MOUNTAIN BUILDING

EDITED BY: György Hetényi, Mark R. Handy and A. Alexander G. Webb
PUBLISHED IN: Frontiers in Earth Science

frontiers Research Topics

ISSN 1664-8714
ISBN 978-2-88971-850-4
DOI 10.3389/978-2-88971-850-4

About Frontiers

Frontiers is more than just an open-access publisher of scholarly articles: it is a pioneering approach to the world of academia, radically improving the way scholarly research is managed. The grand vision of Frontiers is a world where all people have an equal opportunity to seek, share and generate knowledge. Frontiers provides immediate and permanent online open access to all its publications, but this alone is not enough to realize our grand goals.

Frontiers Journal Series

The Frontiers Journal Series is a multi-tier and interdisciplinary set of open-access, online journals, promising a paradigm shift from the current review, selection and dissemination processes in academic publishing. All Frontiers journals are driven by researchers for researchers; therefore, they constitute a service to the scholarly community. At the same time, the Frontiers Journal Series operates on a revolutionary invention, the tiered publishing system, initially addressing specific communities of scholars, and gradually climbing up to broader public understanding, thus serving the interests of the lay society, too.

Dedication to Quality

Each Frontiers article is a landmark of the highest quality, thanks to genuinely collaborative interactions between authors and review editors, who include some of the world's best academicians. Research must be certified by peers before entering a stream of knowledge that may eventually reach the public - and shape society; therefore, Frontiers only applies the most rigorous and unbiased reviews.
Frontiers revolutionizes research publishing by freely delivering the most outstanding research, evaluated with no bias from both the academic and social point of view. By applying the most advanced information technologies, Frontiers is catapulting scholarly publishing into a new generation.

What are Frontiers Research Topics?

Frontiers Research Topics are very popular trademarks of the Frontiers Journals Series: they are collections of at least ten articles, all centered on a particular subject. With their unique mix of varied contributions from Original Research to Review Articles, Frontiers Research Topics unify the most influential researchers, the latest key findings and historical advances in a hot research area! Find out more on how to host your own Frontiers Research Topic or contribute to one as an author by contacting the Frontiers Editorial Office: frontiersin.org/about/contact

MOUNTAIN BUILDING

Topic Editors:
György Hetényi, University of Lausanne, Switzerland
Mark R. Handy, Freie Universität Berlin, Germany
A. Alexander G. Webb, The University of Hong Kong, SAR China

Citation: Hetényi, G., Handy, M. R., Webb, A. A. G., eds. (2021). Mountain Building. Lausanne: Frontiers Media SA. doi: 10.3389/978-2-88971-850-4

Table of Contents

frontiers in Earth Science

EDITORIAL
published: 21 October 2021
doi: 10.3389/feart.2021.789741

Editorial: Mountain Building

György Hetényi[1]*, *A. Alexander G. Webb*[2] *and Mark R. Handy*[3]

[1]University of Lausanne, Lausanne, Switzerland, [2]The University of Hong Kong, Pokfulam, Hong Kong, SAR China, [3]Freie Universität Berlin, Berlin, Germany

Keywords: orogeny (formation of mountains), scales, geological processes, geophysical imaging, earthquakes, modelling

Editorial on the Research Topic

Mountain Building

Mountain building involves the interaction of numerous geological processes that operate on a broad spectrum of spatial and temporal scales. Mountains themselves are geo-archives that preserve the traces of these processes. They document the history of plate boundaries, from the rifting of continents, the spreading and closure of oceans, to the partial subduction and collision of continental lithosphere. Mountains provide a glimpse of how processes shaping the surface interact with crustal structure, including structures that pre-date orogenesis. Rocks exposed in mountains allow us not only to constrain the rates of subduction, metamorphism and exhumation, but also to estimate rates of erosion and surface uplift. Geophysical images of the depths beneath mountains contribute to our understanding of how lower crust, lithospheric mantle and asthenosphere behave during orogenesis. Together with modelling studies, these observations are changing notions on the formation of natural resources and on assessing natural hazards such as earthquakes.

The papers in this volume represent a step forward in understanding how mountain-building processes at the surface affect deep-seated processes, and vice-versa. The prime challenge of this multidisciplinary endeavour is to fill gaps in our knowledge of Earth's 3-D structure, as well as in the record of motion of rock bodies back in time, the fourth dimension. For young orogens, filling the gaps requires complementary datasets from the surface and subsurface. The former come from field-based studies that quantify source-to-sink paths of eroded rocks and the kinematics of subducted and exhumed basement rocks. The latter derive from geophysical imaging of rock bodies with contrasting physical properties such as density, seismic velocities and their anisotropy, electrical conductivity and fluid content. Deeply eroded orogens are natural laboratories for such studies, because their exposures of all levels of the crust, from unmetamorphosed sediments to the lower crust, provide clues to understanding ongoing processes in active orogens.

The contributions below deal with the structure of the Alpine-Himalayan mountain belt. The Alps in particular are a time-honoured testing ground for ideas on mountain building. Asthenospheric flow beneath the Alps revealed by new seismic anisotropy studies varies with depth and records intricate flow patterns around sinking slabs and through gaps in these slabs formed by tearing (Link and Rümpker 2021). The overlying orogenic crust is equally complex, especially in the arc of the Western Alps where new joint inversion of gravity and seismological data yield a refined 3-D geometric view of the famous Ivrea Geophysical Body. There, the lithospheric mantle rises to within only a few km of mantle rocks exposed at the surface (Scarponi et al., 2021). The Alpine Moho appears to be sensitive to local variations in the composition of the (pre-)orogenic crust, as studied in the eastern Southern Alps at its junction with the Dinarides (Sadeghi-Bagherabadi et al., 2021), a site of slow (1–2 mm/yr) Adria-Europe plate convergence. Fault activity at this complex orogenic knot involves episodic fault-valve

OPEN ACCESS

Edited and reviewed by:
Carolina Lithgow-Bertelloni, UCLA Department of Earth, Planetary, and Space Sciences, United States

***Correspondence:**
György Hetényi
gyorgy.hetenyi@unil.ch

Specialty section:
This article was submitted to Solid Earth Geophysics, a section of the journal Frontiers in Earth Science

Received: *05 October 2021*
Accepted: *11 October 2021*
Published: *21 October 2021*

Citation:
Hetényi G, Webb AAG and Handy MR (2021) Editorial: Mountain Building. Front. Earth Sci. 9:789741. doi: 10.3389/feart.2021.789741

behaviour due to the recurrent release of pore pressure trapped in the vicinity of faults that juxtapose rocks with contrasting permeability (Rossi et al., 2021).

The Himalayas are home to the largest continent-continent collision on Earth, forming an orographic and climatic barrier, as well as structural anomaly of the first order. Like the Alps, they show strong lateral (along-strike) variations in orogenic structure, particularly as expressed by crustal and upper mantle thickness (Kumar et al., 2021). At the surface, this variation may be manifested by a subdivision of the orogen into segments with different thrust geometries and separated by so-called cross faults (Hubbard et al., 2021). These faults delimit areas of distinctive seismicity and themselves coincide with zones of enchanced seismicity. A particularly active, deep-crustal fault zone marking the eastern edge of the underthrusting India plate (the Dhubri-Chungthang Fault zone) is connected to a cluster of intermediate-depth (ca. 70 km) seismicity in Southern Tibet. This cluster had been scrutinized by Michailos et al. (2021) with implications for both tectonic and metamorphic processes. On the northern margin of the Tibetan Plateau, variations in the thickness of salt layers in the orogenic foreland are important determinates of the geometry of nappes, as modelled in the foreland thrust-and-fold belt of the Tarim Basin (Li et al., 2021). Along-strike variation in subsurface structure is also manifested in the physical properties of the Himalayan orogenic wedge, as revealed in western and eastern Bhutan by global phase seismic interferometry (Obermann et al., 2021). Surface ruptures, for example, from the Mw 8.1 1714 Bhutan earthquake, suggest that stress is transferred both to the foreland, favouring in-sequence thrusting (Zhao et al., 2021), as well as upward, possibly triggering normal faulting and extension of the orogenic wedge. Indeed, detailed studies of seismic swarms on a normal fault in the hangingwall of the Main Central Thrust following the 2015 Mw 7.8 Gorkha earthquake, Nepal, may be diagnostic of orogenic collapse and stress change involving the migration of CO_2-rich fluids (Adhikari et al., 2021). This post-rupture swarm seismicity may have been enhanced by seasonal variations in the near-surface hydrological load. Earth's surface, particularly its temperature history, is a sensitive recorder of heat advection and cooling during exhumation and surface uplift. Thermochronometry applied to high-relief ranges along the eastern margin of the Tibetan Plateau shows that exhumation related to India-Asia convergence began in late Paleogene time, then accelerated intermittently throughout Neogene time to rates as high as 2 mm/yr along major reactivated thrusts in the central Longmen Shan (Furlong et al., 2021).

The diversity of contributions in this volume serve to emphasize Alfred Wegener's (*1880–1930*) prescient words on Earth Science (paraphrased in translation by M.H.): "Only by integrating all Earth Sciences can we hope to approach truth, i.e., to arrive at a picture that arranges known facts in a way that can be said to have the greatest probability of explaining our observations". These words hold as much today as when they were first written and ushered in a new way of looking at mountains and how they form.

AUTHOR CONTRIBUTIONS

All authors listed have made a substantial, direct and intellectual contribution to the work, and approved it for publication.

ACKNOWLEDGMENTS

We are grateful to all reviewers for their time, care and contributions to the manuscripts published in this special volume. We also thank the editorial team as well as the Frontiers team for their support throughout the process of assembling and publication.

REFERENCES

Adhikari, L. B., Bollinger, L., Vergne, J., Lambotte, S., Chanard, K., Laporte, M., et al. (2021). Orogenic Collapse and Stress Adjustments Revealed by an Intense Seismic Swarm Following the 2015 Gorkha Earthquake in Nepal. *Front. Earth Sci.* 9, 659937. doi:10.3389/feart.2021.659937

Furlong, K. P., Kirby, E., Creason, C. G., Kamp, P. J. J., Xu, G., Danišík, M., et al. (2021). Exploiting Thermochronology to Quantify Exhumation Histories and Patterns of Uplift along the Margins of Tibet. *Front. Earth Sci.* 9, 688374. doi:10.3389/feart.2021.688374

Hubbard, M., Mukul, M., Gajurel, A. P., Ghosh, A., Srivastava, V., Giri, B., et al. (2021). Orogenic Segmentation and its Role in Himalayan Mountain Building. *Front. Earth Sci.* 9, 641666. doi:10.3389/feart.2021.641666

Kumar, A., Kumar, N., Mukhopadhyay, S., and Klemperer, S. L. (2021). Tomographic Image of Shear Wave Structure of NE India Based on Analysis of Rayleigh Wave Data. *Front. Earth Sci.* 9, 680361. doi:10.3389/feart.2021.680361

Li, C., Yin, H., Wu, Z., Zhou, P., Wang, W., Ren, R., et al. (2021). Effects of Salt Thickness on the Structural Deformation of Foreland Fold-And-Thrust Belt in the Kuqa Depression, Tarim Basin: Insights from Discrete Element Models. *Front. Earth Sci.* 9, 655173. doi:10.3389/feart.2021.655173

Link, F., and Rümpker, G. (2021). Resolving Seismic Anisotropy of the Lithosphere-Asthenosphere in the Central/Eastern Alps beneath the SWATH-D Network. *Front. Earth Sci.* 9, 679887. doi:10.3389/feart.2021.679887

Michailos, K., Carpenter, N. S., and Hetényi, G. (2021). Spatio-Temporal Evolution of Intermediate-Depth Seismicity beneath the Himalayas: Implications for Metamorphism and Tectonics. *Front. Earth Sci.* 9, 742700. doi:10.3389/feart.2021.742700

Obermann, A., Ruigrok, E., Bianchi, I., and Hetényi, G. (2021). Constraining the Moho Depth below Bhutan with Global-phase Seismic Interferometry. *Front. Earth Sci.* 9, 658146. doi:10.3389/feart.2021.658146

Rossi, G., Pastorutti, A., Nagy, I., Braitenberg, C., and Parolai, S. (2021). Recurrence of Fault Valve Behavior in a Continental Collision Area: Evidence from Tilt/Strain Measurements in Northern Adria. *Front. Earth Sci.* 9, 641416. doi:10.3389/feart.2021.641416

Sadeghi-Bagherabadi, A., Vuan, A., Aoudia, A., and Parolai, S.AlpArray-Swath-D Working Group (2021). High-Resolution Crustal S-Wave Velocity Model and Moho Geometry beneath the Southeastern Alps: New Insights from the SWATH-D Experiment. *feart* 9, 641113. doi:10.3389/feart.2021.641113

Scarponi, M., Hetényi, G., Plomerová, J., Solarino, S., Baron, L., and Petri, B. (2021). Joint Seismic and Gravity Data Inversion to Image Intra-crustal Structures: The Ivrea Geophysical Body along the Val Sesia Profile (Piedmont, Italy). *Front. Earth Sci.* 9, 671412. doi:10.3389/feart.2021.671412

Zhao, Y., Grujic, D., Baruah, S., Drukpa, D., Elkadi, J., Hetényi, G., et al. (2021). Paleoseismological Findings at a New Trench Indicate the 1714 M8.1 Earthquake Ruptured the Main Frontal Thrust over All the Bhutan Himalaya. *Front. Earth Sci.* 9, 689457. doi:10.3389/feart.2021.689457

Conflict of Interest: The authors declare that the research was conducted in the absence of any commercial or financial relationships that could be construed as a potential conflict of interest.

Publisher's Note: All claims expressed in this article are solely those of the authors and do not necessarily represent those of their affiliated organizations, or those of the publisher, the editors and the reviewers. Any product that may be evaluated in this article, or claim that may be made by its manufacturer, is not guaranteed or endorsed by the publisher.

frontiers in Earth Science

ORIGINAL RESEARCH
published: 31 March 2021
doi: 10.3389/feart.2021.641113

High-Resolution Crustal S-wave Velocity Model and Moho Geometry Beneath the Southeastern Alps: New Insights From the SWATH-D Experiment

Amir Sadeghi-Bagherabadi[1,2], Alessandro Vuan[1], Abdelkrim Aoudia[2], Stefano Parolai[1] and The AlpArray and AlpArray-Swath-D Working Group*

[1] National Institute of Oceanography and Applied Geophysics–OGS, Trieste, Italy, [2] Earth System Physics Section, Abdus Salam International Centre for Theoretical Physics–ICTP, Trieste, Italy

OPEN ACCESS

Edited by:
György Hetényi,
University of Lausanne, Switzerland

Reviewed by:
Irene Molinari,
Istituto Nazionale di Geofisica e Vulcanologia (INGV), Italy
Irene Bianchi,
FWF Austrian Science Fund, Austria

***Correspondence:**
Amir Sadeghi-Bagherabadi
asadeghi@ictp.it

Specialty section:
This article was submitted to Solid Earth Geophysics, a section of the journal Frontiers in Earth Science

Received: *13 December 2020*
Accepted: *02 March 2021*
Published: *31 March 2021*

Citation:
Sadeghi-Bagherabadi A, Vuan A, Aoudia A, Parolai S and The AlpArray and AlpArray-Swath-D Working Group (2021) High-Resolution Crustal S-wave Velocity Model and Moho Geometry Beneath the Southeastern Alps: New Insights From the SWATH-D Experiment. Front. Earth Sci. 9:641113. doi: 10.3389/feart.2021.641113

We compiled a dataset of continuous recordings from the temporary and permanent seismic networks to compute the high-resolution 3D S-wave velocity model of the Southeastern Alps, the western part of the external Dinarides, and the Friuli and Venetian plains through ambient noise tomography. Part of the dataset is recorded by the SWATH-D temporary network and permanent networks in Italy, Austria, Slovenia and Croatia between October 2017 and July 2018. We computed 4050 vertical component cross-correlations to obtain the empirical Rayleigh wave Green's functions. The dataset is complemented by adopting 1804 high-quality correlograms from other studies. The fast-marching method for 2D surface wave tomography is applied to the phase velocity dispersion curves in the 2–30 s period band. The resulting local dispersion curves are inverted for 1D S-wave velocity profiles using the non-perturbational and perturbational inversion methods. We assembled the 1D S-wave velocity profiles into a pseudo-3D S-wave velocity model from the surface down to 60 km depth. A range of iso-velocities, representing the crystalline basement depth and the crustal thickness, are determined. We found the average depth over the 2.8–3.0 and 4.1–4.3 km/s iso-velocity ranges to be reasonable representations of the crystalline basement and Moho depths, respectively. The basement depth map shows that the shallower crystalline basement beneath the Schio-Vicenza fault highlights the boundary between the deeper Venetian and Friuli plains to the east and the Po-plain to the west. The estimated Moho depth map displays a thickened crust along the boundary between the Friuli plain and the external Dinarides. It also reveals a N-S narrow corridor of crustal thinning to the east of the junction of Giudicarie and Periadriatic lines, which was not reported by other seismic imaging studies. This corridor of shallower Moho is located beneath the surface outcrop of the Permian magmatic rocks and seems to be connected to the continuation of the Permian

magmatism to the deep-seated crust. We compared the shallow crustal velocities and the hypocentral location of the earthquakes in the Southern foothills of the Alps. It revealed that the seismicity mainly occurs in the S-wave velocity range between ∼3.1 and ∼3.6 km/s.

Keywords: ambient noise tomography, Eastern Alps, external Dinarides, Friuli plain, Po plain, Moho, basement, phase velocity

INTRODUCTION

The Eastern Alps and external Dinarides across North-Eastern Italy, Austria and Western Slovenia are the result of the collision between the European plate with the Adriatic microplate (e.g., Dewey et al., 1989). Their evolution since Late Cretaceous is mainly controlled by the protrusion of the Adriatic lower crust (e.g., Handy et al., 2010), a relatively rigid and less deformed continental crustal block pushed into weaker parts of the orogen. The Adria microplate, squeezed between the African and European plates, is rotating counterclockwise relatively to Eurasia (e.g., Serpelloni et al., 2005; Le Breton et al., 2017) and its indentation is accommodated by NNW-SSE shortening in the Eastern and Southern Alps. The Eastern Alps and the Southeastern Alps show a complex structure reflecting the interplay between orogen-normal shortening and orogen-parallel motion (e.g., Handy et al., 2015).

The seismicity is mainly located in the upper-middle crust and along the Southeastern Alps foothills (Viganò et al., 2015; Bressan et al., 2016). Fault mechanisms show a compression from NW-SE to N-S, and NNE-SSW, consistent with the geodynamic setting, and seismicity patterns seem to be controlled by the crustal heterogeneities and the different degree of interseismic coupling along the main thrust front.

Seismic experiments carried out during the last two decades, TRANSALP (TRANSALP Working Group, 2002), ALP 2002 (Brückl et al., 2007; Grad et al., 2009; Šumanovac et al., 2009), and CROP (Finetti, 2005) suggested the subduction of Eurasia below the Adria microplate to the west of the Southeastern Alps below the Tauern Window. From the Tauern window to the east, a sudden change in the subduction direction is inferred from teleseismic tomography studies (e.g., Kissling et al., 2006; Handy et al., 2015), and the interaction of the Adriatic microplate and Eurasia is made more complex by its underthrusting below the Dinarides and the Pannonian fragment (Brückl et al., 2010; Šumanovac et al., 2016). The Eastern Alps structural complexity and the existing different tectonic models triggered in the last decade a number of studies on crustal and upper mantle structure, also made possible by the development of more dense seismological networks in the area (AlpArray Seismic Network, 2015; Istituto Nazionale Di Oceanografia E Di Geofisica Sperimentale, 2016; Hetényi et al., 2018a).

By using permanent and temporary stations, seismic tomography studies were carried out at continental and regional scales (e.g., Molinari et al., 2015; Behm et al., 2016; Guidarelli et al., 2017; Tondi et al., 2019). A recent joint inversion of surface wave phase velocities from ambient noise and earthquakes confirmed the heterogeneity of the crustal structure between the Central and Eastern Alps (Kästle et al., 2018). New crustal models from ambient noise tomography have also been recently proposed by Lu et al. (2020), Molinari et al. (2020), Qorbani et al. (2020) improving the resolution of the existing reference models like EPcrust (Molinari and Morelli, 2011).

Receiver function data and the global-phase seismic interferometry, provided by the AlpArray complementary experiment EASI (Hetényi et al., 2018b; Kvapil et al., 2020), with focus on the Eastern Alps, highlighted a complex crustal structure and suggested a possible Adria subduction below Eurasia (Hetényi et al., 2018b; Bianchi et al., 2020). However, the interpretation of the receiver function data is still ambiguous due to the possible presence of slices of lower crust imbricated at the contact between Eurasia and Adria, and therefore not a single interface at depth with an overall acoustic impedance (Bianchi and Bokelmann, 2014; Bianchi et al., 2015).

For mapping in greater detail the Moho discontinuity, investigating its possible fragmentation, and improving the knowledge about the dynamic processes that originated crustal growth, accretion, delamination, and underplating, an array of 154 broadband seismic stations (**Figure 1**, AlpArray-SWATH-D project) in the Eastern Alpine region was completed at the end of 2017 and operated for 2 years (Heit et al., 2017). SWATH-D focuses on a key area of the Alps where the hypothesized flip in the subduction polarity is suggested to occur and where the TRANSALP experiment has imaged a jump in the Moho geometry (TRANSALP Working Group, 2002). The temporary network complemented the larger-scale AlpArray network and existing permanent stations of the Alps-Adria region (Heit et al., 2017). The spatial density of the integrated seismic networks provides the opportunity to improve the lateral resolution for ambient noise and receiver function studies, including greater detail in the crustal and uppermost mantle models.

We apply an ambient noise tomography to a new dataset exploiting the SWATH-D temporary experiment. Rayleigh wave phase velocity measurements obtained for pairs of stations are integrated with the measurements adopted from Nouibat et al. (2021). S-wave velocities are obtained by using non-perturbational and perturbational inversion in an area including the Friuli and Venetian plains, the Alps foothills, the Alpine chain and external Dinarides. A new high-resolution crustal model is computed down to a depth of 60 km and its relation with the main geologic and tectonic features are discussed. The estimated crustal thickness in the Southeastern Alps and external Dinarides is compared with those included in the Northern Adria crust (NAC) model (Magrin and Rossi, 2020) and the Moho map of Spada et al. (2013).

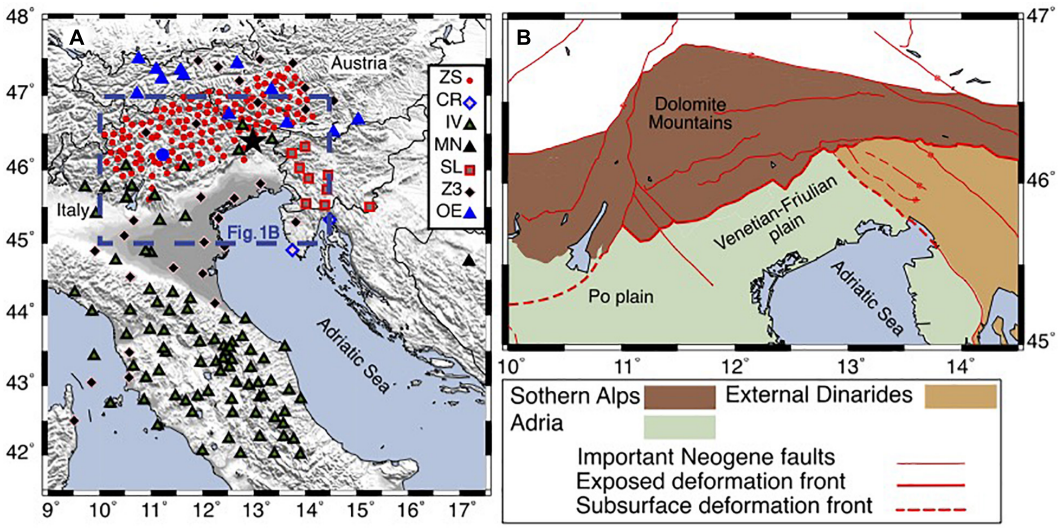

FIGURE 1 | (A) Map showing the seismic stations used in this study. The ZS, CR, SL, and MN stations are used for computation of correlograms in this study. The correlograms computed using up to 4 years of the recordings from the IV, OE, and Z3 stations are adopted from Nouibat et al. (2021). The blue circle shows the location of D024 station of the ZS network and location of the June 14, 2019, Mw 3.7 earthquake is shown by black star. **(B)** Map showing the major tectonic features in the study region modified from Schmid et al. (2004, 2008) and Handy et al. (2010). ZS–SWATH-D temporary network; CR–Croatian seismograph network; IV–Italian national seismic network; MN–Mediterranean very broadband seismographic network; SL–Seismic network of the republic of Slovenia; Z3–AlpArray Z3 network; OE–Austrian seismic network.

DATA AND METHODS

Seismic Data and Cross Correlation

The dataset used in this study is composed of two subsets. The larger subset exploited 10 months of continuous recordings for computation of correlograms. The other smaller complementary subset of correlograms was adopted from Nouibat et al. (2021) (hereafter NBT21), which were calculated using up to 4 years of continuous recordings. Location of the seismic stations used in the two datasets is shown in **Figure 1**. In the following, we will present the description of these datasets.

The SWATH-D temporary experiment deployed 154 broadband seismic stations during 2017–2020. Taking the recording duration and quality of the stations into consideration, we processed 10 months of continuous seismic data recorded between October 2017 and July 2018 from 133 stations of the SWATH-D temporary network (ZS) (Heit et al., 2017). Continuous recordings of 13 permanent stations of the Slovenian (SL) (Slovenian Environment Agency, 2001), Croatian (CR) (University of Zagreb, 2001), and the Mediterranean very broadband (MN) (MedNet Project Partner Institutions, 1990) networks between October 2017 and July 2018 were also used (**Figure 1**).

The continuous data were baseline-corrected and downsampled to 5 Hz, and the instrumental response was removed. We followed the workflow proposed by Bensen et al. (2007) with slight modifications for the computation of cross-correlation of the vertical components. The waveforms were filtered between 0.5 and 100 s and cut to 1 h segments. We applied the time domain normalization and spectral whitening. We then cross-correlated the 1 h-long segments of all the ZS station pairs. We also performed the cross-correlation between the 1 h segments of the permanent stations (i.e., SL, CR, and MN networks) and all the ZS stations. Since the number of permanent station pairs is much smaller than the ZS-permanent station pairs and their ray crossings mainly coincide with those of the ZS-permanent and ZS-ZS station pairs, the cross-correlations between the permanent stations were not included. Subsequently, we stacked up to 24 available correlograms of each day. The resulting daily correlograms were stacked again over 3 months. We checked the quality of the correlograms by means of estimating the signal-to-noise-ratio (SNR). Then the SNR of the 3 month stacked correlograms were compared to investigate the seasonal variation in the quality of the correlograms. Comparison of the 3 month correlograms revealed that the correlograms were temporarily stable during the 10 month period of recording, and their SNR values did not exhibit substantial variations. **Supplementary Figure S1** shows the 3 month correlograms with the SNR value of higher than 5 between station D024 (the blue circle in **Figure 1**) and other contemporaneously operating stations. We also stacked the daily correlograms for the 3–10 month periods to examine the effect of stacking duration on the quality of the correlograms. We fixed the value for the SNR threshold at 10. The results revealed that the SNR values of the majority of the station pairs were higher than the threshold after 7 months of stacking. Therefore, 10 months of stacking was sufficient to obtain stable correlograms (i.e., ZS, SL, MN, and CR station pairs).

At the end of this procedure, we selected 4050 high-quality empirical green functions (EGFs) showing clear and symmetrical signals on both the causal and acausal parts. **Figure 2** shows the cross-correlations computed between station D024 (the blue

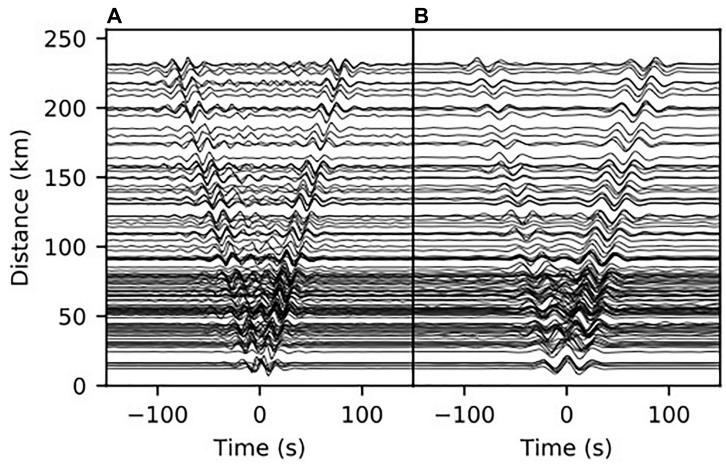

FIGURE 2 | Examples of the stacked correlograms between station D024 (the blue circle in **Figure 1**) and other contemporaneously operating stations. Correlograms filtered in the period range of 10–20 s **(A)** and 20–40 s **(B)**.

circle in **Figure 1**) and other contemporaneously operating stations. Dispersive Rayleigh wave packets are evident on both the causal and acausal parts of the correlograms.

We followed the same procedure to compute the correlograms between some stations of the Italian national seismic network (IV) (INGV Seismological Data Centre, 1997) and the AlpArray Z3 network (Z3) (AlpArray Seismic Network, 2015) and the ZS stations to improve our ray coverage. However, unlike the ZS, SL, MN, and CR station pairs, the 10 month period of recording was not sufficient to satisfy our quality control criteria for the IV-Z3, IV-ZS, Z3-ZS station pairs. Therefore, we adopted 3036 correlograms from NBT21 as a complement to the dataset computed in this work. The correlograms were computed following the procedure explained in Soergel et al. (2020) and using up to 4 years of the continuous recordings of 148 stations of the IV, Austrian (OE) (Zentralanstalt Für Meterologie Und Geodynamik [ZAMG], 1987) and Z3 networks (**Figure 1**). Regardless of the time domain normalization, the preprocessing steps in the Soergel et al. (2020) procedure are mainly similar to the method we applied (i.e., detrending, low-pass filtering, and instrument response correction). This allows for the seamless integration of the correlograms computed in this study and those of NBT21. NBT21 followed the comb filter preprocessing routine for handling of transient high amplitude earthquake signals. They calculated the cross-correlations between each station pair using 4 h windows and stacked them to obtain the final correlogram for each station pair. We controlled the quality of the correlograms and kept 1804 EGFs with SNR values greater than 10 on both the causal and acausal parts to supplement our initial dataset. **Figure 3** shows the variation in the number of EGFs with interstation distances and azimuths before and after inclusion of the high-quality correlograms of NBT21.

Rayleigh Wave Phase Velocity Measurements

The calculated EGFs have been then used to estimate the phase velocity of Rayleigh waves for each couple of stations. It is worth remembering that the largest period for which the phase velocity can be measured is proportional to the interstation distance. In the traditional frequency-time analysis (e.g., Levshin et al., 1992) the wavelength should be smaller than or equal to one-third of the interstation distance (Yao et al., 2006; Lin et al., 2008). However, the method of Ekström et al. (2009) allows for measuring reliable phase velocities up to periods with wavelength comparable to the interstation distance. The technique proposed by Ekström et al. (2009) uses the Aki's spectral formulation to measure the phase velocity directly from the zero crossings of the real part of the correlation spectrum. We used the methodology of Ekström et al. (2009) incorporated into the GSpecDisp package (Sadeghisorkhani et al., 2017) for measuring the phase velocity dispersion curves of the Rayleigh waves. The reliable period range for each couple of stations was conservatively selected so that the interstation distance was 1.5–50 times larger than the considered wavelengths. We visually evaluated the causal and acausal parts of the EGFs and manually picked the dispersion curves exhibiting a clear, smooth and continuous trend of period dependence. The phase velocities were picked at periods where energy level on the real part of the correlogram spectrum is significant.

We also used the multiple-filter approach (Herrmann, 1973, 2013) to measure the phase velocities of some random correlograms and compared them with those obtained from GSpecDisp package. The comparison revealed no substantial difference between the dispersion curves in the period range where 3–50 wavelengths can propagate within the interstation distance. Furthermore, we measured the phase velocities from 44 records of June 14, 2019, Mw 3.7 earthquake (the black star in **Figure 1**) using the multiple-filter approach (Herrmann, 1973, 2013) to further validate the dispersion curves obtained from correlograms. The earthquake epicenter is located close to station D013 of the ZS network. The dispersion curves from June 14, 2019, Mw 3.7 earthquake were in agreement with those from correlograms between D013 and other ZS stations (**Figure 3**). **Figure 3D** shows the dispersion curves picked from the D013-D024 and D013-D086 correlograms as well as the

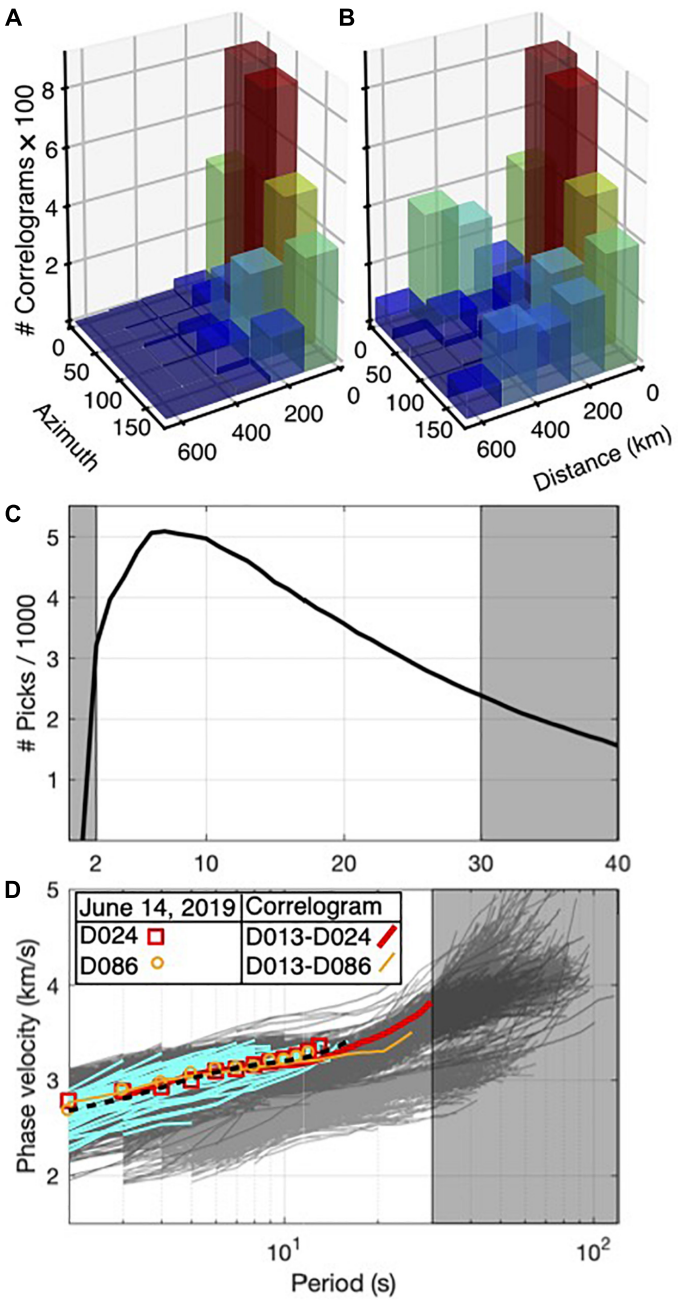

FIGURE 3 | (A) Number of correlograms calculated in this study vs. interstation distance and azimuth. **(B)** Number of correlograms used in this study, including the high quality correlograms of Nouibat et al. (2021), vs. interstation distance and azimuth. **(C)** Number of Rayleigh phase velocity picks at different periods. **(D)** Phase velocity dispersion curves measured from correlograms calculated in this study (dark gray) superimposed on the dispersion curves measured from correlograms adopted from Nouibat et al. (2021) (lighter gray). The phase velocity dispersion curves from 44 records of the June 14, 2019, Mw 3.7 earthquake and the average curve are shown by cyan and black lines, respectively. The dispersion curves from D013-D024 and D013-D086 correlograms and those of the earthquake waveforms recorded by D024 and D086 stations are also shown. The horizontal axis label is shared in **(C,D)**. Gray boxes in **(C,D)** show the periods excluded from tomography.

dispersion curves from the waveforms of June 14, 2019, Mw 3.7 earthquake recorded by D024 (46.21°N, 11.23°E) and D086 (46.64°N, 11.35°E) stations. At periods longer than 30 s, the dispersion curves obtained from the correlogram dataset of NBT21 exhibit two diverging trends. The set of dispersion curves with lower velocities at longer periods are related to the rays crossing the Po and Venetian-Friuli plains, while the dispersion curves of the rays crossing the Alps have higher velocities at periods longer than 30 s.

Figure 3C shows the number of phase velocities obtained from correlograms in the period range of 2–30 s. The number of measurements varies between 2,390 in 30 s and 5,094 in 7 s.

Since the SNR of most of the 3 month stacked correlograms were smaller than the threshold of 10 we were not able to estimate the uncertainty of the phase velocity measurements from seasonal variability as it is proposed by Bensen et al. (2007).

2D Phase Velocity Tomography

The fast-marching surface wave tomography package (FMST) (Rawlinson, 2005) is used for inversion of the reliable Rayleigh wave phase velocity measurements. FMST uses the fast-marching method (Sethian and Popovici, 1999) for the forward prediction of the traveltimes. It applies an iterative subspace inversion to map lateral variations in phase velocity accounting for the non-linear relationship between velocity and traveltime. The study area was parameterized with 0.1° × 0.1°cell grids. The cell grid size is selected so that each cell in the target region contains a minimum of 20 ray crossings. The average of the measured phase velocities at each period was considered as the homogeneous starting model of the inversion. FMST allows the damping and smoothing regularization parameters to be adjusted in order to cope with the problem of non-uniqueness. The damping factor prevents the solution model from departing too much from the starting model, while the smoothing factor avoids unrealistic sudden changes and constrains the smoothness of the solution model. Although the dispersion curves were picked carefully, we first ran the inversions with a high value of damping factor to detect and discard the highly incoherent paths with the traveltime residual greater than three times the average of all the traveltime residuals (Kaviani et al., 2020). We performed the tomographic inversion again with a set of regularization parameter pairs in the range between 0 and 5 to select the optimal damping and smoothing parameters at each period. The optimal damping and smoothing parameters were selected by the construction of the trade-off curves. After careful inspection of the trade-off between data misfit and model variance at each period, the damping factor was chosen. The trade-off curves between misfit and model roughness were used to estimate the optimal smoothing parameters at each period. **Figure 4** shows the smoothing and damping trade-off curves and the selected optimal parameters for periods of 5 and 20 s.

We performed checkerboard tests to elucidate the dimensions of the features that can be resolved through the inversion process. The actual ray coverage and the selected optimal regularization parameters were used in the checkerboard tests. Thanks to the dense ray coverage, the 0.3° × 0.3° blocks at periods shorter than 5 s were recovered in the Southeastern Alps region covered by the ZS network. However, smearing effects are obvious at periods longer than 4 s. Performing the checkerboard tests with anomaly sizes of 0.5° × 0.5° revealed that the anomalies are well recovered in most of the target region (**Figure 5**).

Following Zelt (1998), we quantitatively assessed the semblance between the true and recovered checkerboard anomalies through the calculation of the resolvability factor. The areas in tomographic results with resolvability factor of higher than 0.7, and the tomographic grids with a minimum of 20 ray crossings are shown in **Figure 5**. The final tomographic results are confined within the overlapped area between the resolvability factor of higher than 0.7 and a minimum of 20 ray crossings (**Figure 5**). We initially performed the tomography for the period range between 2 and 40 s. However, considering the checkerboard test results, we decided to confine the final tomographic inversions to the 2–30 s period band in the region covered by ZS network and to the 5–30 s period range in the remaining parts.

1D S-wave Velocity Inversion

We extracted local dispersion curves for each 0.1° × 0.1° grid node of the tomographic model and inverted them for 1D depth-dependent S-wave velocity profiles. We performed the two-step procedure of Haney and Tsai (2017) for non-perturbational and perturbational inversion of Rayleigh-wave velocities. First, we applied the non-perturbational inversion, based on the Dix-type relation for surface waves, and an optimal non-uniform finite-element grid of layers generated based on depth sensitivity of the Rayleigh waves (Haney and Tsai, 2015; **Figure 6**). The 1D velocity profiles obtained were then used as starting models for the subsequent perturbational inversion that relies on the finite-element method resulting in a matrix formulation of the forward problem. It allows for linking the forward and inverse problems using matrix perturbation theory. The perturbational inversion iteratively refines the starting model provided by the non-perturbational Dix-type inversion to find the final model that fits the data. We generated a set of synthetic phase velocity dispersion curves with 2.5% noise from arbitrary velocity models. A comparison of the inverted and true models revealed that the inversion process is capable of producing a smoothed version of the true model (**Supplementary Figure S2**).

Figure 6 shows an example of the measured and predicted dispersion curves as well as the starting and final S-wave velocity models at a grid node. Although the perturbational updating of the non-perturbational starting model has not substantially affected the shallower S-wave velocity structures, it leads to significant fitting improvements at longer period dispersions representing the deeper S-wave velocity structures. We inverted the local dispersion curves for the 1D velocity profiles down to a depth of more than 200 km. However, considering the sensitivity kernels calculated using the final S-wave velocity model, we consider as reliable the results obtained down to 60 km (**Figure 6**). Four examples of the inverted 1D S-wave velocity profiles and their sensitivity kernels are shown in **Supplementary Figure S3**.

RESULTS

3D S-wave Velocity Model

After inverting all the local dispersion curves, we assembled the resulting 1D S-wave velocity profiles into a pseudo-3D crustal S-wave velocity model of the Southeastern Alps (hereafter SEA-Crust). **Figure 7A** shows seven depth slices from the surface down to 60 km. The average velocity is increasing from about 2.0 km/s at the surface to about 4.5 km/s at the depth of 60 km. The average 1D S-wave velocity profiles of the Alps and the Friuli and Venetian plains are shown in **Figure 7B**. The P-wave velocities in **Figure 7B** were calculated considering the average

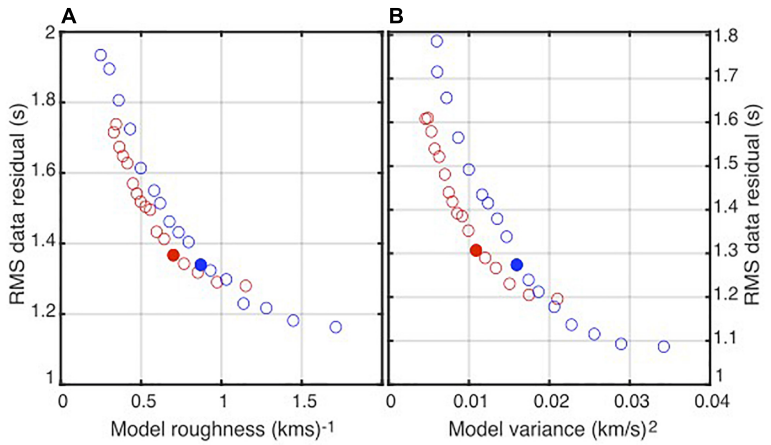

FIGURE 4 | The trade-off curves between misfit and model roughness for different smoothing parameters **(A)** and the trade-off curves between misfit and model variance for different damping parameters **(B)** for periods of 5 s (red) and 20 s (blue). Damping and smoothing parameters change in the range between 0 and 5. The selected optimal smoothing and damping parameters are shown by filled circles.

crustal Poisson ratio of 0.256 (Christensen, 1996). In the depths shallower than about 15 km and to the north of the deformation front, S-wave velocity is higher than the southern parts (i.e., in the Venetian and Friuli plains). In contrast, deeper depth slices reveal higher velocities in the Venetian and Friuli plains compared to the Eastern Alps. Considering both the S-wave velocities of 4.0 and 4.2 km/s as proxies for the Moho depth, the crust in the eastern Alps is, on average, about 15 km thicker than in the Venetian and Friuli plains (**Figure 7**). At 60 km depth, the depth slice is dominated by velocities greater than 4.0 km, implying that the crust in the whole study region should not be thicker than 60 km.

Figures 8A–H shows the variation of S-wave velocity with respect to the average velocity at different depths from 5 to 40 km. **Figure 8I** shows the major faults in the region. The absolute velocities at the same depths are shown in **Supplementary Figure S4**. The Southern prominent low-velocity zone at 5 and 10 km depths is related to the Venetian and Friuli plains. The upper crustal S-wave velocities change considerably from the Friuli and Venetian plains to the Alps foothills. As we expected, in the shallow crust, the S-wave velocities are lower for the Adria plate beneath the Friuli and Venetian plains, where soft sediments and sedimentary rocks are thicker. The S-wave velocity at 10 km depth in the Southeastern Alps reaches the value of about 3.8 km/s that is in agreement with the high P-wave velocity value of 6.8 km/s reported by other works (Behm, 2009; Bressan et al., 2012). Considering the increasing trend of the crustal thickness from the south to the north of the study region, the 15–30 and 20–40 km depth ranges are approximately associated with the middle-lower crust in the Southeastern Alps and Adria, respectively. The maps of absolute velocity in **Supplementary Figure S4** reveal that the middle and lower crust are faster in the southern parts than in the northern parts of the study region. Nonetheless, a more rigid lower and middle crust for the Adria plate is not a new result and is consistent with the efficient wave propagation due to low attenuation of recorded earthquakes and SmS wave propagation (e.g., Bragato et al., 2011; Sugan and Vuan, 2014). The faster middle and lower crust of the Adria compared to the Southeastern Alps is also observed by the other recent tomographies (Kästle et al., 2018; Lu et al., 2018; Qorbani et al., 2020).

The boundary between the higher and lower velocity anomalies to the east of longitude 12°E and in the 15–40 km depth range perfectly mimics the leading edge of the Alpine front responsible for the 1976 Friuli earthquake (Aoudia et al., 2000) to the east and the Bassano-Cansiglio active folding system to the west (**Figure 8**). The presence of a high-velocity body (HV1) deeper than 10 km to the east of the Giudicarie fault is evident. The NNW oriented part of HV1 at 40 km depth is also clearly observed by Molinari et al. (2020) and roughly observed by Kästle et al. (2018) and Lu et al. (2018). On the other hand, such a high-velocity body seems to be absent from both the Love and Rayleigh-wave shear velocity model of Qorbani et al. (2020). The location of the HV1 at 10–20 km depth range coincides with the Permian magmatic rocks at the surface (Schuster and Stüwe, 2008). The eastward extension of HV1 with depth can be considered as the continuation of the Permian magmatic complex within the lower crust. The low-velocity anomaly in the 10–20 km depth range and to the northwest of the study region is also observed by Qorbani et al. (2020).

Crystalline Basement and Moho Depth

Different criteria have been used by receiver function and tomography studies to capture the sedimentary layer-crystalline basement boundary and the Moho discontinuity. Using the iso-velocities at the bottom of the layers is among the most well-established approaches for estimation of the discontinuity depths in seismic imaging studies. However, the S-wave iso-velocities used in the literature range from 1.5 to 3.0 km/s and from 3.9 to 4.3 km/s for depicting the basement and Moho

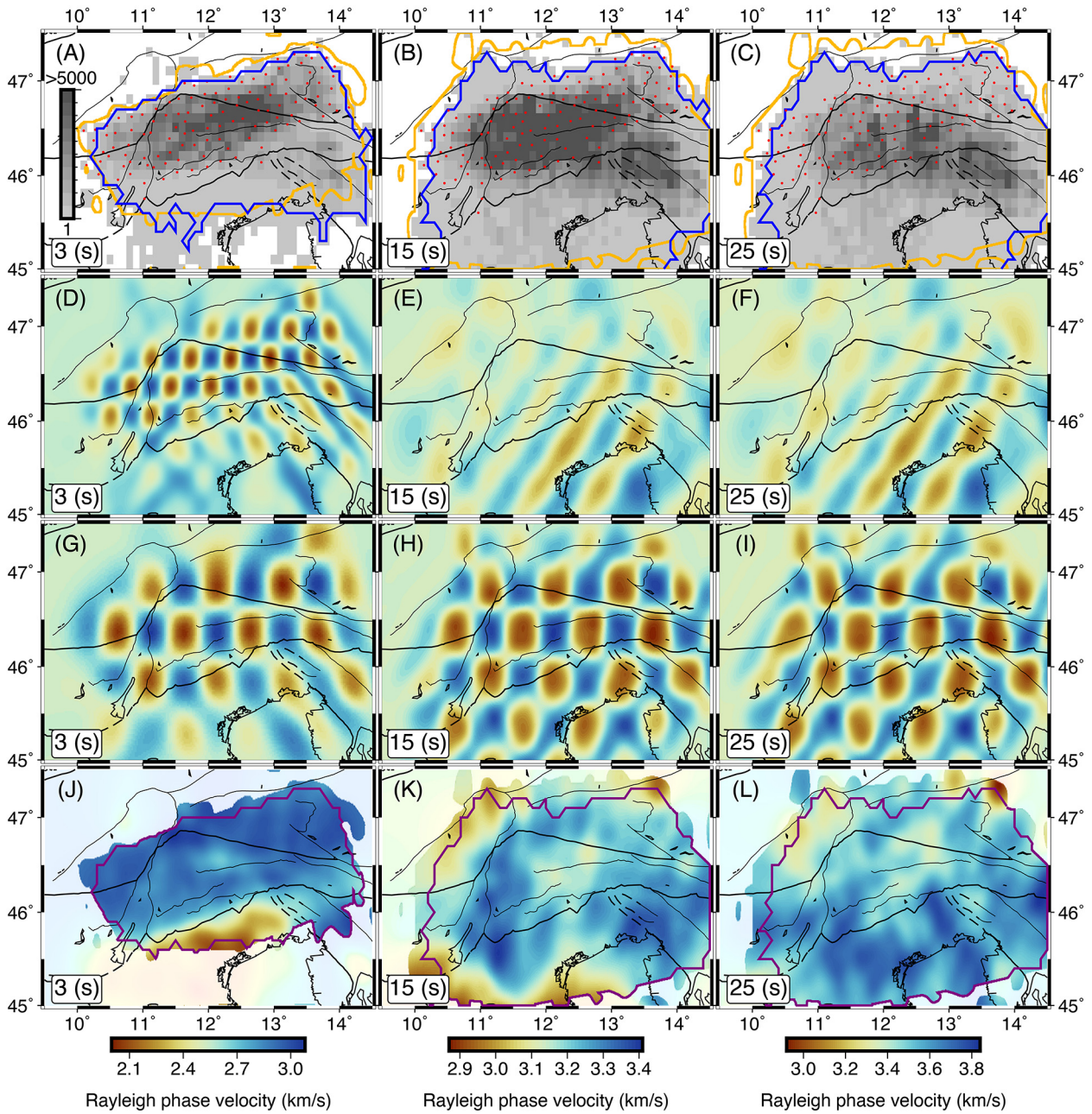

FIGURE 5 | Number of ray crossings in each 0.1° × 0.1° grid cell and stations of the ZS network **(A–C)**. The area with resolvability factor of higher than 0.7 and the tomographic grids with minimum of 20 ray crossings are shown by orange and blue polygons, respectively. Checkerboard reconstruction results with anomaly size of 0.3° × 0.3° **(D–F)** and 0.5° × 0.5° **(G–I)**, and tomographic inversion results at periods of 3, 15, and 25 s **(J–L)**. The purple polygon illustrates the overlapped area between the resolvability factor higher than 0.7 and the minimum of 20 ray crossings.

depths, respectively (Christensen and Mooney, 1995; Brocher, 2005; Moschetti et al., 2010; Molinari and Morelli, 2011; Macquet et al., 2014; An et al., 2015; Guidarelli et al., 2017; Magrin and Rossi, 2020; Planès et al., 2020). Part of this discrepancy originates from the lack of single definitions of the discontinuities and the trade-off between the S-wave velocity and the depth of the discontinuities. If the S-wave velocities of both the top and the bottom layers are estimated, a strong depth gradient of the 1D S-wave velocity profile can be considered as an indicator of the discontinuity.

We used the gradient of the 1D velocity profiles in the top 10 km as a proxy to select the reasonable iso-velocity representing the crystalline basement depth. **Figure 9A** presents the number of maximum depth gradients in various velocities. Considering the histogram, we selected the average depths corresponding to a range of velocities between 2.8 and 3.0 km/s as the indicator

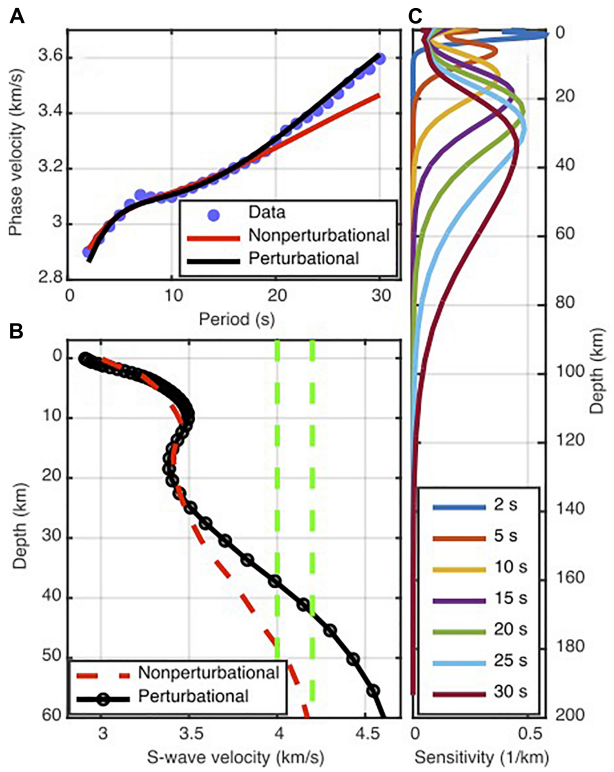

FIGURE 6 | (A) An example local dispersion curve and predicted curves from non-perturbational (initial model) and perturbational (final model) inversions. **(B)** Inverted S-wave velocity depth models using non-perturbational (initial model) and perturbational (final model) inversions. Black circles represent the optimal non-uniform finite-element grid of layers. S-wave velocities of 4.0 and 4.2 km/s as candidate velocities for detecting the Moho at depth are shown by vertical green dashed lines. **(C)** Sensitivity kernel of the final perturbational model.

of the discontinuity. A map illustrating the crystalline basement depth is presented in **Figure 9B**. It shows that the crystalline basement depths in the Po, Venetian and Friuli plains ranges between ∼4 and ∼10 km. In the same region, Qorbani et al. (2020) has also traced a low-velocity anomaly with values of less than 3.0 km/s down the 10 km.

According to Steinhart (1967) and Thybo et al. (2013), the seismic Moho is defined as a rapid increase of the crustal P-wave velocity to a value in the range of 7.6 and 8.6 km/s. In the absence of a sharp increase in velocity, the Moho is the level at which the P-wave velocity exceeds the 7.6 km/s threshold. Taking the average crustal Poisson ratio of 0.256 (Christensen, 1996) into account, the S-wave threshold velocity is 4.3 km (An et al., 2015). In some part of the study region (i.e., beneath the Southeastern Alps) the Moho is deeper than 55 km which is close to the maximum depth of SEA-Crust (Molinari and Morelli, 2011; Spada et al., 2013; Bianchi and Bokelmann, 2014; Bianchi et al., 2015; Hetényi et al., 2018b; Kästle et al., 2018; Lu et al., 2018, 2020; Stipčević et al., 2020). Therefore, in these regions, SEA-Crust is not able to sample the shallow uppermost mantle beneath such a deep Moho and the 1D velocity models vary smoothly with depth, especially toward the deepest parts. Thus, for estimating the crustal thickness we preferred to use the iso-velocity depths rather than depth gradient of the 1D velocity profiles. To this end, we collected a set of available Moho depths from receiver function studies (Bianchi et al., 2014, 2015; Hetényi et al., 2018b; Stipčević et al., 2020) and compared them with different depths of iso-velocities between 3.9 and 4.3 km/s. **Figure 9C** illustrates the receiver function Moho depths vs. iso-velocity depths. The comparison revealed that the 4.2 km/s iso-velocity depths are in a general agreement with the receiver function results. The 4.1 and 4.3 km/s iso-velocities mainly give rise to underestimation and overestimation of the Moho depth, respectively. However, considering the available uncertainty of the receiver function results, some of the 4.1 and 4.3 km/s iso-velocity depths are acceptable. Thus, the average of the iso-velocity depths between 4.1 and 4.3 km/s is taken to be the Moho depth. We calculated the standard deviation of the depths in the same iso-velocity range as a measure of uncertainty of the Moho depth (**Figure 9D**). The general pattern of higher uncertainties for the deeper Moho depth estimates is partly due to the decreasing vertical resolution with depth.

DISCUSSION

Comparison of the Pseudo-3D S-wave Model With Other Studies

We compared SEA-Crust with those of NAC (Magrin and Rossi, 2020) and Kästle et al. (2018) (hereafter KST18) through the calculation of their relative changes (**Supplementary Figures S5–S7**) for fixed-depth slices. Mapping the local differences in the upper crust (5 and 10 km depth, **Supplementary Figure S5**), NAC is faster than SEA-Crust almost everywhere in the Po and Venetian-Friuli plains (more than 20% at 5 km depth). Beneath the southernmost SWATH-D development and at 5 and 10 km depths, the relative change between SEA-Crust and NAC is smaller (∼10%) (**Supplementary Figure S5**). This consistency between SEA-Crust and NAC coincides with the region where NAC is constrained by local earthquake tomographies (Anselmi et al., 2011; Bressan et al., 2012; Viganò et al., 2013). Within the 20–30 km depth range, NAC is, on average, faster (less than 10%) than SEA-Crust beneath the Alps and slower beneath the plains (**Supplementary Figure S5**). NAC also tends to be slower than SEA-Crust (less than 15%) in the lower crust (depth >30 km) and almost everywhere in the study region (**Supplementary Figure S5**).

In the upper crust (depth <10 km), SEA-Crust appears to be on average ∼10% faster and slower than KST18 in the Southeastern Alps and in the plains, respectively (**Supplementary Figure S6**). Within the 20–30 km depth range, KST18 is ∼10% slower than SEA-Crust (**Supplementary Figure S6**). The S-wave velocity differences between KST18 and SEA-Crust increase gradually with depth and reach ∼15% at 35 km. Toward the deeper structures and between 50 and 60 km depths, while the KST18 is slower than SEA-Crust (less than 10%) beneath the plains, it turns out to be faster (less than 10%) beneath the Alps (**Supplementary Figure S6**).

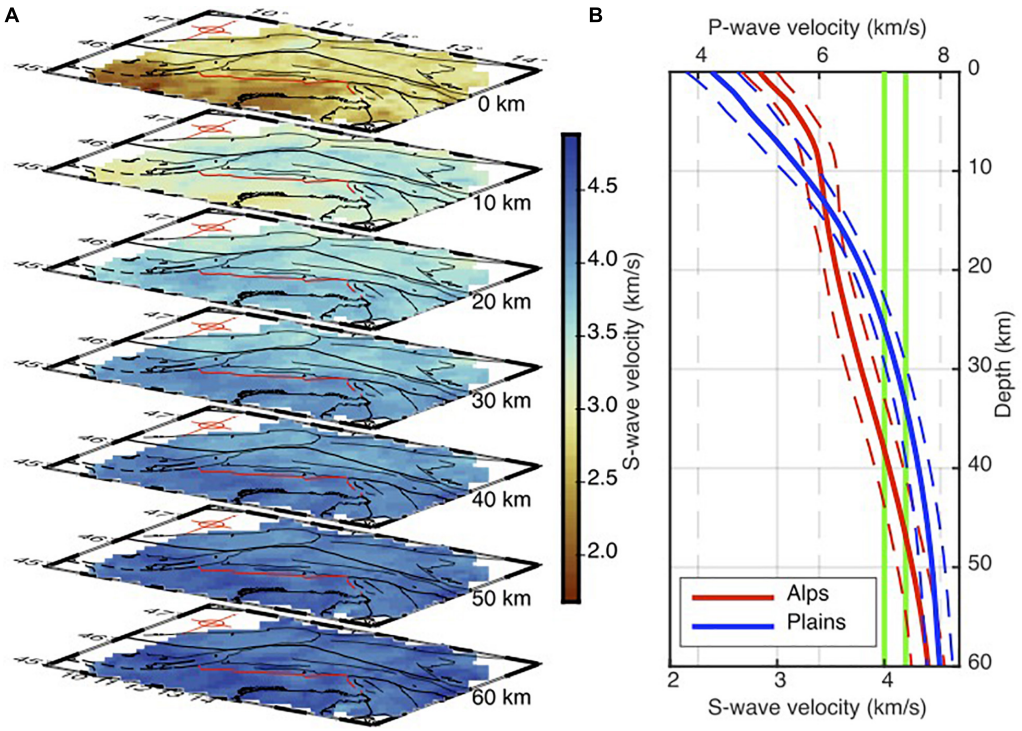

FIGURE 7 | (A) Depth slices showing variation of the S-wave velocity from the surface down to 60 km depth. The border between the Southeastern Alps and the Venetian and Friuli plains is shown by the red line. The thinner black lines depict the Neogene faults (Schmid et al., 2004, 2008; Handy et al., 2010). **(B)** The average 1D S-wave velocity profiles in the Southeastern Alps and the Venetian and Friuli plains. S-wave velocities of 4.0 and 4.2 km/s are shown by vertical green lines. The P-wave velocity profiles are calculated considering the average Poisson ratio of 0.256 for the continental crust (Christensen, 1996).

Extremely variable S-wave velocities characterize the plains, which is also pronounced by differences between NAC and KST18 (**Supplementary Figure S7**). Comparing the three models shows that SEA-Crust in the upper crust is more compatible with KST18 rather than NAC all around the study region. This is probably as a result of the similarities between the approaches used by this study and KST18.

A peculiarity of SEA-Crust is that it exploited the new dataset of phase velocities extracted from the SWATH-D station pairs with short interstation distances. Therefore, we expect SEA-Crust to be more selective and accurate for the paths crossing the plains and the Alpine region at short periods and shallower depths. It can justify the higher relative changes in SEA-Crust with respect to NAC and KST18 in the shallow crust (**Supplementary Figures S5, S6**).

Border of the Po and Venetian-Friuli Plains

The Southern low-velocity anomaly at 5 km in **Figure 8A** coincides with the location of the well-known Po, Venetian and Friuli plains. The S-wave velocity in the region covered by the basins is not homogeneous, and a relatively higher velocity trend beneath the Schio-Vicenza fault divides it into the eastern and western lower velocity parts. The S-wave velocity range between 2.8 and 3.0 km/s used for determination of the basement depth is in the same range as those reported for the Mesozoic carbonates on top of the crystalline basement (Pola et al., 2014; Turrini et al., 2014; Molinari et al., 2020). The estimated basement depth in **Figure 9B** is in turn shallower (∼5 km) beneath the Schio-Vicenza fault compared to its western and eastern deepest parts (∼10 km) to the southwest of the Garda Lake and the northwestern corner of the Adriatic Sea. The topography of the crystalline basement depth correlates well with the depth of the Pliocene base related to the softer sediments (Pola et al., 2014). The N-S cross sections in **Figure 10** also highlight the soft and consolidated sedimentary cover of the Venetian and Friuli plains that is negatively correlated to the topography.

Upper and Middle Crustal Structure vs. Seismicity

The N-S cross sections in **Figure 10** reveal that the middle and lower crust, particularly toward the northern parts is highly heterogeneous. Part of this heterogeneity comes from a vertical sequence of higher and lower velocity layers beneath the Southeastern Alps, which is also detectable in section A. Beneath the Adria plate, there are sharp velocity transitions between the upper, middle and the lower crust; the middle crust seems to be well developed with velocity gradients. However, toward the north, the velocity gradients are laterally distorted by high-velocity bodies in the upper and middle crust starting from the foothills of the Alps. The seismicity we plotted along the cross sections spans from 2008 to 2019 and are extracted from

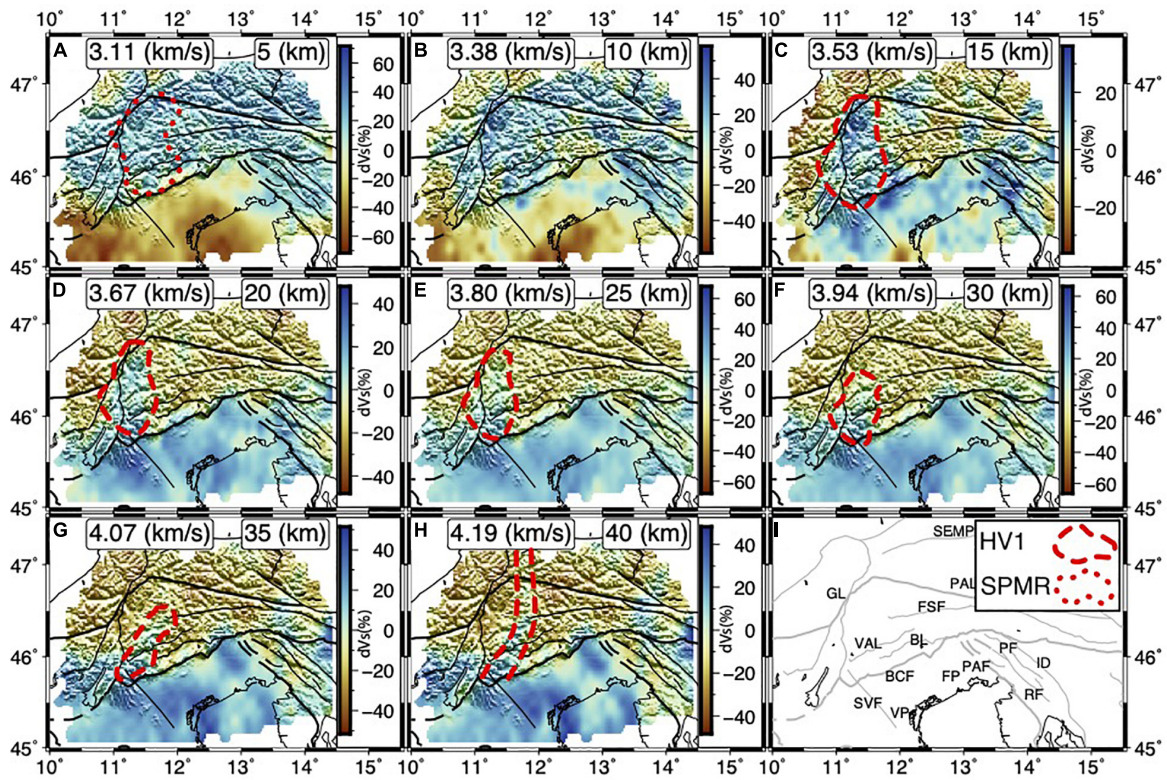

FIGURE 8 | Depth slices showing the S-wave velocity anomalies at 5, 10, 15, 20, 25, 30, 35, and 40 km **(A–H)**. The average S-wave velocity is shown in each panel. Location of the Permian magmatic rocks observed at the surface is shown in **(A)**. **(I)** Map showing the major faults in the region. SPMR, Surface Permian magmatic rocks.

the OGS catalog (Friuli-Venezia Giulia Seismometric Network Bulletin, 2019). The seismicity is mainly located in the southern front of the Alps (i.e., where the elevation increases along the topographic sections) and is confined in a narrow velocity band between ∼3.1 and ∼3.6 km/s (**Figure 10**). The 15 September 1976 (Ms = 6.1) earthquake (Aoudia et al., 2000) is shown in section E, and its adjacent seismicity clearly reveals the concentration of the seismicity on the interface separating the higher velocity from the lower velocity zones. The concentration of the seismic activity in the narrow velocity band is also in agreement with the occurrence of large earthquakes in the upper-crustal density domain boundaries and the regions of the highest geodetic strain rate (Spooner et al., 2019). This supports the hypothesis that the faster middle and lower crust of Adria in this area is more rigid than the Southeastern Alps, while the faster upper crust of southeastern Alps is more rigid than Adria (e.g., Brückl et al., 2007, 2010; Marotta and Splendore, 2014; Magrin and Rossi, 2020).

Moho Topography

During the last two decades, important efforts were made to determine the crustal thickness of the Alps through different approaches (e.g., Kummerow et al., 2004; Spada et al., 2013; Hetényi et al., 2018b; Kästle et al., 2018; Lu et al., 2018, 2020; Spooner et al., 2019; Magrin and Rossi, 2020). The Moho model of Spada et al. (2013) is derived from a combination of receiver function and controlled source seismological studies. The more recently published study of Magrin and Rossi (2020) is focused on the northern tip of the Adria plate (i.e., about the same study area as ours). They integrated the available information about the depth of the main interfaces and the physical properties of the crust to build the NAC model. The continuous Moho map of NAC and the crustal thickness model of Spada et al. (2013) are plotted along all the sections in **Figure 10**.

Figure 9D shows the crustal thickness map from the average depths between 4.1 and 4.3 km/s iso-velocities. The red circles in **Figure 9D** represent the location of the estimation nodes, and their size are inversely proportional to the uncertainty of the estimates. Crustal thickening, as expected, is found in our results from south to north (**Figures 9D**, **10**). Taking the uncertainties into account, while the thinner crust of the Adria plate is shown as gentle undulations that seems to be consistent with NAC, the Moho model of Spada et al. (2013) is about 10 km deeper (see sections B, D, and C in **Figure 10**). Moving toward the north and along the sections B, C, and D, the change in our Moho depth at the Alps foothills is sharper than the other models, and the crustal thickness mirrors the topography, particularly in section D (**Figure 10**). The Moho depth of Kummerow et al. (2004) beneath the TRANSALP profile is depicted in sections B, C, and D.

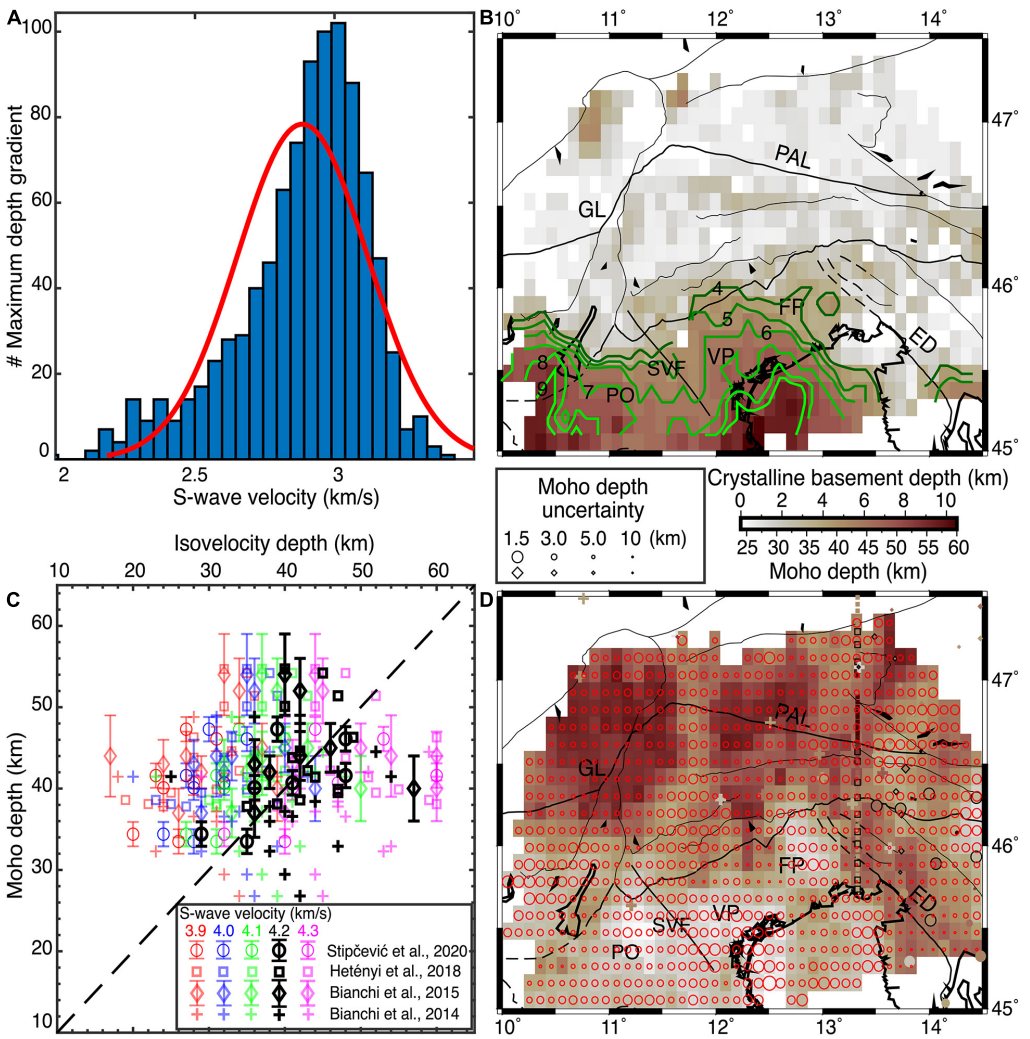

FIGURE 9 | (A) A histogram showing the variation in the number of maximum depth gradients of the 1D S-wave velocity profiles with S-wave velocity. The best fitting normal distribution is shown by red. **(B)** The crystalline basement depth estimated by the average of iso-velocity depths between 2.8 and 3.0 km/s. Green lines portray the basement depth contours from 4 km (darkest green) to 9 km (lightest green). **(C)** Comparison between receiver function Moho depths and the depths obtained from iso-velocities ranging from 3.9 to 4.3 km/s. The horizontal axis label is shown on the top axis. **(D)** Moho depth estimated by the average of iso-velocity depths between 4.1 and 4.3 km/s. The Moho depths adopted from receiver function studies are shown by the same symbols as in **(C)** and their sizes are proportional to their uncertainty (if it was available). The receiver function depths used for the comparison in **(C)** are marked by black outline. The size of the red circles represents the uncertainty of the Moho at each node. PAL, Periadriatic Line; SVF, Schio-Vicenza fault; GL, Giudicarie Line; FP, Friuli Plain; VP, Venetian Plain; PO, Po Plain; ED, External Dinarides.

Surprisingly, considering the three adjacent sections, it appears that the maximum Moho depth beneath the Dolomite Mountains significantly varies from more than 50 km in section B and D to ~40 km in section C which coincides with the location of TRANSALP. In section B, a sharp Moho step with magnitude of more than 15 km is positioned between the Moho gradients in the NAC and Spada et al. (2013) models. In section C, by contrast, the Moho depth remains unchanged at ~40 km toward the north of the Alps foothills. While the magnitude of crustal thickness in section D is similar to section B, the Moho depth increases at a longer wavelength along the profile in section D. Section A, perpendicular to the three adjacent sections, clearly portrays the N-S narrow corridor of crustal thinning. The shallower Moho in section C is located beneath the surface observation of the Permian magmatic rocks and HV1 that can be considered as the continuation of the Permian magmatism to the deep-seated crust. Presence of a much smoother lateral variation in the crustal thickness to the east of the Giudicarie line is reported by Kästle et al. (2018) and Spooner et al. (2019).

Except for the inconsistencies in their middle parts, the Moho depths in sections E, F, and G generally agree with the NAC Moho. The deeper Moho to the north of the Palmanova fault is consistent with the results of the recent receiver function study of Stipčević et al. (2020). The NW-SE thickened crust along the boundary between the Friuli plain and the external Dinarides is mainly formed as a result of the past and ongoing Adria-Europe

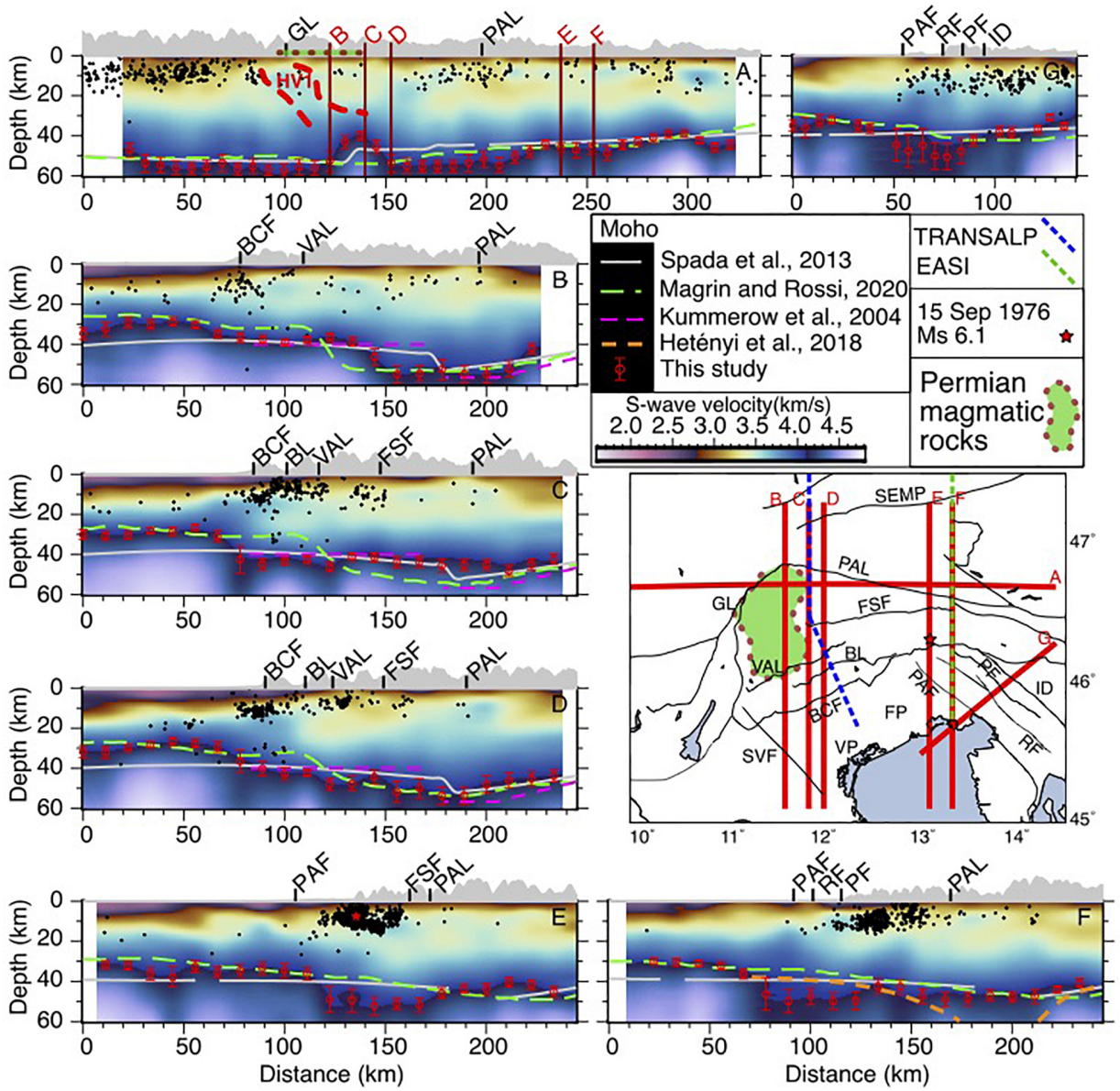

FIGURE 10 | Cross sections of the S-wave velocity model. The seismic events within 0.05° from the profiles are extracted from the OGS catalog (Friuli-Venezia Giulia Seismometric Network Bulletin, 2019) and projected along the sections. PAL, Periadriatic Line; GL, Giudicarie Line; FP, Friuli Plain; VP, Venetian Plain; SEMP, Salzach-Ennstal-Mariazell-Puchberg; VAL, Valsugana thrust; BL, Belluno Line; FSF, Fella-Sava Fault; ID, Idrija Fault; BCF, Bassano-Cansiglio Fault; PAF, Palmanova fault; RA, Rasa fault; PF, Predjama Fault.

convergence, which is accommodated by thrusting and strike slip faulting (Vičič et al., 2019). The crustal thickness from the receiver functions of Hetényi et al. (2018b) along the EASI profile is shown in section F. The EASI Moho beneath the Periadriatic Line reaches the depths of more than 60 km, which is far deeper than the values of the other models. The southern part of the EASI crosses the thickened crust to the east of the Friuli plain (∼50 km). However, the thick crust in this region is not captured by EASI receiver functions (Hetényi et al., 2018b) and it shows a ∼10 km thinner crust which is consistent with Spada et al. (2013) and slightly deeper than the NAC Moho.

CONCLUSION

We compiled a collection of 5854 correlograms calculated using the continuous seismic recordings from the permanent and temporary networks in Italy, Austria, Slovenia and Croatia. Most of the correlograms are computed using the seismic recordings of the AlpArray SWATH-D complementary experiment, and additional 1084 EGFs are provided by Nouibat et al. (2021). We used the GSpecDisp package (Sadeghisorkhani et al., 2017) for measuring the phase velocity dispersion curves of the Rayleigh waves between 2 and 30 s. The FMST package is applied for the

Rayleigh phase velocity tomography in a 0.1° × 0.1° grid covering the Southeastern Alps, the western part of the external Dinarides, and the Friuli and Venetian plains. We inverted the resulting local dispersion curves for 1D S-wave velocity profiles using the non-perturbational and perturbational inversion methods (Haney and Tsai, 2015, 2017). Finally, the 1D S-wave velocity profiles are assembled into a pseudo-3D S-wave velocity model. By using the depth gradient of the 1D S-wave velocity profiles, the depth of the crystalline basement beneath each node is determined. We also compared the iso-velocity depths with the crustal thickness inferred from receiver functions and found the 4.2 km/s iso-velocity to be a reasonable representation of the Moho depth. Taking the resulted S-wave velocity model and the crystalline basement and Moho depth maps into account, the following principal conclusions can be drawn:

- Thanks to the close station spacing of the SWATH-D network, our S-wave velocity model contains more details compared to the other available models (e.g., Kästle et al., 2018; Magrin and Rossi, 2020) particularly at shallower depths.
- The crystalline basement depth in the Po, Venetian and Friuli plains, ranges between ∼4 and ∼10 km.
- The crystalline basement beneath the Schio-Vicenza fault is shallower (∼5 km) than its eastern and western regions implying that the Schio-Vicenza fault can be considered as a prominent structural feature between the Venetian and Friuli plains to the east and the Po-plain to the west.
- Comparison of the shallow crustal velocities and location of the earthquakes in the southern foothills of the Alps reveals that the seismicity mainly occurs in a narrow velocity band between ∼3.1 and ∼3.6 km/s.
- The map of the iso-velocity-based Moho depth illustrates a N-S trending narrow corridor of thinner crust (∼40 km) beneath the Dolomite Mountains and along the TRANSALP profile, which separates the eastern and western thicker (∼55 km) crustal cores.
  -The Moho depth map displays a thickened crust along the boundary between the Friuli Plain and the external Dinarides.

DATA AVAILABILITY STATEMENT

The raw data supporting the conclusions of this article including the pseudo-3D crustal S-wave velocity model, and the Moho and basement depths of the Southeastern Alps, the western part of the external Dinarides, and the Friuli and Venetian plains (SEA-Crust) are publicly accessible at: https://doi.org/10.5281/zenodo.4574022.

AUTHOR CONTRIBUTIONS

AS-B: conceptualization, data curation, methodology, software, writing original draft, writing, review and editing and visualization. AV: data curation, conceptualization, methodology, software, writing original draft, writing, review and editing, visualization, funding acquisition, and supervision. AA: methodology, writing original draft, writing, review and editing, validation, funding acquisition, and supervision. SP: validation, writing review and editing, funding acquisition and Supervision. AlpArray and AlpArray-Swath-D Working Group: design of experiment, data acquisition, data curation, funding acquisition. All authors contributed to the article and approved the submitted version.

FUNDING

AS-B was supported by the ICTP TRIL (Training and Research in Italian Laboratories) programme (ICTP-OGS agreement).

ACKNOWLEDGMENTS

The maps are plotted using perceptually uniform colormaps (Crameri, 2018). AS-B acknowledges support from the ICTP TRIL (Training and Research in Italian Laboratories) programme (ICTP-OGS agreement). We thank the editor, GH, and the reviewers, IM, and IB, for their constructive comments. We thank Ahmed Nouibat and Anne Paul for sharing part of their correlogram dataset and Nick Rawlinson for the FMST tomography code. We appreciate helpful discussions with Andrea Magrin and Giuliana Rossi. The equipment for the SWATH-D array was provided by the Geophysical Instrument Pool Potsdam (GIPP of the GFZ grant number 201717) (https://www.gfz-potsdam.de/gipp) and DSEBRA (http://www.spp-mountainbuilding.de/research/project_reports/DSEBRA_2018.pdf). We acknowledge the AlpArray-Swath D Working Group: B. Heit, M. Weber, C. Haberland, F. Tilmann, the AlpArray-Swath D Field Team: Luigia Cristiano (Freie Universität Berlin, Helmholtz-Zentrum Potsdam Deutsches GeoForschungsZentrum (GFZ), Peter Pilz, Camilla Cattania, Francesco Maccaferri, Angelo Strollo, Günter Asch, Peter Wigger, James Mechie, Karl Otto, Patricia Ritter, Djamil Al-Halbouni, Alexandra Mauerberger, Ariane Siebert, Leonard Grabow, Susanne Hemmleb, Xiaohui Yuan, Thomas Zieke, Martin Haxter, Karl-Heinz Jaeckel, Christoph Sens-Schonfelder (GFZ), Michael Weber, Ludwig Kuhn, Florian Dorgerloh, Stefan Mauerberger, Jan Seidemann (Universität Potsdam), Frederik Tilmann, Rens Hofman (Freie Universität Berlin), Yan Jia, Nikolaus Horn, Helmut Hausmann, Stefan Weginger, Anton Vogelmann [Austria: Zentralanstalt für Meteorologie und Geodynamik (ZAMG)], Claudio Carraro, Corrado Morelli (Südtirol/Bozen: Amt für Geologie und Baustoffprüfung), Günther Walcher, Martin Pernter, Markus Rauch (Civil Protection Bozen), Damiano Pesaresi, Giorgio Duri, Michele Bertoni, Paolo Fabris [Istituto Nazionale di Oceanografia e di Geofisica Sperimentale OGS (CRS Udine)], Andrea Franceschini, Mauro Zambotto, Luca Froner, Marco Garbin (also OGS) (Ufficio Studi Sismici e Geotecnici -Trento) and the institutions that provided permanent station data

in the AlpArray Project. We would like to thank to the AlpArray Seismic Network Team: GH, Rafael Abreu, Ivo Allegretti, Maria-Theresia Apoloner, Coralie Aubert, Simon Besançon, Maxime Bès de berc, Götz Bokelmann, Didier Brunel, Marco Capello, Martina Čarman, Adriano Cavaliere, Jérôme Chèze, Claudio Chiarabba, John Clinton, Glenn Cougoulat, Wayne C. Crawford, Luigia Cristiano, Tibor Czifra, Ezio D'alema, Stefania Danesi, Romuald Daniel, Anke Dannowski, Iva Dasović, Anne Deschamps, Jean-Xavier Dessa, Cécile Doubre, Sven Egdorf, ETHZ-SED Electronics Lab, Tomislav Fiket, Kasper Fischer, Wolfgang Friederich, Florian Fuchs, Sigward Funke, Domenico Giardini, Aladino Govoni, Zoltán Gráczer, Gidera Gröschl, Stefan Heimers, Ben Heit, Davorka Herak, Marijan Herak, Johann Huber, Dejan Jarić, Petr Jedlička, Yan Jia, Hélène Jund, Edi Kissling, Stefan Klingen, Bernhard Klotz, Petr Kolínský, Heidrun Kopp, Michael Korn, Josef Kotek, Lothar Kühne, Krešo Kuk, Dietrich Lange, Jürgen Loos, Sara Lovati, Deny Malengros, Lucia Margheriti, Christophe Maron, Xavier Martin, Marco Massa, Francesco Mazzarini, Thomas Meier, Laurent Métral, IM, Milena Moretti, Anna Nardi, Jurij Pahor, Anne Paul, Catherine Péquegnat, Daniel Petersen, Damiano Pesaresi, Davide Piccinini, Claudia Piromallo, Thomas Plenefisch, Jaroslava Plomerová, Silvia Pondrelli, Snježan Prevolnik, Roman Racine, Marc Régnier, Miriam Reiss, Joachim Ritter, Georg Rümpker, Simone Salimbeni, Marco Santulin, Werner Scherer, Sven Schippkus, Detlef Schulte-Kortnack, Vesna Šipka, Stefano Solarino, Daniele Spallarossa, Kathrin Spieker, Josip Stipčević, Angelo Strollo, Bálint Süle, Gyöngyvér Szanyi, Eszter Szűcs, Christine Thomas, Martin Thorwart, Frederik Tilmann, Stefan Ueding, Massimiliano Vallocchia, Luděk Vecsey, René Voigt, Joachim Wassermann, Zoltán Wéber, Christian Weidle, Viktor Wesztergom, Gauthier Weyland, Stefan Wiemer, Felix Wolf, David Wolyniec, Thomas Zieke, Mladen Živčić, and Helena Žlebčíková.

SUPPLEMENTARY MATERIAL

The Supplementary Material for this article can be found online at: https://www.frontiersin.org/articles/10.3389/feart.2021.641113/full#supplementary-material and https://doi.org/10.5281/zenodo.4574022

Supplementary Figure 1 | Three month correlograms with the SNR value of higher than 5 between station D024 (the blue circle in **Figure 1**) and other contemporaneously operating stations.

Supplementary Figure 2 | Synthetic 1D velocity inversion tests. The True and the inverted models are shown by cyan and red, respectively.

Supplementary Figure 3 | Four examples of the inverted 1D S-wave velocity profiles and their sensitivity kernels. Locations of the 1D profiles are mentioned in the panels.

Supplementary Figure 4 | Depth slices showing the absolute S-wave velocity values at 5, 10, 15, 20, 25, 30, 35, and 40 km. Location of the Permian magmatic rocks observed at the surface is shown in **(A)**. SPMR–Surface Permian magmatic rocks.

Supplementary Figure 5 | Depth slices showing the relative change in the S-wave velocities of SEA-Crust (this study) with respect to NAC (Magrin and Rossi, 2020). The relative change is calculated as [(SEA-Crust–NAC)/NAC]. FP, Friuli Plain; VP, Venetian Plain; PO, Po Plain.

Supplementary Figure 6 | Depth slices showing the relative change in the S-wave velocities of SEA-Crust (this study) with respect to KST18 (Kästle et al., 2018). The relative change is calculated as [(SEA-Crust–KST18)/KST18]. FP, Friuli Plain; VP, Venetian Plain; PO, Po Plain.

Supplementary Figure 7 | Depth slices showing the relative change in the S-wave velocities of NAC (Magrin and Rossi, 2020) with respect to KST18 (Kästle et al., 2018). The relative change is calculated as [(NAC-KST18)/KST18]. FP, Friuli Plain; VP, Venetian Plain; PO, Po Plain.

REFERENCES

AlpArray Seismic Network (2015). AlpArray Seismic Network (AASN) Temporary Component. AlpArray Working Group. Other/Seismic Network. International Federation of Digital Seismograph Networks. doi: 10.12686/alparray/z3_2015

An, M., Wiens, D. A., Zhao, Y., Feng, M., Nyblade, A. A., Kanao, M., et al. (2015). S-velocity model and inferred Moho topography beneath the Antarctic Plate from Rayleigh waves. *J. Geophys. Res. Solid Earth* 120, 359–383. doi: 10.1002/2014jb011332

Anselmi, M., Govoni, A., De Gori, P., and Chiarabba, C. (2011). Seismicity and velocity structures along the South-Alpine thrust front of the Venetian Alps (NE-Italy). *Tectonophysics* 513, 37–48. doi: 10.1016/j.tecto.2011.09.023

Aoudia, A., Saraoì, A., Bukchin, B., and Suhadolc, P. (2000). The 1976 Friuli (NE Italy) thrust faulting earthquake: a reappraisal 23 years later. *Geophys. Res. Lett.* 27, 577–580. doi: 10.1029/1999GL011071

Behm, M. (2009). 3-D modelling of the crustal S-wave velocity structure from active source data: application to the Eastern Alps and the Bohemian Massif. *Geophys. J. Int.* 179, 265–278. doi: 10.1111/j.1365-246X.2009.04259.x

Behm, M., Nakata, N., and Bokelmann, G. (2016). Regional ambient noise tomography in the Eastern Alps of Europe. *Pure Appl. Geophys.* 173, 2813–2840. doi: 10.1007/s00024-016-1314-z

Bensen, G. D., Ritzwoller, M. H., Barmin, M. P., Levshin, A. L., Lin, F., Moschetti, M. P., et al. (2007). Processing seismic ambient noise data to obtain reliable broad-band surface wave dispersion measurements. *Geophys. J. Int.* 169, 1239–1260. doi: 10.1111/j.1365-246X.2007.03374.x

Bianchi, I., Behm, M., Rumpfhuber, E. M., and Bokelmann, G. (2015). A new seismic data set on the depth of the Moho in the Alps. *Pure Appl. Geophys.* 172, 295–308. doi: 10.1007/s00024-014-0953-1

Bianchi, I., and Bokelmann, G. (2014). Seismic signature of the Alpine indentation, evidence from the Eastern Alps. *J. Geodyn.* 82, 69–77. doi: 10.1016/j.jog.2014.07.005

Bianchi, I., Miller, M. S., and Bokelmann, G. (2014). Insights on the upper mantle beneath the Eastern Alps. *Earth Planet. Sci. Lett.* 403, 199–209. doi: 10.1016/j.epsl.2014.06.051

Bianchi, I., Ruigrok, E., Obermann, A., and Kissling, E. (2020). *Moho Topography Beneath the Eastern European Alps by Global Phase Seismic Interferometry, Solid Earth Discuss.* [Preprint]. In review. doi: 10.5194/se-2020-179

Bragato, P. L., Sugan, M., Augliera, P., Massa, M., Vuan, A., and Saraò, A. (2011). Moho reflection effects in the Po plain (northern Italy) observed from instrumental and intensity data. *Bull. Seismol. Soc. Am.* 101, 2142–2152. doi: 10.1785/0120100257

Bressan, G., Gentile, G. F., Tondi, R., de Franco, R., and Urban, S. (2012). Sequential integrated inversion of tomographic images and gravity data: an application to the Friuli area (North-Eastern Italy). *Boll. Geof. Teor. Appl.* 53, 191–212. doi: 10.4430/bgta0059

Bressan, G., Ponton, M., Rossi, G., and Urban, S. (2016). Spatial organization of seismicity and fracture pattern in NE-Italy and W-Slovenia. *J. Seismol.* 20, 511–534. doi: 10.1007/s10950-015-9541-9

Brocher, T. (2005). Empirical relations between elastic wavespeeds and density in the Earth's crust. *Bull. Seismol. Soc. Am.* 95, 2081–2092. doi: 10.1785/0120050077

Brückl, E., Behm, M., Decker, K., Grad, M., Guterch, A., Keller, G. R., et al. (2010). Crustal structure and active tectonics in the Eastern Alps. *Tectonics* 29:TC2011. doi: 10.1029/2009TC002491

Brückl, E., Bleibinhaus, F., Gosar, A., Grad, M., Guterch, A., Hrubcovaì, P., et al. (2007). Crustal structure due to collisional and escape tectonics in the Eastern Alps region based on profiles Alp01 and Alp02 from the ALP 2002 seismic experiment. *J. Geophys. Res. Solid Earth.* 112:B06308.

Christensen, N., and Mooney, W. D. (1995). Seismic velocity structure and composition of the continental crust: a global view. *J. Geophys. Res.* 100, 9761–9788. doi: 10.1029/95JB00259

Christensen, N. I. (1996). Poisson's ratio and crustal seismology. *J. Geophys. Res.* 101, 3139–3156. doi: 10.1029/95JB03446

Crameri, F. (2018). *Scientific Colour-Maps*. Genève: Zenodo: doi: 10.5281/zenodo.1243862

Dewey, J. F., Helman, M. L., Knott, S. D., Turco, E., and Hutton, D. H. W. (1989). Kinematics of the western mediterranean. *Geol. Soc. Lond. Spec. Publ.* 45, 265–283. doi: 10.1144/gsl.sp.1989.045.01.15

Ekström, G., Abers, G. A., and Webb, S. C. (2009). Determination of surface-wave phase velocities across US array from noise and Aki's spectral formulation. *Geophys. Res. Lett.* 36:L18301. doi: 10.1029/2009GL039131

Finetti, I. R. (ed.) (2005). *CROP Project: Deep Seismic Exploration of the Central Mediterranean, and Italy*, Vol. 1. Amsterdam: Elsevier.

Friuli-Venezia Giulia Seismometric Network Bulletin (2019). Available online at: http://www.crs.inogs.it/bollettino/RSFVG/RSFVG.en.html (accessed September 22, 2020).

Grad, M., Brückl, E., Majdan ìski, M., Behm, M., Guterch, A., and CELEBRATION 2000 and ALP 2002 Working Groups (2009). Crustal structure of the Eastern Alps and their foreland: seismic model beneath the CEL10/Alp04 profile and tectonic implications. *Geophys. J. Int.* 177, 279–295. doi: 10.1111/j.1365-246x.2008.04074.x

Guidarelli, M., Aoudia, A., and Costa, G. (2017). 3-D structure of the crust and uppermost mantle at the junction between the southeastern Alps and external dinarides from ambient noise tomography. *Geophys. J. Int.* 211, 1509–1523. doi: 10.1093/gji/ggx379

Handy, M. R., Schmid, S. M., Bousquet, R., Kissling, E., and Bernoulli, D. (2010). Reconciling plate-tectonic reconstructions of Alpine Tethys with the geological-geophysical record of spreading and subduction in the Alps. *Earth Sci. Rev.* 102, 121–158. doi: 10.1016/j.earscirev.2010.06.002

Handy, M. R., Ustaszewski, K., and Kissling, E. (2015). Reconstructing the Alps-carpathians-dinarides as a key to understand switches in subduction polarity, slab gaps and surface motion. *Int. J. Earth Sci.* 104, 1–26. doi: 10.1007/s00531-014-1060-3

Haney, M. M., and Tsai, V. C. (2015). Nonperturbational surface-wave inversion: a dix-type relation for surface waves. *Geophysics* 80, EN167–EN177. doi: 10.1190/geo2014-0612.1

Haney, M. M., and Tsai, V. C. (2017). Perturbational and nonperturbational in- version of Rayleigh-wave velocities. *Geophysics* 82, F15–F28. doi: 10.1190/GEO2016-0397.1

Heit, B., Weber, M., Tilmann, F., Haberland, C., Jia, Y., Carraro, C., et al. (2017). *The Swath-D Seismic Network in Italy and Austria. GFZ Data Services. Other/Seismic Network*. doi: 10.14470/mf7562601148

Herrmann, R. B. (1973). Some aspects of band-pass filtering of surface waves. *Bull. Seismol. Soc. Am.* 63, 663–671.

Herrmann, R. B. (2013). Computer programs in seismology: an evolving tool for instruction and research, Seism. *Res. Lettr.* 84, 1081–1088. doi: 10.1785/0220110096

Hetényi, G., Molinari, I., Clinton, J., Bokelmann, G., Bondár, I., Crawford, W. C., et al. (2018a). The AlpArray seismic network: a large-scale European experiment to image the Alpine orogeny, *Surv. Geophy.* 39, 1009–1033. doi: 10.1007/s10712-018-9472-4

Hetényi, G., Plomerová, J., Bianchi, I., Kampfová Exnerová, H., Bokelmann, G., Handy, M. R., et al. (2018b). From mountain summits to roots: crustal structure of the Eastern Alps and bohemian massif along longitude 13.3°E. *Tectonophysics* 744, 239–255. doi: 10.1016/j.tecto.2018.07.001

INGV Seismological Data Centre (1997). *Rete Sismica Nazionale (RSN)*. Italy: Istituto Nazionale di Geofisica e Vulcanologia [INGV], doi: 10.13127/SD/X0FXnH7QfY

Istituto Nazionale Di Oceanografia E Di Geofisica Sperimentale (2016). *North-East Italy Seismic Network. International Federation of Digital Seismograph Networks*. Sgonico: Istituto Nazionale Di Oceanografia E Di Geofisica Sperimentale, doi: 10.7914/SN/OX

Kästle, E. D., El-Sharkawy, A., Boschi, L., Meier, T., Rosenberg, C., Bellahsen, N., et al. (2018). Surface wave tomography of the Alps using ambient-noise and earthquake phase velocity measurements. *J. Geophys. Res.* 123, 1770–1792. doi: 10.1002/2017JB014698

Kaviani, A., Paul, A., Moradi, A., Mai, P. M., Pilia, S., Boschi, L., et al. (2020). Crustal and uppermost mantle shear wave velocity structure beneath the Middle East from surface wave tomography. *Geophys. J. Int.* 221, 1349–1365. doi: 10.1093/gji/ggaa075

Kissling, E., Schmid, S. M., Lippitsch, R., Ansorge, J., and Fügenschuh, B. (2006). "Lithosphere structure and tectonic evolution of the Alpine arc: new evidence from high- resolution teleseismic tomography," in *European Lithosphere Dynamics*, eds D. G. Gee and R. A. Stephenson (London: Geological Society Memoir), 3229–3145.

Kummerow, J., Kind, R., Oncken, O., Giese, P., Ryberg, T., Wylegalla, K., et al. (2004). A natural and controlled source seismic profile through the Eastern Alps: TRANSALP. *Earth Planet. Sci. Lett.* 225, 115–129. doi: 10.1016/j.epsl.2004.05.040

Kvapil, J., Plomerová, J., Kampfová Exnerová, H., Babuška, V., Hetényi, G., and The AlpArray Working Group (2020). *Transversely Isotropic Lower Crust of Variscan Central Europe imaged by Ambient Noise Tomography of the Bohemian Massif, Solid Earth Discuss. [Preprint]*. In review. doi: 10.5194/se-2020-176.

Le Breton, E., Handy, M. R., Molli, G., and Ustaszewski, K. (2017). Post-20 Ma motion of the Adriatic plate: New constraints from surrounding Orogens and implications for crust-mantle decoupling. *Tectonics* 36, 3135–3154. doi: 10.1002/2016TC004443

Levshin, A., Ratnikova, L., and Berger, J. (1992). Peculiarities of surface-wave propagation across central Eurasia. *Bull. Seismol. Soc. Am.* 82, 2464–2493.

Lin, F. C., Moschetti, M. P., and Ritzwoller, M. H. (2008). Surface wave tomography of the western United States from ambient seismic noise: rayleigh and love wave phase velocity maps. *Geophys. J. Int.* 173, 281–298. doi: 10.1111/j.1365-246X.2008.03720.x

Lu, Y., Stehly, L., Brossier, R., Paul, A., and AlpArray Working Group (2020). Imaging Alpine crust using ambient noise wave-equation tomography. *Geophys. J. Int.* 222, 69–85. doi: 10.1093/gji/ggaa145

Lu, Y., Stehly, L., Paul, A., and AlpArray Working Group (2018). High-resolution surface wave tomography of the European crust and uppermost mantle from ambient seismic noise. *Geophys. J. Int.* 214, 1136–1150. doi: 10.1093/gji/ggy188

Macquet, M., Paul, A., Pedersen, H. A., Villasen Þor, A., Chevrot, S., Sylvander, M., et al. (2014). Ambient noise tomography of the pyrenees and the surrounding regions: inversion for a 3-D vs model in the presence of a very heterogeneous crust. *J. Geophys. Int.* 199, 402–415. doi: 10.1093/gji/ggu270

Magrin, A., and Rossi, G. (2020). Deriving a new crustal model of northern adria: the Northern Adria Crust (NAC) model. *Front. Earth Sci.* 8:89. doi: 10.3389/feart.2020.00089

Marotta, A. M., and Splendore, R. (2014). 3D mechanical structure of the lithosphere below the Alps and the role of gravitational body forces in the regional present-day stress field. *Tectonophysics* 631, 117–129. doi: 10.1016/j.tecto.2014.04.038

MedNet Project Partner Institutions (1990). *Mediterranean Very Broadband Seismographic Network (MedNet)*. Italy: Istituto Nazionale di Geofisica e Vulcanologia, doi: 10.13127/SD/FBBBTDTD6Q

Molinari, I., and Morelli, A. (2011). EPcrust: a reference crustal model for the European Plate. *Geophys. J. Int.* 185, 352–364. doi: 10.1111/j.1365-246X.2011.04940.x

Molinari, I., Obermann, A., Kissling, E., Hetényi, G., Boschi, L., and The AlpArray-Easi Working Group (2020). 3D crustal structure of the Eastern Alpineregion from ambient noise tomography. *Results Geophys. Sci.* 4:100006. doi: 10.1016/j.ringps.2020.100006

Molinari, I., Verbeke, J., Boschi, L., Kissling, E., and Morelli, A. (2015). Italian and Alpine three-dimensional crustal structure imaged by ambient-noise surface-wave dispersion. *Geochem. Geophys. Geosyst.* 16, 4405–4421. doi: 10.1002/2015GC006176

Moschetti, M. P., Ritzwoller, M. H., Lin, F. C., and Yang, Y. (2010). Crustal shear wave velocity structure of the western United States inferred from ambient seismic noise and earthquake data. *J. Geophys. Res.* 115:B10306. doi: 10.1029/2010JB007448

Nouibat, A., Stehly, L., Paul, A., Brossier, R., Bodin, T., Schwartz, S., et al. (2021). *First Step Towards an Integrated Geophysical-Geological Model of the W-Alps: A New Vs Model from Transdimensional Ambient-Noise Tomography, EGU General Assembly 2021, Online, 19 April–30 Apr 2021*. EGU21–EGU3197. doi: 10.5194/egusphere-egu21-3197

Planès, T., Obermann, A., Antunes, V., and Lupi, M. (2020). Ambient-noise tomography of the greater Geneva basin in a geothermal exploration context. *Geophys. J. Int.* 220, 370–383. doi: 10.1093/gji/ggz457

Pola, M., Ricciato, A., Fantoni, R., Fabbri, P., and Zampieri, D. (2014). Architecture of the western margin of the North Adriatic foreland:the Schio-Vicenza fault system. *Ital. J. Geosci.* 133, 223–234. doi: 10.3301/IJG.2014.04

Qorbani, E., Zigone, D., Handy, M. R., Bokelmann, G., and The AlpArray-EASI working group (2020). Crustal structures beneath the Eastern and Southern Alps from ambient noise tomography. *Solid Earth* 11, 1947–1968. doi: 10.5194/se-11-1947-2020

Rawlinson, N. (2005). *FMST: Fast Marching Surface Tomography Package-Instructions, Research School of Earth Sciences*. Canberra: Australian National University.

Sadeghisorkhani, H., Gudmundsson, O., and Tryggvason, A. (2017). GSpecDisp: A matlab GUI package for phase-velocity dispersion measurements from ambient-noise correlations. *Comput. Geosci.* 110, 41–53. doi: 10.1016/j.cageo.2017.09.006

Schmid, S. M., Bernoulli, D., Fügenschuh, B., Matenco, L., Schefer, S., Schuster, R., et al. (2008). The alpine-carpathian-dinaridic orogenic system: correlation and evolution of tectonic units. *Swiss J. Geosci.* 101, 139–183. doi: 10.1007/s00015-008-1247-3

Schmid, S. M., Fügenschuh, B., Kissling, E., and Schuster, R. (2004). Tectonic Map andoverall architecture of the Alpine orogen. *Eclogae Geologicae Helvetiae* 97, 93–117. doi: 10.1007/s00015-004-1113-x

Schuster, R., and Stüwe, K. (2008). Permian metamorphic event in the Alps. *Geology* 36, 603–606. doi: 10.1130/G24703A.1

Serpelloni, E., Anzidei, M., Baldi, P., Casula, G., and Galvani, A. (2005). Crustal velocity and strain-rate fields in Italy and surrounding regions: new results from the analysis of permanent and non-permanent GPS networks. *Geophys. J. Int.* 161, 861–880. doi: 10.1111/j.1365-246X.2005.02618.x

Sethian, J. A., and Popovici, A. M. (1999). 3-D traveltime computation using the fast marching method. *Geophysics* 64, 516–523. doi: 10.1190/1.1444558

Slovenian Environment Agency (2001). *Seismic Network of the Republic of Slovenia. International Federation of Digital Seismograph Networks*. Slovenian: Slovenian Environment Agency, doi: 10.7914/SN/SL

Soergel, D., Pedersen, H. A., Stehly, L., Margerin, L., Paul, A., and AlpArray Working Group (2020). Coda-Q in the 2.5-20 s period band from seismic noise: application to the greater Alpine area. *Geophys. J. Int.* 220, 202–217. doi: 10.1093/gji/ggz443

Spada, M., Bianchi, I., Kissling, E., Agostinetti, N. P., and Wiemer, S. (2013). Combining controlled-source seismology and receiver function informa- tion to derive 3-D moho topography for Ttaly. *Geophys. J. Int.* 194, 1050–1068. doi: 10.1093/gji/ggt148

Spooner, C., Scheck-Wenderoth, M., Götze, H. J., Ebbing, J., and Hetenyi, G. (2019). Density distribution across the Alpine lithosphere constrained by 3-D gravity modelling and relation to seismicity and deformation. *Solid Earth* 10, 2073–2088. doi: 10.5194/se-10-2073-2019

Steinhart, J. S. (1967). "Mohorovičić discontinuity," in *International Dictionary of Geophysics*, ed. S. K. Runcorn (Oxford: Pergamon), 991–994.

Stipčević, J., Herak, M., Molinari, I., Dasovicì, I., Tkalčic, H., and Gosar, A. (2020). Crustal thickness beneath the Dinarides and surrounding areas from receiver functions. *Tectonics* 37:e2019TC005872. doi: 10.1029/2019TC005872

Sugan, M., and Vuan, A. (2014). On the ability of Moho reflections to affect the ground motion in northeastern Italy: a case study of the 2012 Emilia seismic sequence. *Bull. Earthquake Eng.* 12, 2179–2194. doi: 10.1007/s10518-013-9564-y

Šumanovac, F., Hegedu ′′s, E., Oreškovic, J., Kolar, S., Kovaìcs, A. C., Dudjak, D., et al. (2016). Passive seismic experiment and receiver functions analysis to determine crustal structure at the contact of the northern dinarides and southwestern pannonian basin. *Geophys. J. Int.* 205, 1420–1436. doi: 10.1093/gji/ggw101

Šumanovac, F., Oreškovic, J., Grad, M., and ALP 2002 Working Group (2009). Crustal structure at the contact of the dinarides and pannonian basin based on 2-D seismic and gravity interpretation of the Alp07 profile in the ALP 2002 experiment. *Geophys. J. Int.* 179, 615–633. doi: 10.1111/j.1365-246x.2009.04288.x

Thybo, H., Artemieva, I. M., and Kennett, B. (2013). Moho: 100 years after andrija Mohorovičić. *Tectonophysics.* 609, 1–8. doi: 10.1016/j.tecto.2013.10.004

Tondi, R., Vuan, A., Borghi, A., and Argnani, A. (2019). Integrated crustal model beneath the Po Plain (Northern Italy) from surface wave tomography and bouguer gravity data. *Tectonophysics* 750, 262–279. doi: 10.1016/j.tecto.2018.10.018

TRANSALP Working Group (2002). First deep seismic reflection images of the Eastern Alps reveal giant crustal wedges and transcrustal ramps. *Geophys. Res. Lett.* 29, 92.1–92.4. doi: 10.1029/2002GL014911

Turrini, C., Lacombe, O., and Roure, F. (2014). Present-day 3D structural model of the po valley basin Northern Italy. *Mar. Pet. Geol.* 56, 266–289. doi: 10.1016/j.marpetgeo.2014.02.006

University of Zagreb (2001). *Croatian Seismograph Network [Data set]. International Federation of Digital Seismograph Networks*. Zagreb: University of Zagreb, doi: 10.7914/SN/CR

Vičič, B., Aoudia, A., Javed, F., Foroutan, M., and Costa, G. (2019). Geometry and mechanics of the active fault system in western Slovenia. *Geophys. J. Int.* 217, 1755–1766. doi: 10.1093/gji/ggz118

Viganò, A., Scafidi, D., Martin, S., and Spallarossa, D. (2013). Structure and properties of the Adriatic crust in the central-eastern Southern Alps (Italy) from local earthquake tomography. *Terra Nova* 25, 504–512. doi: 10.1111/ter.12067

Viganò, A., Scafidi, D., Ranalli, G., Martin, S., Della Vedova, B., and Spallarossa, D. (2015). Earthquake relocations, crustal rheology, and active deformation in the central-eastern Alps (N Italy). *Tectonophysics* 661, 81–98. doi: 10.1016/j.tecto.2015.08.017

Yao, H., van der Hilst, R. D., and de Hoop, M. V. (2006). Surface-wave array tomography in SE Tibet from ambient seismic noise and two-station analysis - I. Phase velocity maps. *Geophys. J. Int.* 166, 732–744. doi: 10.1111/j.1365-246X.2006.03028.x

Zelt, C. (1998). Lateral velocity resolution from three-dimensional seismic refraction data. *Geophys. J. Int.* 135, 1101–1112. doi: 10.1046/j.1365-246x.1998.00695.x

Zentralanstalt Für Meterologie Und Geodynamik [ZAMG] (1987). *Austrian Seismic Network. International Federation of Digital Seismograph Networks*. ZAMG: Hohe Warte, doi: 10.7914/SN/OE

Conflict of Interest: The authors declare that the research was conducted in the absence of any commercial or financial relationships that could be construed as a potential conflict of interest.

frontiers in Earth Science

REVIEW
published: 23 April 2021
doi: 10.3389/feart.2021.641666

Orogenic Segmentation and Its Role in Himalayan Mountain Building

Mary Hubbard[1], Malay Mukul[2], Ananta Prasad Gajurel[3], Abhijit Ghosh[4], Vinee Srivastava[5], Bibek Giri[1], Neil Seifert[1] and Manuel M. Mendoza[4]*

[1] Department of Earth Sciences, Montana State University, Bozeman, MT, United States, [2] Continental Deformation Laboratory, Department of Earth Sciences, Indian Institute of Technology Bombay, Mumbai, India, [3] Department of Geology, Trichandra Multiple Campus, Tribhuvan University, Kathmandu, Nepal, [4] Department of Earth Sciences, University of California, Riverside, Riverside, CA, United States, [5] Department of Earth and Environmental Sciences, Indian Institute of Science Education and Research, Bhopal, India

The continental collision process has made a large contribution to continental growth and reconfiguration of cratons throughout Earth history. Many of the mountain belts present today are the product of continental collision such as the Appalachians, the Alps, the Cordillera, the Himalaya, the Zagros, and the Papuan Fold and Thrust Belt. Though collisional mountain belts are generally elongate and laterally continuous, close inspection reveals disruptions and variations in thrust geometry and kinematics along the strike of the range. These lateral variations typically coincide with cross structures and have been documented in thrust fault systems with a variety of geometries and kinematic interpretations. In the Himalaya, cross faults provide segment boundaries that, in some cases separate zones of differing thrust geometry and may even localize microseismicity or limit areas of active seismicity on adjacent thrust systems. By compiling data on structural segmentation along the length of the Himalayan range, we find lateral variations at all levels within the Himalaya. Along the Gish fault of the eastern Indian Himalaya, there is evidence in the foreland for changes in thrust-belt geometry across the fault. The Gish, the Ganga, and the Yamuna faults all mark boundaries of salients and recesses at the mountain front. The Benkar fault in the Greater Himalayan sequence of eastern Nepal exhibits a brittle-ductile style of deformation with fabric that crosscuts the older thrust-sense foliation. Microseismicity data from several regions in Nepal shows linear, northeast-striking clusters of epicenters sub-parallel to cross faults. The map pattern of aftershock data from the 2015 Nepal earthquakes has an abrupt northeast-trending termination on its eastern side suggesting the presence of a structure of that orientation that limited slip. The orientations of the recognized cross faults and seismic patterns also align with the extensional zones to the north on the Tibetan Plateau and the Indian basement structures to the south. Results from multiple studies are consistent with a link between cross faults and either of these structural trends to the north or south and suggest that cross faults may play a role in segmenting deformation style and seismic activity along the length of the Himalaya.

Keywords: Himalaya, segmentation, Nepal, India, transverse zone, cross fault

OPEN ACCESS

Edited by:
György Hetényi, University of Lausanne, Switzerland

Reviewed by:
R. Jayangonda Perumal, Wadia Institute of Himalayan Geology, India
Rodolphe Cattin, Université de Montpellier, France

****Correspondence:***
Mary Hubbard
mary.hubbard@montana.edu

Specialty section:
This article was submitted to Structural Geology and Tectonics, a section of the journal Frontiers in Earth Science

Received: *14 December 2020*
Accepted: *29 March 2021*
Published: *23 April 2021*

Citation:
Hubbard M, Mukul M, Gajurel AP, Ghosh A, Srivastava V, Giri B, Seifert N and Mendoza MM (2021) Orogenic Segmentation and Its Role in Himalayan Mountain Building. Front. Earth Sci. 9:641666. doi: 10.3389/feart.2021.641666

INTRODUCTION

The continental collision process has been responsible for the mountain building of many modern mountain ranges as well as a number of those for which we only see the remnants. The Appalachians, the Alps, the Cordillera, the Zagros, and the Papuan Fold and Thrust Belt are a few examples where continental collision or terrane accretion has resulted in mountain belts (Johnson and Harley, 2012). In many of these orogens we can trace thrust fault systems for large distances, however, in most cases there are disruptions and variations in thrust geometry and kinematics along the strike of the range. These lateral variations typically coincide with cross structures and have been documented in thrust fault systems from these mountain belts and other fold and thrust belts with a variety of geometries and kinematic interpretations. In the Alps, the Simplon Line and the Brenner Line are well-known cross structures that have accommodated range-parallel extension, likely accompanied by range-parallel transcurrent kinematics (Selverstone, 1988; Hubbard and Mancktelow, 1992). In the Appalachians and Papuan Fold and Thrust Belt, cross structures have been interpreted as tear faults or lateral ramps (Stearns, 1955; Mahoney et al., 2017). In western North America, structures such as the Charleston-Nebo Salient or the Helena Salient coincide with pre-existing basement structures (Constenius et al., 2003; Sears, 2016). While it is clear that cross structures have been recognized in other orogens, much of the structural focus of research in the Himalaya has been on range-parallel thrusts and extensional zones. Review of the Himalayan literature reveals that the geology of the Himalaya is most commonly presented in the context of the major, range-parallel faults that separate packages of rock of generally differing metamorphic grade and lithotectonic origin (Hodges, 2000). This structural configuration was recognized early on by Heim and Gansser (1939). Since that time researchers have conducted detailed field work locally and utilized modern analytical methods to further refine our understanding of the location, style of deformation, and timing of movement of these fault zones (e.g., summarized in Hodges, 2000; Yin, 2006; Searle and Treloar, 2019). It is through these detailed studies over a period of more than 50 years, that workers have recognized lateral discontinuities (e.g., Sastri et al., 1971; Dasgupta et al., 1987; Mugnier et al., 1999a). Types of lateral discontinuities include differences in foreland sediment thickness (Duvall et al., 2020); salients and recesses at the mountain front (Mukul, 2010); discontinuous, or offset sedimentary units in the lowest part of the range (Mugnier et al., 1999b); interaction between basement structures and foreland propagating thrusts (Sahoo et al., 2000); lateral variations in duplex geometries (Mitra et al., 2010; DeCelles et al., 2020); presence of shear fabric orthogonal to range (Hubbard et al., 2018); and discontinuous patterns of seismicity and other geophysical data (e.g., Rajaure et al., 2013; Hetényi et al., 2016).

Many types of data now support the concept that deformation may have partitioned through time along these range-parallel structures in the Himalaya (Gahalaut and Arora, 2012; Rajaure et al., 2013; Hetényi et al., 2016; Mugnier et al., 2017; Bilham, 2019; Mendoza et al., 2019; DeCelles et al., 2020; Duvall et al., 2020). Both geologic and seismic patterns exhibit lateral changes that coincide spatially with the presence of cross-faults (Paul et al., 2015; Hubbard et al., 2016; Srivastava et al., 2018). Historic earthquake records also suggest there may be segment boundaries limiting rupture extent (Hubbard et al., 2016; Bilham, 2019). To date, there is a recognition of the existence of cross structures, but a lack of data regarding how cross-faults relate to contraction along orogen-parallel structures, to lateral heterogeneities in the geology, and to modern seismicity. We present here a review of what has been observed along the range that may help us as we work to understand how deformation has been partitioned in the past and what we may expect in the future as this mountain belt continues its active role as our preeminent collisional orogen.

HIMALAYAN FRAMEWORK

As the world's highest mountain range and the world's most developed, active, collisional mountain belt, the Himalaya has seen a surge of geoscience research in the past half century. While the general structural and lithotectonic configuration of the Himalaya was worked out early (Heim and Gansser, 1939), recent work has been focused on refining stratigraphic details (e.g., DeCelles et al., 2001), understanding the cooling and exhumation history (reviewed in: Adlakha et al., 2013; Cottle et al., 2015), reconstructing the collisional history (e.g., Orme et al., 2015), and analyzing the seismicity to understand crustal structure in three dimensions (e.g., Mendoza et al., 2019). The Himalayan orogen is the product of the convergence following the collision of the Indian and Eurasian continents. Recent work provides evidence that this collision initiated at 58–61 Ma (DeCelles et al., 2014; Orme et al., 2015). The result of this collisional process in the Himalaya was the southward-directed thrusting of slivers of the leading edge of the Indian continent resulting in a series of range-parallel, dominantly in-sequence thrust faults separating lithotectonic units from successively deeper crustal levels toward the north. From south to north these units include (**Figure 1**): (1) the Sub-Himalayan zone including deformed Siwalik molassic sedimentary units, hanging wall to the Main Frontal Thrust (MFT); (2) the Lesser Himalayan zone, hanging wall to the Main Boundary Thrust (MBT); and (3) the Greater Himalayan Sequence (GHS), hanging wall to the Main Central Thrust (MCT). The Greater Himalaya is bound to the north by a north dipping normal fault system known as the South Tibetan Detachment System (STDS). South of the Himalaya the Indo-Gangetic Plain is underlain by Precambrian units of the Indian craton (see review in Godin et al., 2018) that are covered by a Gondwanan sedimentary sequence and Quaternary alluvial sediments including those of the Ganga Basin (Veevers and Tewari, 1995; Agarwal et al., 2002). Geophysical evidence suggests that the major thrust faults root in a midcrustal detachment known as the Main Himalayan Thrust (MHT) (Zhao et al., 1993; Avouac, 2003; Nabelek et al., 2009), the southernmost expression of which is the MFT (Pandey et al., 1999). A ramp structure in the MHT has been suggested as the cause of

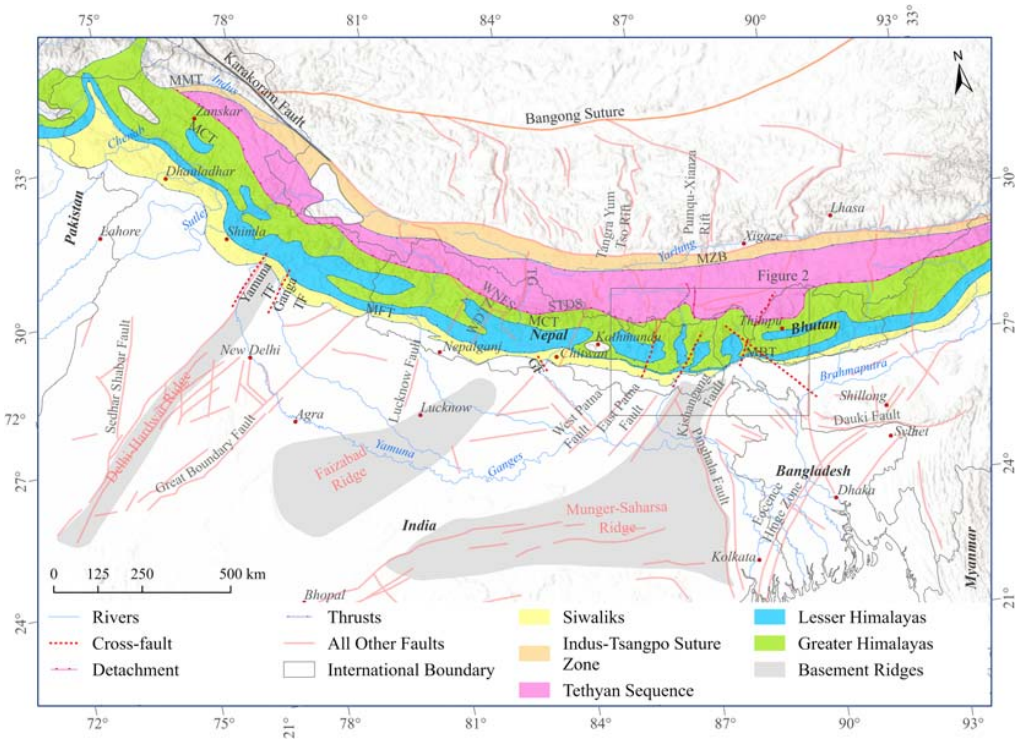

FIGURE 1 | Simplified lithotectonic map of the Himalaya. The heavy, dashed red lines indicate Himalayan cross structures. The brick-colored lines represent extensional structures on the Tibetan Plateau and basement faults on the Indian craton. The light gray shaded areas are basement ridges. GF: Gardi Tear Fault; MBT: Main Boundary Thrust; MCT: Main Central Thrust; MFT: Main Frontal Thrust; STDS: South Tibetan Detachment System; TF: Tear Fault; TG: Thakkhola graben; WNFS: Western Nepal Fault System (source: the Department of Mines and Geology, Nepal; Gansser, 1964; Godin and Harris, 2014; Diehl et al., 2017; Divyadarshini and Singh, 2019; the Geological Survey of India; Sastri et al., 1971; Sahoo et al., 2000; Searle et al., 2003; Jessup et al., 2008; Silver et al., 2015; Seifert, 2019 and compiled by Bibek Giri).

mega-earthquakes as well as the abrupt increase in elevation and interseismic seismicity between the Lesser Himalayan and Greater Himalayan zones (Pandey et al., 1995; Cattin and Avouac, 2000; Nabelek et al., 2009; Elliott et al., 2016).

Timing of in-sequence deformation is thought to generally young to the south, though some recent work has found evidence for younger, out-of-sequence deformation throughout the range (e.g., Mukul et al., 2007; Carosi et al., 2010; Larson and Cottle, 2014; Larson, 2018). Research results also suggest that timing may vary somewhat along the length of the range (Webb et al., 2017). The last few decades have seen debate in the literature about whether movement on the MCT and the STDS were coeval (Beaumont et al., 2004; Hodges, 2006; Kohn, 2008; Searle et al., 2008). While there is evidence that both structures may have been active between ∼22 and 19 Ma (e.g., Hubbard and Harrison, 1989; Burchfiel et al., 1992; Hodges et al., 1992; Kellett et al., 2018), data from several parts of the range suggest that the MCT and other structures within the Greater Himalayan Sequence (GHS) may have been active more recently (Catlos et al., 2002; Montemagni et al., 2019) and the STDS may have initiated as early as 30 Ma and ceased by 19 Ma in some areas (Soucy La Roche et al., 2016) and 12 Ma in others (Godin et al., 2006). The Main Boundary Thrust system is generally less well-exposed than the MCT and constraining its timing has posed a greater challenge. Best estimates are that the MBT deformation initiated at 11–9 Ma and may have continued into the Pliocene (Meigs et al., 1995; DeCelles et al., 1998) with even the possibility of Quaternary displacement (Nakata, 1972; Mukul, 2000; Hossler et al., 2016). DeCelles et al. (2020) propose that the major slip on the MBT is probably younger than ∼5 Ma based on clasts with hanging wall lithologies found in units of the footwall Siwalik Group. It has been recognized along most parts of the range that the Lesser Himalaya has been deformed as a duplex structure, so there was significant shortening taken up between the MCT and the MBT possibly in a similar time frame as the estimates for MBT deformation (Huyghe et al., 2001; Robinson et al., 2001; Szulc et al., 2006; Bhattacharyya and Mitra, 2009; Mitra et al., 2010). The Main Frontal Thrust system is neotectonically active as the southernmost expression of thrust deformation of the Himalaya (Mukul et al., 2007; Srivastava et al., 2016; DeCelles et al., 2020). This structural zone is thought to have been active since the Pliocene based on the cooling ages and depositional ages of the deformed Siwalik group in the hanging wall (Ojha et al., 2000; DeCelles et al., 2020).

Over the years a number of controversies have emerged such as how to define the MCT, the origin of klippen of high-grade lithologies in the Lesser Himalaya, and the amount of shortening accommodated by duplex structures in the Lesser Himalaya

(Hodges, 2006; Searle et al., 2008; Soucy La Roche et al., 2018; DeCelles et al., 2020). In some cases, differences in interpretations may be rooted in structural variations that we are now recognizing along the range (Yin, 2006). There is evidence that lateral heterogeneities exist in all of the tectonic units from the Ganges plain south of the MFT to the Greater Himalayan sequence along the northern edge of the orogen. In some cases, lateral changes are bound by recognized cross structures, but in other cases a lateral change is recognized with either a broad transitional zone or without sufficient field data to pinpoint a specific structure that delineates the change (e.g., Mugnier et al., 1999a; Srivastava and Mukul, 2020).

LATERAL HETEROGENEITIES AND EVIDENCE FOR CROSS FAULTS

Indo-Gangetic Plain

Recognition of geologic features on the Indo-Gangetic Plain that are oriented perpendicular to the trend of the Himalaya goes back to early geological and geophysical studies (Burrard, 1915; Oldham, 1917; Sastri et al., 1971; Rao, 1973; Valdiya, 1976). The great thickness of sediments in the Himalayan foreland, including the Ganga basin, was recognized as early as the time of Suess (1904). Burrard (1915) and Oldham (1917) presented differing interpretations of the presence of the sedimentary sequence based on early geophysical measurements, but it was really during the time of extensive oil and gas-related exploration that geophysical results and drilling revealed transverse structures underlying the foreland sedimentary basin (Sastri et al., 1971; Rao, 1973; Raiverman et al., 1983). Presence of these structures is confirmed in the seismic data (e.g., Dasgupta et al., 2000). Sastri et al. (1971) summarize the basement structure of the Ganga basin as a series of NE-striking basement ridges separated by basement depressions (**Figure 1**). In the east, the Munger-Saharsa ridge lies between the Kishanganj fault and the East Patna fault and has 3,000 m of overlying Neogene sediments. To the west, the depression between the Munger-Saharsa ridge and the Faizabad ridge has up to 6,000 m of sediment including Vindhyan (1.6–1.7 Ga), Paleogene, and Neogene units suggesting that the differential sedimentation and therefore the NE-striking ridge structures pre-date the India-Asia collision. There is also evidence now that faults that bound these basement ridge structures, may also bound blind thrust propagations off of the Main Himalayan Thrust under the modern foreland (Duvall et al., 2020). Duvall et al. (2020) used data from a grid of industry seismic lines from the foreland region in eastern Nepal to map NE-striking strike-slip faults, several of which bound the Munger-Saharsa ridge. These faults penetrate from the basement up through the Quaternary Upper Siwalik units. Between two of the easternmost of their studied faults there is a blind thrust in a region known as the Bhadrapur High (**Figure 2**), with an estimated ∼80–110 m of slip. They suggest that this thrust fault may be the early stages of the formation of a range-front salient. The configuration of cross faults bounding a thrust segment is consistent with the idea that cross faults may play a role in limiting lateral thrust propagation. Based on the seismic imaging data, Duvall et al. (2020) suggest that these cross faults, that originate in the basement, may continue northward into the Himalaya as suggested earlier by Mukul (2010); Godin and Harris (2014), Godin et al. (2018), and Soucy La Roche and Godin (2019).

Sub-Himalayan Zone

The availability of high-resolution topographic data and satellite imagery visually illuminates the lateral heterogeneities in the southern mountain front of the Himalaya. Perhaps most notable are the number of salients and reentrants/recesses along the length of the range (Yeats and Lillie, 1991; Powers et al., 1998; Mukul, 2010). The dun valleys of the Sub-Himalayan zone are enclosed valleys often bound by fault-related folds of the Siwalik Group. These valleys also mark diachronous and contrasting geomorphic expressions of deformation along the range (Kimura, 1999).

In the northwestern Indian Himalaya, there have been several efforts to quantify amounts of shortening and shortening rates in the Sub-Himalayan zone (Powers et al., 1998; Dubey et al., 2001; Srivastava et al., 2018). Dubey et al. (2001) balance multiple cross-sections in the area between Dhauladhar Range and the Shimla (**Figure 1**) and they found significant variability in amounts of shortening from ∼22 to 71% along the range. They conclude that this variability may actually be a result of different approaches to cross section balancing. Dubey (1997) conducted analog modeling of an oblique ramp in a convergent setting and makes a connection to the geometry of reentrants in the northwestern Indian Himalaya.

In the region of the Indian Himalaya where the Yamuna and Ganga rivers emerge, the range front is visibly offset. Sahoo et al. (2000) processed satellite imagery of this area and make an interpretation that tear faults were responsible for this offset (**Figure 1**). Further mapping in that area, which overlies the Delhi-Hardwar basement ridge, has confirmed the presence of cross faults at the recess boundaries (Sahoo et al., 2000; Srivastava et al., 2018). Geologic mapping in deformed molasse and foreland sediment, known as the Siwaliks, of western Nepal demonstrated the need for an orthogonal transfer zone where the structural nature of the range front thrust systems changed abruptly along strike (Mugnier et al., 1999a,b). This transfer zone marks the western boundary of several dun structures in the Sub-Himalayan zone and has been referred to as the West Dang transfer zone, a possible east-dipping lateral ramp (Mugnier et al., 1999a) that may continue northward into the Lesser Himalaya (see section "Discussion" below).

In Central Nepal, in the region of the Chitwan Dun, the range front topography is also irregular. Divyadarshini and Singh (2019) mapped six strands of the MFT at this site, some of which remain distinct for short distances, and others of which merge with each other. These workers have also identified a NNW-striking tear fault above the MFT they call the Gardi Tear Fault.

Farther east, in eastern Nepal and Sikkim, two other cross faults have been recognized at salient-recess boundaries along the range front (**Figure 2**), the Kosi fault in eastern Nepal along the Indian border, and the Gish fault in Sikkim (Mukul, 2010; Srivastava et al., 2017; Mukul et al., 2018). The Kosi fault was recently identified by Mukul et al. (2018) as a possible cross

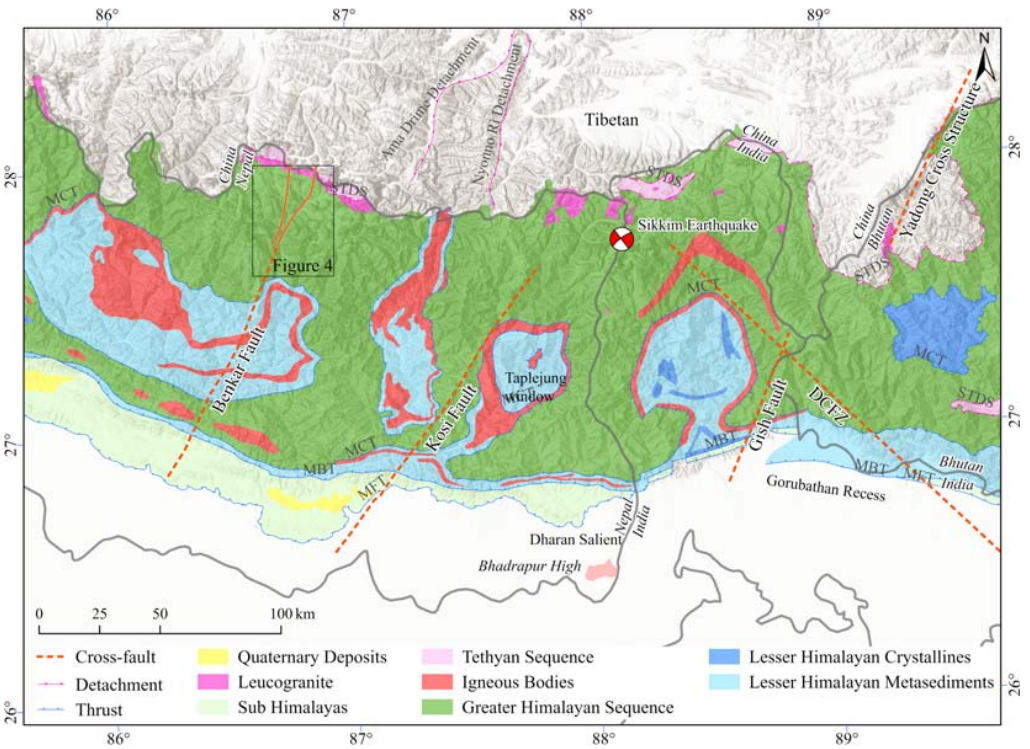

FIGURE 2 | Simplified geologic map of eastern Nepal, India, and western Bhutan. The red dashed lines are the approximate locations of the Benkar, Kosi, Gish, and Dhubri-Chungthang cross faults. The solid yellow lines are the bounds of the Benkar fault zone that have been mapped in the Greater Himalayan Sequence (Seifert, 2019). Sikkim M_w 6.9, 2011 earthquake fault plane solution from Paul et al. (2015). DCFZ: Dhubri-Chungthang Fault Zone; MBT: Main Boundary Thrust; MCT: Main Central Thrust; MFT: Main Frontal Thrust; STDS: South Tibetan Detachment System; [Map data from the Department of Mines and Geology, Nepal, the Geological Survey of India, and Greenwood et al. (2016). Map compiled by Bibek Giri].

fault marking the western boundary of the Dharan salient. This structure aligns with the western boundary of the Munger-Saharsa basement ridge structure in the foreland. Though it has not yet been mapped to the north, its projection may align with the Pumqu Xianza rift of the hinterland (Yin and Taylor, 2011). Microseismicity patterns in the area outline a concentration of events that follows the strike of the Kosi fault suggesting that the structure is active (Pandey et al., 1999; Monsalve et al., 2006; De La Torre et al., 2007). The strike of the fault also aligns with the western edge of the Taplejung window (**Figure 2**) that offsets the MCT in an apparent sinistral sense (Upreti et al., 2003).

The Gish fault has been mapped from the range front into the lesser Himalaya, and the GHS. This fault was first identified in West Bengal/Sikkim region of India (Mukul et al., 2009), where it forms the boundary between the Dharan salient and the Gorubathan recess. Following its recognition, continued research has included geomorphic, structural, and geodetic analysis of the region along, and adjacent to this fault (Srivastava et al., 2017; Mukul et al., 2018; Srivastava and Mukul, 2020). The structural and geomorphic research has focused on the range front of the Himalaya and has documented very different structural styles on either side of the Gish fault, with the Ramgarh Thrust (structurally between the MCT and the MBT) marking the range front in the Gorubathan recess (Matin and Mukul, 2010) and a series of blind thrusts toward the foreland, whereas the Dharan salient has multiple exposed thrusts south of the Ramgarh Thrust. The Ramgarh Thrust is displaced in a sinistral sense across the Gish fault. Deformation style of the Munsiari thrust sheet (structurally between the Ramgarh Thrust and the MCT) differs across the Gish fault and has fold features that are affected by the Gish fault (Matin and Mukul, 2020). Mukul (2010) has traced this fault across the MCT, though the structure has not been mapped in detail in the area of the MCT or further north. The Gish fault aligns with the Kishanganj fault on the eastern edge of the Munger-Saharsa ridge of the Indian basement (**Figure 1**). This region has had a number of strike-slip seismic events (Ni and Barazangi, 1984; Paul et al., 2015).

The Lesser Himalaya

Along-strike variations have been recognized in the Lesser Himalayan zone from topographic data, seismic data, and from cooling history data, suggesting segmentation in tectonic processes (Harvey et al., 2015; van der Beek et al., 2016; Soucy La Roche and Godin, 2019). Hodges et al. (2001) described the topography in the Himalaya along NS transects as having multiple physiographic transitions (PT1, PT2, and PT3). PT2 defined by these authors, is an elevation transition from the highest peaks of the Himalaya, typically consisting of the Greater Himalayan Sequence units, to the region of lower elevations to the south in the Lesser Himalaya. In western Nepal, between the

longitudes of 82.5° E and 81° E, Harvey et al. (2015) show that the PT2 transition bifurcates around an area of relatively low topographic relief. They interpret the PT2S (south) and the PT2N (north) as locations that transition to areas of faster rock uplift and they further document these transitions with the locations of knick points in river channels. Harvey et al. (2015) also present the seismic data from Ader et al. (2012) that shows a broadening of the microseismicity pattern in the area west of ∼82° E and suggest that the ramp in the MHT turns northwestward at that point and that additional duplexing may be occurring at depth in the Lesser Himalayan region. Several other studies have provided additional evidence for a lateral change at ∼82° E longitude. van der Beek et al. (2016) compared stream power and apatite fission track ages (AFT) from a N-S transect west of 82° E and a similar transect in central Nepal. They, too, concluded that there is a likely structural change in the ramp geometry of the MHT, possibly involving a lateral ramp crossing the strike of the range. These changes align with the West Dang Transfer Zone proposed by Mugnier et al. (1999a) based on their work in the Sub-Himalaya to the south. DeCelles et al. (2020) documents changes in duplexing geometry along strike in this zone.

There is further evidence for lateral changes in the MHT in western Nepal that comes from the differences in peak metamorphic temperatures obtained by the Karnali and Jajarkot klippen as well as the timing of metamorphism (Soucy La Roche and Godin, 2019). Exhumation occurred at 20–15 Ma for the Karnali klippe and at 20–25 Ma for the Jajarkot klippe (Soucy La Roche et al., 2019). Soucy La Roche and Godin (2019) interpret these T-t differences to represent a difference in the depth to the MHT of about 13 km and suggest that this exhumation difference reflects segmentation going back to at least the Oligocene. They further interpret re-activation of the Lucknow fault on the west side of the Faizabad ridge to have created a tear fault in the overlying units, thus offsetting the MHT.

The Lesser Himalayan zone is typically characterized along the length of the range as a duplex structure of metasedimentary units from the Kumaon region of India, across Nepal and Sikkim, and into Bhutan (Srivastava and Mitra, 1994; DeCelles et al., 1998; McQuarrie et al., 2008; Bhattacharyya and Mitra, 2009). Structural cross sections from each of these regions reveal significant variations in duplex geometry (e.g., Yin, 2006). While some of these variations may be differences in interpretation, there are clear differences in thickness of the duplex systems, fold geometry, numbers of horses, and shortening estimates in each section (Hauck et al., 1998; DeCelles et al., 2001, 2020; Johnson et al., 2001; Grujic et al., 2002; Mitra et al., 2010; Long et al., 2011). Some of these transitions in style may be gradual, but it has also been noted that duplex or underplating geometry can change across cross faults, tear faults, oblique or lateral ramps (Dubey et al., 2001; Yin, 2006; Harvey et al., 2015).

The Greater Himalaya

Much of the discussion in the literature pertaining to lateral variations in the Greater Himalaya has focused on differences in cooling histories, exhumation rates, and topographic profiles, in some cases extrapolated from the Lesser Himalaya (e.g., Duncan et al., 2003; Robert et al., 2011; Eugster et al., 2018). Further discussions have also included variations in the role of climate on erosion and the differences in the presence or absence of discontinuities within the Greater Himalayan zone (Carosi et al., 2010; Larson and Cottle, 2014). Perhaps one of the most obvious examples of lateral variation is in the Greater Himalayan klippen and Lesser Himalayan windows as seen in map pattern (**Figure 1**; Gansser, 1964; Searle et al., 2008; Thiede et al., 2017). These map pattern variations are largely attributed to variations in the geometries of the Lesser Himalayan duplexing and variations in the presence, absence, or position of a ramp in the MHT (Hodges, 2000; Robinson et al., 2001; Deeken et al., 2011; Kohn, 2014).

In the northwest Himalaya, there are a number of changes that occur in Greater Himalayan cooling ages and inferred exhumation rates between the Sutlej River valley and the Zanskar region (Eugster et al., 2018). Eugster et al. (2018) used low-temperature thermochronology to look at cooling histories for three cross-strike transects from the Sutlej river to the Dhauladhar Range. Their two southeasternmost transects show younger ages in the Greater Himalayan section and therefore suggest a more recent and more rapid exhumation than the Dhauladhar section to the northwest. They also note that there is a change in the topography toward the northwest with an elimination of the PT2 topographic change. A number of factors have been suggested as causes for changes in exhumation history in the northwestern Himalaya such as an increase in the obliquity of convergence (Thakur et al., 2014), a decrease in rainfall at the higher elevations than in the central part of the range (Bookhagen and Burbank, 2006), differences in pre-collisional sediment thickness (Rajendra Prasad et al., 2011) and the re-activation of inherited basement structures (Arora et al., 2012). The changes in obliquity of convergence or rainfall would likely produce broad areas of change whereas changes in sediment thickness or basement fault reactivation could create the more abrupt changes in deformation style, topography, or exhumation that are observed (Eugster et al., 2018).

Thakur et al. (2019) describe the Ropar-Manali lineament, first identified by Virdi (1979), as a dextral strike-slip cross fault that coincides with the segmentation suggested by Hetényi et al. (2016) based on arc-parallel gravity anomalies. In the area of the southern Sutlej River, near Shimla, geologic map pattern suggests a ramp in the MCT such that to the northwest, the MCT ramps up-section to the point that the STDS and the MCT merge (Thakur, 1998; Yin, 2006). This ramp has been referred to as the Mandi ramp (Yin, 2006) and it coincides with the Ropar-Manali lineament described in Thakur et al. (2019).

Low temperature thermochronology coupled with kinematic modeling in central Nepal supports the presence of a ramp in the MHT as is imaged in seismic data (Robert et al., 2011; Elliott et al., 2016). Young apatite fission track ages (AFT) in the Greater Himalaya (<3 Ma) with older ages in the Lesser Himalaya in central and western Nepal contrast with the age pattern in Bhutan which consists of older AFT ages (>3 Ma) in the Greater Himalaya and younger ages (3–5 Ma) in the Lesser Himalaya. Robert et al. (2011) used this data in thermal kinematic modeling and concluded that the MHT ramp that is present in central Nepal is likely absent in Bhutan. These authors also suggest that the topographic differences that result from variations in MHT

geometry further impact the location of higher precipitation and therefore higher erosion rates. Thermochronology data and kinematic modeling of an east and west transect in Bhutan (Coutand et al., 2014) suggests that the MHT ramp geometry changes from west to east and that exhumation rates may decrease to the east. Topographic variations all along the range have also been characterized by river channel steepness (k_{sn}) in the Greater Himalaya with high values of k_{sn} relating to strain accumulation (Cannon et al., 2018). The variability of k_{sn} displays a segmentation along the length of the range. Cannon et al. (2018) suggest that this variability coupled with several other parameters may correspond with variability in the occurrence of major earthquakes along the MHT.

While lateral variations along the Greater Himalaya are clearly expressed in topographic profiles, differences in cooling/exhumation histories, and the presence or absence of leucogranites (Weinberg, 2016), there are limited locations where individual structures have been identified in the field that may be linked to the lateral variations or the segmentation of the range. In eastern Nepal, a fault was recently recognized in the Greater Himalaya that could be related to the segmentation process. The Benkar fault zone was first recognized in the Dudh Kosi valley north of the village of Lukla (Hubbard et al., 2018) and was subsequently mapped across the Greater Himalaya to the north (**Figure 3**; Seifert, 2019; Seifert et al., 2019). Key outcomes from this work were that the NE-striking deformation zone is ∼3–11 km wide with the widening occurring to the north where it bifurcates around leucogranitic exposures (**Figure 4**). The deformation is brittle-ductile with much of the slip having occurred on sillimanite-rich layers. Kinematics are fairly consistently right-lateral, normal on a SE-dipping plane. Mapping has not been completed to the north of the Everest basecamp area or to the south of Lukla. To the north the structure may connect with the NW-striking Tangra Yum Co-Kung Co rift system in the southern Tibetan Plateau region (Maheo et al., 2007). To the south there is topographic evidence for a continuation of the Benkar fault down to the Gangetic plain. This topographic feature aligns with the Motihari-Everest transverse fault suggested by lineament mapping from Satellite images (Dasgupta et al., 1987). The Benkar zone may also align with the West Patna fault on the Indo-Gangetic plain. Timing of displacement along the Benkar fault is unknown, though it is younger than the leucogranites. Preliminary 40Ar/39Ar dating of muscovite separates from three samples along an EW transect indicates that at least some of the movement is younger than 12 Ma (Seifert et al., 2019).

SEGMENTATION AND SEISMICITY

Historic earthquake data shows the episodic and spatially restricted nature of major thrust fault rupture along the length of the Himalaya (Ambraseys and Douglas, 2004; Bilham, 2004, 2019). Wesnousky et al. (2019) recently presented new trench data that when coupled with earlier trench work supports the possible simultaneous rupture of a 250 km long segment of the Main Frontal Thrust (MFT) at ∼1,100 CE. Le Roux-Mallouf et al. (2020) also trenched an area along the MFT in western Bhutan and from evidence of multiple large rupture events interpreted a recurrence interval for great earthquakes of about 550 year. The spatial arrangement of rupture events supports the possibility of segment boundaries that may limit the lateral rupture propagation (Hubbard et al., 2016; Bilham, 2019), though details of most historic events remain poorly known. Aftershock data from the 2015 Gorkha earthquake (Karplus et al., 2020) shows a pattern of seismicity (**Figure 5**) that terminates to the east along an abrupt NE-SW trend (Mendoza et al., 2019). When projected to the Earth's surface, this termination coincides with the Gauri Shankar lineament (Dasgupta et al., 1987) and is similar in orientation to the traces of cross faults that have been mapped in the Sub-Himalaya and the Greater Himalaya elsewhere in the range (Hubbard et al., 2018; Srivastava and Mukul, 2020). Imaging the third dimension of this data on the western side also led Mendoza et al. (2019) to propose a change in structural style based on the change in the patterns of aftershocks. This structural transition to a duplex geometry also occurs along a NE trend. Seismic activity also shows strong lateral variations with a highly active eastern section and low activity to the west of the rupture area. In several areas of the Himalaya, microseismic events align along linear, NE-striking zones (Rajaure et al., 2013) suggesting the presence of cross faults that are active, even if the displacement along them is small. Hoste-Colomer et al. (2017) saw further evidence for cross faults or tear faults in seismic data associated with a 1997 event north of Kathmandu and they comment on similar seismic swarms in eastern and western Nepal.

In 2011, Sikkim experienced an Mw 6.9 earthquake. Using a moment tensor inversion technique, Paul et al. (2015) determined that the main shock origination was at ∼53 km depth and that the earthquake occurred along a NW-striking, near vertical fault and that displacement was dextral along that surface. Aftershocks occurred to the SE of the main shock at depths from 12 to 50 km. These results suggest that much of the deformation was occurring within the subducting Indian plate beneath the MHT. There is evidence from additional earthquake data that the 2011 Sikkim event occurred on the Dhubri-Chungthang fault zone that continues southeastward to the western edge of the Shillong Plateau (Diehl et al., 2017). Further east, in Bhutan, many of the earthquakes from the last century have also had strike-slip displacement on steep fault planes and have occurred at depths ranging from ∼13 to 68 km (Drukpa et al., 2006; Diehl et al., 2017).

In recent years, abundant geodetic data along the Himalaya has led to studies of interseismic coupling (Ader et al., 2012; Stevens and Avouac, 2015; Marechal et al., 2016; Dal Zilio et al., 2020). Ader et al. (2012) and Stevens and Avouac (2016) used data from all along the range and conclude that there is interseismic coupling across the entire length of the range over a 100 km width and that segmentation is not visible in their data. Marechal et al. (2016) used a higher resolution geodetic data set in the area of Bhutan and found that though there was some amount of interseismic coupling along the length of Bhutan, there was lateral variation in the width of the coupled zone. In addition,

FIGURE 3 | Photograph showing strand of Benkar Fault zone. The view is looking north at the west ridge of Taboche (see location in **Figure 4**), a peak in the mapped portion of the Benkar Fault zone, in the Khumbu region of Nepal. Red arrows show a zone of shearing to the right (east) of the leucogranite exposure. The vertical profile in this photo is ~1,100 m. This zone has apparent normal displacement within the NE-striking, Benkar Fault zone that has overall dextral, normal sense of shear (photo by Mary Hubbard).

protracted dynamic triggering in the Central Himalaya indicates that slow slip may play a role in interseismic deformation, stress loading and its lateral variation (Mendoza et al., 2016). Dal Zilio et al. (2020) also found lateral heterogeneity in the interseismic coupling and more specifically, found that regions of high interseismic coupling separated by shorter regions of lower coupling, that are aligned with structures in the Indian basement and that create segment boundaries. These segment boundaries also bound the regions of large earthquake rupture in the last millennium, though Mugnier et al. (2017) suggest that segment barriers may be penetrated during the largest earthquake events.

DISCUSSION

Geologic and geophysical data collected over the past century clearly shows that while much of the Himalaya can be characterized by a continuous series of range-parallel thrust faults, there are also important lateral variations in the architecture of the range. A number of these variations can be tied to specific transverse or cross structures, leading to segmentation of the range. Important questions that come from this recognition of segmentation include the more academic question of what has caused the segmentation and the more applied question of how does the segmentation impact seismicity in terms of fault rupture area and size of earthquake events. We recognize these questions may not be mutually exclusive and the true answers to these questions will require continued data collection, both in the field and in the laboratory, and from multiple disciplines across different space- and time-scales.

To understand possible causes of segmentation, it is useful to look at other collisional mountain belts that also display features of segmentation including cross structures. In some cases, the cross structures are identified as tear faults or lateral ramps (Appalachians and the Papuan Fold and Thrust belt) and in other cases there are transverse extensional structures (Alps). In the Himalayan example, one of the primary explanations for segmentation has been variation in the geometry of the MHT and possibly related variations in duplex geometry in the Lesser Himalaya (e.g., Ader et al., 2012; van der Beek et al., 2016; Mendoza et al., 2019). Geophysical data from the 2015 Gorkha earthquake in Nepal supports these explanations. As to why the MHT and/or duplexing geometries change along the strike of the range, there have been several explanations. Mugnier and Huyghe (2006) note the role of lateral variations

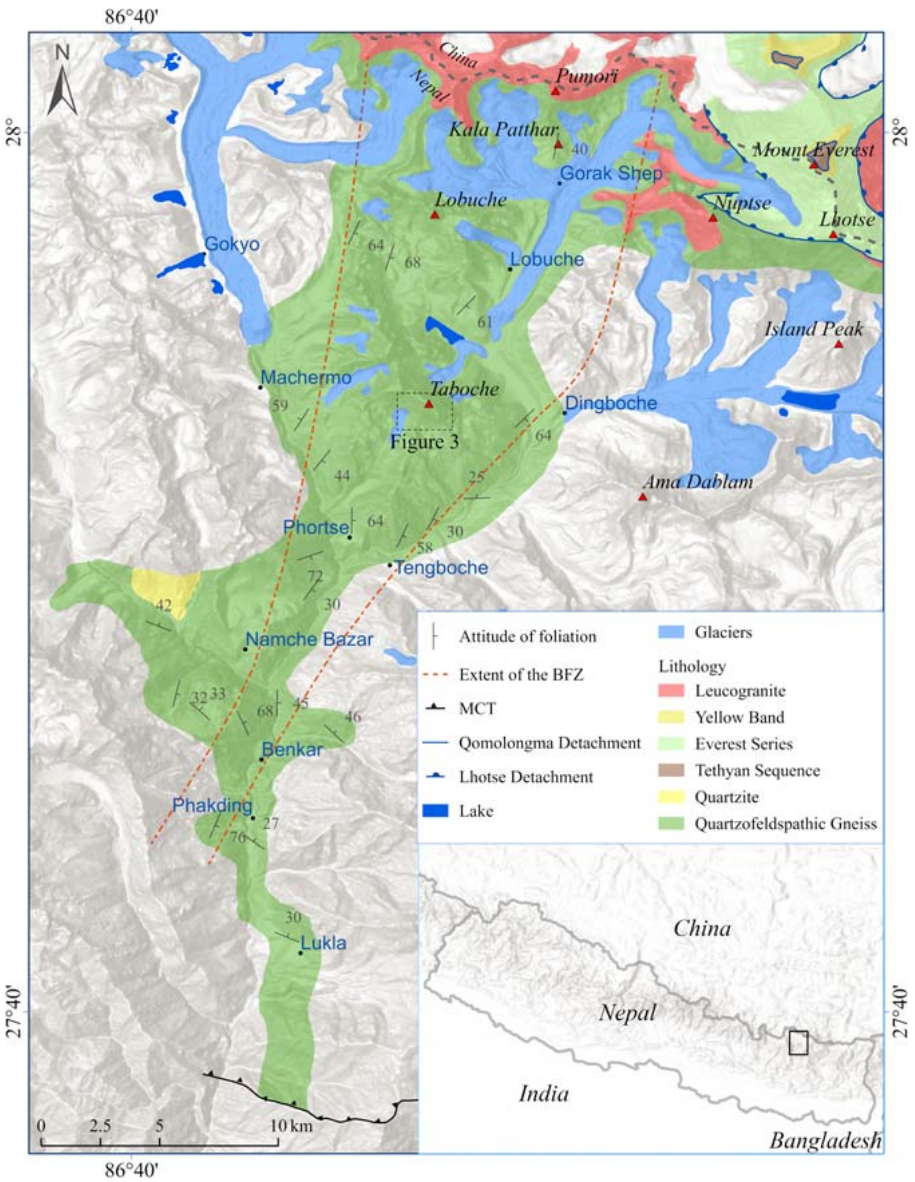

FIGURE 4 | Simplified geologic map of the northern Benkar fault zone. The dotted lines outline the region of non-penetrative, NE-striking shear fabric of the Benkar Fault zone. Kinematics on this shearing are dextral, normal. MCT: Main Central Thrust (after: Seifert, 2019).

in sediment thickness of the Ganga basin in partitioning the basin. These lateral variations are largely controlled by basement structures on the Indian craton. Based on similar orientations and adjacent locations of Indian basement faults and transverse faults in the Lesser Himalaya, Valdiya (1976) proposed that basement faults influenced the development and position of cross faults in the Himalaya. Godin et al. (2018) suggest that basement faults have influenced the lateral changes in structures within the Himalaya, and that they also may have influenced the locations of the NS-striking grabens on the Tibetan plateau. It remains unclear whether structures that are more than 50 km below the Tibetan upper crust could have influenced the location of the graben structures we see today. Future mapping of cross-faults withing the Himalaya may ultimately help us to understand these possible connections. The NE-striking basement structures are imaged in the foreland on seismic profiles (Duvall et al., 2020) and are shown to penetrate from the basement into the overlying sedimentary cover. Earthquake data from events within the Himalaya show strike-slip kinematics and occur down to depths of 50–60 km supporting the idea that the Indian plate basement faults continue to be active under the major Himalayan thrust faults (Paul et al., 2015). This earthquake data implies that at least some of the cross faults or segment boundaries in the Himalaya are tied to the basement structures and are not just tear faults in the hanging wall of the thrusts.

While historic earthquake data from the Himalaya has shown us that major events have been localized temporally and spatially in segments of the range (Bilham et al., 2001; Bilham, 2019), earthquake data from the 2015 Gorkha earthquake in central Nepal has provided a data set that reveals how slip was distributed in three dimensions within a crustal segment of the range (Elliott et al., 2016; Hubbard et al., 2016; Mendoza et al., 2019). The fact that the eastern edge of aftershock data ends abruptly along a NE-trending lineament (**Figure 5**) and that this lineament has been identified as a cross-structure (Mugnier et al., 2017) suggests that cross-structures may play a role in limiting lateral propagation of rupture area and therefore earthquake magnitude (Dowrick and Rhoades, 2004). To the west of Kathmandu there is another transition that occurs about a broad NE-striking zone where the activity of aftershock events shifts from a strongly clustered northern band to a more diffuse band across a >50 km wide zone (Mendoza et al., 2019). Maps of microseismicity across the Himalaya also show that there have been concentrations of events along transverse structures (e.g., **Figure 6**; Rajaure et al., 2013) suggesting that cross-faults could also be capable of slip events like in the 2011 Sikkim earthquake (Paul et al., 2015). Dal Zilio et al. (2021) point out the important role of timescales when looking at the connection between seismicity and segmentation. Whether or not cross fault slip events can generate great earthquakes, or even ameliorate the major Himalayan seismic hazard related to slip along the Main Himalayan thrust, is an important question (Mukul et al., 2018).

The alignment of seismic data with the Indian plate basement structures and the fact that earthquake events with transverse kinematics occur at depths well below the major thrust detachments in the Himalaya, is strong evidence that pre-existing basement structures on the subducting Indian plate are controlling at least some of the segmentation in the mountain building process. Other examples of subducting structures controlling over-riding plate deformation can be seen in oceanic subduction settings. Left lateral strike-slip faults on the continental margin of Oregon and Washington are parallel to, and have been linked to, structures on the subducting Juan de Fuca plate (Goldfinger et al., 1997). A similar scenario has been recognized in NW Sumatra near the site of the 2004 earthquake where N-S striking fracture zone fabric on the subducting plate is suggested to have created N-S striking faults in the overlying accretionary prism (Graindorge et al., 2008). These faults bound

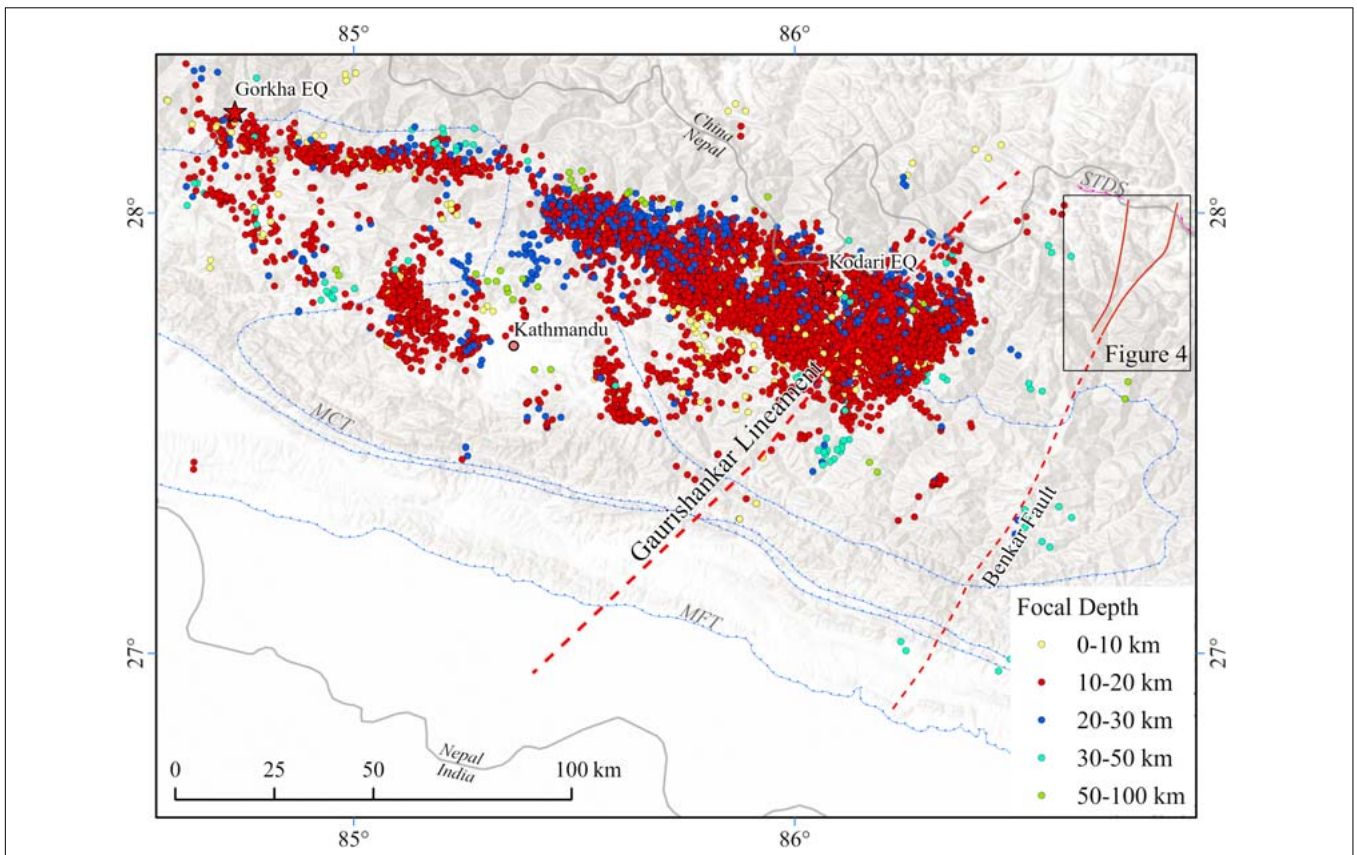

FIGURE 5 | Map of aftershock locations from the 2015 Nepal earthquakes. Epicenters of the two major earthquakes are shown with stars. Colored dots represent the locations of aftershocks. The solid red lines denote the bounds of the mapped portion of the Benkar Fault (Seifert, 2019) and the dotted red lines are the projected traces from satellite imagery of the Benkar Fault and the Gaurishankar lineament (Dasgupta et al., 1987). Note the abrupt termination of the zone of aftershocks on the east side that is sub-parallel to both the Gaurishankar lineament and the Benkar Fault. MBT: Main Boundary Thrust; MCT: Main Central Thrust; MFT: Main Frontal Thrust; STDS: South Tibetan Detachment System (Figure by Bibek Giri with data from Abhijit Ghosh and Mendoza et al., 2019).

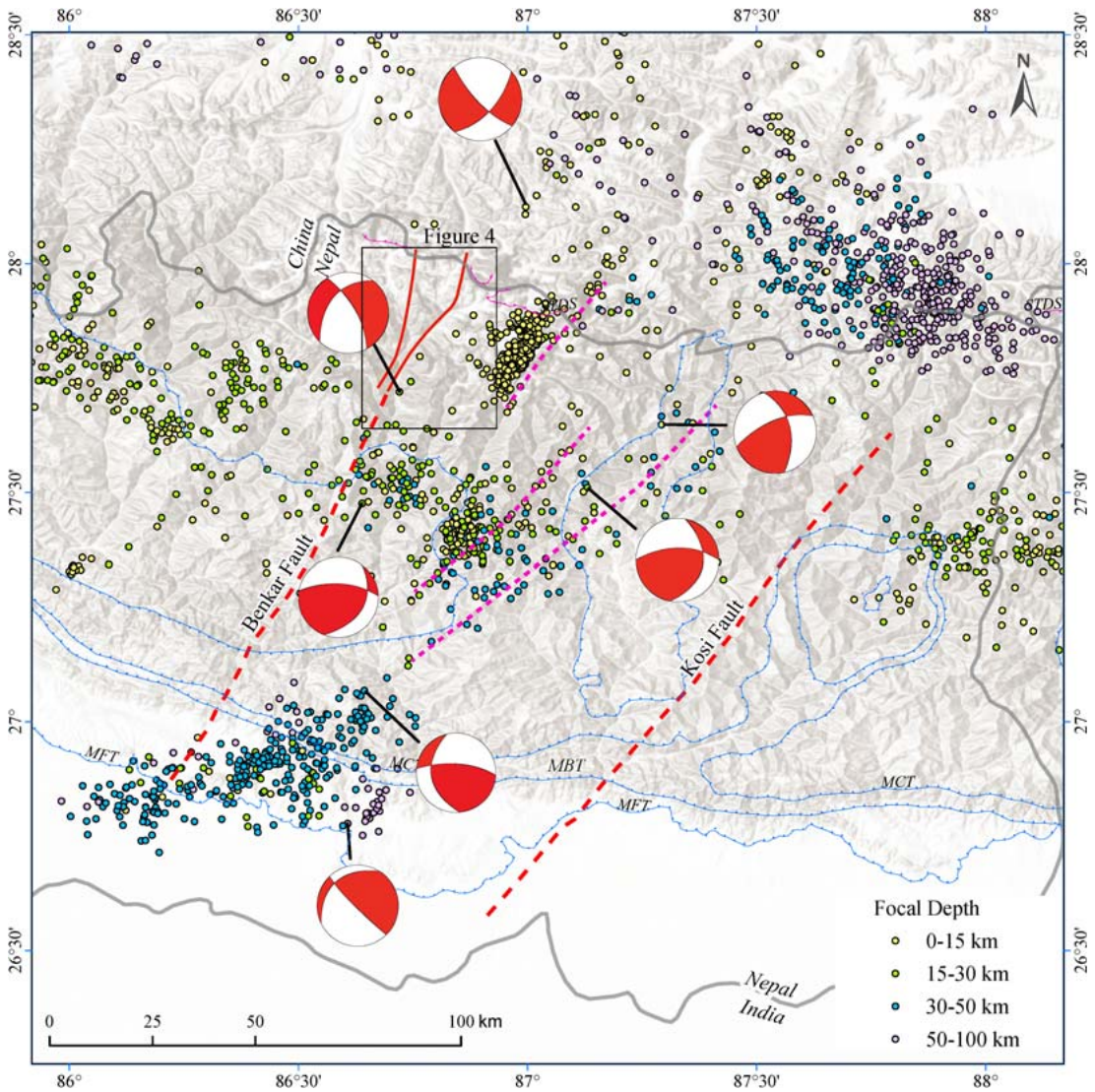

FIGURE 6 | Map of seismic events (magnitude > 1) in eastern Nepal during the time interval 1995–2003. Clusters of microseismicity align with the previously identified Benkar and Kosi Fault zones (red dashed lines), but there are other areas where the seismicity aligns along NE-oriented trends (pink dashed lines). Seismicity locations and depths from Rajaure et al. (2013) and focal mechanisms from Shanker et al. (2011). MBT: Main Boundary Thrust; MCT: Main Central Thrust; MFT: Main Frontal Thrust; STDS: South Tibetan Detachment System.

segments in the prism with alternating vergence of folds. In the offshore region of the Andes near the Peru-Chile border, seismic data from the Mw 8.4 Peru earthquake of 2001 showed that the main fault rupture propagated ∼70 km southward before stalling at a transverse surface (Robinson et al., 2006). After stalling for 30 s the rupture broke through the surface releasing significant energy in the process. That surface was interpreted as a fault that aligns with, and was likely caused by, a subducting fracture zone.

CONCLUSION

In summary, it is clear from geomorphologic, thermochronologic, structural, and geophysical data sets that tectonic processes along the length of the Himalaya have been segmented. Segment boundaries may be diffuse zones or may be discrete structures such as the cross faults. As an active collisional mountain belt, the Himalaya is a perfect place to try to understand the factors that control segmentation and to understand how these factors have evolved through time. Ultimately this understanding may help us to understand mountain building processes that were active in older collisional zones. Moving forward, there is a need for more data on the field expression of segment boundaries and for more data regarding the temporal development of these boundaries. Understanding the location of these boundaries and their role in limiting fault plane rupture and ameliorating MHT-related seismic hazard will help us to better understand the extent of the earthquake hazard in this active mountain range.

AUTHOR CONTRIBUTIONS

MH, MMu, and AGa designed the review. MMu and VS contributed ideas and summaries of their work in the Indian Himalaya to the west and east of Nepal. MH, AGa, BG, and NS contributed summaries of their work on the Benkar Fault and the Khumbu region of Nepal. AGh and MMe contributed their analyses of seismic data from the Gorkha earthquake in Nepal. MH wrote the manuscript. BG drafted the map figures. MMu, AGa, AGh, VS, BG, NS, and MMe improved the manuscript through discussion and revisions. All authors contributed to the article and approved the submitted version.

FUNDING

This work was largely a review article and was not specifically funded by any agency. We acknowledge student support from the Geological Society of America Student Grants.

ACKNOWLEDGMENTS

We thank the Geological Society of America, the Fulbright Foundation, the Nepal Geological Society, and the Himalayan-Karakorum-Tibet workshops that connected us at various conferences and fellowship programs.

REFERENCES

Ader, T., Avouac, J.-P., Liu-Zeng, J., Lyon-Caen, H., Bollinger, L., Galetzka, J., et al. (2012). Convergence rate across the Nepal Himalaya and interseismic coupling on the Main Himalayan Thrust: Implications for seismic hazard. *J. Geophys. Res.* 117:B04403. doi: 10.1029/2011JB009071

Adlakha, V., Patel, R. C., and Lal, N. (2013). Exhumation and its mechanisms: a review of exhumation studies in the Himalaya. *J. Geol. Soc. India* 81, 481–502. doi: 10.1007/s12594-013-0064-0

Agarwal, K., Singh, I., Sharma, M., Sharma, S., and Rajago-Palan, G. (2002). Extensional tectonic activity in the craonward parts (peripheral bulge) of the Ganga Plain foreland basin, India. *Int. J. Earth Sci.* 91, 897–905. doi: 10.1007/s00531-002-0265-z

Ambraseys, N. N., and Douglas, J. (2004). Magnitude calibration of north Indian earthquakes. *Geophys. J. Int.* 159, 165–206. doi: 10.1111/j.1365-246x.2004.02323.x

Arora, B. R., Gahalaut, V. K., and Kumar, N. (2012). Structural control on along-strike variation in the seismicity of the northwest Himalaya. *J. Asian Earth Sci.* 57, 15–24. doi: 10.1016/j.jseaes.2012.06.001

Avouac, J. P. (2003). Mountain building, erosion and the seismic cycle in the Nepal Himalaya. *Adv. Geophy.* 46, 1–80. doi: 10.1016/S0065-2687(03

Beaumont, C., Jamieson, R. A., Nguyen, M. H., and Medvedev, S. (2004). Crustal channel flows: 1. Numerical models with applications to the tectonics of the Himalayan-Tibetan orogen. *J. Geophys. Res.* 109:B06406. doi: 10.1029/2003JB002809

Bhattacharyya, K., and Mitra, G. (2009). A new kinematic evolutionary model for the growth of a duplex—An example from the Rangit duplex. Sikkim Himalaya, India. *Gondwana Res.* 16, 697–715. doi: 10.1016/j.gr.2009.07.006

Bilham, R. (2004). Earthquakes in India and the Himalaya: tectonics, geodesy and history. *Ann. Geophys.* 47, 839–858.

Bilham, R. (2019). ""Himalayan earthquakes: a review of historical seismicity and early 21st century slip potential,"," in *Himalayan Tectonics: a Modern Synthesis*, eds P. J. Treloar and M. P. Searle (London: Geological Society of London Special Publication), 423–482. doi: 10.1144/sp483.16

Bilham, R., Gaur, V. K., and Molnar, P. (2001). Himalayan seismic hazard. *Science* 2001:293.

Bookhagen, B., and Burbank, D. W. (2006). Topography, relief, and TRMM-derived rainfall variations along the Himalaya. *Geophys. Res. Lett.* 33:L08405. doi: 10.1029/2006GL026037

Burchfiel, B. C., Zhiliang, C., Hodges, K. V., Yuping, L., Royden, L. H., Changrong, D., et al. (1992). The South Tibetan Detachment System, Himalayan Orogen: Extension Contemporaneous With and Parallel to Shortening in a Collisional Mountain Belt. *Geolog. Soc. Am. Special Paper* 269, 1–41. doi: 10.1130/SPE269-p1

Burrard, S. G. (1915). Origin of the Indo-Gangetic trough, commonly called Himalayan foredeep. *Proc. R Soc. Lond.* 91A, 220–238. doi: 10.1098/rspa.1915.0014

Cannon, J. M., Murphy, M. A., and Taylor, M. (2018). Segmented strain accumulation in the High Himalaya expressed in river channel steepness. *Geosphere* 14, 1131–1149. doi: 10 .1130/GES01508.1 doi: 10.1130/ges01508.1

Carosi, R., Montomoli, C., Rubatto, D., and Visoná, D. (2010). Late Oligocene high-temperature shear zones in the core of the Higher Himalayan Crystallines (lower Dolpo, Western Nepal). *Tectonics* 2010:29. doi: 10.1029/2008TC002400

Catlos, E. J., Harrison, T. M., Manning, C. E., Grove, M., Rai, S. M., Hubbard, M. S., et al. (2002). Records of the evolution of the Himalayan orogen from in situ Th–Pb ion microprobe dating of monazite: Eastern Nepal and western Garhwal. *J. Asian Earth Sci.* 20, 459–479. doi: 10.1016/s1367-9120(01)00039-6

Cattin, R., and Avouac, M. P. (2000). Modeling mountain building and the seismic cycle in the Himalaya of Nepal. *J. Geophy. Res. 105* 13:407.

Constenius, K., Esser, R. P., and Layer, P. W. (2003). "Extensional collapse of the Charleston-Nebo salient and its relationship to space-time variations in Cordilleran orogenic belt tectonism and continental stratigraphy," in *Cenozoic Systems of the Rocky Mountain Region*, eds R. G. Raynolds and R. M. Flores (Denver, CO: Rocky Mountani SEPM), 303–353.

Cottle, J. M., Larson, K. P., and Kellett, D. A. (2015). How does the mid-crust accommodate deformation in large, hot collisional orogens? A review of recent research in the Himalayan orogen. *J. Struct. Geol.* 78, 119–133. doi: 10.1016/j.jsg.2015.06.008

Coutand, I., Whipp, D. M. Jr., Grujic, D., Bernet, M., Fellin, G., Bookhagen, B., et al. (2014). Geometry and kinematics of the Main Himalayan Thrust and Neogene crustal exhumation in the Bhutanese Himalaya derived from inversion of multithermochronologic data. *J. Geophys. Res.* 119, 1446–1481. doi: 10.1002/2013JB010891

Dal Zilio, L., Hetényi, G., Hubbard, J., and Bollinger, L. (2021). Building the Himalay from tectonic to earthquake scales. *Nat. Rev. Earth Env.* 2021, 143–141. doi: 10.1038/s43017-021-00143-1

Dal Zilio, L., Jolivet, R., and van Dinther, Y. (2020). Segmentation of the Main Himalayan Thrust illuminated by Bayesian inference of interseismic coupling. *Geophys. Res. Lett.* 47:e2019GL086424. doi: 10.1029/2019GL086424

Dasgupta, S., Mukhopadhyay, M., and Nandy, D. R. (1987). Active transverse features in the central portion of the Himalaya. *Tectonophysics* 136, 255–264. doi: 10.1016/0040-1951(87)90028-x

Dasgupta, S., Pande, P., Ganguly, D., and Iqbal, Z. (2000). *Seismotectonic Atlas of India and its Environs*. Calcutta: Geological Survey of India, 1–87.

De La Torre, T. L., Monsalve, G., Sheehan, A. F., Sapkota, S., and Wu, F. (2007). Earthquake processes of the Himalayan collision zone in eastern Nepal and the southern Tibetan Plateau. *Geophys. J. Int.* 171, 718–738. doi: 10.1111/j.1365-246x.2007.03537.x

DeCelles, P. G., Carrapa, B., Ojha, T. P., Gehrels, G. E., and Collins, D. (2020). Structural and thermal evolution of the Himalayan thrust belt in midwestern Nepal. *Geolog. Soc. Am. Special Paper* 547, 1–77. doi: 10.1130/2020.2547(01)

DeCelles, P. G., Gehrels, G. E., Quade, J., and Ojha, T. P. (1998). Eocene–early Miocene foreland basin development and the history of Himalayan thrusting, western and central Nepal. *Tectonics* 17, 741–765. doi: 10.1029/98tc02598

DeCelles, P. G., Kapp, P., Gehrels, G. E., and Ding, L. (2014). Paleocene–Eocene foreland basin evolution in the Himalaya of southern Tibet and Nepal: Implications for the age of initial India-Asia collision. *Tectonics* 33, 824–849. doi: 10.1002/2014TC003522

DeCelles, P. G., Robinson, D. M., Quade, J., Ojha, T. P., Garzione, C. N., Copeland, P., et al. (2001). Stratigraphy, structure, and tectonic evolution of

the Himalayan fold-thrust belt in western Nepal. *Tectonics* 20, 487–509. doi: 10.1029/2000TC001226

Deeken, A., Thiede, R., and Sobel, E. (2011). Exhumational variability within the Himalaya of northwest India. *Earth Planetar. Sci. Lett.* 305, 103–114. doi: 10.1016/j.epsl.2011.02.045

Diehl, T., Singer, J., Hetényi, G., Grujic, D., Clinton, J., Giardini, D., et al. (2017). Seismotectonics of Bhutan: Evidence for segmentation of the Eastern Himalayas and link to foreland deformation. *Earth Planetar. Sci. Lett.* 471, 54–65. doi: 10.1016/j.epsl.2017.04.038

Divyadarshini, A., and Singh, V. (2019). Investigating topographic metrics to decipher structural model and morphotectonic evolution of the Frontal Siwalik Ranges, Central Himalaya, Nepal. *Geomorphology* 337, 31–52. doi: 10.1016/j.geomorph.2019.03.028

Dowrick, D. J., and Rhoades, D. A. (2004). Relations between earthquake magnitude and fault rupture dimensions: how regionally variable are they? *Bull. Seismolog. Soc. Am.* 94, 776–788. doi: 10.1785/0120030151

Drukpa, D., Velasco, A. A., and Doser, D. (2006). Seismicity in the Kingdom of Bhutan (1937–2003): Evidence for crustal transcurrent deformation. *J. Geophys. Res.* 111:B06301. doi: 10.1029/2004JB003087

Dubey, A. K. (1997). Simultaneous development of noncylindrical folds, frontal ramps, and transfer faults in a compressional regime: experimental investigations of Himalayan Examples. *Tectonics* 16, 336–346. doi: 10.1029/96tc02231

Dubey, A. K., Mishra, R., and Bhakuni, S. S. (2001). Erratic shortening from balanced cross sections of the western Himalayan foreland basin causes and implications for basin evolution. *J. Asian Earth Sci.* 19, 765–777. doi: 10.1016/s1367-9120(01)00010-4

Duncan, C., Masek, J., and Fielding, E. (2003). How steep are the Himalaya? Characteristics and implications of along-strike topographic variations. *Geology* 31, 75–78. doi: 10.1130/0091-76132003031<0075:HSATHC<2.0.CO;2

Duvall, M. J., Waldron, J. W. F., Godin, L., and Najman, Y. (2020). Active strike-slip faults and an outer frontal thrust in the Himalayan foreland basin. *Proc. Natl. Acad. Sci.* 117, 17615–17621. doi: 10.1073/pnas.2001979117

Elliott, J. R., Jolivet, R., Gonzalez, P. J., Avouac, J. P., Hollingsworth, J., Searle, M. P., et al. (2016). Himalayan megathrust geometry and relation to topography revealed by the Gorkha earthquake. *Nat. Geosci.* 9, 174–180. doi: 10.1038/ngeo2623

Eugster, P., Thiede, R. C., Scherler, D., Stubner, K., Sobel, E. R., and Strecker, M. R. (2018). Segmentation of the Main Himalayan Thrust Revealed by Low-Temperature Thermochronometry in the Western Indian Himalaya. *Tectonics* 37, 2710–2726. doi: 10.1029/2017TC004752

Gahalaut, V. K., and Arora, B. R. (2012). Segmentation of seismicity along the Himalayan Arc due to structural heterogeneities in the underthrusting Indian plan and overriding Himalayan wedge. *Episodes* 35:4. doi: 10.18814/epiiugs/2012/v3514/006

Gansser, A. (1964). *Geology of the Himalayas*. New York,NY: Wiley Interscience.

Godin, L., and Harris, L. B. (2014). Tracking basement cross-strike discontinuities in the Indian crust beneath the Himalayan orogen using gravity data – relationship to upper crustal faults. *Geophys. J. Int.* 198, 198–215. doi: 10.1093/gji/ggu131

Godin, L., Grujic, D., Law, R. D., and Searle, M. P. (2006). "Channel flow, ductile extrusion and exhumation in continental collision zones: An introduction," in *Channel Flow, Ductile Extrusion and Exhumation in Continental Collision Zones*, eds R. D. Law, M. P. Searle, and L. Godin (London: Geological Society London, Special Publication), 1–23. doi: 10.1144/gsl.sp.2006.268.01.01

Godin, L., Soucy la Roche, R., Waffle, L., and Harris, L. B. (2018). "Influence of inherited Indian basement faults on the evolution of the Himalayan orogen," in *Crustal Architecture and Evolution of the Himalaya–Karakoram–Tibet Orogen*, eds R. Sharma, I. M. Villa, and S. Kumar (London: Geological Society of London Special Publications).

Goldfinger, C., Kulm, L. D., Yeats, R. S., McNeill, L., and Hummon, C. (1997). Oblique strike-slip faulting of the central Cascadia submarine forearc. *J. Geophys. Res.* 102, 8217–8243. doi: 10.1029/96jb02655

Graindorge, D., Klingelhoefer, F., Sibuiet, J. C., McNeill, L., Henstock, T., Dean, S., et al. (2008). Impact of lower plate structure on upper plate deformation at the NW Sumatran convergent margin from seafloor morphology. *Earth Planetar. Sci. Lett.* 275, 201–210. doi: 10.1016/j.epsl.2008.04.053

Greenwood, L. V., Argles, T. W., Parrish, R. R., Harris, N. B., and Warren, C. (2016). The geology and tectonics of central Bhutan. *J. Geol. Soc.* 173, 352–369.

Grujic, D., Hollister, L. S., and Parrish, R. P. (2002). Himalayan metamorphic sequence as an orogenic channel: Insight from Bhutan. *Earth Planetar. Sci. Lett.* 198, 177–191. doi: 10.1016S0012-821X(02)00482-X

Harvey, J. E., Burbank, D. W., and Bookhagen, B. (2015). Along-strike changes in Himalayan thrust geometry: Topographic and tectonic discontinuities in western Nepal. *Lithosphere* 7, 511–518. doi: 10.1130/L444.1

Hauck, M. L., Nelson, K. D., Brown, L. D., Wenjin, Z., and Ross, A. R. (1998). Crustal structure of the Himalayan orogen at ∼90° east longitude from Project INDEPTH deep reflection profiles. *Tectonics* 17, 481–500. doi: 10.1029/98TC01314

Heim, A., and Gansser, A. (1939). *Central Himalaya-Geological Observation of the Swiss Expedition, 1936*. Switzerland: Société Helvetique Science Naturelle.

Hetényi, G., Cattin, R., Berthet, T., Le Moigne, N., Chophel, J., Lechmann, S., et al. (2016). Segmentation of the Himalayas as revealed by arc-parallel gravity anomalies. *Sci. Rep.* 6:33866. doi: 10.1038/srep33866

Hodges, K. V. (2000). Tectonics of the Himalaya and southern Tibet from two perspectives. *Geol. Soc. Am. Bull.* 112, 324–350. doi: 10.1130/0016-7606(2000)112<324:tothas>2.0.co;2

Hodges, K. V. (2006). "A synthesis of the Channel Flow-Extrusion hypothesis as developed for the Himalayan-Tibetan orogenic system," in *Channel Flow, Ductile Extrusion and Exhumation in Continental Collision Zones*, eds R. D. Law, M. P. Searle, and L. Godin (London: Geological Society, London, Special Publications), 71–90. doi: 10.1144/gsl.sp.2006.268.01.04

Hodges, K. V., Hurtado, J. M., and Whipple, K. X. (2001). Southwared extrusion of Tibetan crust and its effect on Himalayan tectonics. *Tectonics* 20, 799–809. doi: 10.1029/2001tc001281

Hodges, K. V., Parrish, R., Housh, T., Lux, D., Burchfiel, B. C., Royden, L., et al. (1992). Simultaneous Miocene extension and shortening in the Himalayan orogen. *Science* 258, 1466–1470. doi: 10.1126/science.258.5087.1466

Hossler, T., Bollinger, L., Sapkota, S. N., Lav, J., Gupta, R. M., and Kandel, T. P. (2016). Surface ruptures of large Himalayan earthquakes in western Nepal: Evidence along a reactivated strand of the Main Boundary thrust. *Earth Planetar. Sci. Lett.* 434, 187–196. doi: 10.1016/j.epsl.2015.11.042

Hoste-Colomer, R., Bollinger, L., Lyon-Caen, H., Burtin, A., and Adhikari, L. B. (2017). Lateral structure variations and transient swarm revealed by seismicity along the Main Himalayan Thrust north of Kathmandu. *Tectonophysics* 71, 107–116. doi: 10.1016/j.tecto.2016.10.004

Hubbard, J., Almeida, R., Foster, A., Sapkota, S. N., Burgi, P., and Tapponnier, P. (2016). Structural segmentation controlled the 2015 MW 7.8 Gorkha earthquake rupture in Nepal. *Geology* 44, 639–642. doi: 10.1130/g38077.1

Hubbard, M., and Harrison, T. M. (1989). 40Ar/39Ar age constraints on deformation and metamorphism in the Main Central Thrust zone and Tibetan Slab, eastern Nepal Himalaya. *Tectonics* 8, 865–880. doi: 10.1029/tc008i004p00865

Hubbard, M., and Mancktelow, N. (1992). Lateral displacement during Neogene convergence in the Western and Central Alps. *Geology* 20, 943–946. doi: 10.1130/0091-7613(1992)020<0943:lddnci>2.3.co;2

Hubbard, M., Gajurel, A. P., Mukul, M., and Seifert, N. (2018). Cross faults and their role in Himalayan Structural Evolution in *Procceeding of the Geological Society of America Abstracts with Programs*. Indiana, USAs

Huyghe, P., Galy, A., Mugnier, J. L., and France-Lanord, C. (2001). Propagation of the thrust system and erosion in the Lesser Himalaya: Geochemical and sedimentological evidence. *Geology* 29, 1007–1010. doi: 10.1130/0091-76132001029<1007:POTTSA<2.0.CO;2

Jessup, M. J., Newell, D. L., Cottle, J. M., Berger, A. L., and Spotila, J. A. (2008). Orogen-parallel extension and exhumation enhanced by denudation in the trans-Himalayan Arun River gorge, Ama Drime Massif, Tibet-Nepal. *Geology* 36, 587–590. doi: 10.1130/g24722a.1

Johnson, M. R. W., and Harley, S. (2012). *Orogenesis: the making of mountains*. Cambridge, MA: Cambridge University Press.

Johnson, M. R. W., Oliver, G. J. H., Parrish, R. R., and Johnson, S. P. (2001). Synthrusting metamorphism, cooling, and erosion of the Himalayan Kathmandu Complex, Nepal. *Tectonics* 20, 394–415. doi: 10.1029/2001TC900005

Karplus, M. S., Pant, M., Sapkota, S. N., Nabelek, J., Valesco, A. A., Adhikari, L. B., et al. (2020). A Rapid response network to record aftershocks of the 2015

Mw 7.8 Gorkha earthquake in Nepal. *Seismolog. Res. Lett.* 2020:0220190394. doi: 101.1758/0220190394

Kellett, D. A., Cottle, J. M., and Larson, K. P. (2018). "The South Tibetan detachment system: History, advances, definition and future directions," in *Himalayan Tectonics: A Modern Synthesis*, eds P. J. Treloar and M. P. Searle (London: Geological Society, London, Special Publication), 377–400. doi: 10.1144/sp483.2

Kimura, K. (1999). Diachronous Evolution of Sub-Himalayan Piggyback Basins. *Island Arc 8.* 1, 99–113. doi: 10.1046/j.1440-1738.1999.00224.x

Kohn, M. J. (2008). P-T-t data from central Nepal support critical taper and repudiate large-scale channel flow of the Greater Himalayan Sequence. *Geol. Soc. Am. Bull.* 120, 259–273. doi: 10.1130/B26252.1

Kohn, M. J. (2014). Himalayan metamorphism and its tectonic implications. *Ann. Rev. Earth Planetar. Sci.* 42, 381–419. doi: 10.1146/annurev-earth-060313-055005

Larson, K. P. (2018). Refining the structural framework of the Khimti Khola region, east-central Nepal Himalaya, using quartz textures and c-axis fabrics. *J. Struct. Geol.* 107, 142–152. doi: 10.1016/j.jsg.2017.12.014

Larson, K. P., and Cottle, J. M. (2014). Midcrustal discontinuities and the assembly of the Himalayan midcrust. *Tectonics* 33, 718–740. doi: 10.1002/2013tc003452

Le Roux-Mallouf, R., Ferry, M., Cattin, R., Ritz, J. F., Drukpa, D., and Pelgay, P. (2020). A 2600-year-long paleoseismic record for the Himalayan Main Frontal Thrust (western Bhutan). *Solid Earth* 11, 2359–2375. doi: 10.5194/se-11-2359-2020

Long, S., McQuarrie, N., Tobgay, T., and Grujic, D. (2011). Geometry and crustal shortening of the Himalayan fold-thrust belt, eastern and central Bhutan. *Geol. Soc. Am. Bull.* 123, 1427–1447. doi: 10.1130/B30203.1

Maheo, G., Leloup, P. H., Valli, F., Lacassin, R., Arnaud, N., Paquette, J.-L., et al. (2007). Post 4 Ma initiation of normal faulting in southern Tibet. Constraints from the Kung Co half graben. *Earth Planetar. Sci. Lett.* 256, 233–243. doi: 10.1016/j.epsl.2007.01.029

Mahoney, L., Hill, K., McLaren, S., and Hanani, A. (2017). Complex fold and thrust belt structural styles: examples from the Greater Juh area of the Papuan Fold and Thrust Belt, Papua New Guinea. *J. Struct. Geol.* 100, 98–119. doi: 10.1016/j.jsg.2017.05.010

Marechal, A., Mazzotti, S., Cattin, R., Cazes, G., Vernant, P., Drukpa, D., et al. (2016). Evidence of interseismic coupling variations along the Bhutan Himalayan arc from new GPS data. *Geophys. Res. Lett.* 43, 399–312. doi: 10.1002/2016GL071163

Matin, A., and Mukul, M. (2010). Phases of deformation from cross-cutting structural relationships in external thrust sheets: insights from small-scale structures in the Ramgarh thrust sheet, Darjeeling Himalaya, West Bengal. *Curr. Sci.* 99, 1369–1377.

Matin, A., and Mukul, M. (2020). Himalayan cross faults affect thrust sheet geometry: An example from the Munsiari thrust sheet near the Gish Transverse fault zone, frontal Darjiling Himalaya, India. *J. Asian Earth Sci.* 199, 104400. doi: 10.1016/j.jseaes.2020.104400

McQuarrie, N., Robinson, D., Long, S., Tobgay, T., Grujic, D., Gehrels, G., et al. (2008). Preliminary stratigraphic and structural architectureof Bhutan: Implications for the along strike architecture of the Himalayan system. *Earth Planetar Sci. Lett.* 272, 105–117. doi: 10.1016/j epsl.2008.04.030

Meigs, A., Burbank, D. W., and Beck, R. A. (1995). Middle-late Miocene (>10 Ma) initiation of the Main Boundary thrust in the western Himalaya. *Geology* 23, 423–426. doi: 10.1130/0091-7613(1995)023<0423:mlmmfo>2.3.co;2

Mendoza, M. M., Ghosh, A., Karplus, M. S., Klemperer, S. L., Sapkota, S. N., Adhikari, L. B., et al. (2019). Duplex in the Main Himalayan Thrust illuminated by aftershocks of the 2015 Mw 7.8 Gorkha earthquake. *Nat. Geosci.* 12, 1018–1022. doi: 10.1038/s41561-019-0474-8

Mendoza, M., Ghosh, A., and Rai, S. S. (2016). Dynamic triggering of small local earthquakes in the central Himalaya. *Geophys. Res. Lett.* 43:GL069969. doi: 10.1002/2016GL069969

Mitra, G., Bhattacharyya, K., and Mukul, M. (2010). The Lesser Himalayan Duplex in Sikkim: implications for variations in Himalayan shortening. *J. Geolog. Soc. India* 75, 276–288.

Monsalve, G., Sheehan, A., Schulte-Pelkum, V., Rajaure, S., Pandsy, M. R., and Wu, F. (2006). Seismicity and one-dimensional velocity structure of the Himalayan collision zone: earthquakes in the crust and upper mantle. *J. Geophys. Res.* 111:B10301. doi: 10.1029/2005JB004062

Montemagni, C., Montomoli, C., Iaccarino, S., Carosi, R., Jain, A. K., Massonne, H.-J., et al. (2019). "Dating protracted fault activities: microstructures, microchemistry and geochronology of the Vaikrita Thrust, Main Central Thrust zone, Garhwal Himalaya, NW India," in *Crustal Architecture and Evolution of the Himalaya-Karakoram-Tibet Orogen*, eds R. Sharma, I. M. Villa, and S. Kumar (London: Geological Society, London, Special Publications).

Mugnier, J. L., Jouanne, F., Bhattarai, R., Cortes-Aranda, J., Gajurel, A., Leturmy, P., et al. (2017). Segmentation of the Himalayan megathrust around the Gorkha earthquake (25 April 2015) in Nepal. *J. Asian Earth Sci.* 141, 236–252. doi: 10.1016/j.jseaes.2017.01.015

Mugnier, J. L., Leturmy, P., Huyghe, P., and Chalaron, E. (1999b). The Siwaliks of western Nepal II. Mechanics of the thrust wedge. *J. Asian Earth Sci.* 17, 643–657. doi: 10.1016/s1367-9120(99)00039-5

Mugnier, J.-L., and Huyghe, P. (2006). The Ganges Basin geometry records a pre-15 Ma isostatic rebound of Himalaya. *Geology* 34, 445–448. doi: 10.1130/G22089.1

Mugnier, J.-L., Leturmy, P., Mascle, G., Huyghe, P., Chalaron, E., Vidal, G., et al. (1999a). The Siwaliks of western Nepal 1: Geometry and kinematics. *J. Asian Earth Sci.* 17, 629–642. doi: 10.1016/S1367-9120(99)00038-3

Mukul, M. (2000). The geometry and kinematics of the Main Boundary Thrust and related neotectonics in the Darjiling Himalayan fold-and-thrust belt, West Bengal, India. *J. Struct. Geol.* 22, 1261–1283. doi: 10.1016/s0191-8141(00)00032-8

Mukul, M. (2010). First-order kinematics of wedge-scale active Himalayan deformation: insights from Darjiling-Sikkim-Tibet (DaSiT) wedge. *J. Asian Earth Sci.* 39, 645–657. doi: 10.1016/j.jseaes.2010.04.029

Mukul, M., Jade, S., and Matin, A. (2009). Active deformation in the Darjiling-Sikkim Himalaya based on 2000-2004 Geodetic Global Positioning System measurements. *GPS Geodesy* 2009, 1–28.

Mukul, M., Jade, S., Ansari, K., Matin, A., and Joshi, V. (2018). Structural insights from geodetic Global Positioning System measurements in the Darjiling-Sikkim Himalaya. *J. Struct. Geol.* 114, 346–356. doi: 10.1016/j.jsg.2018.03.007

Mukul, M., Jaiswal, M., and Singhvi, A. K. (2007). Timing of out-of-sequence active deformation in the frontal Himalayan wedge: Insights from the Darjiling sub-Himalaya. India. *Geology* 35, 999–1002. doi: 10.1130/G23869A.1

Nabelek, J., Hetényi, G., Vergne, J., Sapkota, S., Kafle, B., Jiang, M., et al. (2009). Underplating in the Himalaya−Tibet collision zone revealed by the Hi−CL IMB experiment. *Science* 325, 1371–1374. doi: 10.1126/science.1167719

Nakata, T. (1972). Geomorphic history and crustal movement of the foot-hills of the Himalayas. *Sci. Rep. Tohoku Univ.* 22, 39–177.

Ni, J., and Barazangi, M. (1984). Seismotectonics of the Himalayan Collision Zone: geometry of the underthrusting Indian Plate beneath the Himalaya. *J. Geophys. Res.* 89, 1147–1163. doi: 10.1029/jb089ib02p01147

Ojha, T. P., Butler, R. F., Quade, J., DeCelles, P. G., Richards, D., and Upreti, B. N. (2000). Magnetic polarity stratigraphy of the Neogene Siwalik Group at Khutia Khola, far western Nepal. *Geol. Soc. Am. Bull.* 112, 424–434. doi: 10.1130/0016-76062000112<424:MPSOTN<2.0.CO;2

Oldham, R. D. (1917). Structure of the Himalayas and Indo-Gangetic plains. *Memoir Geolog. Survey India* 1917:156.

Orme, D. A., Reiners, P. W., Hourigan, J. K., and Carrapa, B. (2015). Effects of inherited cores and magmatic overgrowths on zircon (U-Th)/He ages from Greater Himalayan sequence rocks, Mt. Everest region, Tibet. *Geochem. Geophys. Geosyst.* 16, 2499–2507. doi: 10.1002/2015GC005818

Pandey, M. R., Tandukar, R. P., Avouac, J. P., Lavé, J., and Massot, J. P. (1995). Interseismic strain accumulation on the Himalayan crustal ramp (Nepal). *Geophys. Res. Lett.* 22, 751–754. doi: 10.1029/94gl02971

Pandey, M. R., Tandukar, R. P., Avouac, J. P., Vergne, J., Heritier, and Th. (1999). Seismotectonics of the Nepal Himalaya from a local seismic network. *J. Asian Earth Sci.* 17, 703–712. doi: 10.1016/s1367-9120(99)00034-6

Paul, H., Mitra, S., Bhattacharya, S. N., and Suresh, G. (2015). Active transverse faulting within underthrust Indian crust beneath the Sikkim Himalaya. *Geophys. J. Int.* 201, 1070–1081. doi: 10.1093/gji/ggv058

Powers, P. M., Lillie, R. J., and Yeats, R. S. (1998). Structure and shortening of the Kangra and Dehra Dun reentrants, Sub-Himalaya, India. *Geol. Soc. Am. Bull.* 110, 1010–1027. doi: 10.1130/0016-760619 98110

Raiverman, V., Kunte, S. V., and Mukherjea, A. (1983). Basin geometry, Cenozoic sedimentation and hydrocarbon in northwestern Himalaya and Indo-Gangetic plains. *Petrol. Geol. Asia J.* 6, 67–92. doi: 10.1016/0040-1951(80)90136-5

Rajaure, S., Sapkota, S. N., Adhikari, L. B., Koirala, B., Bhattarai, M., Tiwari, D. R., et al. (2013). Double difference relocation of local earthquakes in the Nepal Himalaya. *J. Nepal Geolog. Soc.* 46, 133–142.

Rajendra Prasad, B., Klemperer, S. L., Vijaya Rao, V., Tewari, H. C., and Khare, P. (2011). Crustal structure beneath the Sub-Himalayan fold–thrust belt, Kangra recess, northwest India, from seismic reflection profiling: Implications for late Paleoproterozoic orogenesis and modern earthquake hazard. *Earth Planetar. Sci. Lett.* 308, 218–228. doi: 10.1016/j.epsl.2011.05.052

Rao, M. B. R. (1973). The subsurface geology of the Indo-Gangetic plains. *J. Geolog. Soc. India* 14, 217–242.

Robert, X., van der Beek, P., Braun, J., Perry, C., and Mugnier, J.-L. (2011). Control of detachment geometry on lateral variations in exhumation rates in the Himalaya: Insights from low-temperature thermochronology and numerical modeling. *J. Geophys. Res.* 116:B05202. doi: 10.1029/2010JB007893

Robinson, D. M., DeCelles, P. G., Patchett, P. J., and Garzione, C. N. (2001). The kinematic history of the Nepalese Himalaya interpreted from Nd isotopes. *Earth Planetary Sci. Lett.* 192, 507–521. doi: 10.1016/S0012-821X(01)00451-4

Robinson, D. P., Das, S., and Watts, A. B. (2006). Earthquake Rupture Stalled by a Subducting Fracture Zone. *Science* 312, 1203–1205. doi: 10.1126/science.1125771

Sahoo, P. K., Kumar, S., and Singh, R. P. (2000). Neotectonic study of Ganga and Yamuna tear faults, NW Himalaya, using remote sensing and GIS. *Int. J. Remote Sens.* 21, 499–518. doi: 10.1080/014311600210713

Sastri, V. V., Bhandari, L. L., Raju, A. T. R., and Datta, A. K. (1971). Tectonic framework and subsurface stratigraphy of the Ganga Basin. *J. Geol. Soc. India* 12, 222–233.

Searle, M. P., and Treloar, P. J. (2019). "Introduction to Himalayan tectonics: a modern synthesis," in *Himalayan Tectonics: A Modern Synthesis*, eds P. J. Treloar and M. P. Searle (London: Geological Society of London Special Publications), 1–17. doi: 10.1144/sp483-2019-20

Searle, M. P., Law, R. D., Godin, L., Larson, K. P., Streule, M. J., Cottle, J. M., et al. (2008). Defining the Himalayan Main Central Thrust in Nepal. *J. Geol. Soc. Lond.* 165, 523–534. doi: 10.1144/0016-76492007-081

Searle, M. P., Simpson, R. L., Law, R. D., Parrish, R. R., and Waters, D. J. (2003). The structural geometry, metamorphic and magmatic evolution of the Everest massif, High Himalaya of Nepal–South Tibet. *J. Geol. Soc.* 160, 345–366. doi: 10.1144/0016-764902-126

Sears, J. W. (2016). "Template for the Cordilleran magmatic arc and its detached carapace, Idaho and Montana," in *Belt Basin: Window to Mesoproterozoic Earth*, ed. J. S. MacLean (Boulder, CO: Geological Society of America), 365–384. doi: 10.1130/2016.2522(14)

Seifert, N. (2019). *Structural analysis of the Benkar Fault Zone, a cross structure in the higher Himalaya of the Khumbu Region, eastern Nepal*. Bozeman, MT: Montana State University.

Seifert, N., Hubbard, M. S., Gajurel, A. P., and Shaw, C. A. (2019). "Structural analysis of the Benkar Fault zone, a cross structure in the Higher Himalaya of the Khumbu region, eastern Nepal," in *34th Himalayan-Karakorum-Tibet Workshop*, eds A. Laskowski, D. Orme, M. Hubbard, D. Lageson, and K. Thomson (Bozeman, MT: Montana State University).

Selverstone, J. (1988). Evidence for east-west crustal extension in the eastern alps: implications for the unroofing history of the Tauern Window. *Tectonics* 7, 87–105. doi: 10.1029/tc007i001p00087

Shanker, D., Paudyal, H., and Singh, H. N. (2011). Discourse on seismotectonics of Nepal Himalaya and vicinity. *Geosciences* 1, 1–15. doi: 10.5923/j.geo.20110101.01

Silver, C. R. P., Murphy, M. A., Taylor, M. H., Gosse, J., and Baltz, T. (2015). Neotectonics of the Western Nepal Fault System: Implications for Himalayan strain partitioning. *Tectonics* 34, 2494–2513. doi: 10.1002/2014TC003730

Soucy La Roche, R., and Godin, L. (2019). Inherited cross-strike faults and Oligocene-early Miocene segmentation of the Main Himalayan Thrust, West Nepal. *J. Geophys. Res. Solid Earth* 124, 7429–7444. doi: 10.1029/2019JB017467

Soucy La Roche, R., Godin, L., Cottle, J. M., and Kellett, D. A. (2016). Direct shear fabric dating constrains early Oligocene onset of the South Tibetan detachment in the western Nepal Himalaya. *Geology* 44, 403–406. doi: 10.1130/G37754.1

Soucy La Roche, R., Godin, L., Cottle, J. M., and Kellett, D. A. (2018). Preservation of the early evolution of the Himalayan middle crust in foreland klippen: insights from the Karnali klippe, west Nepal. *Tectonics* 37, 1161–1193. doi: 10.1002/2017TC004847

Soucy La Roche, R., Godin, L., Cottle, J. M., and Kellett, D. A. (2019). Tectonometamorphic evolusion of the tip of the Himalayan metamorphic core in the Jajarkot klippe, west Nepal. *J. Metam. Geol.* 37, 239–269. doi: 10.1111/jmg.12459

Srivastava, P., and Mitra, G. (1994). Thrust geometries and deep structure of the outer and lesser Himalaya, Kumaon and Garhwal (India): Implication for evolution of the Himalayan fold-and-thrust belt. *Tectonics* 13, 89–109. doi: 10.1029/93TC01130

Srivastava, V., and Mukul, M. (2020). Cataclastic strain from external thrust sheets in fold-thrust belts: Insights from the frontal Indian Himalaya. *J. Asian Earth Sci.* 188, G37754.1.

Srivastava, V., Mukul, M., Barnes, J. B., and Mukul, M. (2018). Geometry and kinematics of Main Frontal thrust-related fault propagation folding in the Mohand Range, northwest Himalaya. *J. Struct. Geol.* 115, 1–18. doi: 10.1016/j.jsg.2018.06.022

Srivastava, V., Mukul, Malay, and Barnes, J. B. (2016). Main Frontal Thrust deformation and topographic growth of the Mohand Range, northwest Himalaya. *J. Struct. Geol.* 93, 131–148. doi: 10.1016/j.jsg.2016.10.009

Srivastava, V., Mukul, Manas, Mukul, and Malay. (2017). Quaternary deformation in the Gorubathan recess: Insights on the structural and landscape evolution in the frontal Darjiling Himalaya. *Q. Int.* 462, 138–161. doi: 10.1016/j.quaint.2017.05.004

Stearns, R. G. (1955). Low-angle overthrusting in the central Cumberland Plateau, Tennessee. *Bull. Geol. Soc. Am.* 66, 615–628. doi: 10.1130/0016-7606(1955)66[615:loitcc]2.0.co;2

Stevens, V. L., and Avouac, J. P. (2015). Interseismic coupling on the main Himalayan thrust. *Geophys. Res. Lett.* 42, 5828–5837. doi: 10.1002/2015GL064845

Stevens, V. L., and Avouac, J. P. (2016). Millenary Mw>9.0 earthquakes required by geodetic strain in the Himalaya. *Geophys. Res. Lett.* 43, 1118–1123. doi: 10.1002/2015GL067336

Suess, E. (1904). *The Face of the Earth (Das Antlitz der Erde)*. United Kingdom: Clarendon Press, Oxford, 604.

Szulc, A. G., Najman, Y., Sinclair, H. D., Pringle, M., Bickle, M., Chapman, H., et al. (2006). Tectonic evolution of the Himalaya constrained by detrital 40Ar-39Ar, Sm-Nd and petrographic data from the Siwalik foreland basin succession, SW Nepal. *Basin Res.* 18, 375–391. doi: 10.1111/j.1365-2117.2006.00307.x

Thakur, V. C. (1998). Structure of the Chamba nappe and position of the Main Central Thrust in Kashmir Himalaya. *J. Asian Earth Sci.* 16, 269–282. doi: 10.1016/s0743-9547(98)00011-7

Thakur, V. C., Jayangondaperumal, R., and Joevivek, V. (2019). "Seismotectonics of central and NW Himalaya: plate boundary-wedge thrust earthquakes in thin- and thick-skinned tectonic framework," in *Crustal Architecture and Evolution of the Himalaya-Karakoram Tibet Orogen*, eds R. Sharma, I. M. Villa, and S. Kumar (London: Geological Society of London), doi: 10.1144/SP481.8

Thakur, V. C., Joshi, M., Sahoo, D., Suresh, N., Jayangondapermal, R., and Singh, A. (2014). Partitioning of convergence in Northwest Sub-Himalaya: Estimation of late Quaternary uplift and convergence rates across the Kangra re-entrant, North India. *Int. J. Earth Sci.* 103, 1037–1056. doi: 10.1007/s00531-014-1016-7

Thiede, R., Robert, X., Stübner, K., Dey, S., and Faruhn, J. (2017). Sustained out-of-sequence shortening along a tectonically active segment of the Main Boundary thrust: The Dhauladhar Range in the northwestern Himalaya. *Lithosphere* 9, 717–725. doi: 10.1130/L630.1

Upreti, B. N., Rai, S. M., Sakai, H., Koirala, D. R., and Takigami, Y. (2003). Early Proterozoic granite of the Taplejung Window, far eastern Lesser Nepal Himalaya. *J. Nepal Geol. Soc.* 28, 9–18.

Valdiya, K. S. (1976). Himalayan transverse faults and folds and their parallelism with subsurface structures of North Indian plains. *Tectonophysics* 32, 353–386. doi: 10.1016/0040-1951(76)90069-x

van der Beek, P., Litty, C., Baudin, M., Mercier, J., Robert, X., and Hardwick, E. (2016). Contrasting tectonically driven exhumation and incision patterns, western versus central Nepal Himalaya. *Geology* 44, 327–330. doi: 10.1130/G37579.1

Veevers, J. J., and Tewari, R. C. (1995). *Gondwana master basin of peninsular India between Tethys and the interior of the Gondwanaland province of Pangea*. Boulder: Geological Society of America, Memoirs. 187.

Virdi, N. S. (1979). On the geodynamic significance of mega-lineaments in the outer and lesser regions of western Himalaya. *Himal. Geol.* 9, 79–99.

Webb, A. A. G., Guo, H., Clift, P. D., Husson, L., Müller, T., Costantino, D., et al. (2017). The Himalaya in 3D: Slab dynamics controlled mountain building and monsoon intensification. *Geosphere* 9, 637–651. doi: 10.1130/L636.1

Weinberg, R. F. (2016). Himalayan leucogranites and migmatites: nature, timing and duration of anatexis. *J. Metamorp. Geol.* 34, 821–843. doi: 10.111/jmg.12204

Wesnousky, S. G., Kumahara, Y., Chamlagain, D., and Neupane, P. J. (2019). Large Himalayan Frontal Thrust paleoearthquake at Khayarmara in eastern Nepal. *J. Asian Earth Sci.* 174, 346–351. doi: 10.1016/j.jseaes.2019.01.008

Yeats, R. S., and Lillie, R. J. (1991). Contemporary tectonics of the Himalayan frontal fault system: folds, blind thrusts and the 1905 Kangra earthquake. *J. Struct. Geol.* 13, 215–225. doi: 10.1016/0191-8141(91)90068-t

Yin, A. (2006). Cenozoic tectonic evolution of the Himalayan orogen as constrained by along-strike variation of structural geometry, exhumation history, and foreland sedimentation. *Earth Sci. Rev.* 76, 1–131. doi: 10.1016/j.earscirev.2005.05.004

Yin, A., and Taylor, M. (2011). Mechanics of V-shaped conjugate strike-slip faults and the corresponding continuum mode of continental deformation. *Geol. Soc. Am. Bull.* 123, 1798–1821. doi: 10.1130/B30159.1

Zhao, W., Nelson, K. D., and Project Indepth Team. (1993). Deep seismic reflection evidence for continental underthrusting beneath southern Tibet. *Nat. Geosci.* 366, 557–559. doi: 10.1038/366557a0

Conflict of Interest: The authors declare that the research was conducted in the absence of any commercial or financial relationships that could be construed as a potential conflict of interest.

frontiers in Earth Science

BRIEF RESEARCH REPORT
published: 26 April 2021
doi: 10.3389/feart.2021.658146

Constraining the Moho Depth Below Bhutan With Global-Phase Seismic Interferometry

Anne Obermann[1], Elmer Ruigrok[2], Irene Bianchi[3,4] and György Hetényi[5]*

[1] Swiss Seismological Service, ETH Zurich, Zurich, Switzerland, [2] Royal Netherlands Meteorological Institute, De Bilt, Netherlands, [3] Istituto Nazionale di Geofisica e Vulcanologia, Rome, Italy, [4] Institute of Meteorology and Geophysics, University of Vienna, Vienna, Austria, [5] Institute of Earth Sciences, University of Lausanne, Lausanne, Switzerland

We use a novel technique named global-phase seismic interferometry (GloPSI) to image the lithospheric structure, and in particular the Moho, below two parallel north-south transects belonging to the GANSSER network (2013–2014). The profiles cross the Himalayan orogenic wedge in Bhutan, a tectonically important area within the largest continent-continent collision zone on Earth that is still undergoing crustal thickening and represents a challenging imaging target for the GloPSI approach. GloPSI makes use of direct waves from distant earthquakes and receiver-side reverberations with near vertical incidence. Reflections are isolated from earthquake recordings by solving a correlation integral and are turned into a reflectivity image of the lithosphere below the arrays. Our results compare favorably with first-order features observed from a previous receiver function (RF) study. We show that a combined interpretation of GloPSI and RF results allows for a more in-depth understanding of the lithospheric structure across the orogenic wedge in Bhutan.

Keywords: Bhutan, Himalaya, global-phase seismic interferometry, Moho, Main Himalayan Thrust

OPEN ACCESS

Edited by:
Pascal Audet,
University of Ottawa, Canada

Reviewed by:
Eric Sandvol,
University of Missouri, United States
Florian Millet,
University of Cambridge, United Kingdom

****Correspondence:***
Anne Obermann
anne.obermann@sed.ethz.ch

Specialty section:
This article was submitted to Solid Earth Geophysics, a section of the journal Frontiers in Earth Science

Received: *25 January 2021*
Accepted: *31 March 2021*
Published: *26 April 2021*

Citation:
Obermann A, Ruigrok E, Bianchi I and Hetényi G (2021) Constraining the Moho Depth Below Bhutan With Global-Phase Seismic Interferometry. Front. Earth Sci. 9:658146. doi: 10.3389/feart.2021.658146

INTRODUCTION

The temporary passive seismic experiment GANSSER (Geodynamics ANd Seismic Structure of the Eastern Himalaya Region) continuously recorded seismic data from a total of 37 broadband stations in Bhutan from January 2013 to November 2014. It was the first seismological project to address the lithospheric structure across the eastern third of the Himalayas. This is of interest because the segment beneath Bhutan is the only segment along the Himalayan collision belt where a basement uplift in the foreland, the Shillong Plateau, reaches high elevation, as a result of exhumation since the Pliocene (Biswas et al., 2007; Najman et al., 2016), and the region features mostly strike-slip mechanism earthquakes (Drukpa et al., 2006), unlike the Central Himalaya. Bhutan's structural segment boundaries within the Himalayas are highlighted both by gravity anomaly residuals and by orogen-crossing mid- to lower crustal seismicity of the underthrusting plate (Hammer et al., 2013; Hetenyi et al., 2016a; Diehl et al., 2017). Both the Bhutan Himalayas and the Shillong Plateau can accommodate great earthquakes, as witnessed by the 1714 and 1897 events, respectively (Bilham and England, 2001; Berthet et al., 2014; Hetenyi et al., 2016b, 2018; Le Roux-Mallouf et al., 2016). However, as demonstrated by Coulomb stress modeling, the two regions are seismotectonically less linked than previously proposed (Grujic et al., 2018).

The structure of the orogenic wedge in Bhutan features the Main Himalayan Thrust (MHT), along which the underthrusting plate slides beneath the Himalaya. This is similar to the rest of the mountain belt, however, both the Moho and the MHT geometry present lateral variations between West and East Bhutan, over a distance of ca. 180 km (Singer et al., 2017a), as well as when compared to other cross-sections across the orogen (Subedi et al., 2018). On receiver function (RF) images by Singer et al. (2017a), in the West (along 89.5–90°E) the Moho is at ca. 50 km depth at the front of the orogen in the south, and turns into a ramp ca. 70 km further north. The MHT is less clear, but is at roughly 15 km depth and turns into a ramp, in such a way that the underthrusting crust keeps a constant thickness. The trend at depth of the MHT, and the consequent separation between the over and underthrusted crusts is largely consistent with the thermokinematic modeling results of Coutand et al. (2014). In the East (around 91.5°E), the Moho is at 50 km depth at the front of the orogeny as well, but appears sub-horizontal beneath Bhutan, and steepens gently farther north to connect to deeper Moho segments beneath southern Tibet (Shi et al., 2015). The MHT is somewhat shallower than in the West, being located at ca. 12 km depth. The intra-crustal microseismicity also varies laterally: while it is well focused along the MHT in the East, it is more diffuse and is partly "shifted" below the MHT in the West (Diehl et al., 2017), which corresponds well with the pattern of interseismic coupling obtained from GPS observations (Marechal et al., 2016). Both, the Western and the Eastern line RF images include intra-crustal converters beneath the MHT, which are not constrained by surface geology. These features can result from the deformational Himalayan orogeny (Singer et al., 2017a) or may be inherited elements of the underthrusting plate or terrain. In the upper part of the orogenic wedge, ambient noise tomography from the same seismic network data shows shear-wave anomalies that are well correlated with the tectonic structures known from structural geology at the surface (Singer et al., 2017b).

Here, we exploit data from the GANSSER network for an application of the global-phase seismic interferometry (GloPSI) method (Ruigrok and Wapenaar, 2012; Frank et al., 2014; Bianchi et al., 2021). The main aim is to image the Moho below the two parallel north-south transects crossing the Himalayan orogenic wedge in Bhutan, based on P-wave reflectivity, and to compare it with the RF observations (P- to S-wave conversions). GloPSI makes use of phase arrivals and their receiver-side reverberations from earthquakes at epicental distances of 120–180° (**Figure 2**). These phases impinge on the lithosphere from below with small angles of incidence. The method hereby assumes horizontal and slightly dipping reflectors that extend at least as far as the diameter of the Fresnel volume. The maximum dip that can be imaged with GloPSI, is heavily dependent on the illumination. If there is "full" illumination with global phases, that is good coverage from ray-parameter $p = 0$ until $p = 0.04$ s/km, then the maximum dip that can be imaged is around 14° for reflectors in the lower crust [phi = arcsin(pv), where v is the velocity in the lower crust]. The reflections are isolated from the earthquake recordings with auto-correlation and stacking. For more details on the SI theory illustrated with modeling, please refer to, e.g., Frank et al. (2014), Draganov et al. (2006); Ruigrok et al. (2008), and Ruigrok et al. (2010). With a migration step, the resulting reflection responses are turned into a reflectivity image of the lithosphere below the arrays. In this way, we use a different, independent waveform set to study the Moho. The challenge is twofold: how does GloPSI perform in an environment of relatively thick crust, with traces and imprints of orogenic deformation, and how feasible is it to retrieve useful signals from a relatively small-aperture profile with a small number of, but densely spaced stations, compared to typical GloPSI processing.

DATA AND METHODS

Data

We use 16 months of seismic data records collected from the temporary GANSSER network in Bhutan (data[1]) between January 2013 and November 2014. The stations operated in continuous recording mode, at 100 samples per second, and data recovery rate exceeded 90%. To work along densely spaced profiles, we selected data from the 28 three-component broadband seismometers that were set up along two almost straight, north-south arrays across the Himalayan orogenic wedge in Western (16 stations along a 116 km deployment) and Eastern (12 stations along a 98 km deployment) Bhutan, respectively (**Figure 1A**). Station spacing was as equidistant and linear as access and local conditions allowed. All stations operated for 16 months, and about a third of the stations for the full 22 months.

In the raw seismic records, we looked for direct waves that reach the GANSSER array while traveling through the Earth's core. We are therefore interested in large magnitude $M > 6$ seismic events occurring between 120 and 180° epicentral distance, at any depth range (**Figures 1B**, **2**). For this purpose, we created a list of events occurring within the region of interest from January 2013 to November 2014 from the EMSC website[2]. We then visually selected waveforms with clear P-wave arrivals. For this purpose, we plotted each event for all stations and discarded unclear traces or entire events. We selected 59 earthquakes with $M > 6$ (**Supplementary Table 1**), in the desired epicentral distance range (**Figure 1B**). For each earthquake we selected a time window of 50 s in length, starting at the first arrival (PKiKP, PKP, or PKIKP, Stein and Wysession, 2009) and containing subsequent reverberations in the lithosphere. To limit the occurrence of cross-terms in the autocorrelations that might appear if PKIKP and PKP phase responses are simultaneously present, we use only time windows with one single dominant phase response.

Method

The selected phase responses have a good signal-to-noise ratio and at most, only four traces are missing per event. We can detect PKP over a large distance range, which should enable a stack of sufficient illumination angles to correctly estimate the timing of the main zero-offset reflections. The different data processing

[1]http://data.datacite.org/10.12686/sed/networks/xa

[2]www.emsc-csem.org

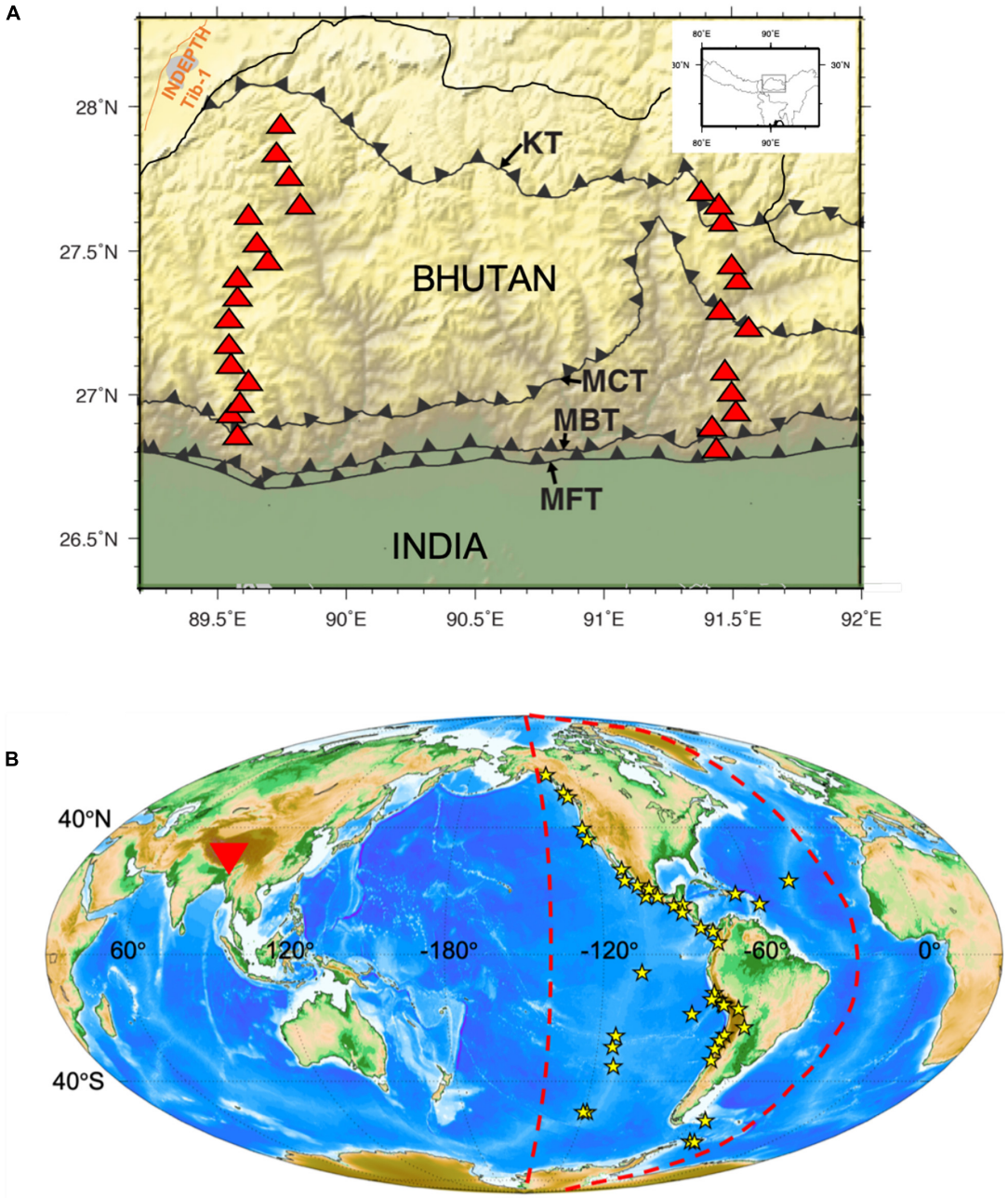

FIGURE 1 | (A) Temporary seismic network stations (red triangles) from the GANSSER project in Bhutan selected for GloPSI application in this study. Main thrust faults are shown on the map: Main Frontal Thrust (MFT), the Main Boundary Thrust (MBT), Main Central Thrust (MCT), and Kakhtang Thrust (KT). The brown line, northwest of Bhutan, indicates the location of the wide-angel reflection profile Tib-1 of the INDEPTH project (e.g., Hauck et al., 1998). **(B)** Selected earthquakes (yellow stars) at epicentral distances of 120–180° (red dashed lines) from Bhutan (red triangle) with a sufficiently high signal-to-noise ratio. We found 59 earthquakes with $M > 6.0$ that satisfy these criteria.

steps are subsequently described and illustrated below in **Figure 3** for Western (left) and Eastern Bhutan (right).

The first step is the application of seismic interferometry, which for GloPSI, amounts to the autocorrelation and stacking of selected time windows, and the flipping of the amplitudes (**Figures 3** A1, B1). The Z-component records are used as a proxy for the P-wave transmission responses. For each phase, we apply a series of processing steps before stacking the autocorrelations. After loading an instrumentally deconvolved phase response, a mild spectral whitening is applied. This whitening function is implemented with a sliding frequency window. The large earthquakes that we typically use have a very low corner frequency. At larger frequencies, there is a significant drop in amplitudes. The whitening is thus necessary to boost the higher

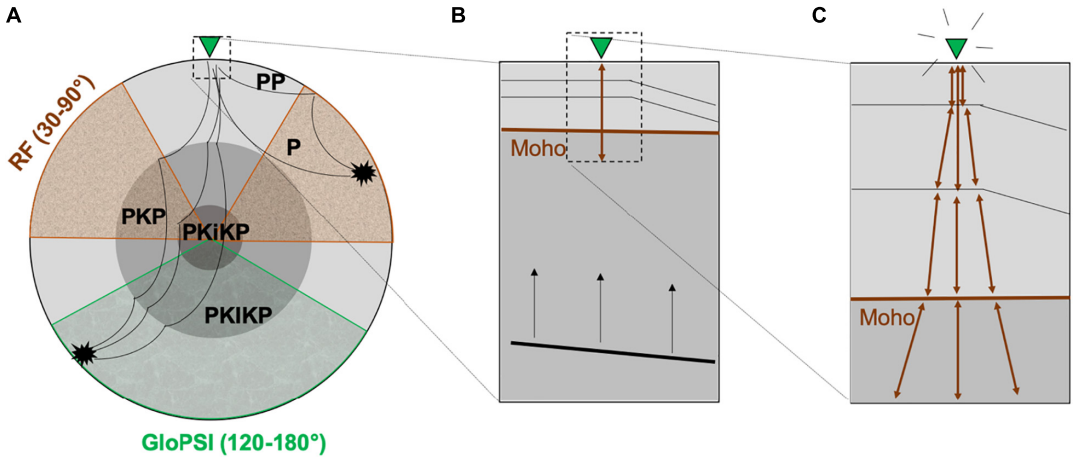

FIGURE 2 | (A) Illustration of raypaths (black lines) between a source (black star) and a receiver (green triangle) for the most prominent P phases. The typical epicentral distances for GloPSI and RF are marked with shading. **(B)** Close-up of the medium below the receiver, with a global phase wavefront just before it impinges on the lithosphere. **(C)** Illustration of exemplary zero-offset reflection responses used in GloPSI (modified from Ruigrok and Wapenaar, 2012).

frequencies and to construct a reflection image with sufficient resolution. The upper limit can be selected at a frequency where there remains a sufficiently high signal-to-noise-ratio for all events. In our case, we applied a spectral whitening in the range of 0.01–1.4 Hz, with a sliding frequency window length of 0.12 Hz. The whitening from very low frequencies onward, boosts the direct P-wave pulse, which can be easily removed with a taper (**Figures 3** A2, B2). Since this part of the signal is of a much higher amplitude than the following wiggles, the signal of interest with relatively lower amplitudes can be better seen after removal. Subsequently, a bandpass filter is applied between 0.2 and 1 Hz in order to remove the low frequency sidelobes and consequently discard the red-to-blue difference from crust to mantle that could be observed in **Figures 3** A1, B1. Similar to the HiCLIMB dataset across Tibet (Ruigrok and Wapenaar, 2012), there were not enough phase responses to stack out the source-side reverberations completely. They were suppressed by substracting the scaled average trace over the array from each individual trace. This processing step introduces collateral damage which suppresses actual horizontal reflectors, if such reflector exists over a large part of the array. Hence, this step is not to be applied to the data for the interior of the continents. Average removal was not needed in Bianchi et al. (2021) who applied GloPSI to an array that was deployed for a similar duration.

We then apply a static correction and eliminate free-surface multiples at the receiver side (step3, **Figures 3** A3, B3) following the method from Verschuur and Berkhout (1997). There could also be triplications of the PKP phase from the source side, or possibly over the D″ discontinuity. As long as the different triplications have a similar ray-parameter, their detrimental effect is also suppressed with this step. However, if there were multiple strong arrivals in one phase response with different angles of incidence, such a panel would need to be excluded from further analysis. Since no strong reflectors are observed beyond a 15 s delay time, in **Figures 3** A4, B4, we show the traces with accurate spatial distribution for the first 15 s delay time only, which corresponds to a depth of ca. 100 km. This is also the depth range to which we migrate the reflectors (**Figure 4**). The limitation to the top 100 km is not inherent to the GloPSI-technique, but a consequence of our spatially sparse data set. We would like to point out that during the processing, no further normalization is applied, except for the whitening. Over the array, and over various depths, the relative amplitudes should be meaningful. However, imaging is done without loss correction and hence the amplitude distribution is somewhat biased in the direction of the middle and upper crust. In the frequency band we selected, there is a strong focus on the Moho and upper mantle. As a last step, the station-wise stacks are time-to-depth converted using the P-wave velocities of the same simplified 1D velocity model that was used by Singer et al. (2017a) for the RF depth migration. The model assumes a constant crustal Vp velocity gradient of 0.0118 s^{-1} starting from 5.9 km/s at the surface. The average Moho depth is set at around 50 km depth, with a Vp jump from 6.5 to 8 km/s. The mantle Vp gradient is then 0.0016 s^{-1}. These gradients are based on a local minimum 1D Vp velocity model obtained from regional earthquakes (Diehl et al., 2017). The resultant first order lithospheric structure across the orogenic wedge in Western and Eastern Bhutan is shown in **Figure 4**. A depth of 100 km is reached after 14.3 s with the 1D Vp model.

RESULTS AND INTERPRETATION

From the obtained final GloPSI images alone (**Figure 4**), it would be difficult to confidently interpret the depth and geometry of the reflectors. We recall that the methods' strength lies in laterally tracing a physical parameter produced by material differences in the crust that produces a similar signal at depth. We cannot resolve fine structures, such as thin layering, but we can resolve larger structures that show continuity in space which can give us important information about the seismic facies. Moreover, because of the large station spacing and the inability to image

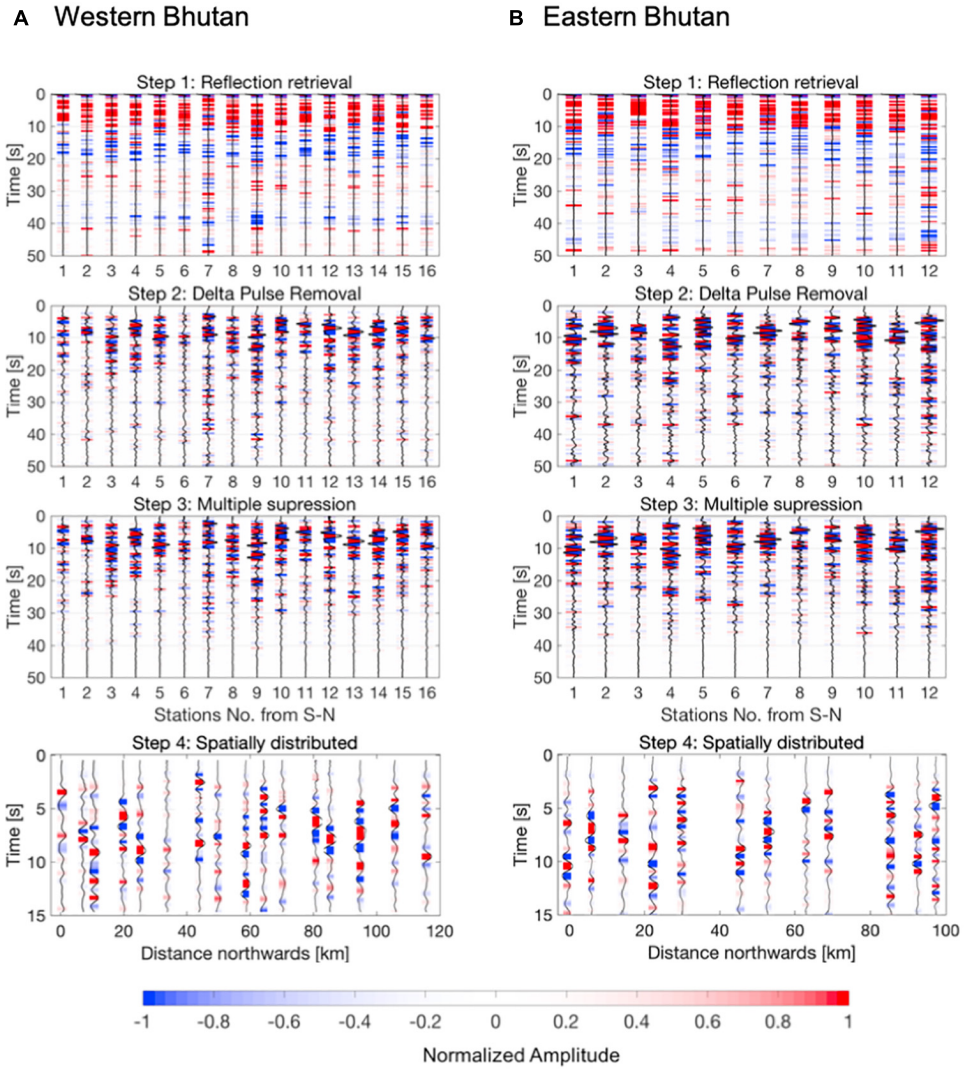

FIGURE 3 | Data processing steps for the profiles in Western **(A)** and Eastern **(B)** Bhutan. After autocorrelation and stacking (step 1), the delta pulse is removed (step 2), and the multiples are suppressed (step 3). In step 4, the traces are shown with accurate spatial distribution for the first 15 s, which correspond to a depth of around 100 km. The amplitudes are normalized to the maximum value after each processing step, which causes the shift in colors after the delta pulse removal.

steep dips, the lateral continuity is not accurately reproduced in the images. This could be potentially improved with more data. From the reflection retrieval, shown in **Figure 3**, step 1, we see a clear change in reflectivity at around 10 s which is an indicator of the boundary between the crust (mostly positive amplitudes) and the mantle (mostly negative amplitudes), for both Eastern and Western Bhutan. For the interpretation of structures, we show our migrated results together with the location of converter points identified in the RF study by Singer et al. (2017a) (shown as filled circles) in **Figure 4**. Thanks to these earlier observations, we can point to the two most prominent reflectors and interpret them, due to known interfaces, as being the Moho and the MHT, and also point to some reflectivity patterns within the crust. In Western Bhutan, the Moho can clearly be identified at around 50 km depth and is slightly dipping toward the North, in agreement with the flexural deepening of the downgoing plate. The shallowest clear horizon is seen at approximately 20 km depth, and is identified as the MHT, with a flat geometry in the East, and northward deepening in the West. In the East, the Moho reflector dips at a lower angle toward the North. The shallowest clear horizon interpreted as MHT is seen at approximately 15 km depth. Within the crust, there is a near parallel layering in the East, while such a pattern is not detected in the West. As a result of the comparison between the two techniques, with RF being especially sensitive to S-wave structure, and GloPSI being especially sensitive to P-wave structure, we can say:

1. The Moho is well visible in Eastern and Western Bhutan with both methods, with matching results. The two techniques corroborate each other for both the flat geometry of the Moho (southern parts of both profiles) and the slightly dipping parts (northern parts). The Moho

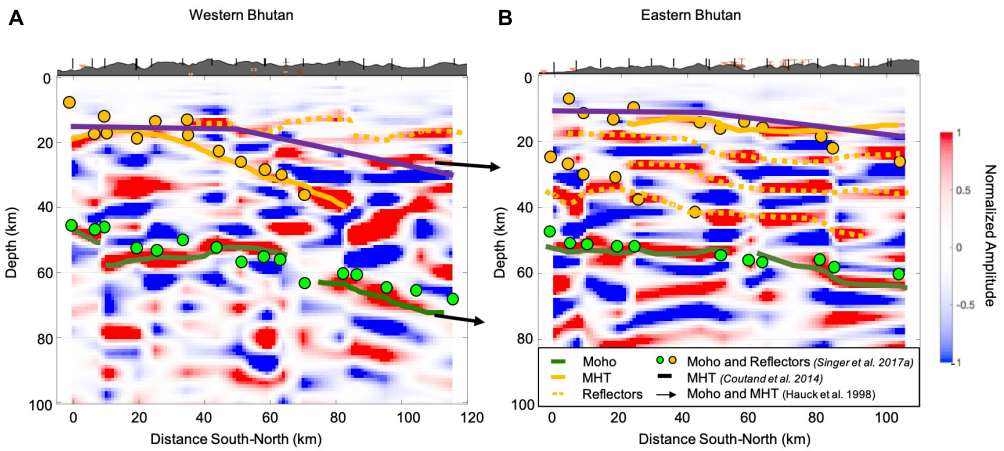

FIGURE 4 | First-order lithospheric structure across the orogenic wedge in Western **(A)** and Eastern **(B)** Bhutan from the depth converted GloPSI reflections. The thick green line indicates the interpreted Moho reflector, the solid orange line the Main Himalayan Thrust (MHT) and dotted orange lines indicate intra-crustal reflectors. The orange and green circles are the interpreted RF converters from Singer et al. (2017a) for crustal interfaces and Moho, respectively. The thick violet line indicates the approximate location of the MHT from multi-thermochronologic data interpreted by Coutand et al. (2014). The black arrows in Western Bhutan show the extrapolated dip of the MHT and Moho, as interpreted from the seismic reflection profile INDEPTH Tib-1 by Hauck et al. (1998). On top of both profiles, the topography is shown and the vertical ticks mark the stations location.

kink is not so obvious from GloPSI; the Moho signal is indeed not visible between approximately 60 and 80 km profile distance (on the Western profile), while it is visible elsewhere. In a similar way, the Moho signal is fading between approximately 60 and 80 km distance along the Eastern profile.

With our image we support previous results (i.e., Hauck et al., 1998; Schulte-Pelkum et al., 2005; Singer et al., 2017a) in the identification of an inclined continuous Moho, instead of a stepped Moho due to imbricated crust (Hirn and Sapin, 1984; Molnar, 1988; Galvé et al., 2002).

2. The shallower reflectors (less than 20 km deep) are well visible in the GloPSI images, better than from the RF. These reflectors are likely linked to the MHT, the predominant intracrustal collision structure in the Himalaya orogen (Coutand et al., 2014). To the images (**Figure 4**, violet line), we added the MHT depth proposed by Coutand et al. (2014). The authors then collected multi-thermochronologic data at various points along similar profiles. In particular, in Eastern Bhutan, the depth and geometry of the MHT correlate well with our results. In Western Bhutan, we added the extrapolated reflectors obtained from the wide-angle seismic reflection profile INDEPTH Tib-1 (**Figure 4A**, black arrows) that was acquired in the Higher Himalayas (Hauck et al., 1998), northwest of Bhutan (**Figure 1**).

In Western Bhutan, the dip of the MHT and the presence of anisotropy associated to it, are structural reasons for preventing a good resolution of that feature by GloPSI, and might cause the discrepancy between the location of the MHT from different studies (yellow and purple lines in **Figure 4A** display some consistent offset). Schulte-Pelkum et al. (2005) interpreted the RF signals from the MHT in eastern Nepal as an anisotropic shear zone representing the upper crustal detachment zone. Singer et al. (2017a) instead imaged the MHT as a negative RF arrival and a ramp structure.

3. Intra-crustal reflectivity in Eastern Bhutan is stronger than in Western Bhutan, hinting at a difference in physical properties or deformational history of the crust penetrating beneath the orogenic wedge (Singer et al., 2017a). Although the flexural shape of the downgoing plate's lithosphere seems to be similar between West and East Bhutan (Hammer et al., 2013; Hetenyi et al., 2016a), physical characteristics of the crust reflect spatially smaller scale properties, for which there is no clear information available, concerning their origins. We speculate that the reflectivity is inherited, but note that further research in the footsteps of e.g., Talwani et al. (2016) and Mallick et al. (2020) is required.

DISCUSSION

With the use of temporary seismic network data and as few as 59 teleseismic events, the GloPSI approach allowed us to outline the main lithospheric structures of the Bhutan Himalaya along two transects. The interpretation was guided by earlier RF observations, however the GloPSI results provided confirmation and useful results. The main conclusion is that the incidence of the Moho and MHT geometry in the two sets of images suggests that P and S waves both yield coherent information about the structure.

A benefit of using GloPSI, is that it only exploits the vertical component of seismic records. Therefore, there is potential to use GloPSI on seismic networks that rely on one-component

sensors, as long as these can record data in the required frequency band (1 s to at least 5 s). Larger aperture networks and a comparatively simple structural environment, complemented with permanent network data, likely increase the chances for GloPSI results to be interpreted alone, without RF or other prior data.

Among the drawbacks of GloPSI, one can note the (partial) loss of relative amplitude information during successive renormalization of waveforms. Moreover, the structure that can be imaged with GloPSI is more limited in space than with RF. With GloPSI, the main contribution comes from structure directly below the stations, whereas with RF, conversion points may be selected that are various distances away from the stations. Hence, for GloPSI, denser array deployments are needed in order to obtain laterally continuous images.

Orogenic regions tend to have strong lateral variability in elastic properties, and even if the incidence angles for GloPSI are closer to vertical than RF studies, the 3D effects should still be visible on the resulting images. The existence of accurate 3D velocity models and denser field arrays would overcome this limitation and allow for more advanced migration techniques. In most areas on Earth, the distribution of sources is more favorable for GloPSI than for RF methods to be applied.

CONCLUSION

From a methodological point of view, the analyses of RFs and global phase interferometry are complementary. Independent datasets in the form of earthquakes from different epicentral distances (RF 30–90°, GloPSI 120–180°) are used, providing complementary illumination and enhancing the coverage for greater interpretation capabilities.

Both methods use transmission responses with different incidence angles below the stations, and different sensitivities to S and P-wave velocity structures, which results in imaging overlap, but also partly exclusive, subsurface information. Combining GloPSI and RF with their individual weaknesses and strengths allows, in general, one to interpret lithospheric structure with a variety of network configurations. With two, rather short but densely spaced profiles across the Himalayan orogenic wedge in Bhutan, we observe a matching pattern of Moho and MHT geometry, as well as east-west differences in shapes and reflectivity patterns.

DATA AVAILABILITY STATEMENT

The raw data supporting the conclusions of this article will be made available by the authors, without undue reservation.

AUTHOR CONTRIBUTIONS

AO processed the data with codes from ER and wrote the initial version of the manuscript. IB and GH contributed to the interpretation and manuscript writing. All authors contributed to the article and approved the submitted version.

FUNDING

The deployment of the temporary seismic GANSSER network in Bhutan was funded by the Swiss National Science Foundation (SNF), Grant 200021-143467 (GH). The GANSSER acronym was chosen to commemorate the famous geologist Augusto Gansser (1910-2012). The instrumental pool of the SED and SEG groups at ETH Zurich provided the station hardware.

ACKNOWLEDGMENTS

We are grateful to the entire field team and the local population for their help in the field experiment, and for the ELAB colleagues from SED for their technical support. IB acknowledges the support of the Austrian Science Fund (FWF) Project J 4314-N29. We like to thank the two reviewers whose help improved the manuscript.

SUPPLEMENTARY MATERIAL

The Supplementary Material for this article can be found online at: https://www.frontiersin.org/articles/10.3389/feart.2021.658146/full#supplementary-material

REFERENCES

Berthet, T., Ritz, J.-F., Ferry, M., Pelgay, P., Cattin, R., Drukpa, D., et al. (2014). Active tectonics of the eastern himalaya: new constraints from the first tectonic geomorphology study in southern bhutan. *Geology* 42, 427–430. doi: 10.1130/g35162.1

Bianchi, I., Ruigrok, E., Obermann, A., Kissling, E., and The AlpArray-EASI Working Group (2021). Moho topography beneath EASI profile in the Eastern European Alps by global phase seismic interferometry. *Solid Earth*. doi: 10.5194/se-2020-179

Bilham, R., and England, P. (2001). Plateau pop-up in the great 1897 Assam earthquake. *Nature* 410, 806–809. doi: 10.1038/35071057

Biswas, S., Coutand, I., Grujic, D., Hager, C., Stöckli, D., and Grasemann, B. (2007). Exhumation and uplift of the shillong plateau and its influence on the eastern himalayas: New constraints from apatite and zircon (U-Th-[Sm])/He and apatite fission track analyses. *Tectonics* 26:TC6013.

Coutand, I., Whipp, D. M. Jr., Grujic, D., Bernet, M., Fellin, M. G., Bookhagen, B., et al. (2014). Geometry and kinematics of the main himalayan thrust and neogene crustal exhumation in the bhutanese himalaya derived from inversion of multithermochronologic data. *J. Geophys. Res. Solid Earth* 119, 1446–1481. doi: 10.1002/2013jb010891

Diehl, T., Singer, J., Hetènyi, G., Grujic, D., Clinton, J., Giardini, D., et al. (2017). Seismotectonics of bhutan: evidence for segmentation of the Eastern Himalayas and link to foreland deformation. *Earth Planet. Sci. Lett.* 471, 54–64. doi: 10.1016/j.epsl.2017.04.038

Draganov, D., Wapenaar, K., and Thorbecke, J. (2006). Seismic interferometry: reconstructing the earth's reflection response. *Geophysics* 71, SI61–SI70.

Drukpa, D., Velasco, A. A., and Doser, D. I. (2006). Seismicity in the Kingdom of Bhutan (1937–2003): evidence for crustal transcurrent deformation. *J. Geophys. Res. Solid Earth* 111:B06301.

Frank, J. G., Ruigrok, E. N., and Wapenaar, K. (2014). Shear wave seismic interferometry for lithospheric imaging: applications to southern Mexico. *J. Geophys. Res. Solid Earth* 119, 5713-5726.

Galvé, A., Sapin, M., Hirn, A., Diaz, J., Lépine, J. C., Laigle, M., et al. (2002). Complex images of Moho and variation of Vp/Vs across the Himalaya and South Tibet, from a joint receiver-function and wide-angle-reflection approach. *Geophys. Res. Lett.* 29:2182.

Grujic, D., Hetenyi, G., Cattin, R., Baruah, S., Benoit, A., Drukpa, D., et al. (2018). Stress transfer and connectivity between the bhutan himalaya and the shillong plateau. *Tectonophysics* 744, 322–332. doi: 10.1016/j.tecto.2018.07.018

Hammer, P., Berthet, T., Hetenyi, G., Cattin, R., Drukpa, D., Chophel, J., et al. (2013). Flexure of the India plate underneath the Bhutan Himalaya. *Geophys. Res. Lett.* 40, 4225–4230. doi: 10.1002/grl.50793

Hauck, M. L., Nelson, K. D., Brown, L. D., Zhao, W., and Ross, A. R. (1998). Crustal structure of the Himalayan orogen at ∼90° east longitude from Project INDEPTH deep reflection profiles. *Tectonics* 17, 481–500. doi: 10.1029/98TC01314

Hetenyi, G., Cattin, R., and Drukpa, D. (2018). Bhutan earthquake opens doors to geophysical studies. *Eos* 100, 26–31. doi: 10.1029/2018EO103055

Hetenyi, G., Cattin, R., Berthet, T., Le Moigne, N., Chophel, J., Lechmann, S., et al. (2016a). Segmentation of the himalayas as revealed by arc-parallel gravity anomalies. *Sci. Rep.* 6:33866.

Hetenyi, G., Le Roux-Mallouf, R., Berthet, T., Cattin, R., Cauzzi, C., Phuntsho, K., et al. (2016b). Joint approach combining damage and paleoseismology observations constrains the 1714 AD Bhutan earthquake at magnitude 8±0.5. *Geophys. Res. Lett.* 43, 10695–10702.

Hirn, A., and Sapin, M. (1984). The Himalayan zone of crustal interaction; suggestions from explosion seismology. *Ann. Geophys.* 2, 123–130.

Le Roux-Mallouf, R., Ferry, M., Ritz, J.-F., Berthet, T., Cattin, R., and Drukpa, D. (2016). First paleoseismic evidence for great surface-rupturing earthquakes in the Bhutan Himalayas. *J. Geophys. Res. Solid Earth* 121, 7271–7283. doi: 10.1002/2015jb012733

Mallick, R., Hubbard, J. A., Lindsey, E. O., Bradley, K. E., Moore, J. D., Ahsan, A., et al. (2020). Subduction initiation and the rise of the Shillong Plateau. *Earth Planet. Sci. Lett.* 543:116351. doi: 10.1016/j.epsl.2020.116351

Marechal, A., Mazzotti, S., Cattin, R., Cazes, G., Vernant, P., Drukpa, D., et al. (2016). Evidence of interseismic coupling variations along the Bhutan Himalayan arc from new gps data. *Geophys. Res. Lett.* 43, 399–312.

Molnar, P. (1988). A review of geophysical constraints on the deep structure of theTibetan Plateau, the Himalaya and the Karakoram, and their geophysicalimplications. *Phil. Trans. R. Soc. Lond. A* 326, 33–88. doi: 10.1098/rsta.1988.0080

Najman, Y., Bracciali, L., Parrish, R. R., Chisty, E., and Copley, A. (2016). Evolving strain partitioning in the Eastern Himalaya: the growth of the shillong plateau. *Earth Planet. Sci. Lett.* 433, 1–9. doi: 10.1016/j.epsl.2015.10.017

Ruigrok, E., and Wapenaar, K. (2012). Global-phase seismic interferometry unveils P-wave reflectivity below the Himalayas and Tibet. *Geophys. Res. Lett.* 39:11303.

Ruigrok, E., Campman, X., Draganov, D., and Wapenaar, K. (2010). High-resolution lithospheric imaging with seismic interferometry. *Geophys. J. Int.* 183, 339–357. doi: 10.1111/j.1365-246x.2010.04724.x

Ruigrok, E., Draganov, D., and Wapenaar, K. (2008). Global-scale seismic interferometry: theory and numerical examples. *Geophys. Prospect.* 56, 395–417. doi: 10.1111/j.1365-2478.2008.00697.x

Schulte-Pelkum, V., Monsalve, G., Sheehan, A., Pandey, M. R., Sapkota, S., Bilham, R., et al. (2005). Imaging the Indian subcontinent beneath the Himalaya. *Nature*, 435, 1222–1225. doi: 10.1038/nature03678

Shi, D., Wu, Z., Klemperer, S. L., Zhao, W., Xue, G., and Su, H. (2015). Receiver function imaging of crustal suture, steep subduction, and mantle wedge in the eastern india–tibet continental collision zone. *Earth Planet. Sci. Lett.* 414, 6–15. doi: 10.1016/j.epsl.2014.12.055

Singer, J., Kissling, E., Diehl, T., and Hetenyi, G. (2017a). The underthrusting indian crust and its role in collision dynamics of the Eastern Himalaya in Bhutan: insights from receiver function imaging. *J. Geophys. Res. Solid Earth* 122, 1152–1178. doi: 10.1002/2016jb013337

Singer, J., Obermann, A., Kissling, E., Fang, H., Hetenyi, G., and Grujic, D. (2017b). Along-strike variations in the himalayan orogenic wedge structure in Bhutan from ambient seismic noise tomography. *Geochem. Geophys. Geosyst.* 18, 1483–1498. doi: 10.1002/2016gc006742

Stein, S., and Wysession, M. (2009). *An Introduction to Seismology, Earthquakes, and Earth Structure*. Hoboken, NJ: John Wiley & Sons.

Subedi, S., Hetenyi, G., Vergne, J., Bollinger, L., Lyon-Caen, H., Farra, V., et al. (2018). Imaging the moho and the main himalayan thrust in western nepal with receiver functions. *Geophys. Res. Lett.* 45, 13222–13230.

Talwani, M., Desa, M. A., Ismaiel, M., and Krishna, K. S. (2016). The tectonic origin of the Bay of Bengal and Bangladesh. *J. Geophys. Res. Solid Earth* 121, 4836–4851. doi: 10.1002/2015jb012734

Verschuur, D. J., and Berkhout, A. J. (1997). Estimation of multiple scattering by iterative inversion, Part II: practical aspects and examples. *Geophysics* 62, 1596–1611. doi: 10.1190/1.1444262

Conflict of Interest: The authors declare that the research was conducted in the absence of any commercial or financial relationships that could be construed as a potential conflict of interest.

frontiers in Earth Science

ORIGINAL RESEARCH
published: 28 May 2021
doi: 10.3389/feart.2021.671412

Joint Seismic and Gravity Data Inversion to Image Intra-Crustal Structures: The Ivrea Geophysical Body Along the Val Sesia Profile (Piedmont, Italy)

Matteo Scarponi[1], György Hetényi[1], Jaroslava Plomerová[2], Stefano Solarino[3], Ludovic Baron[1] and Benoît Petri[4]*

[1] Institute of Earth Sciences, University of Lausanne, Lausanne, Switzerland, [2] Institute of Geophysics, Czech Academy of Sciences, Prague, Czechia, [3] Istituto Nazionale di Geofisica e Vulcanologia, DICCA Università di Genova, Genoa, Italy, [4] UMR7063, CNRS, Institut Terre et Environnement de Strasbourg, Université de Strasbourg, Strasbourg, France

We present results from a joint inversion of new seismic and recently compiled gravity data to constrain the structure of a prominent geophysical anomaly in the European Alps: the Ivrea Geophysical Body (IGB). We investigate the IGB structure along the West-East oriented Val Sesia profile at higher resolution than previous studies. We deployed 10 broadband seismic stations at 5 km spacing for 27 months, producing a new database of ∼1000 high-quality seismic receiver functions (RFs). The compiled gravity data yields 1 gravity point every 1–2 km along the profile. We set up an inversion scheme, in which RFs and gravity anomalies jointly constrain the shape and the physical properties of the IGB. We model the IGB's top surface as a single density and shear-wave velocity discontinuity, whose geometry is defined by four, spatially variable nodes between far-field constraints. An iterative algorithm was implemented to efficiently explore the model space, directing the search toward better fitting areas. For each new candidate model, we use the velocity-model structures for both ray-tracing and observed-RFs migration, and for computation and migration of synthetic RFs: the two migrated images are then compared via cross-correlation. Similarly, forward gravity modeling for a 2D density distribution is implemented. The joint inversion performance is the product of the seismic and gravity misfits. The inversion results show the IGB protruding at shallow depths with a horizontal width of ∼30 km in the western part of the profile. Its shallowest segment reaches either 3–7 or 1–3 km depth below sea-level. The latter location fits better the outcropping lower crustal rocks at the western edge of the Ivrea-Verbano Zone. A prominent, steep eastward-deepening feature near the middle of the profile, coincident with the Pogallo Fault Zone, is interpreted as inherited crustal thickness variation. The found density and velocity contrasts of the IGB agree with physical properties of the main rock units observed in the field. Finally, by frequency-dependent analysis of RFs, we constrain the sharpness of the shallowest portion of the IGB velocity discontinuity as a vertical gradient of thickness between 0.8 km and 0.4 km.

Keywords: joint inversion, seismic receiver functions, gravity anomalies, Ivrea Geophysical Body, Ivrea-Verbano Zone, continental crust, intra-crustal structure

OPEN ACCESS

Edited by:
Claudia Piromallo, Istituto Nazionale di Geofisica e Vulcanologia (INGV), Italy

Reviewed by:
Nicola Piana Agostinetti, University of Vienna, Austria
Paolo Mancinelli, Gabriele d'Annunzio University of Chieti and Pescara, Italy

****Correspondence:***
Matteo Scarponi
matteo.scarponi@unil.ch

Specialty section:
This article was submitted to Solid Earth Geophysics, a section of the journal Frontiers in Earth Science

Received: *23 February 2021*
Accepted: *22 April 2021*
Published: *28 May 2021*

Citation:
Scarponi M, Hetényi G, Plomerová J, Solarino S, Baron L and Petri B (2021) Joint Seismic and Gravity Data Inversion to Image Intra-Crustal Structures: The Ivrea Geophysical Body Along the Val Sesia Profile (Piedmont, Italy). Front. Earth Sci. 9:671412. doi: 10.3389/feart.2021.671412

INTRODUCTION

The geologically defined Ivrea-Verbano Zone (IVZ) and the related but much longer Ivrea Geophysical Body (IGB) belong to the most outstanding features of the whole Alpine domain. They have been the subject of numerous international investigations in the fields of geology, petrology and geophysics (e.g., Schmid et al., 2017; Petri et al., 2019; Kissling et al., 1984 and detailed references below).

The western end of the Southern Alps (**Figure 1A**) is regarded as a nearly complete cross-section of the continental crust, exposing upper to middle and middle to lower crustal composition rocks at its surface in the Serie dei Laghi and the IVZ, respectively (e.g., Fountain, 1976; Khazanehdari et al., 2000). These units belong to a complex tectonic setting, which has been mapped by several groups of authors (e.g., Schmid et al., 2004; Brack et al., 2010; Petri et al., 2019).

This work focuses on the IGB, which constitutes the crustal root of the IVZ and consists of an anomalously dense and seismically fast rock complex. This anomalous crustal complex extends along the whole inner arc of the Western Alps and outcrops in its north-eastern portion as the IVZ. The IGB is nowadays regarded as a sliver of the Adriatic lower lithosphere (e.g., Schmid et al., 2017; Petri et al., 2019), which was involved in the Alpine collision and tectonically emplaced at unusual shallow depths (e.g., Handy et al., 2015). The Adriatic plate, among other micro-plates, was one of the key actors in the Alpine collision and the related orogenic process, which featured the subduction of the former Tethys ocean and the subsequent Adriatic thrusting against the European margin (e.g., Handy et al., 2010).

The IGB is associated with pronounced seismic, gravity and magnetic anomalies (e.g., Lanza, 1982; Kissling et al., 1984; Diehl et al., 2009). The IGB is bounded by the Western Alps along the Insubric line (IL): a main vertical to sub-vertical fault line (Schmid et al., 1987, 1989; Berger et al., 2012) which separates the Adriatic plate from the orogenic wedge (**Figure 2A**).

A long history of investigations has addressed the IGB, both in terms of gravity mapping (e.g., Niggli, 1946; Vecchia, 1968; Masson et al., 1999) and gravity data modeling, with models based on continuous bodies with a sharp and constant density contrast (e.g., Berckhemer, 1968; Kissling et al., 1984), and on heterogeneous-size and -density blocks as well (e.g., Bayer et al., 1989; Bürki, 1990; Rey et al., 1990). Concerning seismic investigations, the IGB was first imaged by refraction experiments (Berckhemer, 1968; Ansorge, 1979), which lead to the birth of an iconic model, usually referred to as the "Bird's Head" in the literature. This became of historical value with subsequent investigations, revealing high level of structural complexities of the IGB (e.g., Ansorge, 1979). In the frame of the ECORS-CROP experiment, the regional crustal structure was investigated via reflection seismics (e.g., Bayer et al., 1989; Nicolas et al., 1990; Thouvenot et al., 1990), guiding the development of several 2D gravity models but also stressing the limitations of controlled-source seismology, in imaging such a complex structure as the IGB (Kissling, 1993). Local earthquake analysis and tomography (LET) studies (e.g., De Franco et al., 1997; Diehl et al., 2009; Solarino et al., 2018) allowed the IGB to be better imaged and interpreted in light of the tectonic setting as well (Schmid and Kissling, 2000). Despite the latest advances in the terms of LET resolution (Diehl et al., 2009 provides the crustal v_P structure on a 25 × 25 × 15 km grid and Solarino et al., 2018 locally higher, up to 15 × 15 × ∼ 10 km), a spatial imaging gap persists between the IGB structure at the geological maps' spatial scale. Therefore, structural questions on the IGB's relation with the exposed IVZ remain open.

Recent gravity investigations, based on new, densely spaced gravity surveys and earlier-existing compiled gravity data (**Figure 2B**) allowed the development of a new 3D IGB gravity model across the IVZ area (Scarponi et al., 2020) and (**Figure 1B**). In this work, we focus on a central cross-section of this most recent 3D IGB model (**Figure 1B**) and we integrate the gravity dataset with new high-resolution broad-band passive seismic data, recorded during the IvreaArray passive seismic experiment (Hetényi et al., 2017). We intend to use the new seismic data to further constrain the most recent IGB 3D density model along the IvreaArray profile (**Figure 2B**). In fact, we investigate the West-East oriented 2D profile along Val Sesia (∼ 45.83°N), crossing the entire IVZ at that latitude (∼ 8.11°E to 8.77°E). We model the IGB along this 2D cross-section as a body below a single discontinuity, and set up a joint inversion scheme to fit the observed gravity anomaly and seismic receiver functions (RFs) from IvreaArray, to constrain both the shape and the physical properties of the IGB. The RF technique enhances smaller-amplitude P-to-S (Ps) converted phases in the P-wave coda, and extracts information on the Earth discontinuities beneath a seismic receiver (Langston, 1979). While RF inversion is routinely performed to investigate the seismic properties of the crust and the upper mantle (Bodin et al., 2012), inverting the RFs-only is in general a strongly non-linear and non-unique problem (Ammon et al., 1990). Joint inversions of RFs along with complementary geophysical observations reduce this non-uniqueness. Such complementary data sets can be, e.g., RFs and surface wave dispersion curves (Julia et al., 2000), also with the addition of magnetotelluric data (Moorkamp et al., 2010) or RFs combined with gravity data and seismic tomography (Basuyau and Tiberi, 2011).

Here, we implement a novel iterative joint inversion algorithm, acting on the gravity and seismic data. This algorithm is meant to explore and characterize the performance of all considered IGB models in non-probabilistic terms, by implementing a performance-driven pseudo-random walk in the model space. The gravity anomaly along the profile and the computed seismic RFs represent our observations. In particular, we combine the sensitivity of gravimetry to the geometry and magnitude of density contrasts in the subsurface structure, with the sensitivity of RFs to the crustal discontinuities beneath the seismic receiver.

DATA AND DATA PRODUCTS

New seismic data has been acquired and recent gravity data has been compiled to produce a higher resolution image of the IGB along the Val Sesia profile. The following paragraphs present

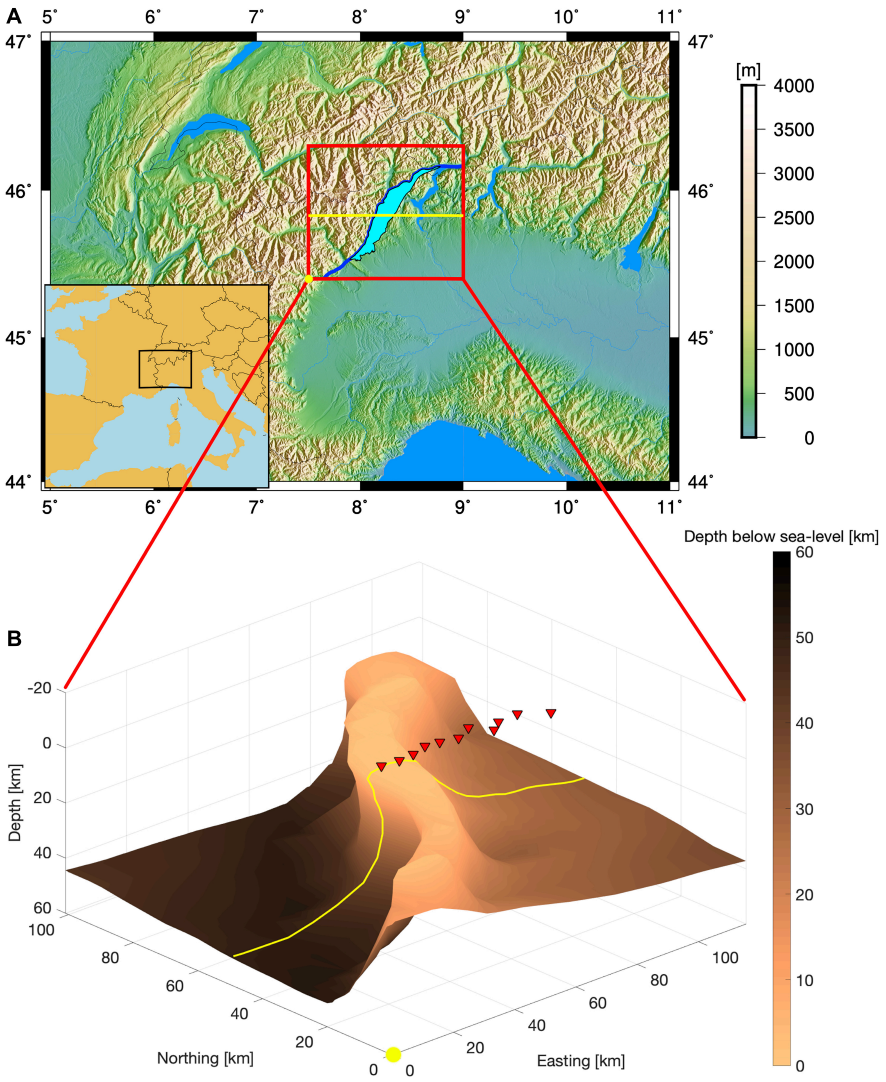

FIGURE 1 | Study area and earlier 3D IGB density model. **(A)** View of the study area. The 2D cross-section investigated in this study, along the 2D West-East IvreaArray seismic profile (red triangles in panel b), is highlighted by a yellow line. This target profile extends across the IVZ (cyan shape), delimited on the West by the Insubric Line (blue line). The yellow circle is the origin of the km-coordinate system used in this study and the subsequent figures (7.5°E, 45.4°N). The inset show the overview map's location in Europe. **(B)** Perspective view of the IGB 3D density model interface, constrained by gravity data modelling in an earlier study (Scarponi et al., 2020).

how the data was obtained and processed prior to the joint inversion. The complete seismic dataset is directly available in the Supplementary Material, in the form of radial (RRF) and transverse (TRF) seismic receiver functions.

The IvreaArray Seismic Network

We collected the new seismic data in the framework of IvreaArray (Hetényi et al., 2017): a temporary seismic network, installed and operated for 27 months (June 2017 to September 2019) as one of the AlpArray complementary experiments.

The main purpose of IvreaArray was to record high-quality seismic signals at a higher spatial resolution in Val Sesia, compared to earlier studies addressing the crustal structure in the Western Alps and in the IVZ.

For this purpose, we deployed 10 broadband three-component seismic stations at 5 km spacing along a West-East linear profile (∼ 45.83°N). The INGV permanent seismic station IV.VARE is included as it located as a natural eastern continuation of IvreaArray (**Figure 2B**). All 10 deployed sensors were the Güralp CMG-3ESP seismometers of the Czech MOBNET pool, with 60 s lower corner frequency. The linear seismic profile crosses the entire IVZ. It starts few km to the west of the IL at ∼ 8.11°E (in the village of Boccioleto), then crosses the lower and middle crustal rocks outcropping in the IVZ and extends to the eastern shore of Lago Maggiore (∼ 8.77°E).

The seismic network operated for 27 months and continuously recorded data at 100 Hz sampling rate on all three components. Data recovery was ∼ 90%. During this time and according to the

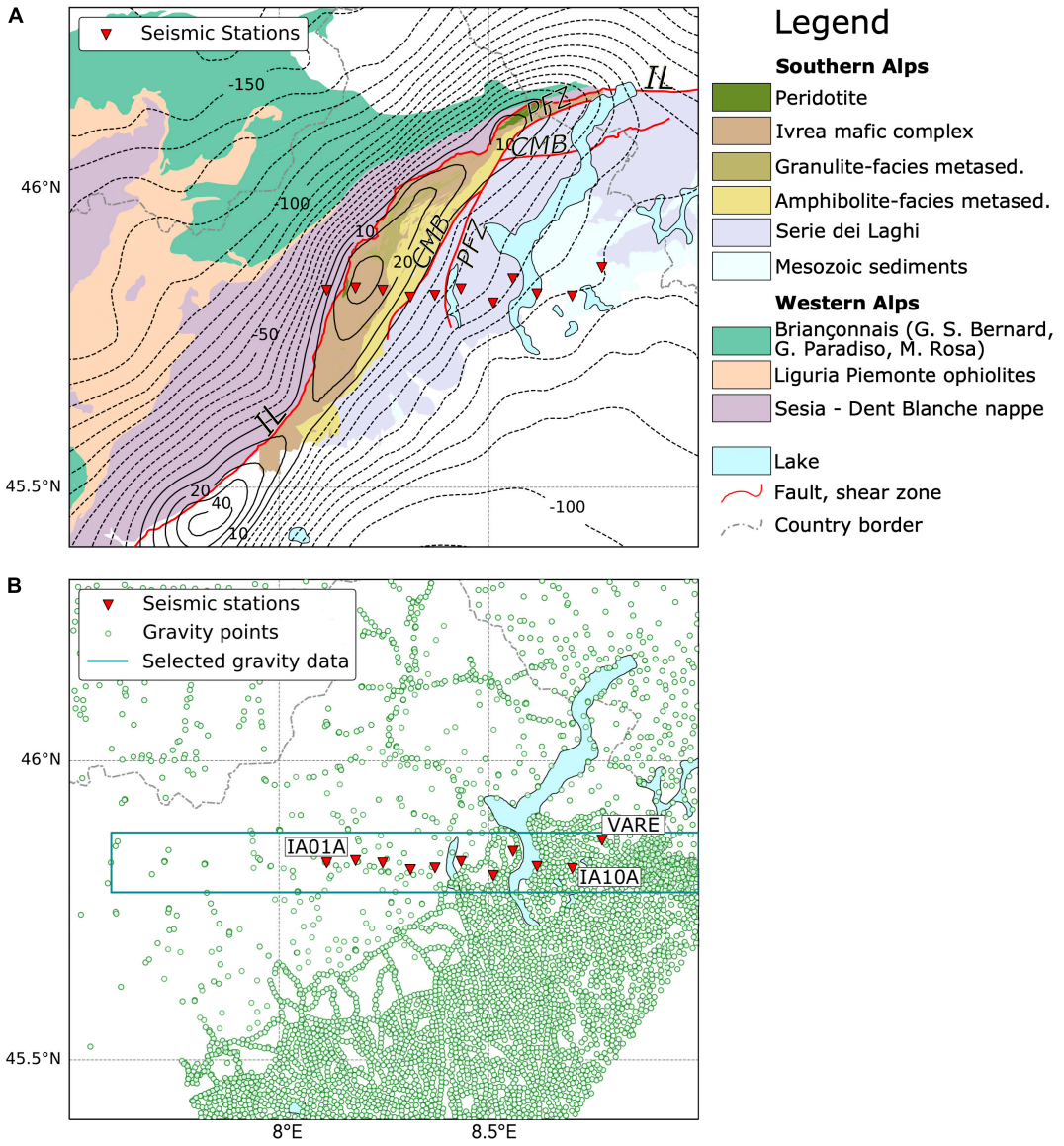

FIGURE 2 | (A) Geological map of the IVZ and the surrounding areas, simplified from Petri et al. (2019) and Schmid et al. (2004) (see legend on the right hand of the figure), together with the location of the 10 IvreaArray broadband seismic stations and the INGV permanent seismic station IV.VARE [red triangles, see station names in **(B)**]. The main faults (red lines), relevant for this study, are indicated as "IL" for Insubric Line, "PFZ" for Pogallo Fault Zone and "CMB" for Cossato-Mergozzo-Brissago Line. Overlaid, the 10 mGal contour lines for the Bouguer gravity anomaly from our data across the study area. **(B)** The compiled gravity data set for this study is shown (green circles), which comprises earlier existing gravity data and recently collected gravity data in the scope of the work of Scarponi et al. (2020). The location of the IvreaArray seismic stations is shown (red triangles) together with the INGV permanent seismic station IV.VARE and their names. The cyan box indicates the gravity data we selected for this study along the 2D IvreaArray profile. The dashed-pointed gray line indicates the Swiss-Italian border as shown in the legend.

USGS earthquake catalog, we selected and retrieved 347 events of interest for our study (magnitude $\geq$ 5.4, epicentral distance $28° \leq \Delta \leq 95°$, **Supplementary Material 1**).

Seismic Receiver Functions

We process the recorded teleseismic signals by computing seismic receiver functions: a deconvolution-based technique which enhances the arrival of P-to-S (Ps) converted phases (Langston, 1979). Ps converted phases follow the direct P-wave arrivals. They are produced when an impinging P-wave encounters a discontinuity – an impendence contrast – in the propagating medium beneath a seismic receiver, thus containing information on the associated Earth structure. A receiver function is mathematically defined as the deconvolution of the seismogram's vertical component from the radial component, yielding a series of delay times with respect to the first P-wave arrival (Langston, 1979). This operation removes the event source time function and the distant-path effects from the trace, favoring a constructive

stacking to investigate the receiver side Earth structure. The analysis of the Ps delay times and amplitudes carries information on the depth of a seismic discontinuity and the shear-wave velocity v_S profile, together with the magnitude of the impedance contrast itself, with a primary sensitivity for the v_S contrast.

We compute RFs based on the time-domain iterative deconvolution technique (Ligorría and Ammon, 1999) by iteratively cross-correlating the vertical and the horizontal (radial) seismic traces and saving the associated delay times, generated by the strongest amplitudes first and by the minor ones later on. The final RF is obtained via convolution of the spike train with a Gaussian pulse, whose width corresponds to the maximum allowed frequency into the seismic signal during pre-filtering (see RRF and TRF in **Supplementary Material**).

In our case, we filtered the seismic data in the 0.1 Hz to 1 Hz frequency band and performed 150 iterations during deconvolution for each RF. Quality control (QC) is applied both on the seismic traces and on the final RFs. First, we look for amplitude similarity for each seismogram component across all the stations for each seismic event, and for teleseismic signal prominence with respect to the background noise. Then, for each computed RF, we verify an acceptable location of the reference direct-P wave signal and for its satisfactory recovery in terms of amplitude. We refer the reader to the work (e.g., Hetényi et al., 2015, 2018; Subedi et al., 2018) for further description of this QC practice. This ensured retrieval of high-quality earthquake signal (in the original seismogram components) and of the direct-P arrival (in the computed RF) prior to the converted phases, providing a final dataset of $\sim$ 1000 high-quality RF traces. The original seismic traces were rotated into the LQT, ray-based coordinate system. This practice allows us to maximize the Ps amplitude and to prevent the direct-P signal from strongly interfering with the peaks' interpretation in case of very shallow interfaces, which are expected in the IVZ. The distribution of all available RFs shows a strong variability in the peak polarities and delay times as a function of the back-azimuth (**Supplementary Material 2**), in particular between the traces coming from the East and the West, which hints at the presence of dipping interfaces. In fact, dipping interfaces and/or anisotropic layers can affect the signal polarity and introduce back-azimuthal periodicities, especially on the transverse RF component (e.g., Levin and Park, 1997). By inspecting all the transverse RF signals from the IvreaArray recordings (see TRF in **Supplementary Material**), we could find some but limited evidence for local dipping structures, but no clear signs of resolvable anisotropy at any of the stations, and therefore decided not to address this particular feature in the subsequent analysis.

Relative to the RF complexity, reverberations cause so-called multiples and small-scale heterogeneities can increase noise. Furthermore, as RFs record delay times, there is a trade-off between layer thickness and average v_P/v_S, which prevents from uniquely inverting for the Earth structure by using RFs Ps phases only (e.g., Ammon et al., 1990).

To address these limitations, and to avoid stacking numerous waveforms sampling a heterogeneous crust in the IVZ, we migrate the observed RFs from time to depth and produce migrated profiles. During migration, we perform ray-tracing for each station–event pair with a vertical resolution of 0.25 km using a 2D velocity model and respecting Snell's law including local interface dip. Then we distribute the RF time sample amplitudes along these ray paths to finally obtain a migrated image, with a final spatial resolution of 0.5 km. The migration spatially re-distributes wave conversions to where they were produced, and gives a structural image of the sub-surface. The areas where the RF amplitudes are stacked constructively represent either an increase or a decrease of seismic velocity with depth. **Figure 3B** shows an example for the 1D *iasp91* velocity model (Kennett and Engdahl, 1991).

While the observed RFs constitute the seismic part of the input to the joint inversion scheme, the computation of RF migration images is incorporated into the iterative inversion procedure, and constitutes the actual mean for the model seismic performance evaluation. The detailed description of the inversion workflow is provided in section "Inversion Approach."

Gravity Anomalies Along Val Sesia

We compiled a gravity dataset by merging earlier and the most recent gravity data acquired across the IVZ. The earlier existing gravity data points were compiled from the Swiss Federal Office of Topography (Swisstopo)[1] and from the Istituto Nazionale di Oceanografia e di Geofisica Sperimentale (OGS)[2], and were merged with the most recent data set in our earlier work (Scarponi et al., 2020). The full dataset was analyzed in the same work (Scarponi et al., 2020), where the original raw relative gravity measurements were processed and transformed into absolute gravity values with the software GravProcess (Cattin et al., 2015), with a final mean uncertainty of 0.22 mGal (1 Gal = 1 cm/s^2). The reader is referred to the work of Scarponi et al. (2020) for full details of the gravity data acquisition practices and processing. In our joint inversion, we use a subset of this data (**Figure 2B**). The compiled dataset reaches a coverage of 1 gravity point every 1 to 2 km along the Val Sesia profile. For the joint inversion presented here, we include all the gravity points up to 5 km to the North and to the South along the IvreaArray seismic profile (**Figure 2B**). As the gravity data points were not uniformly distributed along the IvreaArray profile, we binned the data at 2 km intervals along the profile, obtaining a more balanced spatial distribution and allowing for faster gravity data modeling (0.08s instead of 1s for each test model). For each interval, the considered gravity data points were averaged in location (x and z coordinates) and in the measured gravity anomaly, with mean standard deviation of 3 mGal across the whole profile (**Supplementary Material 5**).

The final gravity data product we use in the inversion of this study is the Niggli gravity anomaly, which is an improved Bouguer anomaly considering surface rock densities for the terrain and plate corrections (Scarponi et al., 2020). This anomaly is obtained by the classical correction of the absolute gravity values for the effect of homogeneous and constant-density 3D topographical masses (i.e., Bouguer plate correction and terrain correction with ρ = 2670 kg/m^3), accounting for the density

[1] https://www.swisstopo.admin.ch/

[2] https://www.inogs.it/

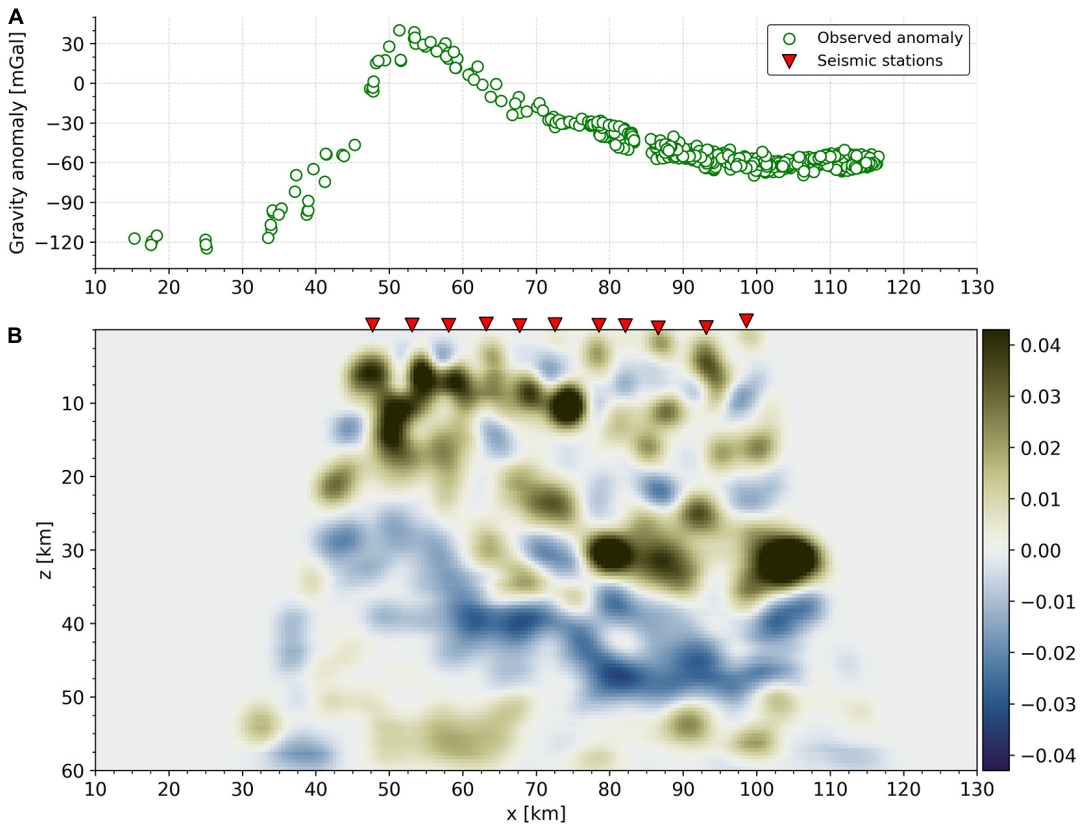

FIGURE 3 | (A) Niggli gravity anomaly computed from observed data and applying rock-density-based terrain corrections (Scarponi et al., 2020) along the West-East IvreaArray profile. **(B)** An example of migrated receiver function profile with the use of the IvreaArray and VARE seismic data and the *iasp91* velocity model for ray-tracing and migration. Colors highlight areas of increasing (brown) and decreasing (blue) seismic velocities with depth.

variations of rocks seen at the surface and extrapolated down to sea-level (i.e., the Niggli correction), which is well justified by the general IVZ vertical structure (e.g., Fountain, 1976; Khazanehdari et al., 2000).

Considering the Niggli gravity anomaly (henceforth simply gravity anomaly) as final gravity observation allows us to focus our modeling effort on the IGB crustal structure below sea level and to analyze it consistently together with seismic RF migration images (**Figure 3**).

INVERSION APPROACH

To reduce the non-uniqueness of RF-only inversion (Ammon et al., 1990), which are sensitive to sharp discontinuities, we jointly invert them with the gravity data, which are sensitive to volumetric anomalies. The RF inversion task has been addressed by many authors in the literature with the application, among others, of different algorithms such as: genetic algorithm (e.g., Shibutani et al., 1996; Levin and Park, 1997), simulated annealing (e.g., Vinnik et al., 2004) and neighborhood algorithm (e.g., Sambridge, 1999). The reader is referred to (Bodin et al., 2012) for further discussion on RF inversion approaches.

For this joint gravity and seismic data inversion, we implemented an iterative algorithm to explore the ensemble of all possible IGB models (i.e., the model space) and to evaluate their performance in terms of their fit to the observations. Even at a simplified parameterization of the model, the high dimension of variables (9 in our case) can require long and computationally expensive efforts (Sambridge and Mosegaard, 2002). To extract more information on models' behaviour in an efficient manner, our iterative algorithm explores in a guided pseudo-random fashion the model space. The algorithm is based on the principles of a Monte Carlo exploration, as at each iteration a new candidate model is proposed upon a random perturbation of the current model, and the exploration evolves as a series of small random steps. Strictly speaking, we implemented a Markov chain property as well, as the candidate model depends only on the current model, and its acceptance is based on the performance of its forward model with respect to the current's one only. If the new candidate model presents a better fit to the data (i.e., the performance), it is always accepted. Otherwise, its acceptance depends on a probability: the poorer the performance, the lower the chance to be accepted.

At each iteration, the evaluation of the overall performance for a given candidate model consists of two parts – the seismic and gravity data modeling, respectively – which are eventually combined together upon comparison with the seismic and gravity observations (**Figure 4**). It develops as follows. Given a candidate model, the associated velocity structure (defined by the candidate

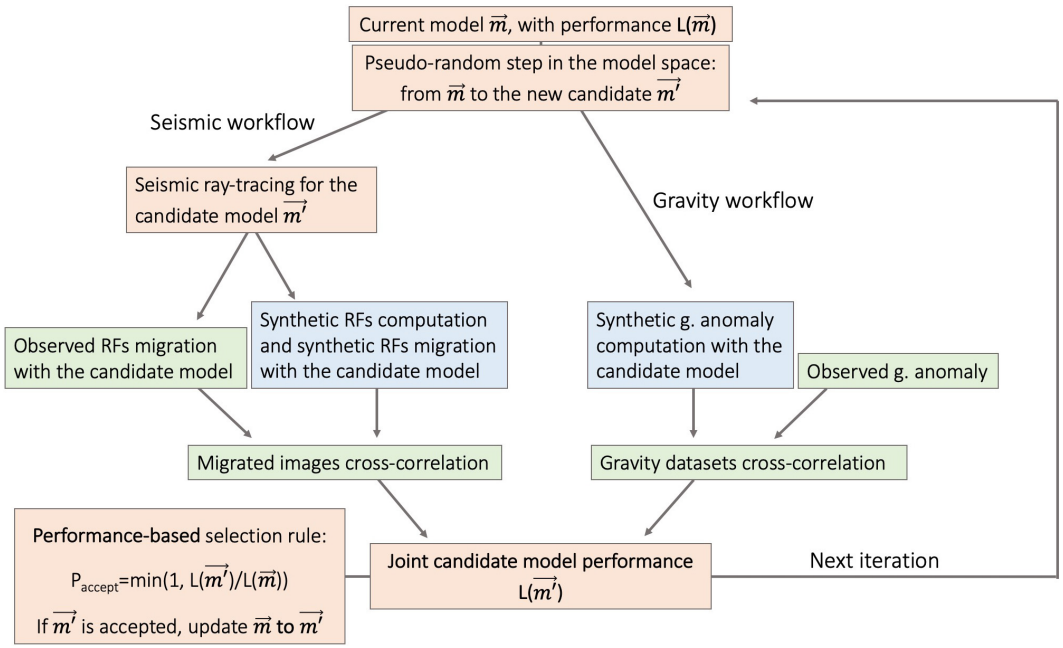

FIGURE 4 | The joint seismic-gravity inversion workflow implements a performance-driven pseudo-random walk in the model space and a performance-based selection rule for the new candidate models. Red boxes refer to the new candidate model generation and evaluation, followed by the forward modeling steps (blue boxes) and by the model performance evaluation (green boxes). At each iteration, a new candidate model is proposed. Successively, the associated seismic and gravity model performances are evaluated and combined into a joint model performance, which determines whether the newly proposed model is accepted or not (following the idea behind the Metropolis-Hastings selection rule). For coherency, the same model is used both for migrating the observed RFs and for generating and migrating the synthetic RFs at each step. The iterative procedure continues by suggesting new model space samples until the maximum number of iterations is reached.

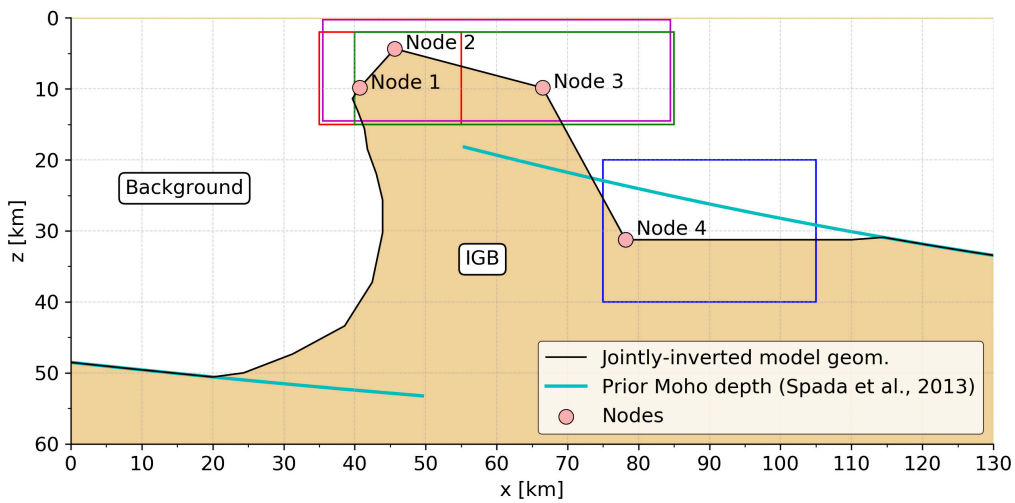

FIGURE 5 | Model parameterization of the IGB shape used for the joint inversion of seismic and gravity data. We invert for the 2D IGB interface geometry (black line), whose configuration depends on the coordinates of four nodes (red, magenta, green, and blue). Spatial positions of each node are investigated within a given perimeter (dashed boxes of respective color) during the inversion, together with the velocity and density contrast of the IGB relative to the surroundings. The far-field model geometry connects to the Moho map (Spada et al., 2013). In the East, the connection is by a horizontal line. In the West, the curved shape is taken from the earlier 3D gravity model of (Scarponi et al. (2020)), as the vertical wall cannot be resolved by converted seismic waves.

IGB model geometry, velocity and density contrasts) is used for both the seismic ray-tracing, and the computation and migration of the synthetic RFs. The same velocity structure and the associated ray-tracing are subsequently used for the migration of the observed RFs. We thus obtain a "synthetic" and an "observed" RF migration image, respectively, which are then

compared to define the candidate model's seismic performance. Similarly, the gravity model performance is evaluated by comparing the observed gravity anomaly to the synthetic gravity anomaly, computed for the same candidate model structure (**Figure 4**). The following paragraphs discuss more in detail the model parameterization, the associated forward problem solution and joint model performance definition, and the technical implementation of the model space exploration.

Model Parameterization

We model the IGB's upper boundary as a single 2D discontinuity with a few segments, associated with sharp density ($\delta\rho$) and shear-wave seismic velocity (δv_S) contrasts (**Figure 5**) representing the IGB bulk physical properties with respect to the surrounding crust. While the former parameters are allowed to vary independently during the inversion, a homogeneous crustal background is assigned to the model and characterized by absolute values of v_S = 3.5 km/s and density = 2700 kg/m^3, which is also a consistent choice of velocity and density values, according to the v_S-density relationship from Brocher (2005) (as further discussed in section "Results"). The choice of the background velocity fits well the upper crustal layer properties of 3.6 ± 0.2 km/s deduced from a short period regional network (De Franco et al., 1997). The v_P/v_S ratio is fixed at 1.73 and 1.8 for the medium above and below the model interface, as indicated by the *iasp91* model for the upper and lower crustal rocks. The number of parameters has been chosen based on the *a priori* knowledge of the IGB and of the associated seismic and gravity anomalies. (Berckhemer, 1968) and (Kissling et al., 1984) provided seismic and gravity evidence for an anomalously dense, eastward-dipping body. Further contributions showed sub-vertical and eastward-dipping units to the East of the Insubric Line (e.g., Zingg et al., 1990; Petri et al., 2019). In addition, the preliminary RF migration with a 1D velocity model (**Figure 3**) clearly points to a shallow interface in the western portion of the profile, and a deeper interface further to the East. In our investigation of the shape of the IGB-top structure, the model boundaries connect to the eastern and the western branches of the regional Moho interface (Spada et al., 2013), acting as far-field constraints on either side of our study's imaging area. We selected this Moho map as the reference crustal thickness only outside our data coverage and modeling domain, and kept it unvaried during the inversion procedure. The IGB model geometry is parameterized by 4 nodes, whose location can vary in space within given boundaries. This allows for a complete exploration in terms of width and depth of IGB head and neck, in analogy with the historical bird model anomaly as a vertical protuberance reaching shallow depths. The locations of the nodes, connected by straight segments, define the IGB model structure within the investigation domain (**Figure 5**). The western connection between node 1 and the Moho mimics the curved shape obtained in the 3D gravity model (Scarponi et al., 2020), as such a steep boundary is not resolvable with converted seismic waves.

We hence expect a shallow, not necessarily flat, discontinuity in the western portion of the profile and an eastward dipping structure – at an undetermined angle – toward the eastern portion of the profile. Therefore, we define four nodes to determine the IGB model geometry, and we prescribe that the depth of node 3 is the same as the depth of node 1. This still allows accounting for the East-West extent of the IGB, its variable eastern slope (due to the relative position of nodes 2 and 4), as well as a shallow interface with two segments, but saves one parameter to invert for.

Then, each IGB model is completely defined by 9 parameters:

$$\vec{m} = \left[\delta V_S, \delta\rho, x_1, x_2, x_3, x_4, z_1, z_2, z_4\right] \quad (1)$$

All these parameters can attain values within a fixed range, with the exception of z_2 and x_2, as node 2 is always prescribed to be located between (along x) and above (along z) node 1 and node 3, in order to investigate the shallowest features of the IGB head. Similarly, node 4 is prescribed to be farther east than node 3. Therefore, the allowed value ranges for x_2, z_2 and x_4 are dynamically adapted at each iteration, depending on the other parameter values. **Figure 5** summarizes the possible range for each of the 9 inverted parameters, with minimum and maximum values based on *a priori* geometry and rock properties. The allowed range of $\delta\rho$ (**Table 1**) is broader than that of the best fit 3D gravity model (400 ± 100 kg/m3, obtained by sensitivity analysis in Scarponi et al., 2020), while the range of δv_S allows changes in a very broad range with respect to lower crust to mantle v_S change in *iasp91* (0.72 km/s). It also includes the full range of velocity variations from upper crust to upper mantle (up to 4.8 km/s) as suggested by the short-period regional network (De Franco et al., 1997).

Forward Calculation and Model Performance

The forward modeling task produces the synthetics to be compared with the respective observations, for a given candidate model. It consists of two separate contributions – the seismic and the gravity part – whose misfits are then combined (see **Figure 6** for an example).

The solution of each seismic forward problem produces two new RF migration images, which we may refer to as the "synthetic" and the "observed" migration images, respectively.

TABLE 1 | Allowed-values range for each of the model space parameters.

Parameter	Min value	Max value
δv_S	0.1 km/s	1.3 km/s
$\delta\rho$	200 kg/m^3	660 kg/m^3
x_1	35 km	55 km
x_2	x_1	x_3
x_3	40 km	85 km
x_4	max[x3, 75 km]	105 km
z_1	2 km	15 km
z_2	0.25 km	z_1
z_4	20 km	40 km

During the inversion, each parameter is free to vary within the given limits, with an exception for x_2 and x_4 which are constrained by the location of the neighboring nodes.

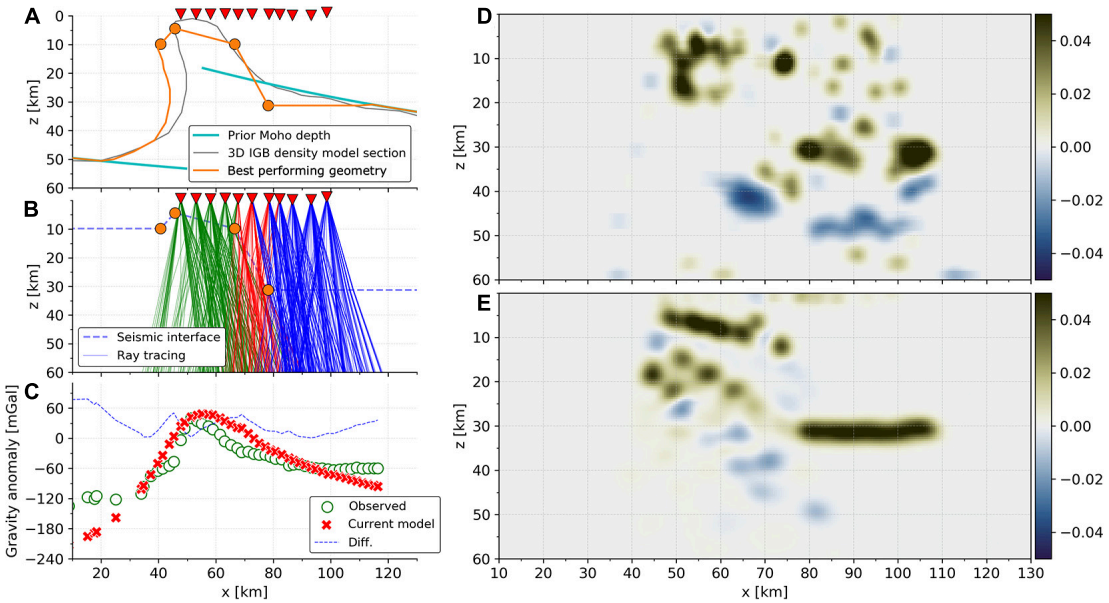

FIGURE 6 | Example of forward model calculation demonstrated on the best performing IGB model. **(A)** The current model geometry (orange line), defined by four nodes (orange circles) and assumptions as in **Figure 5**. **(B)** Seismic ray-tracing across the model interface (blue dashed line segments) for the current velocity model. Seismic rays are colored according to the interface segment they cross along their path. The wave mode conversion respects Snell's law considering the local interface dip. **(C)** Comparison between observed and synthetic gravity anomalies for the current model, and their misfit. **(D)** Observed-RFs migration, including ray-tracing and migration with the velocity structure of the current model. **(E)** Synthetic-RFs migration, using RFs generated by the current velocity structure, and then treated the same way as the observed RFs. The comparison between Observed-RFs and Synthetic-RFs migrations is obtained via image cross-correlation (further details in the text).

The synthetic RF migration image is produced via three main steps: seismic ray-tracing, synthetic RFs computation and synthetic RFs migration (**Figure 4**, Seismic workflow).

Each of these steps always considers the candidate IGB model (or the current in the case of the first iteration): as a first step, we perform the ray-tracing across the candidate 2D velocity model structure for the same seismic catalog – station pairs, identical to the observed dataset. Snell's law is respected at each model interface segment including local dip, meaning that it considers the relative angle between the propagating seismic trace and the dip (and depth) of the local interface segment (**Figure 6B**). The synthetic seismograms are computed via the Raysum software (Frederiksen and Bostock, 2000), whose code is wrapped in our inversion routine and receives as input the local IGB geometry along each ray-path.

Finally, the synthetic RFs are migrated along the candidate velocity structure with the computed ray-tracing, therefore producing the "synthetic" migration image. In addition, the observed RFs are migrated as well along the same candidate model and ray-tracing (**Figures 6D,E**), producing the so-called "observed" migration image. This allows to compare in a consistent manner the observed and the synthetic RFs for each given candidate model. The migrations pictures are spatially smoothed by 2D Gaussian ellipsoidal filter with 1.5 km and 0.75 km horizontal and vertical half-width. Noise, taken as low-amplitude signals at < 15 % of the image maximum amplitude, is removed from the observed migration picture. The final migration pictures have 0.5 km x 0.5 km pixel size.

We define the seismic model performance $L_S(\vec{m})$ as the zero-shift cross-correlation between the observed and synthetic RF migration images (Im_{obs} and Im_{syn}):

$$L_S\left(\vec{m}\right) = \frac{\sum_{i=1}^{N}\left(Im_{obs,i} * Im_{syn,i}\right)}{\sqrt{\sum_{i=1}^{N}\left(Im_{obs,i} * Im_{obs,i}\right)\sum_{i=1}^{N}\left(Im_{syn,i} * Im_{syn,i}\right)}} \quad (2)$$

where i is the pixel index and $L_S(\vec{m})$ is normalized, by definition, between -1 and 1.

For the gravity forward problem, we implemented direct formulas for the computation of gravity anomaly for a given density distribution. The distribution is defined as an n-sided polygon in a two-dimensional plane (Hubbert, 1948; Won and Bevis, 1987), under the assumption that the geometry extends unchanged toward infinity along the direction perpendicular to the profile (i.e., the out-of-plane coordinate). Therefore, we numerically treat the IGB model shape as a 2D polygon associated with a $\Delta\rho$ density contrast with respect to the surrounding background. The synthetic gravity anomaly is then computed for each of the binned gravity points (**Figure 4**, Gravity workflow).

Similarly, to the seismological part, we define the gravity misfit or model performance $L_G(\vec{m})$ as the zero-shift cross-correlation of the observed and synthetic gravity profiles G_{obs} and G_{syn}:

$$L_G\left(\vec{m}\right) = \frac{\sum_{i=1}^{N}\left(G_{obs,i} * G_{syn,i}\right)}{\sqrt{\sum_{i=1}^{N}\left(G_{obs,i} * G_{obs,i}\right)\sum_{i=1}^{N}\left(G_{syn,i} * G_{syn,i}\right)}} \quad (3)$$

where i is the single gravity point index and where $L_G(\vec{m})$ is normalized, by definition, between −1 and 1.

The problem of defining of a joint model performance (or joint misfit), combining the information from different geophysical data sets into the inversion process, has been addressed in the literature via different approaches. Various authors have introduced explicit scalar weighting parameters to accommodate for differences in the dataset's noise and information content (e.g., Julia et al., 2000; Syracuse et al., 2016). Other authors have implicitly incorporated the weighting between different datasets in a more recent Bayesian formulation of their inverse problem (e.g., Bodin et al., 2012).

In our case, the objective functions are not set up on physical properties with values on different orders of magnitudes, but instead they are cross-correlation based. Therefore, in our case, we define our final model performance function as the direct multiplication between the seismic model performance and the gravity model performance, following a maximum likelihood principle (Drahos, 2008):

$$L\left(\vec{m}\right) = L_S\left(\vec{m}\right) * L_G\left(\vec{m}\right) \tag{4}$$

Thus, we obtain a performance measure for which we do not apply any user-defined weighting or scaling factor, and which, by definition, is normalized between −1 and 1.

Model Space Exploration

The model space exploration is carried out in a series of small random steps, with a new model being proposed at each of the iterations. Each of the model space coordinates m_j (with $j = 1,...,9$) has been assigned with a pair of minimum and maximum values, m_j^{min} and m_j^{max}, within which the model coordinates can range during the inversion procedure (**Table 1**).

At each iteration, the exploration starts from the current model space location m^{cur} (i.e., the initial or the latest accepted model sample) and randomly suggests a new candidate model m^{cand}, related to m^{cur} by:

$$m_j^{cand} = m_j^{cur} + r_j * s_j * \left(m_j^{max} - m_j^{min}\right)$$
$$for\ j = 1, \ldots, 9 \tag{5}$$

where r_j is a uniform random deviate and s_j a scaling parameter.

We defined an acceptance rule to guide the acceptance or not of the newly proposed model m^{cand}. Given $L(m^{cand})$ the candidate model's performance and $L(m^{cur})$ the current model's performance, m^{cand} is accepted as model space sample if

$$r < \frac{L\left(m^{cand}\right)}{L\left(m^{cur}\right)} \tag{6}$$

where r is a random number between 0 and 1.

If m^{cand} is accepted, it is updated as new current model and it becomes the starting point for the subsequent iteration; otherwise, the exploration stays at m^{cur} and a new candidate model is proposed.

The acceptance rule we adopted follows the idea behind the Metropolis-Hastings algorithm, which is developed for sampling a probability density function defined over a model space (Sambridge and Mosegaard, 2002). We apply that idea and its acceptance rule here, in non-probabilistic terms, to guide our random walk toward better fitting areas of the model space. In fact, when providing a better fit to the data, the newly proposed model m^{cand} is always accepted [i.e., when $L(m^{cand}) > L(m^{cur})$]. The proposed model m^{cand} can still be accepted, even when it provides a worse fit to the data compared to the current model m^{cur} [i.e., when $L(m^{cand}) < L(m^{cur})$]., as there still is a non-zero probability for the random number r – constrained between 0 and 1 – to be minor than $L(m^{cand})/L(m^{cur})$: the lower the ratio, the lower the probability. The overall acceptance mainly depends on the shape of L(m) and on the distance between the current and the proposed model: $\triangle m = |m^{cand} - m^{cur}|$. In fact, the algorithm requires a fine-tuning of the jump length, which is the only necessary user-defined parameter. Too little steps could cause the model space exploration to be trapped in a local minimum, without escaping and thus leaving wide regions of the model space unexplored. On the other hand, too long steps could provide model proposals too far away from the best fitting areas, causing too many rejections and waste of computational resources. For this reason and based on three preliminary tests we performed on subsets of the data, we rescale the uniform random deviates to be within the [0.05,0.25] interval, which provided a balanced compromise between model space exploration and exploitation.

The inversion on the full dataset was eventually run for 50'000 iterations. As we do not formulate the inverse problem in probabilistic terms, this prevents us from interpreting the sampled models as the realizations of a probability density function. Nevertheless, we used the *a priori* knowledge on the IGB to assign reasonable boundaries to all inversion parameters (as discussed in section "Model parameterization") and we use a performance-driven pseudo-random walk to guide our exploration toward the best-fitting areas of the model space, to retrieve an ensemble of acceptable IGB models, which reproduce and explain the observed datasets.

RESULTS

The inversion algorithm kept 41'363 models out of 50'000 iterations in one week of computation time on a standard computer (2.2GHz Quad-Core Intel Core i7), requiring ∼ 10s to 12s per iteration. Throughout the model space exploration, 20'692 steps were directed toward a better performing model and were therefore retained. The remaining sampled models were accepted based on Equation (6) even if they were not improving the performance with respect to the previous iteration, with an acceptance ratio of ∼ 70%. Exploration has been favored in spite of exploitation. By inspecting the distribution of all sampled models for all the model parameter pairs (**Supplementary Material 3**), a satisfactory model space coverage has been achieved for all the pairs. Less samples cover the worse fitting areas, while a higher sampling density concentrates around the best performing models.

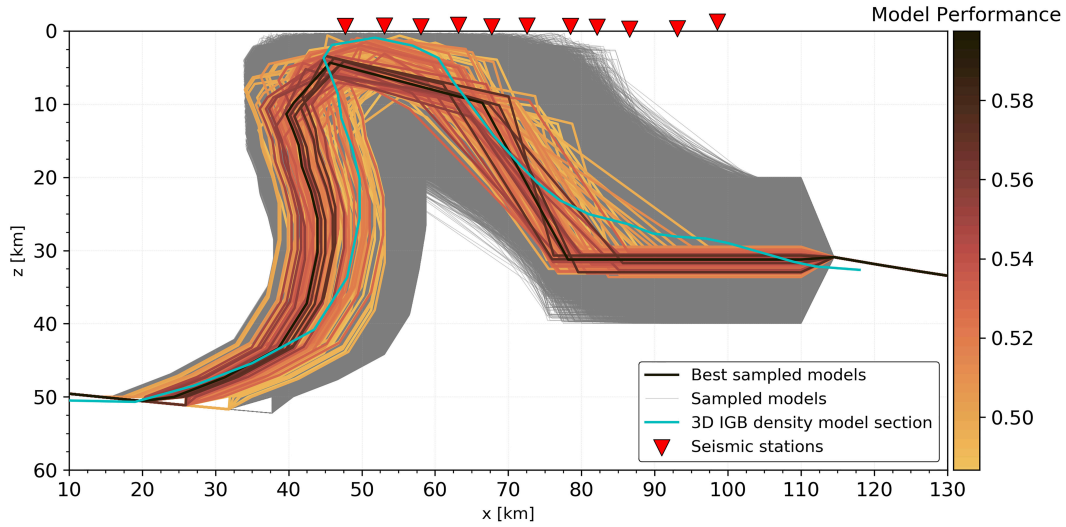

FIGURE 7 | Model geometries resulting from the joint inversion. The 150 best performing models are shown in colored lines according to the model performance. All other sampled and kept models are shown in gray (in total 41'365 models). The cyan dashed line is the cross-section through the 3D IGB gravity model from previous study (Scarponi et al., 2020).

The seismic model performances range from 0 to 0.64 with a nearly symmetric bell-shaped distribution and a median value of 0.26 (negative performances have been discarded by choice). The gravity model performances vary across a narrower range of values, between 0.59 and 0.99, with a negative skew (more frequent higher values) and a median of 0.90 (**Supplementary Material 4**). The better performance of the model with respect to gravity data is not surprising, as our *a priori* choices for the model geometry were driven by the recently constrained 3D gravity model. Therefore, in the final model performance, defined as the multiplication of seismic and gravity fits, the seismic performance acted as a more important guiding factor for the model space exploration. The gravity performance provided finer tuning across the best fitting areas, and also resolved some of the inherent trade-off in RF analysis. Furthermore, jointly inverting with seismic data allowed to constrain geometry features which were not resolvable with a gravity-only inversion, as demonstrated by preliminary tests (**Supplementary Material 6**). The final model performances range between 0 and 0.60, with a median value of 0.22.

The results reproduce well the main features of the observed seismic and gravity anomalies.

First, we describe the best performing model and then we consider the group of 150 best fitting models.

The best performing model fits the gravity anomalies both in terms of location and amplitude, with a slightly broader peak compared to the observations (**Figure 6C**). The vertical part of the IGB model is wider than what was suggested by the earlier, 3D gravity model (Scarponi et al., 2020). Node 2 locates the shallowest IGB portion in the vicinity of the western kink of the previous model (**Figure 6A**), as shallow as 4 km depth, and West of seismological station IA01A and of the IL at the surface. This location is a few kilometers too far to the West considering the local *a priori* geological knowledge. Concerning the migration images, the shallowest interface segment (node 2 to node 3) successfully reproduces the shallowest converted phases in the western portion of the profile, locating a sharp increase of shear-wave velocity right below the surface, between 3 and 7 km depth, and extending for ∼ 20 km to the East from station IA01A to station IA05A (**Figures 6D,E**). Minor local features are recovered as well, such as the positive patch at ∼ 75 km distance and at 12 km depth, and further reverberations at ∼ 45 km distance and 15 km depth, below the shallowest conversion. The eastern portion of the image with prominent signals at ∼ 35 km depth is recovered and consistent with the Moho depth further to the East (**Figures 6A,D,E**).

Using a single interface model prevents us from reproducing the eastern negative amplitudes at ∼ 48 km depth ranging from 80 to 105 km distance, which cannot be regarded a converted-phase multiple reflection (PpSs) from an interface at 34 km depth. Such phase would be expected at a higher delay time (∼ 19 s with the given model structure and therefore migrated at more than 100 km depth). This feature can represent a real decrease of shear-wave seismic velocity with depth, or PpSs multiples of local conversions seen in the upper crust (**Figure 6D**) which are not modeled in this distance range.

A more representative image of the joint inversion results is provided by looking at the ensemble of the 150 best performing models (**Figure 7**). From this, the general characteristics of the retrieved well-fitting IGB model geometries can be outlined. It still is a shallow-reaching, crustal-scale important geophysical anomaly, similar to our earlier 3D gravity model (Scarponi et al., 2020), but without a prominent westward extending horizontal "beak" as in the historical model of Berckhemer (1968),. A shallow interface is always present in the western part of the profile between 1 and 10 km depth, between IA01A and

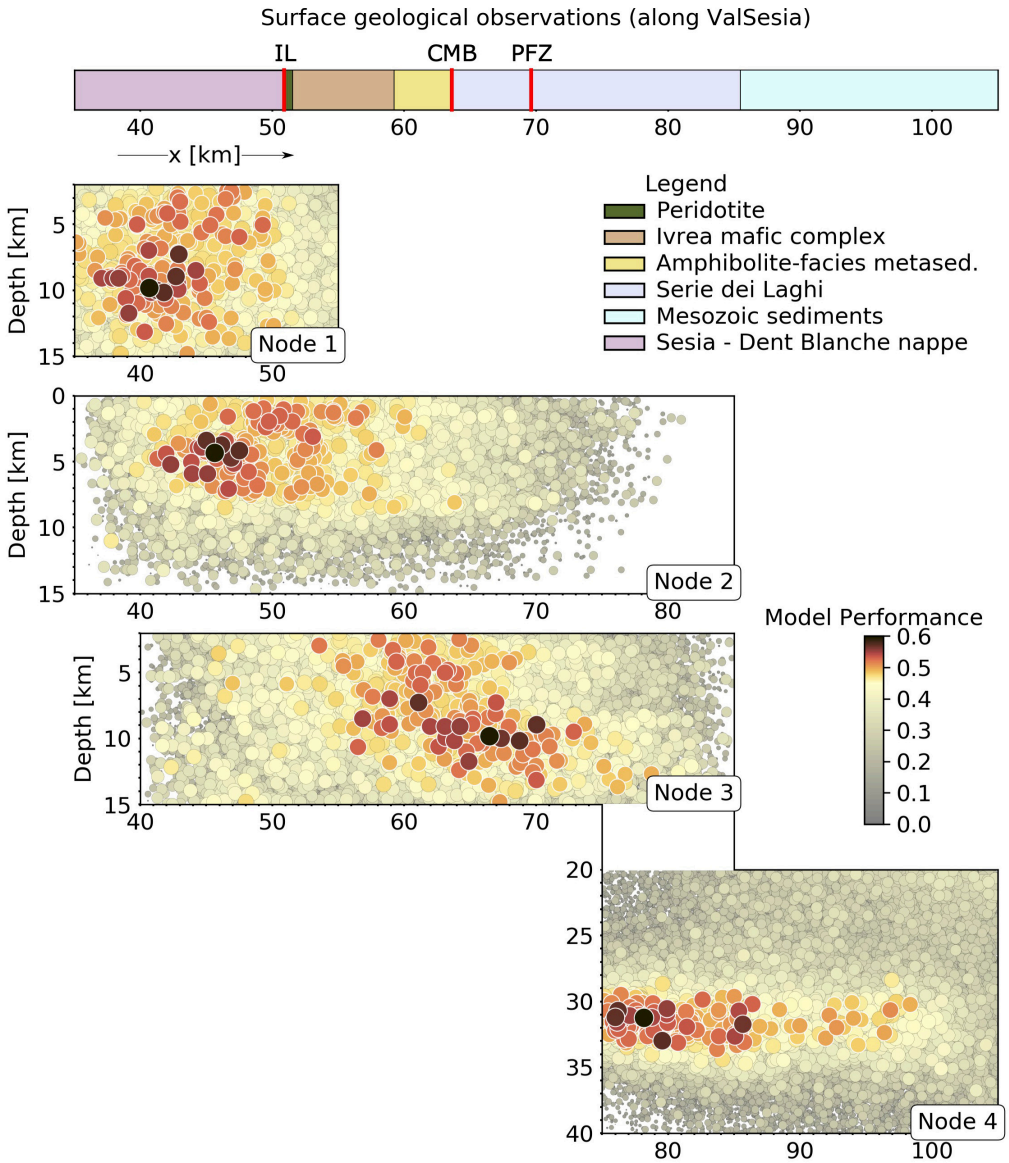

FIGURE 8 | Inversion results on the position of the four nodes, presented in four distance–depth panels. Each panel is showing the locations visited by each single node during the inversion, for each sampled model. All four panels share the same horizontal *X*-axis, but they are shifted along the vertical direction for better visual distinction. Panels of nodes 3 and 4 share the same depth axis, too. All sampled and kept models are shown (in total 41'363), with size and color according to the model performance, plus all models with performance higher than 0.48 are indicated by white edges. Each panel is limited to the allowed range of parameter values. On top, the corresponding surface geological observations from earlier studies (along the same *X*-axis), identifying rock types along the profile (legend on the top right, same as in **Figure 2**). The relevant faults for this study are indicated (as in **Figure 2**) as "IL" for Insubric Line, "CMB" for Cossato-Mergozzo-Brissago Line and "PFZ" for Pogallo Fault Zone.

IA05A stations (~40 to 70 km distance). The position of the vertical structures is less constrained than the horizontal ones, as the steeply dipping structures cannot be imaged by the RFs at all. The shape of the western IGB vertical wall was inherited by the previous 3D gravity model (Scarponi et al., 2020) and its horizontal position was here varied together with node 1. The range of variation of either side of the IGB neck spans ~ 15 km horizontally, while the horizontal segments span a narrower depth range (less than 10 km). In the western part, the neck is on average 30 ± 5 km wide, only a few models deviate up to ± 10 km width. The main IGB discontinuity is tightly constrained in the eastern, flat part of the profile at 35 km depth (**Figure 7**), which is consistent with the Moho structure there (Spada et al., 2013).

How well the IGB-top interface geometry is constrained by the joint inversion can be assessed through the distribution of the sampled model nodes position, which also shows the characteristics of the model space exploration (**Figure 8**). All four nodes have spanned the entire allowed perimeter, with a

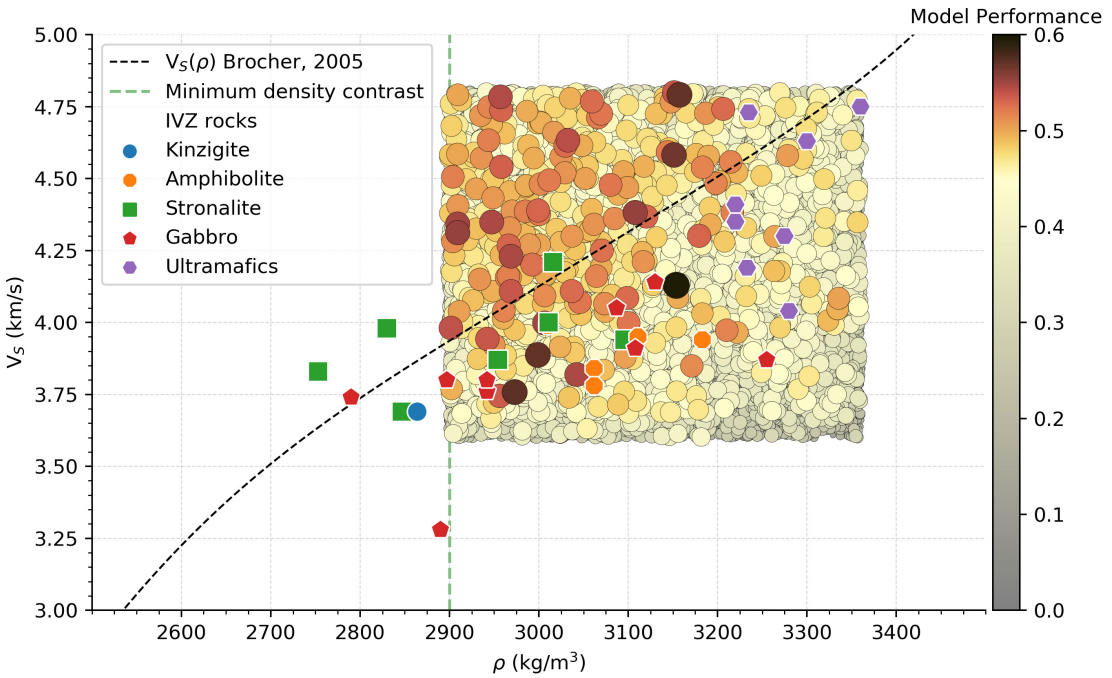

FIGURE 9 | Inversion results on the density and shear-wave velocity contrasts associated with the 2D model interface, shown as gray-contoured circles of size and color according to to the model performance. The background density and the background shear-wave velocity absolute values are common for all models (2700 kg/m^3 and 3.5 km/s, respectively). For comparison, the regression fit for the vs(ρ) relationship from rocks discussed in Brocher (2005) (black dashed line) is shown together with a relevant set of rock physical properties across the IVZ from the SAPHYR catalog (Zappone et al., 2015).

decreasing sampling density toward the worse-fitting external boundaries, and with node 2 being more restricted by definition of its position lying between and above nodes 1 and 3 (**Figure 8**). This proves the efficiency of the implemented algorithm in providing a satisfactory model space exploration, which is computationally much more affordable than a 9-dimensional full grid search at a comparable resolution. In general, node depths are better constrained better than their horizontal locations. The depth-variation range of ∼ 10 km for node 1 to ∼ 4-5 km for node 4.

Node 1 solutions are preferentially at 10 km depth to West of the IL, which is in agreement with the IL being a vertical to sub-vertical dipping feature. Node 2 constrains the shallowest model position and features a bi-modal depth result, with a group of solutions between ∼ 1-3 km at x = 50-55 km. This finding is in agreement with the outcropping dense rocks at the surface. Another group of solutions concentrate at ∼ 3-7 km depth to the West of the surface trace of the IL. Node 3 isn't tightly constrained; nevertheless, it extends the shallow IGB portion to the center of the seismic profile, until the surface trace of the Pogallo Fault Zone (PFZ), prior to high-angle deepening toward node 4 at 31 ± 2 km depth (**Figure 8**).

Concerning the physical property contrasts of the IGB compared to the shallower layer (**Figure 9**), the well-performing models point to a relatively broad range of shear-wave seismic velocity increases. This is mainly constrained by the amplitude of the Ps signals, which is not their most reliable feature due to attenuation. A certain number of better-performing models is associated with a velocity contrast of the order of 0.5 to 1.2 km/s. The best performing density contrasts are in the 200 to 400 kg/m^3 range, with some models at 500 kg/m^3 associated to the higher v_S contrasts. This is in good agreement with the earlier 3D gravity model which suggested that 500 kg/m^3 represents a reasonable higher limit for the IGB density contrast (e.g., Scarponi et al., 2020). We note that models with very high density- and low velocity-contrasts perform poorly (**Figure 9**).

We note that the gravimetric method is able to resolve density contrasts, and not absolute densities. Therefore, the set of inversion results on **Figure 9** can be shifted to the right, to higher density values, by simply assuming that the surrounding crustal density was not 2700 kg/m^3 but higher. A geologically reasonable shift would be around 100 kg/m^3: a density of 2800 kg/m^3 is reasonable for mid-crustal rocks; hence, the well-fitting models from the joint inversion would fall closer to the v_S–ρ relationship trend taken from Brocher (2005). We note that the trend line of Brocher (2005) represents empirical fits, and that actual rock property data dispersions of 0.2 km/s in v_S or of 200 kg/m^3 are reasonable.

DISCUSSION

The inversion results can be interpreted in light of the existing multidisciplinary investigations on the IVZ formation history and the surrounding crustal structures. By inspecting the best performing IGB models (**Figure 7**), two main groups of models can be identified according to the shallow geometry

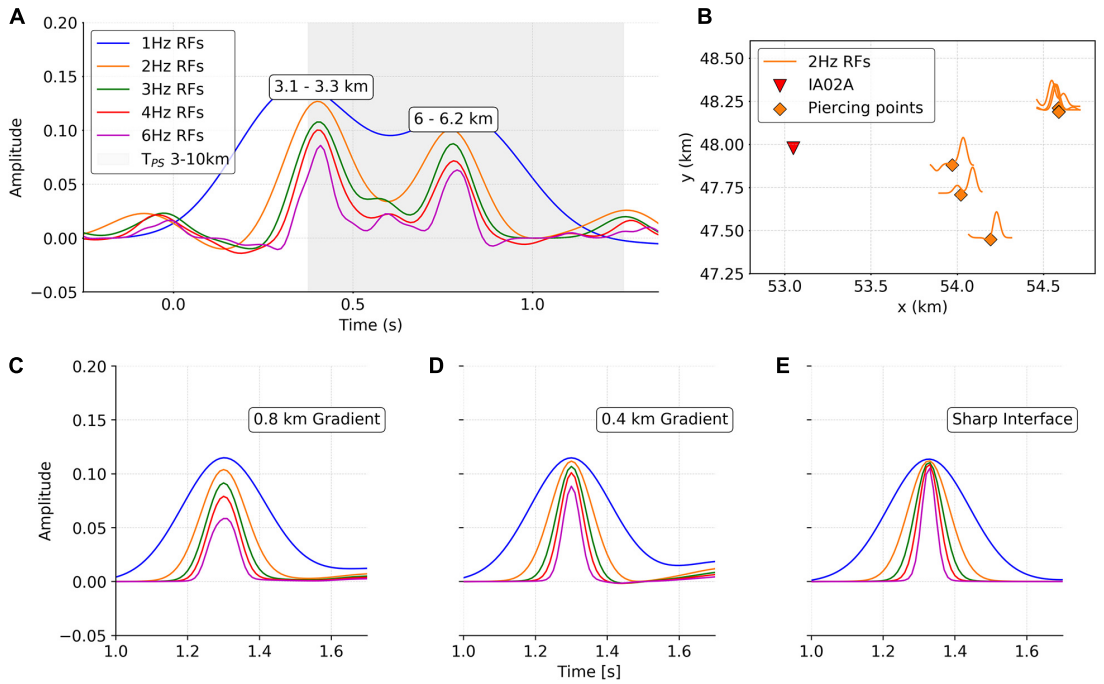

FIGURE 10 | Investigating the sharpness of the seismic interface by frequency-dependent analysis of the highest quality RFs near station IA02A. **(A)** Observed RFs stacked at different frequency ranges, from 0.1 Hz to five different maximum frequencies as specified in the legend. The decreasing signal width, with increasing frequency, points toward a discontinuity sharper than the resolution of the highest frequency waves. The gray band in the background indicates the expected time delay for a P-to-S converted phase from a discountinuity located between 3 and 10 km depth, and with vs = 3.5 km/s above it. The estimated depth of the conversion for the two observed peaks is indicated. For this analysis, a stricter quality control has been applied and only the RFs qualifying at all frequency ranges have been considered. **(B)** Piercing point map (orange squares) for the traces that have been considered in **(A)**, for the frequency range 0.1 Hz to 2 Hz. Next to each piercing point, the time interval 0 to 1s of the associated RFs is plotted, to highlight the spatial variability of the stacked RFs signals. **(C–E)** Synthetic RFs for the same frequencies as in **(A)** demonstrating the effect of velocity gradient sharpness on peak widths and amplitudes.

characteristics of the retrieved IGB models (**Figures 7**, **8**, node 2). The first group of models suggests a gently eastward-dipping interface in the shallow portion, locating the IGB-top head from ∼ 3–7 km depth (node 2) to ∼ 8–12 km depth (node 3) with a minimum horizontal extent of ∼ 20 km. The second group of models features node 2 at clearly shallower depths than nodes 1 and 3, reaching as shallow as 1-3 km depth between seismological stations IA01A and IA03A. While both groups are in agreement with a western boundary associated with a steeply westward dipping IL, the very shallow anomaly of the latter group agrees with the well-known variety of lower to middle crustal rock outcrops observed across the IVZ. Moreover, when compared with the rock properties of *in situ* IVZ samples (Zappone et al., 2015) in v_S–ρ space, the inversion results show good agreement with several gabbro samples, and also with ultramafic rock and amphibolite samples if the aforementioned density-shift is considered (**Figure 9**). These align with indications drawn from studies by Pistone et al. (2020) and Scarponi et al. (2020) on possible rock types. However, we make no further selection of rock types, to avoid potential over-interpretation here, as reality is surely more complex than a single-discontinuity 2D model. Nevertheless, considering the model assumptions, the match with rock properties is satisfactory.

An interesting feature of sampled IGB model structures is the steep eastward-dipping segment at the center of our profile between nodes 3 and 4 (∼ 70-75 km distance, **Figure 7**), representing the eastern flank of the IGB. The steepness of this segment precludes any direct imaging by the RFs. The segment, however, joins the two surrounding and imaged segments (between nodes 2 and 3 and east of node 4) and it compares well with the location at the surface of the Pogallo Fault Zone (PFZ, **Figure 8**). The PFZ is a prominent Jurassic fault zone associated with pre-orogenic crustal thinning episodes, related to the opening of the Alpine Tethys without being subsequently reactivated during the orogenic compression, but only tilted to its present-day vertical position (Handy et al., 1999; Petri et al., 2019).

The PFZ crosses our seismic profile at the surface at the Lago d'Orta, between stations IA05A and IA06A. Several evidences suggest that the PFZ may have offset the Moho during the Jurassic (Handy, 1987) and that the shape of the IGB was determined by a combination of Jurassic crustal thinning and subsequent Alpine orogeny (Schmid et al., 1987). The importance of pre-orogenic inheritance with respect to syn-orogenic processes is however, clearer in the light of our results. Along our profile, the eastern flank of the IGB coincides much more closely with the surface exposure of the PFZ than what was pointed at by previous models (Berckhemer, 1968): the PFZ is likely responsible for shaping the Moho since the Jurassic, implying that the IGB was strongly pre-set by the pre-orogenic rift-related deformations, before being integrated in the Alpine orogeny.

In light of the planned scientific drilling in Val Sesia (Pistone et al., 2017), we further investigated one particular property of the shallowest portion of the IGB interface, namely the sharpness of the velocity discontinuity, by applying frequency-dependent RF analysis. In fact, the frequency content of the observed RFs can put constraints on the resolved thickness of the seismic velocity gradient associated with the converted-wave generating interface itself (James et al., 2003). The narrower the peaks with increasing RF analysis frequency, the sharper the interface at which the conversion was produced. Conversely, if there is a vertical gradient, the highest frequency RFs will remain broad and lose amplitude. We demonstrate this effect by synthetics, which we then compared with the observed RFs. We focused our analysis on station IA02A and stacked a high-quality selection of RFs, for a certain number of high-pass filtering frequencies: 1, 2, 3, 4, and 6 Hz, respectively (**Figure 10A**). We used RFs in the ZRT coordinate system and only for eastward [45-135°] back-azimuths to maximize the Ps conversion amplitude on the inferred eastward dipping interface. The RF stacks show two shallow conversion peaks at ∼ 3 and 6 km depth (**Figure 10A**). Considering the respective piercing points, the two peaks correspond to early arrivals from ENE to late arrivals from ESE. This points to local structural variations at shallow depth beneath the gabbro and norite rocks exposed on the surface (**Figure 10B**). Comparing our results to the synthetics shown in **Figures 10C–E**) indicates that the velocity gradient thickness is more than 0.4 km, and closer to but less than 0.8 km. This is slightly more than the Moho transition zone of 0.5 km proposed for the Kaapvaal craton by James et al. (2003), based on a similar seismic analysis. Our finding is well-resolved as the wavelength of 6 Hz waves at v_S of 3.5 km/s is below 600 m, so this approach would have been able to resolve sharper gradients.

Future contributions could address the IGB structure by inverting for more complicated geometries, including more than one seismic interface. P-to-SH converted phases could be addressed as well, as they do present seismic energy due to the presence of dipping angles and possibly anisotropy, which was not addressed in this contribution as there were strong *a priori* indications for dip. Much finer, high-resolution images of the western part of our area will be revealed with the recently acquired active seismic data with Vibroseis sources and several targets at depth along two long profiles crossing between stations 1 and 2, and carried out as a cooperative project between GFZ Potsdam, Montanuniversität Leoben and the University of Lausanne. We plan to complement these with higher resolution gravimetric and magnetic measurements around the Balmuccia peridotite, to approach the scale of scientific drilling. Subsequent, joint petrological and geophysical investigations will further constrain the lithologies composing the IGB.

CONCLUSION

We implemented and ran a joint inversion algorithm using seismic receiver functions and gravity data to constrain the shape and the physical properties of the Ivrea Geophysical Body (IGB), along a 2D West-East cross-section along the Val Sesia profile and across the Ivrea-Verbano Zone (IVZ). The algorithm executes a performance-driven random walk in the model space, to preferentially explore the better fitting areas of the model space.

Processing the new seismological and recently collected gravity data led to new constraints on the IGB structure. A shallow and relatively sharp interface is resolved over at least 20 km horizontal distance in the western part of the seismic profile (between ∼ 8.11°E and 8.43°E). In particular, we identify two main groups of model geometries for the shallowest portion of the IGB: a flat and gently eastward-dipping interface between 3 and 7 km depth, and a structure with a local peak reaching as shallow as 1-3 km depth, beneath the three westernmost stations (∼ 8.11°E to 8.25°E). While both groups of models agree with a western boundary associated with the steeply westward-dipping Insubric Line, the latter is more consistent with the well-known lower crustal rock complex outcropping at the western edge of the IVZ. Further agreement with the observed geological structures at the surface is found by comparing the IGB model structure with the location of the Pogallo Fault Zone (PFZ). The eastern flank of the protruding IGB coincides with the surface exposure of the Jurassic PFZ, highlighting the role of pre-orogenic processes in shaping the IGB.

The retrieved IGB velocity and density contrasts relative to the surroundings are in general good agreement with the physical properties of the rock samples collected in the area and analyzed in earlier studies. The results span a rather broad range of acceptable shear-wave velocity contrasts (0.5 to 1.2 km/s), providing slightly higher velocities than those from field samples and/or trends in the literature (Brocher, 2005). In terms of density, a reasonably narrow range of better-fitting density contrasts of 200–400 kg/m^3 is found, in agreement or slightly below the recent 3D IGB density model.

We further analyzed the amplitude and frequency content of a stack of selected high-quality receiver functions, to constrain the sharpness of the vertical velocity-gradient associated with the shallow IGB discontinuity. We then compared the observed stack with synthetics, for a range of different pre-deconvolution maximum filtering frequencies, and using various vertical velocity-gradient thicknesses. We found thicknesses of 0.8 km and 0.4 km as reasonable higher and lower limits for the shallow velocity-gradient mimicking the top of the IGB discontinuity. Already acquired but still in-the-processing active seismic campaign data will shed more light on the very shallow structure at high resolution along the same profile, and prepare the ground for deep scientific drilling to deepen our knowledge of the IGB.

DATA AVAILABILITY STATEMENT

The new seismic data will be openly and freely available from September 2022 through the ORFEUS data center, under the FDSN network code XK and is already referenced at the following doi: 10.5281/zenodo.1038209. The gravity dataset is available upon request to either of the first two authors.

AUTHOR CONTRIBUTIONS

MS and GH designed the study. MS, GH, JP, SS, and LB collected the new field data. MS performed the processing and inversion with guidance from GH. MS and GH drafted the manuscript. MS, GH, JP, SS, and BP discussed the obtained results. All authors revised the manuscript and approved the final version.

FUNDING

We acknowledge the Swiss National Science Foundation (SNF) for having supported this research (grant numbers PP00P2_157627 and PP00P2_187199 of project OROG3NY), as well as the Grant Agency of the Czech Republic (No. 21-25710). We also acknowledge project CzechGeo/EPOS No. LM2015079 of the MEYS for funding the MOBNET station pool.

ACKNOWLEDGMENTS

We would like to acknowledge many colleagues for their precious contributions and various inputs that made this work possible, both in the field and during the subsequent steps to P. Jedlièka, J. Kotek, and L. Vecsey from Institute of Geophysics, Czech Academy of Sciences, for installation of seismic stations within this project (stations of MOBNET pool, granted by project CzechGeo/EPOS No. LM2015079 of the MEYS) and for seismic data pre-processing, formatting, and checking; T. Berthet, L. Colavitti, S. Subedi, G. Moradi, C. Alvizuri, and the whole IvreaArray working team for the discussions and fieldwork efforts, together with numerous people in the field area for their help and support during the measurement campaigns, and the seismic sensors installation and maintenance: in particular to the mayors and the local contacts in the communes of Boccioleto, Vocca-Sassiglioni, Varallo, Civiasco, Cesara, Cheggino, Nebbiuno, Calogna, Ispra, and Biandronno; U. Marti, R. Barzaghi, the OGS institution, A. Zappone, T. Diehl, R. Cattin, and S. Mazzotti for sharing background data, internal discussions, and the GravProcess software sharing and editing. We are grateful for the enthusiastic support of many colleagues from the DIVE project, especially Othmar Müntener, Alberto Zanetti, Mattia Pistone, Andrew Greenwod, Luca Ziberna, and Klaus Holliger.

SUPPLEMENTARY MATERIAL

The Supplementary Material for this article can be found online at: https://www.frontiersin.org/articles/10.3389/feart.2021.671412/full#supplementary-material

REFERENCES

Ammon, C. J., Randall, G. E., and Zandt, G. (1990). On the nonuniqueness of receiver function inversions. *Journal of Geophysical Research: Solid Earth* 95, 15303–15318.

Ansorge, J. (1979). Crustal section across the zone of Ivrea-Verbano from the Valais to the Lago Maggiore. *Bollettino di Geofisica Teorica ed Applicata* 21, 149–157.

Basuyau, C., and Tiberi, C. (2011). Imaging lithospheric interfaces and 3D structures using receiver functions, gravity, and tomography in a common inversion scheme. *Computers & geosciences* 37, 1381–1390.

Bayer, R., Carozzo, M., Lanza, R., Miletto, M., and Rey, D. (1989). Gravity modelling along the ECORS-CROP vertical seismic reflection profile through the Western Alps. *Tectonophysics* 162, 203–218.

Berckhemer, H. (1968). Topographie des "Ivrea-Körpers" abgeleitet aus seismischen und gravimetrischen Daten: Schweiz. *Mineral. Petrogr. Mitt* 48, 235–246.

Berger, A., Mercolli, I., Kapferer, N., and Fügenschuh, B. (2012). Single and double exhumation of fault blocks in the internal Sesia-Lanzo Zone and the Ivrea-Verbano Zone (Biella, Italy). *International Journal of Earth Sciences* 101, 1877–1894.

Bodin, T., Sambridge, M., Tkalèiæ, H., Arroucau, P., Gallagher, K., and Rawlinson, N. (2012). Transdimensional inversion of receiver functions and surface wave dispersion. *Journal of Geophysical Research: Solid Earth* 117, B02301.

Brack, P., Ulmer, P., and Schmid, S. M. (2010). A crustal-scale magmatic system from the Earth's mantle to the Permian surface: Field trip to the area of lower Valsesia and Val d'Ossola (Massiccio dei Laghi, Southern Alps, Northern Italy). *Swiss Bulletin für angewandte Geologie* 15, 3–21.

Brocher, T. M. (2005). Empirical relations between elastic wavespeeds and density in the Earth's crust. *Bulletin of the seismological Society of America* 95, 2081–2092.

Bürki, B. (1990). "Geophysical interpretation of astrogravimetric data in the Ivrea Zone," in *Exposed Cross-Sections of the Continental Crust*, eds M. H. Salisbury and D. M. Fountain (Dordrecht: Springer), 545–561.

Cattin, R., Mazzotti, S., and Baratin, L.-M. (2015). GravProcess: An easy-to-use MATLAB software to process campaign gravity data and evaluate the associated uncertainties. *Computers & geosciences* 81, 20–27.

De Franco, R., Biella, G., Boniolo, G., Corsi, A., Demartin, M., Maistrello, M., et al. (1997). Ivrea seismic array: a study of continental crust and upper mantle. *Geophysical Journal International* 128, 723–736.

Diehl, T., Husen, S., Kissling, E., and Deichmann, N. (2009). High-resolution 3-DP-wave model of the Alpine crust. *Geophysical Journal International* 179, 1133–1147.

Drahos, D. (2008). Determining the objective function for geophysical joint inversion. *Geophysical Transactions* 45, 105–121.

Fountain, D. M. (1976). The Ivrea—Verbano and Strona-Ceneri Zones, Northern Italy: a cross-section of the continental crust—new evidence from seismic velocities of rock samples. *Tectonophysics* 33, 145–165.

Frederiksen, A., and Bostock, M. (2000). Modelling teleseismic waves in dipping anisotropic structures. *Geophysical Journal International* 141, 401–412.

Handy, M., Franz, L., Heller, F., Janott, B., and Zurbriggen, R. (1999). Multistage accretion and exhumation of the continental crust (Ivrea crustal section, Italy and Switzerland). *Tectonics* 18, 1154–1177.

Handy, M. R. (1987). The structure, age and kinematics of the Pogallo Fault Zone; Southern Alps, northwestern Italy. *Eclogae Geologicae Helvetiae* 80, 593–632.

Handy, M. R., Schmid, S. M., Bousquet, R., Kissling, E., and Bernoulli, D. (2010). Reconciling plate-tectonic reconstructions of Alpine Tethys with the geological–geophysical record of spreading and subduction in the Alps. *Earth-Science Reviews* 102, 121–158.

Handy, M. R., Ustaszewski, K., and Kissling, E. (2015). Reconstructing the Alps–Carpathians–Dinarides as a key to understanding switches in subduction polarity, slab gaps and surface motion. *International Journal of Earth Sciences* 104, 1–26.

Hetényi, G., Plomerová, J., Bianchi, I., Exnerová, H. K., Bokelmann, G., Handy, M. R., et al. (2018). From mountain summits to roots: Crustal structure of the Eastern Alps and Bohemian Massif along longitude 13.3 E. *Tectonophysics* 744, 239–255.

Hetényi, G., Plomerová, J., Solarino, S., Scarponi, M., Vecsey, L., Munzarová, H., et al. (2017). *IvreaArray—an AlpArray complementary experiment*. doi: 10.5281/zenodo.1038209

Hetényi, G., Ren, Y., Dando, B., Stuart, G. W., Hegedûs, E., Kovács, A. C., et al. (2015). Crustal structure of the Pannonian basin: the AlCaPa and Tisza Terrains and the Mid-Hungarian zone. *Tectonophysics* 646, 106–116.

Hubbert, M. K. (1948). A line-integral method of computing the gravimetric effects of two-dimensional masses. *Geophysics* 13, 215–225.

James, D. E., Niu, F., and Rokosky, J. (2003). Crustal structure of the Kaapvaal craton and its significance for early crustal evolution. *Lithos* 71, 413–429.

Julia, J., Ammon, C., Herrmann, R., and Correig, A. M. (2000). Joint inversion of receiver function and surface wave dispersion observations. *Geophysical Journal International* 143, 99–112.

Kennett, B., and Engdahl, E. (1991). Traveltimes for global earthquake location and phase identification. *Geophysical Journal International* 105, 429–465.

Khazanehdari, J., Rutter, E., and Brodie, K. (2000). High−pressure−high−temperature seismic velocity structure of the midcrustal and lower crustal rocks of the Ivrea−Verbano zone and Serie dei Laghi, NW Italy. *Journal of Geophysical Research: Solid Earth* 105, 13843–13858.

Kissling, E. (1993). Deep structure of the Alps—what do we really know? *Physics of the Earth and Planetary Interiors* 79, 87–112.

Kissling, E., Wagner, J., and Mueller, S. (1984). "Three-dimensional gravity model of the northern Ivrea-Verbano Zone," in *Geomagnetic and Gravimetric Studies of the Ivrea Zone: Matér. Géol. Suisse. Géophys*, Vol. 21, eds J.-J. Wagner and St Müller 55–61.

Langston, C. A. (1979). Structure under Mount Rainier, Washington, inferred from teleseismic body waves: Journal of Geophysical Research. *Solid Earth* 84, 4749–4762.

Lanza, R. (1982). Models for interpretation of the magnetic anomaly of the Ivrea body. *Geologie Alpine* 58, 85–94.

Levin, V., and Park, J. (1997). Crustal anisotropy in the Ural Mountains foredeep from teleseismic receiver functions. *Geophysical Research Letters* 24, 1283–1286.

Ligorría, J. P., and Ammon, C. J. (1999). Iterative deconvolution and receiver-function estimation. *Bulletin of the seismological Society of America* 89, 1395–1400.

Masson, F., Verdun, J., Bayer, R., and Debeglia, N. (1999). Une nouvelle carte gravimétrique des Alpes occidentales et ses conséquences structurales et tectoniques. *Comptes Rendus de l'Académie des Sciences-Series IIA-Earth and Planetary Science* 329, 865–871.

Moorkamp, M., Jones, A., and Fishwick, S. (2010). Joint inversion of receiver functions, surface wave dispersion, and magnetotelluric data. *Journal of Geophysical Research: Solid Earth* 115, B04318.

Nicolas, A., Hirn, A., Nicolich, R., and Polino, R. (1990). Lithospheric wedging in the western Alps inferred from the ECORS-CROP traverse. *Geology* 18, 587–590.

Niggli, E. (1946). Über den Zusammenhang zwischen der positiven Schwereanomalie am Südfuß der Westalpen und der Gesteinszone von Ivrea. *Eclogae Geologicae Helvetiae* 39, 211–220.

Petri, B., Duretz, T., Mohn, G., Schmalholz, S. M., Karner, G. D., and Müntener, O. (2019). Thinning mechanisms of heterogeneous continental lithosphere. *Earth and Planetary Science Letters* 512, 147–162.

Pistone, M., Müntener, O., Ziberna, L., Hetényi, G., and Zanetti, A. (2017). Report on the ICDP workshop DIVE (Drilling the Ivrea–Verbano zonE). *Scientific Drilling* 23, 47–56.

Pistone, M., Ziberna, L., Hetényi, G., Scarponi, M., Zanetti, A., and Müntener, O. (2020). Joint Geophysical−Petrological Modeling on the Ivrea Geophysical Body Beneath Valsesia, Italy: Constraints on the Continental Lower Crust. *Geochemistry, Geophysics, Geosystems* 21, e2020GC009397.

Rey, D., Quarta, T., Mouge, P., Miletto, M., and Lanza, R. (1990). Gravity and aeromagnetic maps of the western Alps: contribution to the knowledge of the deep structures along the ECORS-CROP seismic profile. *Mémoires de la Société géologique de France (1833)* 156, 107–121.

Sambridge, M. (1999). Geophysical inversion with a neighbourhood algorithm—I. Searching a parameter space. *Geophysical journal international* 138, 479–494.

Sambridge, M., and Mosegaard, K. (2002). Monte Carlo methods in geophysical inverse problems. *Reviews of Geophysics* 40, 3–1.

Scarponi, M., Hetényi, G., Berthet, T., Baron, L., Manzotti, P., Petri, B., et al. (2020). New gravity data and 3-D density model constraints on the Ivrea Geophysical Body (Western Alps). *Geophysical Journal International* 222, 1977–1991.

Schmid, S., Aebli, H., Heller, F., and Zingg, A. (1989). The role of the Periadriatic Line in the tectonic evolution of the Alps. *Geological Society, London, Special Publications* 45, 153–171.

Schmid, S. M., Kissling, E., Diehl, T., van Hinsbergen, D. J., and Molli, G. (2017). Ivrea mantle wedge, arc of the western alps, and kinematic evolution of the alps-apennines orogenic system. *Swiss J. Geosci.* 110, 581–612. doi: https://doi.org/10.1007/s00015-016-0237-0

Schmid, S., and Kissling, E. (2000). The arc of the western Alps in the light of geophysical data on deep crustal structure. *Tectonics* 19, 62–85.

Schmid, S., Zingg, A., and Handy, M. (1987). The kinematics of movements along the Insubric Line and the emplacement of the Ivrea Zone. *Tectonophysics* 135, 47–66.

Schmid, S. M., Fügenschuh, B., Kissling, E., and Schuster, R. (2004). Tectonic map and overall architecture of the Alpine orogen. *Eclogae Geologicae Helvetiae* 97, 93–117.

Shibutani, T., Sambridge, M., and Kennett, B. (1996). Genetic algorithm inversion for receiver functions with application to crust and uppermost mantle structure beneath eastern Australia. *Geophysical Research Letters* 23, 1829–1832.

Solarino, S., Malusà, M. G., Eva, E., Guillot, S., Paul, A., Schwartz, S., et al. (2018). Mantle wedge exhumation beneath the Dora-Maira (U) HP dome unravelled by local earthquake tomography (Western Alps). *Lithos* 296, 623–636.

Spada, M., Bianchi, I., Kissling, E., Agostinetti, N. P., and Wiemer, S. (2013). Combining controlled-source seismology and receiver function information to derive 3-D Moho topography for Italy. *Geophysical Journal International* 194, 1050–1068.

Subedi, S., Hetényi, G., Vergne, J., Bollinger, L., Lyon-Caen, H., Farra, V., et al. (2018). Imaging the Moho and the Main Himalayan Thrust in Western Nepal with receiver functions. *Geophysical Research Letters* 45, 13222–13230.

Syracuse, E. M., Maceira, M., Prieto, G. A., Zhang, H., and Ammon, C. J. (2016). Multiple plates subducting beneath Colombia, as illuminated by seismicity and velocity from the joint inversion of seismic and gravity data. *Earth and Planetary Science Letters* 444, 139–149.

Thouvenot, F., Paul, A., Senechal, G., Hirn, A., and Nicolich, R. (1990). ECORS-CROP wide-angle reflection seismics: constraints on deep interfaces beneath the Alps: Mém. *Soc. Géol. France* 156, 97–106.

Vecchia, O. (1968). La zone Cuneo-Ivrea-Locarno, élément fondamental des Alpes. *Géophysique et géologie: Schweizerische Mineralogische Petrographische Mitteilungen* 48, 215–226.

Vinnik, L. P., Reigber, C., Aleshin, I. M., Kosarev, G. L., Kaban, M. K., Oreshin, S. I., et al. (2004). Receiver function tomography of the central Tien Shan. *Earth and Planetary Science Letters* 225, 131–146.

Won, I., and Bevis, M. (1987). Computing the gravitational and magnetic anomalies due to a polygon: Algorithms and Fortran subroutines. *Geophysics* 52, 232–238.

Zappone, A., Wenning, Q. C., and Kissling, E. (2015). "SAPHYR: The Swiss Atlas of physical properties of rocks," in *Proceedings 2015 AGU Fall Meeting2015*, (Washington, D.C: AGU).

Zingg, A., Handy, M., Hunziker, J., and Schmid, S. (1990). Tectonometamorphic history of the Ivrea Zone and its relationship to the crustal evolution of the Southern Alps. *Tectonophysics* 182, 169–192.

Conflict of Interest: The authors declare that the research was conducted in the absence of any commercial or financial relationships that could be construed as a potential conflict of interest.

frontiers in Earth Science

ORIGINAL RESEARCH
published: 02 June 2021
doi: 10.3389/feart.2021.641416

Recurrence of Fault Valve Behavior in a Continental Collision Area: Evidence From Tilt/Strain Measurements in Northern Adria

Giuliana Rossi[1]*, *Alberto Pastorutti*[2], *Ildiko Nagy*[2], *Carla Braitenberg*[2] and *Stefano Parolai*[1]

[1] National Institute of Oceanography and Applied Geophysics-OGS, Sgonico, Italy, [2] Department of Mathematics and Geosciences, University of Trieste, Trieste, Italy

OPEN ACCESS

Edited by:
György Hetényi,
University of Lausanne, Switzerland

Reviewed by:
Alexandre Canitano,
Academia Sinica, Taiwan
Weijian Mao,
Innovation Academy for Precision Measurement Science and Technology (CAS), China
Pierre-Michel Rouleau,
Memorial University of Newfoundland, Canada

***Correspondence:**
Giuliana Rossi
grossi@inogs.it

Specialty section:
This article was submitted to Solid Earth Geophysics, a section of the journal Frontiers in Earth Science

Received: 14 December 2020
Accepted: 19 April 2021
Published: 02 June 2021

Citation:
Rossi G, Pastorutti A, Nagy I, Braitenberg C and Parolai S (2021) Recurrence of Fault Valve Behavior in a Continental Collision Area: Evidence From Tilt/Strain Measurements in Northern Adria. Front. Earth Sci. 9:641416. doi: 10.3389/feart.2021.641416

We analyzed the data recorded by the NE-Italy subsurface tilt and strainmeter network evidencing a coherent transient signal in the recordings of four tiltmeter sites in the 1984–1990 period that produced a tilt along the main fractures. Borrowing from classical seismology techniques, we used the uprise times to locate the transient signal source. The propagation velocity is compatible with a fluid diffusion process that starts from a source located close to the hypocenter of the February 10, 1983 Uccea earthquake, $M_D = 4.2$ at the Italy-Slovenia border, at an estimated depth of 10.8 km. Our results add to the previous interpretation of a transient signal recorded by several global navigation satellite system (GNSS) stations in the 2006–2009 period in terms of fluid diffusion below the Bovec basin (Slovenia). That source was located upon continuation to the northwest of the Ravne fault, few kilometers to the northeast from the present one, and about 6 km from the July 12, 2004 Bovec–Krn earthquake, $M_w = 5.1$, depth ∼6.1 km. These observations suggest that the area is subject to fault valve behavior episodes that released fluids trapped at depth to the surrounding region as pore-pressure bulges. The convergence between Alpine and External Dinarides structures in this area puts highly permeable dolomitic limestones in contact with low-permeable fine-grained limestones and flysch formations. Therefore, the conditions for overpressure generation can be created, whereas fault movements, from time to time, in close relation with seismic events, can enable fluid diffusion in the surroundings. We also estimated the possible fluid influx needed to maintain overpressure and possible discharge across both the faults. The study provides insights on pore–fluid pressure variations related to slow slip events from a context different from subduction or transform margins, i.e., in a continental collision area.

Keywords: tiltmeter, transient signal, EMD analysis, hydrogeophysics, fault-valve behavior, porosity wave propagation

INTRODUCTION

Nowadays, space geodetic observations cover large portions of the Earth, with time series even longer than 20 years, i.e., long enough to allow distinguishing and characterization of periodical or transient variations. The latter consist of variable amplitude signals (from few millimeters to some centimeters, Riel et al., 2014) due to slow slip events often associated with tremors [episodic tremor and slip (ETS)] induced by tectonic or volcanic processes. They have been observed in various parts of the world (e.g., Dragert, 2001; Lowry et al., 2001; a review in Bürgmann, 2018, and references therein).

Besides, crustal deformations at different spatial–temporal scales can also be caused by hydrogeological processes (Watson et al., 2002; van Dam et al., 2007; Longuevergne et al., 2009; Ji and Herring, 2012; Wahr et al., 2013; Devoti et al., 2015, 2018; Silverii et al., 2016, 2019; D'Agostino et al., 2018; Braitenberg et al., 2019). Various types of deformation have been studied considering the elastic response of the crust to the loading forces using increasingly complex models, also taking into account the poroelastic deformations of aquifers and the complicated behavior of karst aquifers (Farrell, 1972; Argus et al., 2014; Devoti et al., 2018; Serpelloni et al., 2018; Silverii et al., 2019) to distinguish and separate hydrological from non-hydrological transient deformations. Some studies (Cervelli et al., 2002; Craig et al., 2017; D'Agostino et al., 2018; Panda et al., 2018, 2020; Chanard et al., 2020) highlighted that rainfalls and consequent groundwater recharge might play a direct role in modulating deformation and seismicity, at least under particular conditions. However, further investigations are needed to confirm these results.

Independently upon the fluid-origin, pore-pressure variations are often thought to be at the origin of slow slip events, ETS, and seismicity (Rice, 1992; Kodaira, 2004; Skarbek and Rempel, 2016; Cruz-Atienza et al., 2018; Nakajima and Uchida, 2018), but most of the voluminous literature regard oceanic–continental plate subduction zones and, in lesser part, volcanic, hotspot, or transform settings (Khoshmanesh and Shirzaei, 2018). Recently, however, fluid migration related to seismic activity has been reported in the Mediterranean, in different parts of the Adria microplate margins (Rossi et al., 2016, 2017, 2018; Nespoli et al., 2018; Console et al., 2020).

In particular, in the northern tip of the Adria microplate, an area of continental collision (Rossi et al., 2016, corrected in 2017–hereafter: RossiI; 2018–hereafter: RossiII), analyzing the global navigation satellite system (GNSS) data from the Friuli Regional Deformation Network (FreDNet) (OGS), Marussi (Friuli Venezia Giulia regional council), and the EUREF networks, reported the occurrence of a transient signal propagating through the region that, between 2006 and 2009, induced a tilt parallel to the principal faulting lineaments. They interpreted the signal as a propagating surge in pore fluid pressure (Revil and Cathles, 2002; Lupi et al., 2011), i.e., a porosity wave. Porosity waves are packets of fluid-filled, hydraulically connected cracks that propagate in response to a pressure gradient set by ambient tectonic stresses (Connolly and Podladchikov, 2013). They have been hypothesized by Skarbek and Rempel (2016) as the transport mechanism of deep fluids triggering ETS in subduction zones. Also, porosity waves can originate in the presence of supra-hydrostatic gradients in fluid pressure across an active fault (Lupi et al., 2011) that may behave as a fluid pressure-activated valve, the so-called fault valve behavior of Sibson (Sibson, 1992, 2014; Fischer et al., 2017; Matsumoto et al., 2021). According to this model, during the interseismic and pre-seismic phases, the fault acts as an impermeable barrier to fluid flow from a region characterized by a supra hydrostatic regime to the overlying layers where the fluid pressure of interconnected pores is hydrostatic (**Figure 1A**). When failure condition is met, through further increase in fluid pressure or accumulation of shear stress, an earthquake occurs, and the fault and the barrier break, allowing fluid discharge along the fault (**Figure 1B**). The scheme in **Figure 1C** shows the time behavior of a fault through time: in the pre-seismic phase (to the left of the earthquakes, indicated as EQ), we observe a slow increase in fluid pressure (P_f) and shear stress (τ). In correspondence with the earthquake, the fault permeability (k) suddenly increases, and the following fluid discharge progressively reduces P_f and τ, with opposite behavior of the frictional shear strength of the fault (τ_f). Progressive healing due to hydrothermal processes decreases permeability, restoring the impermeable barrier, and the cycle can start again.

Although much lower than the fractured fault, the permeability across the fault is not null. Fluids can propagate at a lower rate outside the fault zone in the porous and fractured rocks that constitute a deformable matrix. Hence, a fluid flow would lead to a porosity transient that propagates in a waveform that could be detected by GNSS sensors and tiltmeters, as Braitenberg et al. (2019) demonstrated for pressure changes in karst conduits (**Figure 2**).

In order to support that the transient signal in the different permanent GNSS stations was due to a porosity wave, and, hence, fluid diffusion, RossiI and RossiII inverted the arrival times of the transient, obtaining both propagation velocity and hydraulic diffusivity values consistent with the fluid diffusion hypothesis, and, from these, they inferred permeability. The permeability values turned out to be consistent with the rocks present in the area: highly permeable dolomitic limestones, low permeable fine-grained limestones, and flysch formations. Such rock formations are involved in the overlapped thrusts and imbricate structures created by several tectonic phases that affected the region of study. The contact between permeable and poorly permeable rocks in a compressive and transpressive tectonic regime can give rise to overpressure conditions favorable to the fault valve behavior (Sibson, 1992, 2014). RossiI and RossiII, based on the location they inferred for the porosity-wave source, close to Bovec (Slovenia), hypothesized a valve behavior of the Ravne fault, a transpressive fault of the External Dinarides, recognized as being responsible for the Bovec–Krn seismic events (1998 $M_w = 5.6$ at 6.9 km depth; 2004 $M_w = 5.1$ at 6.1 km depth) (Kastelic et al., 2008). In particular, the transient appeared related to the 2004 earthquake. Unfortunately, there are no GNSS data that could confirm such behavior for the 1998 earthquake.

The hypothesis that the phenomenon reported by RossiI and RossiII is not an isolated episode but could have occurred in the past in the region is at the basis of the present research,

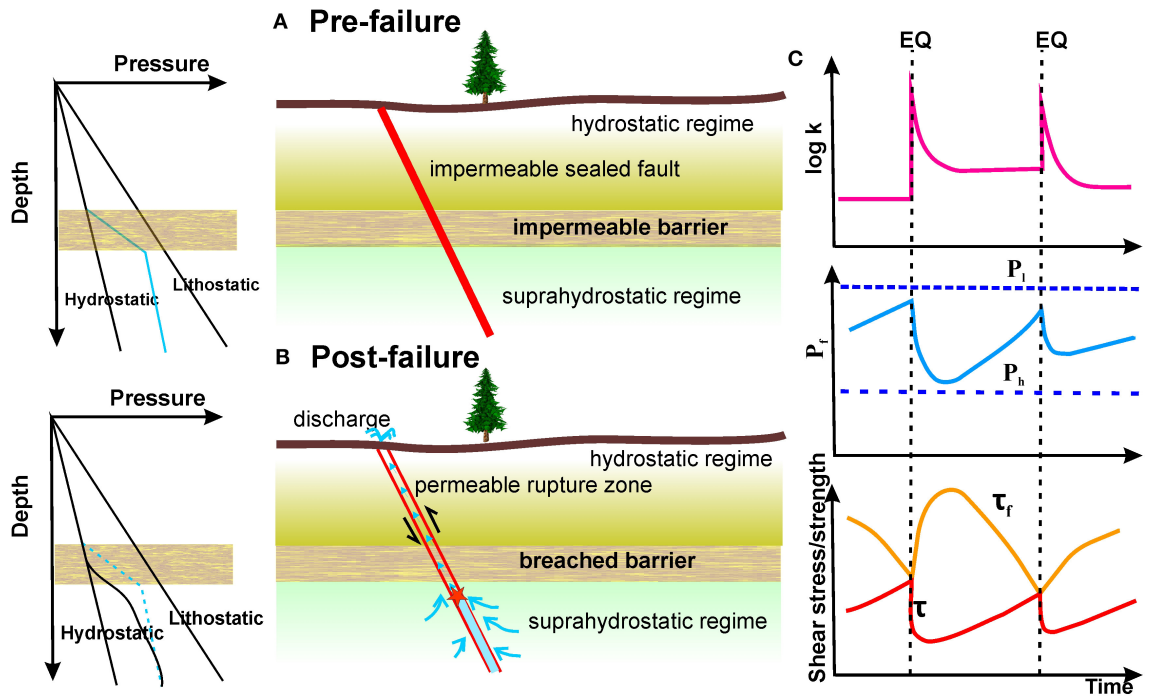

FIGURE 1 | Schematic representation of the fault valve behavior. **(A)** Pre-failure: on the left, the pore pressure gradient in the fault zone, above and below the impermeable barrier, i.e., the transition from the hydrostatic to the supra-hydrostatic flux regime (right); **(B)** post-failure: (right) an earthquake (red star) breaks the barrier, and the fluids rise upwards; on the left, the fluid pressure gradient is nearer to the hydrostatic curve; **(C)** scheme of fault valve action in relation to earthquake occurrence (EQ): when the impermeable barrier is broken, the local permeability k increases, allowing fluid discharge, decreasing fluid pressure P_f, and increasing the frictional strength (τ_f) (from Sibson, 2020, redrawn). P_l, lithostatic pressure; P_h, hydrostatic pressure; τ, tectonic shear stress (From Sibson, 1992, redrawn).

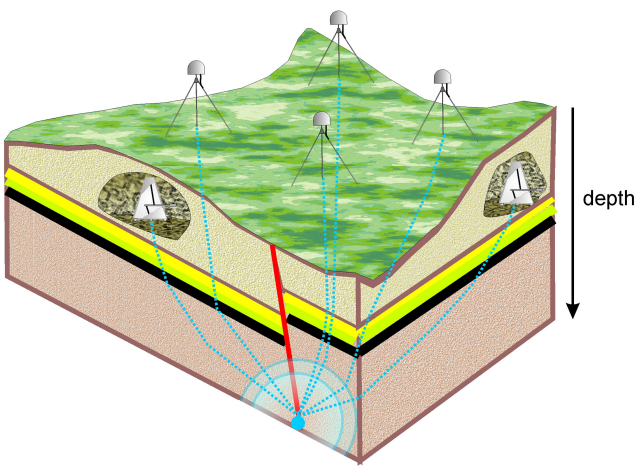

FIGURE 2 | Conceptual model of a porosity wave originating at a fault (red line) and propagating in the hosting rocks. Geodetic instruments, namely, tiltmeters-horizontal pendulums (installed underground, when possible, in natural caves) and GNSS sensors (on the surface) record the induced deformation at different times, depending upon the path of rays, normal to the propagating front (blue dashed lines).

focused on re-analysis of old tiltmeter data in light of more recent GNSS observations.

The region, in fact, has also been continuously monitored for over 50 years by the NE-Italy subsurface tilt and strainmeter network (Braitenberg, 1999). The Grotta Gigante horizontal pendulum station has been active since 1964 (Marussi, 1959; Braitenberg et al., 2006), wherein tiltmeters and strainmeters have been installed starting from 1977. In the 3 years before the 1976 Friuli $M_w > 6$ earthquakes, the Grotta Gigante pendulums recorded "tremors" and an anomalous southward tilt (Chiaruttini and Zadro, 1976; Dragoni et al., 1985). Bonafede et al. (1983) interpreted the tremors in terms of silent earthquakes that originated from the deep non-brittle part of the fault. The frequency is proper for the very low frequency earthquakes (VLFEs) reported by Ito et al. (2007). The suggestion that a transient similar to the 2006–2009 episode could have occurred in the same region in the past came from the observations by Rossi and Zadro (1996) and Zadro and Braitenberg (1999) on long-term variations affecting the signals of the regional tilt-strainmeter network and elastic parameter changes between 1983 and 1986, evidenced by Mao et al. (1989).

Hence, in particular, we focused the analysis on a coherent transient tilt signal, recognizable in the interval 1984–1990, by applying a data-driven approach to the time series. We used the same tomographic approach of RossiI to locate the source of the transient while calculating propagation velocity and hydraulic diffusivity. Finally, we verified whether the associated permeability values are compatible with the rock formation in the region and whether there are conditions for overpressure. To verify the plausibility of the fluid diffusion hypothesis, we also estimated the

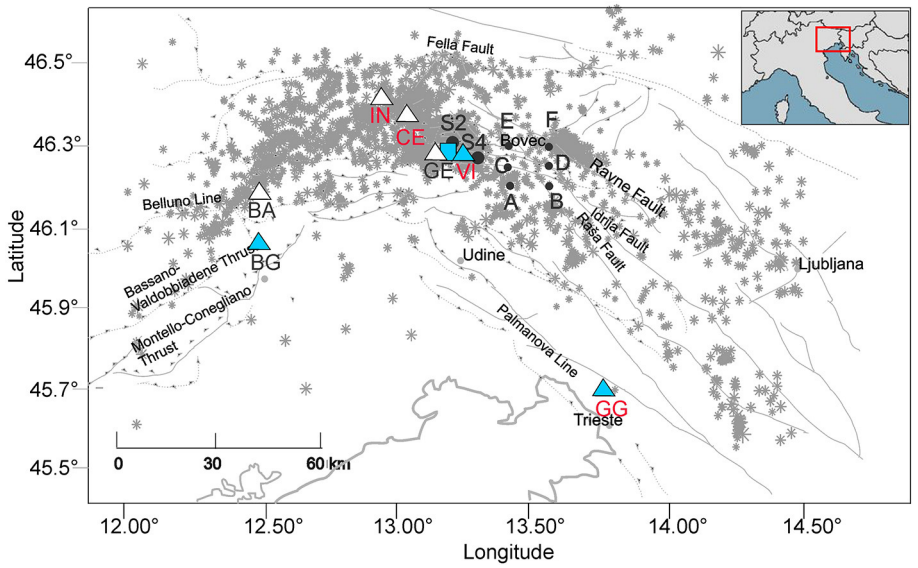

FIGURE 3 | Map with the principal tectonic lineaments and the NE-Italy subsurface tilt and strainmeter network sites: red labels, the sites considered in this study. Blue square: the strainmeter station, presently active; blue triangles: the stations currently active; white triangles: the sites active in the interval 1977–1996. **S2, S4**: location of the vertical profiles from Faccenda et al. (2007); **A,B,C,D,E,F**: location of the six vertical profiles extracted from the model of Bressan et al. (2012). Inset: the location of the region of study. Gray stars: earthquakes recorded in 1988–2012 by the National Institute of Oceanography and Applied Geophysics-OGS seismometric networks (NI doi: 10.7914/SN/NI with University of Trieste, and OX doi: 10.7914/SN/OX; Bragato et al., 2021).

possible fluid flux through the structures involved in the case analyzed in this study and in the one reported by RossiI and RossiII.

THE TECTONIC FRAME AND THE DATA

Several tectonic phases affected the region, originating different tectonic systems interfering with each other. The primary tectonic systems present in the region are those of the Alpine (with S-directed E–W-striking thrusts) and the Dinaric, represented by the External Dinarides (with NW–SE-oriented dextral transpressive faults) (Slejko et al., 1999; Poljak et al., 2000; Bressan et al., 2007). Originated by the collision between the Adria and Eurasia plates and the counter-clockwise rotation of the former, the two systems merge and intersect in the central part of the region. Here, we record the highest seismic activity (**Figure 3**), characterized by an intricate pattern of thrusts and strike–slip fault mechanisms, with a compressional axis oriented from NW–SE to NNW–SSE and N-S (Bressan et al., 2018b).

The strain field has been continuously monitored for over 50 years by the NE-Italy subsurface tilt and strainmeter network (Braitenberg, 1999). Presently, it consists of two long baseline horizontal pendulums installed in Grotta Gigante (GG), near Trieste (installed in 1959; continuous data:1964–present), and two tiltmeter stations located in the Bus de la Genziana (BG) and Villanova (VI) caves, active since 2005 and 1977, respectively (**Figure 3**, **Table 1**; Chiaruttini and Zadro, 1976; Braitenberg, 1999; Zadro and Braitenberg, 1999; Grillo et al., 2018). The VI and BG tiltmeter stations are equipped with two Marussi-type, horizontal pendulums with Zöllner suspension oriented to NS and EW, respectively, with a cast iron conic housing. The nominal angular resolution is 2.5 nrad, and signals are recorded with a sampling rate of 1 h. GG instruments are Zöllner-type horizontal pendulums of exceptional dimensions with an oscillation period of 360 s and an amplification factor of equal to 24,000. VI also hosts three Cambridge wire strainmeters (King and Bilham, 1976) in the N128E, N27E, and N67E directions. The network included at its maximum expansion (1980–1996) four further tiltmeter stations in the Piedmont area of Friuli (CE, BA, IN, and GE) with tiltmeters of the same kind of those in VI and BG (in italic in **Table 1**; **Figure 3**).

This study considers the continuous recordings of GG, VI, CE, and IN stations that worked continuously between 1979 and 1996 (**Figure 4**). Although the raw data have different amplitudes, depending on the instrument and site characteristics (Rossi and Zadro, 1996), some features are recognizable for all stations in the two components (EW and NS). Pluri-annual fluctuations modulate seasonal (annual and semiannual) oscillations. In some cases, a clear linear long-term trend is recognizable (e.g., CE and VI NS-component) (**Figure 4**). Higher frequency signals (some days) (e.g., in the EW component of VI and GG between the end of 1991 and the beginning of 1992) are correlated to hydrological effects (Braitenberg et al., 2019).

The application of a running average over 2 years evidences long-term variations (**Figure 4**). In particular, one fluctuation with a transient character and that affected all the recordings between 1984 and 1990 is evident (blue ellipse in **Figure 4**). For GG, we note another higher amplitude fluctuation in the 1989–1994 period (dashed blue ellipse), which will also be analyzed in the following chapter. The search for

TABLE 1 | Site characteristics of the NE-Italy subsurface tilt-strainmeter network; in italic, the stations that are not presently active.

	ID	Latitude (deg)	Longitude (deg)	Height (m ASL)	Operation period	Geological setting
Grotta gigante	GG	45.4083	13.7633	274	May 1959–present	Natural cave (112 m high vault) in massive Cretaceous limestone
Villanova	VI	46.2564	13.2814	616	January 1977–present (tiltmeters), December 1978–present (strainmeters).	Natural cave in limestone slab overthrusted into Eocene flysch, south of the main overthrust of Alpine system, highly fractured
Bus de la Genziana	BG	46.0581	12.4002	995	October 2005–present	Natural cave in limestones of Upper Cretaceous-Eocene
Cesclans	*CE*	*46.3564*	*13.0583*	*351*	*July 1977–December 1996*	*Human-made underground structure at the contact between limestone and pleistocenic conglomerates, highly fractured by EW oriented overthrusts and NS striking vertical faults*
Invillino	*IN*	*46.4028*	*12.9525*	*480*	*July 1979–December 1996*	*Human-made underground structure in stratified Triassic dolostone with marl intercalations, south of EW oriented overthrust of the Alpine system*
Barcis	*BA*	*46.1858*	*12.6003*	*520*	*December 1978–December 1996*	*Natural cave close to one of the main EW overthrusts of the Alpine system, putting in contact Triassic DolomiaPrincipale with Cretaceous pelagic limestones*
Gemona	*GE*	*46.2719*	*13.1639*	*825*	*September 1980–December 1996*	*Human-made structure in correspondence of one of the EW-oriented thrusts of the Alpine system, putting in contact Triassic DolomiaPrincipale and Cretaceous pelagic limestones*

ID, identification name.

the direction of the maximum amplitude of the transient for each site requires calculation of the tilt component on directions from N to N165°E, spaced 15°: the signal in the complementary directions (N180°E–N340°E) is easily obtained by merely inverting the sign (**Figure 5**; RossiI). The 15° spacing enables a first reasonably accurate scan of the direction with the maximum amplitude to be refined later.

DATA ANALYSIS

Time Series Analysis

As shown in **Figures 4**, **5**, the oscillations have transients and likely dispersive characters, so that uprise and duration could change in the different sites. Hence, intending to exploit the time series in its whole length and avoiding the risk of the filtering parameters conditioning the results, in this study we applied a different method from the filtering of RossiI and RossiII: the data-driven empirical mode decomposition (EMD) technique, initially proposed by Huang et al. (1998). Since its introduction, EMD has been successfully applied in various fields (Ditommaso et al., 2012; Zhang et al., 2019). EMD decomposes a noisy, complex signal into a variable number (N) of intrinsic mode functions (IMFs) through an iterative sifting process. Based on the detection of local maxima and minima in the time series, sifting produces a (generally limited) number of IMFs, each containing higher frequency oscillations than the following IMF component. Orthogonality is not a necessary condition of the EMD technique that provides a complete and adaptive basis for expanding linear, non-linear, and non-stationary data.

The original signal $x(t)$ is expressed as

$$x(t) = \sum_{j=1}^{N} IMF_j(t) + r_n(t) \quad (1)$$

where $r_n(t)$ is the residual.

We performed EMD analysis on the projections calculated every 15° (**Figure 5**). The first 5 IMFs capture the highest frequency signals, including those induced by rainfall, groundwater variations, and co-seismic displacements (red ellipses in original data, IMF1 and IMF2), whereas IMFs 6 and 7 represent the seasonal, periodic, and semi-periodic components (**Figure 6**). IMF 8 contains a longer wavelength term, dominated by a transient surge, recognizable for all the stations (blue ellipse). For each site, once we found the direction in which IMF 8 shows the maximum amplitude, we repeat the analysis by moving from directions 5 and 10° to North and South, to be sure to find the direction of maximum amplitude of our signal, with an uncertainty of only 5°. The maximum absolute amplitude is recorded in directions N85°E for VI, N135°E for CE, N10°E for IN, and N135°E for GG (blue arrows in **Figure 7**). The positive tilt is N85°E for VI, N45°W for CE and GG, and N170°W for IN (darker blue). Due to the time delay between the different sites, the image refers to the end of 1985: GG shows a null tilt (light-blue arrow). Transient oscillation is recognizable in the VI signal in 1983–1987, in CE and IN signals in 1984–1988, with slight differences between the two sites, and in the GG signal in 1988–1992. There is a substantial agreement with both the tectonic lineaments existing in the neighbors of the four sites and the directions in which the lower crust background seismicity tends to align, as evidenced by principal component

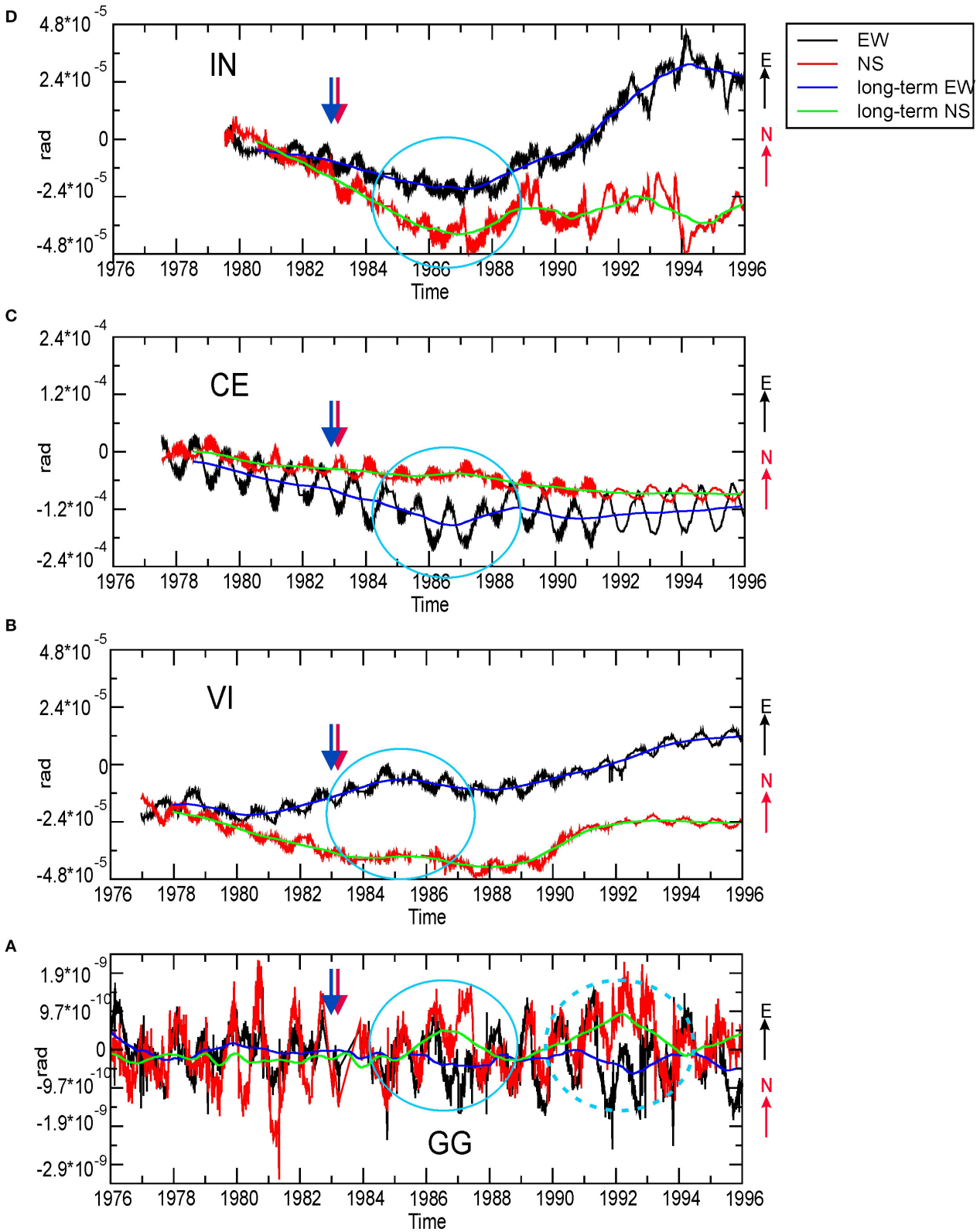

FIGURE 4 | (A–D) Tiltmeter signals for GG, VI, CE, and IN, respectively (1976–1996): original (black and red lines) EW and NS components, and the same, averaged with a running average over 2 years (blue and green lines). The blue ellipse highlights the transient signal; the blue dashed ellipse on GG signals highlights the later transient oscillation. The blue arrow indicates the transient analyzed in this study; the red arrow indicates the 1983, $M_D = 4.2$ Uccea earthquake occurrence. X-axis: time (years). Y-axis: signal amplitude (rad). Positive: North and East, respectively.

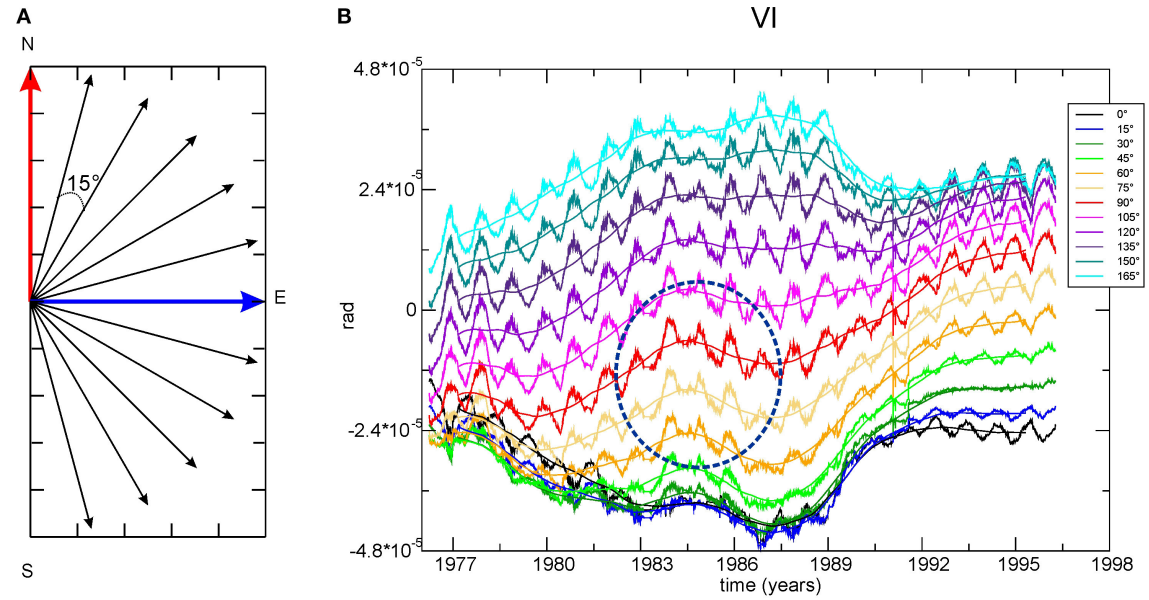

FIGURE 5 | (A) The tilt signal is calculated for directions separated by 15° intervals from N to S, starting from the N–S (red) and E–W (blue) records. **(B)** Example for VI: the time series calculated for various directions are plotted vs. time: in legend, the color corresponding to each direction. The maximum amplitude of oscillation 1983 and 1986 is recorded in N75 and N90°E directions (dashed blue ellipse). X-axis: time (years). Y-axis: signal amplitude (rad). Positive in the directions written in the legend.

analysis (dashed gray arrows in **Figure 7**; Bressan et al., 2016, 2019).

Furthermore, the results are in good agreement with the directions found through the transient analysis that affected the FReDNet GNSS data in the time interval 2006–2009 (red–black arrows for the horizontal component, yellow arrows for the vertical one in **Figure 7**, RossiII). In this case, due to time propagation of the transient signal, the image refers to a particular moment: June 2008. The stations in which the horizontal signal is null at that moment are represented with a black arrow; whereas in the other cases, the red arrow indicates positive horizontal displacement. Similarly, for vertical displacement, the smaller size of the yellow arrow indicates the cases in which the maximum of transient displacement was not reached in June 2008.

The four tiltmeter time series transient uprise times progressively increase, starting with VI, then with CE and IN northwesterly, and with GG southeasterly (**Figure 8**). Notably, the transient uprise time in GG is consistent with the 1989–1994 oscillation observed in the original time series (dashed ellipse in **Figure 4**).

Transient Source Parameters

To locate the source of the unknown transient (in space and in time), we applied a standard, simplified earthquake location procedure based on circles, whose radii are estimated by the arrival times of the transient and its velocity of propagation (RossiI). We estimated the average propagation velocity based on various distance/differential uprise time ratios between couples of tilt recordings. Then, we refined localization through a tomographic approach, i.e., ray tracing in a stratified medium characterized by laterally varying velocities (Böhm et al., 1999), minimizing the observed and calculated travel time differences. The technique is depicted in **Figure 9**. For both the frequencies involved and the limited number of observations, we are aware that we are working at the limits of the method. However, the staggered grid procedure limits the drawbacks of inadequate coverage (Vesnaver and Böhm, 2000). Therefore, we initially chose a very coarse grid, consistent with the broad wavelength of the pulses, to have a rough but reliable velocity distribution.

We started from the RossiI model (**Figure 10A**) and performed ray tracing, following the principle of Fermat. The 3D model origin is at 11.8°E, 45.6°N, and it extends to 14.6°E, 46.7° N, from the Moho surface to the topographic surface, with three surfaces in between at average depths of 2, 4, and 11 km, respectively (Rossi I). We refined the velocity model iteratively, together with the source location. When the difference between the observed and calculated travel times was minimal, we applied to the grid small shifts in x and y directions, and repeated the inversion. At the end of the process, we averaged the results, obtaining a higher resolved image without losing the reliability of the original grid (**Figure 9**; Vesnaver and Böhm, 2000).

The velocities of the final model range between 6.4 and 27 km/year (**Figure 10**). Notwithstanding the more limited area covered by the rays, the values are close to the ones obtained by RossiI. In the second and third layers, the propagation velocity does not exceed 16 km/year (±0.5 km/year; **Figures 10B,C**) in the volumes crossed by the rays. The shallowest layer (layer 1) shows the highest velocity values, up to 27 km/year (±0.9 km/year) (**Figure 10D**). The source of the transient (green circle

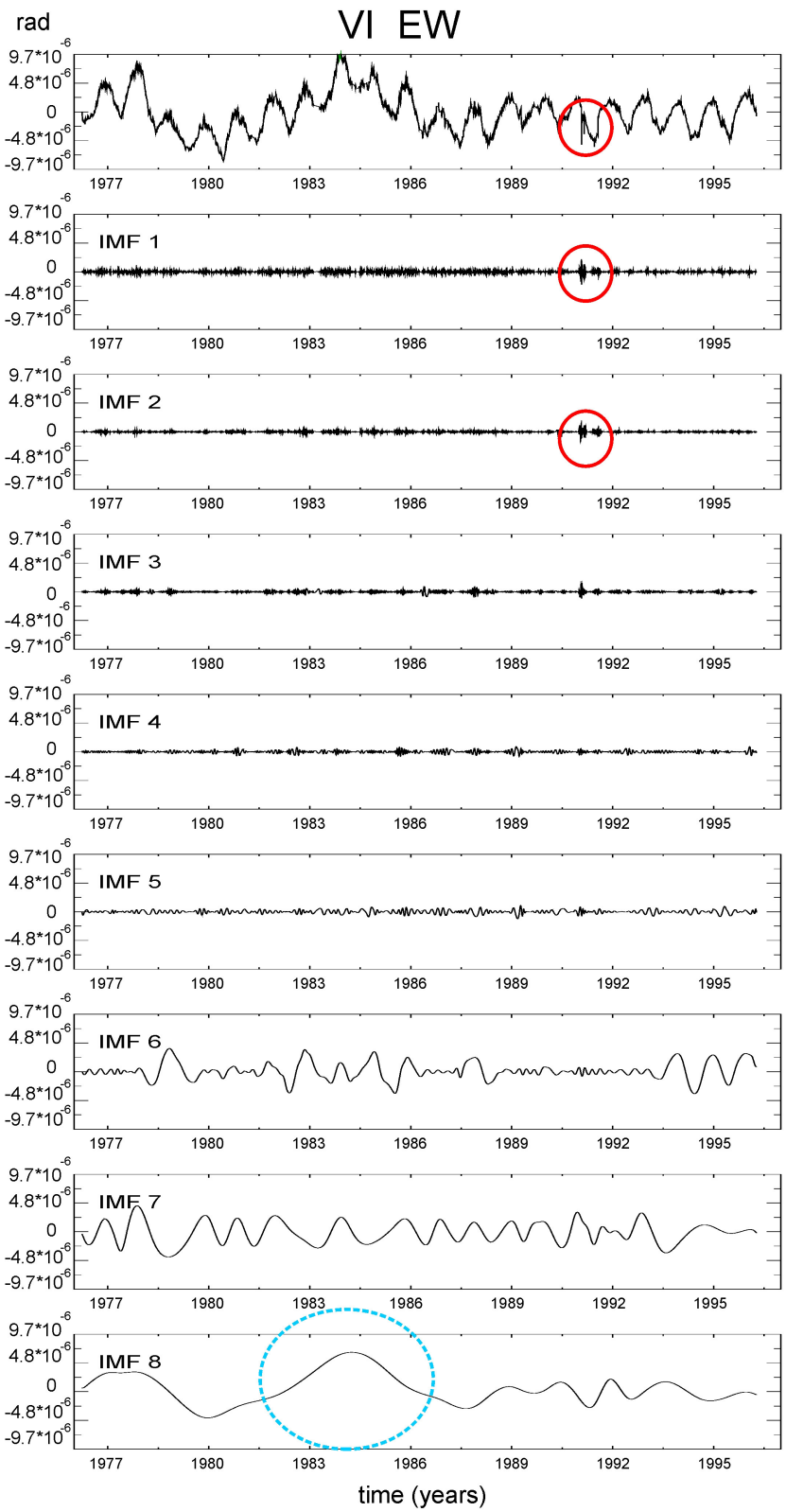

FIGURE 6 | The resulting mode decomposition components from the signal VI (EW): from top to bottom, the original signal, subtracted the long-term trend (the residual of EMD), and the IMFs resulting from EMD: the wavelength of the oscillations increases with the IMF number. IMF1 and IMF2 contain rainfall-induced and co-seismic signals (red ellipse also in the original data). IMF 8 contains the transient of study (fair blue ellipse). Positive: toward East.

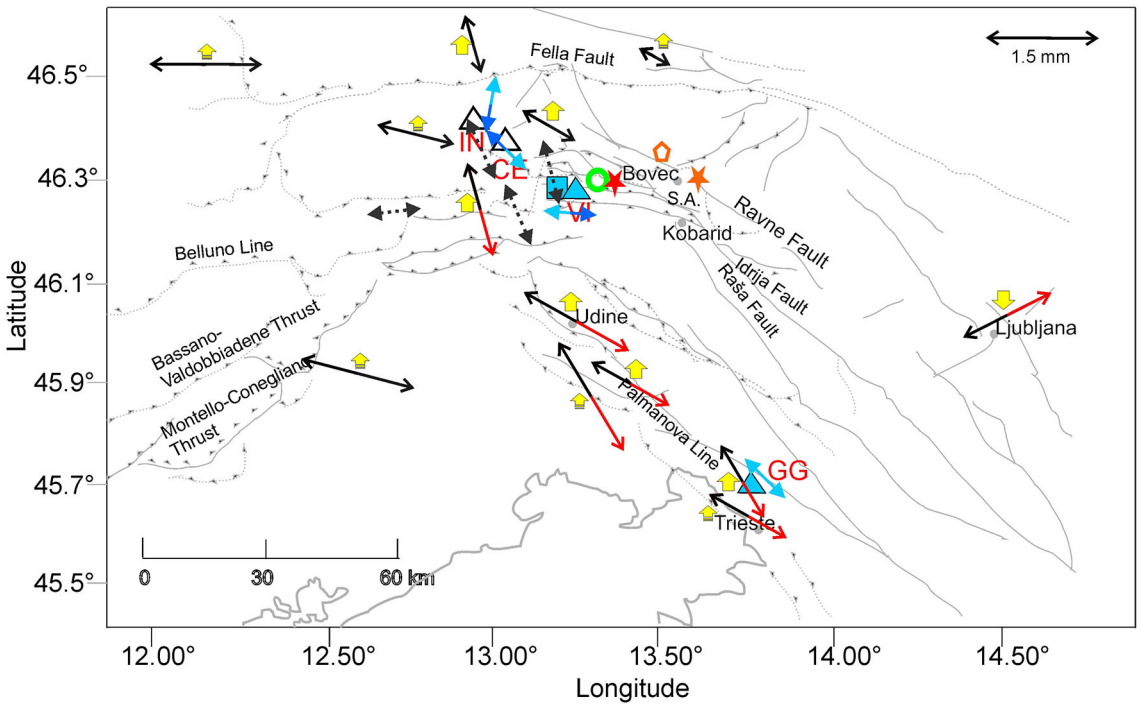

FIGURE 7 | The same map as **Figure 3**, with indication of the directions of the transient 1984–1990 tilting (blue arrows), of the 2006–2009 GNSS transient displacement (Rossill, red-black arrows, yellow arrows), and of the alignment of the background seismicity (Bressan et al., 2016): gray dashed arrows. 1984–1990 tilting- the map refers to the end of 1985: blue color indicates the positive tilting verse, whereas light blue indicates the negative tilting. A light blue two-sided arrow indicates null tilting. 2006–2009 GNSS displacement- the map refers to June 2008: the red-black arrows indicate the direction of horizontal displacement, red for the positive verse of the displacement, whereas black is the negative displacement. A two-sided black arrow means null horizontal displacement. The vertical displacement is represented by the yellow arrows, indicating up or down movement: if the maximum was not reached in June 2008, the arrow is smaller. Green circle: the origin of the transient analyzed in this study, orange pentagon is the source of the transient analyzed by Rossil and Rossill; red star: 1983, $M_D = 4.2$ Uccea earthquake, 10.8 km depth; orange star: 2004, $M_w = 5.1$ Bovec–Krn earthquake; 6.1 km depth. SA, South Alpine thrust.

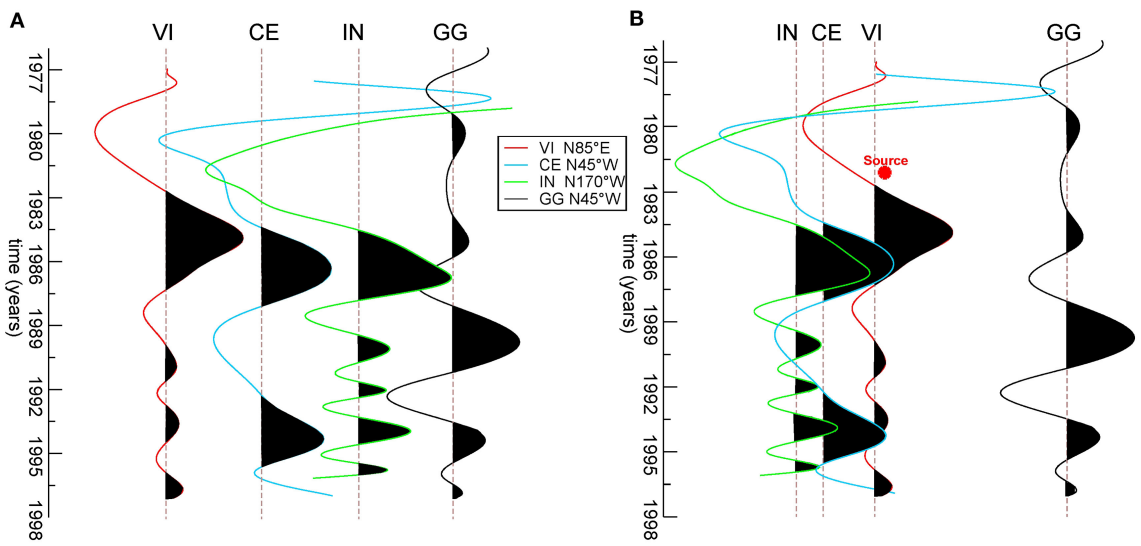

FIGURE 8 | IMF8 for the four stations, in a variable area mode (black area: the positive signal), in the direction in which the transient is maximum and positive. A gain of 10^4 is applied to the GG signal to allow comparison with the other stations. Vertical axis: time (years). **(A)** The time series for each station is ordered following the uprise times, with trace interval fixed. **(B)** The trace interval is proportional to the distance from the calculated source (red star). The traces located to the west of the source of the transient (red star) are on the left, while GG, to the east of the source, on the right.

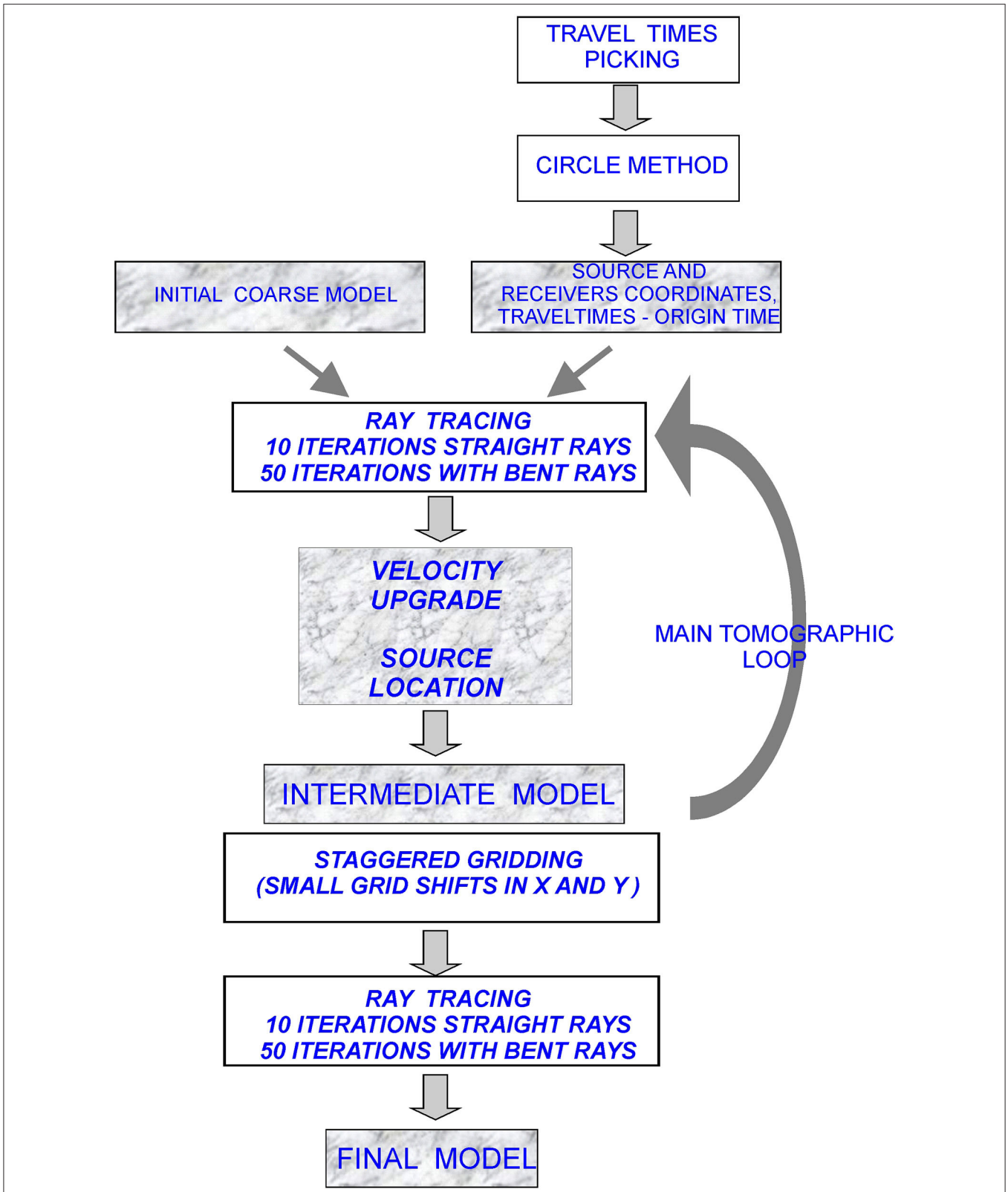

FIGURE 9 | Scheme of the data analysis: retrieval of the source location and origin time (circle method), velocity model refinement (ray tracing method).

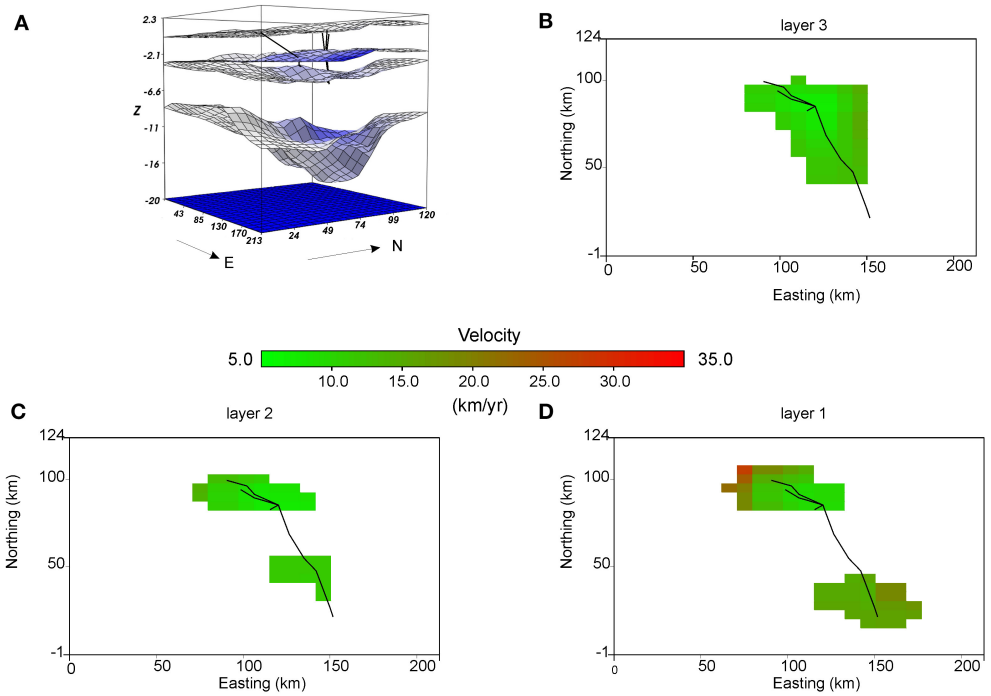

FIGURE 10 | Tomographic inversion. **(A)** 3D Velocity model, with the rays traced (black lines); **(B)** plan view of the velocity distribution in the lowermost layer: the pixels with low ray-coverage are masked in white; **(C)** the same in the intermediate layer; **(D)** the same in the shallowest layer. Black lines in **(A–D)** indicate the ray traces. Origin of model:11.8°E, 45.6°N.

in **Figure 7**) is located at 46°16'50.50 "N, 13°19'0.40" E, hence about 5 km to the East of the VI station, at 6 km depth, with an uncertainty of about 7 km in the plane, and 1 km in depth. Low velocities ($\sim 8 \pm 0.2$ km/year) characterize the "hypocentral" area (**Figure 10B**). Origin time is the end of November 1982 (red star in **Figure 8**), with an uncertainty of 1.5 months.

Fluid Diffusion

We verified whether the uprise times are compatible with an episode of fluid diffusion in the present case, as in the case reported by RossiI. For this aim, we used the uprise times of the transient as input for hydraulic tomographic inversion to obtain hydraulic diffusivity (Brauchler et al., 2013). We followed the scheme shown in **Figure 9**, excluding the source location, which is now fixed, and started from the model of hydraulic diffusivity obtained by RossiI. **Figure 11** shows the hydraulic diffusivity (D_h) values obtained for the same layers, shown in **Figure 10**.

The values are in the range $0.1 \cdot 10^{-3}$–$3.4 \cdot 10^{-2}$ m^2/s ($\pm .02 \cdot 10^{-3}$ m^2/s). The highest values are in the first layer (**Figure 11C**), and the lowest is in the second one (**Figure 11B**), as observed by RossiI. Since permeability is a physical property for which more measurements are available than hydraulic diffusivity, it is more suitable to compare the obtained values with those that can be expected from the lithology present in the region. The equation binding the two quantities is (Talwani et al., 1999).

$$k = D_h \eta_f \left[\varphi \beta_f + (1 - \varphi)\, \beta_r\right] \tag{2}$$

where β_f, β_r, η_f, and ϕ are the fluid and rock compressibility, fluid dynamic viscosity, and rock porosity, respectively, the latter available from a borehole and laboratory measurements (Faccenda et al., 2007). The rays mainly cross the Jurassic limestones and the Cenozoic flysch formations. The finely layered limestones of Jurassic are characterized by permeability values in the order of 10^{-17} m^2, whereas the Cenozoic flysch shows higher permeability ($\sim 4 \cdot 10^{-16}$ m^2) (**Table 2**).

The effective stress σ_0 associated with the pulse is (RossiI)

$$\sigma_0 = \frac{(1 - \varphi)\, g D_h \left(\rho_g - \rho_f\right)}{\phi v} \tag{3}$$

where ρ_f and ρ_g are the density of fluid and rock, g is the gravity acceleration constant, v is the propagation velocity, and D_h is the hydraulic diffusivity. We chose for the Jurassic limestones and the Cenozoic flysch the propagation velocity and hydraulic diffusivity values in locations where these values can be assumed to be dominant at the depth crossed by the rays, based on the available stratigraphic information (Faccenda et al., 2007; ViDEPI, 2009). In the absence of other information, we assumed water density for fluid density. The density of the grains in the rock ρ_g values, known from laboratory measurements, are obtained from Table 2 of RossiII.

The effective stress obtained using Equation (2) is quantified as about 19 MPa, with a standard deviation of 0.11 MPa. To see whether this value implies an overpressure condition, we

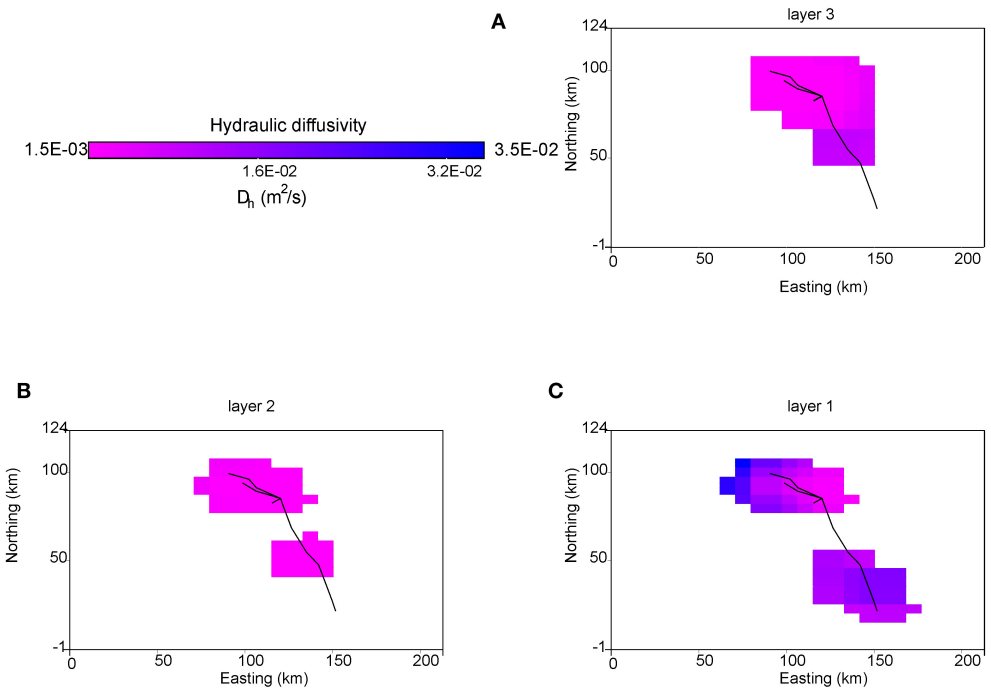

FIGURE 11 | Hydraulic diffusivity tomographic inversion **(A)** plan view of the diffusivity distribution in the lowermost layer; the pixels with low ray-coverage are masked in white; **(B)** the same in the intermediate layer; **(C)** the same in the shallowest layer. Black lines in **(A–C)** indicate the ray traces. Origin of model:11.8°E, 45.6°N.

TABLE 2 | Hydraulic diffusivity (D_h) and permeability (k) calculated for the two regional rock formations crossed by the rays.

	Diffusivity D_h (m^2/s)	D_h uncertainty (m^2/s)	Permeability k (m^2)	k uncertainty (m^2)
Jurassic limestone	$2.2{\cdot}10^{-3}$	$\pm 0.2{\cdot}10^{-4}$	$4.9{\cdot}10^{-17}$	$1.1{\cdot}10^{-19}$
Cenozoic flysch	$1.3{\cdot}10^{-2}$	$\pm 0.2{\cdot}10^{-4}$	$3.9{\cdot}10^{-16}$	$1.5{\cdot}10^{-17}$

calculated the vertical stress due to lithostatic loading σ_v:

$$\sigma_v = \rho_b g z - P_p = (1 - \lambda)\, \rho_b g z \tag{4}$$

where P_p is the pore pressure, λ is the pore fluid ratio (Terzaghi, 1923; Hubbert and Rubey, 1959), and ρ_b is the bulk density of sediment, defined as

$$\rho_b = \varphi \rho_f + (1 - \varphi)\, \rho_g \tag{5}$$

We considered the same vertical profiles reported by RossiII, since they are also very close to the source of the transient in this study (**A,B,C,D,E,F** and **S2,S4** in **Figure 3**). In the present case, given that the origin of the transient is shallower, at a depth of about 6 ± 1.0 km, the lithostatic load is about 167 ± 25 MPa with a standard deviation of ∼2.5 MPa. The pore fluid ratio λ is about 0.89 ± 0.01, indicating condition of a supra-hydrostatic state, with pore pressure very close to the lithostatic load.

DISCUSSION

The study of transient variations in deformation requires several years of observations of long-term inter-seismic strain variations, necessary to reveal a particular region or a repetitive behavior of a structure. Since GNSS and interferometric synthetic aperture radar (InSAR) data are limited to the last 20 years, observations on past episodes of slow slip can come from strainmeters, tiltmeters, and dilatometers that had been continuously recorded in the past. This study focused on long-term oscillation of the strain field in NE-Italy observed in the second half of the last century, reported by Rossi and Zadro (1996) and Zadro and Braitenberg (1999), not correlated with meteorological factors, and that has similarities with the recent GNSS observations in the same region (RossiI and RossiII).

We chose the data-driven EMD technique to delineate, at best, transient non-stationary signals in the recordings. This choice has the advantage of avoiding any *a priori* hypothesis and is independent of any parameter choice while exploiting the time series in its whole length, which is essential when considering transients with some years of duration. The IMF 8 resulting from the tiltmeter data analyses revealed a transient pulse, slowly propagating throughout the region between 1983 and 1987 (**Figure 8**): the uprise times in the various stations slightly increased from VI to IN—to the west of VI—and to GG—to the east of VI. There is a substantial agreement between the

directions of the tilt induced by the transient (blue arrows in **Figure 7**), the directions found through the analysis of the GNSS data (red-black arrows; RossiII), and the directions in which the background seismicity tends to align (gray dashed arrows; Bressan et al., 2016, 2019). We can argue that the propagation follows the primary fractures, presenting the same orientation (Serpelloni et al., 2016; Peterie et al., 2018).

The velocities range between 6.4 and 27 km/year (**Figure 8**), in good agreement with the results of RossiI. Such velocities strongly suggest pore pressure diffusion, and a hydraulic tomographic inversion of the surge times in various tiltmeter stations provided the hydraulic diffusivity values: the values range between $0.1 \cdot 10^{-3}$ and $3.4 \cdot 10^{-2}$ m^2/s. The excellent agreement of the derived values for permeability of the Jurassic limestones and Cenozoic sandstones with the values reported in the literature (Hawle et al., 1967; Sibson and Rowland, 2003) strongly supports the hypothesis that the transient signal is the expression of pore fluid pressure diffusion throughout the region.

The origin time (end of November 1982) and the location of the transient source (**Figure 7**, green circle) indicate a close relationship between fluid surge and the 1983 February 10 $M_D = 4.2$ Uccea earthquake, 6.5 km apart (**Figure 7**, red star). We can estimate the uncertainty in origin time to about 1.5 months, about 7 km for the location in the plane, and about 1 km in depth. The 2006–2009 origin of the transient (RossiI) (orange pentagon in **Figure 7**) was located in the northwestward continuation of the Ravne fault, responsible for the 2004 earthquake ($M_w = 5.1$) (orange star in **Figure 7**), about 6 km from the epicenter of that earthquake (orange star in **Figure 7**). The earthquake occurred 3.5 months after the calculated origin time of the transient. In that case, uncertainty in origin time was estimated at about 15 days, whereas the location uncertainty was about 2 km in the horizontal dimension and 0.8 km in depth.

The two sources are <20 km apart, both in the area where the Dinaric fault system crosses and merges with the Alpine one, near the border between NE-Italy and W-Slovenia. In both cases, the effective stress that can be calculated as an origin for the pore fluid pressure surge results low (19 MPa for this case study, 22 MPa for the 2006–2009 one), implying pore pressures about 0.9 the lithostatic one.

These observations suggest that the area mentioned above is subject to fault valve behavior episodes (Sibson, 1992), releasing fluids to the surrounding region as pore pressure bulges. The tectonic style of the area, a complex superposition of thrusting (Alpine) and transpressive structures (the Dinaric ones), is most favorable to fault valve behaviors (Sibson, 2020). The model of Sibson implies accumulation of a volume of high-pressure fluid beneath a low-permeability seal at the base of a fault zone (interseismic period); an earthquake would break the seal, and the fluid would surge upward immediately following the earthquake (**Figure 1**).

Although the two transients relate to two different faults, some characteristics of the 2004 Bovec–Krn $M_w = 5.1$ earthquake sequence support the interpretation that, at least in that case, the Ravne fault acted as a valve. Gentili (2010) recognized seismic quiescence preceding the 2004 $M_w = 5.1$ Bovec–Krn earthquake, which is compatible with an overpressure condition. On the other hand, the depth distribution of the aftershocks that followed the main shock is compatible with upward spreading, as it would be in the case of a fluid discharge (Bressan et al., 2018a). The seismic monitoring network was still limited at the time of the 1983 Uccea earthquake; however, in the preceding year, we observe a reduction in seismic activity close to the forthcoming epicenter. The aftershocks were few and had tendency to become shallower.

Several models have been proposed to relate overpressurized fluids with faulting (Hickman et al., 1995; Faulkner et al., 2010). The model of Rice (1992), formulated to explain the weakening of a fault, implies that a fault zone behaves as an impermeable barrier to the country rocks. A continuous fluid flux from the lower crust maintains high pore pressure. On the contrary, the model of Byerlee (1990) assumes that water from the country rocks saturates a highly permeable fault zone first, and, when the shearing causes fault zone compaction, is released back to the country rocks, until the flow is arrested because of hydrothermal deposition. It results in a complex system of seal-bound compartments and heterogeneous distribution of overpressurized fluids within a fault zone (Khoshmanesh and Shirzaei, 2018).

Some independent observations can help understand which model can be more suitable in describing the phenomenon of study.

As it is known, the state of overpressure can be related to seismic velocities ratio (V_p/V_s) anomalies (Dvorkin et al., 1999; Chiarabba et al., 2018). The source of the transient in this study coincides with a higher value (1.91) (Bressan et al., 2012). The same authors report a value of 1.86 in correspondence with the source of the 2006–2009 transient. Although high V_p/V_s values are proper for limestones and dolomitic limestones, such values can be interpreted as indicative of a state of overpressure. Unfortunately, these values result from the seismic activity analysis over a relatively long period of time, encompassing different phases of the seismic cycle. A different analysis is reported by Mao et al. (1989), who analyzed the seismic velocities in the same region using a sliding time window. They also compared the amplitude of Earth strain tides observed by the three strainmeters located in the VI station with theoretical ones, in 1978–1986, and recovered the elastic parameters. The results from Mao et al. (1989) can be seen in **Figure 12**, together with the V_p/V_s that we calculated, starting from the velocity values reported in Mao et al. (1989)'s Table 3. It is noteworthy, that they observed changes in velocities and elastic parameters in the same years with a wavelength similar to our transient. In particular, Mao et al. (1989) focused on changes in seismic velocities (3%) and bulk modulus K (50%), started in 1982 and recovered after the 1983 Uccea earthquake, about a year later. The increase in observed bulk modulus (K_O), compared with the theoretical one (K_T) in correspondence with the earthquake could agree with a state of overpressure at the time of the event. Notably, the V_p/V_s ratio markedly increased from the end of 1982 to the end of 1986, in agreement with the surge in the tilt anomaly in VI. However, the information is relative for a broader part of the region and not limited to a single fault, as, e.g., Chiarabba et al. (2018), and, hence, may reflect pore fluid diffusion through the rock formations hosting the fault. The increase in ratio between

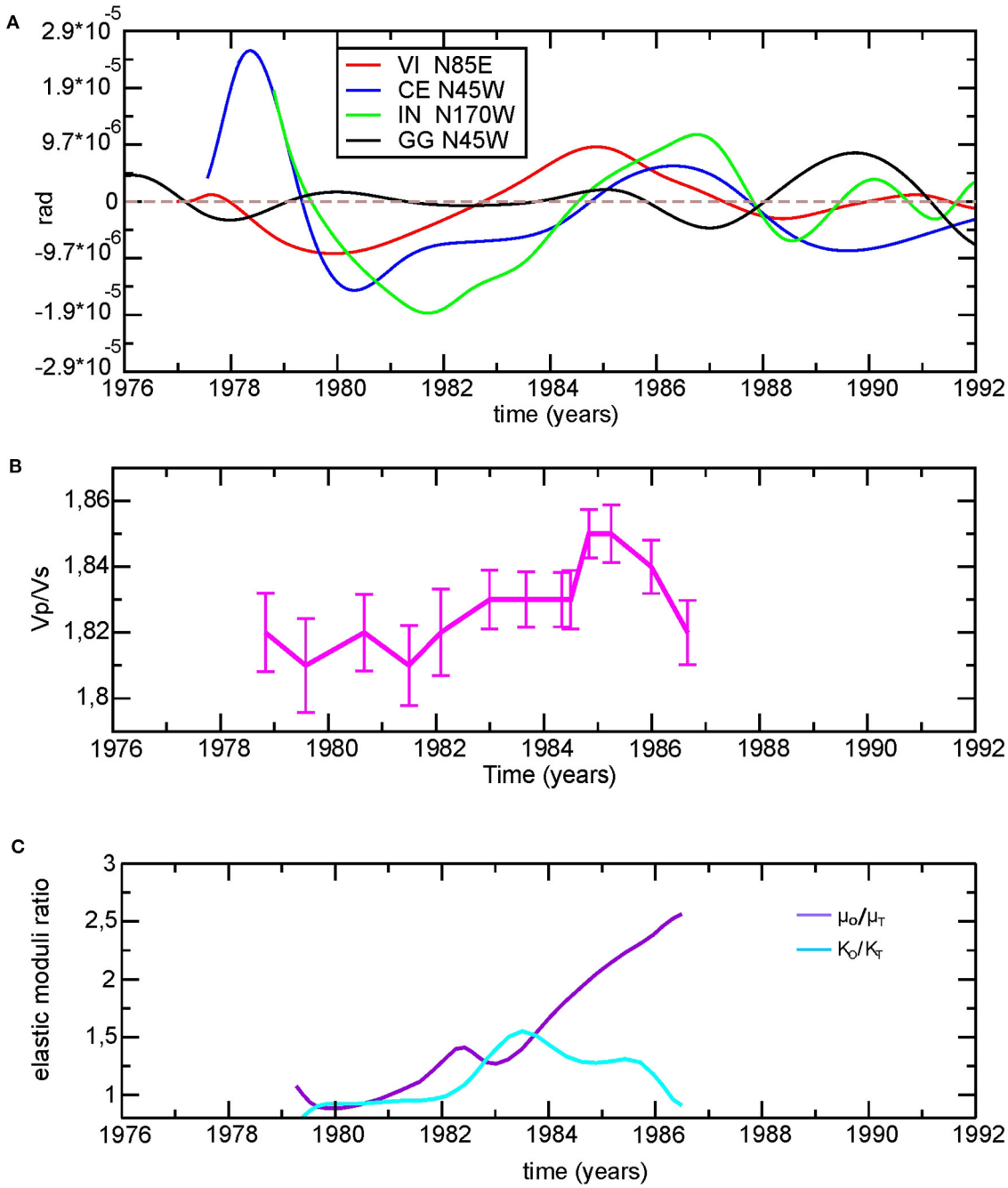

FIGURE 12 | (A) The same curves as **Figure 6** (positive, in the direction indicated in the legend). A gain of 10^4 is applied to the GG signal to allow comparison with the other stations. **(B)** V_p/V_s from Table 3 of Mao et al. (1989), with the error bars; **(C)** the ratio between the observed rigidity (μ_O) and bulk modulus (K_O) and the theoretical rigidity (μ_T) and bulk modulus (K_T), from Mao et al. (1989) redrawn.

the observed shear modulus (μ_O) and the theoretical one (μ_T) that we observe from 1980 to 1986 suggests hardening of the rock matrix with time, interrupted by temporary decrease in the course of 1982, in agreement with the pattern shown in **Figure 1**. We have, however, to remind that the calculation of the shear modulus is strongly affected by the loading tides, and it is unstable, owing to the closeness in values of the two normal strain components of the observed tidal strains (Mao et al., 1989).

Our observations, together with the variations in elastic parameters reported by Mao et al. (1989), are in agreement with the time variation in the fluid content, possibly related to compaction-driven porosity and lateral and temporal variations

in permeability (Byerlee, 1993; Khoshmanesh and Shirzaei, 2018).

The contribution of meteoric water cannot be excluded in the region of study, characterized by karstic phenomena in outcropping and subsurface formations (Cimolino et al., 2010), implying that complex groundwater flow in the rock matrix, fractures, and conduits also inferred from deformations (Devoti et al., 2015; Braitenberg et al., 2019), as in other regions characterized by karst aquifers (Silverii et al., 2016, 2019). In the present case, based on all the observations presented, the models of Rice (1992) and Byerlee (1993) appear the most suitable.

In the absence of geochemical information, the possibility of a fluid source from crustal deeper parts, as in the model of Rice (1992), could not be excluded. We can estimate the flux rate necessary to maintain the overpressure at depth and verify the plausibility of the values for both cases: the one treated in the present study, and the one reported by RossiI and RossiII. The fluid influx q is defined by David et al. (1994) as

$$q = \frac{\xi\left(\rho_b - \rho_f\right) g K_0}{\eta} \tag{6}$$

where K_0 is the permeability, and ξ is the normalized flux given by

$$\xi = \exp\left\{\left(\frac{P(z) - \rho_f g z - \sigma^* ln(1)}{\sigma^*}\right) - ln\left[\exp\left(\frac{\left(\rho_b - \rho_f\right) g z}{\sigma^*}\right) - 1\right]\right\} \tag{7}$$

with σ^* being the characteristic stress.

We used the permeability values shown in **Table 2** for the Jurassic limestones, whereas for permeability and density of the *Dolomia Principale* and Paleozoic sandstones, not crossed by the rays in this case, we referred to RossiII's Table 2.

In this case, we considered the formations that should be present at the depth of the two transient sources. Table 3 of David et al. (1994) gives the values of σ^*: 21.3 MPa for *Dolomia Principale* and the Jurassic limestones and 26.3 MPa for the Paleozoic sandstones. For the two transients, we obtain the values of ξ in the range 0.21–0.33 for the permeable *Dolomia Principale*, and in the range 0.53–0.63 when Jurassic limestones or Paleozoic sandstones are considered, in agreement with the values reported by David et al. (1994).

It follows that for both transients the value of the fluid influx q is in the range 0.47–0.65 m/year for the permeable *Dolomia Principale* and about 0.013–0.015 m/year for the Jurassic limestones, whereas it is 0.023–0.027 m/year for the Paleozoic sandstones. If we use the values of the effective stress we calculated for both transients, instead of σ^*, we have a variation of about 8% for ξ and q. The fluid influx values are reasonable compared with the measurements of the mantle fluid flow in different tectonic environments from geochemical measurements: the highest range of values, 0.42–2.6 m/year, is obtained for the Alpine Fault in New Zealand (Menzies et al., 2016), whereas 0.004–0.14 m/year characterizes the San Andreas Fault (Kennedy et al., 1997; Kulongoski et al., 2013), 0.13–0.19 m/year the North Anatolian Fault (de Leeuw et al., 2010), and −0.012–0.019 m/year the Karakoram fault (Klemperer et al., 2013).

To calculate the approximate areas involved in the flux discharge according to the fault valve model, we use the well-known relationships between magnitude and rupture area (Wells and Coppersmith, 1994), considering the February 1983 $M_D = 4.2$ and July 2004 $M_w = 5.1$ earthquakes. These earthquakes occurred two to three months after the origin of the hypothesized transient. The highest flux discharge corresponds to the more permeable *Dolomia Principale* ($7.2 \cdot 10^5$–$4.0 \cdot 10^6$ m^3/year), whereas, for the much less permeable Jurassic limestones, near-lithostatic pressure would be maintained even with a flux range of $1.7 \cdot 10^4$–$1.1 \cdot 10^5$ m^3/year. In all the cases, we obtain the highest values for the 2006–2009 transient and the greater magnitude of the correlated earthquake.

CONCLUSIONS

Transient variations in crustal deformation data can potentially detect slow pore fluid pressure propagation and associated effective stress fluctuations. The empirical mode decomposition (EMD) method employed here has been efficient in detecting transient tilt signals. Through the present analysis, we demonstrated that the area at the boundary between NE-Italy and W-Slovenia, where the Dinaric fault system crosses and merges with the Alpine one, strongly supports the recurrence of fault valve behavior, releasing fluids from depth to the surrounding region as pore pressure bulges. The pore fluid pressure appears to have migrated from a depth of 6 km upward and through the surrounding as a porosity wave, as inferred from a strong, coherent tilt transient of about 2.5 years in duration in the direction of the main fractures. At the origin of the fluid release, there are overpressure conditions at depth, with pore pressure ∼0.89 the lithostatic one, in agreement with previous and independent observations on elastic parameters and seismic velocity variations. The fluid influx values necessary to maintain such pore pressure values are comparable with other observations in other contexts. Geochemical tracer analysis of the spring water and concretions could help evaluate the budget of meteoric, metamorphic, and mantle fluids. Such information, together with full waveform inversion, more adequate in a near-field case (as for VI and the source of transient), and a pore fluid diffusion model, could better define this complex interaction between fluids, deformation, and seismicity.

Our research provides novel pieces of evidence on the relationship between pore fluid pressure variations and slow slip moderate magnitude events in an area of continental collision. Although based on an almost unique strain data set, our results and observations can help consider

phenomena like the ones reported in this study as a possible cause of deformation and seismicity migration patterns in other regions.

DATA AVAILABILITY STATEMENT

The data that support the findings of this study are available upon request from the authors. Requests to access these datasets should be directed to berg@units.it, apastorutti@units.it.

AUTHOR CONTRIBUTIONS

GR ideated the study, performed data analysis and interpretation of the results, and wrote the manuscript. IN and AP performed the preprocessing of data. CB is responsible for the maintenance of the NE-Italy tilt-strainmeter network of the University of Trieste, and discussed the results and interpretation. SP suggested the EMD technique, designed the EMD software, and participated in EMD data analysis. All the authors read and corrected the manuscript.

FUNDING

We acknowledge funding by the Italian Ministry of University and Research (MUR) Department of Excellence grant, given to the Department of Mathematics and Geosciences of the University of Trieste (Italy) through which AP is supported.

ACKNOWLEDGMENTS

We dedicate this study to the memory of Prof. Maria Zadro, who initiated the NE-Italy tilt-strainmeter network of the University of Trieste, and her scientific curiosity that inspired this research. We thank all the technicians and Dr. Barbara Grillo who, through the years, have helped in the management of the network. We thank Dr. Gianni Bressan for constructive discussions and the relocalization of the Uccea and Bovec–Krn earthquakes. We are grateful to Alexandre Canitano, Weijian Mao, Pierre-Michel Rouleau, and the editor, György Hetényi, for the accurate and thorough revision, stimulating comments, and helpful suggestions.

REFERENCES

Argus, D. F., Fu, Y., and Landerer, F. W. (2014). Seasonal variation in total water storage in California inferred from GPS observations of vertical land motion. *Geophys. Res. Lett.* 41, 1971–1980. doi: 10.1002/2014GL059570

Böhm, G., Rossi, G., and Vesnaver, A. (1999). Minimum-time ray-tracing for 3D irregular grids. *J. Seism. Explor.* 8, 117–131.

Bonafede, M., Boschi, E., and Dragoni, M. (1983). Viscoelastic stress relaxation on deep fault sections as a possible source of very long period elastic waves. *J. Geophys. Res.* 88, 2251–2260. doi: 10.1029/JB088iB03p02251

Bragato, P. L., Comelli, P., Saraò, A., Zuliani, D., Moratto, L., Poggi, V., et al. (2021). The OGS–Northeastern Italy seismic and deformation network: current status and outlook. *Seismol. Res. Lett.* 92, 1704–1716. doi: 10.1785/0220200372

Braitenberg, C. (1999). The Friuli (NE-Italy) tilt/strain gauges and short term observations. *Ann. Geofis.* 42, 637–664.

Braitenberg, C., Pivetta, T., Barbolla, D. F., Gabrovšek, F., Devoti, R., and Nagy, I. (2019). Terrain uplift due to natural hydrologic overpressure in karstic conduits. *Sci. Rep.* 9:3934. doi: 10.1038/s41598-019-38814-1

Braitenberg, C., Romeo, G., Taccetti, Q., and Nagy, I. (2006). The very-broad-band long-base tiltmeters of Grotta Gigante (Trieste, Italy): Secular term tilting and the great Sumatra-Andaman islands earthquake of December 26, 2004. *J. Geodyn.* 41, 164–174. doi: 10.1016/j.jog.2005.08.015

Brauchler, R., Böhm, G., Leven, C., Dietrich, P., and Sauter, M. (2013). A laboratory study of tracer tomography. *Hydrogeol. J.* 21, 1265–1274. doi: 10.1007/s10040-013-1006-z

Bressan, G., Barnaba, C., Bragato, P., Ponton, M., and Restivo, A. (2018b). Revised seismotectonic model of NE Italy and W Slovenia based on focal mechanism inversion. *J. Seismol.* 22, 1563–1578. doi: 10.1007/s10950-018-9785-2

Bressan, G., Barnaba, C., Bragato, P. L., Peresan, A., Rossi, G., and Urban, S. (2019). Distretti sismici del Friuli Venezia Giulia. *Boll. Geof. Teor. Appl.* 60, S1–S74. doi: 10.4430/bgta0300

Bressan, G., Barnaba, C., Magrin, A., and Rossi, G. (2018a). A study on off-fault aftershock pattern at N-Adria microplate. *J. Seismol.* 22, 863–881. doi: 10.1007/s10950-018-9737-x

Bressan, G., Gentile, G. F., Tondi, R., De Franco, R., and Urban, S. (2012). Sequential integrated inversion of tomographic images and gravity data: an application to the Friuli area (north-eastern Italy). *Boll. Geof. Teor. Appl.* 53, 193–212. doi: 10.4430/bgta0059

Bressan, G., Kravanja, S., and Franceschina, G. (2007). Source parameters and stress release of seismic sequences occurred in the Friuli-Venezia Giulia region (Northeastern Italy) and in Western Slovenia. *Phys. EarthPlanet. Inter.* 160, 192–214. doi: 10.1016/j.pepi.2006.10.005

Bressan, G., Ponton, M., Rossi, G., and Urban, S. (2016). Spatial organization of seismicity and fracture pattern in NE Italy and W Slovenia. *J. Seismol.* 20, 511–534. doi: 10.1007/s10950-015-9541-9

Bürgmann, R. (2018). The geophysics, geology and mechanics of slow fault slip. *Earth Planet. Sci. Lett.* 495, 112–134. doi: 10.1016/j.epsl.2018.04.062

Byerlee, J. (1990). Friction, overpressure and fault normal compression. *Geophys. Res. Lett.* 17, 2109–2112. doi: 10.1029/GL017i012p02109

Byerlee, J. (1993). Model for episodic flow of high-pressure water in fault zones before earthquakes. *Geology* 21, 303–306. doi: 10.1130/0091-7613(1993)021<0303:MFEFOH>2.3.CO;2

Cervelli, P., Segall, P., Johnson, K., Lisowski, M., and Miklius, A. (2002). Sudden aseismic fault slip on the south flank of Kilauea volcano. *Nature* 415, 1014–1018. doi: 10.1038/4151014a

Chanard, K., Métois, M., Rebischung, P., and Avouac, J.-P. (2020). A warning against over-interpretation of seasonal signals measured by the global navigation satellite system. *Nat. Commun.* 11:1375. doi: 10.1038/s41467-020-15100-7

Chiarabba, C., Gori, P. D., Cattaneo, M., Spallarossa, D., and Segou, M. (2018). Faults geometry and the role of fluids in the 2016–2017 Central Italy seismic sequence. *Geophys. Res. Lett.* 45, 6963–6971. doi: 10.1029/2018GL077485

Chiaruttini, C., and Zadro, M. (1976). Horizontal pendulum observations at Trieste. *Boll. Geofis. Teor. Appl.* 19, 441–455.

Cimolino, A., Della Vedova, B., Nicolich, R., Barison, E., and Brancatelli, G. (2010). New evidence of the outer Dinaric deformation front in the Grado area (NE-Italy). *Rend. Fis. Acc. Lincei* 21, 167–179. doi: 10.1007/s12210-010-0096-y

Connolly, J. A. D., and Podladchikov, Y. Y. (2013). "A Hydromechanical Model for Lower Crustal Fluid Flow," in *Metasomatism and the Chemical Transformation of Rock: The Role of Fluids in Terrestrial and Extraterrestrial Processes*, eds D. E. Harlov, and H. Austrheim (Berlin: Springer), 599–658. doi: 10.1007/978-3-642-28394-9_14

Console, R., Murru, M., Vannoli, P., Carluccio, R., Taroni, M., and Falcone, G. (2020). Physics-based simulation of sequences with multiple main shocks in Central Italy. *Geophys. J. Int.* 223, 526–542. doi: 10.1093/gji/ggaa300

Craig, T. J., Chanard, K., and Calais, E. (2017). Hydrologically-driven crustal stresses and seismicity in the New Madrid Seismic Zone. *Nat. Commun.* 8:2143. doi: 10.1038/s41467-017-01696-w

Cruz-Atienza, V. M., Villafuerte, C., and Bhat, H. S. (2018). Rapid tremor migration and pore-pressure waves in subduction zones. *Nat. Commun.* 9:2900. doi: 10.1038/s41467-018-05150-3

D'Agostino, N., Silverii, F., Amoroso, O., Convertito, V., Fiorillo, F., Ventafridda, G., et al. (2018). Crustal deformation and seismicity modulated by groundwater recharge of karst aquifers. *Geophys. Res. Lett.* 45, 253–262. doi: 10.1029/2018GL079794

David, C., Wong, T.-F., Zhu, W., and Zhang, J. (1994). Laboratory measurement of compaction-induced permeability change in porous rocks: implications for the generation and maintenance of pore pressure excess in the crust. *Pure Appl. Geophys.* 143, 425–456. doi: 10.1007/BF00874337

de Leeuw, G. A. M., Hilton, D. R., Güleç, N., and Mutlu, H. (2010). Regional and temporal variations in $CO_2/^3He$, $^3He/^4He$ and $\delta^{13}C$ along the North Anatolian Fault Zone, Turkey. *Appl. Geochem.* 25, 524–539. doi: 10.1016/j.apgeochem.2010.01.010

Devoti, R., Riguzzi, F., Cinti, F. R., and Ventura, G. (2018). Long-term strain oscillations related to the hydrological interaction between aquifers in intra-mountain basins: a case study from Apennines chain (Italy). *Earth Planet. Sci. Lett.* 501, 1–12. doi: 10.1016/j.epsl.2018.08.014

Devoti, R., Zuliani, D., Braitenberg, C., Fabris, P., and Grillo, B. (2015). Hydrologically induced slope deformations detected by GPS and clinometric surveys in the Cansiglio Plateau, southern Alps. *Earth Planet. Sci. Lett.* 419, 134–142. doi: 10.1016/j.epsl.2015.03.023

Ditommaso, R., Mucciarelli, M., Parolai, S., and Picozzi, M. (2012). Monitoring the structural dynamic response of a masonry tower: comparing classical and time-frequency analyses. *Bull. Earthquake Eng.* 10, 1221–1235. doi: 10.1007/s10518-012-9347-x

Dragert, H. (2001). A silent slip event on the deeper Cascadia subduction interface. *Science* 292, 1525–1528. doi: 10.1126/science.1060152

Dragoni, M., Bonafede, M., and Boschi, E. (1985). "On the Interpretation of Slow Ground Deformation Precursory to the 1976 Friuli Earthquake," in *Earthquake Prediction*, eds K. Shimazaki, and W. Stuart (Basel: Birkhäuser Basel), 781–792. doi: 10.1007/978-3-0348-6245-5_3

Dvorkin, J., Mavko, G., and Nur, A. (1999). Overpressure detection from compressional- and shear-wave data. *Geophys. Res. Lett.* 26, 3417–3420. doi: 10.1029/1999GL008382

Faccenda, M., Bressan, G., and Burlini, L. (2007). Seismic properties of the upper crust in the central Friuli area (northeastern Italy) based on petrophysical data. *Tectonophysics* 445, 210–226. doi: 10.1016/j.tecto.2007.08.004

Farrell, W. E. (1972). Deformation of the earth by surface loads. *Rev. Geophys.* 10, 761–797. doi: 10.1029/RG010i003p00761

Faulkner, D. R., Jackson, C. A. L., Lunn, R. J., Schlische, R. W., Shipton, Z. K., Wibberley, C. A. J., et al. (2010). A review of recent developments concerning the structure, mechanics and fluid flow properties of fault zones. *J. Struct. Geol. Fault Zones* 32, 1557–1575. doi: 10.1016/j.jsg.2010.06.009

Fischer, T., Matyska, C., and Heinicke, J. (2017). Earthquake-enhanced permeability - evidence from carbon dioxide release following the ML 3.5 earthquake in West Bohemia. *Earth Planet. Sci. Lett.* 460, 60–67. doi: 10.1016/j.epsl.2016.12.001

Gentili, S. (2010). Distribution of seismicity before the larger earthquakes in Italy in the time interval 1994–2004. *Pure Appl. Geophys.* 167, 933–958. doi: 10.1007/s00024-010-0089-x

Grillo, B., Braitenberg, C., Nagy, I., Devoti, R., Zuliani, D., and Fabris, P. (2018). Cansiglio Karst Plateau: 10 Years of Geodetic–Hydrological Observations in Seismically Active Northeast Italy. *Pure Appl. Geophys.* 175, 1765–1781. doi: 10.1007/s00024-018-1860-7

Hawle, H., Kratochvil, H., Schmied, H., and Wieseneder, H. (1967). "Reservoir geology of the carbonate oil and gas reservoir of the Vienna Basin," in 7th *World Petroleum Congress* (Mexico City: OnePetro).

Hickman, S., Sibson, R., and Bruhn, R. (1995). Introduction to special section: mechanical involvement of fluids in faulting. *Pure Appl. Geophys.* 100, 12831–12840. doi: 10.1029/95JB01121

Huang, N. E., Shen, Z., Long, S. R., Wu, M. C., Shih, H. H., Zheng, Q., et al. (1998). The empirical mode decomposition and the Hilbert spectrum for nonlinear and non-stationary time series analysis. *Proc. R. Soc. Lond. A* 454, 903–995. doi: 10.1098/rspa.1998.0193

Hubbert, M. K., and Rubey, W. W. (1959). Role of fluid pressure in mechanics of overthrust faulting. Mechanics of fluid-filled porous solids and its application to overthrust faulting. *Geol. Soc. Am. Bull.* 70, 115–166. doi: 10.1130/0016-7606(1959)70[115:ROFPIM]2.0.CO;2

Ito, Y., Obara, K., Shiomi, K., Sekine, S., and Hirose, H. (2007). Slow earthquakes coincident with episodic tremors and slow slip events. *Science* 315, 503–506. doi: 10.1126/science.1134454

Ji, K. H., and Herring, T. A. (2012). Correlation between changes in groundwater levels and surface deformation from GPS measurements in the San Gabriel Valley, California. *Geophys. Res. Lett.* 39, L01301. doi: 10.1029/2011GL050195

Kastelic, V., Vrabec, M., Cunningham, D., and Gosar, A. (2008). Neo-Alpine structural evolution and present-day tectonic activity of the eastern Southern Alps: the case of the Ravne Fault, NW Slovenia. *J. Struct. Geol.* 30, 963–975. doi: 10.1016/j.jsg.2008.03.009

Kennedy, B. M., Kharaka, Y. K., Evans, W. C., Ellwood, A., DePaolo, D. J., Thordsen, J., et al. (1997). Mantle fluids in the San Andreas Fault System, California. *Science* 278, 1278–1281. doi: 10.1126/science.278.5341.1278

Khoshmanesh, M., and Shirzaei, M. (2018). Episodic creep events on the San Andreas Fault caused by pore pressure variations. *Nat. Geosci.* 11, 610–614. doi: 10.1038/s41561-018-0160-2

King, G., and Bilham, R. (1976). A geophysical wire strainmeter. *Bull. Seismol. Soc. Am.* 66, 2039–2047.

Klemperer, S. L., Kennedy, B. M., Sastry, S. R., Makovsky, Y., Harinarayana, T., and Leech, M. L. (2013). Mantle fluids in the Karakoram fault: Helium isotope evidence. *Earth Planet. Sci. Lett.* 366, 59–70. doi: 10.1016/j.epsl.2013.01.013

Kodaira, S. (2004). High pore fluid pressure may cause silent slip in the Nankai Trough. *Science* 304, 1295–1298. doi: 10.1126/science.1096535

Kulongoski, J. T., Hilton, D. R., Barry, P. H., Esser, B. K., Hillegonds, D., and Belitz, K. (2013). Volatile fluxes through the Big Bend section of the San Andreas Fault, California: Helium and carbon-dioxide systematics. *Chem. Geol.* 339, 92–102. doi: 10.1016/j.chemgeo.2012.09.007

Longuevergne, L., Florsch, N., Boudin, F., Oudin, L., and Camerlynck, C. (2009). Tilt and strain deformation induced by hydrologically active natural fractures: application to the tiltmeters installed in Sainte-Croix-aux-Mines observatory (France). *Geophys. J. Int.* 178, 667–677. doi: 10.1111/j.1365-246X.2009.04197.x

Lowry, A. R., Larson, K. M., Kostoglodov, V., and Bilham, R. (2001). Transient fault slip in Guerrero, southern Mexico. *Geophys. Res. Lett.* 28, 3753–3756. doi: 10.1029/2001GL013238

Lupi, M., Geiger, S., and Graham, C. M. (2011). Numerical simulations of seismicity-induced fluid flow in the Tjörnes Fracture Zone, Iceland. *J. Geophys. Res.* 116:B07101. doi: 10.1029/2010JB007732

Mao, W. J., Ebblin, C., and Zadro, M. (1989). Evidence for variations of mechanical properties in the Friuli seismic area. *Tectonophysics* 170, 231–242. doi: 10.1016/0040-1951(89)90273-4

Marussi, A. (1959). "The University of Trieste station for the study of the tides of the vertical in the Grotta Gigante," in *Proceedings of the III International Symposium on Earth Tides* (Trieste), 45–52.

Matsumoto, Y., Yoshida, K., Matsuzawa, T., and Hasegawa, A. (2021). Fault-valve behavior estimated from intensive foreshocks and aftershocks of the 2017 M 5.3 Kagoshima Bay earthquake sequence, Kyushu, southern Japan. *J. Geophys. Res. Solid Earth.* 126:e2020JB020278. doi: 10.1029/2020JB020278

Menzies, C. D., Teagle, D. A. H., Niedermann, S., Cox, S. C., Craw, D., and Zimmer, M. (2016). The fluid budget of a continental plate boundary fault: Quantification from the Alpine Fault, New Zealand. *Earth Planet. Sci. Lett.* 445, 125–135. doi: 10.1016/j.epsl.2016.03.046

Nakajima, J., and Uchida, N. (2018). Repeated drainage from megathrusts during episodic slow slip. *Nat. Geosci.* 11, 351–356. doi: 10.1038/s41561-018-0090-z

Nespoli, M., Belardinelli, M. E., Gualandi, A., Serpelloni, E., and Bonafede, M. (2018). Poroelasticity and fluid flow modeling for the 2012 Emilia-Romagna earthquakes: hints from GPS and InSAR data. *Geofluids* 2018:e4160570. doi: 10.1155/2018/4160570

Panda, D., Kundu, B., Gahalaut, V. K., Bürgmann, R., Jha, B., Asaithambi, R., et al. (2018). Seasonal modulation of deep slow-slip and earthquakes on the Main Himalayan Thrust. *Nat. Commun.* 9:4140. doi: 10.1038/s41467-018-06371-2

Panda, D., Kundu, B., Gahalaut, V. K., Bürgmann, R., Jha, B., Asaithambi, R., et al. (2020). Reply to "A warning against over-interpretation of seasonal signals

measured by the Global Navigation Satellite System." *Nat. Commun.* 11:1376. doi: 10.1038/s41467-020-15103-4

Peterie, S. L., Miller, R. D., Intfen, J. W., and Gonzales, J. B. (2018). Earthquakes in Kansas induced by extremely far-field pressure diffusion. *Geophys. Res. Lett.* 45, 1395–1401. doi: 10.1002/2017GL076334

Poljak, M., Živčić, M., and Zupančič, P. (2000). "The seismotectonic characteristics of Slovenia," in *Seismic Hazard of the Circum-Pannonian Region*, eds G. F. Panza, M. Radulian, and C. I. Trifu (Basel: Birkhäuser Basel), 37–55. doi: 10.1007/978-3-0348-8415-0_3

Revil, A., and Cathles, L. M. (2002). Fluid transport by solitary waves along growing faults: A field example from the South Eugene Island Basin, Gulf of Mexico. *Earth Planet. Sci. Lett.* 202, 321–335. doi: 10.1016/S0012-821X(02)00784-7

Rice, J. R. (1992). "Chapter 20: fault stress states, pore pressure distributions, and the weakness of the San Andreas Fault," in *International Geophysics, Fault Mechanics and Transport Properties of Rocks*, eds B. Evans and T. F. Wong. International Geophysics (London: Academic Press), 51, 475–503. doi: 10.1016/S0074-6142(08)62835-1

Riel, B., Simons, M., Agram, P., and Zhan, Z. (2014). Detecting transient signals in geodetic time series using sparse estimation techniques. *J. Geophys. Res. Solid Earth* 119, 5140–5160. doi: 10.1002/2014JB011077

Rossi, G., Fabris, P., and Zuliani, D. (2018). Overpressure and fluid diffusion causing non-hydrological transient GNSS displacements. *Pure Appl. Geophys.* 175, 1869–1888. doi: 10.1007/s00024-017-1712-x

Rossi, G., and Zadro, M. (1996). Long-term crustal deformations in NE Italy revealed by tilt-strain gauges. *Phys. Earth Planet. Inter.* 97, 55–70. doi: 10.1016/0031-9201(96)03166-4

Rossi, G., Zuliani, D., and Fabris, P. (2016). Long-term GNSS measurements from the northern Adria microplate reveal fault-induced fluid mobilization. *Tectonophysics* 690, 142–159. doi: 10.1016/j.tecto.2016.04.031

Rossi, G., Zuliani, D., and Fabris, P. (2017). Corrigendum to "Long-term GNSS measurements from the northern Adria microplate reveal fault-induced fluid mobilization." *Tectonophysics* 694, 486–487. doi: 10.1016/j.tecto.2016.10.035

Serpelloni, E., Pintori, F., Gualandi, A., Scoccimarro, E., Cavaliere, A., Anderlini, L., et al. (2018). Hydrologically induced karst deformation: insights from GPS measurements in the Adria-Eurasia plate boundary zone. *J. Geophys. Res. Solid Earth* 123, 4413–4430. doi: 10.1002/2017JB015252

Serpelloni, E., Vannucci, G., Anderlini, L., and Bennett, R. A. (2016). Kinematics, seismotectonics and seismic potential of the eastern sector of the European Alps from GPS and seismic deformation data. *Tectonophysics* 688, 157–181. doi: 10.1016/j.tecto.2016.09.026

Sibson, R. H. (1992). Implications of fault-valve behaviour for rupture nucleation and recurrence. *Tectonophysics* 211, 283–293. doi: 10.1016/0040-1951(92)90065-E

Sibson, R. H. (2014). Earthquake rupturing in fluid-overpressured crust: how common? *Pure Appl. Geophys.* 171, 2867–2885. doi: 10.1007/s00024-014-0838-3

Sibson, R. H. (2020). Preparation zones for large crustal earthquakes consequent on fault-valve action. *Earth Planets Space* 72:31. doi: 10.1186/s40623-020-01153-x

Sibson, R. H., and Rowland, J. V. (2003). Stress, fluid pressure and structural permeability in seismogenic crust, North Island, New Zealand. *Geophys. J. Int.* 154, 584–594. doi: 10.1046/j.1365-246X.2003.01965.x

Silverii, F., D'Agostino, N., Borsa, A. A., Calcaterra, S., Gambino, P., Giuliani, R., et al. (2019). Transient crustal deformation from karst aquifers hydrology in the Apennines (Italy). *Earth Planet. Sci. Lett.* 506, 23–37. doi: 10.1016/j.epsl.2018.10.019

Silverii, F., D'Agostino, N., Métois, M., Fiorillo, F., and Ventafridda, G. (2016). Transient deformation of karst aquifers due to seasonal and multiyear groundwater variations observed by GPS in southern Apennines (Italy). *J. Geophys. Res. Solid Earth* 121, 8315–8337. doi: 10.1002/2016JB013361

Skarbek, R. M., and Rempel, A. W. (2016). Dehydration-induced porosity waves and episodic tremor and slip: Porosity waves and ETS. *Geochem. Geophys. Geosys.* 17, 442–469. doi: 10.1002/2015GC006155

Slejko, D., Neri, G., Orozova, I., Renner, G., and Wyss, M. (1999). Stress field in Friuli (NE Italy) from fault plane solutions of activity following the 1976 main shock. *Bull. Seismol. Soc. Am.* 89, 1037–1052.

Talwani, P., Cobb, J. S., and Schaeffer, M. F. (1999). *In situ* measurements of hydraulic properties of a shear zone in northwestern South Carolina. *J. Geophys. Res.* 104, 14993–15003. doi: 10.1029/1999JB900059

Terzaghi, K. (1923). Die Berechnung der Durchlässigkeitsziffer des Tones aus dem Verlauf der hydrodynamischen Spannungserscheinungen. *Akad. Wissenschaft. Wien* 132, 125–138.

van Dam, T., Wahr, J., and Lavallée, D. (2007). A comparison of annual vertical crustal displacements from GPS and gravity recovery and climate experiment (GRACE) over Europe. *J. Geophys. Res.* 112:B03404. doi: 10.1029/2006JB004335

Vesnaver, A., and Böhm, G. (2000). Staggered or adapted grids for seismic tomography? *Lead. Edge* 19, 944–950. doi: 10.1190/1.1438762

ViDEPI (2009). *Visibilità Dei Dati Afferenti All'attività Di Esplorazione Petrolifera in Italia, Società Geologica Italiana*. Available online at: https://unmig.mise.gov.it/index.php/it/dati/ricerca-e-coltivazione-di-idrocarburi/dati-storici-videpi (accessed November 19, 2020).

Wahr, J., Khan, S. A., van Dam, T., Liu, L., van Angelen, J. H., van den Broeke, M. R., et al. (2013). The use of GPS horizontals for loading studies, with applications to northern California and southeast Greenland: GPS horizontals for loading studies. *J. Geophys. Res. Solid Earth* 118, 1795–1806. doi: 10.1002/jgrb.50104

Watson, K. M., Bock, Y., and Sandwell, D. T. (2002). Satellite interferometric observations of displacements associated with seasonal groundwater in the Los Angeles basin: INSAR and GPS Observations of Los Angeles Basin. *J. Geophys. Res.* 107, ETG 8-1–ETG 8-15. doi: 10.1029/2001JB000470

Wells, D. L., and Coppersmith, K. J. (1994). New empirical relationships among magnitude, rupture length, rupture width, rupture area, and surface displacement. *Bull. Seismol. Soc. Am.* 84, 974–1002.

Zadro, M., and Braitenberg, C. (1999). Measurements and interpretations of tilt–strain gauges in seismically active areas. *Earth Sci. Rev.* 47, 151–187. doi: 10.1016/S0012-8252(99)00028-8

Zhang, S., Liu, K., Liu, Q., Zhang, C., Zhang, Q., and Nan, Y. (2019). Tide variation monitoring based improved GNSS-MR by empirical mode decomposition. *Adv. Space Res.* 63, 3333–3345. doi: 10.1016/j.asr.2019.01.046

Conflict of Interest: The authors declare that the research was conducted in the absence of any commercial or financial relationships that could be construed as a potential conflict of interest.

frontiers in Earth Science

ORIGINAL RESEARCH
published: 16 June 2021
doi: 10.3389/feart.2021.688374

Exploiting Thermochronology to Quantify Exhumation Histories and Patterns of Uplift Along the Margins of Tibet

Kevin P. Furlong[1], Eric Kirby[2], C. Gabriel Creason[3], Peter J. J. Kamp[4], Ganqing Xu[4], Martin Danišík[4], Xuhua Shi[5] and Kip V. Hodges[6]*

[1]Department of Geosciences, Penn State University, University Park, PA, United States, [2]Department of Geological Sciences, University of North Carolina, Chapel Hill, NC, United States, [3]CEOAS, Oregon State University, Corvallis, OR, United States, [4]School of Science, University of Waikato, Hamilton, New Zealand, [5]Key Laboratory of Geoscience Big Data and Deep Resource of Zhejiang Province, School of Earth Sciences, Zhejiang University, Hangzhou, China, [6]School of Earth and Space Exploration, Arizona State University, Tempe, AZ, United States

OPEN ACCESS

Edited by:
A. Alexander G. Webb, The University of Hong Kong, Hong Kong

Reviewed by:
Yuntao Tian, Sun Yat-Sen University, China
Sergio Llana-Fúnez, University of Oviedo, Spain

***Correspondence:**
Kevin P. Furlong
kpf1@psu.edu

Specialty section:
This article was submitted to Structural Geology and Tectonics, a section of the journal Frontiers in Earth Science

Received: *30 March 2021*
Accepted: *28 May 2021*
Published: *16 June 2021*

Citation:
Furlong KP, Kirby E, Creason CG, Kamp PJJ, Xu G, Danišík M, Shi X and Hodges KV (2021) Exploiting Thermochronology to Quantify Exhumation Histories and Patterns of Uplift Along the Margins of Tibet. Front. Earth Sci. 9:688374. doi: 10.3389/feart.2021.688374

The utilization of thermal-chronological data to constrain mountain building processes exploits the links among rock uplift, exhumation, and cooling during orogenesis. Conceptually, periods of rapid uplift and associated denudation will lead to cooling of rocks as they approach Earth's surface. The linkage between uplift and exhumation can be complex, but in practice exhumation is often assumed to directly track uplift. The reconstruction of temperature-time histories via thermochronologic systems provides a proxy method to relate the cooling of rock as it is exhumed toward the surface to orogenesis. For the rapid exhumation rates that can occur in active orogenic systems the thermal history will be complex as a result of heat advection, rates of propagation of thermal perturbations, and other processes that affect the cooling behavior. These effects become amplified as exhumation rates increase, and in regions experiencing exhumation rates greater than ~0.2–0.3 mm/yr (0.2–0.3 km/Ma) simple assumptions of cooling through a constant geotherm will bias the subsequent interpretation. Here we explore, through a suite of generalized models, the impact of exhumation rate and duration on the resulting thermal history and apparent age results. We then apply lessons from these simple exhumation systems to data sets from the high-relief ranges along the eastern margin of the Tibetan Plateau to determine exhumation histories constrained by those data. The resulting exhumation histories provide constraints on the onset of Cenozoic exhumation, the subsequent pace of exhumation, and on the tectonic history of one of the major fault systems in the central Longmen Shan.

Keywords: thermo-chronology, modeling mountain building processes, temperature histories during exhumation, Longmen Shan, Xuelongbao Massif, Pengguan Massif

THERMOCHRONOLOGY AND MOUNTAIN BUILDING

The utilization of thermal-chronological data to estimate rates and patterns of exhumation during mountain building exploits the links among rock uplift, exhumation, and cooling associated with crustal thickening during orogenesis. Conceptually, periods of rapid crustal thickening will be accompanied by rapid uplift, and associated denudation, which will lead to cooling of rocks as they approach Earth's surface. The linkage between uplift and exhumation can be complex, as topographic relief evolves in response to rapid erosion and increased surface slope (Whipple et al., 1999; Montgomery and Brandon, 2002), but in practice exhumation is often assumed to directly track uplift (e.g., Bullen et al., 2003; Stockli et al., 2003). Our ultimate goal is to place constraints on the processes associated with mountain building, and in particular determine timing and rates of deformation associate with orogenesis. The evolution of a mountain system can be linked to processes of burial and exhumation, with assumptions of crustal thickening, fault movements and other kinematics. Those processes can be related to surface and near surface processes of uplift and exhumation.

Because neither uplift or exhumation is readily observed, the reconstruction of temperature-time histories via thermochronologic systems (Reiners and Brandon, 2006; Hodges, 2014) provides a proxy method to relate the cooling of rock, as it is exhumed toward the surface (e.g., Ehlers, 2005), to the evolution of the orogen. The link between the cooling experienced by a rock sample and the exhumation history is often assumed to be similarly direct (e.g., Liu et al., 2013; Lease et al., 2021), but for rapid exhumation rates, often occurring in active orogenic systems, the thermal history will differ from

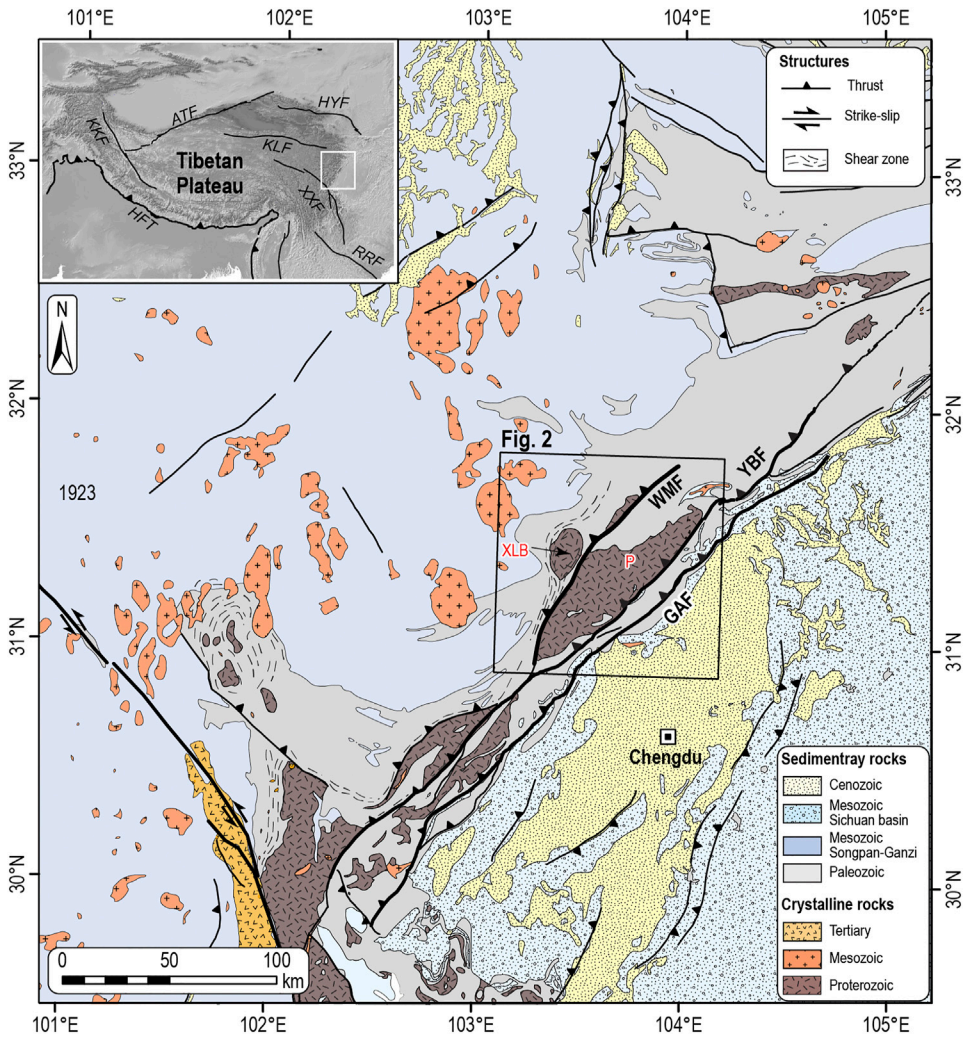

FIGURE 1 | Tectonic setting of the eastern margin of the Tibetan Plateau adjacent to the Sichuan Basin. Geology after Kirby et al., 2002; Airaghi et al., 2018a. Primary fault systems in the Longmen Shan region are abbreviated as follows: GAF, Guanxian–Anxian Fault; YBF, Yingxiu–Beichuan Fault; WMF, Wenchuan–Maowen Fault. Inset map shows location of study area relative to the Tibetan Plateau and major active faults. HFT, Himalayan Frontal Thrust; KKF, Karakorum Fault; ATF, Altyn Tagh Fault; HYF, Haiyuan Fault; KLF, Kunlun Fault; XXF, Xianshuihe–Xiaojiang Fault; and RRF, Red River Fault.

simple cooling with exhumation as a result of heat advection, propagation rates of thermal perturbations, and other processes that affect the cooling behavior (Moore and England, 2001; Braun, 2003; Ehlers, 2005). These effects become amplified as exhumation rates increase, and so although simple assumptions of constant temperature gradient may be adequate to describe a slowly eroding system, in regions experiencing exhumation rates greater than ~0.2–0.3 mm/yr (0.2–0.3 km/Ma) such assumptions will bias the subsequent interpretation. Additionally, in most orogenic events, deformation is often unsteady, and the superimposition of time-varying uplift and exhumation influences the resultant evolution of crustal thermal structure.

Here we explore, through a suite of generalized models, the impact of exhumation rate and duration on the resulting thermal history and apparent age results. We then apply these lessons from simply exhuming systems to a data set from the high-relief ranges that demarcate the eastern margin of the Tibetan Plateau (e.g., Kirby et al., 2013) in order to determine exhumation histories involving non-steady rates of exhumation, constrained by that data. Comparison of the exhumation history to the results of a similar study from the nearby Pengguan Massif (Wang et al., 2012) provide constraints on the onset of Cenozoic exhumation, the subsequent pace of exhumation, and on the tectonic history of one of the major fault systems in the central Longmen Shan.

Tectonic Setting of the Longmen Shan

The Longmen Shan refers broadly to the collection of high mountain ranges that mark the eastern margin of the Tibetan Plateau adjacent to the Sichuan Basin (**Figure 1**). The tectonic evolution of this region remains enigmatic and has played a central role in debates over the role of lower crustal flow during plateau development (c.f., Clark and Royden, 2000; Hubbard and Shaw, 2009). Topographic relief between the peaks in the range and the adjacent basin exceeds 5–6 km (Clark and Royden, 2000; Kirby et al., 2002) along the mountain front and corresponds to an abrupt increase in crustal thickness from ~40 km beneath the Sichuan Basin to >60 km beneath the plateau margin (Robert et al., 2010). The modern topographic front is coincident with the Longmen Shan Thrust Belt, a series of east-vergent thrust faults that developed during the Late Triassic—Early Jurassic Indosinian orogeny (Dirks et al., 1994; Burchfiel et al., 1995) and emplaced allochthonous rocks of the Songpan-Ganzi flysch basin atop the western margin of the Yangtze craton (Chen et al., 1994; Jia et al., 2006). These fault systems were reactivated during the Cenozoic growth of the Tibetan Plateau (Burchfiel et al., 1995; Jia et al., 2010), but most workers agree that Cenozoic shortening appears to be limited to ~30–35 km (Burchfiel et al., 1995; Hubbard and Shaw, 2009; Hubbard et al., 2010). This observation, combined with the absence of a modern flexural basin (Burchfiel et al., 2008), suggests that present-day topography did not grow entirely by shortening and thickening of the upper crust (Royden et al., 1997; Royden et al., 2008).

The exhumation of rocks within the Longmen Shan, as recorded by thermochronology, plays a central role in the understanding of the timing and rates of growth of high topography (Arne et al., 1997; Xu and Kamp, 2000; Kirby et al., 2002; Wang et al., 2012) and places constraints on the total amount of Cenozoic slip along fault systems in the thrust belt (e.g., Godard et al., 2009; Wang et al., 2012; Tan et al., 2017; Ansberque et al., 2018; Shen et al., 2019). In addition, recent studies of the Mesozoic metamorphic conditions experienced during Indosinian crustal thickening (Airaghi et al., 2017; Airaghi et al., 2018a; Airaghi et al., 2018b) provide important constraints on depth and temperature of the rocks prior to the Cenozoic. These results are briefly summarized in terms of three tectonostratigraphic domains that are separated by major fault systems in the central Longmen Shan (**Figure 1**):

Along the western margin of the Sichuan Basin, autochthonous strata of the carbonate-dominated passive margin sequence (Burchfiel et al., 1995; Li et al., 2003) are deformed in a fold and thrust belt in the footwall of the Yingxiu-Beichuan fault (**Figure 1**). The rocks in this region exhibit no indication of elevated metamorphic conditions (Airaghi et al., 2017) and apatite fission-track ages are largely unreset (Arne et al., 1997). Partial resetting of fission-track ages appears to be confined to folds at the leading edge of the fold belt (Richardson et al., 2008).

In the hanging wall of the Yingxiu–Beichuan fault, crystalline basement rocks of the Pengguan Massif are imbricated in a series of thrust nappes that contain a strongly deformed stratigraphic package of metapelites and carbonates that are paraautochthonous relative to the sedimentary successions in the Sichuan Basin (Burchfiel et al., 1995). Nappe emplacement was associated with the development of a foreland basin of Late Triassic to early Jurassic age (Chen et al., 1994; Burchfiel et al., 1995; Chen and Wilson, 1996; Jia et al., 2006). Notably, basement rocks in the Pengguan Massif experienced a greenschist facies metamorphic event with temperatures between 250 and 300°C and pressures of ~7 kbar at ca. 140 Ma (Airaghi et al., 2017), suggesting the possibility that the Yingxiu–Beichuan fault was reactivated at that time. Zircon fission-track ages from the massif yield ages >200 Ma (Wang et al., 2012), consistent with residence of these rocks below the closure temperature of ~250–300°C (Reiners and Brandon, 2006). Systematic age-elevation relationships from thermochronologic systems with lower closure temperatures, however, yield important constraints on the exhumation of the massif (Wang et al., 2012). Although during early Cenozoic time, the region was characterized by modest rates of exhumation (~100 m/Myr), exhumation rates increased dramatically around 30 Ma to ~800 m/Myr, marking the onset of Cenozoic mountain-building in this range (Wang et al., 2012). Notably, variations in the thermochronologic data require a hiatus in exhumation, and a subsequent acceleration, in the Late Cenozoic (Wang et al., 2012). These data will be discussed further below.

The external zone of paraautochthonous nappes is separated from allochthonous strata of pelitic sediments and flysch of the Songpan-Ganzi terrane (Harrowfield and Wilson, 2005; Roger

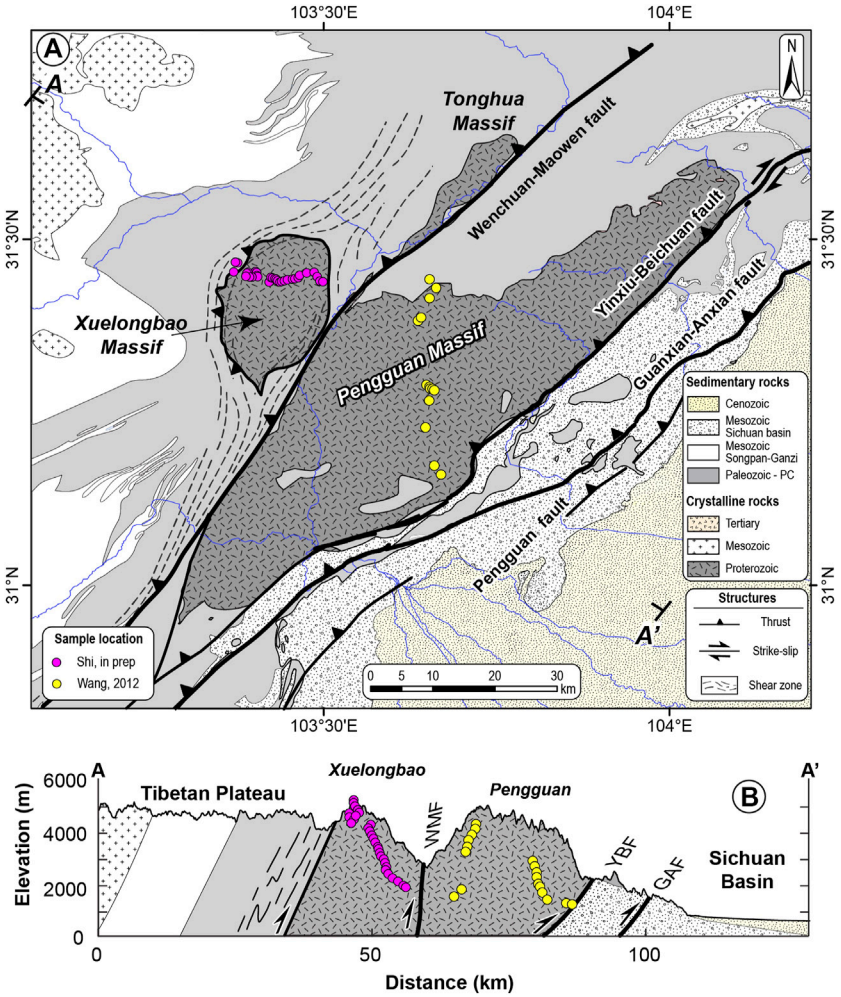

FIGURE 2 | (A) Simplified geology of the Longmen Shan and western Sichuan Basin after Burchfiel et al., 1995; Kirby et al., 2002; Airaghi et al., 2018a. Sample locations of data used in this paper are shown in colored circles. Yellow—data from Wang et al., 2012 in the Pengguan Massif. Pink—data from Shi et al. (in preparation)[1] from the Xuelongbao Massif. **(B)** Cross-section showing the location of sample transects relative to major structures in the Longmen Shan.

et al., 2011) by the Wenchuan–Maowen fault (**Figures 1**, **2**). This sub-vertical fault is marked by a thick zone of fault gouge and cataclastic fabric (Burchfiel et al., 1995) that overprints the eastern margin of a shear zone that developed in the Late Triassic—Early Jurassic (Dirks et al., 1994). This regionally extensive zone of high strain is interpreted to reflect a mid-to-lower crustal décollement, that soles beneath the Songpan-Ganzi flysch and allowed emplacement of allochthonous units over the external nappe complex (Mattauer et al., 1992; Burchfiel et al., 1995; Airaghi et al., 2018a). Metamorphic conditions during fabric formation in the high strain zone surrounding the Xuelongbao and Tonghua massifs (**Figures 1**, **2**) reached amphibolite facies (Dirks et al., 1994), with peak temperatures in excess of 530–580°C and pressures of 9–12 kbar (Airaghi et al., 2017; Airaghi et al., 2018b). This event was overprinted by retrograde metamorphism at greenschist facies, with temperatures of 350–400°C and pressures between 2 and 5 kbar (Airaghi et al., 2017; Airaghi et al., 2018b). The abrupt step in peak temperatures across the present-day trace of the Wenchuan–Maowen fault suggests that this fault marks a persistent structural boundary that accommodated differential exhumation during Mesozoic orogenesis (Airaghi et al., 2018a). Notably, however, rocks now exposed in basement massifs west of the Wenchuan–Maowen fault (the Xuelongbao and Tonghua massifs) appear to have resided at similar crustal levels by the late Cretaceous (ca. 140 Ma; Airaghi et al., 2018a). Young cooling ages for thermochronologic systems west of the Wenchuan–Maowen fault (Arne et al., 1997; Godard et al., 2009; Kirby et al., 2013; Creason et al., 2016; Tan et al., 2017; Shen et al., 2019) imply significant differential exhumation during the Late Cenozoic across this fault.

[1]Shi, X., Kirby, E., Furlong, K., Creason, G., Kamp, P., Xu, G., Danišík, M., Wang, G., He, J., Fan, C., Xu, G., Su, Z., and Wang, E., in preparation, Protracted Exhumation from Oligocene to Present in the Xuelongbao Massif.

Despite these extensive studies of the exhumation history of rocks in the central Longmen Shan, several outstanding questions remain. First, the onset of rapid cooling associated with Cenozoic mountain building is not well-constrained in many places. Much of the allochthonous strata and many of the Triassic plutons that are exposed on the Tibetan Plateau west of the Longmen Shan appear to have experienced slow cooling and limited exhumation during the Cretaceous and early Tertiary (Kirby et al., 2002; Roger et al., 2004, Roger et al., 2011). These studies suggest that the onset of rapid cooling in the Late Cenozoic marks the onset of mountain building associated with the modern plateau. Although studies of lower-temperature thermochronologic systems reveal widespread, rapid exhumation during the Late Miocene to present (Kirby et al., 2002; Godard et al., 2009; Tan et al., 2017; Shen et al., 2019), few of these studies precisely determined when exhumation initiated. In the Pengguan Massif, a densely sampled age-elevation transect and multiple thermochronometers spanning closure temperatures from ~250 to ~60°C constrain this transition to around 30 Ma (Wang et al., 2012). A similar exhumation event in Oligocene - Early Miocene has been recognized in SE Tibet, along the Yulong Shan thrust belt (Zhang et al., 2016; Cao et al., 2019), but the regional significance remains uncertain. In the central Longmen Shan, whether Oligocene exhumation was confined to the external massifs (Wang et al., 2012) or whether it also occurred within the basement massifs west of the Wenchuan–Maowen fault is unresolved.

The second outstanding question centers on the pace and tempo of exhumation during Cenozoic time. Although it is clear that differential exhumation occurred across two of the primary fault systems in the central Longmen Shan (Yingxiu-Beichuan fault and Wenchuan–Maowen fault), the timing, duration, and rates of differential exhumation are not well known. Moreover, the significance of discrete, greenschist-grade shear zones along the western margins of the basement massifs remains enigmatic. These structures appear to have accommodated top-down-to-the-NW shear (Burchfiel et al., 1995; Tian et al., 2016), but the timing and magnitude of this extension are uncertain. Recent 40Ar/39Ar dating of white mica suggests that many of these fabrics may have been active in the late Cretaceous (Tian et al., 2016; Airaghi et al., 2018b; Xue et al., 2021). Determining differential exhumation histories among blocks has the potential to provide new insight into the question of how much shortening and crustal thickening these structures accommodated during Cenozoic development of the plateau.

Finally, one of the most challenging questions is to what extent the modern elevations in the eastern Tibetan Plateau reflect crustal thickening that occurred in Mesozoic time vs. during the Cenozoic. A number of workers have argued that the exceptionally slow cooling (1–3°C/Myr) and low exhumation rates (>10 m/Myr) during the Cretaceous (Kirby et al., 2002; Roger et al., 2011) is inconsistent with the modern topographic relief and must have occurred on a low-relief landscape. In contrast, the somewhat more modest rates of exhumation inferred for the Late Cretaceous - early Tertiary in the external Pengguan Massif (~100 m/Myr; Wang et al., 2012; Airaghi et al., 2017) imply subdued relief at that time (Wang et al., 2012). Developing a more quantitative estimate of topographic relief and the histories of exhumation across the margin of the Tibetan Plateau and Sichuan Basin will help address the question of whether the present-day crustal thickness in eastern Tibet developed during flow and/or thickening of lower crust (Royden et al., 1997; Clark and Royden, 2000).

Thermal History Modeling of Orogenic Systems

For orogenic belts that develop as a result of rapid uplift and exhumation, such as the eastern margin of Tibet, low-temperature thermochronology can provide primary constraints on the recent stages of the event. In such systems we can place timing and rate constraints on the exhumation (and associated uplift) typically involving rock passage through the upper 10 km of the crust. At exhumation rates of 1–2 mm/yr this represents the past 5–10 Ma. However, rates of orogenic activity and mountain building do not occur at constant rates; rather, they appear to occur in intervals of rapid uplift/exhumation interspersed with times of slower exhumation and thermal relaxation. Simple analyses of thermochronologic age data oftentimes assume constant geothermal gradients in depth or time and infer rates and timing of such events from the simple application of fixed geotherms to the apparent ages and closure temperatures for various low-T thermochronologic systems. Our modeling results indicate that for exhumation rates exceeding ~100 m/Ma, such assumptions may significantly bias the interpretation.

Here we explore these non-steady state thermal effects and assess their role in biasing estimates of rates and timing of orogenesis in active systems experiencing relatively rapid exhumation such as the eastern margin of Tibet, New Zealand's Southern Alps, and Taiwan. The generalized models presented here to explore these effects are intentionally kept simple to isolate the effects of exhumation rate on thermal evolution. Clearly, in applications to actual orogenic system (which we investigate later in this paper) exhumation rates vary through time. As a result, the transient effects from a later period of exhumation will be superimposed on non-steady state thermal conditions further complicating the evolution. However, with the intuition we develop through these simple models, we can better understand the observations from orogenic systems and better utilize more complex thermal model realizations.

To model these effects, we use a 1-D, numerical (finite difference) code that allows us to specify standard crustal geothermal properties (conductivity, diffusivity, radiogenic heat production), and act on that initial condition with periods of burial, exhumation, thrusting, and variations in basal heat flux. The code, TQTec, has been used in a variety of previous studies (e.g., Furlong and Edman, 1989; Furlong and Guzofski, 2000; Guzofski and Furlong, 2002; Wang et al., 2012; Furlong and Chapman, 2013; and; Piotraschke et al., 2015), and allows substantial flexibility in defining tectonic events and determining the resultant thermal history effects.

For analyzing the thermal effects of exhumation, we specify exhumation rates and timing in the models and calculate the evolving thermal regime. The upward advection of heat with exhumation (or downward with burial) is accomplished (in the

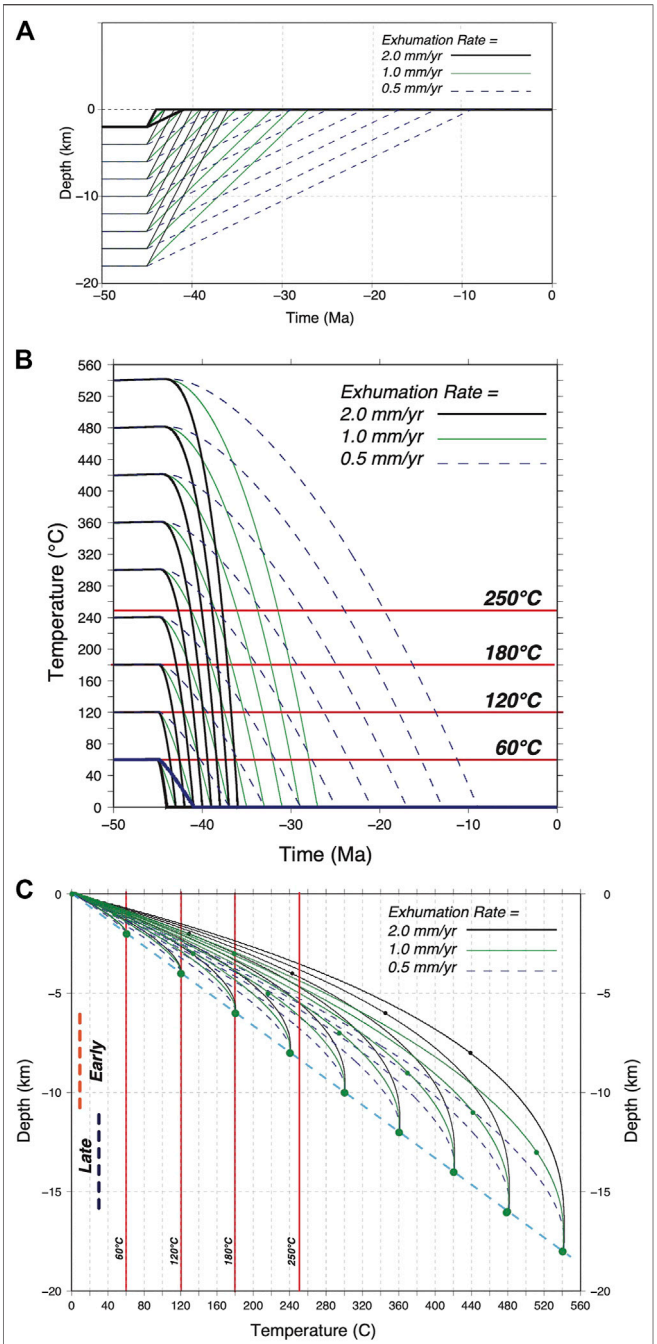

FIGURE 3 | Results of simple numerical exhumation models on thermal structure and history. **(A)** Simple exhumation histories used in the models. Three rates of exhumation are explored [0.5, 1.0, and 2.0 mm/yr (km/Ma)]. Horizons at 2 km depth intervals from 2 to 18 km are monitored. **(B)** Temperature histories for the monitored units. Red lines labeled with temperatures indicate approximate closure T for specific low-T thermochronologic systems [60°C—Apatite (U-Th)/He; 120°C Apatite Fission Track; 180°C, Zircon (U-Th)/He]; and 250°C, Zircon Fission Track). **(C)** Temperature—depth histories for monitored units. Dashed blue line indicates initial crustal geotherm (75 mW/m^2; k = 2.5 W/m-K; dT/dz = 30°C/km).

finite-difference scheme) by explicitly removing (adding) finite thickness units at the top of the model at specified times and allowing the system to continue to thermally evolve. The specified boundary conditions are surface temperature, and a basal heat flow applied at a depth of 60 km, along with specifications of crustal material properties and the distribution of heat generation in the crust. For the simple models here, the conditions are:

$$\text{Surface } T\,(T_0) = 0^{o}\text{C}$$
$$\text{Surface heat flow}\,(q_0) = 75\text{mW}/\text{m}^2$$
$$\text{Crustal Thermal Conductivity}\,(k) = 2.5\ \text{W/m} - \text{K}$$
$$\text{Heat Production}\ (\text{A}_0) = 0$$

These conditions, particularly the lack of a crustal heat production component, lead to an initial constant thermal gradient of 30°C/km throughout the model. The models are run for 50 Ma (model time), with exhumation starting at 45 Ma, and the models run forward in time until 0 Ma. When horizons being tracked reach the surface (depth = 0 km) their thermal histories continue at the assigned surface T. Note that models later in this paper that test the exhumation history of the Xuelongbao data use different initial and boundary conditions, appropriate for that setting.

Simple Exhumation Models

We explore thermal histories for upper-crustal layers at exhumation rates of 0.5 mm/yr (km/Ma), 1.0, and 2.0 mm/yr. In each case the interval of exhumation begins 5 Ma after the start of the model, and continues as long as necessary to exhume 18 km of crust. That is at 0.5 mm/yr the exhumation lasts for 36 Ma, at 1 mm/yr - 18 Ma, and at 2 mm/yr - 9 Ma. Although the exhumation histories are extremely simple, even such simple assumptions lead to significant variations in the resulting thermal history (and hence thermochronologic observations).

Three aspects of the exhumation and thermal history are shown in **Figure 3**. **Figure 3A** records the exhumation history, tracking nine positions in the crust (2 km apart), initially spanning depths from 2 to 18 km. **Figure 3B** shows the resulting temperature history at the three exhumation rates for the points tracked. **Figure 3C** shows the Temperature–Depth (T–Z) history for each tracked horizon. It is important to remember that although the overall time interval for all models is 50 Ma, the interval of active exhumation (which brings all tracked units to the surface) represented in **Figure 3C** varies from 9 Ma for the most rapid (2 mm/yr) exhumation rate to 36 Ma for the slowest (0.5 mm/yr) exhumation rate. On the temperature plots we also indicate the approximate closure temperature for four standard low-T thermochronologic systems: 250°C for Zircon Fission Track (ZFT); 180°C for Zircon (U-Th)/He (ZHe); 120°C for Apatite Fission Track (AFT), and 60°C for Apatite (U-Th)/He (AHe) systems. We recognize these are simply approximations to actual closure and retention/annealing processes, but they serve as useful markers of approximate apparent ages.

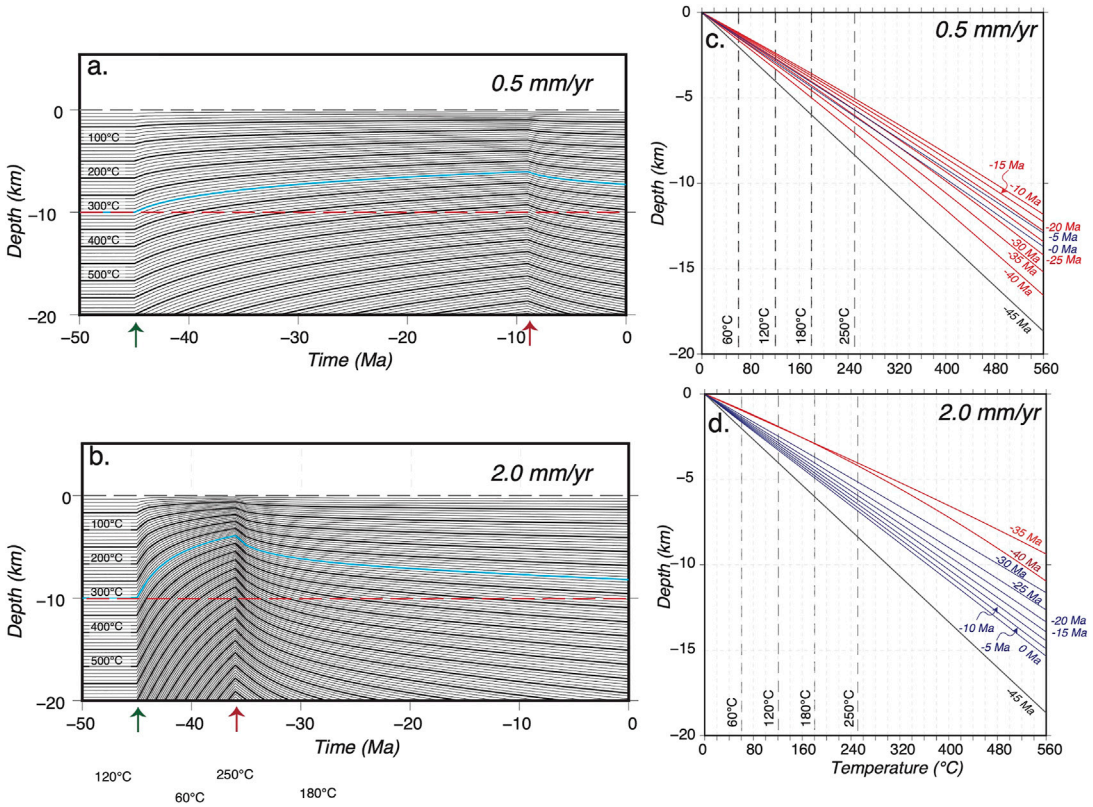

FIGURE 4 | Transient thermal response to a single exhumation event. Comparison between slower (0.5 mm/yr) and faster (2.0 mm/yr) exhumation rates. Results are for models shown in **Figure 3**. In both cases total exhumation is 18 km. Arrows along time-line indicate the start (green) and end (red) of the exhumation event. Left panels **(A,C)** show the behavior of isotherms during and after exhumation. The blue line traces the 300°C isotherm; the red dashed line maps the 10 km depth level. Right panels **(B,D)** show geotherms at various times through the thermal evolution. Red geotherms are during the exhumation event and blue geotherms are after the end of exhumation when the thermal field is relaxing toward equilibrium.

There are several things that are immediately clear in the results shown in these figures. For the three exhumation rates shown (0.5, 1.0, 2.0 mm/yr), the cooling history of the rock units does not simply follow along the initial (30°C/km) geotherm (blue dashed line in **Figure 3C**). In general, cooling rates are slower initially, particularly for the units that are more deeply buried. Over time, as the units approach the surface, cooling rates increase. This is a consequence of the geotherm (initially a simple constant T-gradient with depth) becoming perturbed by the exhumation and heat advection. The result, typical of most exhumation scenarios is initial exhumation along a low T-gradient increasing to a much higher T-gradient as rocks near Earth's surface. The actual temperature path followed by a particular horizon is shown in **Figure 3C**, and it is clear that a non-linear temperature gradient trajectory is followed by each horizon.

As is discussed later, it should also be noted that the T–Z path followed by different horizons at the same exhumation rate, and over the same depth intervals differs. For example (using **Figure 3C**), for the same exhumation rate of 1 mm/yr, a rock horizon initially at 10 km depth would be at ~220°C when it reached 5 km depth, whereas a unit starting at 16 km depth would be at ~260°C when it reached that same 5 km depth. These effects are more exaggerated as the exhumation rate increases. As discussed later, this effect can introduce systematic bias into age-elevation vertical transects. The depth at which rock units may cross critical temperatures (and acquire their exhumation age) can vary as a result of whether reaching that depth is early or late in the exhumation event.

The key effect shown in these simple results, is that for the same initial geotherm, the depth at which horizons will cross critical temperatures (e.g., closure T or equivalent) will vary both as a function of exhumation rate at faster unroofing rates the critical T will be at shallower depths, and whether it is early or late in an exhumation event later in the event the critical T will be shallower. Both of these effects will potentially lead to interpretations of higher than actual exhumation rates, and/or an apparent increase in exhumation rate as the exhumation event proceeds.

Transient Thermal Evolution During Exhumation

During an exhumation event, even at relatively slow rates of 0.1–0.2 mm/yr, the temperature structure is perturbed by advection and assumptions of a constant temperature gradient are not met. Previous studies have described techniques to utilize analytical methods to approximate these effects (e.g., Moore and England, 2001; Willett and Brandon, 2013). However, such

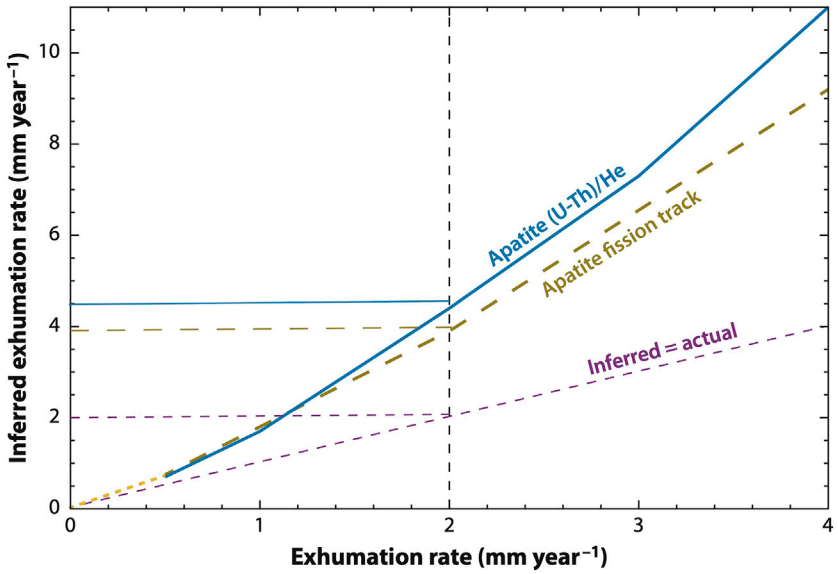

FIGURE 5 | Inferred vs actual exhumation rates for models of simple exhumation. Models assumed a 25°C/km initial geotherm, 5°C surface temperature, and a 60°C closure T for Apatite (U-Th)/He and 120°C for Apatite Fission Track (Note: we also calculated the Apatite Fission Track results using a kinetic model of track annealing and got the same results.) At exhumation rates of 2 mm/yr (2 km/Ma), rates inferred using apparent age and an assumed geotherm will be approximately a factor of two greater than actual exhumation rates.

methods need to make significant assumptions about the duration and amount of exhumation events. Even in cases of relatively slow exhumation (0.1 mm/yr) it may take up to ~100 Ma for the system to reach a dynamic steady state. Prior to that time the geotherm will be changing. These effects are magnified at higher exhumation rates, but the impact on interpretations of thermochronologic data are not always considered. Here we assess the impact of simple exhumation scenarios for the position of isotherms and the associated geotherm during significant exhumation events. These results represent the steady, single-event exhumation histories shown in **Figure 3**, and involve a total exhumation of 18 km. The duration of each event varies based on its exhumation rate. **Figure 4** shows the evolution of isotherms and geotherms during single exhumation events from **Figure 3** for exhumation at 0.5 mm/yr and 2.0 mm/yr; spanning typical ranges of exhumation rates for orogenesis. In these cases, significant upward movement of isotherms occurs during the main phase of exhumation. For example, during exhumation the 300°C isotherm moves upward (**Figure 4**) approximately 6 km in the 2.0 mm/yr case (i.e., an average rate of 0.67 mm/yr), and approximately 4.4 km in the 0.5 mm/yr case (~0.12 mm/yr). If a constant temperature gradient is assumed, these effects can seriously bias the interpretation (as shown in **Figure 5**). In the case of the rapid exhumation model (2.0 mm/yr), the thermal regime is still far from equilibrium even after ~35 Ma of thermal relaxation; the 300°C isotherm in this example is still elevated by more than 2 km (**Figure 5**). These effects are generally recognized for rapid exhumation, but are difficult to correct for with simple models linking depth to temperature during exhumation. There is also a general assumption that at exhumation rates less than ~0.2 mm/yr these transient effects are minor. However even at a rate of 0.1 mm/yr, the 300°C isotherm will rise approximately 1 km during 3.6 km of exhumation; surface heat flow will increase by almost 15%. These effects will have the effect of biasing exhumation rates determined using methods that rely on the slope of age-elevation data, as those approaches require an assumption of constant depth of key isotherm during the time interval represented. Quantification of this effect is discussed below, but for studies of relatively shallow crustal exhumation associated with low-T thermochronometers, these effects may be a significant fraction of the total exhumation.

These results indicate several key points to consider in analyses of low-T thermochronologic data (**Figure 4**).

After long periods of continued exhumation, the thermal regime is still non-steady state, even at rates as low as 0.1 mm/yr. Assumptions of a constant geotherm during exhumation are almost never met.

Similarly, there is a long period of thermal relaxation after an exhumation event. For units in the upper crust (depth <10 km), this period of secular cooling lasts for tens of millions of years. Upper crustal units could cool through several characteristic closure temperatures during this relaxation phase, which might be interpreted as a period of continued exhumation.

This cooling behavior will be superimposed on later exhumation events perturbing them away from "single event" type behavior. That is the ongoing thermal evolution from previous events will influence the temperature history during a subsequent sequence of exhumation events.

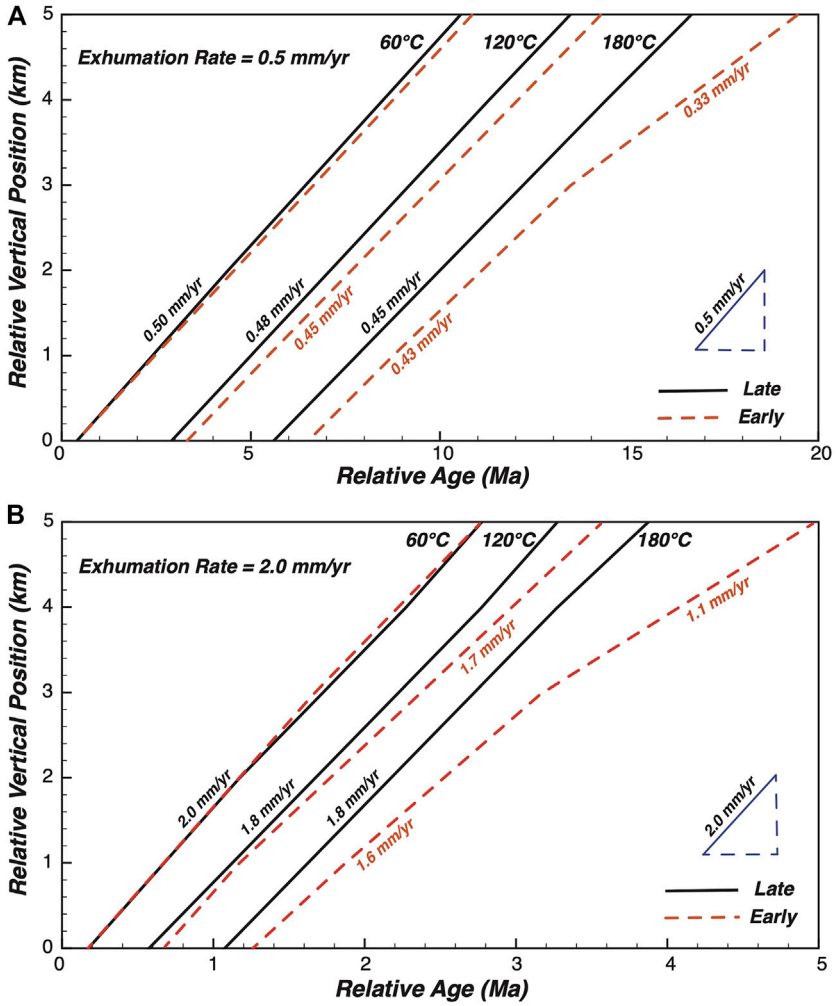

FIGURE 6 | Apparent Exhumation Rate determined from vertical age-elevation profiles for a range of thermochronologic closure temperatures and relative time of age acquisition during the exhumation event. The 5-km depth intervals for samples used to generate this figure (early vs. late) is indicated on the T–z plot (**Figure 3C**).

This transient behavior during and following an exhumation event provides an important constraint in linking observed thermochronologic data to tectonic events. Although it makes it difficult to directly link a thermal history obtained from direct inversion of thermochronologic data, it does provide the opportunity to identify multiple events and periods of hiatus or slow exhumation during the evolution of an orogen.

Bias in Exhumation Interpretations

These variations in thermal structure associated with exhumation rate that also may change during an exhumation event, can lead to systematic bias in the results. For example, the assumption of a simple constant geotherm (25°C/km, surface T of 5°C), will lead to an increasing over-estimation of the exhumation rate as the actual exhumation rate increases (Furlong and Chapman, 2013). In **Figure 5** we show the results for various exhumation rates, and the apparent exhumation rate one would infer using the Apatite low-T systems ((U-Th)/He, Fission Track). At low exhumation rates the over-estimate is relatively small. As actual exhumation rates increase, the apparent or inferred exhumation rate becomes 2–3 times larger than the actual rates.

As noted above (**Figures 3B,C**), there are differences in cooling rates between periods early in an exhumation event, and later in the same event. Using these simple exhumation histories, we can explore how this effect may be manifest in vertical age transects using various low-T thermochronometers. In general, having thermochronologic data along a vertical transect mitigates many of the issues related to the evolution of the crustal geothermal during exhumation or burial. Implicit however in using the slope of the age-elevation vertical profile is the assumption that the depths of critical temperatures remain constant during the period recorded by the thermochronologic data. During an exhumation event, the geotherm through the upper crust will become increasingly steep (**Figure 4**). This effect can also be seen in **Figures 3B,C** where units shallower in the crustal section cross critical temperatures at greater depths (and lower cooling rates) than units that started the exhumation process at greater depths.

Early vs. Late-Stage Cooling Histories

In particular, units that are higher in the vertical profile will tend to show lower apparent exhumation rates than units that were initially deeper, and units whose age is acquired earlier in the exhumation event will have lower apparent exhumation rates than those later in the event. For a vertical section that captures the early parts of the event, the result would be an apparent increase in exhumation rate over time, as seen in the 180°C curves in **Figure 6**. Irrespective of the initial horizon depth, the inferred exhumation rate is lower than actual for deeper (higher T) samples in the early stages of the event, and that effect is greatest at the shallower levels.

For example, in **Figure 6B**, for a vertical section for which we had data from multiple low-T thermochronologic systems, we see that the lowest T system (shallowest, youngest, and hence latest in the exhumation event) best reflects the actual exhumation rate of 2.0 mm/yr, while the higher T systems (which will record ages deeper and earlier in the exhumation event), underestimate the exhumation rate, implying a substantially lower exhumation rate (almost 50% decrease) during the earliest part of the event (1.1 mm/yr in the 180°C case for the shallowest units that acquired their age earliest, compared to the actual rate of 2.0 mm/yr). This effect may be wrongly interpreted to reflect either an acceleration in exhumation rate, or the capturing of a partial retention/annealing zone in the data.

Implications for Simple Exhumation Models

Although the model results shown here are for very simple exhumation histories and might represent only one segment of actual multi-stage exhumation history associated with the development of an orogen, they allow us to identify and isolate various effects that may bias our interpretations of low-T thermochronologic data. For analyzing the tectonic evolution of an actual orogen (as is discussed for a case study in eastern Tibet later) we can use the same modeling approach, but incorporate the effects of multiple exhumation/burial events with differing rates and exhumation amounts, along with periods of relative hiatus in the evolution, (e.g., Wang et al., 2012). From these simple analyses we develop a set of points that should be considered in most interpretations of exhumation associated with mountain building.

Thermochronologic data can be interpreted by assuming a depth to the closure temperature, and dividing that assumed depth by age to get an exhumation rate (e.g., Lease et al., 2021), such an approach implicitly assumes that rock cooling during uplift and exhumation will occur along a simple geotherm (c.f., **Figure 3C**). In cases of slow exhumation (i.e., <~0.1–0.2 mm/yr) this assumption is approximately met, and the impact of a non-stationary geotherm on the inferred exhumation rates is minimal. However, at exhumation rates more typical of active orogenic systems (>0.5 mm/yr), an assumption of a fixed geotherm can lead to significantly over-estimated exhumation rates, by a factor of two or greater. This effect is most pronounced for lower-T thermochronologic systems, where the closure temperature and depth are at shallower levels (**Figure 5**).

Age-elevation profiles can mitigate many of the issues associated with low-T thermochronology. When multiple thermochronologic systems, with different closure temperatures, are available, age-elevation profiles can provide the best estimates of actual exhumation history. However simple interpretation tools, such as linear fits to age-elevation profiles, may lead to misleading results. Our simple modeling shows that such simple linear fits will often-times underestimate the actual exhumation rates, particularly for the slightly higher-T thermochronologic systems such as zircon (U-Th)/He system (nominal closure temperature of ~180°C, Reiners and Brandon, 2006). This effect of underestimating the actual exhumation rate is amplified early in the exhumation history, and for units that acquire apparent ages at shallower levels (**Figure 5**). This combined with effects that lead to apparent increases in exhumation rates closer to the surface can lead to an interpretation of an increase in exhumation rate as the event proceeds (moving from higher-T to lower-T thermochronometers, and higher in the vertical section to lower in the vertical section). Because of its effects on the observed apparent age, this change in slope of the age-elevation profile at higher elevations may also be interpreted to reflect that those samples had resided in (near the bottom of) a partial annealing/retention zone prior to the initiation of the exhumation event.

Multi-Stage Exhumation Models and Geotherms

Most orogenic events likely do not proceed as simple single-stage tectonic events with a constant-rate exhumation/uplift history. Rather, it is more common for an orogenic event to wax and wane in intensity with intervals of rapid uplift and/or exhumation separated by periods of limited tectonic activity, all within the lifetime of an orogenic event. It is these details of orogenic evolution that are key to understanding the underlying tectonic drivers and feedbacks between the tectonics and the resulting geologic signature left in the rock record. Moving from observations of apparent ages to estimates of the actual tectonic history is a major target of studies utilizing low-T thermochronologic systems to evaluate thermal histories.

There are a range of possible methods to move from observed, apparent age data to the causative tectonic or exhumation history. As discussed above, simple estimates of exhumation rate, typically using individual sample ages, or vertical age-elevation profiles can be used to estimate exhumation rates averaged over specified time intervals. This is often done assuming a background heat flow or geothermal gradient, which is used to map from temperature to depth, in order to move from a closure temperature to a closure depth and exhumation rate. Additionally, apparent age data from multiple thermochronologic systems, with differing temperature sensitivities and closure temperatures, can be analyzed (oftentimes with an inversion methodology), estimating a time-temperature history for the samples (e.g., Gallagher, 2012). To convert from such a time-temperature history to an exhumation (or uplift) history requires mapping the temperatures to their equivalent depths. This can be done assuming a constant or specified geotherm over the time

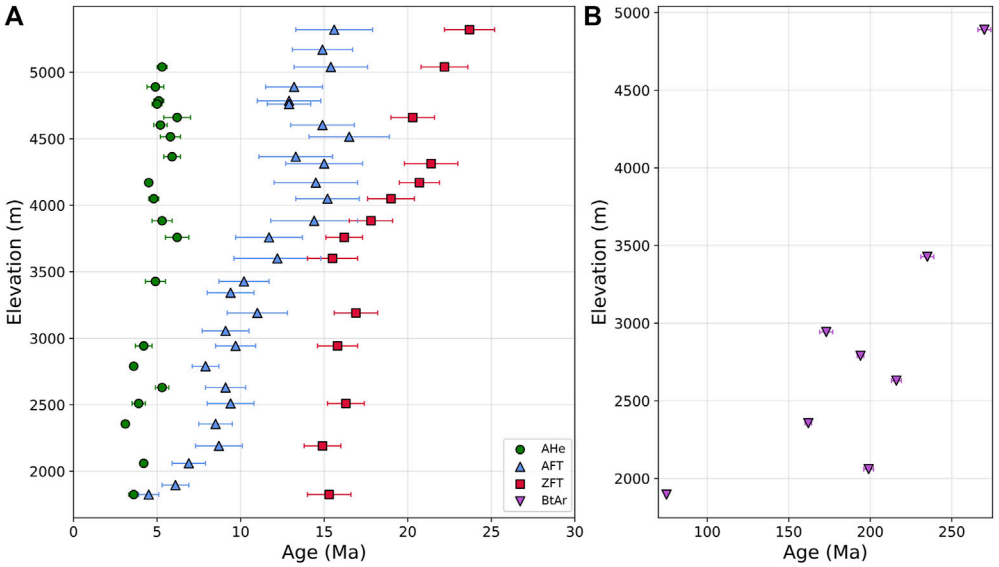

FIGURE 7 | Age-Elevation data from the Xuelongbao Massif analyzed in this study. **(A)** Apatite (U-Th)/He (AHe), Apatite Fission Track (AFT), and Zircon Fission Track (ZFT) data (with 1σ uncertainties). **(B)** Biotite Ar/Ar (BtAr) data (with 2σ uncertainties).

interval of interest (e.g., Lease et al., 2021). There are also methods available to approximate the transient effects and link thermal histories to equivalent exhumation or uplift histories (e.g., Willett and Brandon, 2013), but these approaches generally work best for single-stage exhumation events.

As shown above, even at relatively low exhumation rates (<0.1–0.2 mm/yr), the crustal geotherm can be significantly perturbed as a result of heat advection with the exhumation/burial events. How this affects multi-stage exhumation is more complex than in the simple single-stage models shown above. To develop a sense of the style of these effects, their time lags, and the magnitudes of the effects, we have modeled a multi-stage exhumation event, and compared the actual (modeled) exhumation and thermal histories with those that would be obtained assuming constant heat flow or thermal gradient during the event.

This difference between a simple linkage between cooling rate and exhumation rate presents problems for directly interpreting thermochronologic data. Standard approaches, many based on the early analyses of Stockli et al. (2000), Stockli et al. (2003), follow one of several routes. In cases where there is a vertical age-elevation profile (preferably with multiple low-T thermochronometers used), the slope of the age-elevation data can be assumed to represent the exhumation rate during the age interval considered. As shown in **Figure 6**, this slope may underestimate the exhumation rate, and also will vary for the same exhumation event depending on when during the exhumation event (early vs. late) that the age data are acquired. These perturbations are least pronounced for the lower-T age systems.

Another approach is to utilize an age data-thermal history inversion tool (e.g., Ketcham, 2005; Gallagher, 2012), which construct time-temperature histories that will produce the observed age (and in fission track analyses also the track length distribution) for a multi-system sample. To convert this temperature history to an exhumation/uplift history, a range of assumptions of the temperature gradient need to be made. Although the T histories obtained through these inversions may produce the observed ages, transforming these T-histories to uplift/exhumation histories requires a number of assumptions about the crustal thermal structure. As seen in **Figure 3**, the T-history (for the same exhumation history) varies significantly both as a function of depth, and time during an exhumation event. Assuming a constant crustal geotherm (temperature gradient) during rapid exhumation is not consistent with actual crustal thermal processes. Additionally, periods of slow exhumation or hiatus are hard to discern with this approach, as during a hiatus after a period of rapid exhumation, the crustal thermal regime will continue to cool, but following this approach, that additional cooling might be interpreted as further exhumation.

Case Study: Multi-Stage Exhumation in Eastern Tibet

To illustrate these principles, we use a densely sampled age-elevation transect from the Xuelongbao Massif, in the central Longmen Shan (**Figures 1**, **2**) to explore the effects variations in exhumation history. The massif is composed primarily of granodiorite and tonalite plutonic rocks of Neoproterozoic age (748 ± 7 Ma; Zhou et al., 2006) in intrusive contact with Mesoproterozoic schists and paragneisses along its eastern and southern margins (Zhou et al., 2006). Sheared Paleozoic units

form a carapace around the western and northern margins of the massif. We collected an age-elevation transect that spans elevations from ~1,600 m at the base of the massif to nearly the summit just below 5,500 m (**Figure 7**). These data have been described in Kirby et al. (2013), Creason et al. (2016), and Shi et al. (2018), and complete analytical details are in Shi et al. (in preparation)[1]. We describe briefly the primary results and trends in these data that motivate the thermal models. Although other data exist from this massif (e.g., Godard et al., 2009; Tan et al., 2017; Shen et al., 2019), we focus on this single data set here for simplicity. The Godard et al. (2009) data set includes Zircon (U-Th)/He age results for samples from locations near the samples of this study. These data lie between and compliment the AFT and ZFT results shown in **Figure 7**, as expected based on the relative closure temperatures of these systems. However, the vertical extent of these data is limited and do not substantively inform the exhumation history.

One of the key aspects of thermochronologic studies that seek to characterize the *onset* of mountain building is the need to estimate the initial depth and thermal conditions at the start of the tectonic event. For regions experiencing relatively limited exhumation, this is typically estimated from the break in slope of age-elevation data for low-temperature thermochronometers such as AHe or AFT (e.g., Clark et al., 2005; Ehlers, 2005). However, in regions subjected to rapid and/or deeper exhumation, age-elevation arrays may be relatively uniform (see AHe data in **Figure 7**), and the slope of the line only provides a guide to exhumation rate, if heat advection in the shallow crust can be reasonably modeled (as discussed above). In these cases, the application of multiple thermochronometers with a range of closure temperatures can provide significantly improved information regarding the pace and tempo of cooling and exhumation, as the age difference between different thermochronometers contains information about both the rate and timing of exhumation.

In the Xuelongbao massif, 40Ar/39Ar ages of biotite exhibit significant scatter, but generally define a trend of increasing age with elevation (**Figure 7**, right panel). Notably, a cluster of samples exhibit ages between ~150 and ~200 Ma, which are consistent with temperature estimates for the regrograde, greenschist facies metamorphic conditions experienced by the nearby cover sequence (Airaghi et al., 2018a). In our data, the lowest elevation sample yields an age of ~75 Ma, providing an indication of relatively slow cooling following peak metamorphic temperatures, similar to ages observed in the southern Longmen Shan along strike (Tian et al., 2016). Thus, these data imply that the ~4 km crustal section currently exposed in the massif resided at or near ~350°C (Grove and Harrison, 1996; Reiners and Brandon, 2006) until at least the latest Cretaceous. This allows us to constrain the initial temperatures and depths for the thermal models.

Significant cooling (and exhumation) is recorded by systematic age-elevation relationships in ZFT (closure T of ~230–250°C, Reiners and Brandon, 2006), AFT (closure T of ~110 –120°C, Ketcham et al., 1999), and AHe (closure T of ~60°C, Flowers et al., 2009) systems. Importantly, we do not expect a significant effect of radiation damage on the systematics of He retention in apatite (Flowers et al., 2009) for such young samples that cooled rapidly from well above temperatures where such damage anneals (Shi et al. (in preparation)[1]). These data reveal three important characteristics of the cooling history that any exhumation model needs to honor. First, there is a break in slope of the ZFT data at ~3,500 m elevation that marks an apparent increase in exhumation rate. Second, ZFT ages are nearly invariant (at ~ 15 Ma) with elevation below this point, and AFT ages are similar at higher elevations. As we discuss below, this is characteristic of rapidly cooled crustal sections, but is rarely observed in transects with more limited topographic relief. Third, AFT ages from the lowermost samples are nearly the same age as paired AHe samples. This requires a second relatively recent period of accelerated cooling and exhumation, as explained below.

Constraints of Model Boundary Conditions

To guide the development of exhumation history models to help explain the data in the Xuelongbao vertical transect, we can place constraints on the initial conditions (timing and temperature) of the units exposed and sampled. As described above we have age data from four thermochronologic systems (Apatite (U-Th)/He and Fission Track (AHe and AFT); Zircon Fission Track (ZFT); and Biotite Ar/Ar) (BtAr). With the exception of the BtAr data, all samples indicate young ages (<30 Ma) indicating the vertical section sampled was all hotter (deeper) than the ZFT total annealing T of approximately 250°C. The BtAr data generally show old ages ranging from about 270–150 Ma, indicating those samples were likely cooler than the partial retention temperatures for BtAr. However, one sample near the base of the transect (i.e., initially most deeply buried) has an apparent age of ~75 Ma. We interpret that the apparent age of this sample could represent partial retention, indicating it was initially (i.e., at the 100 Ma start of our modeling) near the top of the partial retention zone, and thus all samples were at a temperature of <~350°C, with the lowest elevation sample at ~350°C.

This helps provide a constraint on the initial depth and thermal gradient of the modeled section—the initial ~4 km section was located at depths spanning a temperature range of approximately 350–250°C. Using this information to guide multiple modeling simulations, we have found that geotherm conditions that produce a temperature gradient of ~25°C/km or less at initial the depths of samples (assumed heat flow of ~75 mW/m^2, with upper crustal radiogenic heat production of 2.0 $\mu W/m^3$, and thermal conductivity of approximately 2.5 W/(m-K), at the time of model initiation (~100 Ma) provide the most consistent results and are what are shown in the following.

Exhumation Models for Xuelongbao Age-Elevation Transects

The nearly 4 km vertical extent of our low-T thermochronologic data allow us to develop a thermal—tectonic history for the Xuelongbao region, delineating a sequence of well-constrained exhumation events since ~30 Ma. We show the results from three

TABLE 1 | Exhumation models.

Model	Exhumation stage	Initiation (Ma)	Duration (Ma)	Exhumation rate (m/Ma)
XLB-4P-1a (4 stage)	1	100	73	10
	2	27	10	400
	3	17	2	2,000
	4	15	15	485
XLB-5P-1b (5 stage)	1	100	73	10
	2	27	10	400
	3	17	2	2,000
	4	15	9	1,50
	5	6	6	986
XLB-5P-1c (5 stage)	1	100	73	10
	2	27	10	400
	3	17	2	2,000
	4	15	9	95
	5	6	6	1,069

of those models that provide good fits to specific aspects of the data, and also provide examples of the trade-offs and constraints provided by the data.

Before comparing these model results to the observed age-elevation profiles for the Xuelongbao Massif, it is instructive to explore the effects of the differences in such multi-stage exhumation histories for the thermal evolution of rocks initially residing at different crustal levels (**Table 1**). **Figure 8** shows exhumation models and resulting thermal evolution histories for three related models that produce synthetic age-elevation profiles that share characteristics with those we observe in our data. These three models have common exhumation histories from their initiation at 100 Ma (only the time interval after 50 Ma is shown in the figures) until the start of enhanced exhumation at 27 Ma. From 27 Ma until 15 Ma they share the same 2-stage exhumation (which, we will see, is constrained by the ZFT data). The three models differ in terms of the exhumation/uplift history since 15 Ma. The simplest model (**Figure 8A**) has a single constant-rate exhumation event for 15–0 Ma, whereas the other two models (**Figures 8B,C**) break that time interval into two events—a slower event initially (15–6 Ma), followed by a more rapid exhumation from 6 to 0 Ma. Models shown in **Figures 8B,C** differ only slightly in the relative rates of the two events (same total exhumation). They both differ from the simple (**Figure 8A**) history by having an extended interval (~9 Ma in duration) of low exhumation separating two intervals of rapid exhumation. The introduction of this relative hiatus in exhumation is motivated by the separation in timing of the upper and lower elevation AFT results. This hiatus is similar to the exhumation history we previously modeled in the Pengguan Massif (Wang et al., 2012); this study concluded that the uplift of that region was accomplished over two time intervals, separated by a period of slower exhumation.

The primary thermal effect of this change from a constant exhumation over the past 15 MA to a 2-stage (slow/fast) exhumation (compare **Figures 8A–C**) is that the shallowest (highest elevation) rock units will pass through the AFT closure T (blue line at 120°C in **Figure 8**—right panels) during the 17–15 Ma period of rapid exhumation, and an increasing delay moving to deeper samples (lower elevation) for that particular thermochronometer age. The more subtle difference between the models shown in **Figures 8B,C**, primarily produces small changes in the relative ages of the lowest-T thermochronometers. These thermal histories can then be mapped into apparent ages for different thermochronologic systems based on closure temperatures and AFT track-length annealing kinetics. Those synthetic age-elevation profiles can then be compared with our observations (**Figure 9**).

Simple Exhumation Models

The simpler model (XLB-4P-1a) involves a 2-stage exhumation history between 27 and 15 Ma, followed by a single stage exhumation event from 15 to 0 Ma. A focus of this simpler model is to constrain the initiation of exhumation affecting the Xuelongbao Massif. That initial period of exhumation is recorded in the higher-T (ZFT) age-elevation results (**Figure 9**). At the time of initiation of this stage of exhumation the rocks sampled were at depths of >15 km and so there is a time delay between the onset of exhumation and when cooling reaches the depth of the samples. We have found that with exhumation beginning approximately 27 Ma, we best match the ~24 Ma age of the highest-elevation ZFT sample, while also fitting the slope of the age-elevation profile. These data (ZFT) also show an increase in the slope of the age-elevation data (for rocks initially more deeply buried) starting at approximately 17 Ma. This motivates the modeled increase in exhumation at 17 Ma, lasting ~2 Ma. Part of the difference in age-elevation slope of the ZFT data between the older (higher in the section) and the younger (lower in the section) data is a consequence of the apparent increase in exhumation between older/deeper and younger/shallower cooling (cf. **Figure 5**), but that effect is not sufficient to explain the entire observed change in slope. The rapid exhumation between 17 Ma and 15 Ma is also motivated by the AFT observations for the samples above elevation 3.75 km. As seen in **Figure 8**, the higher elevation samples will pass through the approximate AFT closure during this interval of rapid exhumation, ending at ~15 Ma. The distinct age-offset between these higher elevation AFT results, and the shallower results is one indication of the hiatus in exhumation starting at ~15 Ma. All

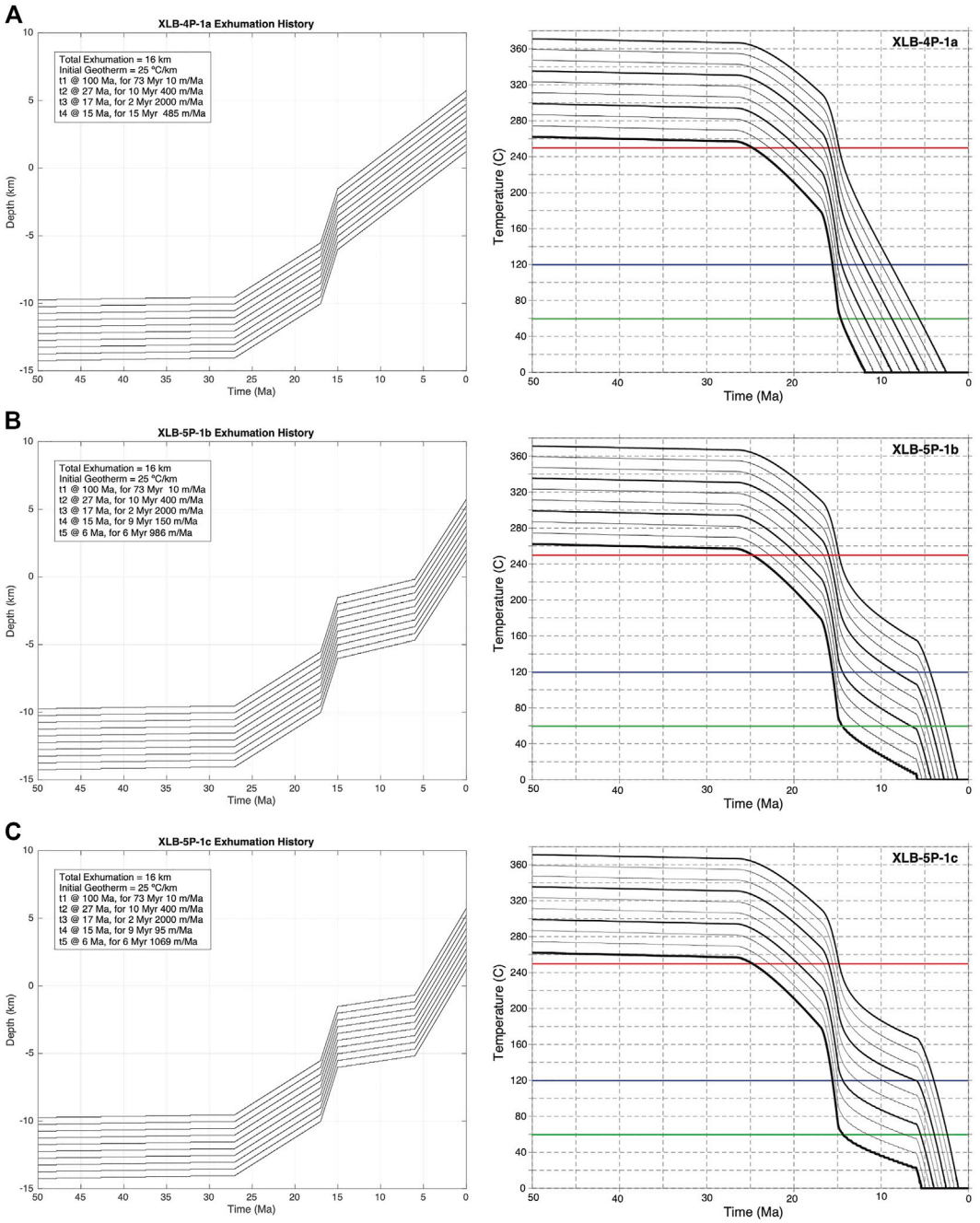

FIGURE 8 | Exhumation **(left)** and thermal **(right)** histories for three tectonic scenarios used to satisfy the observed Age - Elevation vertical profiles for the Xuelongbao transect Details in **Table 1**. All scenarios involve approximately 16 km of exhumation over the past 100 Ma. The exhumation prior to 15 Ma is the same for each model, but differs since that time. Horizons shown represent the range of initial depths and their final positions that are consistent with the elevation and extent of the samples evaluated. Samples reach a surface T of 0°C when they reach of depth of 0 km, and remain at that T during the rest of their history (i.e., at depths above 0 km). **(A)** Simple 4-stage exhumation history with constant exhumation rate since 15 Ma. **(B)** 5 stage exhumation history with post-15 Ma separated into two exhumation periods (15–6 and 6–0 Ma). **(C)** 5 stage exhumation history as in panel **(B)** with slightly slower exhumation rates in the 15–6 Ma interval and slightly faster rates in the 6–0 Ma interval. Implications of these variations in exhumation history are seen in the model fits of **Figure 9** (Note: Deepest buried units in exhumation plot are top curves in Temperature plots).

models share this same exhumation history prior to 15 Ma, but the poor fit of this model (XLB-4P-1a) to the lower-elevation AFT results and the AHe results indicate that a simple constant exhumation since 15 Ma is not able to satisfy the observations, indicating the need for a more complex exhumation history since 15 Ma.

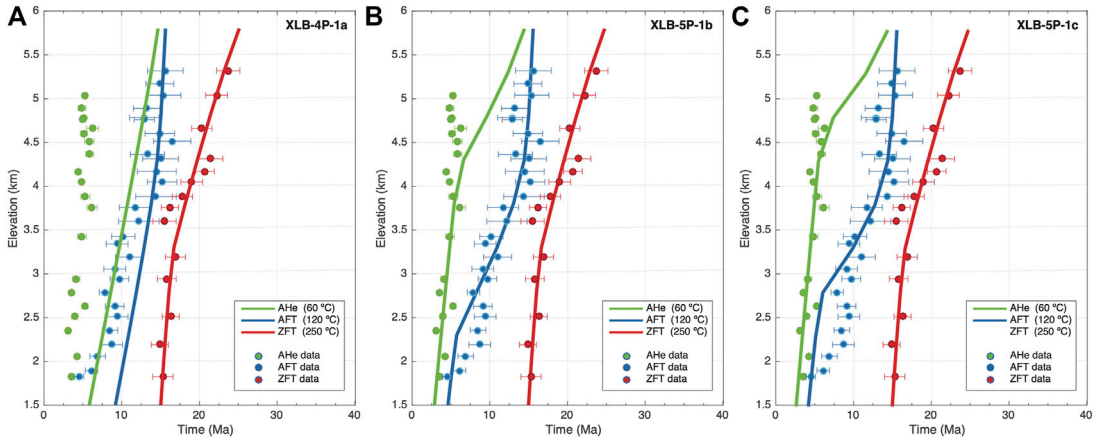

FIGURE 9 | Model results for exhumation histories shown in **Figure 8** and **Table 1**. **(A)** simple 4-stage exhumation history satisfies age-elevation data with apparent ages older than ~15 Ma. **(B)** 5-stage exhumation history with 2-stage exhumation since 15 Ma. **(C)** 5-stage exhumation history similar to panel **(B)**, with slight modifications to rates during each of the post-15 Ma exhumation stages.

More Complex Exhumation Models

In the simpler model (**Figure 9A**), with a single post-15 Ma exhumation history, we see that both the lower elevation AFT data and the AHe data are poorly fit by the temperature history. In particular there is not sufficient age separation between the AHe and AFT results, (and also the lower elevation AFT and ZFT data). This separation and the change in slope of the AFT profile at elevations below ~3.5 km implies that there is a hiatus or other slowing of cooling for a period of time. This led us to the more complex models, which divide the last 15 Ma of exhumation into two stages, in which we have an interval of slow exhumation (hiatus) followed by faster exhumation (**Figures 8B**,C and **9B**,C). Including this interval of reduced exhumation is required to produce the observed age separation. This is a similar effect to what we saw in the Pengguan analyses (Wang et al., 2012), although the timing of the hiatus in this case is more recent.

The subtle difference in the rates of the slow-to-faster exhumation since 15 Ma (**Figures 8B**,**C** and **9B**,C) produces small, but perhaps important, differences in the fit of the synthetic age-elevation profiles to the observed data. In particular the model with the slightly slower initial exhumation, followed by slightly faster 2nd-stage exhumation better fits the entire extent of the AHe data, but indicates younger ages than observed for the lower elevation AFT data. Certainly, more complex exhumation histories could be derived that slightly change the fits, but that is not the intent of this current analysis. Our primary goal in these modeling analyses is not to simply "fit the data"; rather, our intent is to demonstrate the interactions among the superimposed exhumation events and develop insight into the rates, timing, and amount of exhumation that occurred in building this orogen, which we then can use to inform our interpretations of its tectonic evolution.

The thermal history of the crust during multiple exhumation events is hard to characterize by simple patterns of behavior. The effects of heat advection, time lags in cooling, and the superposition of secular and active cooling processes combine to create thermal histories that may produce thermochronologic signatures that may be superficially misleading. As we see in the set of models applied to the data set from the Xuelongbao Massif, although age elevation profiles appear relatively straightforward, a simple exhumation history (**Figures 8A** and **9A**) does not fit the suite of data. In particular, the age differences observed among the three chronometers require a reduction in exhumation rate post-15 Ma, after a period of rapid exhumation. As seen in the subtle differences between model fits for XLB-5P-1b and XLB-5P-1c (**Figures 8B**,**C** and **9B**,C), details of that slow-down or hiatus can produce potentially measurable effects. Focusing on the thermal evolution for model XLB-5P-1c (**Figure 10**), we see several key aspects of a multi-stage exhumation history; similar to what was seen in **Figure 4**.

Even at relatively slow exhumation rates, there is advection of heat and a slight shallowing of isotherms.

During the interval immediately following the rapid mid-Miocene exhumation (17–15 Ma), there is a relaxation of the thermal field leading to a deepening of isotherms. This is partially offset by the upward advection effects of the continued (albeit substantially slower) exhumation during the post-15 Ma period.

As seen in **Figures 8C** and **10**, rock units within the observed thermochronologic data set will acquire their apparent ages during intervals when both the exhumation rates are changing significantly (~0.1–1.0 mm/yr) and the geothermal gradient (heat flow) is varying by 50% or more.

Although the 15 and 0 Ma geotherms are very similar (**Figure 10**), between 15 Ma and the present the gradient changes substantially (from 130 mW m^{-2} at 15 Ma to 85 mW m^{-2} at 10 Ma, returning to 120 mW m^{-2} at 0 Ma).

This superposition of changing exhumation rates and geotherms is difficult to account for in many of the tools used to link thermal histories to exhumation/uplift histories.

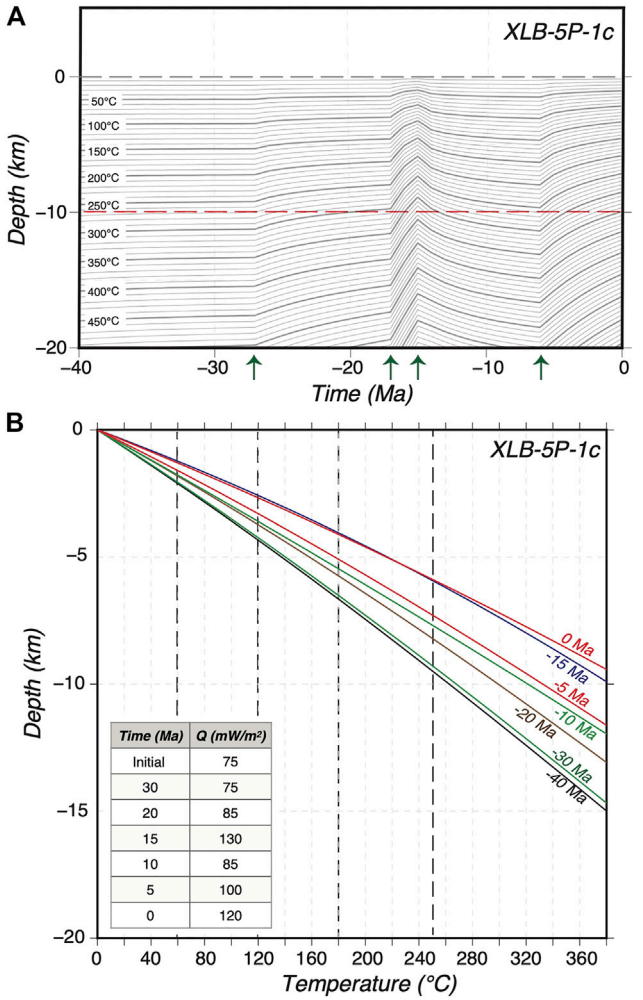

FIGURE 10 | Isotherm and geotherm histories for multi-stage exhumation history. **(A)** Isotherm evolution for exhumation history given by Model XLB-5P-1c. Times of changes in exhumation rates are indicated by arrows. Red dashed line indicates depth of 10 km. Depth to 300°C isotherm varies by approximately 4 km during this tectonic history. **(B)** Geotherms at selected times during thermal evolution. Table indicates surface heat flow for each geotherm shown.

Exhumation Histories for the Central Longmen Shan Orogenic Belt (Xuelongbao–Pengguan Massifs) Derived From Thermal Models

The exhumation histories modeled here, the associated thermal histories, and the resulting fits to the observed age-elevation profiles provide an estimate of the rock uplift history of the Xuelongbao Massif and the hanging wall of the Wenchuan–Maowen Fault (WMF). We can use that history to develop tectonic scenarios for the development of this orogen. In particular, by combining these results, with our previous results for the uplift/exhumation history of the Pengguan Massif (Wang et al., 2012) we can develop a broader regional model of orogen evolution, and in particular constrain the relative exhumation histories of these two major massifs and the amount and timing of vertical displacement along WMF that separates the two massifs (**Figure 11**).

The exhumation histories of the two adjacent massifs show similarities in duration of exhumation and approximate timing of the initiation of the modern period of more rapid exhumation (~30–27 Ma). The exhumation of the Xuelongbao Massif has brought a significantly deeper crustal section to the surface as compared to the exhumation of the Pengguan Massif (16 vs. 10 km, minimum initial depth), and the extreme relief (3.5–4.0 km) and the availability of a range of thermochronologic systems allow the identification of specific stages of exhumation. The similarity in the onset of exhumation for the two massifs indicates that mountain building and the growth of the present-day relief along the topographic margin of the plateau began ~30 Ma. Similarly rapid exhumation occurred along the Yulong Shan thrust belt in SE Tibet (Zhang et al., 2016; Cao et al., 2019) around the same time and points to regional shortening along the eastern margin of Tibet. However, whether crustal thickening was confined to the thrust belt, or whether it was widespread beneath the eastern plateau cannot yet be distinguished from this data.

Of particular importance in piecing together a tectonic history for the region are the differences in exhumation history between the two major massifs (**Figure 11**). Between ~30 and 15 Ma, it appears that the Pengguan region (in the external zone of the thrust belt) experienced faster uplift initially while the results from the Xuelongbao region indicate an acceleration in exhumation at ~17 Ma, at a time when the Pengguan region was unroofing more slowly. Both regions underwent periods of reduced exhumation during the Miocene, followed by a subsequent increase in exhumation during the Late Miocene. Overall rates of exhumation for the Xuelongbao Massif are higher, resulting in the exposure a deeper crustal section and the full resetting of the Zircon FT samples (**Figure 7**). In contrast, un-reset Zircon FT samples from the Pengguan massif (Wang et al., 2012) reflect residence of these rocks at shallower crustal levels. Prior to the Neogene start of exhumation, both massifs appear to have experienced similar background thermal regimes, with a common tectonic history prior to the activation of the faults (e.g., Airaghi et al., 2018a) such that the differences in thermal history reflect differential exhumation across the WMF (Shen et al., 2019).

The two exhumation histories we have obtained (Pengguan and Xuelongbao massifs) allow us to place constraints on rates and timing of activities on the various major fault systems in the region (**Figure 2B**). From the Wang et al. (2012) study we can primarily place constraints on the uplift rates associated with the faults to the east of the Pengguan Massif. Between ~30 and 20 Ma, our modeling showed there was an ~5 Ma interval with rapid exhumation and thus inferred rapid uplift along those frontal faults at a rate of approximately 0.8 mm/yr (0.8 km/Ma). During this time, exhumation rates in the Xuelongbao region are lower, most likely indicating little differential motion across the WMF and lower exhumation,

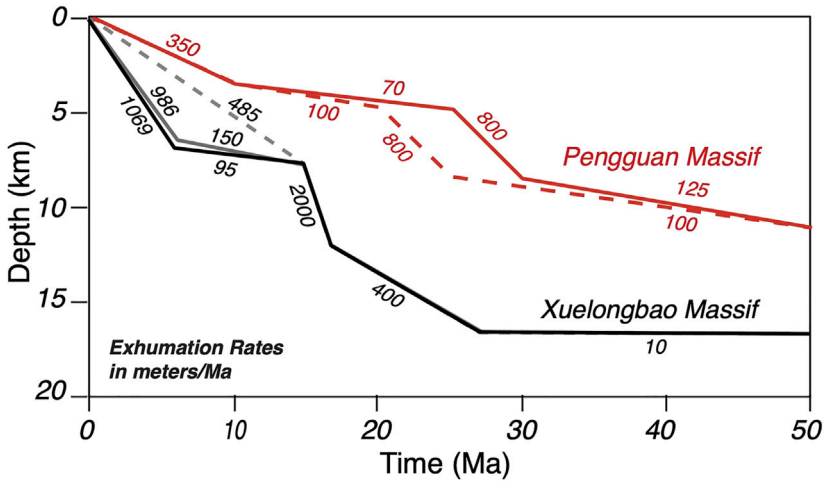

FIGURE 11 | Modeled Exhumation Histories for the Pengguan Massif (Wang et al., 2012) and the Xuelongbao Massif (this study) since 50 Ma. Exhumation rates (meters/Ma) for each exhumation stage are labeled on the graph. The two curves for the Pengguan Massif model reflect the range of models determined in that study. The three curves for the Xuelongbao model are the three models presented in **Figures 8**, **9**.

perhaps because the site is more distant from the mountain front. To convert these exhumation (uplift) rates to fault slip rates requires knowledge of faults attitude. For assumed high angle thrust fault orientations (at least at shallow crustal levels), the exhumation rates we have determined should be scaled by factors of ~1.4 (45° dip) to 1.15 (60° dip) to estimate slip rates on the faults.

The WMF may have begun significant motion at about 20 Ma (when higher exhumation rates relative to the Pengguan begin in Xuelongbao; **Figure 11**), with differential vertical motion along that fault at a rate of ~0.3 mm/yr (0.3 km/Ma). Continued exhumation in the Pengguan Massif suggests that the frontal faults (Yingxui-Beichuan fault) remained active but perhaps at more modest rates of ~0.1 mm/yr (0.1 km/Ma). By ~ 17 Ma, the exhumation rate in the Xuelongbao Massif accelerated to an extremely high value of >1.9 mm/yr (1.9 km/Ma), with uplift (at ~0.1 mm/yr) continuing on the frontal faults. At approximately 15 Ma, the fault systems appear to dramatically slow or enter into a hiatus (lasting ~ 5–10 Ma), where exhumation rates are much lower. The observed data could be explained by no motion on the WMF during this time and all uplift occurring on the frontal faults at a rate of ~0.1 mm/yr (0.1 km/Ma).

Over the past 6–10 Ma, both the frontal faults and the WMF are inferred to accommodate significant rates of displacement relative to the unexhumed margin of the Sichuan Basin. During that time, the frontal faults appear to have accommodated differential exhumation of ~0.35 mm/yr (0.35 km/Ma), and differential exhumation across the WMF appears to be >0.6 mm/yr (0.6 km/Ma) in the past ~6 Ma. These results imply that, of the 6–8 km of difference in crustal level exposed between the Pengguan and Xuelongbao Massifs, approximately 4 km was differentially exhumed over a very short period of time (~2 Ma) in the middle Miocene. Whether this substantial rate of dip-slip motion occurred along the entire WMF at this time, or was restricted to the central Longmen Shan is unclear from these data sets. Numerous other studies present low-T thermochronologic evidence for late Miocene to Recent exhumation further south along the southern Longmen Shan (Arne et al., 1997; Xu and Kamp, 2000; Kirby et al., 2002; Godard et al., 2009; Ansberque et al., 2018; Tan et al., 2017; Tian et al., 2013, Tian et al., 2018), although it is not clear whether these record the same temporal history as we find for this study or in Wang et al. (2012).

These rates of multiple mm/yr of sustained fault motion are high for intra-crustal faults, and likely reflect significant displacements on mid-crustal structures at depth. The analyses we have done here do not allow us to specify details of those mid-to-lower crustal tectonics, but these results do allow us to reach some specific conclusions about the evolution of this region.

Prior ~30 Ma, rocks currently exposed in the Xuelongbao Massif resided near the middle crust at depth levels between 15 and 17 km. Thus, our results are consistent with greater exhumation of the hanging wall of the Wenchuan–Maowen fault (Tan et al., 2017; Shen et al., 2019) relative to rock units exposed in the Pengguan Massif (Wang et al., 2012).

Average exhumation rates since 30 Ma for the region are at least 0.5 mm/yr (0.5 km/Ma), sufficiently high to perturb the thermal history and preclude simple mapping of cooling rate to exhumation rate. Periods of very high exhumation rates (perhaps as high as 2 mm/yr) introduce significant biases into interpretations using standard approaches to analyzing vertical age-elevation profiles.

The application of thermal modeling approaches (explicitly incorporating exhumation) for analyzing the apparent age data allows us to isolate periods of rapid and slower exhumation, which we are able to link to periods of activity on major structures in the region.

DATA AVAILABILITY STATEMENT

The original contributions presented in the study are included in the article/Supplementary Material, further inquiries can be directed to the corresponding author.

AUTHOR CONTRIBUTIONS

KF and EK conceived and designed the project, analyzed data, accomplished the modeling, and wrote the paper. CGC did preliminary modeling to constrain models used in **Figures 8** and **9**. Contributions to the data shown in **Figure 7** are as follows: XS organized and executed the field sampling; PK oversaw the (U-Th)/He and FT analyses; GX did the whole mineral separations and the AFT and ZFT analyses; MD did the (U-Th)/He analyses; KVH did the Ar/Ar analyses.

ACKNOWLEDGMENTS

The authors thank the two reviewers of this paper for very insightful and helpful reviews. This research was supported by NSF grants EAR-1757581 (to KF) and EAR-0911587 (to KF and EK). Research funding for the acquisition of FT and Helium thermochronology data were provided by the New Zealand Government - MBIE Contract: CONT-42907-EMTR-UOW (to PK).

REFERENCES

Airaghi, L., de Sigoyer, J., Guillot, S., Robert, A., Warren, C. J., and Deldicque, D. (2018a). The Mesozoic Along-Strike Tectonometamorphic Segmentation of Longmen Shan (Eastern Tibetan Plateau). *Tectonics* 37, 4655–4678. doi:10.1029/2018TC005005

Airaghi, L., de Sigoyer, J., Lanari, P., Guillot, S., Vidal, O., Monié, P., et al. (2017). Total Exhumation across the Beichuan Fault in the Longmen Shan (Eastern Tibetan Plateau, China): Constraints from Petrology and Thermobarometry. *J. Asian Earth Sci.* 140, 108–121. doi:10.1016/j.jseaes.2017.04.003

Airaghi, L., Warren, C. J., de Sigoyer, J., Lanari, P., and Magnin, V. (2018b). Influence of Dissolution/reprecipitation Reactions on Metamorphic Greenschist to Amphibolite Facies mica40Ar/39Ar Ages in the Longmen Shan (Eastern Tibet). *J. Metamorph Geol.* 36, 933–958. doi:10.1111/jmg.12420

Ansberque, C., Godard, V., Olivetti, V., Bellier, O., de Sigoyer, J., Bernet, M., et al. (2018). Differential Exhumation across the Longriba Fault System: Implications for the Eastern Tibetan Plateau. *Tectonics* 37, 663–679. doi:10.1002/2017TC004816

Arne, D., Worley, B., Wilson, C., Chen, S. F., Foster, D., Luo, Z. L., et al. (1997). Differential Exhumation in Response to Episodic Thrusting along the Eastern Margin of the Tibetan Plateau. *Tectonophysics* 280, 239–256. doi:10.1016/s0040-1951(97)00040-1

Braun, J. (2003). Pecube: a New Finite-Element Code to Solve the 3D Heat Transport Equation Including the Effects of a Time-Varying, Finite Amplitude Surface Topography. *Comput. Geosci.* 29, 787–794. doi:10.1016/s0098-3004(03)00052-9

Bullen, M. E., Burbank, D. W., and Garver, J. I. (2003). Building the Northern Tien Shan: Integrated Thermal, Structural, and Topographic Constraints. *J. Geol.* 111, 149–165. doi:10.1086/345840

Burchfiel, B. C., Chen, Z., Liu, Y., and Royden, L. H. (1995). Tectonics of the Longmen Shan and Adjacent Regions, central China. *Int. Geol. Rev.* 37, 661–735. doi:10.1080/00206819509465424

Burchfiel, B. C., Royden, L. H., van der Hilst, R. D., Hager, B. H., Chen, Z., King, R. W., et al. (2008). A Geological and Geophysical Context for the Wenchuan Earthquake of 12 May 2008, Sichuan, People's Republic of China. *GSA Today* 18, 4–11. doi:10.1130/gsatg18a.1

Cao, K., Wang, G., Leloup, P. H., Mahéo, G., Xu, Y., van der Beek, P. A., et al. (2019). Oligocene-Early Miocene Topographic Relief Generation of Southeastern Tibet Triggered by Thrusting. *Tectonics* 38, 374–391. doi:10.1029/2017TC004832

Chen, S. F., and Wilson, C. J. L. (1996). Emplacement of the Longmen Shan Thrust-Nappe Belt along the Eastern Margin of the Tibetan Plateau. *J. Struct. Geol.* 18, 413–430. doi:10.1016/0191-8141(95)00096-v

Chen, S. F., Wilson, C. J. L., Luo, Z. L., and Deng, Q. D. (1994). The Evolution of the Western Sichuan Foreland Basin, Southwestern China. *J. Southeast Asian Earth Sci.* 10, 159–168. doi:10.1016/0743-9547(94)90016-7

Clark, M. K., and Handy Royden, L. (2000). Topographic Ooze: Building the Eastern Margin of Tibet by Lower Crustal Flow. *Geology* 28, 703–706. doi:10.1130/0091-7613(2000)028<0703:tobtem>2.3.co;2

Clark, M. K., House, M. A., Royden, L. H., Whipple, K. X., Burchfiel, B. C., Zhang, X., et al. (2005). Late Cenozoic Uplift of southeastern Tibet. *Geol* 33, 525–528. doi:10.1130/g21265.1

Creason, C. G., Shi, X., Shi, X., Kirby, E., Furlong, K. P., Wang, G., et al. (2016). Rapid Exhumation along the Longmen Shan Sustained for >30 Ma: Implications for Mountain Building along the Eastern Margin of Tibet. *Geol. Soc. America Abstr. Programs* 48, 7. doi:10.1130/abs/2016AM-284775

Dirks, P. H. G. M., Wilson, C. J. L., Chen, S., Luo, Z. L., and Liu, S. (1994). Tectonic Evolution of the NE Margin of the Tibetan Plateau; Evidence from the central Longmen Mountains, Sichuan Province, China. *J. Southeast Asian Earth Sci.* 9, 181–192. doi:10.1016/0743-9547(94)90074-4

Ehlers, T. A. (2005). Crustal thermal Processes and the Interpretation of Thermochronometer Data. *Rev. Mineral. Geochem.* 58, 315–350. doi:10.2138/rmg.2005.58.12

Flowers, R. M., Ketcham, R. A., Shuster, D. L., and Farley, K. A. (2009). Apatite (U-Th)/He Thermochronometry Using a Radiation Damage Accumulation and Annealing Model. *Geochim. Cosmochim. Acta* 73, 2347–2365. doi:10.1016/j.gca.2009.01.015

Furlong, K. P., and Chapman, D. S. (2013). Heat Flow, Heat Generation, and the Thermal State of the Lithosphere. *Annu. Rev. Earth Planet. Sci.* 41, 385–410. doi:10.1146/annurev.earth.031208.100051

Furlong, K. P., and Edman, J. D. (1989). "Hydrocarbon Maturation in Thrust Belts: Thermal Considerations," in *Origin and Evolution of Sedimentary Basins and Their Energy and Mineral Resources, AGU Geophys. Mon.* (Stanford: Stanford University Press), 137–144.

Furlong, K. P., and Guzofski, C. (2000). "Thermal Rheological Evolution of the Franciscan Crust: Implications for Earthquake Processes," in Proceedings of the 3rd Conference on Tectonic Problems of the San Andreas Fault System. Editors G. Bokelmann and R. L. Kovach (Stanford: Stanford University Press), 112–127.

Gallagher, K. (2012). Transdimensional Inverse thermal History Modelling for Quantitative Thermochronology. *J. Geophys. Res. Solid Earth* 117, B2. doi:10.1029/2011jb008825

Godard, V., Pik, R., Lave, J., Cattin, R., Tibari, B., de Sigoyer, J., et al. (2009). Late Cenozoic Evolution of the central Longmen Shan, Eastern Tibet: Insight from (U-Th)/He Thermochronometry. *Tectonics* 28, 121. doi:10.1029/2008tc002407

Grove, M., and Harrison, T. M. (1996). 40Ar (Super *) Diffusion in Fe-Rich Biotite. *Am. Mineral.* 81, 940–951. doi:10.2138/am-1996-7-816

Guzofski, C. A., and Furlong, K. P. (2002). Migration of the Mendocino Triple junction and Ephemeral Crustal Deformation: Implications for California Coast Range Heat Flow. *Geophys. Res. Lett.* 29 (1), 12-1–12-4. doi:10.1029/2001gl013614

Harrowfield, M. J., and Wilson, C. J. L. (2005). Indosinian Deformation of the Songpan Garzê Fold Belt, Northeast Tibetan Plateau. *J. Struct. Geol.* 27, 101–117. doi:10.1016/j.jsg.2004.06.010

Hodges, K. V. (2014). "Thermochronology in Orogenic Systems," in *Treatise on Geochemistry*. 2nd Edition (Stanford: Stanford University Press), 281–308. doi:10.1016/B978-0-08-095975-7.00308-9

Hubbard, J., and Shaw, J. H. (2009). Uplift of the Longmen Shan and Tibetan Plateau, and the 2008 Wenchuan (M = 7.9) Earthquake. *Nature* 458, 194–197. doi:10.1038/nature07837

Jia, D., Li, Y., Lin, A., Wang, M., Chen, W., Wu, X., et al. (2010). Structural Model of 2008 Mw 7.9 Wenchuan Earthquake in the Rejuvenated Longmen Shan Thrust belt, China. *Tectonophysics* 491, 174–184. doi:10.1016/j.tecto.2009.08.040

Jia, D., Wei, G., Chen, Z., Li, B., Zeng, Q., and Yang, G. (2006). Longmen Shan Fold-Thrust belt and its Relation to the Western Sichuan Basin in central China: New Insights from Hydrocarbon Exploration. *Bulletin* 90, 1425–1447. doi:10.1306/03230605076

Ketcham, R. A., Donelick, R. A., and Carlson, W. D. (1999). Variability of Apatite Fission-Track Annealing Kinetics; III, Extrapolation to Geological Time Scales. *Am. Mineral.* 84, 1235–1255. doi:10.2138/am-1999-0903

Ketcham, R. A. (2005). Forward and Inverse Modeling of Low-Temperature Thermochronometry Data. *Rev. Mineral. Geochem.* 58, 275–314. doi:10.2138/rmg.2005.58.11

Kirby, E., Furlong, K. P., Cook, K., Ouimet, W., Shi, X., Wang, E., Kamp, P. J. J., and Hodges, K. V. (2013). "On the Extent and Significance of Oligocene Mountain Building in Eastern Tibet: *Eos Trans*," in AGU, Fall Meet. Suppl., Abstract T22E-01.

Kirby, E., Reiners, P. W., Krol, M. A., Whipple, K. X., Hodges, K. V., Farley, K. A., et al. (2002). Late Cenozoic Evolution of the Eastern Margin of the Tibetan Plateau: Inferences from 40Ar/39Ar and (U-Th)/He Thermochronology. *Tectonics* 21, 1-1–1-20. doi:10.1029/2000tc001246

Lease, R. O., Haeussler, P. J., Witter, R. C., Stockli, D. F., Bender, A. M., Kelsey, H. M., et al. (2021). Extreme Quaternary Plate Boundary Exhumation and Strike Slip Localized along the Southern Fairweather Fault, Alaska, USA. *Geology* 49, 602–606. doi:10.1130/G48464.1

Li, Y., Allen, P. A., Densmore, A. L., and Qiang, X. (2003). Evolution of the Longmen Shan Foreland basin (Western Sichuan, China) during the Late Triassic Indosinian Orogeny. *Basin Res.* 15, 117–138. doi:10.1046/j.1365-2117.2003.00197.x

Liu, J., Zhang, P., Lease, R. O., Zheng, D., Wan, J., Wang, W., et al. (2013). Eocene Onset and Late Miocene Acceleration of Cenozoic Intracontinental Extension in the North Qinling Range-Weihe Graben: Insights from Apatite Fission Track Thermochronology. *Tectonophysics* 584, 281–296. doi:10.1016/j.tecto.2012.01.025

Mattauer, M., Malavieille, J., Calassou, S., Lancelot, J., Roger, R., Hao, Z., et al. (1992). Le chaine Triassique de Songpan-Garze (Ouest Sichuan et est Tibet): Une chaine de plissement-decollement sur marge passive. *Comptes Rendus de L'Academie Des Sci.* 314, 619–626.

Montgomery, D. R., and Brandon, M. T. (2002). Topographic Controls on Erosion Rates in Tectonically Active Mountain Ranges. *Earth Planet. Sci. Lett.* 201, 481–489.

Moore, M. A., and England, P. C. (2001). On the Inference of Denudation Rates from Cooling Ages of Minerals. *Earth Planet. Sci. Lett.* 185, 265–284. doi:10.1016/s0012-821x(00)00380-0

Piotraschke, R., Cashman, S. M., Furlong, K. P., Kamp, P. J. J., Danišík, M., and Xu, G. (2015). Unroofing the Klamaths-Blame it on Siletzia? *Lithosphere* 7 (4), 427–440. doi:10.1130/l418.1

Reiners, P. W., and Brandon, M. T. (2006). Using Thermochronology to Understand Orogenic Erosion. *Annu. Rev. Earth Planet. Sci.* 34, 419–466. doi:10.1146/annurev.earth.34.031405.125202

Richardson, N. J., Densmore, A. L., Seward, D., Fowler, A., Wipf, M., Ellis, M. A., et al. (2008). Extraordinary Denudation in the Sichuan Basin: Insights from Low-Temperature Thermochronology Adjacent to the Eastern Margin of the Tibetan Plateau. *J. Geophys. Res.-Solid Earth* 113, 21. doi:10.1029/2006jb004739

Robert, A., Zhu, J., Vergne, J., Cattin, R., Chan, L. S., Wittlinger, G., et al. (2010). Crustal Structures in the Area of the 2008 Sichuan Earthquake from Seismologic and Gravimetric Data. *Tectonophysics* 491, 205–210. doi:10.1016/j.tecto.2009.11.010

Roger, F., Jolivet, M., Cattin, R., and Malavieille, J. (2011). Mesozoic-Cenozoic Tectonothermal Evolution of the Eastern Part of the Tibetan Plateau (Songpan-Garzê, Longmen Shan Area): Insights from Thermochronological Data and Simple thermal Modelling. *Geol. Soc. Lond. Spec. Publications* 353, 9–25. doi:10.1144/SP353.2

Roger, F., Malavieille, J., Leloup, P. H., Calassou, S., and Xu, Z. (2004). Timing of Granite Emplacement and Cooling in the Songpan-Garzê Fold Belt (Eastern Tibetan Plateau) with Tectonic Implications. *J. Asian Earth Sci.* 22, 465–481. doi:10.1016/s1367-9120(03)00089-0

Royden, L. H., Burchfiel, B. C., King, R. W., Wang, E., Chen, Z., Shen, F., et al. (1997). Surface Deformation and Lower Crustal Flow in Eastern Tibet. *Science* 276, 788–790. doi:10.1126/science.276.5313.788

Royden, L. H., Burchfiel, B. C., and van der Hilst, R. D. (2008). The Geological Evolution of the Tibetan Plateau. *Science* 321, 1054–1058. doi:10.1126/science.1155371

Shen, X., Tian, Y., Zhang, G., Zhang, S., Carter, A., Kohn, B., et al. (2019). Late Miocene Hinterland Crustal Shortening in the Longmen Shan Thrust belt, the Eastern Margin of the Tibetan Plateau. *J. Geophys. Res. Solid Earth* 124, 11972–11991. doi:10.1029/2019JB018358

Shi, X., Kirby, E., Furlong, K., Creason, G., Kamp, P., Xu, G., Wang, G., He, J., Fan, C., Xu, G., Su, Z., and Wang, E. (2018). "Protracted Cenozoic Exhumation in the Hanging wall of the Longmen Shan Thrust belt: Implications for Fault System Architecture and Evolution," in International Conference for the Decade Memory of the Wenchuan Earthquake, Chengdu, China.

Stockli, D. F., Dumitru, T. A., McWilliams, M. O., and Farley, K. A. (2003). Cenozoic Tectonic Evolution of the White Mountains, California and Nevada. *Geol. Soc. America Bull.* 115 (7), 788–816. doi:10.1130/0016-7606(2003)115<0788:cteotw>2.0.co;2

Stockli, D. F., Farley, K. A., and Dumitru, T. A. (2000). Calibration of the Apatite (U-Th)/He Thermochronometer on an Exhumed Fault Block, White Mountains, California. *Geology* 28 (11), 983–986. doi:10.1130/0091-7613(2000)028<0983:cotaut>2.3.co;2

Tan, X.-B., Xu, X.-W., Lee, Y.-H., Lu, R.-Q., Liu, Y., Xu, C., et al. (2017). Late Cenozoic Thrusting of Major Faults along the central Segment of Longmen Shan, Eastern Tibet: Evidence from Low-Temperature Thermochronology. *Tectonophysics* 712-713, 145–155. doi:10.1016/j.tecto.2017.05.016

Tian, Y., Kohn, B. P., Gleadow, A. J. W., and Hu, S. (2013). Constructing the Longmen Shan Eastern Tibetan Plateau Margin: Insights from Low-Temperature Thermochronology. *Tectonics* 32, 576–592. doi:10.1002/tect.20043

Tian, Y., Kohn, B. P., Phillips, D., Hu, S., Gleadow, A. J. W., and Carter, A. (2016). Late Cretaceous-Earliest Paleogene Deformation in the Longmen Shan Fold-And-Thrust belt, Eastern Tibetan Plateau Margin: Pre-Cenozoic Thickened Crust? *Tectonics* 35, 2293–2312. doi:10.1002/2016TC004182

Tian, Y., Li, R., Tang, Y., Xu, X., Wang, Y., and Zhang, P. (2018). Thermochronological Constraints on the Late Cenozoic Morphotectonic Evolution of the Min Shan, the Eastern Margin of the Tibetan Plateau. *Tectonics* 37, 1733–1749. doi:10.1029/2017TC004868

Wang, E., Kirby, E., Furlong, K. P., van Soest, M., Xu, G., Shi, X., et al. (2012). Two-phase Growth of High Topography in Eastern Tibet during the Cenozoic. *Nat. Geosci* 5, 640–645. doi:10.1038/NGEO1538

Whipple, K. X., Kirby, E., and Brocklehurst, S. H. (1999). Geomorphic Limits to Climate-Induced Increases in Topographic Relief. *Nature* 401, 39–43.

Willett, S. D., and Brandon, M. T. (2013). Some Analytical Methods for Converting Thermochronometric Age to Erosion Rate. *Geochem. Geophys. Geosyst.* 14 (1), 209–222. doi:10.1029/2012GC004279

Xu, G., and Kamp, P. J. J. (2000). Tectonics and Denudation Adjacent to the Xianshuihe Fault, Eastern Tibetan Plateau: Constraints from Fission Track Thermochronology. *J. Geophys. Res.* 105, 19231–19251. doi:10.1029/2000jb900159

Xue, Z., Lin, W., Chu, Y., Faure, M., Chen, Y., Ji, W., et al. (2021). An Intracontinental Orogen Exhumed by Basement-Slice Imbrication in the Longmenshan Thrust Belt of the Eastern Tibetan Plateau. *GSA Bull.* 11, 24. doi:10.1130/B35826.1

Zhang, H., Oskin, M. E., Liu-Zeng, J., Zhang, P., Reiners, P. W., and Xiao, P. (2016). Pulsed Exhumation of interior Eastern Tibet: Implications for Relief Generation Mechanisms and the Origin of High-Elevation Planation Surfaces. *Earth Planet. Sci. Lett.* 449, 176–185. doi:10.1016/j.epsl.2016.05.048

Zhou, M.-F., Yan, D.-P., Wang, C.-L., Qi, L., and Kennedy, A. (2006). Subduction-related Origin of the 750 Ma Xuelongbao Adakitic Complex (Sichuan Province, China): Implications for the Tectonic Setting of the Giant Neoproterozoic Magmatic Event in South China. *Earth Planet. Sci. Lett.* 248, 286–300. doi:10.1016/j.epsl.2006.05.032

Conflict of Interest: The authors declare that the research was conducted in the absence of any commercial or financial relationships that could be construed as a potential conflict of interest.

frontiers in Earth Science

CORRECTION
published: 18 August 2021
doi: 10.3389/feart.2021.747231

Corrigendum: Exploiting Thermochronology to Quantify Exhumation Histories and Patterns of Uplift Along the Margins of Tibet

Kevin P. Furlong[1], Eric Kirby[2], C. Gabriel Creason[3], Peter J. J. Kamp[4], Ganqing Xu[4], Martin Danišík[4], Xuhua Shi[5] and Kip V. Hodges[6]*

[1]Department of Geosciences, Penn State University, University Park, PA, United States, [2]Department of Geological Sciences, University of North Carolina, Chapel Hill, NC, United States, [3]CEOAS, Oregon State University, Corvallis, OR, United States, [4]School of Science, University of Waikato, Hamilton, New Zealand, [5]Key Laboratory of Geoscience Big Data and Deep Resource of Zhejiang Province, School of Earth Sciences, Zhejiang University, Hangzhou, China, [6]School of Earth and Space Exploration, Arizona State University, Tempe, AZ, United States

Keywords: thermo-chronology, modeling mountain building processes, temperature histories during exhumation, Longmen Shan, Xuelongbao Massif, Pengguan Massif

A Corrigendum on

Exploiting Thermochronology to Quantify Exhumation Histories and Patterns of Uplift Along the Margins of Tibet

by Kevin P., Furlong, Eric, Kirby, C., Gabriel, Creason, Peter J. J., Kamp, Ganqing, Xu, Martin, Danišík, Xuhua, Shi, and Kip V., Hodges. (2021). Front. Earth Sci. 9:688374. doi: 10.3389/feart.2021.688374

In the original article, there was a mistake in the legend of **Figure 2** as published. An incorrect citation for Shi et al. (in preparation) was given. The correct legend appears below.

Further, a few of the authors of the article were not initially included in the published version. The corrected authors list now includes C. Gabriel Creason, Peter J. J. Kamp, Ganqing Xu, Martin Danišík, Xuhua Shi, and Kip V. Hodges.

The corrected **Author Contributions** statement appears below.

AUTHOR CONTRIBUTIONS

KF and EK conceived and designed the project, analyzed data, accomplished the modeling, and wrote the paper. CGC did preliminary modeling to constrain models used in Figures 8 and 9. Contributions to the data shown in Figure 7 are as follows: XS organized and executed the field sampling; PK oversaw the (U-Th)/He and FT analyses; GX did the whole mineral separations and the AFT and ZFT analyses; MD did the (U-Th)/He analyses; KVH did the Ar/Ar analyses.

In the original article, the reference for Shi et al. (in preparation) was incorrectly written as 'Shi, X., Kirby, E., Furlong, K., Creason, G., Kamp, P., Xu, G., et al.2020Protracted Exhumation from Oligocene to Present in the Xuelongbao Massif*J. Asian Earth Sci.*1412710.1016/j.jseaes.2010.03.008'

This should be 'Shi, X., Kirby, E., Furlong, K., Creason, G., Kamp, P., Xu, G., Danišík, M., Wang, G., He, J., Fan, C., Xu, G., Su, Z., and Wang, E.', in preparation, Protracted exhumation from Oligocene to present in the Xuelongbao massif.

OPEN ACCESS

Approved by:
Frontiers Editorial Office, Frontiers Media SA, Switzerland

****Correspondence:***
Kevin P. Furlong
kpf1@psu.edu

Specialty section:
This article was submitted to Structural Geology and Tectonics, a section of the journal Frontiers in Earth Science

Received: *25 July 2021*
Accepted: *30 July 2021*
Published: *18 August 2021*

Citation:
Furlong KP, Kirby E, Creason CG, Kamp PJ J, Xu G, Danišík M, Shi X and Hodges KV (2021) Corrigendum: Exploiting Thermochronology to Quantify Exhumation Histories and Patterns of Uplift Along the Margins of Tibet. Front. Earth Sci. 9:747231. doi: 10.3389/feart.2021.747231

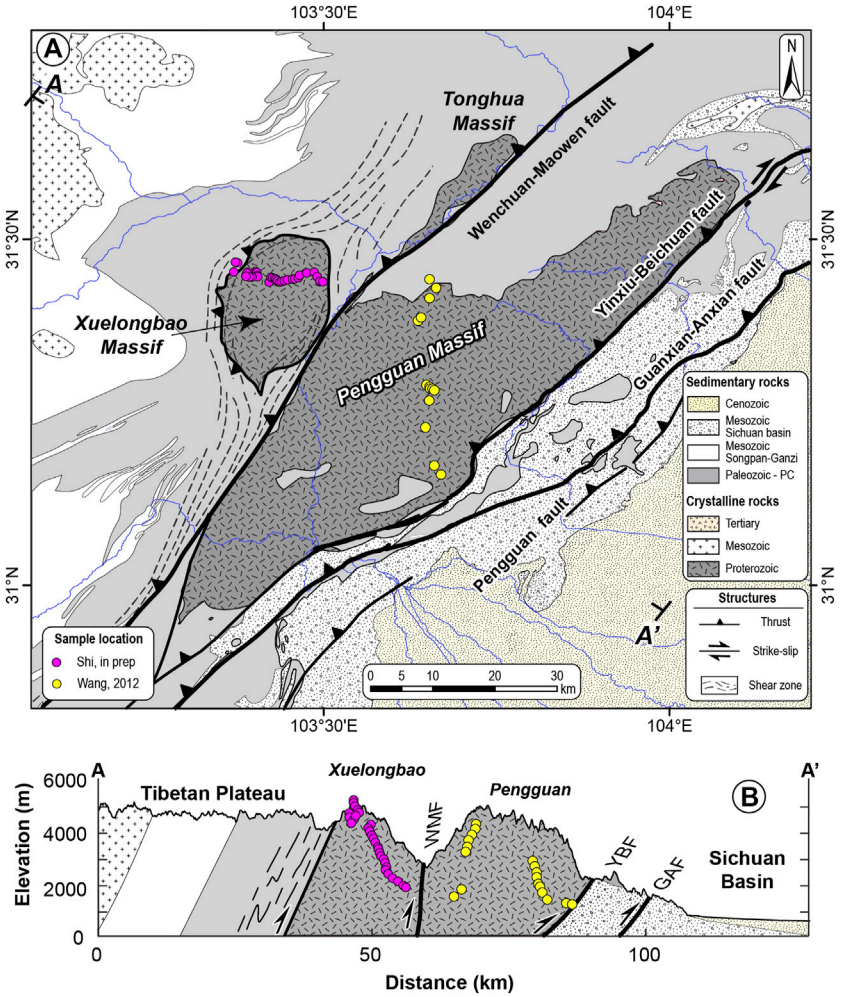

FIGURE 2 | (A) Simplified geology of the Longmen Shan and western Sichuan Basin after Burchfiel et al., 1995; Kirby et al., 2002; Airaghi et al., 2018a. Sample locations of data used in this paper are shown in colored circles. Yellow—data from Wang et al., 2012 in the Pengguan Massif. Pink—data from Shi et al. (2020) from the Xuelongbao Massif. **(B)** Cross-section showing the location of sample transects relative to major structures in the Longmen Shan.

There are also errors with the citation of the reference in multiple locations in the article. A correction has been made to the section **'Case Study: Multi-stage Exhumation in Eastern Tibet,'** Paragraph 1:

'To illustrate these principles, we use a densely sampled age-elevation transect from the Xuelongbao Massif, in the central Longmen Shan (Figures 1, 2) to explore the effects variations in exhumation history. The massif is composed primarily of granodiorite and tonalite plutonic rocks of Neoproterozoic age (748 ± 7 Ma; Zhou et al., 2006) in intrusive contact with Mesoproterozoic schists and paragneisses along its eastern and southern margins (Zhou et al., 2006). Sheared Paleozoic units form a carapace around the western and northern margins of the massif. We collected an age-elevation transect that spans elevations from ~1,600 m at the base of the massif to nearly the summit just below 5,500 m (Figure 7). These data have been described in Kirby et al. (2013), Creason et al. (2016), and Shi et al. (2020), and complete analytical details are in Shi et al. (in prep.). We describe briefly the primary results and trends in these data that motivate the thermal models. Although other data exist from this massif (e.g., Godard et al., 2009; Tan et al., 2017; Shen et al., 2019), we focus on this single data set here for simplicity. The Godard et al. (2009) data set includes Zircon (U-Th)/He age results for samples from locations near the samples of this study. These data lie between and compliment the AFT and ZFT results shown in Figure 7, as expected based on the relative closure temperatures of these systems. However, the vertical extent of these data is limited and do not substantively inform the exhumation history'.

A correction has also been made in Paragraph 4:

'Significant cooling (and exhumation) is recorded by systematic age-elevation relationships in ZFT (closure T of

~230°C–250°C, Reiners and Brandon, 2006), AFT (closure T of ~110°C–120°C, Ketcham et al., 1999), and AHe (closure T of ~60°C, Flowers et al., 2009) systems. Importantly, we do not expect a significant effect of radiation damage on the systematics of He retention in apatite (Flowers et al., 2009) for such young samples that cooled rapidly from well above temperatures where such damage anneals (Shi et al., in prep). These data reveal three important characteristics of the cooling history that any exhumation model needs to honor. First, there is a break in slope of the ZFT data at ~3,500 m elevation that marks an apparent increase in exhumation rate. Second, ZFT ages are nearly invariant (at ~ 15 Ma) with elevation below this point, and AFT ages are similar at higher elevations. As we discuss below, this is characteristic of rapidly cooled crustal sections, but is rarely observed in transects with more limited topographic relief. Third, AFT ages from the lowermost samples are nearly the same age as paired AHe samples. This requires a second relatively recent period of accelerated cooling and exhumation, as explained below'.

The **Acknowledgements** are also modified in light of change of authorship.

ACKNOWLEDGMENTS

The authors thank the two reviewers of this paper for very insightful and helpful reviews. This research was supported by NSF grants EAR-1757581 (to KF) and EAR-0911587 (to KF and EK). Research funding for the acquisition of FT and Helium thermochronology data were provided by the New Zealand Government - MBIE Contract: CONT-42907-EMTR-UOW (to PK).

The authors apologize for these errors and state that this does not change the scientific conclusions of the article in any way. The original article has been updated.

frontiers in Earth Science

ORIGINAL RESEARCH
published: 22 July 2021
doi: 10.3389/feart.2021.659937

Orogenic Collapse and Stress Adjustments Revealed by an Intense Seismic Swarm Following the 2015 Gorkha Earthquake in Nepal

Lok Bijaya Adhikari[1,2], Laurent Bollinger[3], Jérôme Vergne[4], Sophie Lambotte[4], Kristel Chanard[2], Marine Laporte[3], Lily Li[5], Bharat P. Koirala[1], Mukunda Bhattarai[1], Chintan Timsina[1], Nabina Bishwokarma[1], Nicolas Wendling-Vazquez[3], Frédéric Girault[2] and Frédéric Perrier[2]*

[1]Department of Mines and Geology, National Earthquake Monitoring and Research Center, Kathmandu, Nepal, [2]Université de Paris, Institut de Physique du Globe de Paris, CNRS, IGN, Paris, France, [3]CEA, DAM, DIF, Bruyères-le-Châtel, France, [4]Institut Terre et Environnement de Strasbourg, CNRS, Université de Strasbourg, Strasbourg, France, [5]Beijing National Earth Observatory, Institute of Geophysics, China Earthquake Administration, Beijing, China

OPEN ACCESS

Edited by:
A. Alexander G. Webb, The University of Hong Kong, China

Reviewed by:
Abhijit Ghosh, University of California, Riverside, United States
Jie Deng, University of California, Los Angeles, United States

***Correspondence:**
Lok Bijaya Adhikari
lbadhikari@hotmail.com

Specialty section:
This article was submitted to Solid Earth Geophysics, a section of the journal Frontiers in Earth Science

Received: *28 January 2021*
Accepted: *16 June 2021*
Published: *22 July 2021*

Citation:
Adhikari LB, Bollinger L, Vergne J, Lambotte S, Chanard K, Laporte M, Li L, Koirala BP, Bhattarai M, Timsina C, Bishwokarma N, Wendling-Vazquez N, Girault Fé and Perrier Fé (2021) Orogenic Collapse and Stress Adjustments Revealed by an Intense Seismic Swarm Following the 2015 Gorkha Earthquake in Nepal. Front. Earth Sci. 9:659937. doi: 10.3389/feart.2021.659937

The April 25, 2015 M_w 7.9 Gorkha earthquake in Nepal was characterized by a peak slip of several meters and persisting aftershocks. We report here that, in addition, a dense seismic swarm initiated abruptly in August 2017 at the western edge of the afterslip region, below the high Himalchuli-Manaslu range culminating at 8156 m, a region seismically inactive during the past 35 years. Over 6500 events were recorded by the Nepal National Seismological Network with local magnitude ranging between 1.8 and 3.7 until November 2017. This swarm was reactivated between April and July 2018, with about 10 times less events than in 2017, and in 2019 with only sporadic events. The relocation of swarm earthquakes using proximal temporary stations ascertains a shallow depth of hypocenters between the surface and 20 km depth in the High Himalayan Crystalline slab. This swarm reveals an intriguing localized interplay between orogenic collapse and stress adjustments, involving possibly CO_2-rich fluid migration, more likely post-seismic slip and seasonal enhancements.

Keywords: Gorkha earthquake, aftershock, seismic swarm, seismicity and tectonics, relocation, himalaya

INTRODUCTION

Crustal processes are particularly important to understand in the Himalayas, where the convergence between India and Eurasia plates is able to produce in the near future a megaquake expected to affect Nepal and Northern India, one of the most-densely populated area on Earth (*e.g.*, Bilham, 2019). In the Himalayas, earthquakes also contribute to the orogenic growth, rise and support of the high topography, which results from the competition between geodynamical and climatic conditions at the geological timescale. The front of the high Himalayan range is located above the downdip-end of locked fault segments (*e.g.*, Avouac et al., 2001; Bollinger et al., 2004; Ader et al., 2012; Lindsey et al., 2018; Ingleby et al., 2020) of the shallow dipping Main Himalayan Thrust (MHT) fault system (Nabelek et al., 2009). These segments break during large and great earthquakes, leading instantly to the coseismic subsidence of the high mountain range. These episodes are followed by decades or centuries of postseismic and interseismic deformation during which the range locally rises, prior to the occurrence of another large earthquake. The strain and stress rates within the hanging wall of the

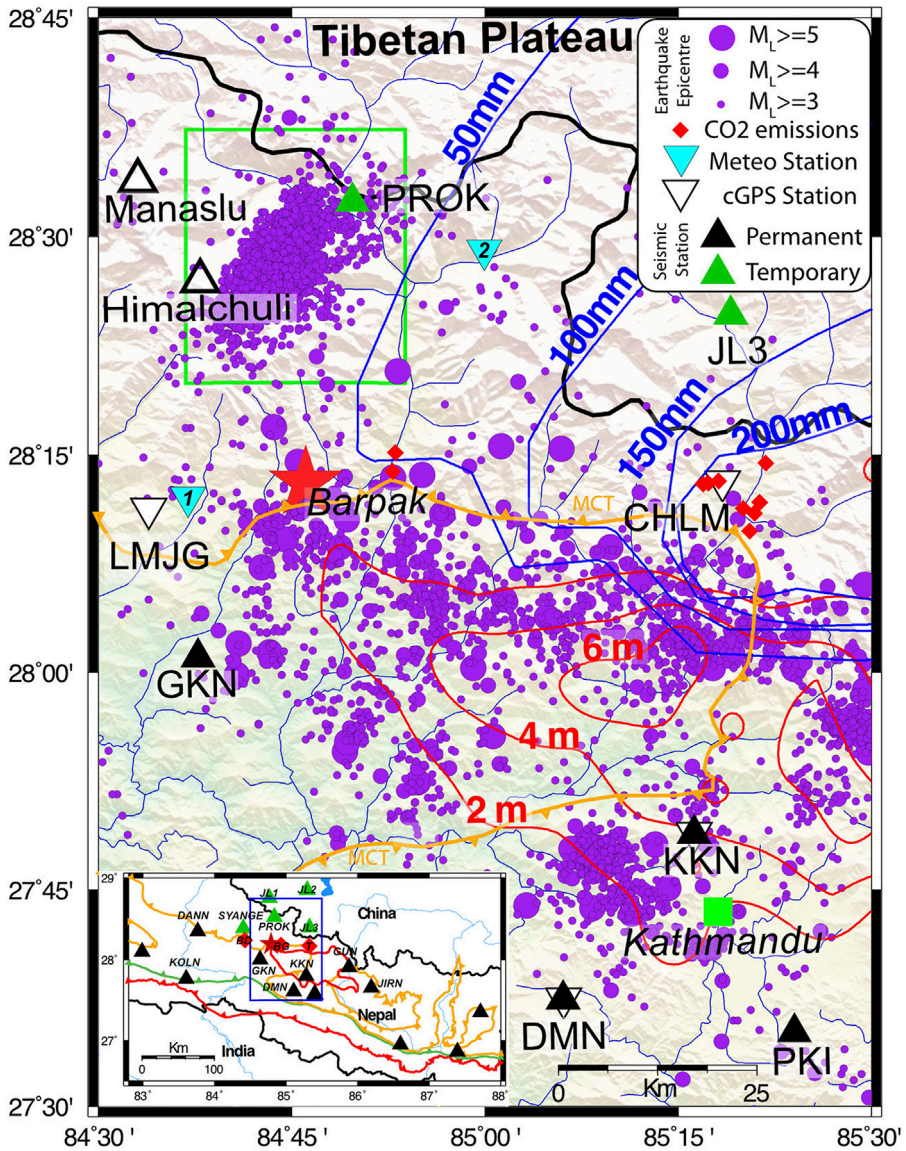

FIGURE 1 | Seismicity after the Mw 7.8 Gorkha earthquake of April 25, 2015. Earthquakes with local magnitude ML ≥ 3.0 are recorded by the permanent NSC network (stations shown in inset) plotted in purple circles. Red star represents the Gorkha mainshock. Green triangles represent the temporary seismic stations installed following the activation of Himalchuli swarm. Light blue triangles represent the meteorological stations (numbers 1 and 2 respectively for Gharedhunga and Chhekampar). Red contours correspond to coseismic slip (Grandin et al., 2015). Blue contours correspond to post-seismic slip deduced from cGPS stations (Zhao et al., 2017). At a larger spatial scale, the inset presents the seismic stations (black triangle), and three CO_2 emission sites (red diamond), where BD, BG, and T stand for Bahundanda, Budhi Gandaki, and Trisuli sites, respectively.

MHT vary therefore significantly during the period separating two interseismic stages. This may impact the seismic behavior of faults located in the high range.

These processes could be studied in detail after the deadly M_w 7.9 2015 Gorkha earthquake in Nepal (e.g. Avouac et al., 2015; Galetzka et al., 2015; Grandin et al., 2015; Elliott et al., 2016). Indeed, this earthquake was the first large Himalayan earthquake with extensive instrumental coverage. Monitoring of deformation in Nepal and Tibet revealed the interplay between afterslip and viscoelastic relaxation (*e.g.*, Gualandi et al., 2017; Zhao et al., 2017; Wang and Fialko, 2018; Jiang et al., 2019; Jouanne et al., 2019; Tian et al., 2020; Liu-Zeng et al., 2020). Aftershocks are being monitored by the 21-station National Earthquake Monitoring and Research Center (NEMRC) network (Adhikari et al., 2015), continuously in operation since 1994 (Pandey et al., 1995), and temporarily complemented by local and nearby networks (Bai et al., 2016; Mendoza et al., 2019; Yamada et al., 2020). These aftershocks, still active in 2020, are mostly located in the vicinity of the rupture zone in Central Nepal, between the epicenters of the main shock and of the May 12, 2015 shock (Adhikari et al., 2015; Baillard et al., 2017).

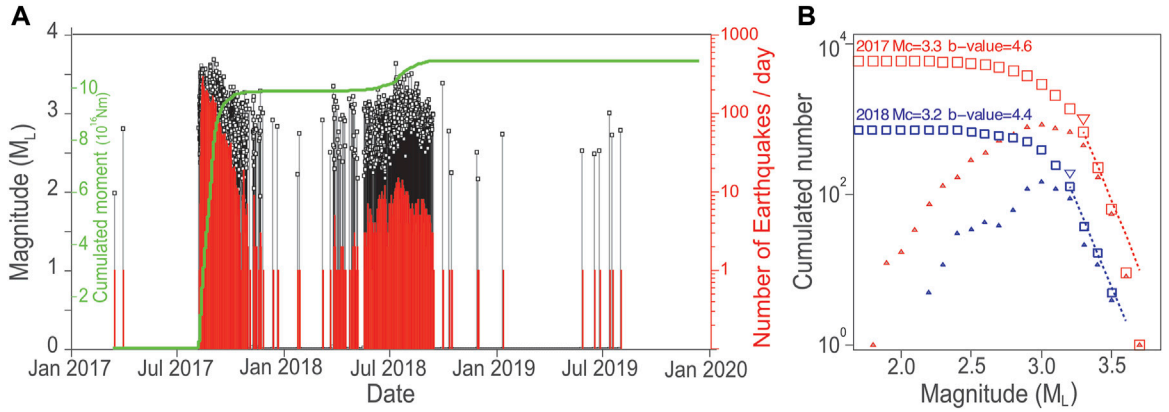

FIGURE 2 | Seismicity in the region affected by the swarm (source: NSC catalogue). **(A)** Magnitude versus time (in black). In red, the number of recorded earthquakes per day versus time. In green, cumulated seismic moment released by the earthquakes. **(B)** Cumulated number of events versus local magnitude in 2017 (in red) and in 2018 (in blue). Triangles and squares correspond to the number of events and to the cumulated number of events above a given magnitude, respectively.

In addition to aftershocks, and to earthquakes resulting from interseismic stress buildup along the downdip end of the locked fault zone, the NSC network also recorded very rare transient seismic swarms (Hoste-Colomer et al., 2017). The study of these unusual swarms revealed stress triggering and/or fluid diffusion in the crust (Hoste-Colomer et al., 2017), mechanisms that were documented elsewhere thanks to robust earthquake catalogues (*e.g.*, Hainzl, 2004; Kraft et al., 2006; Lohman and McGuire, 2007; Cappa et al., 2009; Duverger et al., 2015; De Barros et al., 2019).

In this paper, we report a new and peculiar feature of the seismicity after the Gorkha earthquake. An intense swarm developed suddenly in the summer of 2017 under the very high topography of the Manaslu-Himalchuli range, about 30 km North of the epicenter of Gorkha earthquake, outside of the aftershock zone (**Figure 1**), and in a region where no significant earthquake activity had been recorded since 1994 (**Supplementary Figure 1**) and where no large earthquake occurred since the 14th century. This swarm is the most intense swarm ever recorded in the whole Himalayan range. Using records from the NSC network, complemented by local temporary stations, we constrain the location of this seismicity. We then discuss our observations, their possible causes and their implications in term of regional geodynamical setting.

EVENTS AND DATA

The M_w 7.9 Gorkha earthquake, which struck Central Nepal on April 25, 2015 at 11:56 local time, ruptured a 140 km-long and-50 km-wide patch of the MHT. The main shock, which accommodated several meters of coseismic slip (*e.g.*, Avouac et al., 2015; Grandin et al., 2015; Elliott et al., 2016), was immediately followed by an intense seismic activity, mainly located at the periphery of the rupture (**Figure 1**).

These aftershocks of the Gorkha earthquake were continuously recorded by the NSC network which consists in 17 short period (1 s) vertical component stations (ZM500) and 4 broad-band stations (0.1–120 s) operated since 1994 by the Department of Mines and Geology (DMG) in collaboration with the Département Analyse Surveillance Environnement (DASE, France). The instruments cover the whole Nepalese territory, but lie primarily at the front of the High Himalayan range (**Figure 1**). The seismic signals captured at these stations are telemetered in real time to the seismological centers located in Kathmandu (Central Nepal) and in Surkhet (Western Nepal).

In total, over 43,000 earthquakes were recorded in Nepal between April 2015 and April 2020, among them over 31,000 aftershocks of the Gorkha earthquake. These events tend to be clustered and fall principally within a few kilometers from the edges of the fault plane that ruptured during the main shock, a region also associated with a centimetric afterslip (*e.g.*, Mencin et al., 2016; Gualandi et al., 2017; Zhao et al., 2017; Jouanne et al., 2019; Liu-Zeng et al., 2020; Ingleby et al., 2020). In the meantime, larger afterslip happened North of the downdip end of the rupture. This reincreased the Coulomb stress by ≥0.05 MPa along 30% of the downdip end of the rupture during the first year of postseismic slip (Liu-Zeng et al., 2020).

Most of the seismic clusters persisted, but their activity decreased progressively during the 4 years following the main shock. However, a major exception to this behavior occurred 30 km North from the Gorkha mainshock epicenter (**Figure 1**), under the Himalchuli-Manaslu mountain range, where a large seismic swarm developed mainly in 2017, and repeated with lower intensity in 2018. This swarm occurred 45 km North of GKN, the closest station from the permanent network, in a region only reached after 5 days of walking. This region had been seismically inactive over the past 35 years (**Supplementary Figure 1**). No historical seismicity was reported either. The crisis began on August 7, 2017 with a sharp onset, the first event recorded being followed by 18 events within a day and more than 100 events within 3 days. The rate of earthquakes detected by the NSC network continued to increase until day 7 then stationed around 200 ± 50/day from the next day onwards (**Figure 2** and **Supplementary Figure 2**). The local magnitude

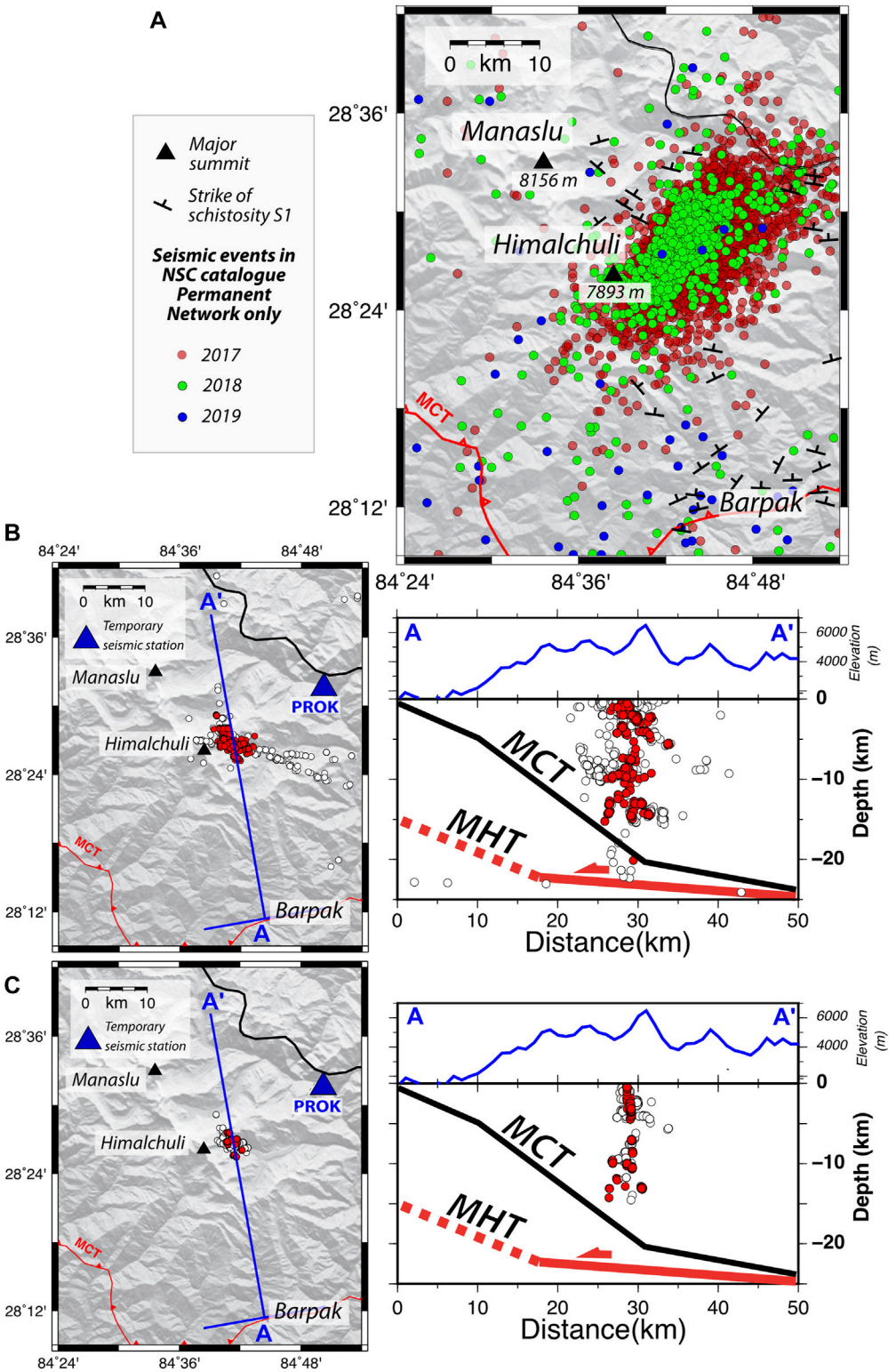

FIGURE 3 | (A) Seismicity recorded by the permanent NSC network. Red, green, and blue circles correspond to events recorded in 2017, 2018, and 2019, respectively. The red contour corresponds to the surface trace of MCT. **(B)** Map and cross section through the seismic events detected using template matching and relocated including at least one temporary station (PROK or JL). Open circles show all the events located with Hypo71; red circles show the events located with at least 9 phases. **(C)** Map and cross section through the best events relocated using HypoDD.

of the events, deduced from the maximum amplitude of the (Sn, Sg, Lg) (See Adhikari et al., 2015), peaked several times between local magnitude M_L 3.6 and 3.7 (reached by an event on 27/08/2017). The b-value, calculated using the maximum likelihood method, remained higher than 4 (**Figure 2**), a value totally different from the average b-value around 0.8 determined elsewhere along strike (Pandey et al., 1999; Adhikari et al., 2015).

Since the hypocentral depths and location of the events remained associated with large uncertainties, mainly due to the poor azimuthal coverage and relatively large distances to the permanent seismic stations of the network, we installed temporary three component stations (KVS500 and Le3D5s respectively on a EDR-X7000 @50Hz and a Nanometrics - Taurus @ 100Hz) and an accelerometer (Güralp CMG5T on a Staneo digitizer) in a village named Prok (station codename PROK installed on August 21, 2017 for 7 days of acquisition, **Figure 1**) and later in fall in Syangje (stations codename SYNGE, inset of **Figure 1**), at kilometric distances from the swarm to the East and West (**Figure 1**). The local earthquakes were also recorded by three broadband stations, deployed northward on the Tibetan plateau by the Chinese Earthquake Administration (JL1-2-3, **Figure 1**) on September 2, 2017 and available until September 18, 2017. In 2018 and 2019, the seismicity was only monitored by the permanent stations of the national network.

METHODS AND EARLY PROCESSING

Arrival times of (Pg, Pn) and (Sg, Sn) waves of the seismic events were picked manually by analysts at the NSC in Kathmandu. The maximum amplitude of (Sg, Sn) seismic phases was measured at stations on the 0.8–8.0 Hz band-pass filtered seismic signals to compute local magnitude (M_L) of the seismic events (Adhikari et al., 2015). A 1D/3 layers velocity model is used (Pandey, 1985), with P and S wave velocities of 5.56, 6.50, 8.10 and 3.18, 3.71, 4.63 km s^{-1}, respectively, with depth interfaces at 23 and 55 km for the Moho discontinuity.

In total, NSC analysts manually picked 74,759 phases, mainly Pg and Sg, locating a total of 6,756 earthquakes in the swarm from August 7, 2017 to September 13, 2019 with M_L ranging from 1.8 to 3.7 in the region of interest (from 28.35° to 28.60°N latitude and from 84.55° to 84.90°E longitude). Preliminary discrete fixed depth values (2, 6, 10, 15, 20, and 25 km) are attributed to the events by this processing, minimizing the time residuals. The earthquakes epicenters resulting from this first step of processing are spread over a 25 x 15 km^2 SW-NE area. The events that occurred in 2018 and 2019 are centered on the 2017 seismicity spread (**Figure 3A** and **Supplementary Figure 3**). The hypocentral depths range from 0 to 30 km. No clear spatial organization emerged at this stage; the swarm appears as an apparent seismicity spread oriented along an axis perpendicular to the orientation of the permanent network.

The events that were also captured by the temporary stations were then relocated in order to better determine the true shape of the seismicity cluster (**Figure 3B**). For that purpose, we refined the catalogue of phase picks on the temporary stations using EQcorrscan, a matched filter and subspace detection package (Chamberlain et al., 2017). After an examination of the signals, seven and five templates were selected at PROK and JL, respectively. The templates span the variety of signals acquired and could mostly correspond to events at various depths. This approach allowed detecting 1800 almost repeating earthquakes within 8 days at PROK, and 1217 within 16 days at JL. These earthquakes include all events picked at NSC at the permanent stations. The additional events represent an increase of 67 % of the database for the considered days. The hypocentral locations of the events detected by template matching were determined with Hypo71 using the NSC velocity model (Pandey, 1985), integrating the phase arrival time deduced from template matching and the phases initially picked by the analysts. Among these events, 1532 were located with more than nine picks, including at least one temporary station (**Figure 3B** and **Supplementary Table 1**). These template matched events were then relocated using a double-difference scheme under HypoDD (Waldhauser and Ellsworth, 2000), requiring a cross correlation coefficient of the signals at 0.8 (**Figure 3C** and **Supplementary Figures 4, 5**).

Synthetic tests were then performed in order to determine the robustness of the hypocentral locations and the influence of the biases induced by the network geometries. For that purpose, we generated synthetic catalogues of earthquakes taking into account the average time and spatial uncertainties estimated from the events manually picked at NSC. The synthetic events were then relocated using a double-difference scheme under HypoDD, considering the three seismic network geometries available during the seismic crisis (See **Supplementary Figure 6** for full description and used parameters). The results of these synthetic tests are used to support our conclusions below.

RESULTS: SPATIO-TEMPORAL VARIATIONS OF THE HIMALCHULI SWARM SEISMICITY

General Behavior of the Swarm

The first results from the data analysis reveal the peculiar behavior of the Himalchuli swarm, both persistent over weeks and with a possible strong seasonal modulation. With 6793 M_L>1.8 events, this is the largest swarm ever recorded in the Himalayas. The onset of the seismicity in 2017 is sharp and not following at all the typical mainshock-aftershocks pattern.

Indeed, after a first M_L 2.8 earthquake on August 7, 2017 at 00:29:21 UTC, the swarm expanded quickly over a surface similar to the final extension of its overall seismicity. The beginning of this seismic sequence do not coincide with the occurrence of a large earthquake at regional or teleseismic distance. We found therefore no candidate for a dynamic triggering by long-period surface waves, a phenomenon described further west in Kumaon-Garhwal Himalaya, with local microearthquake activity triggered by the surface waves of the 2007 Mw 8.5 earthquake (Mendoza et al., 2016). The number of events per day increased from 1 to 294 in 7 days, contributing then to a dense seismic activity near the barycenter of the swarm (**Figure 2** and **Supplementary Figures 2, 3**). The rate of earthquakes decreased more

progressively than it rose until early September 2017. A few additional earthquakes occurred from 16 September to November 2017 (**Figure 2** and **Supplementary Figure 2**). The seismic activity rate reached a low level with 1 event every 10 days until March 2018 and the beginning of a new period of activity (**Figure 2** and **Supplementary Figure 2**). The rate of earthquakes increased more progressively from the May 17, 2018, reaching a peak of activity on July 14, 2018, with 15 earthquakes that day. This episode was followed by a decrease of the seismicity that ended on September 12, 2018. Then, almost no earthquakes were detected until the summer 2019, when sporadic local earthquakes occurred (**Figure 3A**). The higher seismicity rates of the swarm during the summer for these three successive years cannot be attributed to a temporal decrease of the seismic noise. Indeed, the high frequency seismic noise at the NSC stations is higher in summer than in winter due to river and landslide activity (Burtin et al., 2009), leading to less event detection (Bollinger et al., 2007). The largest event, with M_L 3.8, occurred on November 5, 2017.

The seismic moment released by the crisis was evaluated from the M_w converted from the M_L of the earthquakes obtained at NSC, using the following relation (Ader et al., 2012): $M_w=0.84M_L+0.21$. We obtained that the 5992 events recorded in 2017 progressively released 9.92×10^{16} Nm, the 759 events in 2018 released 1.19×10^{16} Nm, while 2019 events released only 5.13×10^{13} Nm. The total seismic moment released reached then 1.11×10^{17} Nm, a value equivalent to a single earthquake of M_w 5.3.

Earthquake Relocation and Geometry of the Swarm

The earthquake catalogues also show that the seismicity spreads within a single-continuous patch (**Figures 1**, **2**, **3A**). However, the genuine size and orientation of the spread are not sufficiently well constrained in the original NSC catalogue. Indeed, the addition of one or the other temporary stations (PRK, between the 21 and 28/08/2017 or JL, between the 02 and 18/09/2017), which efficiently closes the azimuthal detection gap, reshapes the cluster. The synthetic tests performed for every network geometry available during the seismic crisis help to quantify the hypocentral location biases (**Supplementary Material** "Synthetic tests" and **Supplementary Figure 6**). They demonstrate the robustness of the catalogue generated when the network was complemented by these temporary stations closing the azimuthal gap. This relocated catalogue, which contains only the 20% of best located earthquakes, is illustrated in **Figure 3B**.

The structure of the seismicity deduced from the relocated catalogues is significantly different from the original one (**Figure 3A**). The seismicity swarm does not spread over nor is elongated along a NE-SW axis, but is organized within a narrow (2–4 km-thick) steeply northward dipping, $7 \times 15\ km^2$ region located at the foot of the Himalchuli summit (**Figure 3B**). The difference observed in comparison with the original catalogue is expected, since the shape and width of the original seismicity spread were largely controlled by the network geometry (a result illustrated by synthetic catalogue testing described in

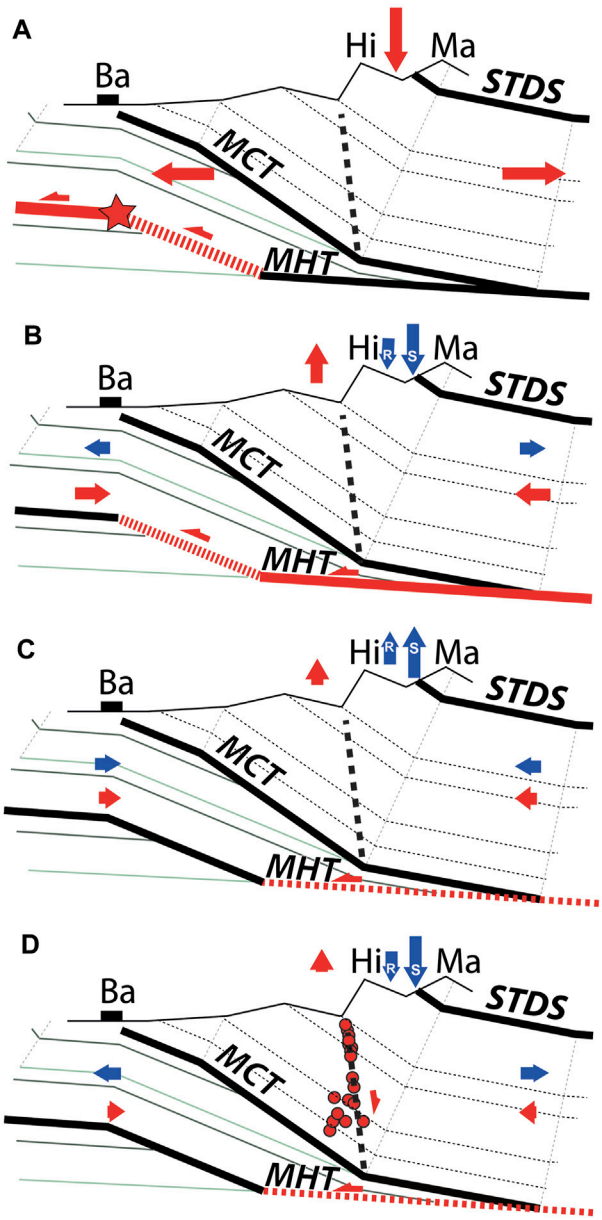

FIGURE 4 | Conceptual model of the transient and seasonal straining and the seismic swarm (see text). Geological section is deduced from field mapping (Colchen et al., 1986). Ba, Hi, and Ma stand for Barpak, Himalchuli, and Manaslu, respectively. MHT, MCT, and STDS stand for Main Himalayan Thrust, Main Central Thrust, and Southern Tibetan Detachment System, respectively. The bold dashed line corresponds to the fault activated during the seismic crisis. The red arrows are related to the effects of the tectonic forcing. The blue arrows are related to the effects of the hydrological surface loads, R for Regional, S for local Snow load. **(A)** April 25, 2015. Coseismic damage, following the rupture of the upper decollement of the MHT in red, generates localized extension and subsidence of the High range. **(B)** Summer 2015. Afterslip associated with immediate fault clamping. **(C)** Fall-Winter 2016. Seasonal fault clamping resulting from tectonics, regional and local straining. **(D)** August 2017. Orogenic collapse and/or fluid/gas migration associated with seasonal extension related to regional seasonal straining and local snow loading. Hypocenters from relocated earthquakes are shown as red circles (plotted in **Figure 3C**).

Supplementary Material and **Supplementary Figure 6**). The difference is also not a bias related to the short period and limited number of events covered by the temporary stations. Indeed, the density map of events considered for the relocation shows similarities with the density map of all earthquakes happening in 2017 or 2018, the location and shape of the area of highest density remaining similar (**Supplementary Figure 3**). This suggests that the geometry described by a small number of well-relocated events may be representative of the overall distribution of the swarm. The events in 2018 and 2019 could also line up with the same inferred fault, no migration of the densest area of the seismicity or change of the shape of this region being detectable (**Supplementary Figure 3**). The depth of the relocated events ranges between 0 and 28 km, when considering all events, most of the best located events (95%) falling between 0 and 15 km. An average seismic slip of 2.85 cm on such a 7 × 15 km^2 plane would have been enough to release the total seismic moment of the swarm (1.11×10^{17} Nm). However, the swarm geometry defined by the microseismicity remains associated with large uncertainties, while the kinematics on the fault remains uncharacterized, limiting the possibility for a convincing interpretation of this seismicity taken out of its geological or seismotectonic context. We therefore attempted at determining the focal mechanisms of the largest earthquakes of the seismic swarm in order to benefit from a fault plane orientation and slip vector. The attempts at waveform inversion at regional distances failed because all earthquakes are too small (below M_w 3) for being studied at KKN, the nearest permanent broadband station installed 90 km from the cluster. In parallel, we attempted at determining focal mechanisms with first motion polarities of the direct P-wave. For most of the largest earthquakes selected, the signals are not very impulsive and the polarities are difficult to ascertain. Furthermore, for all of them, the distribution of the polarities on the focal sphere is far from optimal, due to the large azimuthal gap, the range of hypocentral distances covered by the stations and the shallow depths of the earthquakes. The events of M_{Lv} 3.5 and 3.1 (resp. M_w 2.8 and 2.5) that occurred on August 26 and 29, 2017, respectively (and were recorded at PROK), are among the best recorded for determining a focal mechanism (see **Supplementary Material**). However, the result we obtained for the two are not consistent, precluding the validation or invalidation of some possible geometries based on the observed polarities (**Supplementary Figure 7**).

Structure of the Fault Plane Likely Activated by the Swarm

The updip-end, shallow trace, of the swarm defined by the best located earthquakes, recorded during the few days when the local station of PROK was available, falls precisely at the toe of Himalchuli Southeastern face, along a glacial valley. They did occur on a steep plane. The geological survey of the region by Colchen et al. (1986) revealed no active fault trace but a large slab of High Himalayan Crystalline (HHC) units, slightly dipping to the North. The slab is associated with almost East-West structural fabrics. The bedding of the local quartzite/gneisses, complemented by the bedding of the Lesser Himalayan unit southward, helped tying a local balanced cross-section (**Figure 3A** and **Figure 4A**). Most, if not all, of the seismic swarm develops through the Formations I and II of the HHC, above a change of dip of the units in the hanging-walls of the Main Central Thrust (MCT) and MHT fault systems (**Figure 4A**). A structure activated with the same orientation as the main structural fabrics is likely, but the activation of a structure across the main fabrics remains possible. To our knowledge, the valley along the south-eastern slope of the Himalchuli was not the focus of any extensive tectonic survey, and its morpho-glacial activity probably precludes the preservation of the neotectonic landforms of active faults. Without an opportunity to survey the area, we visually inspected the high resolution GoogleEarth™ and ArcGIS™ Wayback imagery of the world images available in the vicinity of the seismic swarm before and after the Gorkha earthquake and the first swarm sequence (Supplementary section Imagery and **Supplementary Figure 8**). We checked in particular possible ~NS and NE-SW structures consistent with the orientation of the closest active normal faults, mapped 60 km to the North-East in Gyirong graben (Armijo et al., 1986). This examination confirmed the main East-West orientation of the rocks bedding, schistosity and/or structural fabrics (**Supplementary Figure 8**), but was not relevant to identify any active fault trace in the area, along or across fabrics within that area, highly covered by snow and ice.

DISCUSSION

Relations With the Gorkha Earthquake Rupture and Afterslip

This shallow seismicity swarm of more than 6500 earthquakes with M_L>1.8 located at the foot of the High Himalayan range is unusual, falling in a region where swarms had never been recorded since 1994. The clustered seismicity, however, developed 30 km North of the 2015 M_w 7.9 Gorkha earthquake epicenter in a region prone, since the main shock, to large variations of strain and stresses. We found no evidence of dynamic triggering, founding no large earthquake possibly associated with the onset of the swarm.

The earthquake ruptured a 140 × 50 km^2 locked fault patch to the South-East which was responsible for the subsidence of the high Himalayan range (*e.g.*, Avouac et al., 2015; Grandin et al., 2015; **Figure 4A**). This subsidence locally exceeded 1 m. Despite lower values in the Himalchuli area, the coseismic strain and stress changes applied to the geological medium were likely significant (**Figure 4A**). Indeed, the peak of coseismic slip on the MHT was observed 80 km to the southeast of the study area, exceeding 5 m (*e.g.*, Avouac et al., 2015; Grandin et al., 2015). A displacement of 1–2 m at depth is also estimated on the fault segments 10–20 km to the South of the Himalchuli. The discrepancy between the source models and the relatively low resolution of the slip accommodated at depth on the midcrustal ramp of the MHT, precludes any precise estimate of the stress buildup at short distances. Nevertheless, the whole hanging wall of the MHT was necessarily considerably affected by the main shock in this region of high slip gradients and localized

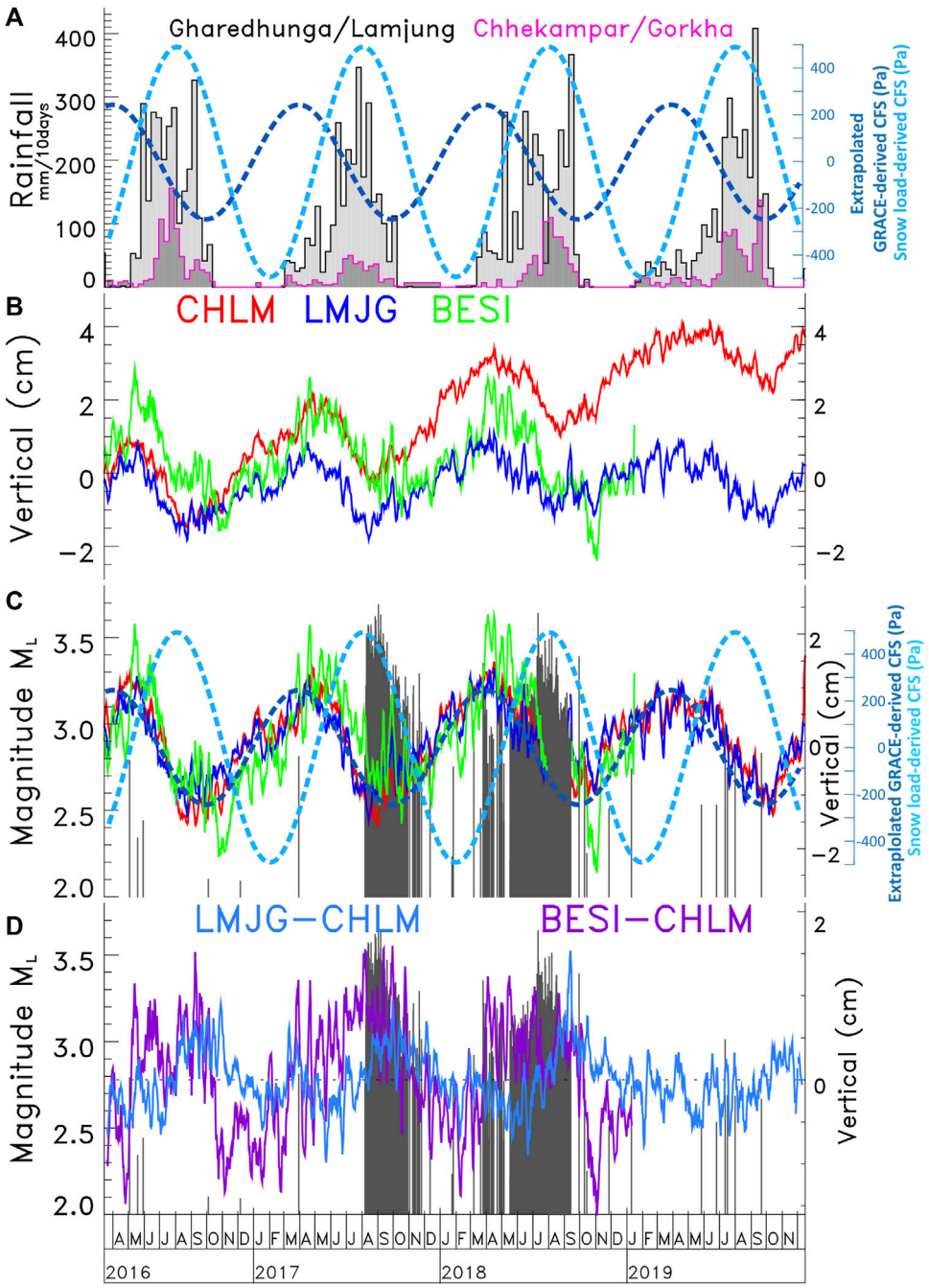

FIGURE 5 | (A) Pink and black histograms represent the rainfall measured at two meteorological stations (Chhekampar and Gharedhunga located in **Figure 1**). The modulation of the Coulomb Failure Stress (CFS), related to the regional straining, is extrapolated from GRACE (dark blue), and that related to the local straining, is derived from local snow loads (light blue) **(B)** Vertical displacements measured at the cGPS stations of Chilime (CHLM in red), Lamjung (LMJG in blue) and Besisahar (BESI in green) **(C)** Detrended vertical displacement confronted with the magnitude versus time distribution of the seismicity (in grey) and with **(D)** LMJG–CHLM and BESI–CHLM cGPS baselines.

extension (**Figure 4A**). The earthquake was immediately followed by deep afterslip, poroelastic rebound and viscous relaxation (**Figure 4B**) (*e.g.*, Gualandi et al., 2017; Zhao et al., 2017; Wang and Fialko, 2018; Jiang et al., 2019; Jouanne et al., 2019; Tian et al., 2020; Liu-Zeng et al., 2020). The deep afterslip, within the 3 months following the mainshock, exceeded 1 cm and reached locally as much as 5 cm after a year, a value which corresponds to 2.5 years of interseismic loading (Gualandi et al., 2017; Zhao et al., 2017; Ingleby et al., 2020; Liu-Zeng et al., 2020; Tian et al., 2020).

Knowing the large postseismic relaxation and afterslip of the Gorkha earthquake, in the following, we discuss different types of forcing that may modulate, induce or trigger the seismicity in the Himalchuli swarm and the mountain collapse including surface hydrological loading and fluid migration.

Effects of the Surface Hydrological Loads on the Fault

The strain and stress rates that resulted from the early postseismic behavior of the fault were significantly larger than those induced by surface hydrological loading of the Earth. However, these postseismic effects dampen with time as the tectonic system relaxes, becoming locally less influential on the strain and stress within the upper crust than the hydrological surface loading. Indeed, in the Himalayas, surface mass redistribution of continental hydrology induces measurable transient and seasonal deformation. Seasonal amplitudes of regional horizontal and vertical displacements, as recorded by cGPS stations located in the high range, reach a few mm to a few cm (Bettinelli et al., 2008; Chanard et al., 2014; Larochelle et al., 2018) (**Figure 5**). Seasonal hydrology not only induces seasonal strain but also seasonal stress variations at depth on the fault systems. These stress variations are suspected to be responsible for the seasonal modulation of the midcrustal seismicity along the MHT (Bollinger et al., 2007; Bettinelli et al., 2008; Ader and Avouac, 2013).

Here, we quantitatively estimated the strain and stress induced by regional and local surface loading (see **Supplementary Methods 1, 2**). We first take advantage of satellite gravity measurements from the Gravity and Recovery Climate Experiment (GRACE) to quantify spatial and temporal variations in regional surface loading. We then calculate the full displacement field characterizing the solid-Earth's response to surface variations in hydrological loading inferred from GRACE, using a spherical layered elastic Earth model (Chanard et al., 2018). Our calculation is validated by comparison with observed displacements at cGPS stations (**Supplementary Figure 9**), and then used to evaluate stress perturbations on steeply dipping fault planes N080-N100E, dipping 70N-90N, a fault geometry consistent with the pattern of the swarm (**Figure 3**) and the main structural fabrics of the area. We compute change in Coulomb stress (CFS) as an indicator of the fault susceptibility to failure under annual stresses derived from GRACE. This shows a maximum of CFS in spring and a maximum rate of CFS at the onset of the monsoon, with amplitudes reaching up to 800 Pa (**Figure 5**, **Supplementary Figures 10–12**).

The spatial resolution of the GRACE data is only of a few hundred of km (~300 km). This leads to averaging loads over large areas, resolving the large wavelengths of the surface forcing on the faults. This may lead in this area to a significant mis-determination of the static stress change applied on shallow faults, which are also sensitive to localized loads, such as short wavelength snow accumulation on top of faults. Indeed, during summer monsoon, the freezing-thawing altitude reaches nearly 6000 m. The precipitations under this altitude favor rapid snow melt. Water is evacuated into rivers, while a thick snowpack is formed above 6000 m. According to the precipitations recorded at Gharedunga and Chhekampar, two meteorological stations at close distance from the Himalchuli (**Figures 1**, **5**), surface load of the summer monsoon due to snow accumulation could reach 1 m -water equivalent- above 6000 m in the hanging wall of the suspected northward dipping fault, while no snow accumulates in the footwall which remains below the zero isotherm. This leads to a potential large stress increase on the fault plane. This would favor the normal fault failure during the summer monsoon. To test this hypothesis, we compute stress fields induced by 1 m snow loads localized on the surface of the hanging wall, over the Himalchuli or Manaslu mountain ranges using the Boussinesq solution (Boussinesq, 1878; see **Supplementary Methods 2**). **Supplementary Figure 13** shows the two settings of snow surface load at 6 km on the Himalchuli or Manaslu, as well as the resulting depth profiles of the largest stress component σ_{zz}. We then evaluate the CFS at a depth of 10 km for an East-West steeply dipping (80°N) fault plane (see **Figure 5**, **Supplementary Methods 2** and **Supplementary Figure 13**). **Supplementary Figure 13** shows results of CFS as a function of the distance to the center of snow load, with a maximum amplitude reaching up to 600 Pa, 10 km BSL, below the load for the combination of both the Manaslu and Himalchuli snow loads. A larger load in term of water equivalent, or a depth shallower than 10 km BSL will lead to values that can overcome the 2 kPa (see **Supplementary Figures S13a,b**) which correspond to the CFS variations suspected to modulate the secular stress buildup of a few kPa/yr and its associated seismicity along the MHT at midcrustal depth (Bettinelli et al., 2008).

This is not surprising, snow loads having been suspected to be the forcing which modulate seismicity elsewhere, inhibiting the seismicity in winter in Japan on shallow dipping thrust faults and strike slip faults parallel to the snow loads (Heki, 2003). The tectonic setting here is different from the Japanese case, because of the orientation of the geological structures and their kinematics, but the effect could be similar in term of the amplitude of the Coulomb stress modulation on the fault system. Note that if the receiver faults are normal faults oriented NS or NE-SW, steeply dipping toward the highest topography to the West, the results would have not been drastically different.

Note that this local effect adds to the seasonal modulation of the stress by regional forcing previously described with a time structure favoring earthquakes in April and enhancing the seismicity rate in summer, the seismicity rate being expected to vary in proportion to the stress rate (**Figures 4B,C**) (Bettinelli et al., 2008).

A Collapse Possibly Accompanied by Fluid Migration

To decipher the processes behind the seismic swarm, another important information is that large carbon dioxide (CO_2) emissions and hydrothermal disturbances followed the Gorkha earthquake at the front of the High Himalayan range (Girault et al., 2018). Several plausible causative scenarios for the failure and seismogenesis of the area can then be considered.

We consider a scenario involving the progressive collapse of the mountain under its own weight along a normal fault system. Indeed, the basement of the Himalchuli-Manaslu, which is the

highest mountain group affected by subsidence along the Gorkha rupture, was probably weakened due to instant stretching and damages resulting from the mainshock (**Figure 4A**). Although not mapped by previous geological surveys, possibly hidden under the local glacier, a northward dipping fault is highly probable and both consistent with the shape of relocated swarm of earthquakes (**Figure 3B** and **Figure 4D**) and the local stress field imposed by the high topography. The failure was probably delayed by the deep afterslip on the MHT, responsible for clamping the steep northward dipping normal fault (**Figure 4B**). During this period of afterslip at depth, the fault is also solicited by the seasonal variations of the surface loads (**Figure 4B** for summer 2015 and 2016 and 4C for fall and winter 2015 and 2016). In August 2017, the normal fault is activated at the peak of local seasonal stresses (**Figure 5C**). During the two years that follow, the seismicity is then modulated by the stresses related to the surface hydrological loads (**Figure 5C**). The transient slip and swarm are reactivated in two stages in 2018: 1) at the peak of the regional Coulomb failure stress applied on the fault, involving a first increase of the seismicity rate in spring, and 2) during the summer monsoon, (a) when the local load in the hanging wall of the normal fault contributes to facilitating the rupture and (b) when the stress rate is optimal. The time structure of the sporadic events recorded in 2019 suggest that this scenario repeated two years after the initiation of the swarm (**Figure 5C**).

These mechanisms could be possibly accompanied by fluid migration that affects fracture strength. This would explain the high b-value obtained (**Figure 2**), the seismicity exhibiting a deficiency of large earthquakes, a signature often associated with the presence of fluids (*e.g.*, Murru et al., 1999; Bachmann et al., 2012). In addition to pore pressure changes which could be the driver of the failure, alternative scenarios can involve changes in poroelastic stresses contributing to the generation of induced seismicity. Instead of resulting from the sole fault clamping by afterslip, the delay between the Gorkha mainshock, and/or an initial fluid injection, and the beginning of the swarm development could be due to the time necessary to increase enough the fluid pressure for triggering seismicity. These delays between injection and earthquake realizations have been illustrated elsewhere (*e.g.*, Zhai et al., 2019). The seasonal deformations that follow the first swarm realization in 2017 can lead to repeated episodes in which the rock is hydraulically fractured due to additional poro-elastic stresses.

Several examples of seismicity driven by fluids involved deep CO_2-rich fluids upwelling through fractured rocks (*e.g.*, Cappa et al., 2009; Weinlich, 2014; Ingebritsen et al., 2015; Miller et al., 2004; Chiodini et al., 2020). In the Nepal Himalayas, CO_2 produced by metamorphic reactions is released mainly in the MCT zone in the dissolved form as hot spring waters and in gaseous form as tectonic fumaroles and diffuse degassing structures (*e.g.*, Girault et al., 2014; **Figure 1**). The 2015 M_w 7.9 Gorkha earthquake strongly affected Central Nepal triggering significant perturbations of the whole CO_2 emitting region (Girault et al., 2018): increases and decreases of gaseous CO_2 emissions at diffuse degassing structures and of dissolved CO_2 emissions in springs, up to a complete cessation of flow in the Trisuli valley (Inset map **Figure 1**).

Other valleys, less than 30 km away from the swarm, such as the Budhi Gandaki and Marsyandi valleys, also release significant CO_2 and are at closer distances (**Figure 1**). Repeated CO_2 flux measurements at the Bahundanda hydrothermal system (Inset map **Figure 1**) during active and inactive periods of the swarm did not show any clear change. The available time-series of soil-gas radon-222 concentration at this site show variations associated with the monsoon and steady signals during winter. Carbon isotopic values of CO_2 ($\delta^{13}C$) in the Budhi Gandaki valley remain relatively similar: for gaseous CO_2 emissions, -5.4 ± 0.1 ‰ in January 2017 and -5.6 ± 0.1 ‰ in January 2018 at Khorlabesi, -3.0 ± 0.1 ‰ versus -3.1 ± 0.1 ‰ at Machhakhola; for dissolved CO_2 in hot spring waters, -0.5 ± 0.2 ‰ versus $+1.1 \pm 0.1$ ‰ at Machhakhola. In the Marsyandi valley, at Bahundanda, the $\delta^{13}C$ values of gaseous CO_2 emissions (-2.2 ± 0.1 ‰ in January 2017, -3.6 ± 0.1 ‰ in August 2018) and of dissolved CO_2 in hot spring waters ($+0.2 \pm 0.2$ ‰ versus $+0.9 \pm 0.1$ ‰, and -0.2 ± 0.3 ‰ versus $+0.6 \pm 0.1$ ‰) show a slight difference possibly due to an increase in CO_2 degassing or to monsoonal rain effects (Girault et al., 2018; C. France-Lanord and P. Agrinier, private communications). At this stage, we cannot identify any clear excursion of carbon isotopic values of CO_2 in gas and hot water at these hydrothermal sites during the period covered by the swarm.

Thus, no hydrothermal changes at known hydrothermal sites nearby were noticed in measurements available during the specific period of activity of the Himalchuli swarm. However, the potential presence of CO_2 emission zones or CO_2-rich springs in the immediate vicinity of the swarm has not been investigated yet. Despite the very high b-value, the particular behavior of the seismicity, the presence of numerous fluid/gas vents in the region affected by the seismicity, there are no other compelling evidence for a fluid-driven swarm activity.

Whereas some of these plausible forcing generate unique seismic temporal structures, or particular seismic spatial patterns, their respective contributions to the triggering of the seismic events emphasized here are difficult to further resolve. Indeed, we were unable to resolve any migration of the seismicity front, nor to determine the volume and time of fluid injection possibly triggering the observed seismicity, as well as to overcome the absence of well-constrained focal mechanisms. Finally, while we lack time-series of near-field InSAR and cGPS data covering the whole crisis, this seismic cluster located below the highest Himalayan summits and found in the trace of the Gorkha earthquake, at the edge of the western Nepal seismic gap, offers unique and challenging observations.

CONCLUSION

A peculiar seismic swarm initiated in August 2017 at the front of the High Himalayas, about 30 km North-West of the epicenter of the M_w 7.9 2015 Gorkha earthquake in Nepal. This swarm produced more than 6500 events with M_L larger than 1.8 in three months in 2017. It was then reactivated in 2018 and again mildly in 2019. No comparable seismic swarm was recorded before in the Himalayas, the previous swarms being much smaller in size and intensity (Hoste-Colomer et al., 2017, 2018).

The Himalchuli swarm reveals a new possible feature of the seismicity following large earthquakes in the Himalayas. Beyond aftershocks in and around the rupture zone, seismicity can happen in the extended region affected by post-seismic relaxation, in the form of swarms, as observed in other contexts (*e.g.*, Hainzl, 2004). Such swarms may help to diagnose the stress conditions of the seismogenic crust. However, they can only be detected by permanent networks, as temporary networks, while dense and more sensitive, are not necessarily installed in an adequate location and are usually not maintained sufficiently long after large earthquakes.

The occurrence of this swarm is a major concern, the area being situated at the northeastern edge of a large MHT segment that has not ruptured since the 14th century (Bollinger et al., 2016). Furthermore, it is the first example of a recurrent seismic swarm under the front of the high range. The relocation of this seismicity, using nearby temporary stations, shows that the earthquakes happened along a northward dipping plane between the sub-surface and the basal décollement of the MHT. Thus, the relocated seismicity does not suggest any clear connection to the next megaquake. Rather, the spatial structure of the seismicity relative to the high topography suggests a definite relation with the collapse of the high mountain range, associated on average with 2–3 cm of seismic slip along a 7×15 km^2 long plane. This collapse happens at the foot of the Himalchuli-Manaslu group, the only mountain range above 8000 m-high along the Gorkha earthquake rupture. The high b-value and the deficit of large earthquakes suggest that this episode was accompanied by fluid injection and/or migration in the High Himalayan Crystalline rocks. However, the data available are yet too limited to distinguish between the various possible mechanisms of earthquake triggering. Nevertheless, the occurrence of such strong seismic swarm indicate that this system is highly sensitive to small deformation rates related to hydrologically-driven seasonal strain in the Himalayas and is therefore under near-critical conditions. Careful monitoring of small magnitude earthquake swarms in this region should therefore be an essential task in the future.

DATA AVAILABILITY STATEMENT

The raw data supporting the conclusions of this article will be made available by the authors, without undue reservation.

AUTHOR CONTRIBUTIONS

LA, LB, JV and FP contributed to conception and design of the study. All authors contributed at various stages of the analysis of the seismological data. LA, LB, JV and FP wrote the manuscript with contributions from KC, ML and FG. All authors contributed to manuscript revision, read, and approved the submitted version.

ACKNOWLEDGMENTS

We thank DMG (Nepal) as well as DASE (France) for facilitating the early exchanges during the crisis, as well as the data acquisition and treatment. DMG director general Sarbjit Prasad Mahato, Rajendra Khanal, Soma Nath Sapkota and Ram Prasad Ghimire are thanked for support over the years. Nepal Ministry of Home Affairs Nepal and DASE provided helicopter for installation and service of the temporary seismological station. We acknowledge early discussions with Pascal Bernard (IPGP) and Héléne Lyon-Caen (ENS Paris) and feedback from Yves Gaudemer. Kamal Kaphle, Arjun Bandhari and Destin Nziengui were involved in the processing. The Ambassador François-Xavier Léger and the French Embassy in Kathmandu are thanked for assistance. Two reviewers provided constructive comments that helped improve the original manuscript. This is IPGP contribution number 4229.

SUPPLEMENTARY MATERIAL

The Supplementary Material for this article can be found online at: https://www.frontiersin.org/articles/10.3389/feart.2021.659937/full#supplementary-material

REFERENCES

Ader, T., Avouac, J.-P., Liu-Zeng, J., Lyon-Caen, H., Bollinger, L., Galetzka, J., et al. (2012). Convergence Rate across the Nepal Himalaya and Interseismic Coupling on the Main Himalayan Thrust: Implications for Seismic hazard. *J. Geophys. Res.* 117 (B4), a–n. doi:10.1029/2011jb009071

Ader, T. J., and Avouac, J.-P. (2013). Detecting Periodicities and Declustering in Earthquake Catalogs Using the Schuster Spectrum, Application to Himalayan Seismicity. *Earth Planet. Sci. Lett.* 377–378, 97–105. doi:10.1016/j.epsl.2013.06.032

Adhikari, L. B., Gautam, U. P., Koirala, B. P., Bhattarai, M., Kandel, T., Gupta, R. M., et al. (2015). The Aftershock Sequence of the 2015 April 25 Gorkha-Nepal Earthquake. *Geophys. J. Int.* 203, 2119–2124. doi:10.1093/gji/ggv412

Armijo, R., Tapponnier, P., Mercier, J. L., and Han, T.-L. (1986). Quaternary Extension in Southern Tibet: Field Observations and Tectonic Implications. *J. Geophys. Res.* 91 (B14), 13803–13872. doi:10.1029/jb091ib14p13803

Avouac, J.-P., Bollinger, L., Lavé, J., Cattin, R., and Flouzat, M. (2001). Le cycle sismique en Himalaya. *Comptes Rendus de l'Académie des Sci. - Ser. IIA - Earth Planet. Sci.* 333 (9), 513–529. doi:10.1016/s1251-8050(01)01573-7

Avouac, J.-P., Meng, L., Wei, S., Wang, T., and Ampuero, J.-P. (2015). Lower Edge of Locked Main Himalayan Thrust Unzipped by the 2015 Gorkha Earthquake. *Nat. Geosci.* 8 (9), 708–711. doi:10.1038/ngeo2518

Bachmann, C. E., Wiemer, S., Goertz-Allmann, B. P., and Woessner, J. (2012). Influence of Pore-Pressure on the Event-Size Distribution of Induced Earthquakes. *Geophys. Res. Lett.* 39, 9302. doi:10.1029/2012GL051480

Bai, L., Liu, H., Ritsema, J., Mori, J., Zhang, T., Ishikawa, Y., et al. (2016). Faulting Structure above the Main Himalayan Thrust as Shown by Relocated Aftershocks of the 2015Mw7.8 Gorkha, Nepal, Earthquake. *Geophys. Res. Lett.* 43 (2), 637–642. doi:10.1002/2015gl066473

Baillard, C., Lyon-Caen, H., Bollinger, L., Rietbrock, A., Letort, J., and Adhikari, L. B. (2017). Automatic Analysis of the Gorkha Earthquake Aftershock Sequence: Evidences of Structurally Segmented Seismicity. *Geophys. J. Int.* 209 (2), 1111–1125. doi:10.1093/gji/ggx081

Bettinelli, P., Avouac, J. P., Flouzat, M., Bollinger, L., Ramillien, G., Rajaure, S., et al. (2008). Seasonal Variations of Seismicity and Geodetic Strain in the Himalaya Induced by Surface Hydrology. *Earth Planet. Sci. Lett.* 266 (3-4), 332–344. doi:10.1016/j.epsl.2007.11.021

Bilham, R. (2019). Himalayan Earthquakes: a Review of Historical Seismicity and Early 21st century Slip Potential. *Geol. Soc. Lond. Spec. Publications* 483 (1), 423–482. doi:10.1144/sp483.16

Blewitt, G., Hammond, W., and Kreemer, C. (2018). Harnessing the GPS Data Explosion for Interdisciplinary Science. *Eos* 99, 485. doi:10.1029/2018EO104623

Bollinger, L., Avouac, J. P., Cattin, R., and Pandey, M. R. (2004). Stress Buildup in the Himalaya. *J. Geophys. Res.* 109 (B11), B11405. doi:10.1029/2003jb002911

Bollinger, L., Perrier, F., Avouac, J.-P., Sapkota, S., Gautam, U., and Tiwari, D. R. (2007). Seasonal Modulation of Seismicity in the Himalaya of Nepal. *Geophys. Res. Lett.* 34 (8), L08304. doi:10.1029/2006gl029192

Bollinger, L., Tapponnier, P., Sapkota, S. N., and Klinger, Y. (2016). Slip Deficit in central Nepal: Omen for a Repeat of the 1344 AD Earthquake?. *Earth, Planets and Space* 68 (1), 12. doi:10.1186/s40623-016-0389-1

Boussinesq, J. (1878). Équilibre D'élasticité D'un Sol Isotrope Sans Pesanteur, Supportant Différents Poids. *CR Math. Acad. Sci. Paris* 86, 1260–1263.

Burtin, A., Bollinger, L., Cattin, R., Vergne, J., and Nábělek, J. L. (2009). Spatiotemporal Sequence of Himalayan Debris Flow from Analysis of High-Frequency Seismic Noise. *J. Geophys. Res.* 114 (F4), 1198. doi:10.1029/2008JF001198

Cappa, F., Rutqvist, J., and Yamamoto, K. (2009). Modeling Crustal Deformation and Rupture Processes Related to Upwelling of Deep CO2-rich Fluids during the 1965-1967 Matsushiro Earthquake Swarm in Japan. *J. Geophys. Res.* 114 (B10), B10304. doi:10.1029/2009jb006398

Chamberlain, C. J., Boese, C. M., and Townend, J. (2017). Cross-correlation-based Detection and Characterisation of Microseismicity Adjacent to the Locked, Late-Interseismic Alpine Fault, South Westland, New Zealand. *Earth Planet. Sci. Lett.* 457, 63–72. doi:10.1016/j.epsl.2016.09.061

Chanard, K., Avouac, J. P., Ramillien, G., and Genrich, J. (2014). Modeling Deformation Induced by Seasonal Variations of continental Water in the Himalaya Region: Sensitivity to Earth Elastic Structure. *J. Geophys. Res. Solid Earth* 119 (6), 5097–5113. doi:10.1002/2013jb010451

Chanard, K., Fleitout, L., Calais, E., Rebischung, P., and Avouac, J. P. (2018). Toward a Global Horizontal and Vertical Elastic Load Deformation Model Derived from GRACE and GNSS Station Position Time Series. *J. Geophys. Res. Solid Earth* 123 (4), 3225–3237. doi:10.1002/2017jb015245

Chiodini, G., Cardellini, C., Di Luccio, F., Selva, J., Frondini, F., Caliro, S., et al. (2020). Correlation between Tectonic CO_2 Earth Degassing and Seismicity Is Revealed by a 10-year Record in the Apennines. *Italy. Sci. Adv.* 6, eabc2938. doi:10.1126/sciadv.abc2938

Colchen, M., LeFort, P., and Pêcher, A. (1986). *Recherches géologiques dans l'Himalaya du Népal*. Paris: CNRS.

De Barros, L., Baques, M., Godano, M., Helmstetter, A., Deschamps, A., Larroque, C., et al. (2019). Fluid-Induced Swarms and Coseismic Stress Transfer: A Dual Process Highlighted in the Aftershock Sequence of the 7 April 2014 Earthquake (Ml 4.8, Ubaye, France). *J. Geophys. Res. Solid Earth* 124 (4), 3918–3932. doi:10.1029/2018jb017226

Duverger, C., Godano, M., Bernard, P., Lyon-Caen, H., and Lambotte, S. (2015). The 2003-2004 Seismic Swarm in the Western Corinth Rift: Evidence for a Multiscale Pore Pressure Diffusion Process along a Permeable Fault System. *Geophys. Res. Lett.* 42 (18), 7374–7382. doi:10.1002/2015gl065298

Elliott, J. R., Jolivet, R., González, P. J., Avouac, J.-P., Hollingsworth, J., Searle, M. P., et al. (2016). Himalayan Megathrust Geometry and Relation to Topography Revealed by the Gorkha Earthquake. *Nat. Geosci.* 9 (2), 174–180. doi:10.1038/ngeo2623

Galetzka, J., Melgar, D., Genrich, J. F., Geng, J., Owen, S., Lindsey, E. O., et al. (2015). Slip Pulse and Resonance of the Kathmandu basin during the 2015 Gorkha Earthquake, Nepal. *Science* 349 (6252), 1091–1095. doi:10.1126/science.aac6383

Girault, F., Adhikari, L. B., France-Lanord, C., Agrinier, P., Koirala, B. P., Bhattarai, M., et al. (2018). Persistent CO2 Emissions and Hydrothermal Unrest Following the 2015 Earthquake in Nepal. *Nat. Commun.* 9 (1), 2956. doi:10.1038/s41467-018-05138-z

Girault, F., Bollinger, L., Bhattarai, M., Koirala, B. P., France-Lanord, C., Rajaure, S., et al. (2014). Large-scale Organization of Carbon Dioxide Discharge in the Nepal Himalayas. *Geophys. Res. Lett.* 41, 6358–6366. doi:10.1002/2014gl060873

Grandin, R., Vallée, M., Satriano, C., Lacassin, R., Klinger, Y., Simoes, M., et al. (2015). Rupture Process of theMw = 7.9 2015 Gorkha Earthquake (Nepal): Insights into Himalayan Megathrust Segmentation. *Geophys. Res. Lett.* 42 (20), 8373–8382. doi:10.1002/2015gl066044

Gualandi, A., Avouac, J.-P., Galetzka, J., Genrich, J. F., Blewitt, G., Adhikari, L. B., et al. (2017). Pre- and post-seismic Deformation Related to the 2015, Mw7.8 Gorkha Earthquake, Nepal. *Tectonophysics* 714–715, 90–106. doi:10.1016/j.tecto.2016.06.014

Hainzl, S. (2004). Seismicity Patterns of Earthquake Swarms Due to Fluid Intrusion and Stress Triggering. *Geophys. Res. Int.* 159, 1090–1096. doi:10.1111/j.1365-246x.2004.02463.x

Heki, K. (2003). Snow Load and Seasonal Variation of Earthquake Occurrence in Japan. *Earth Planet. Sci. Lett.* 207 (1–4), 159–164. doi:10.1016/s0012-821x(02)01148-2

Hoste-Colomer, R., Bollinger, L., Lyon-Caen, H., Adhikari, L. B., Baillard, C., Benoit, A., et al. (2018). Lateral Variations of the Midcrustal Seismicity in Western Nepal: Seismotectonic Implications. *Earth Planet. Sci. Lett.* 504, 115–125. doi:10.1016/j.epsl.2018.09.041

Hoste-Colomer, R., Bollinger, L., Lyon-Caen, H., Burtin, A., and Adhikari, L. B. (2017). Lateral Structure Variations and Transient Swarm Revealed by Seismicity along the Main Himalayan Thrust north of Kathmandu. *Tectonophysics* 714–715, 107–116. doi:10.1016/j.tecto.2016.10.004

Ingebritsen, S. E., Shelly, D. R., Hsieh, P. A., Clor, L. E., Seward, P. H., and Evans, W. C. (2015). Hydrothermal Response to a Volcano-Tectonic Earthquake Swarm, Lassen, California. *Geophys. Res. Lett.* 42, 9223–9230. doi:10.1002/2015gl065826

Ingleby, T., Wright, T. J., Hooper, A., Craig, T. J., and Elliott, J. R. (2020). Constraints on the Geometry and Frictional Properties of the Main Himalayan Thrust Using Coseismic, Postseismic, and Interseismic Deformation in Nepal. *J. Geophys. Res. Solid Earth* 125 (2), e2019JB019201. doi:10.1029/2019jb019201

Jiang, G., Wang, Y., Wen, Y., Liu, Y., Xu, C., and Xu, C. (2019). Afterslip Evolution on the Crustal Ramp of the Main Himalayan Thrust Fault Following the 2015 Mw 7.8 Gorkha (Nepal) Earthquake. *Tectonophysics* 758, 29–43. doi:10.1016/j.tecto.2019.03.005

Jouanne, F., Gajurel, A., Mugnier, J.-L., Bollinger, L., Adhikari, L. B., Koirala, B., et al. (2019). Postseismic Deformation Following the April 25, 2015 Gorkha Earthquake (Nepal): Afterslip versus Viscous Relaxation. *J. Asian Earth Sci.* 176, 105–119. doi:10.1016/j.jseaes.2019.02.009

Kraft, T., Wassermann, J., Schmedes, E., and Igel, H. (2006). Meteorological Triggering of Earthquake Swarms at Mt. Hochstaufen, SE-Germany. *Tectonophysics* 424 (3–4), 245–258. doi:10.1016/j.tecto.2006.03.044

Larochelle, S., Gualandi, A., Chanard, K., and Avouac, J. P. (2018). Identification and Extraction of Seasonal Geodetic Signals Due to Surface Load Variations. *J. Geophys. Res. Solid Earth* 123 (12), 11–31. doi:10.1029/2018jb016607

Lindsey, E. O., Almeida, R., Mallick, R., Hubbard, J., Bradley, K., Tsang, L. L. H., et al. (2018). Structural Control on Downdip Locking Extent of the Himalayan Megathrust. *J. Geophys. Res. Solid Earth* 123 (6), 5265–5278. doi:10.1029/2018jb015868

Liu-Zeng, J., Zhang, Z., Rollins, C., Gualandi, A., Avouac, J. P., Shi, H., et al. (2020). Postseismic Deformation Following the 2015 Mw7. 8 Gorkha (Nepal) Earthquake: New GPS Data, Kinematic and Dynamic Models, and the Roles of Afterslip and Viscoelastic Relaxation. *J. Geophys. Res. Solid Earth* 125 (9), e2020JB019852. doi:10.1029/2020JB019852

Lohman, R. B., and McGuire, J. J. (2007). Earthquake Swarms Driven by Aseismic Creep in the Salton Trough, California. *J. Geophys. Res. Solid Earth* 112 (B4), jb004596. doi:10.1029/2006jb004596

Mencin, D., Bendick, R., Upreti, B. N., Adhikari, D. P., Gajurel, A. P., Bhattarai, R. R., et al. (2016). Himalayan Strain Reservoir Inferred from Limited Afterslip Following the Gorkha Earthquake. *Nat. Geosci.* 9 (7), 533–537. doi:10.1038/ngeo2734

Mendoza, M. M., Ghosh, A., Karplus, M. S., Klemperer, S. L., Sapkota, S. N., Adhikari, L. B., et al. (2019). Duplex in the Main Himalayan Thrust Illuminated by Aftershocks of the 2015 Mw 7.8 Gorkha Earthquake. *Nat. Geosci.* 12 (12), 1018–1022. doi:10.1038/s41561-019-0474-8

Mendoza, M. M., Ghosh, A., and Rai, S. S. (2016). Dynamic Triggering of Small Local Earthquakes in the central Himalaya. *Geophys. Res. Lett.* 43 (18), 9581–9587. doi:10.1002/2016gl069969

Miller, S. A., Collettini, C., Chiaraluce, L., Cocco, M., Barchi, M., and Kaus, B. J. P. (2004). Aftershocks Driven by a High-Pressure CO2 Source at Depth. *Nature* 427 (6976), 724–727. doi:10.1038/nature02251

Murru, M., Montuori, C., Wyss, M., and Privitera, E. (1999). The Locations of Magma chambers at Mt. Etna, Italy, Mapped Byb-Values. *Geophys. Res. Lett.* 26 (16), 2553–2556. doi:10.1029/1999gl900568

Nabelek, J., Hetényi, G., Vergne, J., Sapkota, S., Kafle, B., Jiang, M., et al. (2009). Underplating in the Himalaya-Tibet Collision Zone Revealed by the Hi-CLIMB experiment. *Science* 325 (5946), 1371–1374. doi:10.1126/science.1167719

Pandey, M. R. (1985). Seismic Model of central and Eastern Lesser Himalaya of Nepal. *J. Geol. Soc. Nepal* 3, 1–11. doi:10.3126/jngs.v3i0.32655

Pandey, M. R., Tandukar, R. P., Avouac, J. P., Lavé, J., and Massot, J. P. (1995). Interseismic Strain Accumulation on the Himalayan Crustal Ramp (Nepal). *Geophys. Res. Lett.* 22 (7), 751–754. doi:10.1029/94gl02971

Pandey, M. R., Tandukar, R. P., Avouac, J. P., Vergne, J., and Heritier, T. (1999). Seismotectonics of the Nepal Himalaya from a Local Seismic Network. *J. Asian Earth Sci.* 17 (5-6), 703–712. doi:10.1016/s1367-9120(99)00034-6

Tian, Z., Freymueller, J. T., and Yang, Z. (2020). Spatio-temporal Variations of Afterslip and Viscoelastic Relaxation Following the Mw 7.8 Gorkha (Nepal) Earthquake. *Earth Planet. Sci. Lett.* 532, 116031. doi:10.1016/j.epsl.2019.116031

Waldhauser, F., and Ellsworth, W. L. (2000). A Double-Difference Earthquake Location Algorithm: Method and Application to the Northern Hayward Fault, California. *Bull. Seismological Soc. America* 90 (6), 1353–1368. doi:10.1785/0120000006

Wang, K., and Fialko, Y. (2018). Observations and Modeling of Coseismic and Postseismic Deformation Due to the 2015 Mw 7.8 Gorkha (Nepal) Earthquake. *J. Geophys. Res. Solid Earth* 123 (1), 761–779. doi:10.1002/2017jb014620

Weinlich, F. H. (2014). Carbon Dioxide Controlled Earthquake Distribution Pattern in the NW Bohemian Swarm Earthquake Region, Western Eger Rift, Czech Republic - Gas Migration in the Crystalline Basement. *Geofluids* 14, 143–159. doi:10.1111/gfl.12058

Yamada, M., Kandel, T., Tamaribuchi, K., and Ghosh, A. (2020). 3D Fault Structure Inferred from a Refined Aftershock Catalog for the 2015 Gorkha Earthquake in Nepal. *Bull. Seismological Soc. America* 110 (1), 26–37. doi:10.1785/0120190075

Zhai, G., Shirzaei, M., Manga, M., and Chen, X. (2019). Pore-pressure Diffusion, Enhanced by Poroelastic Stresses, Controls Induced Seismicity in Oklahoma. *Proc. Natl. Acad. Sci. USA* 116 (33), 16228–16233. doi:10.1073/pnas.1819225116

Zhao, B., Bürgmann, R., Wang, D., Tan, K., Du, R., and Zhang, R. (2017). Dominant Controls of Downdip Afterslip and Viscous Relaxation on the Postseismic Displacements Following the M W 7.9 Gorkha, Nepal, Earthquake. *J. Geophys. Res. Solid Earth* 122 (10), 8376–8401. doi:10.1002/2017jb014366

Conflict of Interest: The authors declare that the research was conducted in the absence of any commercial or financial relationships that could be construed as a potential conflict of interest.

frontiers in Earth Science

ORIGINAL RESEARCH
published: 05 August 2021
doi: 10.3389/feart.2021.689457

Paleoseismological Findings at a New Trench Indicate the 1714 M8.1 Earthquake Ruptured the Main Frontal Thrust Over all the Bhutan Himalaya

Yuqiu Zhao[1], Djordje Grujic[1], Santanu Baruah[2], Dawchu Drukpa[3], Joanne Elkadi[4], György Hetényi[5], Georgina E. King[4], Zoë K. Mildon[6], Nityam Nepal[3] and Caroline Welte[7]*

[1]Department of Earth and Environmental Sciences, Dalhousie University, Halifax, NS, Canada, [2]Geoscience and Technology Division, CSIR-North East Institute of Science and Technology, Jorhat, India, [3]Earthquake and Geophysics Division, Department of Geology and Mines, Thimphu, Bhutan, [4]Institute of Earth Surface Dynamics, University of Lausanne, Lausanne, Switzerland, [5]Institute of Earth Sciences, University of Lausanne, Lausanne, Switzerland, [6]School of Geography, Earth and Environmental Sciences, University of Plymouth, Plymouth, United Kingdom, [7]Department of Earth Sciences, ETH Zurich, Zurich, Switzerland

The 1714 Bhutan earthquake was one of the largest in the Himalaya in the last millennium. We show that the surface rupture caused by this earthquake extended further to the east than previously known, it was at least 175 km long, with slip exceeding 11 m at our study site. The age of the surface rupture was constrained by a combination of radiocarbon and traditional optically stimulated luminescence dating of affected river sediments. Computations using empirical scaling relationships, fitting historical observations and paleoseismic data, yielded a plausible magnitude of Mw 8.1 ± 0.4 and placed the hypocentre of the 1714 Bhutan earthquake on the flat segment of the Main Himalayan Thrust (MHT), the basal décollement of the Himalayan orogen. Calculations of Coulomb stress transfer indicate that great earthquakes along the leading part of the MHT would cause surface rupture. In contrast, distal earthquakes may not immediately trigger surface rupture, although they would increase the stresses in the leading part of the MHT, facilitating future surface-rupturing earthquakes. Frontal earthquakes would also transfer stress into the modern foreland basin facilitating southward propagation of the MHT as a blind basal décollement. In conclusion, studies of surface-rupturing events alone likely underestimate the seismic slip along the Himalayan megathrust.

Keywords: surface rupture, stress transfer, Himalaya, optically stimulated luminescence dating, radiocarbon dating

OPEN ACCESS

Edited by:
Alexander Cruden,
Monash University, Australia

Reviewed by:
R. Jayangonda Perumal,
Wadia Institute of Himalayan Geology, India
Mark Quigley,
The University of Melbourne, Australia

****Correspondence:***
Djordje Grujic
dgrujic@dal.ca

Specialty section:
This article was submitted to Structural Geology and Tectonics, a section of the journal Frontiers in Earth Science

Received: *31 March 2021*
Accepted: *05 July 2021*
Published: *05 August 2021*

Citation:
Zhao Y, Grujic D, Baruah S, Drukpa D, Elkadi J, Hetényi G, King GE, Mildon ZK, Nepal N and Welte C (2021) Paleoseismological Findings at a New Trench Indicate the 1714 M8.1 Earthquake Ruptured the Main Frontal Thrust Over all the Bhutan Himalaya. Front. Earth Sci. 9:689457. doi: 10.3389/feart.2021.689457

INTRODUCTION

Understanding the evolution of convergent tectonic plate systems and determining their role in generating great earthquakes (>magnitude 8; USGS earthquake magnitude classes) requires integrating the record of fault behaviors preserved in fault rocks from all crustal depths with geophysical observations. Mapping and dating surface ruptures allow building earthquake catalog to calculate the slip rates, accumulated slip, and missing slip and thus calculate the seismic hazard and identify modes of propagation of an orogenic wedge into its foreland. Paleoseismic studies in the Himalaya have likely identified most of the great surface-rupturing events during the last 1,000 years. However, their low dating resolution may limit the ability to distinguish a series of events from distinct, much larger events, i.e., great earthquakes spread over decades may appear as a single great

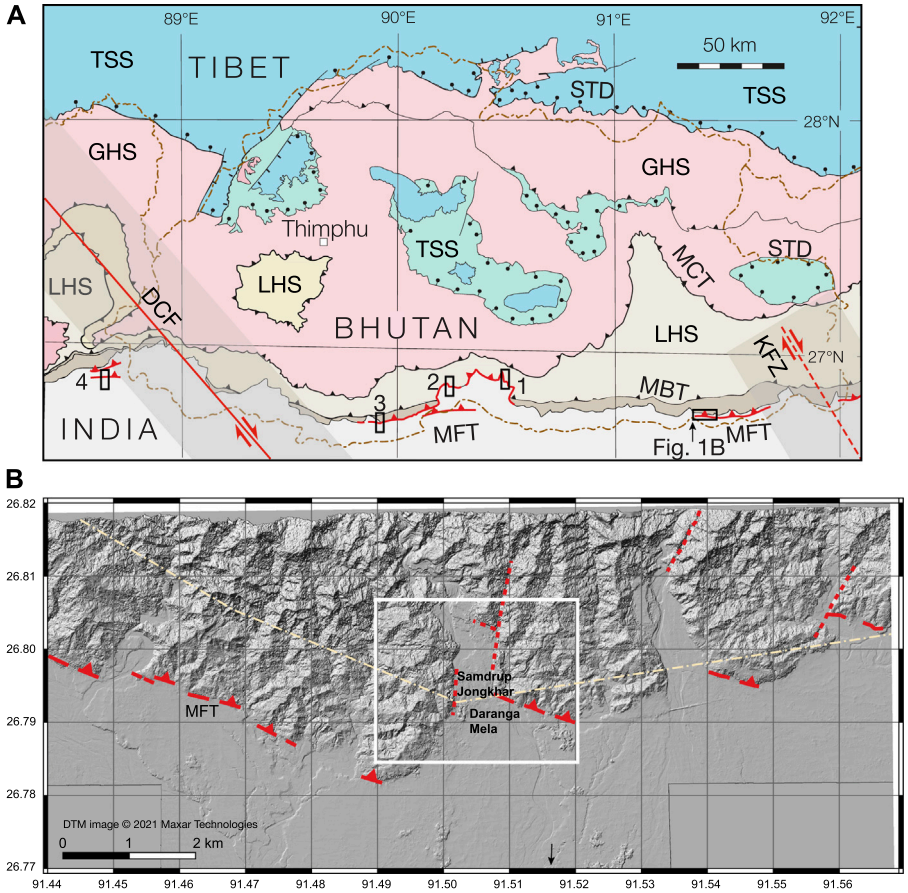

FIGURE 1 | (A) Simplified geology of the Bhutan Himalaya, with the area of Panel **(B)** shown with the black square in the SE corner. Previous paleoseismological studies in the area are indicated with vertical rectangles: **1**: Gelephu (Berthet et al., 2014); **2**: Sarpang (Le Roux-Mallouf et al., 2016); **3**: Piping (Le Roux-Mallouf et al., 2020); **4**: Chalsa (Kumar et al., 2010). STD: South Tibetan Detachment; MCT: Main Central thrust; MBT: Main Boundary Thrust; MFT: Main Frontal Thrust; TSS: Tethyan Sedimentary Sequence; GHS: Greater Himalayan Sequence; LHS: Lesser Himalayan Sequence. **DCF**: Dhubri–Chungthang fault zone (Diehl et al., 2017); **KFZ**: Kopili Fault zone (Sutar et al., 2017). **(B)** Topography of the Himalayan foothills and foreland basin in eastern Bhutan. The Himalayan Frontal Thrust consists of an *en échelon* arrangement of short segments. White square indicates the area of **Figure 2**. The digital terrain model (DTM) with a horizontal resolution of 0.5 m and vertical resolution of 8 m was derived from Maxar stereo pair imagery by Maxar Technologies and further processed using QGIS (v. 3.16.3).

earthquake, or even an M 9 earthquake (e.g., Le Roux-Mallouf et al., 2016). In addition, the low precision of surface rupture length determination causes large errors in the inferred magnitudes.

The segment of the in eastern Bhutan is thought to host a potential slip of more than 10–12 m (Bilham, 2019; Robinson, 2020), the greatest in the Himalayas, implying high seismic hazard (Stevens et al., 2020). Conversely, the Bhutanese Himalaya experience fewer instrumental earthquakes than the central and western Himalayas (Gahalaut et al., 2011; Stevens and Avouac, 2015; Jayangondaperumal et al., 2018). However, this apparent gap in the Himalayan seismic belt may be only an observational gap caused by a lack of permanent seismometers in Bhutan until recent years. The apparent gap on the scale of the seismic cycle also roots in the fact that this region is a relatively less explored part of the Himalayas.

Here we present new information based on new paleoseismological findings in eastern Bhutan, interpreted in terms of possible earthquake location and magnitude that further close the seismic gap. Our results agree with the recent hypothesis of bimodal seismicity along the Main Himalayan Thrust (MHT) (Dal Zilio et al., 2019), which purports that a sequence of blind earthquakes is required to cause a great surface-rupturing event.

MORPHOTECTONIC SETTING

Main Himalayan Thrust and Main Frontal Thrust

The basal décollement of the Himalayan orogen is the MHT, equivalent to a subduction zone megathrust, along which the Indian plate has been underthrusting beneath the Himalayan belt. The Main Frontal Thrust (MFT) is the surface expression of the MHT frontal ramp along the Himalayan orogenic front. The MFT places the Siwalik Group (locally the Lesser Himalayan

Sequence) against Quaternary foreland sediments (**Figure 1A**). The trace of the MHT composite is discontinuous and in West Bengal and Central Bhutan–within large re-entrants–involves at least three traces: one at the topographic break, the Topographic Frontal thrust (TFT), and two outboards of the orogen (Nakata, 1972), seemingly affecting only the sediments of the foreland basin. The intermediate trace is a north-directed back thrust, interpreted as an element of a juvenile triangle zone (Stockmal et al., 2001) at the Himalayan orogenic front (Dasgupta et al., 2013; Chakrabarti Goswami et al., 2019). The southern tip of the MFT in the foreland basin may also be a blind basal décollement with an incipient back thrust (Duvall et al., 2020). Although the first-order trace of the MFT (at the topographic break) appears curved but continuous, detailed maps indicate that the trace consists of segments arranged in a left-stepping *en échelon* geometry (**Figure 1B**). These segments are separated by strike-slip faults, pressure ridges or relay ramps, characteristic of fault growth by linkage extensively investigated in extensional tectonic settings (e.g., Mansfield and Cartwright, 2001).

Thrusting on the MFT began at ~2 Ma in central Nepal (Mugnier et al., 2004; van der Beek et al., 2006) and ~1 Ma in Arunachal Pradesh in NE India (Chirouze et al., 2013); however, the onset of the MFT in Bhutan is still unconstrained (Coutand et al., 2016). The MHT was first imaged in Southern Tibet along the western border of Bhutan (Hauck et al., 1998). The MHT has a ramp-flat-ramp geometry that varies along strike between western and eastern Bhutan (Coutand et al., 2014) but consists of three main segments. The southernmost frontal ramp in eastern Bhutan is north-dipping at 65–70° (Hirschmiller et al., 2014) but flattens toward the surface, which is typical of ruptures along thrust faults because of decreasing lithostatic pressure (e.g., Philip and Meghraoui, 1983; Lee et al., 2001). However, the detailed geometry, which is essential for estimating slip and slip rates, is more complex (Drukpa et al., 2018). The frontal ramp is rooted at ~12 km in the west and ~10 km in the east. The flat middle section dips sub-horizontally by 3–5° to the north. In western Bhutan, this section is 100–110 km wide (Coutand et al., 2014; Diehl et al., 2017). Although the cosmogenic nuclide denudation analyses suggest a wider flat portion (Le Roux-Mallouf et al., 2015), we adopt the former geometry because the data are more mutually consistent. In eastern Bhutan, the flat portion is somewhat narrower at ~95 km (Coutand et al., 2014; Diehl et al., 2017) but is more difficult to constrain (Singer et al., 2017). The northernmost segment of the MHT is a mid-crustal ramp dipping northward at ~30° (Hauck et al., 1998). Smaller ramps have been inferred by cross-section balancing (Long et al., 2012).

The difference in MHT geometry between western and eastern Bhutan is reflected in the variations in coupling along with the detachment. In western and central Bhutan, the width of the fully locked zone on the MHT is reported as ~100 km (Li et al., 2020) to 135–155 km (Marechal et al., 2016). At its northernmost boundary, it is limited by an abrupt down-dip transition, representing an area of interseismic stress build-up according to the seismicity (Diehl et al., 2017). Le Roux-Mallouf et al. (2015) suggested that the wider and gentle coupling zone on the MHT could have greater seismogenic potential in western Bhutan. In eastern Bhutan, the fully coupled zone is narrower (100–120 km) and confined up-dip and down-dip by partial coupling zones (Marechal et al., 2016; Li et al., 2020). GPS data indicate that the up-dip frontal ramp exhibits an aseismic slip rate of 5.5–14.5 mm/a within 50 km north of the MFT (Marechal et al., 2016).

The convergence rates based on GPS measurements in the Sikkim Himalaya are 17.2 ± 1.9 mm/a (Li et al., 2020), which agree with the slip rate of ~18 mm/a measured by Mukul et al. (2018). The estimated convergence rates in western Bhutan and eastern Bhutan are 18.5 ± 1.0 and 16.2 ± 1.5 mm/a, respectively (Li et al., 2020), both of which are similar to the 17 ± 2 mm/a estimated by Marechal et al. (2016). The cumulative deformation values derived from paleoseismic data yield an average slip rate of 24.9 ± 10.4 mm/a along the MFT over the last 2,600 years (Le Roux-Mallouf et al., 2020). Across western Arunachal Pradesh (to the east of Bhutan), the age and geometry of uplifted river terraces indicate a convergence rate of 23 ± 6.2 mm/a (Burgess et al., 2012). The potential discrepancy between the millennial-scale slip rate from geological studies and geodetic estimates suggests that some of the interseismic deformations in Bhutan could be anelastic.

Active Tectonics of Bhutan

The seismotectonic of the Bhutanese Himalaya differ from those in the central Himalaya in the following two aspects:

1) The Bhutanese Himalaya and especially its foreland are bound by two oblique strike-slip zones (the Dhubri–Chungthang fault zone (DCF) in the west, evidently extending beneath the orogen (Diehl et al., 2017) and the Kopili fault zone in the east with a more diffuse and less clear continuation N of the Himalayan front (Sutar et al., 2017). Both fault zones are capable of generating earthquakes with Mw > 7 (ibid.). Both fault zones appear to affect only the Indian basement, that is, the Himalayan crust beneath the MHT (Diehl et al., 2017; Grujic et al., 2018), and define a distinct segment of the orogen in terms of flexure (Hammer et al., 2013; Hetényi et al., 2016).
2) Active deformation of the Indian basement in the Himalayan foreland. The two strike-slip fault zones extend south of the Himalaya and border the Shillong Plateau to the west and east, respectively. The Shillong Plateau is bound to the south by the Dauki fault (Biswas et al., 2007; Clark and Bilham, 2008), which exhibits cumulative displacement of >10 km (Biswas et al., 2007), but no related major earthquakes have been observed or recorded. To the north, the Shillong Plateau is affected by the Oldham fault, which produced an earthquake of 8.15 < Mw < 8.35 in 1897 (England and Bilham, 2015). In contrast to the Dauki fault, the Oldham fault has no mappable displacement, and its surface trace remains elusive (Rajendran et al., 2004).

The 2009 Mw 6.1 earthquake (USGS, 2020) is the only earthquake instrumentally observed in Bhutan with a focal solution compatible with slip along the MHT. All other earthquakes with a reported focal mechanism have been strike-slip or oblique-slip (Drukpa et al., 2006; Diehl et al., 2018). According to paleoseismic investigations, south-central Bhutan has been struck by at least five large earthquakes (E1–E5)

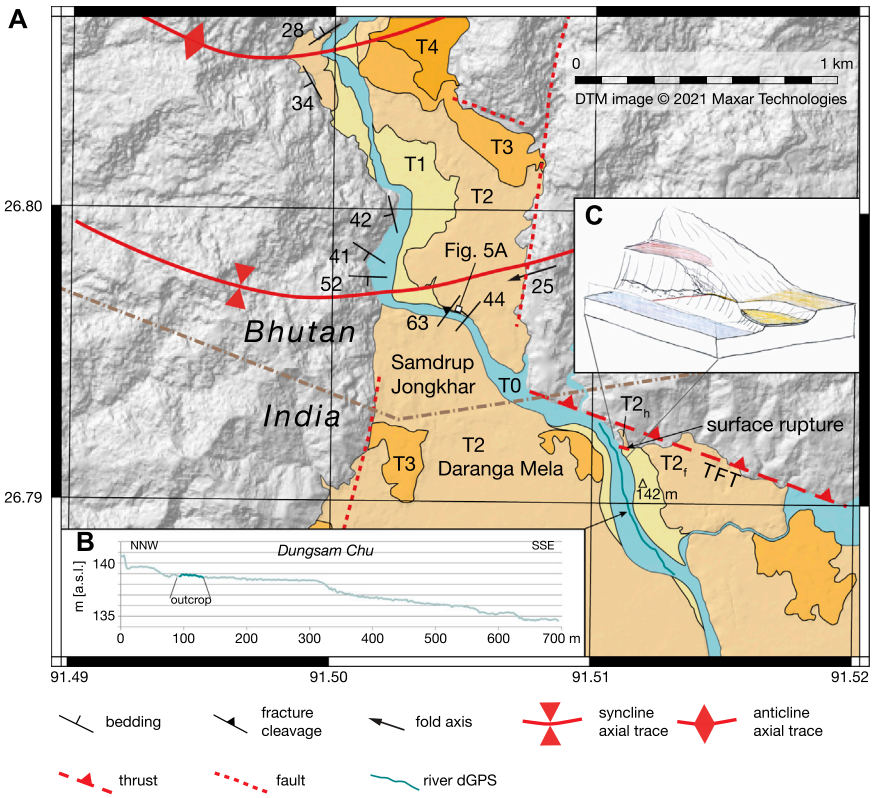

FIGURE 2 | Geomorphic and structural map of the study area. **(A)** The digital terrain model (DTM) with a horizontal resolution of 0.5 m was derived from Maxar stereo pair imagery by Maxar Technologies and further processed using QGIS (v. 3.16.3). The geological observations are from Grujic et al. (2018) and our observations. The river terraces were mapped on the original DTM. **(B)** River profile acquired by the differential GPS. The mapped segment of the river is indicated on the map. **(C)** Draft of the paleoseismic exposure by Luca Malatesta, LM (U of Lausanne, 2019). River terraces T1 and T2 were observed and measured in the field; terrace T2h (hanging wall) in red is inferred to be the same as terrace T2f (footwall) in orange but uplifted by the surface-rupturing earthquake. Point marked 142 is the elevation above sea level in meters and location of the base station for differential GPS survey.

between 485 ± 125 BCE and 1714 CE (Le Roux-Mallouf et al., 2020).

E1: Historically, the most recent earthquake that provoked massive destruction in the region was the 1714 CE earthquake, previously described by Ambraseys and Jackson (2003) as the 1713 CE earthquake with an epicentre in Arunachal Pradesh. By combining more recently identified historical and palaeoseismic constraints (Hetényi et al., 2016), determined that this earthquake occurred on May 4, 1714 and reached Mw 7.5–8.5 with a modeled hypocentre located in central or western Bhutan. E1 was possibly observed by palaeoseismic studies (**Figure 1A**) at the Piping site (Le Roux-Mallouf et al., 2020), Sarpang, and Gelephu (Berthet et al., 2014; Le Roux-Mallouf et al., 2016). This faulting event caused 1.5 ± 0.5 m of coseismic dip-slip at the Piping site and up to 0.5 m of vertical offset in Sarpang.

E2: This is the largest known seismic event observed in Bhutan. At the Piping site, it was dated to between 1204 CE and 1464 CE, 1344 ± 130 CE (Le Roux-Mallouf et al., 2020), and between 1140 CE and 1520 CE (Le Roux-Mallouf et al., 2016). This event was associated with 12.2 ± 2.8 m of coseismic dip-slip, an Mw > 8.5 earthquake at the Piping site (Le Roux-Mallouf et al., 2020), and 16–23 m of coseismic surface slip with an inferred Mw of ~8.7 (Le Roux-Mallouf et al., 2016).

Events E3, E4, and E5, observed at the Piping site, occurred at 300 ± 70 CE, 100 ± 160 CE, and 485 ± 125 BCE, respectively (Le Roux-Mallouf et al., 2020). All five events provide an average recurrence interval of 550 ± 211 years and a cumulative slip of 40.4 ± 10.8 m of slip (E2+E3+E4) (Le Roux-Mallouf et al., 2020).

MATERIALS AND METHODS

Field Investigation

The new study site is located between Samdrup Jongkhar (SE Bhutan) and Daranga Mela (N Assam, India) along the left bank of Dungsam Chu (**Figure 2**), which is a tributary of the Pagaldiya River that flows southwards to the Brahmaputra (**Figure 1B**). Geomorphic analyses were performed using transects acquired by differential GPS and landscape analysis of a digital terrain model (DTM) with a horizontal resolution of 0.5 m.

Sample Collection

To constrain the burial ages of the faulted units, we collected pairs of radiocarbon and optically stimulated luminescence (OSL) samples from seven locations (**Tables 1**, **2**).

TABLE 1 | Results of AMS analysis on samples selected from organic-rich layers and the total organic carbon (TOC) content of various fractions of sediments. BP = before present (before 1950 AD). F14C is the concentration measured in the sample, corrected for fractionation, and normalized to the 1950 value and the corresponding 14C age. δC13 is a value measured on graphite and can include additional fractionation. C/N ratio is an atomic ratio (C/N) × (14/12). The mass C is the final carbon content of the sample. Calibration was performed using the OxCal calibration with the INTCAL20 calibration curve (Reimer et al., 2020). The samples with $F^{14}C > 1$ indicate the post-1950 source of carbon (modern). The corresponding calendar ages were obtained using Bomb Peak ^{14}C data (Hua et al., 2013; Levin et al., 2013) and the online calibration software http://calib.org/CALIBomb/.

Unit	Material	Sample code	Sample Nr. ETH-#	C^{14} age BP	± 1σ	$F^{14}C$	±1σ	$\delta^{13}C$ ‰	± 1σ	C mg	C/N	Calibrated ranges (95.4 % conf. level) CE, -BCE	
T1-soil 0	charcoal	1-1	90350	–926	21	1.1222	0.0030	–28.7	1	1.00		1994	1996
T1-soil 1	charcoal	1-2	90351	–3326	33	1.5129	0.0062	–35.3	1	0.18	88.54	1970	1972
T1-soil 3	charcoal	1-3	90352	36	22	0.9956	0.0027	–25.0	1	0.99	111.38	1697	1911
CW1-sand	charcoal	19-10c	101046	7376	61	0.3992	0.0030	–19.0	1	0.46	1.70	–6386	–6082
CW1-sand	charcoal	2-2	90354	>50,000		0.0019	0.0001	–21.1	1	0.99	48.78		
CW1-sand	pollen	19-10p	115685.1.2	7520	25	0.3921	0.0013	–23.0	1	0.531		–6443	–6262
T2h-U1	charcoal	18-1	101038	383	22	0.9534	0.0026	–26.7	1	0.99	140.09	1449	1623
T2f-U1	macrofossil	2f-0	90353	4246	40	0.588	0.0030	–30.9	1	0.20	110.17	–2923	–2674
T2f-U1	pollen	2f-1p	115686.1.2	14215	40	0.1704	0.0009	–21.5	1	0.585		–15450	–15148
T2f-U1	pollen	2f-2p	115687.1.2	19870	60	0.0843	0.0007	–22.6	1	0.698		–22139	–21819
T2f-U1	charcoal	2f-3	90357	3082	74	0.6814	0.0063	–27.2	1	0.05		–1501	–1126
T2f-U1	charcoal	18-4	101040	–123	21	1.0154	0.0027	–29.9	1	0.83	18.40	1955	1957
T2f-U3	undefined	19-2	101042	–177	21	1.0223	0.0027	–29.5	1	0.86	40.92	1955	1957

TABLE 2 | Conventional OSL dating from the Dungsam Chu site. Results of OSL analysis on samples. The input variables for individual samples used for dose rate and age calculations are listed in **Supplementary Table S1**.

Sample	Equivalent dose (Gy)	No. of aliquots	Dose rate (Gy/ka)				Age (ka)
			β	γ	Cosmic	Total	
T1-1	1.02 ± 0.20	43	0.943 ± 0.034	0.740 ± 0.025	0.215 ± 0.021	1.897 ± 0.047	0.540 ± 0.105
T1-2	4.16 ± 0.78	25	1.349 ± 0.051	1.093 ± 0.036	0.203 ± 0.020	2.644 ± 0.066	1.57 ± 0.30
T2H-1	1.05 ± 0.15	38	1.358 ± 0.059	1.159 ± 0.046	0.209 ± 0.021	2.725 ± 0.078	0.385 ± 0.055
T2F-1	1.39 ± 0.26	30	1.576 ± 0.096	1.247 ± 0.068	0.129 ± 0.013	2.951 ± 0.119	0.47 ± 0.09
T2F-2	8.31 ± 0.79	34	1.571 ± 0.133	1.306 ± 0.101	0.179 ± 0.018	3.056 ± 0.168	2.72 ± 0.30
T2F-3	9.65 ± 0.37	33	1.455 ± 0.124	1.231 ± 0.095	0.158 ± 0.016	2.844 ± 0.157	3.39 ± 0.23
T2F-4	15.89 ± 2.83	26	1.683 ± 0.092	1.478 ± 0.074	0.145 ± 0.015	3.306 ± 0.119	4.81 ± 0.87
T2F-5	16.60 ± 1.82	29	0.995 ± 0.038	0.810 ± 0.026	0.140 ± 0.014	1.945 ± 0.048	8.53 ± 0.96

Note: F – footwall and H – hanging wall.

Radiocarbon Dating

Twenty-one samples were selected for radiocarbon analysis of the MFT exposure, including six fluvial deposits and two colluvial wedge samples. Three of the six fluvial deposit samples originated from terrace T1, with all others taken from terrace T2. Datable materials discovered in the samples included charcoal, bulk sediments (grain-size < 125 μm), and isolated plant and animal microfossils such as pollen, seeds, and insect shells. Physical and chemical pre-treatments were performed to isolate the samples from the surrounding matrix and remove post-depositional contaminants (Bronk Ramsey, 2008; Hajdas, 2008). Physical pre-treatments were performed at Dalhousie University (Canada), whereas chemical treatments were performed at the ETH accelerator facility in Zurich (Switzerland). The procedure for physical cleaning and inspection involved 1) manual picking with tweezers after visual examination of large pieces of organic matter; 2) flotation using deionized water accompanied by an ultrasonic bath to separate large pieces from the surrounding matrix; 3) drying below 60°C in an oven for 12–24 h after flotation; and 4) sieving for bulk sediments < 125 μm, following microscopic observations of the carbon content. To avoid contamination, acid-base-acid (ABA) treatment was applied at 60°C to remove the contamination caused by carbonates and humic acids, as follows: 1) initial acid treatment washed carbonates away from the sample surfaces using 0.5 M HCl solution, followed by sample rinsing with deionized water; 2) a base wash using 0.1 M NaOH solution removed humic acids, which was also followed by sample rinsing with deionized water; 3) a weak acid solution (0.1 M HCl) removed carbonates dissolved during previous pre-treatments. The ABA treatment ended with a final rinsing with deionized water. For pollen dating 400 μL aliquots of the samples and of three processing blanks were transferred to glass vials and freeze-dried. About 1.5 mg dried material was wrapped in cleaned Al capsules (Welte et al., 2018) and converted to

graphite (Wacker et al., 2010b). Accelerator mass spectrometry (AMS) was performed at the Laboratory of Ion Beam Physics, ETH Zurich, Switzerland (Wacker et al., 2010a).

$F^{14}C$ represents the concentration of ^{14}C measured in the samples normalized and corrected for fractionation ($\delta^{13}C$). Conventional radiocarbon ages were calculated using Libby's half-life for ^{14}C (Stuiver and Polach, 1977; Reimer et al., 2004). The $\delta^{13}C$ values used for the correction of $F^{14}C$ (Reimer et al., 2004) were measured on graphite samples. Radiocarbon dates were calibrated using OxCal V4.4 (Bronk Ramsey, 2017) and the atmospheric calibration curve IntCal20 (Reimer et al., 2020), with a 95.4% confidence interval for 2σ error.

Optically Stimulated Luminescence Dating

Nine samples were dated by OSL, including eight overbank fluvial deposits and one colluvial wedge sample. Samples were prepared under subdued red-light conditions at Dalhousie University and the University of Lausanne using the following standard methods: sieving to isolate the 150–250 μm grain-size, removal of magnetic minerals using a hand-magnet, chemical treatment to remove carbonates and organic material, and density separation to isolate the quartz-rich mineral fractions. The quartz-rich fraction was purified by HF etching for 60 min using 40% HF.

Quartz OSL measurements were performed using a single aliquot regenerative dose protocol (Murray and Wintle, 2000) with three Risø TL-DA-20 readers and dose rates ranging from 0.089 to 0.24 s^{-1}. Small aliquots of 2 mm diameter were measured. A preheat (and cut heat) temperature of 270°C was used, as well as a high-temperature optical wash at the end of each measurement cycle. The selected measurement conditions were validated using preheat plateau tests and successful dose recovery. An IR-depletion test was used to screen all aliquots for feldspar contamination (Duller, 2008).

Data were accepted using the following criteria: a recycling ratio within 10% of unity, an IR-depletion test within 10% of unity, a maximum test dose error of <10%, and recuperation of <10% of the natural signal. At least 25 D_e values were accepted for each of the measured samples. Overdispersion values (Galbraith et al., 1999) were calculated using the Luminescence package in RStudio (Kreutzer et al., 2016), which yielded values in excess of 20% for almost all samples (**Supplementary Figure S2**). For this reason, the three-component minimum age model was applied with an assumed overdispersion σ_b = 0.2 (see Supplementary material for details).

Sample radionuclide concentrations were determined using inductively coupled plasma mass spectrometry (ICP-MS). Environmental dose rates were calculated using DRAC v.1.2 (Durcan et al., 2015) and the conversion factors of (Guérin et al., 2011), the alpha grain-size attenuation factors of (Brennan et al., 1991), the beta grain-size attenuation factors of (Guérin et al., 2012) and the etch depth attenuation factors of Bell (1979) assuming an etch depth of 8 μm.

RESULTS

Geomorphology of the Study Area

The MFT, i.e., the TFT, crosses the Dungsam Chu at 26.79194°N, 91.51085°E. Despite large vertical displacement along the MFT, the talweg is flat along a stretch of ~240 m. Fifty meters upstream of the MFT trace is a 1-m-high knickpoint. A 1.5-m-high knickpoint is located ~180 m downstream, from which the river flows south at ~0.5° (**Figure 2B**), indicating that the coseismic knickpoint migrated upstream and was rapidly eroded, as observed in recent earthquakes (Liu and Yang, 2015). Such a rapid channel response is compatible with a high sediment supply and discharge. The rate of channel adjustment depends on the erodibility of the boundary, river discharge, slope, and sediment supply rate (e.g., Whipple and Tucker, 1999; Lague, 2014).

The MFT separates the flat, mostly undeformed, recent to active deposits of the alluvial plain to the south from alluvial terraces deposited by the Dungsam Chu over the Siwalik Group. These terraces are composed of well-stratified cobbles to boulders (the dominant lithologies are quartzite and slate from the Lesser Himalayan Sequence) within a sandy matrix. The lower (younger) terraces (T1, T2) are located along the present stream at low elevations, ~3.5 and ~9 m above the present stream, respectively. T2 is a fill terrace on which T1 formed as a cut-in-fill terrace. The intermediate terrace (T3) is strongly dissected by natural and anthropogenic processes. Alternatively, it could be interpreted as remnants of an alluvial fan. T4 was mapped only locally upstream of Dungsam Chu. T3 and T4 were identified from the DTM and were not observed in the field.

MFT Exposure

The natural river-cut exposure of the MFT was straightened and refreshed with a backhoe (**Supplementary Figure S1**). The orthorectified photomosaic of the outcrop (**Figure 3**) was constructed using Agisoft Metashape software. Because the MFT has a strike of 110° and the outcrop strikes 150°, the outcrop log (**Figure 4**) is a projection of the photomosaic perpendicular to the fault strike and parallel to the slickenlines observed in the fault gouge.

The MFT trace is discontinuous and consists of segments arranged *en échelon* and offset by N-S striking to NNE-SSW striking faults observed in the field and mapped on the DTM. For comparison, in central Bhutan, the TFT strikes 102–104° (Le Roux-Mallouf et al., 2016; Le Roux-Mallouf et al., 2020). In the center of Samdrup Jongkhar, in a small river-cut since walled over, the Siwalik bedding is strongly overprinted by pervasive fracture cleavage, suggesting top down to the west movement (**Figure 5A**). The fracture cleavage has the same orientation as the N-S striking faults between the MFT segments (**Figure 2**).

In the cross-section, the MFT is straight and simple, dipping approximately 24° to the north. The footwall block consists of the ~8-m-thick T2, containing four irregular interbedded sandstone and conglomerate units with sharp boundaries,

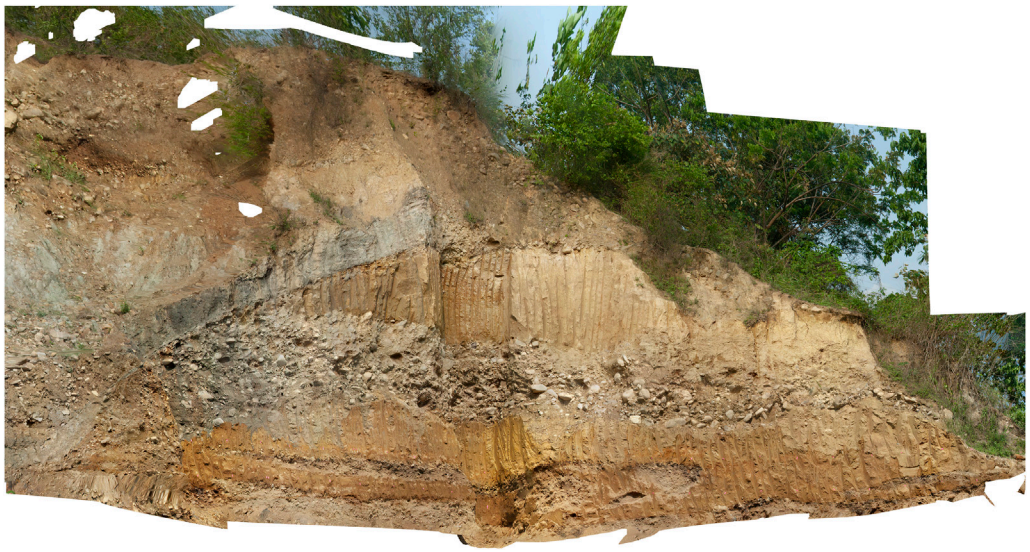

FIGURE 3 | The orthorectified photomosaic of the outcrop (see also the associated **Supplementary Video S1**) was constructed with Agisoft Metashape software using 136 field photographs. The MFT, i.e., the TFT, crosses the Dungsam Chu at 26.79194°N, 91.51085°E.

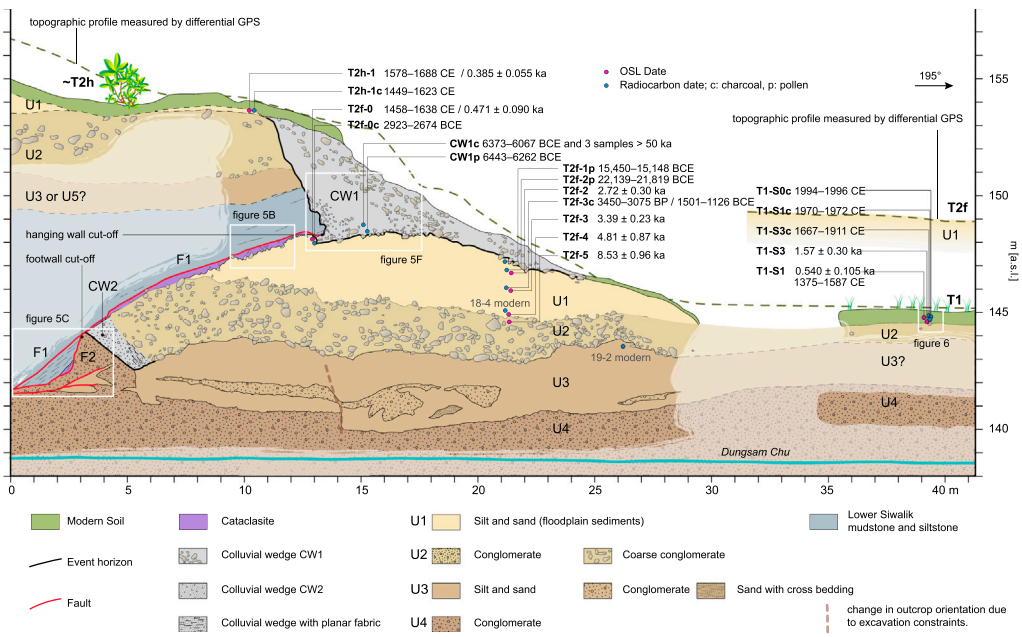

FIGURE 4 | Detailed map of the Dungsam Chu palaeoseismic exposure. This map is a projection of the photomosaic (**Figure 3**) into the kinematic plane, perpendicular to the trace of the fault and parallel to the slickenlines observed along the clay smears within the F1 surface. The map was constructed by observations on the photomosaic, individual photographs, and by field observations. The topographic profile, including the surface of T1 and T2f to the south of the MFT trace, were measured by a dGPS. The dGPS measurements were made along the slope, away from the cliff edge, and are slightly higher. The topographic profile and T2f were projected onto the map of the exposure. The Dungsam Chu bed is also measured by the dGPS (darker blue segment on **Figure 2B**). Faded colors indicate a lack of exposure.

labeled U4, U3, U2, and U1 from oldest to youngest (**Figure 4**). Unit U4 is a clast-supported fluvial conglomerate composed of poorly sorted and poorly rounded granules, pebbles, and cobbles in a sandy matrix (**Supplementary Figure S3A**). The sandy matrix is overprinted by oxidation and local concentrations of manganese oxide. The base of U4 is currently below the water table, so it could not be logged. Unit U3 overlying Unit U4 is a silt to medium sand-sized fluvial deposit ~1.5–3.0 m thick, which includes

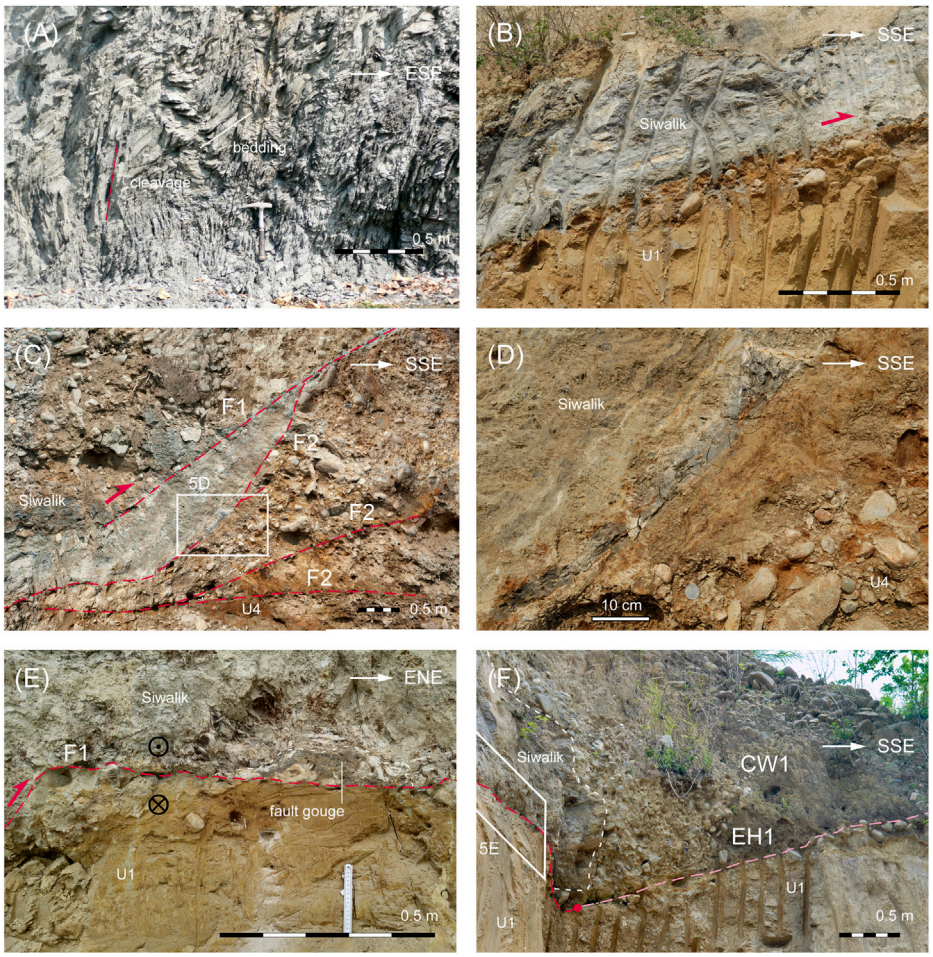

FIGURE 5 | Field photographs of characteristic structures at the Dungsam Chu MFT exposure. **(A)** Moderately west-dipping Siwaliks siltstone layering strongly overprinted by steeper fracture cleavage indicating top down to the west faulting. Location in the center of Samdrup Jongkhar indicated in **Figure 2**. **(B)** F1 separating Siwaliks in the hanging wall and the U1 of terrace 2. Notice the layer of pebbles dragged up from lower stratigraphic levels. **(C)** Bottom of the north end of the paleoseismic exposure indicating branching of older faults F2 cut-off by the most recent fault F1. Between F1 and upper F2 is a lens of cataclasite. **(D)** Close up of Panel 5**(C)** showing the cataclasite, which is derived both from Siwalik and T2 lithologies. Coin for the scale is in the middle bottom of the photograph. **(E)** Tip of the F1 fault, looking NNW. In the hanging wall, there is a lens of cataclasite, probably derived from Siwalik sediments, it the footwall, there are few pebbles as in Panel 5**(B)**. **(F)** Colluvial wedge 1. Showing the tip of the F1 fault (circle), the leading edge of the Siwalik in the hanging wall (white dashed line), and the Event Horizon 1 (pale pink line). Location of the photograph in Panel 5**(D)** is on the left side.

~20–80-cm-thick lenses of granular or pebble conglomerates and lenses of coarse sand with cross bedding (**Supplementary Figures S3A–D**). Unit U2 is an ~1.8–3.0-m-thick, poorly sorted, and well-rounded pebble-cobble-boulder conglomerate with a sandy matrix. Unit U2 is distinguished from unit U4 by a generally larger clast size and a lesser degree of orange coloration due to oxidation. The topmost unit U1 is the youngest in the footwall, measuring up to 2.2 m thick, consisting of sandy to silty fluvial deposits. U4 is finer in grain-size and lighter in color than unit U2.

The cut-in-fill terrace T1 exposed to the south of the palaeoseismic exposure is ~65 cm thick, comprising organic material-rich soil that caps the pebble-to-boulder gravel layer U2 (**Figure 6**). The T1 shows likely four soil profiles, mainly consisting of soil horizons A and B. The uppermost and lowermost soil profiles exhibit a clear sequence of local soil with horizons A, Bt (showing clay accumulation in the form of coatings on ped surfaces or in pores), and B. The middle soil profiles display white leached clay or clayey silt clasts identified as Ae1 in the top section, overlying a weakly developed Bw1 horizon and a possible fluvial sand deposit C1 horizon that buried a soil simply including horizons A2 and Bt2. The presence of Ae1, Bw1, and C1 indicates no erosion but still lots of water to leach the sediments in the middle layer. Considering all the age constraints in T1, the middle soil profile with horizons Ae1, Bw1, and C1 might be influenced seismically, and the lowermost soil may be formed pre-seismically. Based on the overlying C1 having an older burial age than the underlying buried soil, an alternative interpretation would be a possible earthquake-induced injected sand in the middle section instead of C1, even though the OSL burial ages calculated using the minimum age model (MAM)

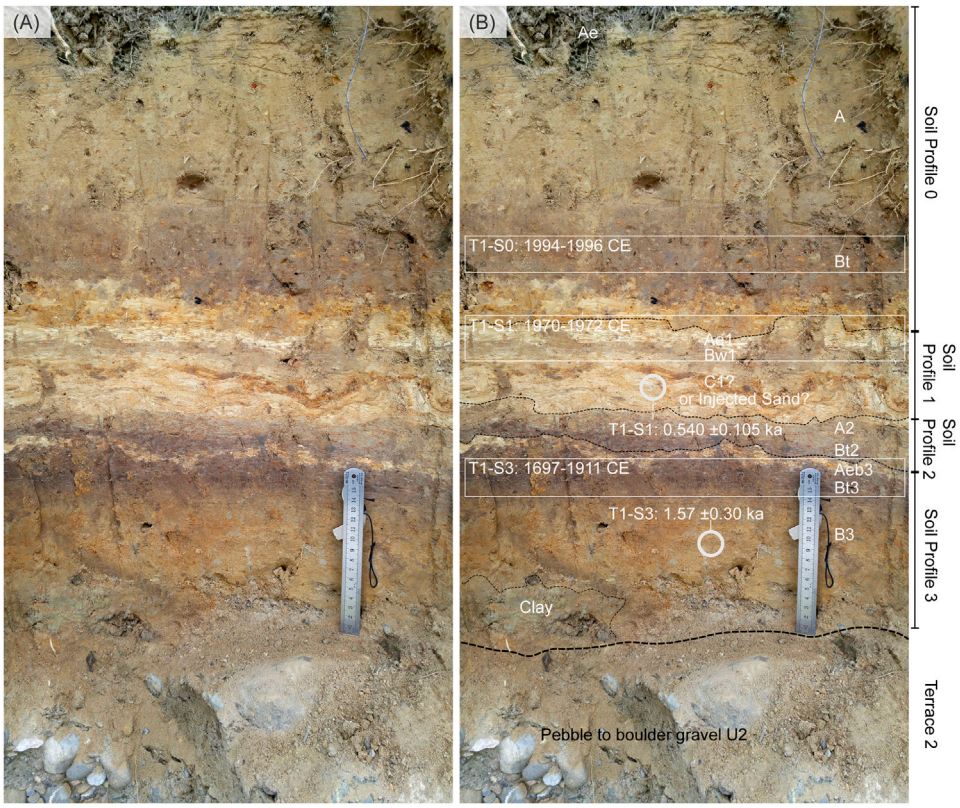

FIGURE 6 | Terrace 1 at the southern end of the palaeoseismic exposure (**Figure 4**). **(A)** original photograph, **(B)** interpreted photograph. Terrace 1 is interpreted as a cut-in-fill terrace on top of layer U2 of Terrace 2. Material for radiocarbon dating was collected along horizons indicated with white rectangles. The deposits of T1 are interpreted as overbank deposits being converted to modern soil. The injected sand layer was interpreted based on the age distribution and photograph analysis (see main text for alternative interpretations).

might be still overestimated due to incompletely bleached grains in the samples. However, no other injection features were exposed to confirm this alternative.

The hanging wall block of the MFT consists of dark gray mudstone and siltstone layers of Unit 1 of the Siwalik Group (Coutand et al., 2016). These deposits represent different parts of a river-dominated deltaic system, developed in either a lacustrine or marine environment (Coutand et al., 2016). This outcrop is separated by faults and gaps in exposure from the continuous, 2,200-m-thick sedimentary section of the Siwalik Group that was deposited between ~7 and 1 Ma (Coutand et al., 2016); therefore, we could not determine the depositional age at this outcrop. Late Miocene Siwalik sediments are discordantly overlain by the ~2.5-m-thick T2, which includes three layers of interbedded sandstone and conglomerate (**Figure 4**). Sandstone lies over an evident erosion and weathering surface, pelma (Schirmer, 2020) that cuts through the Siwalik north-dipping stratigraphy. Soil horizon A was observed at the top of the hanging wall block. Except for modern soil, there were no continuous deposits over the fault trace.

We interpret CW1 and CW2 as two scarp-derived colluvial wedge units deposited during or shortly after coseismic displacement along with F1 and F2, respectively (**Figure 4**). The tip of F2 was sealed by CW2 during the earlier coseismic event, E2. Unit CW2 comprises pebbles in a dark sandy matrix with rare cobbles and caps the tops of the uppermost and middle F2 splays (**Figure 5C**), which is presumably derived from units U1 and U2 and contemporary soil. Unit CW1 originates from T2 and soil in the hanging wall and consists of cobble layers on the south side of the triangular unit, coarse sand in the middle, pebble layers on the north side, and a sandy matrix (**Figure 5E**).

Two events were identified: the most recent event, E1, and the penultimate event, E2. Pebbles dragged by E1 adorn the top of the footwall block (**Figure 5B**). Cataclasite is present between the two F2 splays and at the tip of F1 **Figures 4C,D**. The two tips of the surface ruptures (**Figure 4**) formed during the respective seismic events indicate that the throw of the last event was approximately 4.5 m, i.e., 10.5 ± 0.5 m of coseismic slip was produced during E1. Retrodeforming the E1 slip along the MFT places the terrace on the hanging wall of the MFT at the same level as the event horizon 1 and the top of the terrace T2 (**Figure 7**). Because only one cut-off line is visible for E2, we propose a minimum vertical displacement of 3 m for E2.

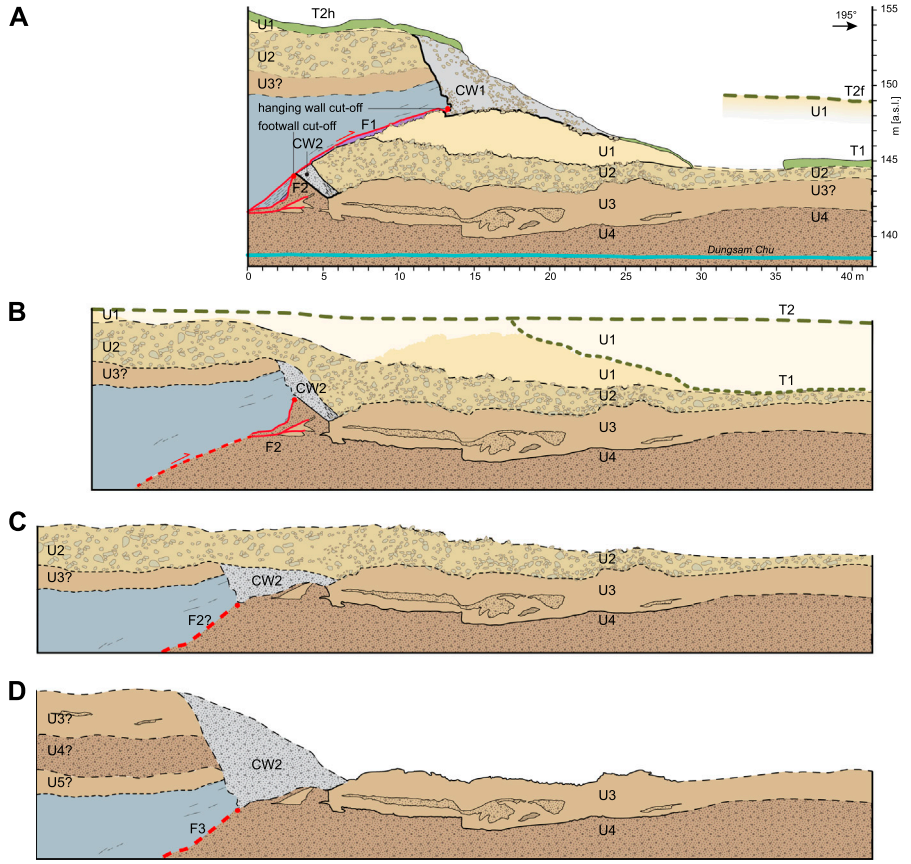

FIGURE 7 | Retrodeformed section. **(A)** Current situation. **(B)** Pre 1714, this is a conservative restoration in which the inferred cut-off lines (**Figure 4**) were placed together. No other adjustments were made. Notice that the top of the hanging wall is restored to the same level as the current top of the terrace 2. Lateral variations of layer thicknesses are interpreted as a common feature of alluvial deposits and the result of the incision of terrace 1 into terrace 2. Notice the steepening of the F2, similar to the phenomenon observed by Le Roux-Mallouf et al. (2020). Indicated is the maximum northward extent of the cut in terrace T1. Tapering of U1 deposits is due either to their overlapping an older fill-cut terrace or more likely a minor displacement of U2 by F2 **(C)** Retroderformed section at the end of the deposition of U2, before the minor event F2. **(D)** Section after the event along the F3 and after the formation of the related colluvial wedge.

AMS ^{14}C and OSL Dating Results

Table 1 summarizes the results of the AMS ^{14}C analysis. Only ten samples yielded radiocarbon ages that were dendrochronologically corrected (Reimer et al., 2013); three samples yielded ages >50 ka, whereas the C content was too low in all other samples. Almost all samples produced OSL ages (**Table 2**), except for sample CW2, which was contaminated with feldspar. In the hanging wall, sample 2H-1 yielded a calibrated ^{14}C age of 1445–1623 CE, which matches the OSL burial age of 1578–1688 CE for sample T2H-1 at the same sampling site. All five OSL samples in the footwall yielded increasing ages with depth (**Figure 3**). In the footwall, three OSL samples (T2F-1, T2F-2, and T2F-3) yielded ages of 1458–1638 CE (0.471 ± 0.090 ka), 2.72 ± 0.30 ka, and 3.39 ± 0.23 ka, from top to bottom. The OSL age of sample T2F-3 also matches the ^{14}C age of 3450–3075 BP at the same location. These suggest deposition of U1 between ~3.39 and ~0.47 ka. Two samples in the topmost and top sections of U2 in the footwall yielded OSL ages of 4.81 ± 0.87 and 8.53 ± 0.96 ka, respectively. The OSL age of sample T2F-1 (1458–1638 CE) is different from the calibrated ^{14}C age of 2923–2674 BCE at the same location, which indicates the mixing of material in the fault zone. One detrital charcoal collected in CW2, sample 2-1 (**Figure 4**), yielded a ^{14}C age of 6373–6067 BCE, which suggests the source of unit CW2, but cannot be used to constrain its age. Three samples that yielded ages >50 ka are most likely Permian coal fragments from the Gondwana unit outcropping at the headwaters of Dungsam Chu [see, e.g., Figures 2, 3 in Long et al. (2011)].

Three charcoal samples and two OSL samples were collected from cut-in-fill terrace T1 (**Figure 6**). Three charcoal samples found in the bottom organic staining section of horizon A and the top and bottom organic staining sections of the leached and depleted E horizon yielded calibrated ^{14}C ages of 1994–1996 CE, 1970–1972 CE, and 1697–1911 CE, respectively (**Figures 4**, **6**). Two OSL samples taken from the middle sand section of a leached and depleted E horizon and the middle of the B horizon yielded OSL ages of 1375–1587 CE and 1.57 ± 0.30 ka, respectively. Large overdispersion (σ_b) value for these samples indicates incomplete bleaching; therefore we applied the MAM.

DISCUSSION

Great Medieval Earthquakes

Palaeoseismological studies highlight one to several great medieval earthquakes in the. A large historical rupture around 1100 CE was reported in east-central Nepal (Upreti et al., 2000; Lavé et al., 2005). The largest event mapped in trenches in West Bengal (Kumar et al., 2010), central Bhutan (Le Roux-Mallouf et al., 2016; Le Roux-Mallouf et al., 2020), and eastern Arunachal Pradesh (Kumar et al., 2010) could exhibit consistent coseismic slip and chronology with the ~1100 CE earthquake. Radiocarbon-modelled constraints on the timing of this event by Le Roux-Mallouf et al. (2016) yielded a scenario of a single mega-event between 1090 and 1145 CE with a 95.4% probability.

The second Great Medieval Earthquake was the historically recorded 1255 Kathmandu earthquake (Pant, 2002), also documented by palaeoseismologic studies (Mugnier et al., 2013; Sapkota et al., 2013; Bollinger et al., 2014) and also suggested to have occurred in West Bengal (Mishra et al., 2016); however, this interpretation was strongly disputed by Pierce and Wesnousky (2016). Alternative modeling of radiocarbon data (Le Roux-Mallouf et al., 2016) supports the latter event but, instead of supporting one mega-event, indicates a series of events between 1025 CE and 1520 CE. The second Great Medieval Earthquake was the largest seismic event observed in Bhutan. At the Piping site, it was dated to between 1204 CE and 1464 CE (Le Roux-Mallouf et al., 2020) or to between 1140 CE and 1520 CE (Le Roux-Mallouf et al., 2016). This event was associated with 12.2 ± 2.8 m of coseismic dip-slip, an Mw > 8.5 earthquake at the Piping site (Le Roux-Mallouf et al., 2020), and 16–23 m of coseismic surface slip with an inferred Mw of ~8.7 at the Sarpang site (Le Roux-Mallouf et al., 2016).

Nearest trenches where great medieval events were rerecorded lie 124 km to the west (Le Roux-Mallouf et al., 2016) and 130 km to the east (Kumar et al., 2010) of our study site. Therefore, evidence of a medieval earthquake of Mw > 8 would also be expected at our site. However, according to our structural interpretation and dating, E2 in Daranga Mela is older than 8 ka. If the tremendous medieval events had affected this segment of the MHT, the evidence for surface rupture may have been overprinted by the E1 event, or eroded by surface processes. Alternatively, the slip caused by medieval events may not have reached the surface, or has propagated further south into the foreland basin. The lack of traces for medieval events reduces the likeliness of one mega-event rupturing the whole front and puts more weight on the scenario of multiple events.

1714 Bhutan Earthquake

The 1714 Bhutan earthquake has been identified in palaeoseismological trenches in western (Le Roux-Mallouf et al., 2020), central (Berthet et al., 2014; Le Roux-Mallouf et al., 2016), and eastern Bhutan (this study). The structure of the surface-rupturing faults is different; complicated by several splays and several events in the west and central Bhutan but very straight and simple in the east. In the western and eastern Bhutan Late Miocene, Siwalik sediments were thrust over Quaternary fluvial sediments, whereas the entire Siwalik appears to be missing in central Bhutan, where metasediments of the Lesser Himalayan Sequence are thrust over Quaternary alluvial sediments.

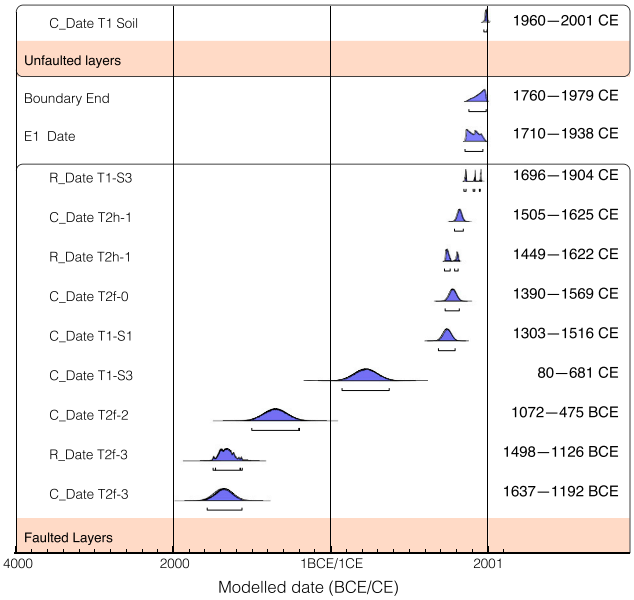

FIGURE 8 | ^{14}C ages of detrital charcoal (R_Date) from Dungsam Chu palaeoseismic exposure calibrated using the phase model of OxCal. The OSL data were input by converting the laboratory OSL age to calendar date (C_Date), including the laboratory uncertainties (Lienkaemper and Ramsey, 2009). In this scenario, the two oldest OSL ages were excluded to present the younger ages at a higher resolution. Dark gray areas show posterior probability distributions resulting from the Bayesian phase model of OxCal. Light gray areas show the standard (unmodelled) probability distributions.

The 1714 event was not recognized at palaeoseismological sites west and east of Bhutan (Kumar et al., 2010). Equivalent to our comment about the medieval earthquakes, one must be careful in interpreting a lack of evidence as an absence of the 1714 event. In central Bhutan, there are at least three splays and traces of the MFT (Nakata, 1972; Berthet et al., 2014). The northernmost branch, also known as the TFT, has been investigated in all palaeoseismic studies in Bhutan. In contrast, the palaeoseismic trenches in West Bengal and Arunachal Pradesh lie across the southernmost branch of the MFT, south of the topographic front, where Quaternary sediments are thrust over other Quaternary sediments. Neither the traces in the Bhutan Himalaya foreland nor surfaces ruptures along with the TFT in West Bengal, and Arunachal Pradesh were not yet dated. In addition, the youngest mapped and dated layer in West Bengal and Arunachal Pradesh trenches, besides modern soil, is 1388–1455 CE (Kumar et al., 2010). Therefore, sedimentary conditions did not allow observation of a potential younger surface-breaking event.

F1 cuts unit U1 and is sealed by unit CW2; thus, event 1 occurred after unit U1 and likely triggered the deposition of unit CW2. The age of the uppermost section of U1 in the footwall given by the topmost OSL sample T2F-1 is consistent with the pair of radiocarbon and OSL dates in the hanging wall, confirming the identity of U1 from the footwall to the

hanging wall and constrains E1 from rupturing the surface after 1690 CE. Due to the lack of an undisturbed layer sealing the fault, we could not determine the minimum age of the E1 event. The timing of formation of the injected sand would constrain the timing of the earthquake, causing this liquefaction feature to after formation of the soil horizon, with ^{14}C dates of 1697–1911 CE.

In addition to simple calibration, a Bayesian model of OxCal was used to calibrate all samples with $F^{14}C < 1$ and positive ^{14}C ages (**Figure 8**), along with a chronostratigraphic model (aka phase model) for deposition episodes (alluvial units T1 and T2, colluvial wedge CW1) and surface-rupturing events E1 at the Dungsam Chu exposure. The model is built from abutting relationships between stratigraphy and faulting and is constrained by ^{14}C and OSL ages. We evaluated several scenarios, all of which yielded similar results. All of the alluvial deposits on the primary exposure were affected by faulting. In the second scenario, we included data from T1 to the south of the MFT trace. The soil horizon 3 with a ^{14}C age of 1697–1911 CE was injected with sand exhibiting older OSL ages; therefore, it was also considered "faulted." In the third scenario, we included four ages from central Bhutan deposited on top of the event 1 horizon. All scenarios gave the same result for the end of the "phase," which is interpreted to have been caused by E1. The variations of each scenario included the "event" in 1714 CE and the modern soil, which was not affected by faulting.

Through a combination of observations, chronostratigraphic modeling, and the historical record (Hetényi et al., 2016), we conclude that the E1 surface rupture was caused by the 1714 Bhutan earthquake.

Magnitude and Location of the 1714 Bhutan Earthquake

The simplest and most common palaeo-earthquake magnitude estimate is based on the scaling relationship between the rupture length and magnitude (Wells and Coppersmith, 1994; Leonard, 2010). The distance between the trenches in which the 1714 event was observed was 175 km; the nearest trenches in which the event was not observed (Kumar et al., 2010) were 96 and 130 km to the west and east, respectively. Therefore, the minimum length of the surface rupture was 175 km, and the maximum was ~400 km, which is likely unrealistic. If we assume that the two oblique strike-slip zones in the underthrusting basement constrain the extent of surface rupture along the MHT, the maximum surface rupture length could have been ~290 km. The 175–290 km surface rupture length estimated for the 1714 Bhutan earthquake corresponds to Mw 7.8–8.1. According to Leonard (2010), the corresponding average surface displacement would be 3.7–5.6 m, whereas the maximum surface displacement should be double that value (Wells and Coppersmith, 1994; Leonard, 2010), i.e., 7.4–11.2 m. The larger value is consistent with the displacement of 11.3 ± 0.5 m, estimated from our outcrop log.

Following the approach of Hetényi et al. (2016), we performed a full grid search of earthquake scenarios using empirical scaling relationships relating the magnitude to the intensity, source location, and rupture geometry to constrain the size and possible hypocentral location of the 1714 event. The intensity observations and intensity prediction equations (IPE) by Allen et al. (2012) and Szeliga et al. (2010) are fully described in Hetényi et al. (2016). In addition to scaling equations by Wells and Coppersmith (1994) used in Hetényi et al. (2016), we also used those by Leonard (2010), and added the surface rupture observations from Le Roux-Mallouf et al. (2020) and this study. The tested scenarios and parameters used in the calculations are listed in **Table 3**. The set of four results, combining the two possible IPEs with two possible scaling laws (**Figure 9**), point to a magnitude range of 7.7–8.5 for plausible solutions, that is, Mw 8.1 ± 0.4. Note that the red fields in **Figure 9** outline the area of possible hypocentre locations, not the rupture extent. The relatively lower magnitude models (until M~8) locate the hypocentre in central Bhutan; the higher magnitude models extend the possible solution area to cover western Bhutan and also toward eastern Bhutan.

The length-to-width scaling by Leonard (2010) for intracontinental dip-slip faults yielded a rupture width of 31–44 km for surface rupture lengths of 175–290 km. Alternatively, using the scaling equations by Leonard (2010) to the earthquake magnitude range obtained by modeling yields rupture length and width of 118 and ~42 km for Mw 7.7, and rupture length and width of ~358 and ~88 km for Mw 8.5. All these values imply that only the frontal third to half of the fully locked MHT (Li et al., 2020) would have slipped during the 1714 Bhutan earthquake; or that the aspect ratio of rupture length and width differed from the average. However, compared to the Gorkha earthquake of Mw 7.8 that has not ruptured the surface and the model of bimodal seismicity in Dal Zilio et al. (2019), the width parameter is poorly constrained. Nevertheless, with this magnitude range (7.7–8.5), we are confident that the 1714 Bhutan earthquake ruptured the flat portion of the MHT and the frontal ramp between the two strike-slip zones.

Stress Transfer

It has been observed that large instrumental earthquakes that rupture the deep ramp of the MHT do not always cause surface ruptures (Mugnier et al., 2013; Elliott et al., 2016). Therefore paleoseismic on-fault determinations of slip may not provide evidence for these deeper earthquakes in pre-instrumental times (Quigley et al., 2016). Coulomb stress transfer (CST) changes the state of stress around the rupture fault, with some areas (or receiver faults) experiencing an increase in Coulomb stress and others experiencing a decrease in stress (Lin and Stein, 2004). Typically, changes in stress along or across strike are investigated for planar faults, however the MHT has a ramp-flat geometry, thus CST modeling for non-planar faults (Stahl et al., 2016; Hughes et al., 2020) is better suited. Therefore, we use CST to try and determine the potential interaction and triggering between deep ramp earthquakes and the shallow ramp and flat portion of the MHT.

We performed calculations of coseismic stress changes using a realistic ramp-flat geometry of the MHT and the strike-variable surface trace of the MFT. The method used to generate strike-variable fault planes from surface fault traces was developed by Mildon et al. (2016) and dip-variable fault planes in Hughes et al. (2020). The MHT was modeled as a series of 20-km rectangular

TABLE 3 | Tested scenarios and parameters used in the magnitude calculations. Combinations of equations and parameters used for estimated magnitude calculations of the 1714 Bhutan earthquake shown in **Figure 9**. For the intensity observations please see (Hetényi et al., 2016).

Tested scenarios	Allen and W&C: M7.7-8.3	Szeliga and Leonard: M7.8-8.5
Allen and Leonard: M7.7-8.3	IPE of Allen et al. (2012): $I\ (M, R_{hyp})$, where $c_0 = 2.085$, $c_1 = 1.428$, $c_2 = -1.402$, $c_4 = 0.078$, $S = 0$, $m_1 = -0.209$, and $m_2 = 2.042$	Scaling relations of Leonard (2010): $RW \sim RLD$, $M_0 \sim RLD$, $M \sim M_0$, where $\mu = 3.3 \times 10^{10}$ Nm^{-2}, $C_1 = 17.5$ and $C_2 = 3.8 \times 10^{-5}$, and RLD and RW in meters.
Szeliga and W&C: M7.8-8.5	Scaling relations of Wells and Coppersmith (1994): $M \sim RLD$, $M \sim RW$, where $a_1 = -2.42$, $b_1 = 0.58$, $a_2 = -1.61$, and $b_2 = 0.41$, and RLD and RW in km.	IPE of Szeliga et al. (2010): $I\ (M, R_{hyp})$, where $a = 6.05$, $b = 1.11$, $c = -0.0006$, and $d = -3.91$

Note: I, *expected intensity,* M, *magnitude,* R_{hyp}, *hypocentral distance to the earthquake focus,* RW, *downdip rupture width,* RLD, *subsurface rupture length, and* M_0, *scalar moment (Nm).*

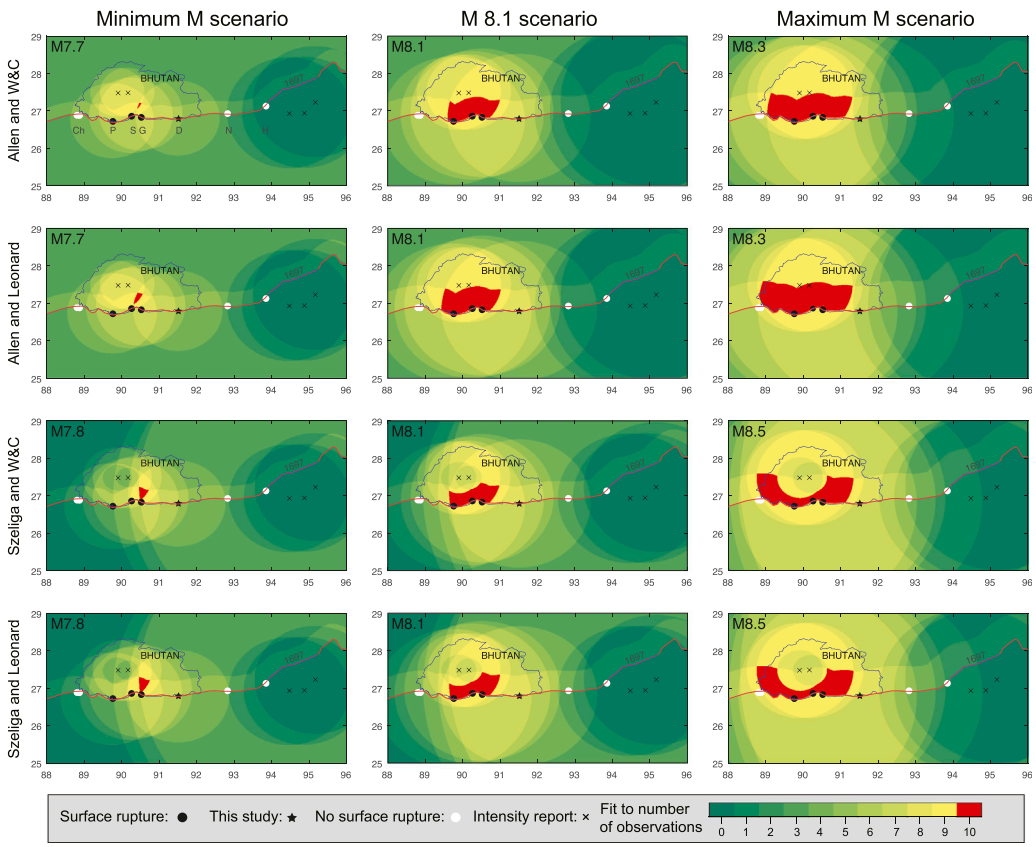

FIGURE 9 | Various earthquake scenarios fitting historical damage and paleoseismology observations. Rows correspond to the different combinations of intensity prediction equations by Allen et al. (2012) and Szeliga et al. (2010) combined with scaling relationship equations by Leonard (2010) and Wells and Coppersmith (1994), as explained in Hetényi et al. (2016). The three columns show minimum magnitude, M8.1, and large magnitude scenarios, respectively. The color bar shows the number of observations fitted at the location on the map for a given magnitude; the red area represents hypocentre locations fitting all observed data points. Palaeoseismological trenches where surface rupture caused by the 1714 earthquake was identified are shown in black circles; trenches showing no evidence of surface rupture in the 18th century are shown as white circles. **Ch**: Chalsa; **P**: Piping; **S**: Sarpang; G: Gelephu; **D:** Dungsam Chu; **N**: Nameri; **H**: Harmutty. Intensity reports (Hetényi et al., 2016) are indicated with black crosses. Red line is the simplified trace of the Main Frontal Thrust. Purple segment in the east is the maximum portion of the MHT ruptured by the 1697 Sadiya earthquake (Pandey et al., 2021). Bhutan's approximate border is shown in blue for reference. Map coordinates are in degrees N and E.

elements comprising the non-planar fault surface. The ramp-flat geometry of the MHT is based on Coutand et al. (2014) and Singer et al. (2017). All CST calculations were performed in Coulomb 3.4 (Toda et al., 2005), with the coefficient of friction as 0.4 and a Young's modulus of 80 GPa (Grujic et al., 2018). An earthquake of magnitude 8.1 with a concentric slip distribution

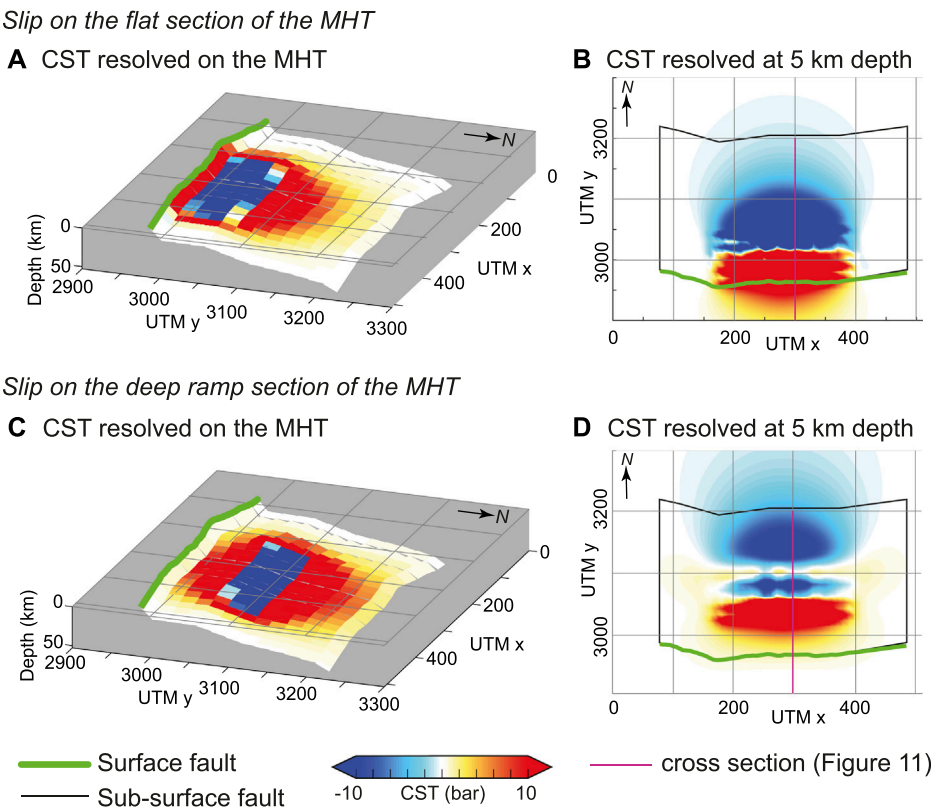

FIGURE 10 | Models of Coulomb Stress Transfer (CST) for representative earthquakes. The color scale of CST is the same for all figures. **(A)**. slip on the flat section of the MHT with stress resolved onto the rest of the MHT, **(B)**. slip on the flat section with stress resolved at 5 km depth onto receiver faults with the geometry 270/45/90 (strike/dip/rake), **(C)**. slip on the deep ramp (>15 km depth) of the MHT with stress resolved onto the rest of the MHT, **(D)**. slip on the deep ramp with stress resolved at 5 km depth onto receiver faults with the geometry 270/45/90.

(see Mildon et al., 2016) over an area of 230 × 70 km [utilizing the scaling relationships in Wells and Coppersmith (1994)] was generated. Although this is a simple assumption, a hypocentre neither need be in the middle of the fault nor at the location of strongest shaking. For example, the maximum slip of the 2004 Aceh earthquake was located ~200 km northwest of the hypocenter (Cattin et al., 2009). If the area of the fault that slips stays the same, but the distribution within the area varies, e.g., is skewed to one end, then the regions of positive and negative stress stay approximately the same, though the magnitudes undoubtedly vary (Mildon et al., 2017). Two earthquake scenarios were modeled, one with the slip on the deep ramp and one with the slip on the flat section. Although it has been documented that the MHT ramp has been creeping (Dal Zilio et al., 2021), we use this scenario to simulate earthquakes on the internal part of the MHT. The magnitude of Coulomb stress changes caused by coseismic slip on a fault also depends on the assumed elastic structure, which in this work is oversimplified (homogeneous half-space).

When the great earthquake slip is on the flat portion of the MHT (between 14 and 15 km depth), this transfers high positive Coulomb stresses (>10 bar) onto the frontal thrust (**Figure 10A**), indicating that earthquakes that predominantly slip the flat section will promote rupture on the frontal thrust, and therefore are likely to generate surface ruptures. The CST calculations indicate that an earthquake along the deep ramp on the MHT would transfer considerable amounts (up to and over 10 bar) of positive Coulomb stress onto the flat portion of the fault; however, much less (<2 bar) is transferred onto the frontal ramp (**Figure 10C**). In cross-section (**Figure 11**), we show the distribution of stress changes projected on subhorizontal planes and the optimally oriented thrust faults. Seismic slip along the ramp of the MHT would cause positive changes in the Coulomb stress along the shallow, flat segment of the MHT located in the end-fault lobe of the ramp (**Figure 11A**). However, clamping effects (i.e., compressive changes of normal stress) in the frontal part of the MHT are important (**Figure 11B**) impeding propagation of the slip to the surface (i.e., MFT). A similar stress pattern is observed for the optimally oriented thrust faults; although the Coulomb stress change along the MHT is neutral, the unclamping effect (i.e., tensile changes of normal stress) is modest (**Figures 11C,D**). Consequently, deep slip on the MFT may increase elastic strain in upper crustal levels, including shallow MFT, which is then accommodated by slip on the shallow MFT. The Coulomb stress increase along the flat portion of the MHT would promote future earthquakes along the frontal

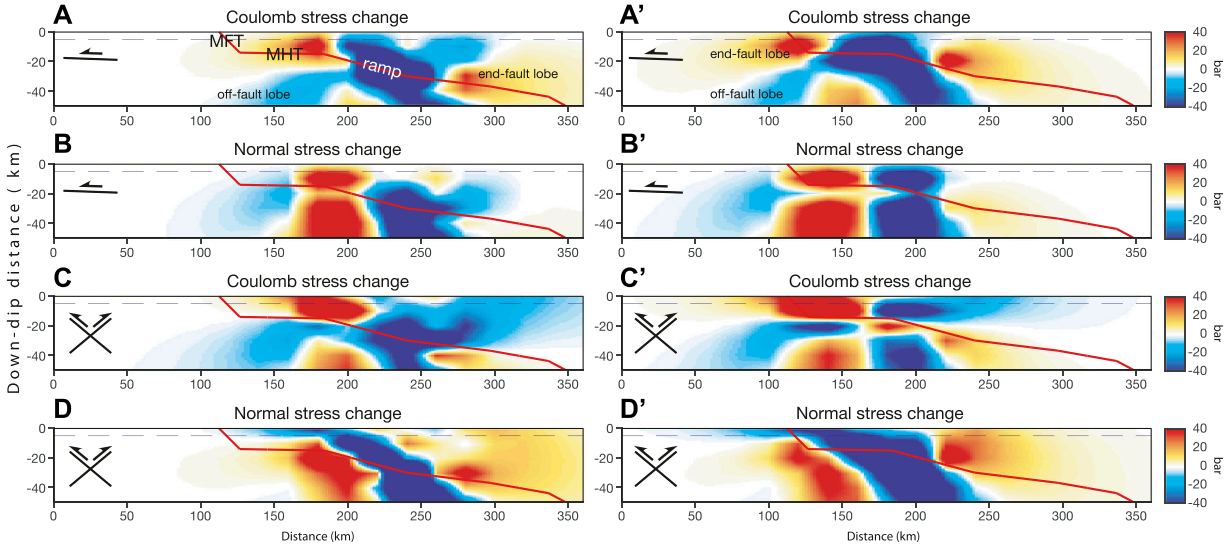

FIGURE 11 | Cross-section view of the distribution of static stress changes caused by the 1714 Bhutan earthquake along a profile perpendicular to the strike of the MFT. The left-hand panels show the Coulomb stress **(A,C)** normal stress **(B,D)** changes caused by a shock with hypocentre on the deep ramp of the MHT. The right-hand panels show the Coulomb stress **(A′,C′)** normal stress **(B′,D′)** changes caused by a shock with hypocentre on the flay segment of the MHT. Static stress changes are calculated for the subhorizontal planes with the geometry 270/02/90 (**A**,**A′**,**B**,**B′**) and optimally oriented thrust faults with the geometry 270/40/90 (**C**,**C′**,**D**,**D′**).

segment of the MHT and thus along with the frontal thrust. The down-dip end-fault stress lobes for both horizontal faults and optimally oriented faults are positive (**Figures 11A′–D′**), which is not the case for the deep slip (**Figures 11A–D**). It is important to note that the up-dip end-fault Coulomb stresses lobe is associated with a lobe of positive normal stress change (unclamping effect) (**Figures 11A′,B′**). Although the positive Coulomb stress change is larger for the thrust faults (cf. **Figures 11A′,C′**) there is a significant clamping effect (**Figure 11D′**), promoting MHT propagation into the foreland basin in the form of a blind basal décollement. Such a structure has been observed within or below the lower Siwalik Group in the subsurface of the foreland basin of the eastern Nepalese Himalaya (Duvall et al., 2020). Blind basal décollement may exist in the Bhutan Himalayan foreland basin as suggested by juvenile triangle zones in West Bengal and western Assam (Dasgupta et al., 2013; Chakrabarti Goswami et al., 2019). Therefore, palaeoseismic studies around the surface trace of the MFT may overestimate the slip potential where un-recognized faults or distributed deformation provide additional sources of strain release. In the case of the blind basal décollement in the foreland basin, the region of pre-seismic strain accumulation is only 20–40 km wide, the maximum slip that can be stored and released, no matter how long the interval since the previous earthquake, is only a couple of meters (Bilham, 2019).

CONCLUSION

Combined radiocarbon and OSL dating of river sediments at a new paleoseismic site, supported by historical records, indicated that the most recent surface rupture along the MFT in Eastern Bhutan was caused by the 1714 Bhutan earthquake. The surface rupture length was at least 175 km and likely up to ~290 km. The largest observed coseismic surface displacement was ~10.5 m. The scaling relationship between the rupture length and magnitude (Wells and Coppersmith, 1994; Leonard, 2010) indicated a minimum magnitude of Mw of 7.8–8.1. Computations using empirical scaling relationships, historical intensity data, and palaeoseismologically determined surface ruptures in the Bhutan Himalaya yielded plausible magnitudes of 7.7–8.5. The same calculations placed the epicentre of the 1714 Bhutan earthquake on the flat segment of the MHT. CST calculations suggested that distal earthquakes do not promote rupture on the frontal thrust. In contrast, a great earthquake along the flat portion of the MHT would cause slip along the frontal ramp (MFT), and would promote the propagation of the MHT into the foreland basin in the form of a blind thrust.

The current state of Himalayan palaeoseismological knowledge (Bilham, 2019) suggests that the majority of great surface-rupturing earthquakes during the last millennium have been identified, although the dating precision for some of them is low. However, great earthquakes that did not lead to surface rupture caused stress transfer into the flat frontal portion, promoting subsequent surface-rupturing events along the MFT.

DATA AVAILABILITY STATEMENT

The original contributions presented in the study are included in the article/**Supplementary Material**, further inquiries can be directed to the corresponding author. The code to model strike- and dip-variable faults in Coulomb 3.4 is available from https://github.com/ZoeMildon/3D-faults.

AUTHOR CONTRIBUTIONS

YZ: Fieldwork, data acquisition data interpretation, writing; DG: project concept and funding, field work, data acquisition data interpretation, writing; SB: field work, data acquisition; DD: field work, data acquisition; JE: data acquisition; GH: data interpretation, data modelling, writing; GK: data acquisition, data interpretation; ZM: data modelling, data interpretation. NN: field work, data acquisition; CW: data acquisition, data interpretation.

FUNDING

The study was supported by the Natural Sciences and Engineering Research Council of Canada (NSERC) grant RGPIN/4297-2014 to DG, and the National Geographic Society (Scientific research grant 83118-07 to DG). ZM acknowledges the support from NERC Studentship NE/L501700/1 and JSPS Short Term Fellowship PE15776 for developing the method to model stress changes on faults with variable geometry. Mitacs Globalink Research Award and the GSA student award provided the financial support to YZ for her work visit to the University of Lausanne. GH acknowledges the support of the Swiss National Science Foundation for project OROG3NY (grant number PP00P2_157627).

ACKNOWLEDGMENTS

We are grateful to Etho Metho travel agency for logistic support in Bhutan and to Abhijit Chowdhury and his team for field assistance in Assam. Palynological Laboratory Services Ltd (UK) performed the pollen separation. We also thank Isabelle Coutand, Roman Kislitsyn, John Gosse, Olivia Rolfe, and Luca Malatesta for laboratory assistance and discussion. Critical comments by reviewers RJ and MQ are greatly acknowledged.

SUPPLEMENTARY MATERIAL

The Supplementary Material for this article can be found online at: https://www.frontiersin.org/articles/10.3389/feart.2021.689457/full#supplementary-material

REFERENCES

Allen, T. I., Wald, D. J., and Worden, C. B. (2012). Intensity Attenuation for Active Crustal Regions. *J. Seismol* 16 (3), 409–433. doi:10.1007/s10950-012-9278-7

Ambraseys, N., and Jackson, D. (2003). A Note on Early Earthquakes in Northern India and Southern Tibet. *Curr. Sci.* 84, 570–582.

Bell, W. (1979). Attenuation Factors for the Absorbed Radiation Dose in Quartz Inclusions for Thermoluminescence Dating. *Ancient TL* 8 (2), 12.

Berthet, T., Ritz, J.-F., Ferry, M., Pelgay, P., Cattin, R., Drukpa, D., et al. (2014). Active Tectonics of the Eastern Himalaya: New Constraints from the First Tectonic Geomorphology Study in Southern Bhutan. *Geology* 42 (5), 427–430. doi:10.1130/g35162.1

Bilham, R. (2019). Himalayan Earthquakes: a Review of Historical Seismicity and Early 21st century Slip Potential. *Geol. Soc. Lond. Spec. Publications* 483 (1), 423–482. doi:10.1144/sp483.16

Biswas, S., Coutand, I., Grujic, D., Hager, C., Stöckli, D., and Grasemann, B. (2007). Exhumation and Uplift of the Shillong Plateau and its Influence on the Eastern Himalayas: New Constraints from Apatite and Zircon (U-Th-[Sm])/He and Apatite Fission Track Analyses. *Tectonics* 26 (6), a–n. doi:10.1029/2007tc002125

Bollinger, L., Sapkota, S. N., Tapponnier, P., Klinger, Y., Rizza, M., Van Der Woerd, J., et al. (2014). Estimating the Return Times of Great Himalayan Earthquakes in Eastern Nepal: Evidence from the Patu and Bardibas Strands of the Main Frontal Thrust. *J. Geophys. Res. Solid Earth* 119 (9), 7123–7163. doi:10.1002/2014jb010970

Brennan, B., Lyons, R., and Phillips, S. (1991). Attenuation of Alpha Particle Track Dose for Spherical Grains. *Int. J. Radiat. Appl. Instrumentation. D. Nucl. Tracks Radiat. Measurements* 18 (1-2), 249–253. doi:10.1016/1359-0189(91)90119-3

Burgess, W. P., Yin, A., Dubey, C. S., Shen, Z.-K., and Kelty, T. K. (2012). Holocene Shortening across the Main Frontal Thrust Zone in the Eastern Himalaya. *Earth Planet. Sci. Lett.* 357, 152–167.

Cattin, R., Chamot-Rooke, N., Pubellier, M., Rabaute, A., Delescluse, M., Vigny, C., et al. (2009). Stress Change and Effective Friction Coefficient along the Sumatra-Andaman-Sagaing Fault System after the 26 December 2004 (Mw= 9.2) and the 28 March 2005 (Mw= 8.7) Earthquakes. *Geochem. Geophys. Geosystems* 10 (3). doi:10.1029/2008gc002167

Chakrabarti Goswami, C., Jana, P., and Weber, J. C. (2019). Evolution of Landscape in a piedmont Section of Eastern Himalayan Foothills along India-Bhutan Border: A Tectono-Geomorphic Perspective. *J. Mt. Sci.* 16 (12), 2828–2843. doi:10.1007/s11629-018-5208-7

Chirouze, F., Huyghe, P., Van Der Beek, P., Chauvel, C., Chakraborty, T., Dupont-Nivet, G., et al. (2013). Tectonics, Exhumation, and Drainage Evolution of the Eastern Himalaya since 13 Ma from Detrital Geochemistry and Thermochronology, Kameng River Section, Arunachal Pradesh. *Geol. Soc. America Bull.* 125 (3-4), 523–538. Available at: http://gsabulletin.gsapubs.org/cgi/doi/10.1130/B30697.1. doi:10.1130/b30697.1

Clark, M., and Bilham, R. (2008). Miocene Rise of the Shillong Plateau and the Beginning of the End for the Eastern Himalaya. *Earth Planet. Sci. Lett.* 269 (3), 337–351. Available at: http://linkinghub.elsevier.com/retrieve/pii/S0012821X0800071X. doi:10.1016/j.epsl.2008.01.045

Coutand, I., Barrier, L., Govin, G., Grujic, D., Hoorn, C., Dupont-Nivet, G., et al. (2016). Late Miocene-Pleistocene Evolution of India-Eurasia Convergence Partitioning between the Bhutan Himalaya and the Shillong Plateau: New Evidences from Foreland basin Deposits along the Dungsam Chu Section, Eastern Bhutan. *Tectonics* 35 (12), 2963–2994. doi:10.1002/2016tc004258

Coutand, I., Whipp, D. M., Jr, Grujic, D., Bernet, M., Fellin, M. G., Bookhagen, B., et al. (2014). Geometry and Kinematics of the Main Himalayan Thrust and Neogene Crustal Exhumation in the Bhutanese Himalaya Derived from Inversion of Multithermochronologic Data. *J. Geophys. Res. Solid Earth* 119 (2), 1446–1481. doi:10.1002/2013jb010891

Dal Zilio, L., Hetényi, G., Hubbard, J., and Bollinger, L. (2021). Building the Himalaya from Tectonic to Earthquake Scales. *Nat. Rev. Earth Environ.* 6, 1–18.

Dal Zilio, L., van Dinther, Y., Gerya, T., and Avouac, J.-P. (2019). Bimodal Seismicity in the Himalaya Controlled by Fault Friction and Geometry. *Nat. Commun.* 10 (1), 48. doi:10.1038/s41467-018-07874-8

Dasgupta, S., Mazumdar, K., Moirangcha, L. H., Gupta, T. D., and Mukhopadhyay, B. (2013). Seismic Landscape from Sarpang Re-entrant, Bhutan Himalaya Foredeep, Assam, India: Constraints from Geomorphology and Geology. *Tectonophysics* 592, 130–140. doi:10.1016/j.tecto.2013.02.021

Diehl, T., Singer, J., Hetényi, G., Grujic, D., Clinton, J., Giardini, D., et al. (2017). Seismotectonics of Bhutan: Evidence for Segmentation of the Eastern Himalayas and Link to Foreland Deformation. *Earth Planet. Sci. Lett.* 471, 54–64. doi:10.1016/j.epsl.2017.04.038

Drukpa, D., Gautier, S., Cattin, R., Namgay, K., and Le Moigne, N. (2018). Impact of Near-Surface Fault Geometry on Secular Slip Rate Assessment Derived from Uplifted River Terraces: Implications for Convergence Accommodation across the Frontal Thrust in Southern Central Bhutan. *Geophys. J. Int.* 212 (2), 1315–1330. doi:10.1093/gji/ggx478

Drukpa, D., Velasco, A. A., and Doser, D. I. (2006). Seismicity in the Kingdom of Bhutan (1937-2003): Evidence for Crustal Transcurrent Deformation. *J. Geophys. Res.* 111 (B06301), a–n. doi:10.1029/2004JB003087

Duller, G. A. T. (2008). Single-grain Optical Dating of Quaternary Sediments: Why Aliquot Size Matters in Luminescence Dating. *Boreas* 37 (4), 589–612. doi:10.1111/j.1502-3885.2008.00051.x

Durcan, J. A., King, G. E., and Duller, G. A. T. (2015). DRAC: Dose Rate and Age Calculator for Trapped Charge Dating. *Quat. Geochronol.* 28, 54–61. doi:10.1016/j.quageo.2015.03.012

Duvall, M. J., Waldron, J. W. F., Godin, L., and Najman, Y. (2020). Active Strike-Slip Faults and an Outer Frontal Thrust in the Himalayan Foreland basin. *Proc. Natl. Acad. Sci. USA* 117 (30), 17615–17621. doi:10.1073/pnas.2001979117

Elliott, J. R., Jolivet, R., González, P. J., Avouac, J.-P., Hollingsworth, J., Searle, M. P., et al. (2016). Himalayan Megathrust Geometry and Relation to Topography Revealed by the Gorkha Earthquake. *Nat. Geosci.* 9 (2), 174–180. doi:10.1038/ngeo2623

England, P., and Bilham, R. (2015). The Shillong Plateau and the Great 1897 Assam Earthquake. *Tectonics* 34 (9), 1792–1812. doi:10.1002/2015tc003902

Gahalaut, V. K., Rajput, S., and Kundu, B. (2011). Low Seismicity in the Bhutan Himalaya and the Stress Shadow of the 1897 Shillong Plateau Earthquake. *Phys. Earth Planet. Interiors* 186, 97–102. doi:10.1016/j.pepi.2011.04.009

Galbraith, R. F., Roberts, R. G., Laslett, G. M., Yoshida, H., and Olley, J. M. (1999). Optical Dating of Single and Multiple Grains of Quartz from Jinmium Rock Shelter, Northern Australia: Part I, Experimental Design and Statistical Models. *Archaeometry* 41 (2), 339–364. doi:10.1111/j.1475-4754.1999.tb00987.x

Grujic, D., Govin, G., Barrier, L., Bookhagen, B., Coutand, I., Cowan, B., et al. (2018). Formation of a Rain Shadow: O and H Stable Isotope Records in Authigenic Clays from the Siwalik Group in Eastern Bhutan. *Geochem. Geophys. Geosyst.* 19 (9), 3430–3447. doi:10.1029/2017gc007254

Grujic, D., Hetényi, G., Cattin, R., Baruah, S., Benoit, A., Drukpa, D., et al. (2018). Stress Transfer and Connectivity between the Bhutan Himalaya and the Shillong Plateau. *Tectonophysics* 744, 322–332. doi:10.1016/j.tecto.2018.07.018

Guérin, G., Mercier, N., and Adamiec, G. (2011). Dose-rate Conversion Factors: Update. *Ancient TL* 29 (1), 5–8.

Guérin, G., Mercier, N., Nathan, R., Adamiec, G., and Lefrais, Y. (2012). On the Use of the Infinite Matrix assumption and Associated Concepts: a Critical Review. *Radiat. Measurements* 47 (9), 778–785. doi:10.1016/j.radmeas.2012.04.004

Hammer, P., Berthet, T., Hetényi, G., Cattin, R., Drukpa, D., Chophel, J., et al. (2013). Flexure of the India Plate underneath the Bhutan Himalaya. *Geophys. Res. Lett.* 40 (16), 4225–4230. doi:10.1002/grl.50793

Hauck, M. L., Nelson, K. D., Brown, L. D., Zhao, W., and Ross, A. R. (1998). Crustal Structure of the Himalayan Orogen at ~90° East Longitude from Project INDEPTH Deep Reflection Profiles. *Tectonics* 17 (4), 481–500. doi:10.1029/98tc01314

Hetényi, G., Cattin, R., Berthet, T., Le Moigne, N., Chophel, J., Lechmann, S., et al. (2016). Segmentation of the Himalayas as Revealed by Arc-Parallel Gravity Anomalies. *Scientific Rep.* 6 (1), 1–10. doi:10.1038/srep33866

Hetényi, G., Le Roux-Mallouf, R., Berthet, T., Cattin, R., Cauzzi, C., Phuntsho, K., et al. (2016). Joint Approach Combining Damage and Paleoseismology Observations Constrains the 1714 A.D. Bhutan Earthquake at Magnitude 8 ± 0.5. *Geophys. Res. Lett.* 43 (20), 10,695–10,702. doi:10.1002/2016GL071033

Hirschmiller, J., Grujic, D., Bookhagen, B., Coutand, I., Huyghe, P., Mugnier, J.-L., et al. (2014). What Controls the Growth of the Himalayan Foreland Fold-And-Thrust belt? *Geology* 42 (3), 247–250. doi:10.1130/g35057.1

Hua, Q., Barbetti, M., and Rakowski, A. Z. (2013). Atmospheric Radiocarbon for the Period 1950-2010. *Radiocarbon* 55 (4), 2059–2072. doi:10.2458/azu_js_rc.v55i2.16177

Hughes, A., Bell, R., Mildon, Z., Rood, D., Whittaker, A., Rockwell, T., et al. (2020). Three-Dimensional Structure, Ground Rupture Hazards, and Static Stress Models for Complex Nonplanar Thrust Faults in the Ventura Basin, Southern California. *J. Geophys. Res. Solid Earth* 125 (7), e2020JB019539. doi:10.1029/2020jb019539

Jayangondaperumal, R., Thakur, V., Joevivek, V., Rao, P. S., and Gupta, A. K. (2018). *Active Tectonics of Kumaun and Garhwal Himalaya*. Springer. doi:10.1007/978-981-10-8243-6

Kreutzer, S., Dietze, M., Burow, C., Fuchs, M., Schmidt, C., Fischer, M., et al. (2016). *Comprehensive Luminescence Dating Data Analysis (R Package)*. See Available at: https://cran.r-project.org/web/packages/Luminescence/index.html.

Kumar, S., Wesnousky, S. G., Jayangondaperumal, R., Nakata, T., Kumahara, Y., and Singh, V. (2010). Paleoseismological Evidence of Surface Faulting along the Northeastern Himalayan Front, India: Timing, Size, and Spatial Extent of Great Earthquakes. *J. Geophys. Res.* 115 (B12), B12422. Available at: http://www.agu.org/pubs/crossref/2010/2009JB006789.shtml. doi:10.1029/2009jb006789

Lague, D. (2014). The Stream Power River Incision Model: Evidence, Theory and beyond. *Earth Surf. Process. Landforms* 39 (1), 38–61. doi:10.1002/esp.3462

Lavé, J., Yule, D., Sapkota, S., Basant, K., Madden, C., Attal, M., et al. (2005). Evidence for a Great Medieval Earthquake (1100 A.D.) in the Central Himalayas, Nepal. *Science* 307 (5713), 1302–1305. doi:10.1126/science.1104804

Le Roux-Mallouf, R., Ferry, M., Ritz, J. F., Berthet, T., Cattin, R., and Drukpa, D. (2016). First Paleoseismic Evidence for Great Surface-rupturing Earthquakes in the Bhutan Himalayas. *J. Geophys. Res. Solid Earth* 121 (10), 7271–7283.

Le Roux-Mallouf, R., Godard, V., Cattin, R., Ferry, M., Gyeltshen, J., Ritz, J. F., et al. (2015). Evidence for a Wide and Gently Dipping Main Himalayan Thrust in Western Bhutan. *Geophys. Res. Lett.* 42 (9), 3257–3265.

Le Roux-Mallouf, R., Ferry, M., Cattin, R., Ritz, J.-F., Drukpa, D., and Pelgay, P. (2020). A 2600-Year-Long Paleoseismic Record for the Himalayan Main Frontal Thrust (Western Bhutan). *Solid Earth* 11 (6), 2359–2375. doi:10.5194/se-11-2359-2020

Lee, J.-C., Chen, Y.-G., Sieh, K., Mueller, K., Chen, W.-S., Chu, H.-T., et al. (2001). A Vertical Exposure of the 1999 Surface Rupture of the Chelungpu Fault at Wufeng, Western Taiwan: Structural and Paleoseismic Implications for an Active Thrust Fault. *Bull. Seismological Soc. America* 91 (5), 914–929.

Leonard, M. (2010). Earthquake Fault Scaling: Self-Consistent Relating of Rupture Length, Width, Average Displacement, and Moment Release. *Bull. Seismological Soc. America* 100 (5A), 1971–1988. doi:10.1785/0120090189

Levin, I., Kromer, B., and Hammer, S. (2013). Atmospheric Δ14CO2 Trend in Western European Background Air from 2000 to 2012. *Tellus B: Chem. Phys. Meteorology* 65 (1), 20092. doi:10.3402/tellusb.v65i0.20092

Li, S., Tao, T., Gao, F., Qu, X., Zhu, Y., Huang, J., et al. (2020). Interseismic Coupling beneath the Sikkim-Bhutan Himalaya Constrained by GPS Measurements and its Implication for Strain Segmentation and Seismic Activity. *Remote Sensing* 12 (14), 2202. doi:10.3390/rs12142202

Lienkaemper, J. J., and Ramsey, C. B. (2009). OxCal: Versatile Tool for Developing Paleoearthquake Chronologies--A Primer. *Seismological Res. Lett.* 80 (3), 431–434. doi:10.1785/gssrl.80.3.431

Liu, F., and Yang, S. (2015). The Effect of the Wenchuan Earthquake on the Fluvial Morphology in the Longmen Shan, Eastern Tibetan Plateau: Discussion and Speculation. *Quat. Int.* 371, 280–289. doi:10.1016/j.quaint.2014.09.021

Long, S., McQuarrie, N., Tobgay, T., Rose, C., Gehrels, G., and Grujic, D. (2011). Tectonostratigraphy of the Lesser Himalaya of Bhutan: Implications for the Along-Strike Stratigraphic Continuity of the Northern Indian Margin. *Geol. Soc. America Bull.* 123 (7-8), 1406–1426. doi:10.1130/B30202.1

Long, S. P., McQuarrie, N., Tobgay, T., Coutand, I., Cooper, F. J., Reiners, P. W., et al. (2012). Variable Shortening Rates in the Eastern Himalayan Thrust belt, Bhutan: Insights from Multiple Thermochronologic and Geochronologic Data Sets Tied to Kinematic Reconstructions. *Tectonics* 31 (5). Available at: http://www.agu.org/pubs/crossref/2012/2012TC003155.shtml. doi:10.1029/2012tc003155

Mansfield, C., and Cartwright, J. (2001). Fault Growth by Linkage: Observations and Implications from Analogue Models. *J. Struct. Geology.* 23 (5), 745–763. doi:10.1016/s0191-8141(00)00134-6

Marechal, A., Mazzotti, S., Cattin, R., Cazes, G., Vernant, P., Drukpa, D., et al. (2016). Evidence of Interseismic Coupling Variations along the Bhutan Himalayan Arc from New GPS Data. *Geophys. Res. Lett.* 43 (24), 399–312. doi:10.1002/2016gl071163

Mildon, Z. K. (2017). *The Link between Earthquakes and Structural Geology; the Role of Elapsed Time, 3D Geometry and Stress Transfer in the central Apennines*. Italy: (Doctporal dissertation), UCL (University College London).

Mildon, Z. K., Toda, S., Faure Walker, J. P., and Roberts, G. P. (2016). Evaluating Models of Coulomb Stress Transfer: Is Variable Fault Geometry Important?. *Geophys. Res. Lett.* 43 (24), 407–412. doi:10.1002/2016gl071128

Mishra, R. L., Singh, I., Pandey, A., Rao, P., Sahoo, H., and Jayangondaperumal, R. (2016). Paleoseismic Evidence of a Giant Medieval Earthquake in the Eastern Himalaya. *Geophys. Res. Lett.* 43 (11), 5707–5715. doi:10.1002/2016GL068739

Mugnier, J.-L., Gajurel, A., Huyghe, P., Jayangondaperumal, R., Jouanne, F., and Upreti, B. (2013). Structural Interpretation of the Great Earthquakes of the Last Millennium in the central Himalaya. *Earth-Science Rev.* 127, 30–47. doi:10.1016/j.earscirev.2013.09.003

Mugnier, J., Huyghe, P., Leturmy, P., and Jouanne, F. (2004). "Episodicity and Rates of Thrust Sheet Motion in Himalaya (Western Nepal)," in *Thrust Tectonics and Hydrocarbon Systems*. Editor K. R. Mc Clay (American Association of Petroleum Geologists Memoir), 91–114.

Mukul, M., Jade, S., Ansari, K., Matin, A., and Joshi, V. (2018). Structural Insights from Geodetic Global Positioning System Measurements in the Darjiling-Sikkim Himalaya. *J. Struct. Geology* 114, 346–356. doi:10.1016/j.jsg.2018.03.007

Murray, A. S., and Wintle, A. G. (2000). Luminescence Dating of Quartz Using an Improved Single-Aliquot Regenerative-Dose Protocol. *Radiat. measurements* 32 (1), 57–73. doi:10.1016/s1350-4487(99)00253-x

Nakata, T. (1972). Geomorphic History and Crustal Movement of the Foot-hills of the Himalayas, The Science Reports of the Tohoku University 7th series. *Geography* 22 (1), 39–177.

Pandey, A., Jayangondaperumal, R., Hetényi, G., Priyanka, R. S., Singh, I., Srivastava, P., et al. (2021). Establishing Primary Surface Rupture Evidence And Magnitude of The 1697 CE Sadiya Earthquake At The Eastern Himalayan Frontal Thrust, India. *Sci. Rep.* 11, 879. doi:10.1038/s41598-020-79571-w

Pant, M. R. (2002). A Step toward a Historical Seismicity of Nepal. *Adarsa* 2, 29–60.

Philip, H., and Meghraoui, M. (1983). Structural Analysis and Interpretation of the Surface Deformations of the El Asnam Earthquake of October 10, 1980. *Tectonics* 2 (1), 17–49. doi:10.1029/tc002i001p00017

Pierce, I., and Wesnousky, S. G. (2016). On a Flawed Conclusion that the 1255 A.D. Earthquake Ruptured 800 Km of the Himalayan Frontal Thrust East of Kathmandu. *Geophys. Res. Lett.* 43 (17), 9026–9029. doi:10.1002/2016gl070426

Quigley, M. C., Hughes, M. W., Bradley, B. A., van Ballegooy, S., Reid, C., Morgenroth, J., et al. (2016). The 2010-2011 Canterbury Earthquake Sequence: Environmental Effects, Seismic Triggering Thresholds and Geologic Legacy. *Tectonophysics* 672-673, 228–274. doi:10.1016/j.tecto.2016.01.044

Rajendran, C., Rajendran, K., Duarah, B., Baruah, S., and Earnest, A. (2004). Interpreting the Style of Faulting and Paleoseismicity Associated with the 1897 Shillong, Northeast India, Earthquake: Implications for Regional Tectonism. *Tectonics* 23 (4). doi:10.1029/2003tc001605

Ramsey, C. B. (2017). Methods for Summarizing Radiocarbon Datasets. *Radiocarbon* 59 (6), 1809–1833. doi:10.1017/rdc.2017.108

Reimer, P. J., Austin, W. E. N., Bard, E., Bayliss, A., Blackwell, P. G., Bronk Ramsey, C., et al. (2020). The IntCal20 Northern Hemisphere Radiocarbon Age Calibration Curve (0-55 Cal kBP). *Radiocarbon* 62 (4), 725–757. doi:10.1017/rdc.2020.41

Reimer, P. J., Bard, E., Bayliss, A., Beck, J. W., Blackwell, P. G., Ramsey, C. B., et al. (2013). IntCal13 and Marine13 Radiocarbon Age Calibration Curves 0-50,000 Years Cal BP. *Radiocarbon* 55 (4), 1869–1887. doi:10.2458/azu_js_rc.55.16947

Reimer, P. J., Brown, T. A., and Reimer, R. W. (2004). Discussion: Reporting and Calibration of post-bomb 14C Data. *Radiocarbon* 46 (3), 1299–1304.

Robinson, T. R. (2020). Scenario Ensemble Modelling of Possible Future Earthquake Impacts in Bhutan. *Nat. Hazards* 103 (3), 3457–3478. doi:10.1007/s11069-020-04138-x

Sapkota, S. N., Bollinger, L., Klinger, Y., Tapponnier, P., Gaudemer, Y., and Tiwari, D. (2013). Primary Surface Ruptures of the Great Himalayan Earthquakes in 1934 and 1255. *Nat. Geosci.* 6 (1), 71–76. doi:10.1038/ngeo1669

Schirmer, W. (2020). Edifice of Fluvial Terrace Flights, Stacks and Rows. *Geosciences* 10 (12), 501.

Singer, J., Obermann, A., Kissling, E., Fang, H., Hetényi, G., and Grujic, D. (2017). Along-strike Variations in the H Imalayan Orogenic Wedge Structure in B Hutan from Ambient Seismic Noise Tomography. *Geochem. Geophys. Geosyst.* 18 (4), 1483–1498. doi:10.1002/2016gc006742

Stahl, T., Quigley, M. C., McGill, A., and Bebbington, M. S. (2016). Modeling Earthquake Moment Magnitudes on Imbricate Reverse Faults from Paleoseismic Data: Fox Peak and forest Creek Faults, South Island, New Zealand. *Bull. Seismological Soc. America* 106 (5), 2345–2363. doi:10.1785/0120150215

Stevens, V. L., and Avouac, J. P. (2015). Interseismic Coupling on the Main Himalayan Thrust. *Geophys. Res. Lett.* 42 (14), 5828–5837. doi:10.1002/2015gl064845

Stevens, V. L., De Risi, R., Le Roux-Mallouf, R., Drukpa, D., and Hetényi, G. (2020). Seismic hazard and Risk in Bhutan. *Nat. Hazards* 104 (3), 2339–2367. doi:10.1007/s11069-020-04275-3

Stockmal, G. S., Lebel, D., Mcmechan, M. E., and Mackay, P. A. (2001). Structural Style and Evolution of the triangle Zone and External Foothills, Southwestern Alberta: Implications for Thin-Skinned Thrust-and-fold belt Mechanics. *Bull. Can. Pet. Geology* 49 (4), 472–496. doi:10.2113/49.4.472

Stuiver, M., and Polach, H. A. (1977). Discussion Reporting of 14C Data. *Radiocarbon* 19 (3), 355–363. doi:10.1017/s0033822200003672

Sutar, A. K., Verma, M., Pandey, A. P., Bansal, B. K., Rajendra Prasad, P., Rama Rao, P., et al. (2017). Assessment of Maximum Earthquake Potential of the Kopili Fault Zone in Northeast India and strong Ground Motion Simulation. *J. Asian Earth Sci.* 147, 439–451. doi:10.1016/j.jseaes.2017.07.035

Szeliga, W., Hough, S., Martin, S., and Bilham, R. (2010). Intensity, Magnitude, Location, and Attenuation in India for Felt Earthquakes since 1762. *Bull. Seismological Soc. America* 100 (2), 570–584. doi:10.1785/0120080329

Toda, S., Stein, R. S., Richards-Dinger, K., and Bozkurt, S. B. (2005). Forecasting the Evolution of Seismicity in Southern California: Animations Built on Earthquake Stress Transfer. *J. Geophys. Res. Solid Earth* 110 (B5). doi:10.1029/2004jb003415

Upreti, B., Nakata, T., Kumahara, Y., Yagi, H., Okumura, K., Rockwell, T., et al. (2000). The Latest Active Faulting in Southeast Nepal. Paper presented at the Proceedings of the Hokudan International symposium and School in active faulting.

USGS (2020). M 6.1 - Bhutan. Retrieved from Available at: https://earthquake.usgs.gov/earthquakes/eventpage/usp000h1r4/executive.

van der Beek, P., Robert, X., Mugnier, J.-L., Bernet, M., Huyghe, P., and Labrin, E. (2006). Late Miocene - Recent Exhumation of the central Himalaya and Recycling in the Foreland basin Assessed by Apatite Fission-Track Thermochronology of Siwalik Sediments, Nepal. *Basin Res.* 18 (4), 413–434. doi:10.1111/j.1365-2117.2006.00305.x

Wacker, L., Bonani, G., Friedrich, M., Hajdas, I., Kromer, B., Němec, M., et al. (2010a). MICADAS: Routine And High-Precision Radiocarbon Dating. *Radiocarbon* 52 (2), 252–262. doi:10.1017/S0033822200045288

Wacker, L., Němec, M., and Bourquin, J. (2010b). A Revolutionary Graphitisation System: Fully Automated, Compact and Simple. *Nucl. Instrum. Methods Phys. Res. B* 268 (7-8), 931–934. doi:10.1016/j.nimb.2009.10.067

Wells, D. L., and Coppersmith, K. J. (1994). New Empirical Relationships Among Magnitude, Rupture Length, Rupture Width, Rupture Area, and Surface Displacement. *Bull. seismological Soc. America* 84 (4), 974–1002.

Welte, C., Hendriks, L., Wacker, L., Haghipour, N., Eglinton, T. l., and Günther, D. (2018). Towards The Limits: Analysis Of Microscale 14C Samples Using EA-AMS. *Nucl. Instrum. Methods Phys. Res. B* 437, 66–74. doi:10.1016/j.nimb.2018.09.046

Whipple, K. X., and Tucker, G. E. (1999). Dynamics of the Stream-Power River Incision Model: Implications for Height Limits of Mountain Ranges, Landscape Response Timescales, and Research Needs. *J. Geophys. Res.* 104 (B8), 17661–17674. doi:10.1029/1999jb900120

Conflict of Interest: The authors declare that the research was conducted in the absence of any commercial or financial relationships that could be construed as a potential conflict of interest.

frontiers in Earth Science

ORIGINAL RESEARCH
published: 24 August 2021
doi: 10.3389/feart.2021.655173

Effects of Salt Thickness on the Structural Deformation of Foreland Fold-and-Thrust Belt in the Kuqa Depression, Tarim Basin: Insights From Discrete Element Models

Changsheng Li[1,2,3], Hongwei Yin[3], Zhenyun Wu[1,2]*, Peng Zhou[4], Wei Wang[3], Rong Ren[5], Shuwei Guan[5], Xiangyun Li[6], Haoyu Luo[6] and Dong Jia[3]*

[1]State Key Laboratory of Nuclear Resources and Environment, East China University of Technology, Nanchang, China, [2]School of Earth Sciences, East China University of Technology, Nanchang, China, [3]School of Earth Sciences and Engineering, Nanjing University, Nanjing, China, [4]Resource Exploration Office, Tarim Oilfield Branch Company, PetroChina, Korla, China, [5]PetroChina Research Institute of Petroleum Exploration and Development, Beijing, China, [6]Research Institute of Petroleum Exploration and Development, Tarim Oilfield Branch Company, PetroChina, Korla, China

OPEN ACCESS

Edited by:
A. Alexander G. Webb,
The University of Hong Kong, China

Reviewed by:
Junpeng Wang,
China University of Geosciences Wuhan, China
Daniel Mège,
Space Research Center (PAN), Poland

***Correspondence:**
Hongwei Yin
hwyin@nju.edu.cn
Zhenyun Wu
zhenyun_wu@ecut.edu.cn

Specialty section:
This article was submitted to Structural Geology and Tectonics, a section of the journal Frontiers in Earth Science

Received: *18 January 2021*
Accepted: *19 July 2021*
Published: *24 August 2021*

Citation:
Li C, Yin H, Wu Z, Zhou P, Wang W, Ren R, Guan S, Li X, Luo H and Jia D (2021) Effects of Salt Thickness on the Structural Deformation of Foreland Fold-and-Thrust Belt in the Kuqa Depression, Tarim Basin: Insights From Discrete Element Models. Front. Earth Sci. 9:655173. doi: 10.3389/feart.2021.655173

The salt layer is critical for the structural deformation in the salt-bearing fold-and-thrust system, which not only acts as the efficient décollement layer but also flows to form salt tectonics. Kuqa Depression has a well-preserved thin-skinned fold-and-thrust system with the salt layer as the décollement. To investigate the effects of salt thickness on the structural deformation in the Kuqa Depression, three discrete element models with different salt thicknesses were constructed. The experiment without salt was controlled by several basal décollement dominant faults, forming several imbricate sheets. The experiments with salt developed the decoupled deformation with the salt layer as the upper décollement (subsalt, intrasalt, and suprasalt), significantly similar to the Kuqa Depression along the northern margin of Tarim Basin. Basal décollement dominant imbricated thrusts formed at the subsalt units, while the monoclinal structure formed at the suprasalt units. The decoupled deformation was also observed in the tectonic deformation graphics, distortional strain fields, and max shear stress fields. However, the salt layer was thickened in the thick salt model, and the salt thickness of the thin salt model varied slightly because the thin salt weakened the flowability of the salt. The lower max shear stress zone was easily formed in the distribution region of salt under the action of compression stress, which is conducive to the flow convergence of salt and the crumpled deformation of interlayer in salt. The results are well consistent with the natural characteristics of structural deformation in the Kuqa Depression. Our modeling result concerns the structural characteristics and evolution of salt-related structures and the effects of salt thickness on the structural deformation in the compressional stress field, which might be helpful for the investigations of salt-related structures in other salt-bearing fold-and-thrust belts.

Keywords: salt-related structures, salt thickness, Kuqa Depression, DEM, strain-stress

INTRODUCTION

The Kuqa Depression is a peripheral foreland basin placed at the southern piedmont of Tianshan Orogen, Northwest China (**Figure 1**). It develops from the Late Permian to Quaternary with strong compressional deformation since the late Cenozoic (Nishidai and Berry (1990); (Lu et al., 1994; Yin et al., 1998; Lu et al., 1999; Liu et al., 2000)). Bounded by the Kuqa River, the depression can be divided into the eastern Kuqa Depression and the western Kuqa Depression (Xin et al., 2002). From the north to south, five main structural belts are divided according to the different structural features in the western Kuqa Depression: the North structural belt (NSB), Kelasu structural belt (KLSSB), Baicheng sag (BCS), Qiulitage structural belt (QLTGSB), and the South basement slope belt (SBSB) (**Figure 1**) (Yin et al., 1998; Xin et al., 2002). As one of the most important hydrocarbon-bearing evaporite basins in China (Yu et al., 2014; Feng et al., 2018; Song et al., 2019), numerous salt-related structures were widely developed in the Kuqa Depression, especially in the Kelasu structural belt with obvious topographic relief features and obvious structural deformation features (Tang et al., 2004; Wu et al., 2014; Yu et al., 2014; Wu et al., 2015a; Zhao and Wang, 2016; Wang et al., 2017; Neng et al., 2018).

In recent years, based on structural analysis of seismic profiles with the application of several structural analysis techniques, such as the interpretation or balanced analysis of seismic profiles (Li and Qi, 2012; Neng et al., 2012; Neng et al., 2013; Yu et al., 2015; Hou et al., 2019), the area–depth–strain method (Xie et al., 2015; Wang et al., 2017), and the Coulomb wedge theory (Suppe, 2007; Lin et al., 2017), and structural simulated techniques, such as the sandbox physical simulation (Wang et al., 2010; Yin et al., 2011; Li and Qi, 2012; Xu et al., 2012; Wu et al., 2014) and numerical simulation (Wang et al., 2010; Xu et al., 2012; Li W. et al., 2017; Duan et al., 2017; Li, 2019; Li et al., 2020), further understanding has been obtained on the research of structures in the Kelasu structural belt. In many compressional salt-bearing basins around the world, the rock salt, as the important décollement layer, has been demonstrated to have important impact on regional structural evolution (Cotton and Koyi, 2000; Wu et al., 2014; Wu et al., 2015b). Meanwhile, much attention has been paid on the differential thickness distribution of Kumugeliemu salt and Jidike salt in the western and eastern Kuqa Depression (Chen et al., 2004; Tang et al., 2004; Li et al., 2012; Yu et al., 2014; Tang et al., 2015; Zhao and Wang, 2016; Wang et al., 2017). How did differential thickness distribution of these two salt layers influence the structural deformation in the western and eastern depression? It is worthy of further research to explore the influence of the differential thickness of rock salt on the structural evolution, especially from the perspective of experimental simulation.

In this study, two seismic profiles were presented to reveal the differential structural deformation caused by the difference in the thickness of the salt layers. Besides, three two-dimensional discrete element models with different salt thicknesses were constructed to investigate the characteristics of the differential structural deformation in the western Kuqa Depression. The experimental setup, the model construction technique, the material, and the wall properties were prescribed. Based on three simulation experiments, we focused on the internal relationship between the experimental results and structural deformation characteristics in the northern margin of the Kuqa area, e.g., the formation of the "accommodative space" in the salt strata and the crumpled deformation of the dolomite interbed in the Kelasu structural belt.

GEOLOGICAL SETTING

The Kelasu structural belt is a strong structural deformation belt placed at the northern part of the western Kuqa Depression (**Figure 1**). The stratigraphy of the Kuqa Depression has been

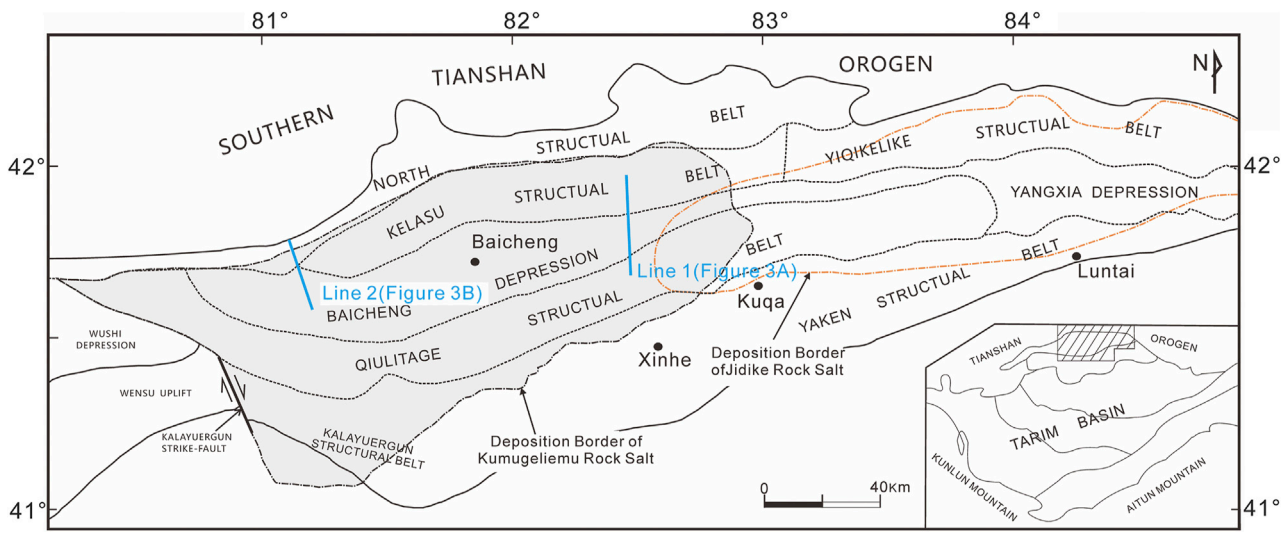

FIGURE 1 | Structural units of the Kuqa Depression, Tarim Basin.

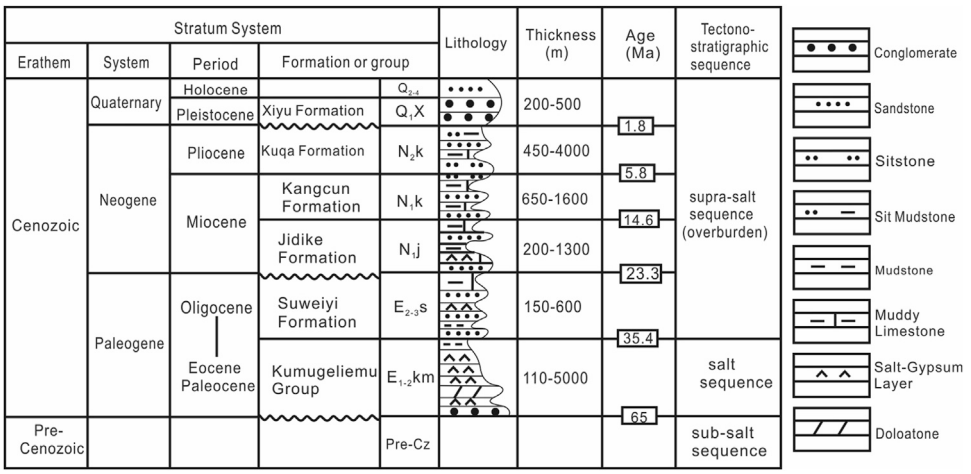

FIGURE 2 | Stratigraphy of the Kuqa Foreland Basin.

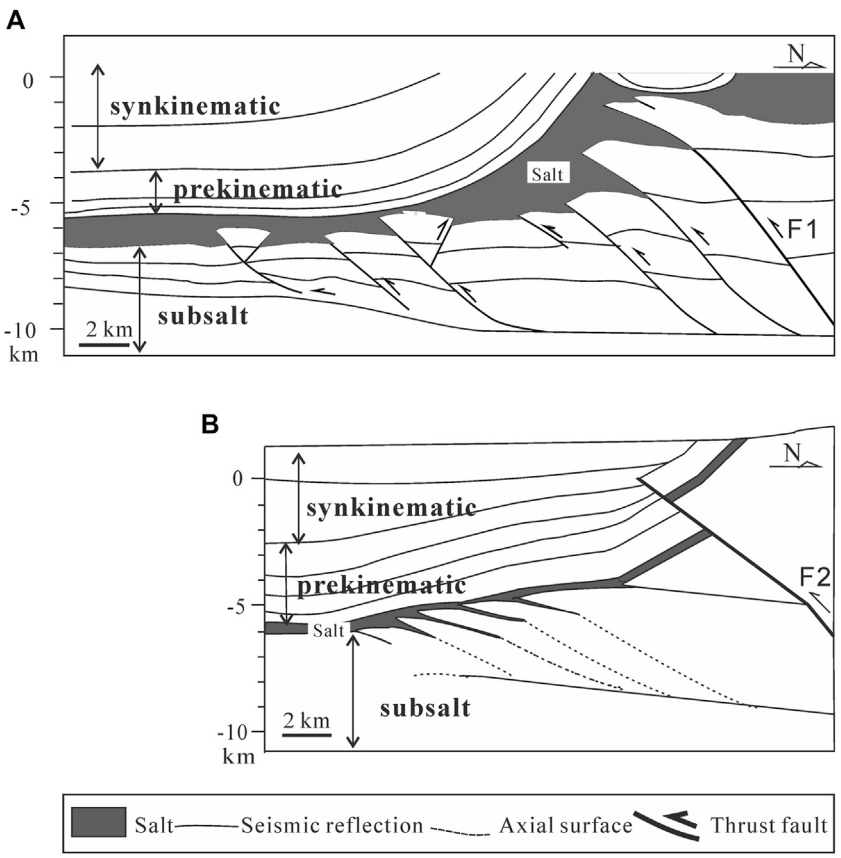

FIGURE 3 | Two interpreted models of seismic profiles in the northern margin of western Kuqa Depression. **(A)** The thick salt model. Interpreted seismic section Line 1 (see **Figure 1** for location) of the western Kelasu structure in the western Kuqa Depression; data revised from Wang et al. (2017). **(B)** The thin salt model. Interpreted seismic section Line 2 (see **Figure 1** for location) of the eastern Kelasu structure in the western Kuqa Depression; data revised from Wu et al. (2014). The prekinematic strata (syn, isopachous layer) interval whose initial stratigraphic thickness is constant above a salt structure. It records sedimentation before salt movement. The synkinematic layer accumulated during salt flow and may include internal onlap or truncation. The subsalt strata were sedimentary units immediately underlying salt.

summarized regionally (Yin et al., 1998; Chen et al., 2004; Wang et al., 2011). Isolated by the evaporative rock salt, the stratigraphic column could be subdivided into three parts (**Figure 2**): (1) Palaeozoic and Mesozoic subsalt basement; (2) the Palaeocene–Eocene Kumugeliemu ($E_{1\text{-}2}$km) evaporative rock salt; and (3) Eocene–Quaternary overburden which is composed of old strata to young strata by Suweiyi formation ($E_{2\text{-}3}$s), Jidike formation (N_1j), Kangcun formation (N_1k), Kuqa formation (N_2k), and Xiyu formation (Q_1x). The strata E_{2-3}s to N_1k were interpreted as prekinematic strata (**Figure 3A**) which were deposited before salt flow began. The prekinematic strata (syn, isopachous layer) interval's initial stratigraphic thickness is constant above a salt structure (Jackson and Talbot, 1991). These record sedimentation before salt movement. The strata N_2k to the Quaternary (Q) were interpreted as synkinematic strata (**Figure 3A**) which accumulated during salt flow and may include internal onlap or truncation (Jackson and Talbot, 1991; Wu et al., 2014). The thickness of the synkinematic sedimentation is about 6–8 km in the western Kuqa Depression (Wang et al., 2011). According to the interpreted seismic profiles (**Figure 3**), the differential thickness and the vertical distribution of the salt layer were presented, i.e., the thick salt model with ca. 1,000 m salt in the western Kelasu structural belt (Wu et al., 2014) and the thin salt model with ca. 200 m salt in the eastern Kelasu structural belt (Wang et al., 2017). Several typical structural characteristics were summarized as follows based on the comprehensive comparison and analysis of typical seismic profiles.

The Western Kelasu Structural Belt

The salt layer was thickened in the thick salt model (**Figure 3A**) because the flowability of the salt could be enhanced. The fault F1 (**Figure 3A**) pinched out on the salt layer. Two major décollement levels exist in Kuqa Depression, i.e., an upper décollement with salt–gypsum lithologies (the Paleogene–Miocene Kumgeliem and Jidike strata) and the lower décollement mostly within Jurassic coal and mudstone strata (Wang et al., 2011). Imbricate thrust faults and duplex structures linking the two décollements developed with salt that flowed into the cores of the duplex structure (F1, **Figure 3A**). The differences in the geometries of salt structures in different regions show that the thickness of the salt sequences has an important influence on the development of salt-cored décollement folds and related thrust faults in the Tarim Basin (Wu et al., 2014).

The Eastern Kelasu Structural Belt

The fault F2 (**Figure 3B**) in the piedmont thrust fold belt of the Kuqa Depression directly cuts through all the layers and nappes to the shallow strata from the deep of orogenic belts. The thin salt between the salt substratum and the slat superstratum shows no obvious rheological properties, so the salt thickness shows little variation (**Figure 3B**).

EXPERIMENTAL METHOD AND MODEL SETUP

The discrete element method (DEM) has been applied to the study of geological and geophysical problems in recent decades (Hardy et al., 2009; Yin et al., 2009; Liu et al., 2015; Morgan, 2015; Botter et al., 2016; Buiter et al., 2016; Morgan and Bangs, 2017; Li, 2019; Li et al., 2020; Xu et al., 2021). A full, detailed description of the theory behind this modeling approach and its application to geological problems is given by Morgan (2015) and Li C. et al. (2017, 2018, 2021), Li (2019). A geological body is simplified into an assemblage of ball elements which obey Newton's equations of motion and can move under the action of the forces which are generated by interaction with pairs by elastic springs. Our implementation of DEM in the discrete element software ZDEM was summarized by Li (2019).

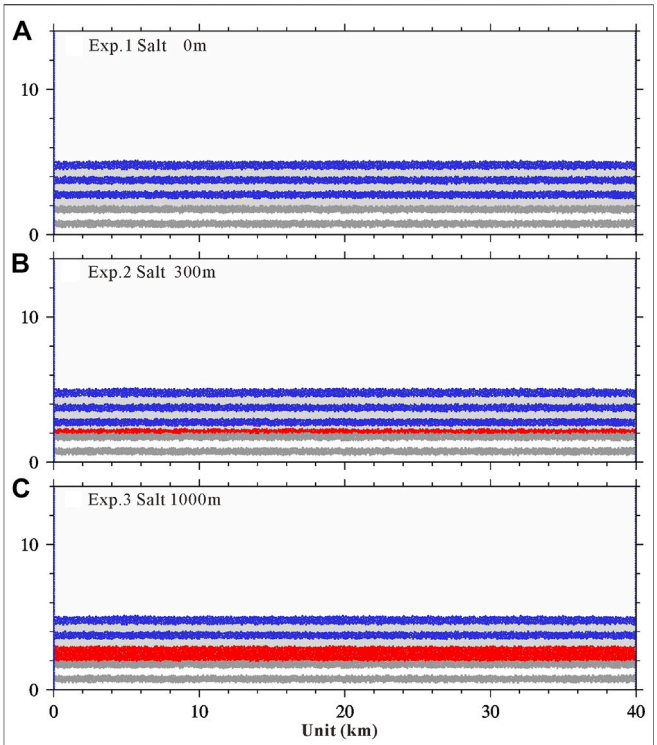

FIGURE 4 | Initial models. **(A)** Reference experiment without salt. **(B)** Experiment with thin salt (ca. 300 m tall). **(C)** Experiment with thick salt (ca. 1,000 m tall). White and gray denote the subsalt stratum. Red denotes the salt layer. Blue and gray denote the prekinematic layer.

Three experiments presented here were all initialized by randomly generating particles within a 40 km wide × 14 km–tall domain. Particles were allowed to settle under gravity, bound by two vertical walls and a basal row of fixed particles. The resulting particle assembly was 40 km wide and 5 km thick, and values were chosen to allow typical sedimentary covers to be modeled, large absolute values of convergence to be achieved, and model boundaries to be far from the locus of deformation (**Figure 4**). The particle packing consisted of 12,234 particles, with uniform distribution radii of 60.0 and 80.0 m. To examine the influence of salt thickness on the structural deformation, three experiments were carried out on initially identical homogeneous packings and boundary and initial conditions and dimensions but using different sets of the salt thickness (**Figure 4**). As a reference experiment, there is no salt layer in Exp. 1. The salt thickness of Exp. 2 was set to ca. 300 m tall, and the salt thickness of Exp. 3 was set to ca. 1,000 m tall.

TABLE 1 | Particle properties and basic parameters for DEM simulation.

Quantity	Value
Density (kg m^{-3})	2,500.0 (rock), 2,200.0 (salt)
Radii (m)	60.0, 80.0
Shear modulus (Pa)	2.9e9
Poisson's ratio	0.2
Friction coefficient	0.3 (rock), 0.15 (foot wall), 0.0 (salt)
Local damping coefficient	0.4
Time step (s)	0.05
Gravitational acceleration (m s^{-2})	10.0
Wall velocity (m s^{-1})	2.0

TABLE 2 | Interparticle bond properties of rock layers for DEM simulation.

Quantity	Value
Young's modulus (Pa)	2.0e8
Shear modulus (Pa)	2.0e8
Tensile strength (Pa)	1.0e7
Cohesion (Pa)	2.0e7

The particle properties of experiments are presented in **Table 1**. Upon settling, bonds of assigned strengths (**Table 2**) were introduced at all interparticle contacts, except salt layers. Interparticle friction was set to 0.3 throughout the bonded domain (i.e., rock layer). There are two major décollement levels existing in the Kuqa Depression, i.e., an upper décollement in the salt layer and the lower décollement mostly within Jurassic coal and mudstone strata (Wang et al., 2011). As the low décollement, the interparticle friction of the foot wall was set to 0.15. As the upper décollement, the interparticle friction of the salt layers was set to 0.0 to ensure its lower strength.

The bulk mechanical properties of the numerical materials used in these experiments were prescribed by particle properties and bond parameters in **Tables 1** and **2**. These parameters in **Tables 1** and **2** were consistent with previous studies (Morgan, 2015; Li, 2019). They were calibrated through a series of repose angles and two-dimensional biaxial tests based on the method presented by Li, (2019; 2021) and Morgan (2015). In numerical simulations, a local damping coefficient, which was the one most commonly used (Potyondy and Cundall, 2004; Itasca Consulting Group 2008; Kozicki and Donzé, 2008; O'Sullivan, 2011; Scholtès and Donzé, 2013; Weatherley et al., 2014; Zhao, 2015; Li, 2019; Xu et al., 2021), was added to damp the reflected waves from the boundary of the particle and to avoid buildup of kinetic energy in the closed system (Itasca Consulting Group 2008; Li, 2019). The meaning of the other parameters in **Tables 1** and **2** was given by Morgan (2015) and Li (2019). The value of cohesion of rock layer and salt layer is, respectively, ca. 10.5 MPa and ca. 1.8 MPa (Li, 2019). The values of friction angles of rock layer and salt layer are ca. 18.6° and ca. 4.3°, respectively (Li, 2019). The value of cohesion is consistent with the strength of shallow crustal sediments (Camac et al., 2009; Jaeger et al., 2009; Schumann et al., 2014). Note that the values of friction angle are significantly lower than the typical value of friction angle, 30° (Jaeger et al., 2009; Wu et al., 2014), which is a common characteristic of these numerical materials (Morgan, 1999; Aharonov and Sparks, 2004; Morgan, 2004; Vidal and Bonneville, 2004; Dean et al., 2013; Gray et al., 2014; Morgan, 2015; Li, 2019), and consistent with shear experiments on smooth glass rods (Frye and Marone, 2002; Sun et al., 2016; Li, 2019).

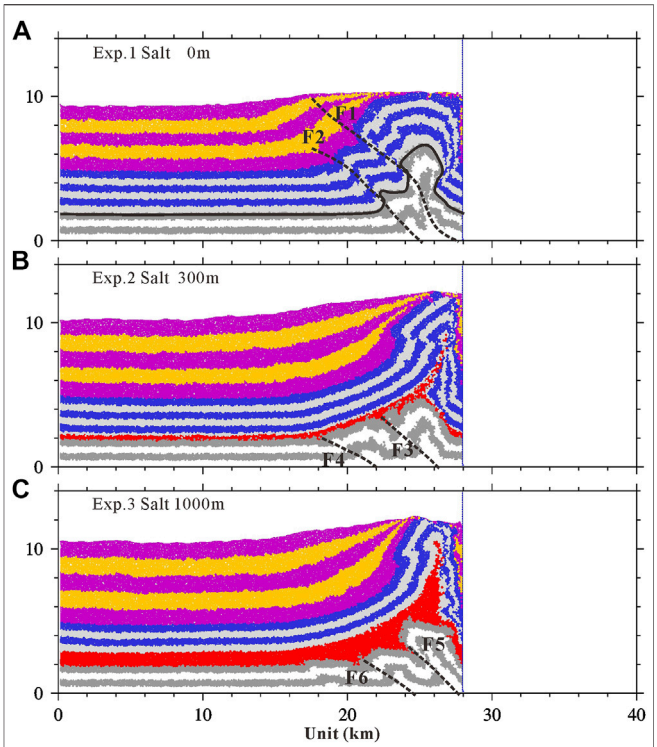

FIGURE 5 | Final deformations of three shortening experiments with different salt thicknesses after 12 km of shortening. **(A)** Reference experiment. **(B)** Experiment with thin salt (ca. 300 m). **(C)** Experiment with thick salt (ca. 1,000 m). White and gray denote the subsalt layer. Red denotes the salt layer. Blue and gray denote the prekinematic layer. Violet and yellow denote the synkinematic layer. Bonds of assigned strengths (**Table 2**) were introduced at all interparticle contacts, except the synkinematic layer (violet and yellow) and salt layer (red). Dashed lines denote faults. The figures of each step are included in the **Supplementary Material**.

The horizontal contraction was initiated by capturing particles along the right sidewall and applying a constant velocity of 2.0 m/s to the left. The time step per cycle was 0.05 s, producing 0.1 m of wall displacement per cycle. The synkinematic sedimentation played an important role in structural deformation in Kuqa Depression (Yin et al., 2011; Wu et al., 2014). After the first thrust was formed (ca. 2 km of shortening), ca. 0.5 km-thick synkinematic layer was deposited for every 1 km of shortening. The final thickness of the synkinematic layer was ca. 5 km.

EXPERIMENT RESULTS

Distribution Deformation

Comparative plots of the final particle configurations (12 km wall displacement) of the three experiments with different salt

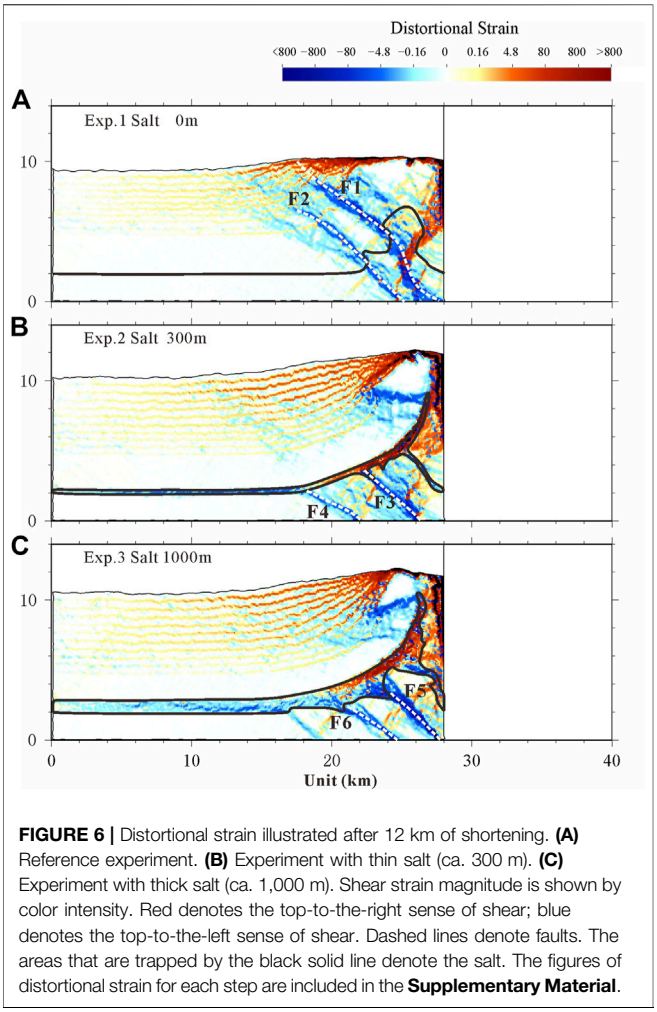

FIGURE 6 | Distortional strain illustrated after 12 km of shortening. **(A)** Reference experiment. **(B)** Experiment with thin salt (ca. 300 m). **(C)** Experiment with thick salt (ca. 1,000 m). Shear strain magnitude is shown by color intensity. Red denotes the top-to-the-right sense of shear; blue denotes the top-to-the-left sense of shear. Dashed lines denote faults. The areas that are trapped by the black solid line denote the salt. The figures of distortional strain for each step are included in the **Supplementary Material**.

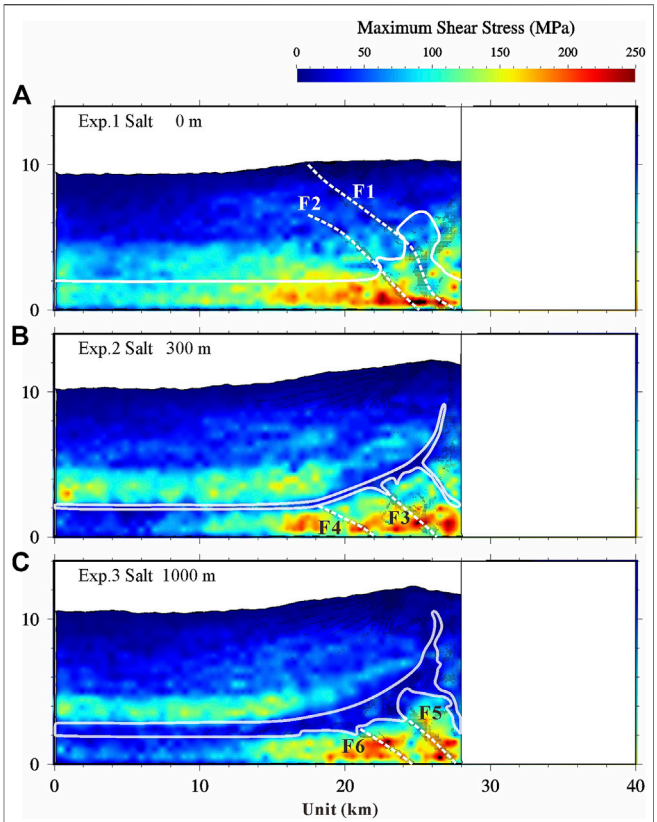

FIGURE 7 | Max shear stress illustrated after 12 km of shortening. **(A)** Reference experiment. **(B)** Experiment with thin salt (ca. 300 m). **(C)** Experiment with thick salt (ca. 1,000 m). The final structure of each series is superimposed by plotting regions of high distortional strain (i.e., the absolute value is greater than 4.8 in **Figure 6**) in black. Dashed lines denote faults. The areas that are trapped by the white solid line denote the salt. The figures of max shear stress for each step are included in the **Supplementary Material**.

thicknesses are shown in **Figure 5**. Three experiments have the same initial model but use different sets of salt thickness. As the reference experiment, Exp. 1 is without salt (**Figure 5A**). The salt thickness is ca. 300 m in Exp. 2 with thin salt (**Figure 5B**), while salt thickness is ca. 1,000 m in Exp. 3 with thick salt (**Figure 5C**).

Two faults form in Exp. 1 without salt layer, and the growth strata show the features of fault-propagation fold in accordance with the fault activity (**Figure 5A**). But, the deformation was apparently divided into two parts in Exp. 2 (ca. 300 m salt, **Figure 5B**) and Exp. 3 (ca. 1,000 m salt, **Figure 5C**) containing the salt layer. Deformation above and below the salt layer was decoupled, with the imbricate structure formed in the subsalt units and back-thrust fault formed in suprasalt units.

In **Figure 3B**, continuous progradation from the southern Tianshan piedmont until the end of the late Miocene–early Pliocene made Kumugeliemu salt flow basinward and F2 developed (Li et al., 2012). Accelerated crustal shortening since the end of the late Pliocene–early Pleistocene amplified the Misikantake anticline and formed the Quele salt nappe, and several new forward subsalt structures developed and they do not extend to the surface (Li et al., 2012). Previous studies have shown that frictional resistance increases with salt pinch-out (Dooley et al., 2007) and buttressing effects of a distal salt pinch-out can control the location and style of distal salt structures (Costa and Vendeville, 2002; Couzens-Schultz et al., 2003; Dooley et al., 2007). Faults can easily cut through rock layers without salt layers (**Figure 5A**), but they rarely cut the thick salt layers; instead, they detach along with the salt layers (**Figure 3A**, **5C**).

Distortional Strain

The distortional strain was used to quantify the results for DEM and was calculated according to the study by Morgan (2015). Distortional strain, i.e., strain-induced distortion, can be quantified as the second invariant of the deviatoric finite strain tensor (Morgan, 2015). Throughout the experiments, particle positions and interparticle forces were output every 10,000 cycles (1 km wall displacement), an interval referred to as an "increment." Subsequent calculations of particle displacements are made at whole increments, and this unit is used for plotting purposes.

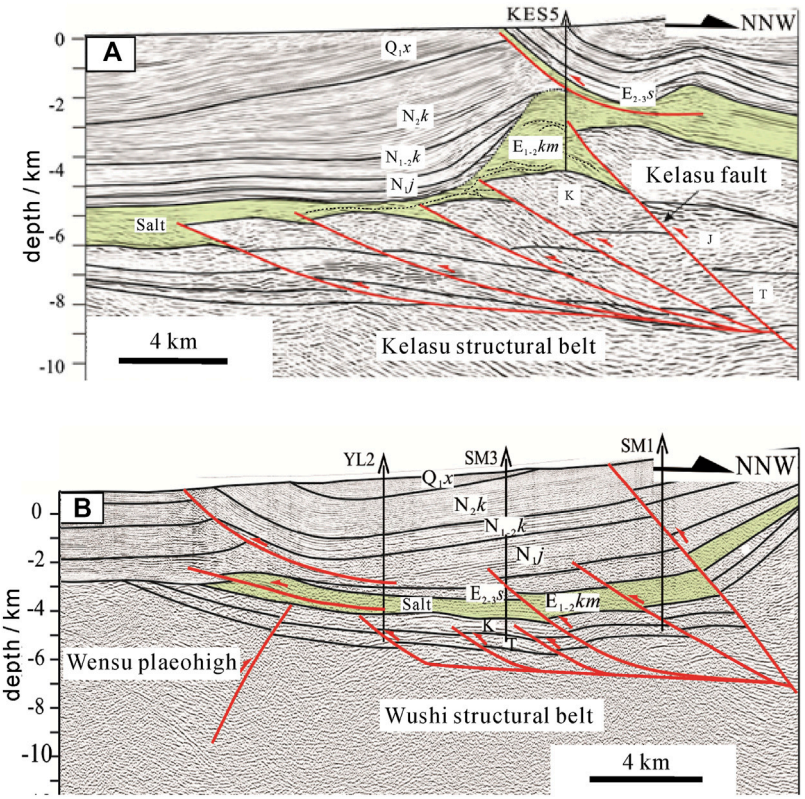

FIGURE 8 | Structural deformation characteristics caused by the differential thickness of the salt layer in **(A)** the Kelasu structural belt and **(B)** the Wushi structural belt; seismic profiles cited from Yang (2017).

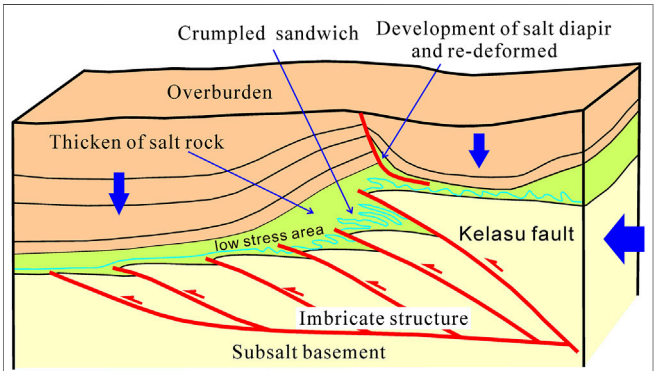

FIGURE 9 | Deformation model of the dolomite interbeds in the Kelasu structural belt; the crumpled data from Yang (2017).

The results of the three experiments are shown in **Figure 6** with plots of cumulative distortional strain after 12 km (the shortening rate 20%) of shortening. The experiments were accommodated by largely distributed shear deformation with occasional local zones of more intense top-to-the-left shearing (**Figure 6**, blue zones). Dip angles of the forward thrust (**Figure 6**, blue zones) were ca. 45° in all three experiments. They were in the same range as the dip angles (ca. 30°–50°, **Figures 3A,B**) of the forward thrust in the subsalt units.

As shown in **Figure 6B,C**, F3–F6 did not cut through the salt layer; instead, they detached along with the salt layer because of the flow of salt that contributes significantly to structural relief in this part of the Kuqa fold-and-thrust belt. On the contrary, F1 and F2 (**Figure 6A**) could easily cut through the rock layer. The salt layer was obviously thickened near the right wall when the initial thickness of salt was ca. 1,000 m (**Figure 6C**). The thickness of salt had a little change when the initial thickness of salt was ca. 300 m (**Figure 6B**) because the flowability of thin salt is weaker. The salt could be one of the main factors leading to differential tectonics. The contour map of distortional strain (**Figures 6A–C**) shows local strain concentration around the fault, indicating that faulting played an important role in the fracture development in the damage zone surrounding the fault. This mechanism explained the higher density of shear fractures that developed in the near-fault area and the salt layers.

Max Shear Stress

Stress invariants for all of the systems are calculated and plotted for 1 × 1 km elements (summing over ca. 25 particles), with colors scaled by stress magnitude. The final structure of each series (**Figure 7**) is superimposed by plotting regions of high distortional strain (i.e., the absolute value is greater than 4.8 in **Figure 6**) in black. Similar to the simulation results of Morgan (2015), there is a distinct variability within the wedges about the maximum shear stress, τ_{max} (**Figures**

7A–C). τ_{max} increased with depth due to the combined increase in both vertical and horizontal stresses with burial (Morgan, 2015). Moreover, τ_{max} was relatively high near the moving wall and in the foot walls of major shear zones. The highest values of τ_{max} usually appeared directly in front of the frontal thrusts, outlining regions of unfaulted material that still supported high shear stresses (Morgan, 2015). The frontal regions of high τ_{max} expanded with decreasing salt thickness (**Figure 7**), demonstrating the flowability of salt layers to dissipate shear stresses. The stress also had obvious stratification characteristics in the experiments with the salt layer.

DISCUSSION

Both the regional geological structure analysis and the structural simulation experiments show that if there is a regional distribution of salt rock as an important décollement layer in the fold orogenic belt and its foreland basin, the strata will undergo obvious structural stratification deformation in the vertical direction (**Figures 5**, **6**) (Wang et al., 2010; Yin et al., 2011; Xu et al., 2012; Wu et al., 2014; Yang, 2017; Neng et al., 2018; Li, 2019; Li et al., 2020; Sun et al., 2021; Xu et al., 2021). The results of these experiments well reflect the regional structural characteristics of the northern margin of the western Kuqa Depression (**Figure 8**). In the northern margin of the western section of Kuqa Depression, the basement involved thrust faults into the salt with a large displacement. When the salt is thick, the thrust fault will make the overlying salt significantly thicken and create favorable "accommodative space," which is conducive to the formation of the salt anticline and salt diapir (**Figure 3A**, **8A**). When the salt is thin, it is easy to cut through by faults, which is not conducive to the formation of favorable "accommodative space" (**Figure 3B**, **8B**).

The results of the three simulations also show that a lower max shear stress zone is easily formed in the distribution region of salt under the action of compression stress, which is conducive to the flow convergence of salt and the crumpled deformation of interlayer in salt (**Figures 7**, **9**). When the thickness of salt decreases, the fluidity of salt decreases obviously which is not conducive to salt convergence to form salt-related structures (**Figure 8B**). While the salt is thick enough, its fluidity is obviously enhanced which is conducive to the flow and convergence of salt from the high-stress area to the low-stress area and forms larger salt structures, such as salt anticline or salt diapir structures (**Figure 8A**)

There are a fewer imbricate faults of the subsalt units in three discrete element simulations (**Figure 5C**) than in the interpreted seismic sections of the Kelasu structure in the Kuqa Depression (**Figure 3A**, **8A**). The displacement of shortening, the slope, and the thickness of substrate décollement may control the distribution range and the number of imbricate faults in the subsalt units. We would make further analysis in the later study.

CONCLUSION

Effects of salt thickness on the structural deformation were discussed using different seismic profiles in the foreland fold-and-thrust belt of the Kuqa Depression, which indicated that the thickness of the salt had an important influence on the structural styles.

The experiment without salt was controlled by several basal décollement dominant faults, forming several imbricate sheets. The experiments with salt developed the decoupled deformation with the salt layer as the upper décollement (subsalt, intrasalt, and suprasalt), significantly similar to the Kuqa Depression in the northern margin of Tarim Basin. Basal décollement dominant imbricated thrusts formed at the subsalt units, while the monoclinal structure formed at the suprasalt units. The decoupled deformation was also observed in the tectonic deformation graphics, distortional strain fields, and max shear stress fields. However, the salt layer was thickened in the thick salt model and the salt thickness of the thin salt model varied slightly because the thin salt weakened the flowability of the salt evidently. The lower max shear stress zone was easily formed in the distribution region of salt under the action of compression stress, which is conducive to the flow convergence of salt and the crumpled deformation of interlayer in salt. These phenomena are well consistent with the natural characteristic of structural deformation in the Kuqa Depression, Tarim Basin.

The modeling results in this study concern the structural characteristics and evolution of salt-related structures and the effects of salt thickness on the structural deformation in the compressional stress field, which might be helpful for the investigations of salt-related structures in other salt-bearing fold-and-thrust belts.

DATA AVAILABILITY STATEMENT

The original contributions presented in the study are included in the article/**Supplementary Material**; further inquiries can be directed to the corresponding author.

AUTHOR CONTRIBUTIONS

Conceptualization: CL and HY; methodology: CL, HY, and ZW; formal analysis and investigation: CL, HY, ZW, PZ, and WW; writing—original draft preparation: CL and ZW; writing—review and editing: HY, ZW, DJ, SG, RR, XL, and HL; funding acquisition: HY, CL, ZW, DJ, SG, and RR.

FUNDING

The authors gratefully acknowledge the financial support provided by the National Natural Science Foundation of China (grants 41972219, 41927802, 41572187, and 41602208), National S&T Major Project of China (grants 2016ZX05026-002-007, 2016ZX05003-001, and 2016ZX005008-001-005), the PhD

Starting Foundation of East China University of Technology (grants DHBK2019024 and DHBK2019053), and Project of PetroChina Company Limited (grant 2018A-0101). CL was also supported by program B for being an outstanding PhD candidate of Nanjing University.

ACKNOWLEDGMENTS

The authors would like to thank Julia K. Morgan and Thomas Fournier for generously sharing their postprocessing scripts and algorithms, which have been used to process and display the model outputs presented here. HY would like to thank Prof. Morgan for generously sharing her discrete element code RICEBAL (v. 5.1, modified from Peter Cundall's TRUBAL v. 1.51) and Rice University for hosting his collaborative visit in 2009, providing him with the opportunity to further develop his knowledge of DEM and geomechanics principles and learn the capabilities of these methods. The authors also would like to thank Wenqiao XU for the fruitful discussions on this manuscript. The authors are grateful for thoughtful reviews by two reviewers, which resulted in significant improvements in this paper. The authors acknowledge Beijing PARATERA Tech CO., Ltd. (https://paratera.com) for providing HPC resources that have contributed to the research results reported within this paper. Data used in this paper and the discrete element software ZDEM will be available online at https://geovbox.com, and more examples are given on this website. Modeling results and information can be obtained by contacting CL at lichangsheng@ecut.edu.cn.

SUPPLEMENTARY MATERIAL

The Supplementary Material for this article can be found online at: https://www.frontiersin.org/articles/10.3389/feart.2021.655173/full#supplementary-material

REFERENCES

Aharonov, E., and Sparks, D. (2004). Stick-slip Motion in Simulated Granular Layers. *J. Geophys. Res.* 109, a–n. doi:10.1029/2003JB002597

Botter, C., Cardozo, N., Hardy, S., Lecomte, I., Paton, G., and Escalona, A. (2016). Seismic Characterisation of Fault Damage in 3D Using Mechanical and Seismic Modelling. *Mar. Pet. Geology.* 77, 973–990. doi:10.1016/j.marpetgeo.2016.08.002

Buiter, S. J. H., Schreurs, G., Albertz, M., Gerya, T. V., Kaus, B., Landry, W., et al. (2016). Benchmarking Numerical Models of Brittle Thrust Wedges. *J. Struct. Geology.* 92, 140–177. doi:10.1016/j.jsg.2016.03.003

Camac, B. A., Hunt, S. P., and Boult, P. J. (2009). Predicting Brittle Cap-Seal Failure of Petroleum Traps: an Application of 2D and 3D Distinct Element Method. *Pet. Geosci.* 15, 75–89. doi:10.1144/1354-079309-796

Chen, S., Tang, L., Jin, Z., Jia, C., and Pi, X. (2004). Thrust and Fold Tectonics and the Role of Evaporites in Deformation in the Western Kuqa Foreland of Tarim Basin, Northwest China. *Mar. Pet. Geology.* 21, 1027–1042. doi:10.1016/j.marpetgeo.2004.01.008

Costa, E., and Vendeville, B. C. (2002). Experimental Insights on the Geometry and Kinematics of Fold-And-Thrust Belts above Weak, Viscous Evaporitic Décollement. *J. Struct. Geology.* 24, 1729–1739. doi:10.1016/S0191-8141(01)00169-9

Cotton, J. T., and Koyi, H. A. (2000). Modeling of Thrust Fronts above Ductile and Frictional Detachments: Application to Structures in the Salt Range and Potwar Plateau, Pakistan. *Geol. Soc. America Bull.* 112, 351–363. doi:10.1130/0016-7606(2000)112%3C351:MOTFAD%3E2.0.CO;2

Couzens-Schultz, B. A., Vendeville, B. C., and Wiltschko, D. V. (2003). Duplex Style and triangle Zone Formation: Insights from Physical Modeling. *J. Struct. Geology.* 25, 1623–1644. doi:10.1016/S0191-8141(03)00004-X

Dean, S. L., Morgan, J. K., and Fournier, T. (2013). Geometries of Frontal Fold and Thrust Belts: Insights from Discrete Element Simulations. *J. Struct. Geology.* 53, 43–53. doi:10.1016/j.jsg.2013.05.008

Dooley, T. P., Jackson, M. P. A., and Hudec, M. R. (2007). Initiation and Growth of Salt-Based Thrust Belts on Passive Margins: Results from Physical Models. *Basin Res.* 19, 165–177. doi:10.1111/j.1365-2117.2007.00317.x

Duan, Y., Shaoying, H., Li, W., Zhang, H., Ma, X., and Liao, F. (2017). Using Discrete Element Numerical Simulation Method to Study Salt Tectonic Deformation Mechanism of Kelasu Structural Belt. *Xinjiang Pet. Geology.* 38, 1. 2017. (in Chinese with English abstract). doi:10.7657/XJPG20170406

Feng, J., Dai, J., Lu, J., and Li, X. (2018). Quantitative Prediction of 3-D Multiple Parameters of Tectonic Fractures in Tight sandstone Reservoirs Based on Geomechanical Method. *IEEE Access* 6, 39096–39116. doi:10.1109/ACCESS.2018.2847723

Frye, K. M., and Marone, C. (2002). The Effect of Particle Dimensionality on Granular Friction in Laboratory Shear Zones. *Geophys. Res. Lett.* 29, 22-1–22-4. doi:10.1029/2002GL015709

Gray, G. G., Morgan, J. K., and Sanz, P. F. (2014). Overview of Continuum and Particle Dynamics Methods for Mechanical Modeling of Contractional Geologic Structures. *J. Struct. Geology.* 59, 19–36. doi:10.1016/j.jsg.2013.11.009

Hardy, S., McClay, K., and Anton Muñoz, J. (2009). Deformation and Fault Activity in Space and Time in High-Resolution Numerical Models of Doubly Vergent Thrust Wedges. *Mar. Pet. Geology.* 26, 232–248. doi:10.1016/j.marpetgeo.2007.12.003

Hou, G., Sun, S., Zheng, C., Tang, Y., Zhou, L., and Mo, T. (2019). Subsalt Structural Styles of Keshen Section in the Kelasu Tectonic Belt. *Xinjiang Pet. Geology.* 40, 21. (in Chinese with English abstract). doi:10.7657/XJPG20190103

Itasca Consulting Group (2008). *PFC2D (Particle Flow Code in 2 Dimensions) Online Manual*. Version 4.0. Minnesota: Itasca Consulting Group Inc.

Jackson, M., and Talbot, C. J. (1991). *A Glossary of Salt Tectonics Geological Circular*. Austin, TX, USA: The University of Texas at AustinBureau of Economic Geology, 1–44.

Jaeger, J. C., Cook, N. G., and Zimmerman, R. (2009). *Fundamentals of Rock Mechanics*. John Wiley & Sons. doi:10.1007/978-3-540-92128-8

Kozicki, J., and Donzé, F. V. (2008). A New Open-Source Software Developed for Numerical Simulations Using Discrete Modeling Methods. *Comput. Methods Appl. Mech. Eng.* 197, 4429–4443. doi:10.1016/j.cma.2008.05.023

Li, C. (2019). *Quantitative Analysis and Simulation of Structural Deformation in the Fold and Thrust belt Based on Discrete Element Method. Doctor Thesis*. Nanjing, China: NanJing University. (in Chinese with English abstract).

Li, C., Yin, H., Jia, D., Zhang, J., Wang, W., and Xu, S. (2018). Validation Tests for Discrete Element Codes Using Single-Contact Systems. *Int. J. Geomechanics* 18, 06018011. doi:10.1061/(ASCE)GM.1943-5622.0001133

Li, C., Yin, H., Liu, C., and Cai, S. (2017a). Design and Test of Parallel Discrete Element Method Program of Shared Memory Type. *J. Nanjing University(Natural Science)* 53, 1161–1170 (in Chinese with English abstract). doi:10.13232/j.cnki.jnju.2017.06.018

Li, C., Yin, H., Wu, C., Zhang, Y., Zhang, J., Wu, Z., et al. (2021). Calibration of the Discrete Element Method and Modeling of Shortening Experiments. *Front. Earth Sci.* 9, 636512. doi:10.3389/feart.2021.636512

Li, J., Zhang, Y., Wang, H., and Wang, D. (2020). Three-dimensional Discrete Element Numerical Simulation of Paleogene Salt Structures in the Western Kuqa Foreland Thrust belt. *Pet. Exploration Develop.* 47, 68–79. doi:10.1016/S1876-3804(20)60006-4

Li, S., Wang, X., and Suppe, J. (2012). Compressional Salt Tectonics and Synkinematic Strata of the Western Kuqa Foreland basin, Southern Tian Shan, China. *Basin Res.* 24, 475–497. doi:10.1111/j.1365-2117.2011.00531.x

Li, W., Li, J., Wang, H., Huang, S., and Neng, Y. (2017b). Deformation Mechanisms of Kelasu Tectonic belt in Kuqa Foreland Thrust belt: Insight from Discrete Element Numerical Simulation. *Geotectonica et Metallogenia* 41, 1001–1010. (in Chinese with English abstract). doi:10.16539/j.ddgzyckx.2017.06.001

Li, Y., and Qi, J. (2012). Delamination Contractional Deformation and it Main Controlled Factors of Kelasu Structural Zone in Kuqa Depression. *Chin. J. Geology. (Scientia Geologica Sinica)*. (in Chinese with English abstract).

Lin, C., Yin, H., Wang, W., Li, C., Neng, Y., Zhou, P., et al. (2017). Application of the Critical Taper Model in the Subsalt Structural Wedges—Example from Kelasu Structure belt of Kuqa Depression. *Geol. J. China Universities* 23, 491–498. (in Chinese with English abstract). doi:10.16108/j.issn1006-7493.2016209

Liu, C., Pollard, D. D., Gu, K., and Shi, B. (2015). Mechanism of Formation of Wiggly Compaction Bands in Porous sandstone: 2. Numerical Simulation Using Discrete Element Method. *J. Geophys. Res. Solid Earth* 120, 8153–8168. doi:10.1002/2015JB012374

Liu, Z. H., Lu, H., Li, X., Jia, C. Z., Lei, G., Chen, C. M., et al. (2000). Tectonic Evolution of Kuqa Rejuvenated Foreland basin. *Scientia Geologica Sinica* 35, 482–492. (in Chinese with English abstract).

Lu, H., Howell, D. G., Jia, D., Cai, D., Wu, S., Chen, C., et al. (1994). Rejuvenation of the Kuqa Foreland basin, Northern Flank of the Tarim basin, Northwest China. *Int. Geology. Rev.* 36, 1151–1158. doi:10.1080/00206819409465509

Lu, H., Jia, D., Chen, C., Liu, Z., Wang, G., and Jia, C. (1999). Nature and Timing of the Kuqa Cenozoic Structures. *Earth Sci. Front.* 6, 215–221. (in Chinese with English abstract).

Morgan, J. K., and Bangs, N. L. (2017). Recognizing Seamount-Forearc Collisions at Accretionary Margins: Insights from Discrete Numerical Simulations. *Geology* 45, 635–638. doi:10.1130/G38923.1

Morgan, J. K. (2015). Effects of Cohesion on the Structural and Mechanical Evolution of Fold and Thrust Belts and Contractional Wedges: Discrete Element Simulations. *J. Geophys. Res. Solid Earth* 120, 3870–3896. doi:10.1002/2014JB011455

Morgan, J. K. (1999). Numerical Simulations of Granular Shear Zones Using the Distinct Element Method: 2. Effects of Particle Size Distribution and Interparticle Friction on Mechanical Behavior. *J. Geophys. Res.* 104, 2721–2732. doi:10.1029/1998jb900055

Morgan, J. K. (2004). Particle Dynamics Simulations of Rate- and State-dependent Frictional Sliding of Granular Fault Gouge. *Comput. Earthquake Sci.* 161, 1877–1891. doi:10.1007/978-3-0348-7873-9_5

Neng, Y., Sun, H., Xu, L., and Cao, S. (2013). Research on Structural Transfer Based on 3D Seismic Data----A Case Study from KL1 and KL2 Structures of Foreland Thrust Belt, Kuqa Depression. *China Pet. Exploration* 18, 12. doi:10.3969/j.issn.1672-7703.2013.03.002

Neng, Y., Xie, H., Li, Y., Lei, G., and Yang, X. (2012). The character of deformation style and its distribution law in the middle Part of Kuqa depression, northern margin of Tarim Basin, NW China. *Dizhi Kexue/Chin. J. Geology.* 47, 629–639. (in Chinese with English abstract).

Neng, Y., Xie, H., Yin, H., Li, Y., and Wang, W. (2018). Effect of basement structure and salt tectonics on deformation styles along strike: An example from the Kuqa fold-thrust belt, West China. *Tectonophysics* 730, 114–131. doi:10.1016/j.tecto.2018.02.006

Nishidai, T., and Berry, J. L. (1990). Structure and hydrocarbon potential of the Tarim Basin (NW China) from satellite imagery. *J. Pet. Geol* 13, 35–58. doi:10.1111/j.1747-5457.1990.tb00250.x

O'Sullivan, C. (2011). *Particulate Discrete Element Modelling*. Taylor & Francis. doi:10.1201/9781482266498

Potyondy, D. O., and Cundall, P. A. (2004). A bonded-particle model for rock. *Int. J. Rock Mech. Mining Sci.* 41, 1329–1364. doi:10.1016/j.ijrmms.2004.09.011

Scholtès, L., and Donzé, F.-V. (2013). A DEM model for soft and hard rocks: Role of grain interlocking on strength. *J. Mech. Phys. Sol.* 61, 352–369. doi:10.1016/j.jmps.2012.10.005

Schumann, K., Behrmann, J. H., Stipp, M., Yamamoto, Y., Kitamura, Y., and Lempp, C. (2014). Geotechnical behavior of mudstones from the Shimanto and Boso accretionary complexes, and implications for the Nankai accretionary prism. *Earth, Planets and Space* 66, 129. doi:10.1186/1880-5981-66-129

Song, X., Lü, X., Shen, Y., and Guo, S. (2019). Hydrocarbon migration and accumulation history in deep reservoirs: a case study of Mesozoic sandstone gas reservoirs in the Kelasu-Yiqikelike structural belt of the Kuqa Depression, Tarim Basin. *Geosci. J.* 23, 69–86. doi:10.1007/s12303-018-0011-6

Sun, C., Jia, D., Yin, H., Chen, Z., Li, Z., Shen, L., et al. (2016). Sandbox modeling of evolving thrust wedges with different preexisting topographic relief: Implications for the Longmen Shan thrust belt, eastern Tibet. *J. Geophys. Res. Solid Earth* 121, 4591–4614. doi:10.1002/2016JB013013

Sun, C., Li, Z., Wu, S., He, Z., Zhao, S., and Wang, P. (2021). Structural Significance of the Mid-level Décollement Within the Western Sichuan Fold-And-Thrust Belt (WSFTB), Insights From Sandbox Modeling. *Front. Earth Sci.* 9, 109. doi:10.3389/feart.2021.631405

Suppe, J. (2007). Absolute fault and crustal strength from wedge tapers. *Geol* 35, 1127–1130. doi:10.1130/G24053A.1

Tang, L.-J., Jia, C.-Z., Jin, Z.-J., Chen, S.-P., Pi, X.-J., and Xie, H.-W. (2004). Salt tectonic evolution and hydrocarbon accumulation of Kuqa foreland fold belt, Tarim Basin, NW China. *J. Pet. Sci. Eng.* 41, 97–108. doi:10.1016/S0920-4105(03)00146-3

Tang, P., Rao, G., Li, S., and Wang, R. (2015). The impact of salt layer thickness on the structural characteristics and evolution of detachment folds in the leading edge of Kuqa fold and thrust belt. *Earth Sci. Front.* 22, 312–327. doi:10.13745/j.esf.2015.01.027

Vidal, V., and Bonneville, A. (2004). Variations of the Hawaiian hot spot activity revealed by variations in the magma production rate. *J. Geophys. Res.* 109. doi:10.1029/2003JB002559

Wang, W., Yin, H., Jia, D., and Li, C. (2017). A sub-salt structural model of the Kelasu structure in the Kuqa foreland basin, northwest China. *Mar. Pet. Geology.* 88, 115–126. doi:10.1016/j.marpetgeo.2017.08.008

Wang, X., Suppe, J., Guan, S., Hubert-Ferrari, A., Gonzalez-Mieres, R., and Jia, C. (2011). "Cenozoic structure and tectonic evolution of the Kuqa fold belt, southern Tianshan, China," in *Thrust Fault-Related Folding: AAPG Memoir 94*. Editors K. McClay, J. H. Shaw, and J. Suppe, 215–243. doi:10.1306/13251339M94389

Wang, X., Wang, Z., Xie, H., Li, S., Tang, P., Yin, H., et al. (2010). Cenozoic salt tectonics and physical models in the Kuqa depression of Tarim Basin, China. *Sci. China Earth Sci.* 40, 1655–1668. (in Chinese with English abstract).

Weatherley, D., Hancock, W., Abe, S., and Boros, V. (2014). *ESyS-Particle Tutorial and User's Guide* Brisbane, Queensland, Australia. Version 2.3.1

Wu, Z., Yin, H., Wang, X., and Xu, S. (2015a). The Structural features and formation mechanism of exposed salt diapirs in the front of fold-thrust belt, western Kuqa Depression. *J. Nanjing Univ. (Natural Sciences)* 51, 612–625. (in Chinese with English abstract). doi:10.13232/j.cnki.jnju.2015.03.018

Wu, Z., Yin, H., Wang, X., Zhao, B., and Jia, D. (2014). Characteristics and deformation mechanism of salt-related structures in the western Kuqa depression, Tarim basin: Insights from scaled sandbox modeling. *Tectonophysics* 612-613, 81–96. doi:10.1016/j.tecto.2013.11.040

Wu, Z., Yin, H., Wang, X., Zhao, B., Zheng, J., Wang, X., et al. (2015b). The structural styles and formation mechanism of salt structures in the Southern Precaspian Basin: Insights from seismic data and analog modeling. *Mar. Pet. Geology.* 62, 58–76. doi:10.1016/j.marpetgeo.2015.01.010

Xie, H., Yin, H., Tang, Y., Wang, W., Wei, H., and Wu, Z. (2015). Research on subsalt structure in the central Kelasu structure belt based on the area-depth technique. *Geotectonica et Metallogenia* 39, 1033–1040. (in Chinese with English abstract). doi:10.16539/j.ddgzyckx.2015.06.005

Xin, W., Chengzao, J., Shufeng, Y., Hubert-Ferrari, A., and Suppe, J. (2002). The time of deformation on the Kuqa fold-and-thrust belt in the southern Tianshan-based on the Kuqa river area. *Acta Geologica Sinica* 76, 55–63. (in Chinese with English abstract).

Xu, W., Yin, H., Jia, D., Li, C., Wang, W., Yang, G., et al. (2021). Structural Features and Evolution of the Northwestern Sichuan Basin: Insights From Discrete Numerical Simulations. *Front. Earth Sci.* 9, 653395. doi:10.3389/feart.2021.653395

Xu, Z., Xie, H., Li, Y., Lei, G., Wu, C., and Neng, Y. (2012). Characteristics and controlling factors of the subsalt differential structure in the Kelasu structural belt, Kuqa Depression. *Nat. Gas Geosci.* 6, 1034–1038. (in Chinese with English abstract).

Yang, K. (2017). *Differential Structural Deformations and Controlling Factors of Salt Tectonic in the Middle Segment of the Kuqa Depression*. Beijing, China: Doctor ThesisChina University of Petroleum (Beijing. (in Chinese with English abstract). doi:10.1130/abs/2017am-298817

Yin, A., Nie, S., Craig, P., Harrison, T. M., Ryerson, F. J., Xianglin, Q., et al. (1998). Late Cenozoic tectonic evolution of the southern Chinese Tian Shan. *Tectonics* 17, 1–27. doi:10.1029/97TC03140

Yin, H., Wang, Z., Wang, X., and Wu, Z. (2011). Characteristics and mechanics of Cenozoic salt-related structures in Kuqa foreland basins: Insights from physical modeling and discussion. *Geol. J. China Universities* 17, 308–317. (in Chinese with English abstract). doi:10.16108/j.issn1006-7493.2011.02.020

Yin, H., Zhang, J., Meng, L., Liu, Y., and Xu, S. (2009). Discrete element modeling of the faulting in the sedimentary cover above an active salt diapir. *J. Struct. Geology*. 31, 989–995. doi:10.1016/j.jsg.2008.10.007

Yu, H., Qi, J., Shi, J., Wu, C., Zhang, W., Fan, S., et al. (2015). Basement fault activities have influenced on caprock tectonic deformation in Kuqa depression. *Chin. J. Geology*. 50, 50–62. (in Chinese with English abstract). doi:10.3969/j.issn.0563-5020.2015.03

Yu, Y., Tang, L., Yang, W., Huang, T., Qiu, N., and Li, W. (2014). Salt structures and hydrocarbon accumulations in the Tarim Basin, northwest China. *Bulletin* 98, 135–159. doi:10.1306/05301311156

Zhao, B., and Wang, X. (2016). Evidence of early passive diapirism and tectonic evolution of salt structures in the western Kuqa depression (Quele area), southern Tianshan (NW China). *J. Asian Earth Sci.* 125, 138–151. doi:10.1016/j.jseaes.2016.05.021

Zhao, G.-F. (2015). *High Performance Computing and the Discrete Element Model: Opportunity and challenge*. Elsevier.

Conflict of Interest: The authors PZ, SG, RR, XL, and HL were employed by the PetroChina Company Limited (PetroChina).

The remaining authors declare that the research was conducted in the absence of any commercial or financial relationships that could be construed as a potential conflict of interest.

Publisher's Note: All claims expressed in this article are solely those of the authors and do not necessarily represent those of their affiliated organizations, or those of the publisher, the editors, and the reviewers. Any product that may be evaluated in this article, or claim that may be made by its manufacturer, is not guaranteed or endorsed by the publisher.

frontiers in Earth Science

ORIGINAL RESEARCH
published: 03 September 2021
doi: 10.3389/feart.2021.679887

Resolving Seismic Anisotropy of the Lithosphere–Asthenosphere in the Central/Eastern Alps Beneath the SWATH-D Network

Frederik Link and Georg Rümpker*

Institute of Geosciences, Goethe-University Frankfurt, Frankfurt, Germany

The Alpine orogeny is characterized by tectonic sequences of subduction and collision accompanied by break-off events and possibly preceded by a flip of subduction polarity. The tectonic evolution of the transition to the Eastern Alps has thus been under debate. The dense SWATH-D seismic network as a complementary experiment to the AlpArray seismic network provides unprecedented lateral resolution to address this ongoing discussion. We analyze the shear-wave splitting of this data set including stations of the AlpArray backbone in the region to obtain new insights into the deformation at depth from seismic anisotropy. Previous studies indicate two-layer anisotropy in the Eastern Alps. This is supported by the azimuthal pattern of the measured fast axis direction across all analyzed stations. However, the temporary character of the deployment requires a joint analysis of multiple stations to increase the number of events adding complementary information of the anisotropic properties of the mantle. We, therefore, perform a cluster analysis based on a correlation of energy tensors between all stations. The energy tensors are assembled from the remaining transverse energy after the trial correction of the splitting effect from two consecutive anisotropic layers. This leads to two main groups of different two-layer properties, separated approximately at 13°E. We identify a layer with a constant fast axis direction (measured clockwise with respect to north) of about 60° over the whole area, with a possible dip from west to east. The lower layer in the west shows N–S fast direction and the upper layer in the east shows a fast axis of about 115°. We propose two likely scenarios, both accompanied by a slab break-off in the eastern part. The continuous layer can either be interpreted as frozen-in anisotropy with a lithospheric origin or as an asthenospheric flow evading the retreat of the European slab that would precede the break-off event. In both scenarios, the upper layer in the east is a result of a flow through the gap formed in the slab break-off. The N–S direction can be interpreted as an asthenospheric flow driven by the retreating European slab but might also result from a deep-reaching fault-related anisotropy.

Keywords: shear-wave splitting, cluster analysis, anisotropy, mantle flow, Alpine orogeny, Eastern Alps, lithosphere, asthenosphere

OPEN ACCESS

Edited by:
György Hetényi,
University of Lausanne, Switzerland

Reviewed by:
Götz Bokelmann,
University of Vienna, Austria
Simone Salimbeni,
Istituto Nazionale di Geofisica e Vulcanologia, sezione di Bologna, Italy
A. Alexander G. Webb,
The University of Hong Kong, China

****Correspondence:***
Frederik Link
link@geophysik.uni-frankfurt.de

Specialty section:
This article was submitted to Solid Earth Geophysics, a section of the journal Frontiers in Earth Science

Received: *12 March 2021*
Accepted: *16 July 2021*
Published: *03 September 2021*

Citation:
Link F and Rümpker G (2021) Resolving Seismic Anisotropy of the Lithosphere–Asthenosphere in the Central/Eastern Alps Beneath the SWATH-D Network. Front. Earth Sci. 9:679887. doi: 10.3389/feart.2021.679887

INTRODUCTION

The development of seismic anisotropy is significantly affected by tectonic processes and the dynamics of the Earth's interior (Savage 1999). The lithosphere and the asthenosphere are the dominant source regions of seismic anisotropy in the crust and upper mantle. In the crust, anisotropy results from the stress-induced alignment of cracks (Christensen, 1966; Nur and Simmons, 1969; Nur, 1971; Crampin 1987; Yousef and Angus 2016) in alternating layers of different seismic velocities like folded sediments (Backus 1962; Savage 1999) or (in the lower crust) an alignment of intrinsically anisotropic minerals. The latter also occurs in the upper mantle lithosphere as frozen-in anisotropy. In the asthenosphere, seismic anisotropy is dominated by the lattice-preferred orientation of olivine crystals that align along the strain direction (Silver 1996; Karato et al., 2008), in response to mantle flow processes (Long and Becker 2010). The most robust observable for measuring seismic anisotropy is the splitting of shear waves, which is commonly inferred from core–mantle converted phases (Silver and Chan 1991; Savage 1999). Shear-wave splitting characterizes anisotropy by a fast axis, which is parallel to the preferred orientation of the mantle minerals in a simple mantle flow–dominated anisotropic model, and a lag time, which scales with the strength of anisotropy and the extent of the anisotropic volume. However, the diverse tectonic history and complex present-day dynamics influence the anisotropy of the upper mantle and lithosphere. Also, large or local shear faults may produce an extended crustal and lithospheric anisotropy above an asthenospheric mantle flow (e.g., Savage 1999; Reiss et al., 2016; Reiss et al., 2018). Lithospheric fragments of subducted slabs can carry frozen-in anisotropy. They result in a pronounced layered anisotropy when they sink (after possible break-off) into the mantle, due to a replacement flow of asthenospheric mantle material (Qorbani et al., 2015a).

The Alpine orogeny is a result of an ensemble of subduction, extension, and collision sequences driven by the convergence of the African and Eurasian plates (Dewey et al., 1973; Dewey et al., 1989; Handy et al., 2010). Prior to the collision of the Adriatic–African and European plates at around 35 Ma, Alpine Tethys and the distal European margin subducted during the convergence initiated at 84 Ma with Adria as the upper plate (Schmid et al., 2004; Handy et al., 2010). With the collision, the Adriatic plate was pushed by the African plate deep into Europe, which led to the formation of a complicated subduction geometry (Handy et al., 2010; Király et al., 2018). Concurrently, a slab break-off was initiated after the completed subduction of the Tethyan units and separated the crustal European units from the subducted lithosphere below the Eastern Alps (von Blanckenburg and Davies, 1995; Lippitsch, 2003; Harangi et al., 2006; Kissling et al., 2006). This was possibly accompanied or preceded by a subduction polarity switch (Schmid et al., 2004; Vignaroli et al., 2008; Handy et al., 2010; Molli and Malavieille 2011; Handy et al., 2015). Especially the subduction polarity below the Eastern Alps is under debate (Kästle et al., 2020), as tomographic studies indicate a northward dip of a possibly Adriatic subduction below Europe (Schmid et al., 2004; Ustaszewski et al., 2008; Schmid et al., 2013), which might be a result of a polarity switch accompanied by a break-off of the previously subducted European slab (Handy et al., 2010; Schmid et al., 2013). For further detailed descriptions of possible models, we refer to the study by Kästle et al. (2020). The present-day tectonic structure can be identified as accreted European units in the Central and Eastern Alps, partially showing metamorphism from deep subduction (Froitzheim et al., 1996; Handy et al., 2010, see also **Figure 1**). This is separated from the Southern Alps, consisting of Adriatic units by the Tonale Fault (TF) and the Periadriatic Fault (PAF). The main irregularity of the orogen parallel E–W trending faults arises by the Giudicarie Fault (GF), which formed during the indentation of the Adriatic microplate (Handy et al., 2015).

To address the question of subduction polarity and tectonic evolution in the transition of the Central to the Eastern Alps, the recently established seismic network SWATH-D provides a unique opportunity due to its unprecedented dense station coverage (AlpArray Seismic Network, 2015; Heit et al., 2017; Hetényi et al., 2018a). The 154 stations cover the critical transition between the TRANSALP (Lüschen et al., 2004) and the EASI experiment (Hetényi et al., 2018b) along the Periadriatic Fault (Handy et al., 2010). While the Moho geometry in the TRANSALP experiment was still unclear (Lüschen et al., 2004), the EASI experiment seems to image the Adriatic Moho below the European plate, which indicates an Adriatic subduction (Hetényi et al., 2018b; Kästle et al., 2020). While tomographic studies lack evidence for the subduction polarity in the Eastern Alps (Kästle et al., 2020 and references therein), they clearly suggest a European subduction in the Western and in the Central Alps (Lippitsch, 2003; Zhao et al., 2016). The result from EASI therefore indicates a polarity switch, possibly in the area covered by the SWATH-D complementary network. The present study addresses open questions regarding the slab break-off, slab geometry, and tectonic evolution in this key area of the Alpine system by analyzing the splitting of core–mantle phases due to seismic anisotropy beneath the network. Based on the findings from previous studies and our individual splitting measurements, we specifically account for two-layer anisotropic models which can account for both frozen-in lithospheric and asthenospheric mantle flows, or a present-day two-layer flow in the asthenosphere.

METHOD AND DATA

Individual Shear-Wave Splitting Measurements

When a shear wave propagates through an anisotropic medium, the wave is split into a fast and a slow phase polarized perpendicular to each other (Savage 1999). The polarization directions coincide with the horizontal projection of the fast and slow directions of the anisotropic medium. Usually, core–mantle converted phases (e.g., SKS, SKKS, PKS, and PKKS) are used for the analysis, as their initial polarization is determined by the event-station geometry, when they leave the Earth's core. Assuming a radially symmetric isotropic Earth, no splitting occurs, and the initial polarization in the radial direction

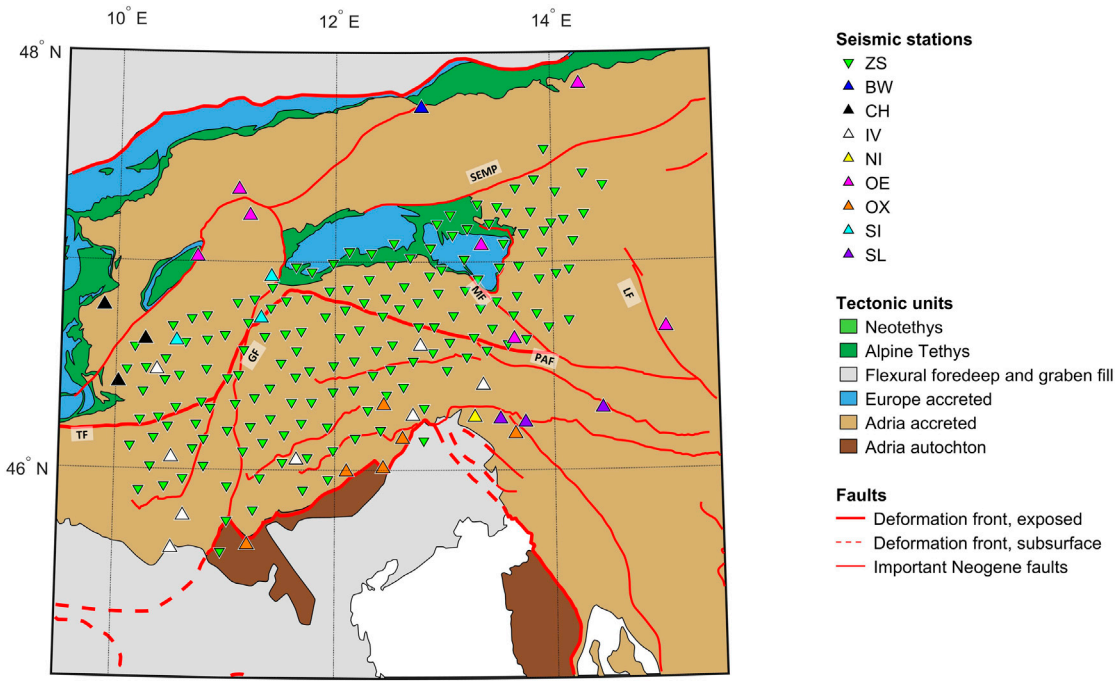

FIGURE 1 | Station distribution of the dense SWATH-D complementary seismic network (ZS) and permanent stations of national networks in the same region. Major faults are GF, Giudicarie Fault; PAF, Periadriatic Fault; TF, Tonale Fault; SEMP, Salzach–Ennstal–Mariazell–Puchberg fault system; MF, Mölltal Fault; and LF, Lavanttal Fault. The background shows the geological map compiled by M.R. Handy with units and major lineaments simplified from the works of Bigi et al. (1992), Froitzheim et al. (1996), Schmid et al. (2004), Schmid et al. (2008), Handy et al. (2010), Bousquet et al. (2012), Handy et al. (2015), and Handy et al. (2019).

is preserved in the recording at the receiver. In contrast, after the propagation through an anisotropic medium, seismic energy may be present on the transverse component due to shear-wave splitting. This anisotropic effect can be investigated by applying an inverse splitting operator with the aim to remove the splitting from the recorded data (Silver and Chan 1991). Here, we use the SplitRacer toolbox (Reiss and Rümpker 2017) to analyze the splitting of the core–mantle converted phases, which also includes standard procedures for requesting and processing large amounts of data from (virtual) seismic networks based on FDSN web services.

Assembling Data and Processing

The SWATH-D (Heit et al., 2017) network provides 2 years of continuous seismic data at 154 stations between 2017 and 2019. This data set is accessible from the GEOFON archive. We include data from permanent stations in the area for longitudes between 10 and 14.5°E and for latitudes between 45.5 and 47.5°N. The data are assembled from the networks BW, CH, IV, NI, OE, OX, SI, and SL (see **Figure 1** and **Supplementary Table S1** in the supplements), which are also part of the AlpArray backbone (AlpArray Seismic Network, 2015; Hetényi et al., 2018a). Teleseismic events with magnitudes above 5.8 and within the distance range from 89 to 140° are selected for download. Data with gaps are discarded in the first quality check. The traces are cut into 100-s windows centered around the arrival of an expected core–mantle converted phase. A signal-to-noise ratio is calculated based on the normalized signal energy in a 25-s window subsequent to the expected arrival time of the phase and the normalized noise energy in a 20-s window preceding this arrival time. Phases with a signal-to-noise ratio below 2.5 are discarded. The traces are band-pass filtered with corner frequencies of 0.02 and 0.25 Hz for all stations. The windows containing the phases for later analysis are then selected by visual inspection. The long period signal of the selected phases is used to determine their initial polarization (Rümpker and Silver 1998), which allows us to identify a possible station misorientation. We correct for the mean misorientation and consider temporal changes at affected stations (see also **Supplementary Table S2**). The phases are individually analyzed for splitting in a grid search for a pair of splitting time and fast axis direction, minimizing the remaining transverse energy after applying the inverse splitting operator (Silver and Chan 1991). The fast axis direction is measured clockwise with respect to north in this study. The results are categorized after manual inspection as good, average, and null according to the quality of the measurement. Poor measurements are discarded and not considered for further analysis. The quality is assessed based on the ellipticity of the waveform, noise contamination, energy reduction, and error of the results. Phases with linear particle motion and low noise contamination are considered as null measurements. If phases show an elliptic particle motion and a considerable improvement in energy reduction on the transverse component after applying the inverse splitting operator, the measurements are considered as good for low noise contamination and average for moderate noise contamination. If the error exceeds realistic measures, the phases are discarded as poor measurements.

Analysis for Two-Layer Anisotropy at Station Clusters

Previous studies have found evidence for a two-layer anisotropy in the eastern part of the region covered by the SWATH-D network (Qorbani et al., 2015a). We therefore search for two anisotropic layers in our analysis. Instead of fitting calculated effective (or apparent) splitting parameters to the observed results obtained from an event-by-event splitting analysis, we choose to perform the more stable two-layer joint-splitting approach (Silver and Savage 1994; Rümpker and Silver 1998; Homuth et al., 2016). This also allows us to include null measurements and serves to improve the statistical significance of the results. In the two-layer joint-splitting approach, an inverse splitting operator is calculated for a set of four parameters (Silver and Savage 1994; Rümpker and Silver 1998), a splitting time, δt, and a fast axis, ϕ, characterizing the anisotropic effect of each layer. By applying the inverse splitting operator to an XKS waveform, the splitting of the two-layer model is removed from this phase. How well the existing splitting is removed is expressed by the remaining transverse energy. The inverse operator is applied for a range of splitting parameters, the delay time, and fast axis direction, for each of the two layers. The remaining energy is stored, which results in a four-dimensional matrix of the remaining transverse energy, which is directly related to the misfit function of the two-layer anisotropic model. For a single phase, a search for the minimum will result in highly ambiguous solutions. We therefore include (or join) all available phases by summing up the four-dimensional misfit function to search for the overall best fitting solution, which ideally minimizes the transverse energy of all phases simultaneously. This technique has produced more stable results in previous studies (Homuth et al., 2016; Reiss and Rümpker 2017) and should produce equivalent results to those of the waveform-based technique of Menke and Levin (2003). The joint-splitting technique is much less computationally expensive and less dependent on model assumptions than the modeling technique of Yuan et al. (2008), who, in return, were able to search for a plunge of the fast axis. However, a detailed comparison of the different techniques available is beyond the scope of this article.

For our data set, 2 years of data are not sufficient for reliably determining two-layer splitting parameters at a single station. Therefore, we introduce a modification of the two-layer joint-splitting approach provided in the SplitRacer software. In view of the dense station spacing of the SWATH-D network and by considering the extent of typical XKS Fresnel zones in the upper mantle, we can assume that core–mantle converted phases largely sample the same anisotropic regime for neighboring stations. Therefore, we aim for the simultaneous analysis of neighboring stations (groups), with similar anisotropic patterns. As a measure of similarity between two data sets, we use their correlation coefficients (Everitt et al., 2011). We found that the four-dimensional distribution of transverse energy allows sufficient characterization of anisotropic features and waveform variability beneath a station. Therefore, we choose this as the basis for our measurement of correlation. The following describes our stepwise analysis procedure:

- We first apply the regular joint-splitting analysis for two anisotropic layers to every station j and store the individual contribution, $T_{ij}(x)$, of every phase i to the overall misfit function, $TE_j(x)$, separately. The variable x depicts the parameter vector $(\delta t_1, \phi_1, \delta t_2, \phi_2)$, where the indices 1 and 2 depict the lower and upper layers, respectively.
- In a second step, we cross-correlate the four-dimensional energy tensor (or misfit function) of each station to produce a correlation matrix, $c_{jk} = \frac{\sum_x \left((TE_j(x) - \bar{TE_j}) \cdot (TE_k(x) - \bar{TE_k}) \right)}{\left(\sum_x (TE_j(x) - \bar{TE_j})^2 \sum_x (TE_k(x) - \bar{TE_k})^2 \right)^{\frac{1}{2}}}$. Here, we only consider stations that have at least one phase categorized as good (see also **Figures 2A,B**). This provides a measure of similarity of the energy tensor from each station and, therefore, similar anisotropic structures sampled at the stations.
- Based on this assumption, a cluster analysis using a complete linkage is performed (Everitt et al., 2011). The hierarchical clustering is a stepwise approach. Data points are merged into one group, based on the distance to each other (measured using the correlation coefficient). The new distances of all data points to the merged set are then based on the maximum distance (or the maximum value of the dissimilarity matrix) from them to one of the points in the set. In the hierarchical clustering, this procedure can be done from all data points treated as single individuals to one group, which contains all data points (for more details, see Everitt et al., 2011). The ideal number of groups has to be chosen by the analyst and depends on the data set and the purpose of the investigation. The correlation matrix can then be sorted for the groups, to visualize the similarity of the clusters, which produces patches of high values around the diagonal elements of the matrix for similar groups (see also **Figure 2C**).
- For each group found in the cluster analysis, a joint-splitting analysis of all phases measured at the dedicated stations is performed. Thus, four splitting parameters are identified, which minimize the overall transverse energy of all phases in this group. We base the joint splitting on a bootstrap approach with 1,000 assembled subsets (Efron 1979), to test the stability of the result. Each subset is sampled randomly from the set of phases in each group with replacement preserving the size of each set. The joint analysis for the subset is found for the stack of all individual energy tensors previously stored in the joint analysis of the stations. We discard results where both layers show a similar fast axis direction ($\phi \pm 20^\circ$) or a phase shift of 90° [$(\phi + 90^\circ) \pm 20^\circ$], as this would be an indication for a single-layer anisotropy. If no two-layer anisotropic model can be found, a single-layer joint-splitting analysis is calculated. We determine the final result from the mean and the standard deviation of a Gaussian curve fitting the distribution from the bootstrapping.

RESULTS

Individual Measurements

The splitting analysis of individual events provides, in total, 3,123 pairs of splitting parameters. 792 of them are categorized as good, 1,467 as average, and 863 as null measurement. The splitting time

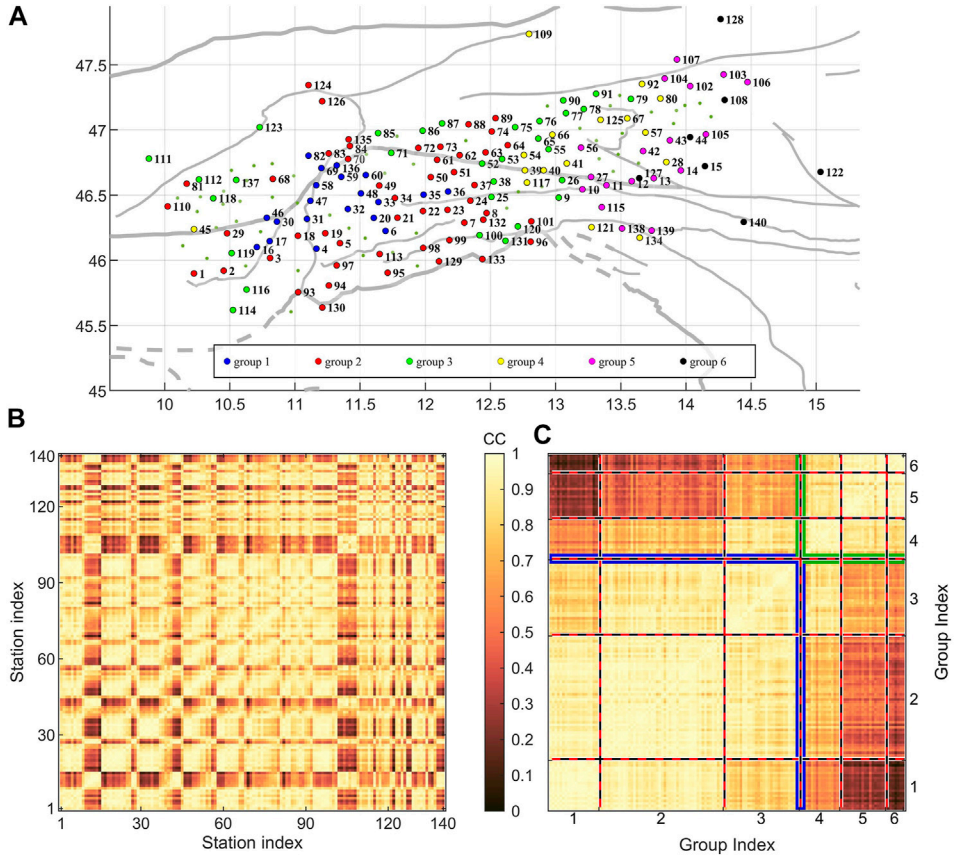

FIGURE 2 | Cluster analysis for stations of similar anisotropic two-layer transverse-energy patterns. **(A)** Map of stations with index (as used in the correlation matrix), if at least one good measurement was recorded. The colored dots indicate the resulting six groups from the hierarchical clustering. **(B)** Matrix of correlation coefficients from inter-station correlation of the remaining transverse energy grid after joint splitting for two anisotropic layers. The color scales with the value of the correlation coefficient (CC). **(C)** Matrix of the same correlation coefficients as in **(B)** but sorted for groups based on the hierarchical cluster analysis with complete linkage. Six groups have been allowed (separated by red-black dashed lines), while two main groups are identified with blue (first three groups) and green (last three groups) frames.

for good and average measurements varies mainly between 1.3 ± 0.5 s and shows no major lateral variation. The dominant fast axis direction is between 50° and 65°, although there is a trend toward larger angles of 90° and up to 145°, which appear mainly with growing longitude. At first sight, the individual results can be interpreted as gentle clockwise rotation of anisotropic fast axis orientation from west to east (see **Figure 3**). However, the permanent stations in the east show a large variation of the individual results, which can also be seen to be less pronounced in the west. We further investigate the azimuthal distribution of the good measurements with respect to their station position in longitude (see **Figure 4**). The splitting measurements change laterally, mainly with longitude. The lateral and azimuthal change of the splitting parameters can be visualized in one representation, if we consider the longitude position of the station, where the measurements are recorded, as the radius in a polar plot, where the polar angle represents the back azimuth of the incoming event (see **Figure 4A**). While the measurements have the same lateral pattern for events coming from the opposite direction (see 45°–90° and 225°–270°, respectively), their fast axis orientation changes for events coming from different angles. This is clear evidence for the events sampling the same anisotropic origin, whereas the azimuthal variation points toward a possible anisotropic layering. Stations with a longitude greater than 13°E show the same fast axis direction for events coming from 180° to 225° and for events coming from 270° to 315°, indicating a 90° periodicity. This favors a multilayer anisotropic origin in the east. In a more classical representation of the splitting time and fast axis direction (see **Figure 4B**), the azimuthal variation for the stations located east of 13°E becomes evident. We estimate the two-layer characteristics of the single measurements by fitting synthetic apparent splitting parameters for a two-layer anisotropic model to our measured parameters. The synthetic splitting time and fast axis direction are calculated using the expressions introduced by Silver and Savage (1994). The apparent parameters are calculated for a two-layer model, where the splitting time of each layer is varied for 0.2 s between 0 and 4 s. The fast axis direction of each layer is varied in 10° steps between 0 and 180°. One synthetic pair of parameters for each measured pair is calculated considering the initial polarization defined by the back azimuth of the event.

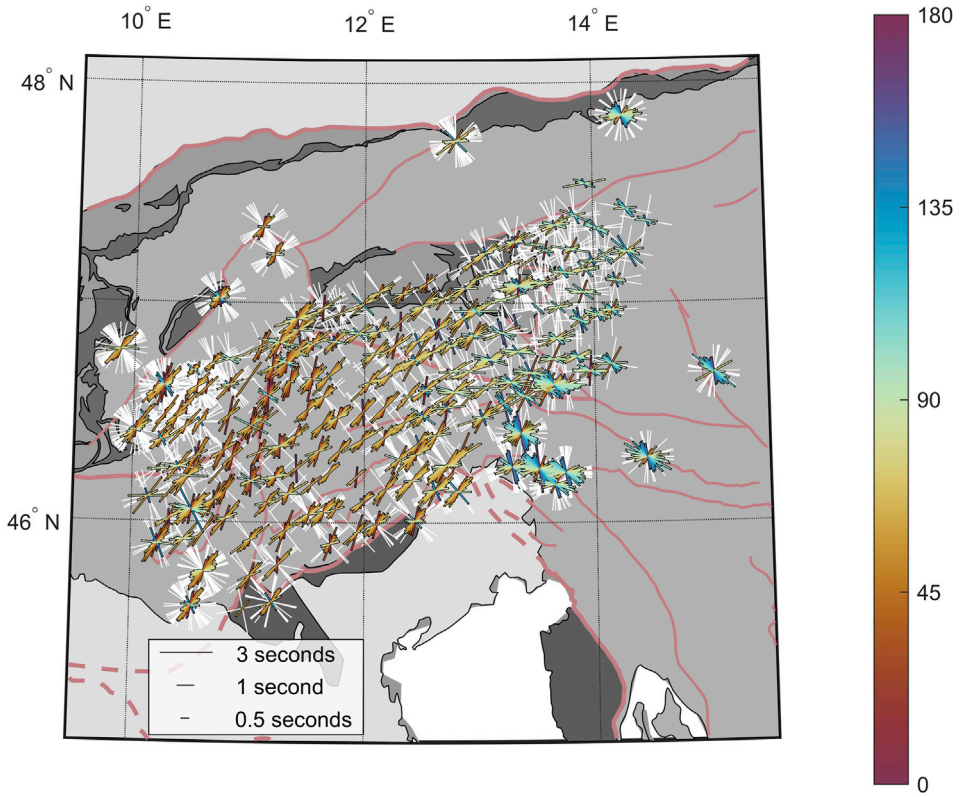

FIGURE 3 | Results from single-splitting analysis. Measurements of categories good and average are presented as bars aligned with the fast axis direction and scale with strength of anisotropy. The color of the bars indicates the fast axis direction. Null measurements are shown as white crosses in the direction of the back azimuth and with 90° phase shift.

This allows us to define a misfit between the measured and synthetic parameters and leads to a favored model with minimum misfit. We find the best fitting model, which is defined by two equally strong anisotropic layers, an upper layer with a splitting time of 1 s and a fast axis direction of 120° and a lower layer defined by a splitting time of 1.6 s and a fast axis direction of 70°. This agrees well with the azimuthal pattern observed by Qorbani et al. (2015a) and their anisotropic model. However, while the central part of the network between 12°E and 13°E shows no significant change in the fast axis direction, a similar periodicity of weak azimuthal variation can be seen for stations west of 12°E. We investigate this further by analyzing the azimuthal variation for stations in the longitude range between 11 and 12°E. Here, we observe again a clear azimuthal variation in the splitting-parameter plots (see **Figure 4C**). The corresponding best fitting two-layer anisotropic model shows one dominating upper layer with a splitting time of 1.4 s and a fast axis direction of 50°. The lower layer is weaker but still considerably strong with a splitting time of 0.6 s. The fast axis direction of the deeper layer points toward 170°. This indicates a layered anisotropy for the western part of the network also, which will be further tested in a joint analysis of multiple events for two anisotropic layers in the following section. Based on the single measurements, we would expect a much smaller two-layer effect with one dominating layer (possible locally confined) in the west, compared to the east with the very pronounced variation in the anisotropic parameters.

Joint Analysis of Multiple Events for Two-Layer Anisotropy

In the following section, we test the entire data set for layered anisotropy, by searching for splitting parameters of two anisotropic layers which best fit the data. We include all stations, as this analysis also allows us to test for one dominating layer with the other layer showing only minor splitting. Therefore, no previous selection on stations to be used for this analysis is necessary. A cluster analysis is performed, where we search for stations with similarities in their four-dimensional matrix of the remaining transverse energy derived from a two-layer joint-splitting analysis, as described above. We discard stations without any good measurements for this analysis to avoid a distortion caused by noise-contaminated stations. From the complete linkage using the correlation matrix of station-wise correlated four-dimensional misfit functions, we can visually identify two main groups of similar energy tensors (see **Figures 2A,C**), which are separated at 12.5°E–13°E. However, we allow for additional variation within these two groups by introducing six different groups in total to consider minor lateral variation

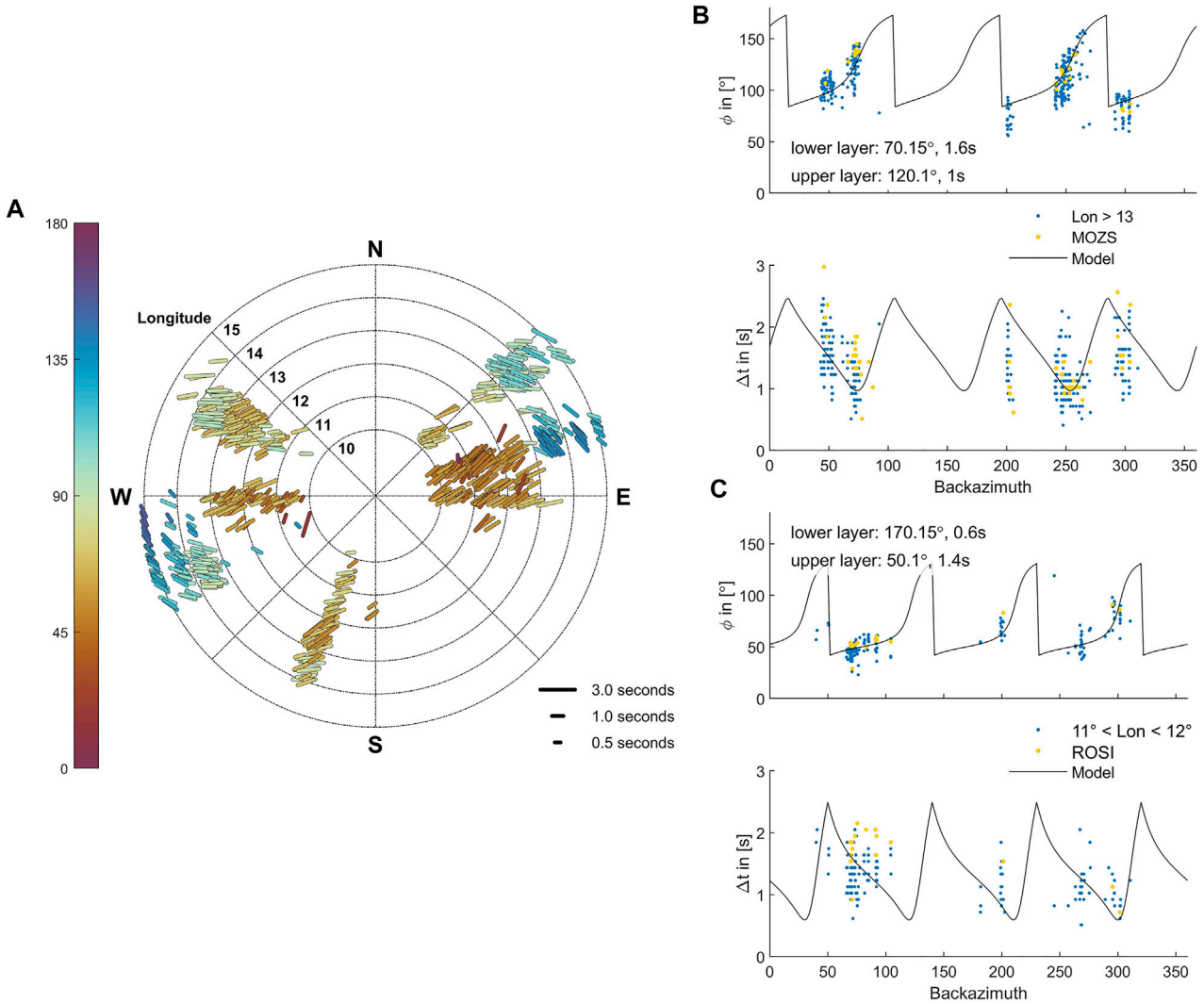

FIGURE 4 | (A) Azimuthal variation of the measurements categorized as good with respect to longitude of the station (radius) and the back azimuth of the event. The color of the bars indicates the fast axis direction. **(B)** Synthetic apparent splitting parameters for the best fitting two-layer anisotropic model to the measurements of stations with longitude larger than 13°E (solid line). Blue circles indicate the individual splitting measurements categorized as good of all stations in this area. The yellow circles show the measurements of the exemplary station MOZS. **(C)** Synthetic apparent splitting parameters for the best fitting two-layer anisotropic model to the measurements of stations between the longitude of 11°E–12°E. Similar to **(B)** for station ROSI.

in the (one- or) two-layer anisotropic pattern (compare **Figure 2A**).

The results from the joint splitting of the six groups all show robust splitting results (**Figure 5**). Three groups (1–3, see **Figures 5A–C**) are characterized by an upper layer with a fast axis between 55 and 70° and a lower layer with a fast axis between 1 and 37°. The splitting time of these groups (1–3) show a dominance of the upper layer with a value of 0.8–1.2 s. Only group 1 (see **Figure 5A**) shows a clear, pronounced second layer with a splitting time of 0.5 s and a small error for splitting time and fast axis direction in both layers. Group 2 (**Figure 5B**) is characterized by a considerable splitting of 0.4 s, but the error from the bootstrapping statistics of ±0.3 s shows the minor confidence in this parameter. Therefore, a one-layer solution might explain the data equally well. The splitting time for group 3 (**Figure 5C**) itself is very weak with only 0.2 s and is therefore also explained equally well using a one-layer model. The larger error in the fast axis direction of the lower layer is also indicative of the minor relevance of the two-layer anisotropy. For the remaining three groups (4–6, see **Figures 5D–F**), the lower layer shows strong splitting with a splitting time of 0.8–1 s. The fast axis direction for the lower layer shows values between 65° and 73°. While group 4 (**Figure 5D**) exhibits an upper layer with a splitting time of only 0.4 s, the other two groups (5 and 6, **Figures 5E,F**) show an equally pronounced splitting as the lower layer with 0.9 s. All three groups show a similar direction for the fast axis of the upper layer (106°–114°). Group 4 (**Figure 5D**) also shows a larger error for the fast axis in the weaker upper layer, which is

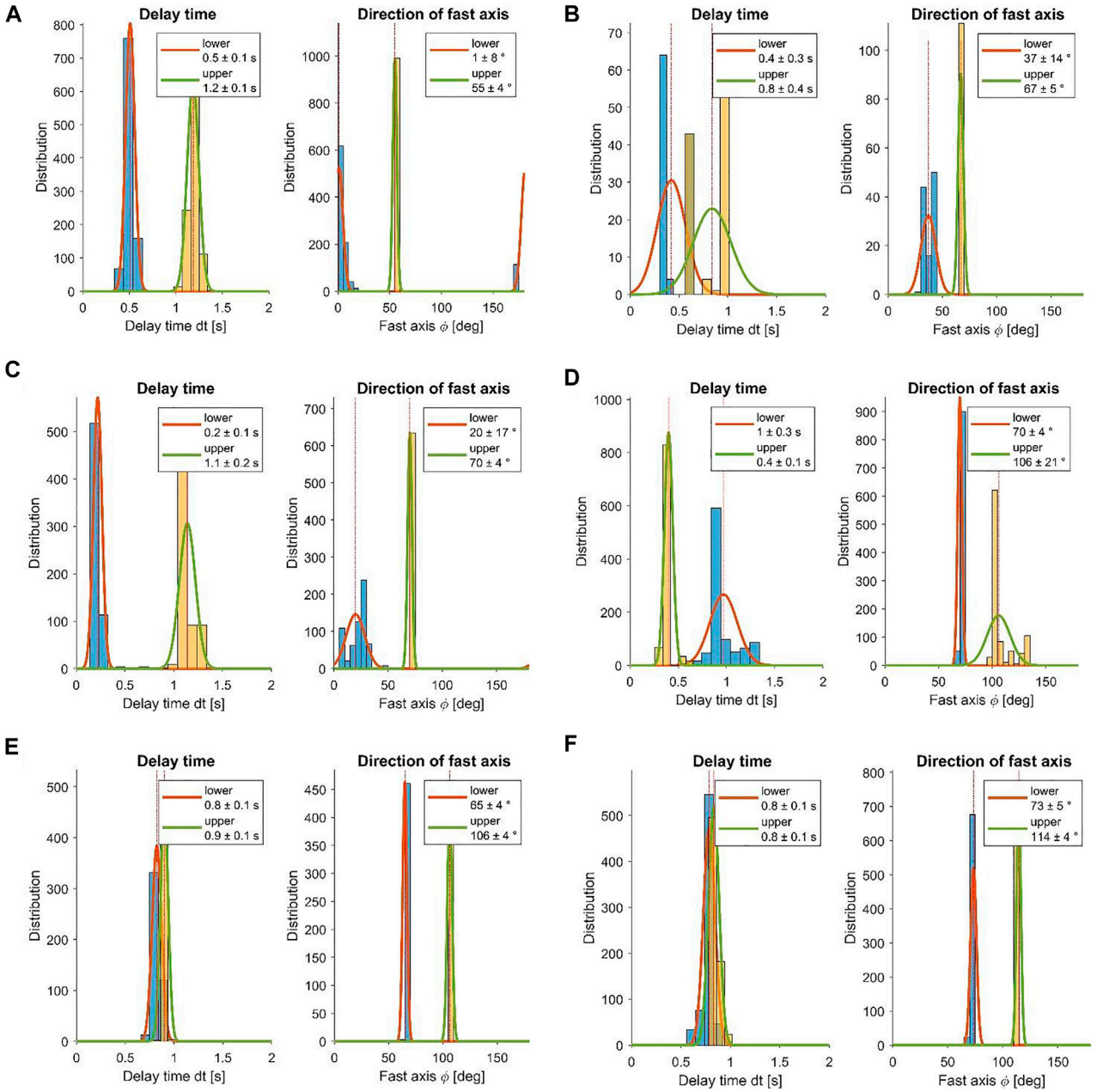

FIGURE 5 | Results for the bootstrap statistics of the groups 1–6 [**(A–F)** in order of the groups] found in the cluster analysis. Blue bars show the histograms for the lower layer and yellow bars the histograms for the upper layer. The lines show a fit of a Gaussian curve to the distribution of each parameter given by its mean and standard deviation.

indicative of a smaller significance of the two-layer anisotropy, similar to group 2 (**Figure 5B**). The two main groups (1-3 and 4–6) clearly separate into a western and an eastern subdomain at a longitude between 12.5°E and 13°E (**Figure 6**). This coincides with the location of the EASI profile (AlpArray Seismic Network, 2014) and also with the location between 12 and 12.5°E, where Qorbani et al. (2015a) found a transition of anisotropic effects in this region. The western part is (at least locally) characterized by a lower layer of almost N–S aligned fast axis direction (unit D in **Figure 6C**) and an upper layer of approximately 60° fast axis direction consistently measured for the whole western area (unit C in **Figure 6C**). The eastern part is characterized by a lower layer with the same direction as the previous upper layer, a fast axis direction of 60° (unit B in **Figure 6C**). The fast axis in the upper layer of the eastern region is aligned roughly along 110° (unit A in **Figure 6C**). The larger error of the fast axis direction associated with group 4 may indicate that the error is introduced by the transition from the eastern to the western area, as parts of the rays

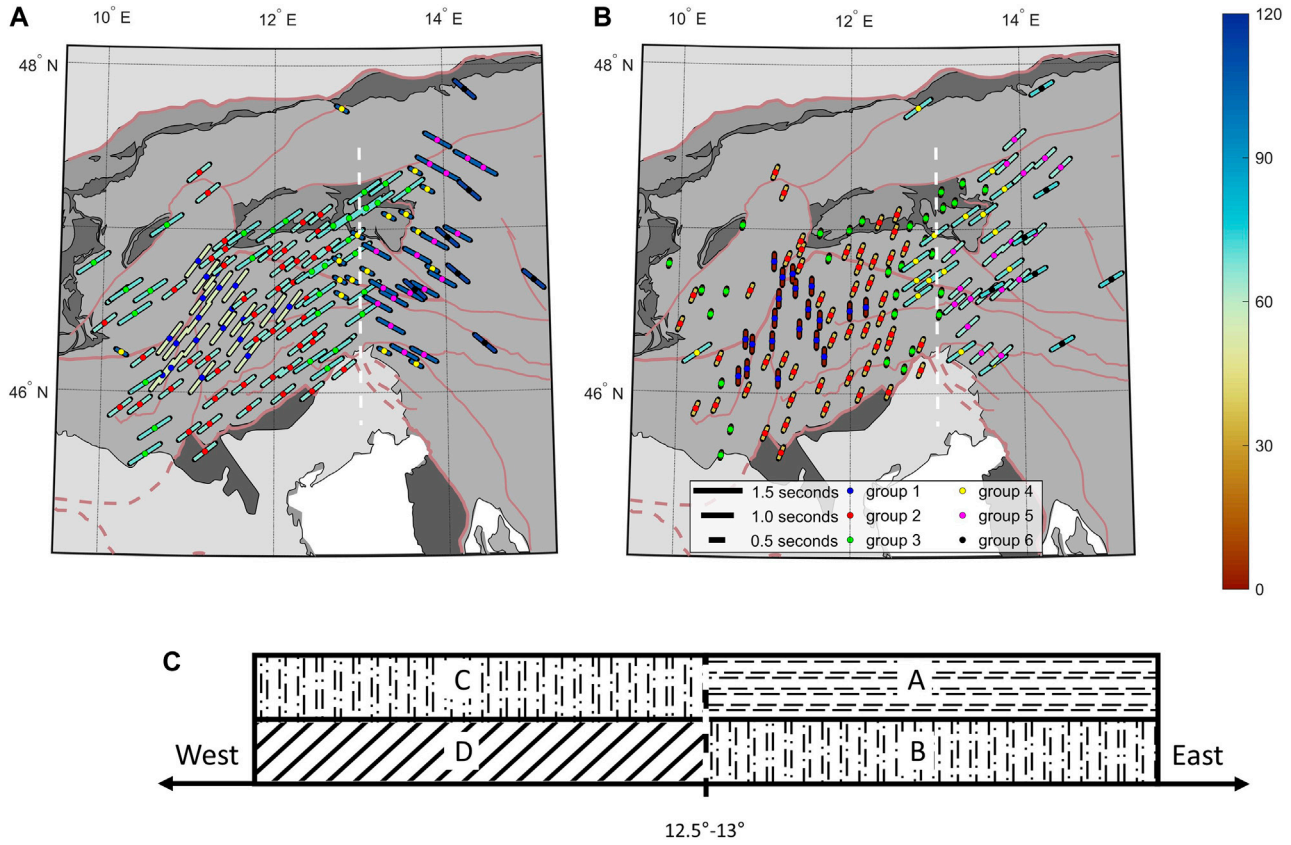

FIGURE 6 | Two-layer splitting results in two separate maps indicating three different anisotropic sources. **(A)** Upper layer and **(B)** lower layer anisotropy from the joint-splitting analysis (see **Figure 5**). The dashed white line indicates the separation of the western and the eastern subareas at ~13°E longitude. **(C)** 2D block model of main anisotropic units. A represents the upper layer in the east and B and C show the same anisotropic direction but represent the lower layer in the east (B) and the upper layer in the west (C). D represents the lower anisotropic layer in the west.

coming from the west might intersect a larger portion of the eastern regime. This lateral change is not considered in the rather simplified two-layer anisotropy, where only vertical variation is assumed. The confidence in the two-layer anisotropy for group 4 (**Figure 5D**) is supported by the small error in the splitting time of only 0.1 s.

DISCUSSION

We find a lateral and a vertical variation in the anisotropic properties of the Eastern Alps, similar to Qorbani et al. (2015a). However, the statistical approach based on bootstrapping in combination with the joint-splitting analysis also allows us to identify a two-layer anisotropy for the area west of 13°E, which was previously thought to be characterized by only a single anisotropic layer (Barruol et al., 2011; Bokelmann et al., 2013; Qorbani et al., 2015a; Petrescu et al., 2020a). The dense station spacing also allows a high lateral resolution of the anisotropic pattern, which supports the abrupt change between the eastern and western parts with a distinct boundary at 12.5°E–13°E. The two-layer joint splitting allows us to separate the study area into a western and an eastern subdomain. Both domains show a layer with a fast axis of ~60°, defining the upper layer in the west and the lower layer in the east. While the lower layer in the western subdomain shows only weak anisotropy and N–S–direction, the upper layer in the eastern subdomain is equally pronounced as the lower layer and shows a fast axis of 100°–115°.

When observing a possible vertical variation of seismic anisotropy, the crust is likely contributing at least part of this effect. Qorbani et al. (2015b) found wide similarities of single anisotropic directions to kinematic data for lower crustal material in the Tauern Window and alignment with fault structures. This is interpreted as vertical coherent deformation of the crust and the lithospheric mantle, mainly controlled by the indentation of the Adriatic microplate. Our study area is further extended to the south and covers a larger longitudinal range, which includes the main Alpine suture marked by the Tonale Fault (TF) (see also **Figure 1** and **Figure 7**) and the Periadriatic Fault (PAF). The Giudicarie Fault (GF) differs from the mainly E–W aligned fault systems and forms a displacement of the two major faults. To investigate a possible alignment with deep-reaching surface geological features, we back-projected the

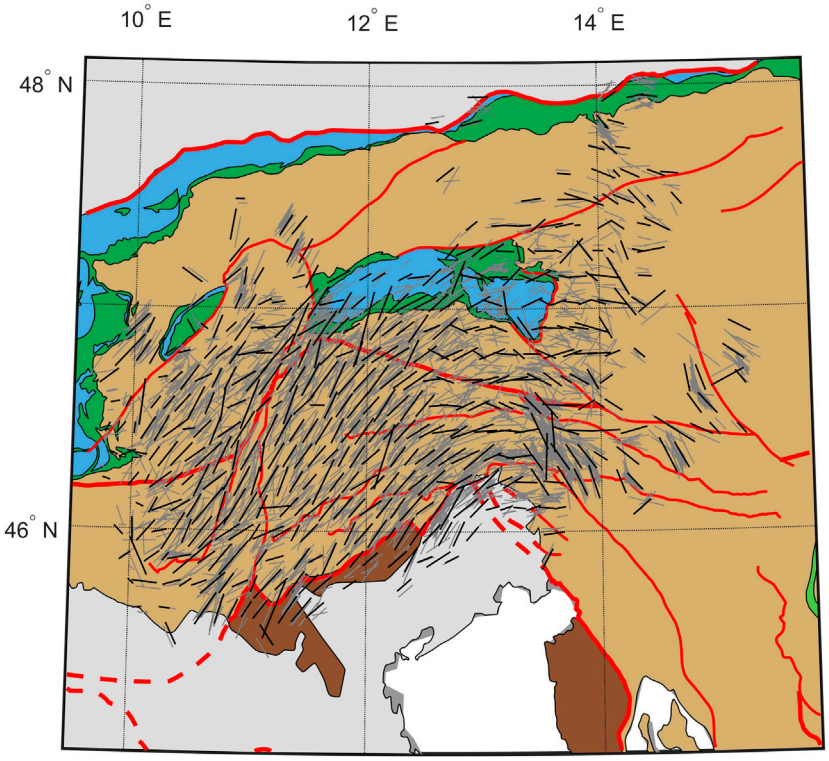

FIGURE 7 | Single splitting measurements with quality good and average projected into a depth of 120 km (gray bars). For better visualization, the measurements are averaged on a regular grid, which are shown as black bars. Same tectonic map as in **Figure 1**.

individual measurements into a depth of 120 km (see **Figure 7**), which is the maximum base of the lithosphere for the area of the Tauern Window (Jones et al., 2010; Bianchi and Bokelmann, 2014; Qorbani et al., 2015b). While Qorbani et al. (2015b) found a very good agreement of the fast axis direction and kinematic data with the faults in the small area around the Tauern Window [in particular with the Mölltal Fault (MF)], we see such an alignment only for a limited number or only part of the faults. At the Mölltal Fault (MF), only measurements that are very close to the fault appear to align with the surface structure. They extend to the north to a region of more variable fast axis direction. A large depth extent of the fault and therefore a considerable effect is not to be expected from this very localized apparent alignment. The measurements around the Lavanttal Fault (LF) system might also be interpreted as an aligned pattern of the fast axis with the fault. However, the measurements appear to have a rotational pattern around the station location, which coincides well with the pattern of the fast axis direction for the neighboring station in the S–W and the north. This favors a deeper origin (e.g., multilayer anisotropy) as for these other stations, no alignment with surface features is visible and the rotational pattern indicates a 90° periodicity. It is remarkable that the Periadriatic Fault (PAF) and the Tonale Fault (TF), as major sutures for the European–Adriatic collision, show no significant correlation with the fast axis directions. Only the Giudicarie Fault (GF) with the northern and southern parts seems to produce a more significant imprint on the fast axis direction. The single measurements align with the fault and also show (to its west) an irregular NNE–SSW alignment along the fault, which is not visible for the measurements in the vicinity. In summary, we only see the Giudicarie Fault (GF) as a major surface feature, which seems to connect to larger depths, producing a possible anisotropic effect in the shear-wave splitting. The remaining faults seem to produce either only a very locally confined effect or produce, surprisingly, no effect at all, for example, the Periadriatic Fault (PAF) and the Tonale Fault (TF).

Seismic tomography can provide insight into slab geometries and lithospheric thinning as well as asthenospheric upwelling in terms of positive and negative velocity perturbations. However, so far, studies based on body waves show only a limited agreement of velocity anomalies with flow patterns derived from shear-wave splitting (see Qorbani et al., 2015a and references therein; Lippitsch, 2003; Koulakov et al., 2009). A recent surface wave tomography by Kästle et al. (2018), Kästle et al. (2020) provides significantly improved resolution for relatively shallow structures (between 50 and 200 km). The latter shows a distinct weakening in the positive velocity perturbation of the European slab at a depth of ~120 km at the transition to the Eastern Alps. The start of the weakening of the positive anomaly is located at a longitude

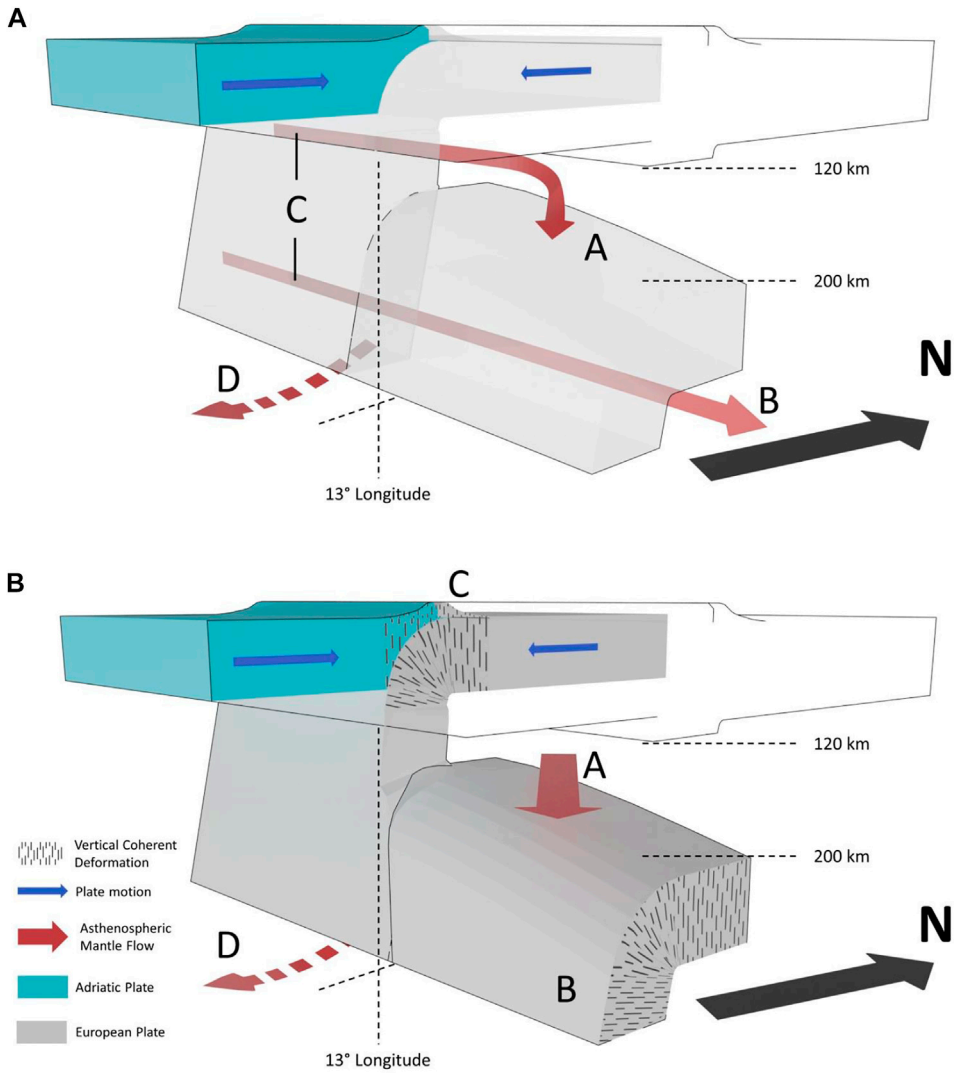

FIGURE 8 | Schematic model of the lithospheric/asthenospheric interaction in the study region. A to D correspond to the anisotropic units shown in **Figure 6** **(A–B)** European plate subducts below the Adriatic plate. During the subduction process, the European plate is pushed back and produces a weak N–S directed plate motion–induced flow at the bottom of the slab (D). At around 35 Ma, a slab break-off initiated, which opened a gap for asthenospheric flow at a depth between ~120 and ~200 km. **(A)** Asthenosphere produces a toroidal flow around the retreating European slab (B and C). The opening of the break-off causes a reorientation of the minerals parallel to the orogen C into the new flow direction A of 115°N. **(B)** As a result of the compressive regime, anisotropy develops parallel to the orogeny (B and C) within the crust and lithosphere due to vertical coherent deformation (VCD). This anisotropy is stored in the subducting European plate. The opening of the slab break-off results in asthenospheric flow of 115°N (A). While the compressional regime in the west remains constant with the VCD causing the measured upper-layer anisotropy and plate motion–induced flow causing the lower-layer anisotropy, the change of deformation in the eastern part is perturbed by the break-off event. Here, the upper-layer anisotropy is caused by the asthenospheric flow above the detached slab, which preserves the VCD of the former collision causing the lower-layer (frozen-in) anisotropy B.

of ~13°E and therefore coincides well with the changing anisotropic pattern found in our study. This weakening can also be identified in images from body wave tomography (Zhao et al., 2016 ; Kästle et al., 2020). The weakening of the positive velocity anomaly has been interpreted as the discontinuous European slab and marks a break-off at depths of about 120–200 km. If we assume 4% anisotropy and a mantle shear velocity of 4.5 km/s, the required thickness of the anisotropic volume is about 90–100 km to satisfy the splitting times found for the upper layer in the east. The depth range between the lithospheric base and the slab fragment is found to be around 80 km and agrees with the required volume (within errors).

The dominant anisotropy (of about 60°) in the western part coincides well with the Alpine orogeny and is aligned parallel-to-subparallel to the strike of the mountain belt. This is evidence for a vertical coherent deformation with coupled anisotropy from the lithosphere to the upper asthenosphere as proposed by Silver (1996). The fast axis is not perfectly aligned with the mountain axis but shows a constant trade-off of about 10–20°. While this

disagrees with an ideal coherent deformation of the crust and the mantle lithosphere, the overall regional changes of anisotropy in the Alpine area clearly rejects the simple asthenospheric flow model. In that case, the fast polarizations are expected to align more-or-less parallel to the absolute plate motion. The high variability within the plate therefore favors a shallower origin of the anisotropy. The deviation of the orogen-parallel alignment may be indicative of fossil anisotropy that is mainly preserved in the deeper crust in combination with the mantle lithosphere related to a previous stage of the European–Adriatic collision. The fast axis direction would then point to the alignment of the pre-collisional front during the subduction of the Piemont–Valais oceanic units (Handy et al., 2015).

An alternative scenario for the origin of the observed pattern in the western part of the study area is a slab-controlled flow that is mainly driven by the Adriatic intender causing a steep European subduction. The blocked mantle flow is then forced to flow around the retreating European slab, causing the alignment parallel to the orogeny (see **Figure 8A**, and Király et al., 2018; Petrescu et al., 2020a). Both scenarios seem equally likely for the western region, where the dominant upper layer exhibits fast axes oriented subparallel to the orogenic belt. However, our observations for the eastern subdomain show discrepancies with a slab-controlled orogen-parallel flow behind the Alpine Front; as part of the asthenospheric domain behind the slab is reoriented in the direction of the upper layer (representing the flow through the gap produced by the break-off), we would expect to observe a weakening in the slab-controlled splitting. As a consequence, the volume pushed back by the retreating slab is shortened, leading to a weaker anisotropic effect parallel to the orogeny. However, the measured direction and the strength of the anisotropy are preserved in the lower layer of the eastern subdomain and resemble the anisotropy of the upper layer in the west. Therefore, our two-layer splitting results support a lithospheric origin and the vertical coherent deformation model with orogen-parallel anisotropy or fossil anisotropy parallel to the pre-collisional subduction front (see **Figure 8B**). The upper layer in the east can be interpreted as an asthenospheric flow that is controlled by the break-off event, which initiated 35 Ma ago (Handy et al., 2015) when the subduction of the Tethys oceanic plate was completed. The contact of the Adriatic plate with the more rigid European continental plate favored the break-off and changed the dynamic condition in the collision. This led to a perturbation of the coherent deformation with a cancellation of the anisotropic effect in the upper lithosphere. The orogeny-parallel direction remains preserved in the detached slab fragment, which we measure as lower-layer anisotropy in the east. It may be noted that splitting observations further to the east in the Pannonian Basin and the Carpathians exhibit a similar fast axis direction to the upper layer in the eastern subdomain (Petrescu et al., 2020b and references therein). This is evidence for a larger-scale feature that is connected to the upper-layer anisotropy found in the eastern subdomain of our study area.

In contrast, the N–S directed anisotropy, which we resolve in the western subdomain, is quite weak and is only locally a stable feature, while the fast axis directions of all groups in the area point in a similar direction. The generally small delay times indicate less significant anisotropy or a non-horizontal fast axis, which may also be present across a wider region, but is suppressed, due to one or more dominating anisotropic layers. If we interpret the N–S directed anisotropy in the east as an asthenospheric flow below the lithosphere, such large-scale distribution would be necessary. The asthenospheric flow would then represent the return flow of mantle material following the dip of the subducting plate and submerge below the retreating European slab that is pushed by the Adriatic intender (see **Figure 8** and compare with Funiciello et al., 2006 for laboratory experiments). The close vicinity of the group with clear two-layer results in the west to the Giudicarie Fault might favor this geologic feature as the origin of an apparent two-layer effect. As the back-projected single measurements also show an alignment with the fault (see **Figure 7**), this provides additional evidence for a deep-reaching fault, which affects the splitting. While the order of the layers is a counterargument, as the N–S layer (parallel to the strike of the fault) is found to be the lower layer in contrast to the shallow surface feature, the conditions for the two-layer analysis are not ideal. The number of measurements and the azimuthal coverage are limited. It seems logical that the laterally confined feature of the fault leads to an effect on events of only a limited azimuthal range. That, in combination with the limited azimuthal event coverage, can lead to an apparent two-layer model. Still, the strong effect on the splitting measurements requires a deep-reaching fault likely extending into the mantle lithosphere. This is not supported by Moho contours of the suture, where a displacement, as seen at the surface, is not visible (Spada et al., 2013; Handy et al., 2015). Whether the measured two-layer effect in the western subdomain originates in the mantle or is influenced by the crust could be resolved with a longer measurement period of a similarly dense network. This would allow the application of techniques based on receiver functions or ambient noise, which may be able to resolve shallower features in more detail.

CONCLUSION

This study addresses the open questions regarding a possible slab break-off accompanied by a subduction polarity flip in the transition of the Central to the Eastern Alps. We approach this question based on tectonic implications given by shear-wave splitting measurements at the dense SWATH-D complementary network and stations of the AlpArray backbone in the same area. As previous studies imply a two-layer anisotropy in the Eastern Alps (Qorbani et al., 2015a), we investigate this further and search for a possible two-layer anisotropic model. A depth-dependent anisotropic structure is also supported by the observed azimuthal variation of the single splitting measurements. The temporary character of the SWATH-D experiment and the associated limited amount of data do not allow for a conventional single-station two-layer analysis in this area. Therefore, we combine measurements of multiple stations based on a cluster analysis to resolve the splitting parameters of two layers. While allowing for further

variation in up to six groups, the cluster analysis yields two main groups of similar splitting effects separated approximately at a longitude of 13°E. The western part is characterized by a lower layer of N–S direction and an upper layer with a fast direction of roughly 60°. The eastern part shows a lower layer with a fast direction of 60° and an upper layer with a fast direction of 110°, which is in agreement with previous observations (Qorbani et al., 2015a).

As the upper layer of the western part shows the same direction as the lower layer in the east, a common origin for the anisotropy seems likely. We interpret this as lithospheric anisotropy frozen in the European subducting slab with vertical coupling into the asthenosphere. Weak N–S aligned anisotropy in the west indicates either a return flow at the bottom of the retreating European slab pushed by the Adriatic plate or, alternatively, a deep-reaching Giudicarie Fault, which may produce an apparent two-layer effect. The abrupt change of the two-layer anisotropic pattern with an equally pronounced splitting of the upper layer in the east is evidence for a break-off event initiated 35 Ma ago (Handy et al., 2015). While the slab fragment is sinking into the mantle (a connection to the European slab is likely to remain), the gap provides an opening for asthenospheric flow from the Alpine Front to the Pannonian Basin.

While this interpretation provides evidence for the subduction of the European plate below the Adriatic intender with a break-off event in the eastern part of the Alps, the splitting measurements cannot constrain a possible subsequent subduction of the Adriatic plate below Europe, filling the gap (Lippitsch, 2003; Handy et al., 2015; Kästle et al., 2020). Therefore, further investigation is required to resolve the subduction polarity in the Eastern Alps.

DATA AVAILABILITY STATEMENT

Publicly available datasets were analyzed in this study. These data can be found here: ZS, GEOFON Data Archive (doi: 10.14470/MF7562601148); BW, Department of Earth and Environmental Sciences, Geophysical Observatory, University of Munchen (doi: 10.7914/SN/BW); CH, Swiss Seismological Service (SED) at ETH Zurich (doi: 10.12686/sed/networks/ch); IV, SI, INGV Seismological Data Centre (doi: 10.13127/SD/X0FXnH7QfY); NI, OGS (Istituto Nazionale di Oceanografia e di Geofisica Sperimentale) and University of Trieste (doi: 10.7914/SN/NI); OE: ZAMG-Zentralanstalt für Meterologie und Geodynamik (doi: 10.7914/SN/OE); OX, OGS (Istituto Nazionale di Oceanografia e di Geofisica Sperimentale) (doi: 10.7914/SN/OX); SL, Slovenian Environment Agency (doi: 10.7914/SN/SL).

AUTHOR CONTRIBUTIONS

FL developed and performed the data analysis and wrote the first draft of the manuscript. FL and GR jointly discussed the results and their interpretation and revised the manuscript.

FUNDING

This study was supported by the Deutsche Forschungsgemeinschaft (DFG) within the priority program "Mountain Building Processes in Four Dimensions" (SPP 4D-MB).

ACKNOWLEDGMENTS

We would like to thank two reviewers for their constructive and very helpful comments. We acknowledge the operation of the SWATH-D complementary seismic network with the support of the Geophysical Instrument Pool Potsdam (GIPP), see Heit al. (2017), and the permanent seismic networks used in this study: BW, Department of Earth and Environmental Sciences, Geophysical Observatory, University of München; CH, Swiss Seismological Service (SED) at ETH Zurich; IV, SI, INGV Seismological Data Centre; NI, OGS (Istituto Nazionale di Oceanografia e di Geofisica Sperimentale) and University of Trieste; OE: ZAMG-Zentralanstalt für Meterologie und Geodynamik; OX, OGS (Istituto Nazionale di Oceanografia e di Geofisica Sperimentale); SL, Slovenian Environment Agency. We acknowledge the scientific exchange and cooperation within the AlpArray Working Group (http://www.alparray.ethz.ch) and would like to thank the AlpArray Seismic Network Team: György HETÉNYI, Rafael ABREU, Ivo ALLEGRETTI, Maria-Theresia APOLONER, Coralie AUBERT, Simon BESANÇON, Maxime BÈS DE BERC, Götz BOKELMANN, Didier BRUNEL, Marco CAPELLO, Martina ČARMAN, Adriano CAVALIERE, Jérôme CHÈZE, Claudio CHIARABBA, John CLINTON, Glenn COUGOULAT, Wayne C. CRAWFORD, Luigia CRISTIANO, Tibor CZIFRA, Ezio D'ALEMA, Stefania DANESI, Romuald DANIEL, Anke DANNOWSKI, Iva DASOVIĆ, Anne DESCHAMPS, Jean-Xavier DESSA, Cécile DOUBRE, Sven EGDORF, ETHZ-SED Electronics Lab, Tomislav FIKET, Kasper FISCHER, Wolfgang FRIEDERICH, Florian FUCHS, Sigward FUNKE, Domenico GIARDINI, Aladino GOVONI, Zoltán GRÁCZER, Gidera GRÖSCHL, Stefan HEIMERS, Ben HEIT, Davorka HERAK, Marijan HERAK, Johann HUBER, Dejan JARIĆ, Petr JEDLIČKA, Yan JIA, Hélène JUND, Edi KISSLING, Stefan KLINGEN, Bernhard KLOTZ, Petr KOLÍNSKÝ, Heidrun KOPP, Michael KORN, Josef KOTEK, Lothar KÜHNE, Krešo KUK, Dietrich LANGE, Jürgen LOOS, Sara LOVATI, Deny MALENGROS, Lucia MARGHERITI, Christophe MARON, Xavier MARTIN, Marco MASSA, Francesco MAZZARINI, Thomas MEIER, Laurent MÉTRAL, Irene MOLINARI, Milena MORETTI, Anna NARDI, Jurij PAHOR, Anne PAUL, Catherine PÉQUEGNAT, Daniel PETERSEN, Damiano PESARESI, Davide PICCININI, Claudia PIROMALLO, Thomas PLENEFISCH, Jaroslava PLOMEROVÁ, Silvia PONDRELLI, Snježan PREVOLNIK, Roman RACINE, Marc RÉGNIER, Miriam REISS, Joachim RITTER, Georg RÜMPKER, Simone SALIMBENI, Marco SANTULIN, Werner SCHERER, Sven SCHIPPKUS, Detlef SCHULTE-KORTNACK, Vesna ŠIPKA, Stefano SOLARINO, Daniele SPALLAROSSA, Kathrin SPIEKER, Josip STIPČEVIĆ, Angelo STROLLO, Bálint SÜLE, Gyöngyvér SZANYI, Eszter SZÚCS, Christine

THOMAS, Martin THORWART, Frederik TILMANN, Stefan UEDING, Massimiliano VALLOCCHIA, Luděk VECSEY, René VOIGT, Joachim WASSERMANN, Zoltán WÉBER, Christian WEIDLE, Viktor WESZTERGOM, Gauthier WEYLAND, Stefan WIEMER, Felix WOLF, David WOLYNIEC, Thomas ZIEKE, Mladen ŽIVČIĆ and Helena ŽLEBČÍKOVÁ. We would also like to thank to the SWATH-D Working Group: Ben HEIT, Michael WEBER, Christian HABERLAND, Frederik TILMANN (Helmholtz-Zentrum Potsdam Deutsches GeoForschungsZentrum [GFZ]) and the SWATH-D Field Team: Luigia CHRISTIANO, Peter PILZ, Camilla CATTANIA, Francesco MACCAFERRI, Angelo STROLLO, Susanne HEMMLEB, Stefan MROCZEK, Thomas ZIEKE, Günter ASCH, Peter WIGGER, James MECHIE, Karl OTTO, Patricia RITTER, Djamil AL-HALBOUNI, Alexandra MAUERBERGER, Ariane SIEBERT, Leonard GRABOW, Xiaohui YUAN, Christoph SENS-SCHONFELDER, Jennifer DREILING, Rob GREEN, Lorenzo MANTILONI, Jennifer JENKINS, Alexander JORDAN, Azam Jozi NAJAFABADI, Susanne KALLENBACH (Helmholtz-Zentrum Potsdam Deutsches GeoForschungsZentrum [GFZ]), Ludwig KUHN, Florian DORGERLOH, Stefan MAUERBERGER, Jan SEIDEMANN (Universität Potsdam), Rens HOFMAN (Freie Universität Berlin), Nikolaus HORN, Stefan WEGINGER, Anton VOGELMANN (Austria: Zentralanstalt für Meteorologie und Geodynamik [ZAMG]), Simone KASEMANN (Universität Bremen), Claudio CARRARO, Corrado MORELLI (Südtirol/Bozen: Amt für Geologie und Baustoffprüfung), Günther WALCHER, Martin PERNTER, Markus RAUCH (Civil Protection Bozen), Giorgio DURI, Michele BERTONI, Paolo FABRIS (Istituto Nazionale di Oceanografia e di Geofisica Sperimentale [OGS] [CRS Udine]), Andrea FRANCESCHINI, Mauro ZAMBOTTO, Luca FRONER, Marco GARBIN (also OGS) (Ufficio Studi Sismici e Geotecnici-Trento).

SUPPLEMENTARY MATERIAL

The Supplementary Material for this article can be found online at: https://www.frontiersin.org/articles/10.3389/feart.2021.679887/full#supplementary-material

REFERENCES

AlpArray Seismic Network (2015). AlpArray Seismic Network (AASN) Temporary component. *AlpArray Working Group*. Other/Seismic Network. doi:10.12686/alparray/z3_2015

AlpArray Seismic Network (2014). Eastern Alpine Seismic Investigation (EASI) - AlpArray Complementary Experiment. *AlpArray Working Group*. doi:10.12686/alparray/xt_2014

Backus, G. E. (1962). Long-wave elastic anisotropy produced by horizontal layering. *J. Geophys. Res.* 67, 4427–4440. doi:10.1029/jz067i011p04427

Barruol, G., Bonnin, M., Pedersen, H., Bokelmann, G. H. R., and Tiberi, C. (2011). Belt-parallel mantle flow beneath a halted continental collision: The Western Alps. *Earth Planet. Sci. Lett.* 302, 429–438. doi:10.1016/j.epsl.2010.12.040

Bianchi, I., and Bokelmann, G. (2014). Seismic signature of the Alpine indentation, evidence from the Eastern Alps. *J. geodynamics* 82, 69–77. doi:10.1016/j.jog.2014.07.005

Bigi, G., Cosentino, D., Parotto, M., Sartori, R., and Scandone, P. (1992). Structural model of Italy, 1:500.000. *CNR Progetto Finalizzato Geodinamica* 114 (3).

Bokelmann, G., Qorbani, E., and Bianchi, I. (2013). Seismic anisotropy and large-scale deformation of the Eastern Alps. *Earth Planet. Sci. Lett.* 383, 1–6. doi:10.1016/j.epsl.2013.09.019

Bousquet, R., Schmid, S. M., Zeilinger, G., Oberhänsli, R., Rosenberg, C., Molli, G., et al. (2012). "Tectonic framework of the Alps," in *Lithosphere Structure and Tectonics of the Alps* (Paris: CCGM/CGMW).

Christensen, N. I. (1966). Shear wave velocities in metamorphic rocks at pressures to 10 kilobars. *J. Geophys. Res.* 71, 3549–3556. doi:10.1029/jz071i014p03549

Crampin, S. (1987). The basis for earthquake prediction. *Geophys. J. Int.* 91, 331–347. doi:10.1111/j.1365-246X.1987.tb05230.x

Dewey, J. F., Helman, M. L., Knott, S. D., Turco, E., and Hutton, D. H. W. (1989). Kinematics of the western Mediterranean. *Geol. Soc. Lond. Spec. Publications* 45 (1), 265–283. doi:10.1144/gsl.sp.1989.045.01.15

Dewey, J. F., Pitman, W. C., Ryan, W., and Bonnin, J. (1973). Plate Tectonics and the evolution of the Alpine system. *Geol. Soc. America Bull.* 84 (10), 3137–3180. doi:10.1130/0016-7606(1973)84<3137:ptateo>2.0.co;2

Efron, B. (1992). Bootstrap Methods: Another Look at the Jackknife. *Ann. Stat.* 7 (1), 569–593. doi:10.1007/978-1-4612-4380-9_41

Everitt, B. S., Landau, S., Leese, M., and Stahl, D. (2011). *Cluster Analysis* Chichester: Wiley. doi:10.1002/9780470977811

Froitzheim, N., Schmid, S. M., and Frey, M. (1996). Mesozoic paleogeography and the Timing of eclogite-facies metamorphism in the Alps: A working hypothesis. *Eclogae Geologicae Helv.* 89 (1), 81.

Funiciello, F., Moroni, M., Piromallo, C., Faccenna, C., Cenedese, A., and Bui, H. A. (2006). Mapping mantle flow during retreating subduction: Laboratory models analyzed by feature Tracking. *J. Geophys. Res.* 111 (B3), a–n. doi:10.1029/2005jb003792

Handy, M. R., Giese, J., Schmid, S. M., Pleuger, J., Spakman, W., Onuzi, K., et al. (2019). Coupled Crust-Mantle Response to Slab Tearing, Bending, and Rollback Along the Dinaride-Hellenide Orogen. *Tectonics* 38, 2803–2828. doi:10.1029/2019tc005524

Handy, M. R., M. Schmid, S., Bousquet, R., Kissling, E., and Bernoulli, D. (2010). Reconciling plate-Tectonic reconstructions of Alpine Tethys with the geological-geophysical record of spreading and subduction in the Alps. *Earth-Science Rev.* 102, 121–158. doi:10.1016/j.earscirev.2010.06.002

Handy, M. R., Ustaszewski, K., and Kissling, E. (2015). Reconstructing the Alps-Carpathians-Dinarides as a key to understanding switches in subduction polarity, slab gaps and surface motion. *Int. J. Earth Sci. (Geol Rundsch)* 104, 1–26. doi:10.1007/s00531-014-1060-3

Harangi, S., Downes, H., and Seghedi, I. (2006). Tertiary-Quaternary subduction processes and related magmatism in the Alpine-Mediterranean region. *Geol. Soc. Lond. Mem.* 32, 167–190. doi:10.1144/gsl.mem.2006.032.01.10

Heit, B., Weber, M., Tilmann, F., Haberland, C., Jia, Y., and Pesaresi, D. (2017). *The Swath-D Seismic Network in Italy and Austria*. GFZ Data Services. Other/Seismic Network. doi:10.14470/MF7562601148

Hetényi, G., Molinari, I., Molinari, I., Clinton, J., Bokelmann, G., Bondár, I., et al. (2018a). The AlpArray seismic network: a large-scale European experiment to image the Alpine orogen. *Surv. Geophys.* 39 (5), 1009–1033. doi:10.1007/s10712-018-9472-4

Hetényi, G., Plomerová, J., Bianchi, I., Kampfová Exnerová, H., Bokelmann, G., Handy, M. R., et al. (2018b). From mountain summits to roots: Crustal structure of the Eastern Alps and Bohemian Massif along longitude 13.3°E. *Tectonophysics* 744, 239–255. doi:10.1016/j.tecto.2018.07.001

Homuth, B., Löbl, U., Batte, A. G., Link, K., Kasereka, C. M., and Rümpker, G. (2016). Seismic anisotropy of the lithosphere/asthenosphere system beneath the Rwenzori region of the Albertine Rift. *Int. J. Earth Sci. (Geol Rundsch)* 105, 1681–1692. doi:10.1007/s00531-014-1047-0

Jones, A. G., Plomerova, J., Korja, T., Sodoudi, F., and Spakman, W. (2010). Europe from the bottom up: A statistical examination of the central and northern European lithosphere-asthenosphere boundary from comparing seismological and electromagnetic observations. *Lithos* 120, 14–29. doi:10.1016/j.lithos.2010.07.013

Karato, S.-i., Jung, H., Katayama, I., and Skemer, P. (2008). Geodynamic Significance of Seismic Anisotropy of the Upper Mantle: New Insights from Laboratory Studies. *Annu. Rev. Earth Planet. Sci.* 36, 59–95. doi:10.1146/annurev.earth.36.031207.124120

Kästle, E. D., El-Sharkawy, A., Boschi, L., Meier, T., Rosenberg, C., Bellahsen, N., et al. (2018). Surface Wave Tomography of the Alps Using Ambient-Noise and Earthquake Phase Velocity Measurements. *J. Geophys. Res. Solid Earth* 123 (2), 1770–1792. doi:10.1002/2017jb014698

Kästle, E. D., Rosenberg, C., Boschi, L., Bellahsen, N., Meier, T., and El-Sharkawy, A. (2020). Slab break-offs in the Alpine subduction zone. *Int. J. Earth Sci. (Geol Rundsch)* 109, 587–603. doi:10.1007/s00531-020-01821-z

Király, Á., Faccenna, C., and Funiciello, F. (2018). Subduction Zones Interaction Around the Adria Microplate and the Origin of the Apenninic Arc. *Tectonics* 37, 3941–3953. doi:10.1029/2018tc005211

Kissling, E., Schmid, S. M., Lippitsch, R., Ansorge, J., and Fügenschuh, B. (2006). Lithosphere structure and Tectonic evolution of the Alpine arc: new evidence from high-resolution Teleseismic Tomography. *Geol. Soc. Lond. Mem.* 32, 129–145. doi:10.1144/gsl.mem.2006.032.01.08

Koulakov, I., Kaban, M. K., Tesauro, M., and Cloetingh, S. (2009). P- andS-velocity anomalies in the upper mantle beneath Europe from Tomographic inversion of ISC data. *Geophys. J. Int.* 179 (1), 345–366. doi:10.1111/j.1365-246x.2009.04279.x

Lippitsch, R. (2003). Upper mantle structure beneath the Alpine orogen from high-resolution Teleseismic Tomography. *J. Geophys. Res.* 108. doi:10.1029/2002jb002016

Long, M. D., and Becker, T. W. (2010). Mantle dynamics and seismic anisotropy. *Earth Planet. Sci. Lett.* 297, 341–354. doi:10.1016/j.epsl.2010.06.036

Lüschen, E., Lammerer, B., Gebrande, H., Millahn, K., and Nicolich, R. (2004). Orogenic structure of the Eastern Alps, Europe, from TRANSALP deep seismic reflection profiling. *Tectonophysics* 388, 85–102. doi:10.1016/j.tecto.2004.07.024

Menke, W., and Levin, V. (2003). The cross-convolution method for interpretingSKSsplitting observations, with application to one and Two-layer anisotropic earth models. *Geophys. J. Int.* 154 (2), 379–392. doi:10.1046/j.1365-246x.2003.01937.x

Molli, G., and Malavieille, J. (2011). Orogenic processes and the Corsica/Apennines geodynamic evolution: insights from Taiwan. *Int. J. Earth Sci. (Geol Rundsch)* 100, 1207–1224. doi:10.1007/s00531-010-0598-y

Nur, A. (1971). Effects of Stress on Velocity Anisotropy in Rocks With Cracks. *J. Geophy. Res.* 76 (8), 2022–2034. doi:10.1029/JB076I008P02022

Nur, A., and Simmons, G. (1969). Stress-induced velocity anisotropy in rock: An experimental study. *J. Geophys. Res.* 74 (27), 6667–6674. doi:10.1029/jb074i027p06667

Petrescu, L., Pondrelli, S., Salimbeni, S., Faccenda, M., and Group, A. W. (2020a). Mantle flow below the central and greater Alpine region: insights from SKS anisotropy analysis at AlpArray and permanent stations. *Solid Earth* 11 (4), 1275–1290. doi:10.5194/se-11-1275-2020

Petrescu, L., Stuart, G., Houseman, G., and Bastow, I. (2020b). Upper mantle deformation signatures of craton-orogen interaction in the Carpathian-Pannonian region from SKS anisotropy analysis. *Geophys. J. Int.* 220 (3), 2105–2118. doi:10.1093/gji/ggz573

Qorbani, E., Bianchi, I., and Bokelmann, G. (2015a). Slab detachment under the Eastern Alps seen by seismic anisotropy. *Earth Planet. Sci. Lett.* 409 (1), 96–108. doi:10.1016/j.epsl.2014.10.049

Qorbani, E., Kurz, W., Bianchi, I., and Bökelmann, G. (2015b). Correlated crustal and mantle deformation in the Tauern Window, Eastern Alps. *Ajes* 108, 159–171. doi:10.17738/ajes.2015.0010

Reiss, M. C., and Rümpker, G. (2017). SplitRacer: MATLAB Code and GUI for Semiautomated Analysis and Interpretation of Teleseismic Shear-Wave Splitting. *Seismological Res. Lett.* 88 (2A), 392–409. doi:10.1785/0220160191

Reiss, M. C., Rümpker, G., Tilmann, F., Yuan, X., Giese, J., and Rindraharisaona, E. J. (2016). Seismic anisotropy of the lithosphere and asthenosphere beneath southern Madagascar from Teleseismic shear wave splitting analysis and waveform modeling. *J. Geophys. Res. Solid Earth* 121, 6627–6643. doi:10.1002/2016jb013020

Reiss, M. C., Rümpker, G., and Wölbern, I. (2018). Large-scale Trench-normal mantle flow beneath central South America. *Earth Planet. Sci. Lett.* 482, 115–125. doi:10.1016/j.epsl.2017.11.002

Rümpker, G., and Silver, P. G. (1998). Apparent shear-wave splitting parameters in the presence of vertically varying anisotropy. *Geophys. J. Int.* 135 (3), 790–800. doi:10.1046/j.1365-246x.1998.00660.x

Savage, M. K. (1999). Seismic anisotropy and mantle deformation: What have we learned from shear wave splitting? *Rev. Geophys.* 37, 65–106. doi:10.1029/98RG02075

Schmid, S. M., Bernoulli, D., Fügenschuh, B., Matenco, L., Schefer, S., Schuster, R., et al. (2008). The Alpine-Carpathian-Dinaridic orogenic system: correlation and evolution of Tectonic units. *Swiss J. Geosci.* 101, 139–183. doi:10.1007/s00015-008-1247-3

Schmid, S. M., Fügenschuh, B., Kissling, E., and Schuster, R. (2004). Tectonic map and overall architecture of the Alpine orogen. *Eclogae geol. Helv.* 97, 93–117. doi:10.1007/s00015-004-1113-x

Schmid, S. M., Scharf, A., Handy, M. R., and Rosenberg, C. L. (2013). The Tauern Window (Eastern Alps, Austria): a new Tectonic map, with cross-sections and a Tectonometamorphic synthesis. *Swiss J. Geosci.* 106, 1–32. doi:10.1007/s00015-013-0123-y

Silver, P. G., and Chan, W. W. (1991). Shear wave splitting and subcontinental mantle deformation. *J. Geophys. Res.* 96 (B10), 16429–16454. doi:10.1029/91JB00899

Silver, P. G., and Savage, M. K. (1994). The interpretation of shear-wave splitting parameters in the presence of Two anisotropic layers. *Geophys. J. Int.* 119 (3), 949–963. doi:10.1111/j.1365-246x.1994.tb04027.x

Silver, P. G. (1996). Seismic anisotropy beneath the continents: Probing the depths of geology. *Annu. Rev. Earth Planet. Sci.* 24 (1), 385–432. doi:10.1146/annurev.earth.24.1.385

Spada, M., Bianchi, I., Kissling, E., Agostinetti, N. P., and Wiemer, S. (2013). Combining controlled-source seismology and receiver function information to derive 3-D Moho Topography for Italy. *Geophys. J. Int.* 194, 1050–1068. doi:10.1093/gji/ggt148

Ustaszewski, K., Schmid, S. M., Fügenschuh, B., Tischler, M., Kissling, E., and Spakman, W. (2008). A map-view restoration of the Alpine-Carpathian-Dinaridic system for the Early Miocene. *Swiss J. Geosci.* 101, 273–294. doi:10.1007/s00015-008-1288-7

Vignaroli, G., Faccenna, C., Jolivet, L., Piromallo, C., and Rossetti, F. (2008). Subduction polarity reversal at the junction between the Western Alps and the Northern Apennines, Italy. *Tectonophysics* 450, 34–50. doi:10.1016/j.tecto.2007.12.012

von Blanckenburg, F., and Davies, J. H. (1995). Slab breakoff: A model for syncollisional magmatism and Tectonics in the Alps. *Tectonics* 14, 120–131. doi:10.1029/94tc02051

Yousef, B. M., and Angus, D. A. (2016). When do fractured media become seismically anisotropic? Some implications on quantifying fracture properties. *Earth Planet. Sci. Lett.* 444, 150–159. doi:10.1016/j.epsl.2016.03.040

Yuan, H., Dueker, K., and Schutt, D. L. (2008). Testing five of the simplest upper mantle anisotropic velocity parameterizations using Teleseismic S and SKS data from the Billings, Montana PASSCAL array. *J. Geophys. Res.* 113, B03304. doi:10.1029/2007jb005092

Zhao, D., Yu, S., and Liu, X. (2016). Seismic anisotropy Tomography: New insight into subduction dynamics. *Gondwana Res.* 33, 24–43. doi:10.1016/j.gr.2015.05.008

Conflict of Interest: The authors declare that the research was conducted in the absence of any commercial or financial relationships that could be construed as a potential conflict of interest.

The handling editor GH and the reviewers SS and GB declared a shared research group, the AlpArray Working Group, with one of the authors, GR, at the time of review.

frontiers in Earth Science

ORIGINAL RESEARCH
published: 01 October 2021
doi: 10.3389/feart.2021.742700

Spatio-Temporal Evolution of Intermediate-Depth Seismicity Beneath the Himalayas: Implications for Metamorphism and Tectonics

Konstantinos Michailos[1]*, *N. Seth Carpenter*[2,3] *and György Hetényi*[1]

[1]Institute of Earth Sciences, University of Lausanne, Lausanne, Switzerland, [2]Kentucky Geological Survey, University of Kentucky, Lexington, KY, United States, [3]Department of Earth and Environmental Sciences, University of Kentucky, Lexington, KY, United States

Intermediate-depth earthquakes (>40 km) have been observed beneath the central Himalayas over decades, with little known about their nature and characteristics. Here, we apply a state-of-the-art systematic processing routine, starting from continuous waveform data, to obtain the most comprehensive high-quality earthquake catalog with a focus on the intermediate-depth seismicity beneath the central Himalayas. We construct a catalog containing 414 robust earthquake locations with depths ranging from 40 to 110 km spanning from late 2001 till mid-2003. We calculate earthquake magnitudes in a consistent way and obtain values ranging between M_L 0.8 and 4.5 with a magnitude of completeness of M_C 2.4. This information allows us to study the spatiotemporal characteristics of the seismicity in great detail. Earthquakes mainly take place in a cluster, consisting of two linear segments at ca. 35° azimuth difference, situated beneath the high Himalayas in NE Nepal and adjacent S. Tibet. Seismicity there does not feature any mainshock-aftershock patterns but presents a few sequences with potential seismicity migration rates compatible with linear or diffusive migration. This result, along with previous studies in the lower Indian crust, allows interpreting these events as related to metamorphic reactions involving dehydration processes. However, given the geodynamic context, a tectonic interpretation with a dextral basement fault zone propagating beneath the Himalaya and continuing as a westward propagating tear fault would also be possible. This represents a continuous fault zone from the deep crust in S. Tibet, across the Himalaya along the Dhubri-Chungthang fault zone (DCFZ) to the Shillong plateau, which could be an inherited tectonic feature.

Keywords: Himalayas, seismicity, spatio-temporal evolution, metamorphism, tectonics

OPEN ACCESS

Edited by:
Nibir Mandal,
Jadavpur University, India

Reviewed by:
Supriyo Mitra,
Indian Institute of Science Education and Research Kolkata, India
José Borges,
University of Evora, Portugal

***Correspondence:**
Konstantinos Michailos
konstantinos.michailos@unil.ch
konstantinos.michailos@gmail.com

Specialty section:
This article was submitted to Solid Earth Geophysics, a section of the journal Frontiers in Earth Science

Received: *16 July 2021*
Accepted: *06 September 2021*
Published: *01 October 2021*

Citation:
Michailos K, Carpenter NS and Hetényi G (2021) Spatio-Temporal Evolution of Intermediate-Depth Seismicity Beneath the Himalayas: Implications for Metamorphism and Tectonics. Front. Earth Sci. 9:742700. doi: 10.3389/feart.2021.742700

1 INTRODUCTION

The Himalayan orogen is a unique and complex geological structure that comprises the highest mountain chain on Earth. The kinematics of the orogen are controlled by the continental collision between the Indian and Eurasian plates (e.g., Molnar and Tapponnier, 1975). The collision began 65–50 Ma (Yin and Harrison, 2000) and has a current convergence rate of ~2 cm/yr (Bettinelli et al., 2006). The crustal structure and geometry of the Himalayan orogen has been the focus of several international scientific experiments (INDEPTH, HIMNT, Hi-CLIMB, GANSSER, Hi-KNET;

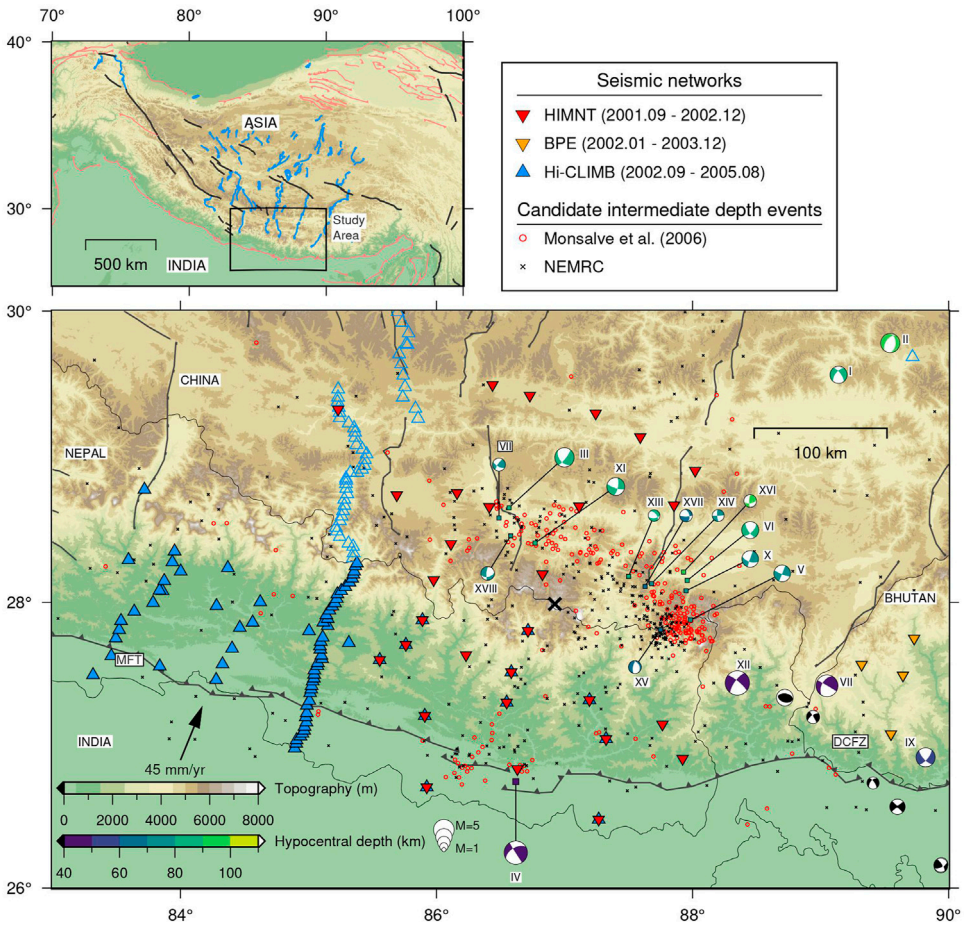

FIGURE 1 | Spatial distribution of seismic networks operating in the Himalayas between late 2001 and mid-2003. Red and orange inverted triangles show the HIMNT and BPE seismic sites, respectively. Blue triangles depict Hi-CLIMB. Empty blue triangles show the locations of the Hi-CLIMB seismic sites not used in this study. Red circles and black crosses indicate the epicenters of the candidate intermediate-depth events (Details can be found in **Table 1**). Black cross highlights the location of Mt Everest. Active faults are shown as thick gray lines. The black arrow indicates the local velocity of Indian Plate relative to Eurasia (~45 mm/yr; DeMets et al., 2010). MFT is the Main Frontal Thrust and DCFZ is the Dhubri-Chungthang fault zone. Focal mechanisms colored according to their hypocentral depths and noted with Roman numerals from I to XVIII (see more details in **Supplementary Table S1** of the supplementary material) depict moment tensor inversions determined by the Global CMT catalog and previous studies for intermediate-depth events in the region (Chen et al., 1981; Molnar and Chen, 1983; Chen, 1988; Chen and Kao, 1996; Zhu and Helmberger, 1996; de la Torre et al., 2007; Alvizuri and Hetényi, 2019). Black focal mechanisms show shallower than 40 km depth earthquakes determined by Diehl et al. (2017) that lie along the Dhubri-Chungthang fault zone (DCFZ). Inset shows the location of the study area in the broader region. Active faults (Styron et al., 2010) are colored according to the type of faulting (red for thrust, blue for normal, and black for strike-slip faults).

Nelson et al., 1996; Schulte-Pelkum et al., 2005; Nábělek et al., 2009; Diehl et al., 2017; Hoste-Colomer et al., 2018) along with many active and passive seismic studies (e.g., Kind et al., 2002; Wittlinger et al., 2004; Mitra et al., 2005; Priestley et al., 2008; Acton et al., 2011; Caldwell et al., 2013; Paul and Mitra, 2017; Singer, 2017) and seismic velocity model studies (Monsalve et al., 2008; Huang et al., 2009; Sheehan et al., 2014). These studies have highlighted a gradually thickening Indian crust while crossing the orogen from the South to the North (i.e., ~40 km in the southern edges; 60–65 km beneath the high Himalayas; 75–90 km beneath southern Tibet) a feature that is generally constant along the length of the central part of the orogen (e.g., Priestley et al., 2019).

The orogen's active tectonics have caused a number of devastating earthquakes in the past (Mugnier et al., 2013; Bilham, 2019). In addition to shallow events, which are responsible for the seismic hazard, intermediate-depth earthquakes (40–100 km) also take place beneath the orogen near the plate interface and intra-slab regions (**Figure 1**; Chen and Molnar, 1983; Monsalve et al., 2006; Priestley et al., 2008; Paul et al., 2015; Schulte-Pelkum et al., 2019; Wang et al., 2020). These events have been identified over decades now (e.g., Chen et al., 1981; Chen and Molnar, 1983), and their significance and location relative to the Moho contributed to advancing the understanding of the rheology of the continental lithosphere (e.g., Chen and Molnar, 1983; Maggi et al., 2000; Jackson, 2002; Jackson et al., 2004).

Under normal conditions, and apart from subduction settings, earthquakes would not occur in continents at depths ranging between 40 and 100 km, but the unique tectonic setting of the Himalayas allows this, although the mechanisms and processes

causing this intermediate-depth seismicity beneath the Himalayan orogen are debated. Eclogitization metamorphic reactions have been suggested to take place in the underthrusted continental crust (Henry et al., 1997). Within this process, water is considered to play an important role (Jackson et al., 2004; Hetényi et al., 2007). There are two models on the origin of this water: it may be introduced from an external source (Jackson et al., 2004; Priestley et al., 2008), or underthrust with the hydrous minerals of the Indian lower crust (ILC) and then dehydrate (Hetényi et al., 2007; Hetényi et al., 2021). In either case, eclogitization leads to volume reduction affecting the local stress field, and dehydration increases pore fluid pressure and hence enables brittle failure. The fluids can ultimately migrate upwards, as documented by magnetotelluric (Lemonnier et al., 1999; Unsworth et al., 2005) and seismic data (Nelson et al., 1996) along the INDEPTH transect, and *via* local low seismic velocity zones as observed elsewhere in southern Tibet (Hetényi et al., 2011). Alternatively, Craig et al. (2012) proposed a rheological model for the underthrusted ILC beneath Tibet and related it to seismicity distribution. They assume a cold anhydrous underthrusting ILC that is being heated up sufficiently slowly to remain seismogenic at great depths beneath the orogen, without particular emphasis on fluids.

Understanding whether metamorphic reactions play a role in intermediate-depth seismicity in the Himalayas is of particular importance as these earthquakes serve as the primary modern analogue for interpreting petrological observations of the former Caledonides orogen mid-crust, now exposed at the surface in Norway. Starting with the seminal paper of Austrheim (1987) describing fluid migration and eclogitization, there has been nearly 35 years of research involving mineralogical, petrological, rock physics, mechanical, seismic, deformation and other, complementary studies on this topic (e.g., Petley-Ragan et al., 2019; Zertani et al., 2019; Malvoisin et al., 2020; Zertani et al., 2020). The occurrence of present-day intermediate-depth seismic events in the Himalayas that can potentially help explain the petrological observations made at the surface in Norway remains an exciting prospect. For this reason, a detailed examination of the spatiotemporal evolution and characteristics of these intermediate-depth events can be helpful with testing and interpreting the mechanisms causing seismogenesis at such depths. Detailed earthquake catalogs can provide information on the properties of seismic deformation taking place and potentially pinpoint to mechanisms that drive seismogenesis (e.g., Hainzl and Ogata, 2005; Lohman and McGuire, 2007; Hauksson et al., 2019; De Barros et al., 2020; Ross et al., 2020). Such catalogs may assist with answering questions: Are these events characteristic of tectonic processes, with possibly mainshock-aftershock sequences? Are there swarms or patterns that can be interpreted as fluid migration? Answering such questions first requires determining whether or not the available data facilitate making such a distinction at present.

Previous seismicity studies in the central Himalayas have mainly focused on the shallow seismic activity (e.g., Pandey et al., 1995; Monsalve et al., 2006; Liang et al., 2008; Carpenter et al., 2010; Baillard et al., 2017; Hoste-Colomer et al., 2017; Hoste-Colomer et al., 2018) and have paid little attention to intermediate-depth events. The most comprehensive analysis of the local seismicity beneath the central Himalayas was performed by Monsalve et al. (2006). They used almost 20 months of seismic data from the Himalaya Nepal Tibet Seismic Experiment (HINMT; de la Torre and Sheehan, 2005) and observed a bimodal distribution of hypocentral depths of seismicity that included 139 intermediate-depth events. de la Torre et al. (2007) determined focal mechanism solutions for some of these intermediate-depth locations with focal depths ranging from 60 to 90 km near the Moho beneath the central Himalayas. This analysis suggested that strike-slip faulting and east-west deformation takes place near and below the Moho (see focal mechanisms in **Figure 1**). Alvizuri and Hetényi (2019) calculated the full seismic moment tensor for the largest and best constrained intermediate-depth event, initially detected by Monsalve et al. (2006). The moment tensor solution contained components of both double couple and tensile crack, which supports local dehydration embrittlement processes beneath the Himalayas.

Here we address the need for a detailed intermediate-depth earthquake catalog for the central Himalayas orogen especially given that the space and time evolution of these events has not been addressed so far. In particular, starting with continuous waveform data and applying modern detection and analyses methods, we present the most comprehensive intermediate-depth earthquake catalog for the central Himalayas. We examine the spatial and temporal characteristics of the seismicity and discuss possible mechanisms for seismogenesis at such depths to explain our seismological observations.

2 MATERIALS AND METHODS

2.1 Seismic Data

We use continuous waveform data from three different temporary seismic networks that operated in the central Himalayas region from late 2001 till mid-2003 (HIMNT, Hi-CLIMB, BPE; de la Torre and Sheehan, 2005; Monsalve et al., 2006; Nábělek et al., 2009; Miller, 2002; Velasco et al., 2007). The composite seismic network consists of 114 seismic sites in total. We do not use all the Hi-CLIMB seismic sites and only use the initial phase of the Hi-CLIMB network that complemented and re-occupied some of the HIMNT locations. We choose not to use the later Hi-CLIMB phases as they occupied the transect sites at times that were not suitable for earthquake location purposes. **Figure 1** shows the spatial distribution of the composite seismic network. The number of operational seismic sites and spatial coverage of the composite seismic network varies substantially with time. Details for all seismic networks used here can be found in the supplementary material (**Supplementary Figure S1**). We also include data from individual seismic site IC.LSA in Tibet. All the continuous waveform data used here are archived at the Incorporated Research Institutions for Seismology Data Management Center (IRIS–DMC). Waveform access and processing were performed using the ObsPy package in Python (Krischer et al., 2015).

TABLE 1 | Details of candidate intermediate-depth events (recorded with ≥40 km hypocentral depths) from existing catalogs. Dates are in month/year format (mm.yyyy).

Source	Number of events	Time period spanning
NEMRC	792	09.2001 – 04.2003
Monsalve et al. (2006)	139	09.2001 – 04.2003
All catalogs	**931**[a]	09.2001 – 04.2003

[a]*This number contains duplicate events.*

2.2 Candidate Intermediate-Depth Events

As a first step, we create a list of candidate events of all the available intermediate-depth earthquakes located in the central Himalayas with hypocentral depths greater or equal to 40 km. In particular, we combine existing catalogs from the previous study of Monsalve et al. (2006) and the National Earthquake Monitoring and Research Center (NEMRC) of Nepal. This process provided us with 931 candidate intermediate-depth events (**Table 1** and **Figure 1**). We note that this number of events potentially contains many duplicates as the two catalogs overlap in both time and space.

2.3 Earthquake Catalog Compilation

We start with the 931 candidate events (**Table 1** and **Figure 1**) and locate as many events as possible given the waveform data availability. We apply a semi-automatic processing and locating method, similar to the one described in Michailos et al. (2019). In brief, we cut all the available continuous waveform data within the time windows around the origin times of the candidate events (extending 10 s before and 50 s after the earthquake's origin time). We identify and pick *P* and *S* phases within the cut waveforms, using an automatic phase picker called *kpick* (Rawles and Thurber, 2015). All automatic *P* and *S* wave phases are then manually inspected on unfiltered seismograms, false or uncertain picks are removed, and new manual picks are added where appropriate. This analysis yields 226 intermediate-depth events based on 2,604 *P* and 1,654 *S* high-quality phase picks, roughly half of which are manual.

By applying this analysis and not solely creating a composite earthquake catalog in which we would combine information from the two previous catalogs, we avoid inconsistencies and heterogeneities due to the use of different location methods, velocity models, seismic networks, magnitude scales. Also, by applying this processing, we ensure that the earthquake catalog is devoid of duplicate events that otherwise would be extremely hard to distinguish if we were to use only their location information (i.e., origin time and hypocenter). We note, however, that this initial catalog of 226 candidate events is based on origin times from two different catalogs that were not compiled in the same way. Therefore this initial catalog, based on analysis of segments of the waveform data, is likely to include inconsistencies due to the use of different earthquake detection methods used by the previous study Monsalve et al. (2006) and NEMRC.

To overcome this inherent heterogeneity in the catalog and obtain a broader and more complete picture of the seismicity, we analyze the continuous waveform data using a recently developed earthquake signal detector and phase picker called EQTransformer (Mousavi et al., 2020). EQTransformer uses a deep learning model trained on earthquake observations (1 million earthquake and 300,000 noise waveforms) from around the globe and synchronously performs earthquake detection and phase picking (Mousavi et al., 2020). We use this algorithm for the same period as our initial earthquake catalog and only keep the additional events. We manually inspect the additional events (in addition to the initial 221 candidate intermediate-depth events from this analysis) and refine picks where appropriate. This process provides us with 122 additional intermediate-depth earthquakes locations. In total, we locate 348 intermediate-depth events that correspond to high-quality 3,852 *P*, and 2,765 *S* phase picks. This analysis also yielded 347 robust earthquake locations with hypocenters shallower than 40 km depth, which we do not investigate further.

2.4 Matched-Filter Earthquake Detection

We use matched-filter earthquake detection techniques to extend further the intermediate-depth catalog (hypocentral depths greater than 40 km). In particular, we use EQcorrscan (Chamberlain et al., 2017), an open-source Python package for detecting repeating and near-repeating seismicity. We create templates of 6 s lengths (starting 0.2 s before *P* and *S* phases of earthquakes) recorded on at least four seismic sites. Tests with different template lengths (2, 4, 6, and 8 s) were performed and templates of 6 and 8 s gave very similar results that detected more intermediate-depth events compared to the rest. We choose 6 s over 8 s templates for computational efficiency. Templates and continuous waveforms are down-sampled to 50 Hz and bandpass filtered between 1.0 and 10.0 Hz. We discard noisy templates that have a signal-to-noise ratio (SNR) smaller than 4.0. After applying this analysis, we retain 277 templates (out of 348). We then scan these templates through the continuous data spanning late 2001 till mid-2003 and calculate network cross-correlation sums (NCCS) based on aligned single-channel cross-correlation coefficients. When NCCS exceeds 10 times the Median Absolute Deviation (MAD) of the daily NCCS, an earthquake detection is defined. This process provides us with ~2,000 earthquake detections in total.

To ensure the robustness of these detections and remove false detections, we use an automatic location process, described in Michailos et al. (2019), that iteratively determines earthquake locations keeping the locations that meet some given quality criteria (i.e., earthquake recorded on at least four stations and an RMS value < 1 s). As a final quality control step, we manually inspect all the automatically determined locations, and we obtain 64 additional, robustly located intermediate-depth earthquake locations. This relatively low number of final earthquake locations obtained from matched filter detection is due to the sparse seismic network in northeastern Nepal where the majority of our templates are located and strict quality criteria we apply in order to maintain only the robustly located events. To check that the matched filter detection routine performed well, we manually inspected a subset of the initial ~2,000 matched filter detections. These detections contained earthquake signals but were ultimately rejected because they were detected in fewer than four stations.

2.5 Earthquake Location

2.5.1 Initial Absolute Earthquake Locations

We calculate preliminary absolute earthquake locations using the probabilistic non-linear earthquake location algorithm, NonLinLoc (Lomax et al., 2000). We consider four different 1-D velocity models: 1) Tibet (Monsalve et al., 2006), 2) Nepal (Pandey et al., 1995; Cotte et al., 1999; Monsalve et al., 2006), 3) gradational version of the Tibet velocity model, 4) the global iasp91 velocity model (Kennett and Engdahl, 1991). We examine the effect on the hypocentral depths of the earthquakes by using these different velocity models. Overall, all four velocity models, apart from the one developed by Monsalve et al. (2006) for the Nepal region, yield similar results (see more details in supplementary material). Because the majority of the intermediate-depth earthquakes are located near southern Tibet; we choose to use the 1-D velocity model developed by Monsalve et al. (2006) for the southern Tibet region that is in agreement with receiver-function calculations (e.g., Moho depth of ~70 km; Schulte-Pelkum et al., 2005). We use a constant V_P/V_S ratio of 1.77 (same value used to construct the velocity models).

We select NonLinLoc to obtain preliminary earthquake locations as 1) earthquake locations are represented as a posterior probability density function (PDF; that can be plotted as a cloud of possible locations surrounding the maximum likelihood hypocenter) which includes the effects of the location uncertainties deriving from the seismic network geometry and arrival time calculations, 2) NonLinLoc includes station elevation information for the creation of the velocity grid and the calculation of the travel times that are of great importance given the high topography of the Himalayas. We do not apply any weighting scheme on the quality of the picks, that is to say, all picks are equally weighted because all picks were manually inspected and refined. During this initial NonLinLoc run, we also calculate station corrections.

2.5.2 Final Absolute Earthquake Locations With Station Corrections

For the final absolute earthquake locations, we improve the accuracy of the arrival travel times by including station corrections (estimated during the preliminary NonLinLoc run; **Supplementary Figure S6** in supplementary material). To do so, we use the equal differential-time (EDT) function, which is known to cope well with outliers in arrival travel times (Lomax, 2005). Using a method like EDT, we address issues arising from: a) the use of a 1-D velocity model for a broader region than what it was developed for (i.e., unmodeled velocity structures throughout the examined region), b) misidentifying phase picks (especially for S-wave picks), or c) uncertain absolute arrival times at specific sites due to interrupted or limited satellite communication.

The robustness of earthquake locations and the accuracy of the hypocentral depth estimates depend upon the knowledge of the crustal structures, the number and quality of the phase picks, and the network geometry (Pavlis, 1986; Havskov and Ottemöller, 2010). As a general rule, hypocentral depth errors increase near the boundaries and outside of the regions covered by the seismic networks. Keeping this in mind, we retain events with distances to the closest station smaller than the two times their hypocentral depth (mean distance to closest station 72.7 ± 32.5 km; **Supplementary Figure S7** in supplementary material). We also discard events with fewer than eight total picks, events lacking at least two S-phase picks, and events that have a root mean square (RMS) larger than 1 s. Hypocentral uncertainties of absolute earthquake locations have average values of 11.4 and 14.1 km on the horizontal and vertical directions, respectively (**Supplementary Figure S8** in supplementary material).

2.5.3 Relative Earthquake Locations

To refine the earthquake locations, better examine the internal seismicity structure, and to better identify any potential seismicity migration, we use double-difference earthquake location techniques. This technique leverages the high precision of differential travel time measurements and minimizes the effects of unknown velocity structures that may exist within the source-receiver ray paths (Waldhauser and Ellsworth, 2000). In particular, we use HypoDD (Waldhauser, 2001) and the 1-D velocity model of (Monsalve et al., 2006).

Of the 414 absolute earthquake locations, we are able to relocate 298 events using HypoDD. The difference in hypocentral depths between the absolute and relative earthquake locations is generally smaller than 5 km (90th percentile of 4.6 km; see **Supplementary Figure S9** in the supplementary material), which is smaller than the absolute earthquake location uncertainties. We perform an uncertainty analysis, a modified bootstrapping approach (Efron and Robert, 1994; Waldhauser and Ellsworth, 2000), to assess the robustness of the final relocations, and we obtain mean values of 1.2 and 2.3 km for horizontal and vertical directions.

It has to be stressed, however, that the robustness and accuracy of these techniques are strongly dependent on the correctness of the velocity model, along with the accuracy of the absolute earthquake locations used (Michelini and Lomax, 2004). Thus double-difference methods can provide a very detailed and accurate pattern for the earthquakes within a cluster of similar events, but the overall position of the cluster remains dependent on the starting absolute earthquake locations and might not always be accurate (Wolfe, 2002; Menke and Schaff, 2004). In addition to this, the use of a 1-D velocity model over a 3-D one that is not available for the region introduces limitations in the precision of the relative earthquake locations (e.g., Matoza et al., 2013) caused by lateral variations in velocity structures. Nevertheless, we proceed with migration analysis under the assumption that the relative locations are not adversely affected by such biases.

2.6 Magnitude Estimation

We estimate local magnitudes to quantify the earthquakes' physical size consistently using a formula calculated by Adhikari et al. (2015). The local magnitude scale formula we use here was developed for the broader Nepal region and it includes geometric spreading and elastic attenuation correction terms. We do not include station correction terms. We automatically define amplitude picks (4,410 in total) on the vertical components of seismograms (band-passed 0.3–7 Hz) in a 1-s time window starting after the *S* wave picks, using a utility function from the EQcorrscan Python package (Chamberlain et al., 2017). Amplitude picks are measured on

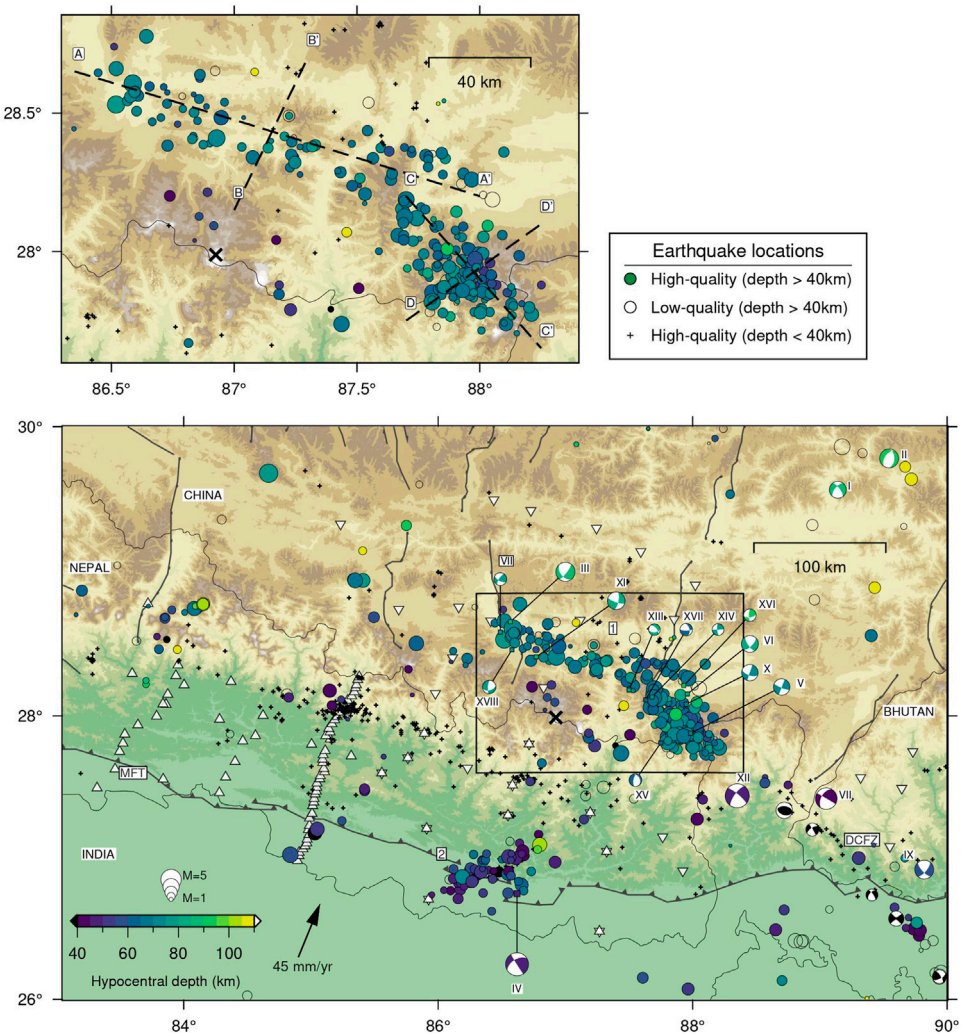

FIGURE 2 | Epicenters of 414 relative and absolute earthquake locations calculated using HypoDD (Waldhauser, 2001) and NonLinLoc (Lomax et al., 2000) with a 1D velocity model (Monsalve et al., 2006). Well constrained earthquake locations (high-quality) are shown by colored circles scaled by their respective magnitudes. Poorly constrained earthquake locations (low-quality) are indicated by empty black circles. Black crosses depict the high-quality shallow seismicity located in this study. The large black cross depicts the location of Mount Everest. MFT is the Main Frontal Thrust and DCFZ is the Dhubri-Chungthang fault zone. Framed numbers 1 and 2 show the seismicity clusters described in the text. Focal mechanisms are the same as in **Figure 1**. Inset shows the expanded view of the region marked by the box, focusing on Cluster 1. Black dashed lines with capital letters indicate cross-sections shown in **Figures 3**, **4**.

synthetic Wood-Anderson seismograms on the vertical components. We use the vertical components as they have been found to be less sensitive to local amplification effects (Havskov and Ottemöller, 2010).

Using the amplitudes and the formula, we calculate magnitudes at individual seismic sites and the average value of these is kept as the earthquake's magnitude. Because the local magnitude formula was initially developed for a different region (i.e., broader Nepal region), we examine the consistency and robustness of our magnitude estimates by comparing a sample of our magnitudes to the ones from the same earthquakes recorded by existing catalogs (NEMRC; Monsalve et al., 2006). Our local magnitude estimates are on average 0.38 ± 0.07 (95% CI) magnitude units underestimated compared to magnitude values of Monsalve et al. (2006) and NEMRC, but provide consistent estimates within our dataset, which is essential for the spatio-temporal analysis performed here (**Supplementary Figure S10** of the supplementary material). In addition, we calculate the magnitude residuals, and we find no bias with hypocentral distance (**Supplementary Figure S11** supplementary material).

3 RESULTS

3.1 Spatial Distribution of Intermediate Depth Seismicity

We present 414 high-quality intermediate-depth earthquake locations beneath the central Himalayas orogen spanning from late 2001 through mid-2003. Hypocentral depths of the seismic

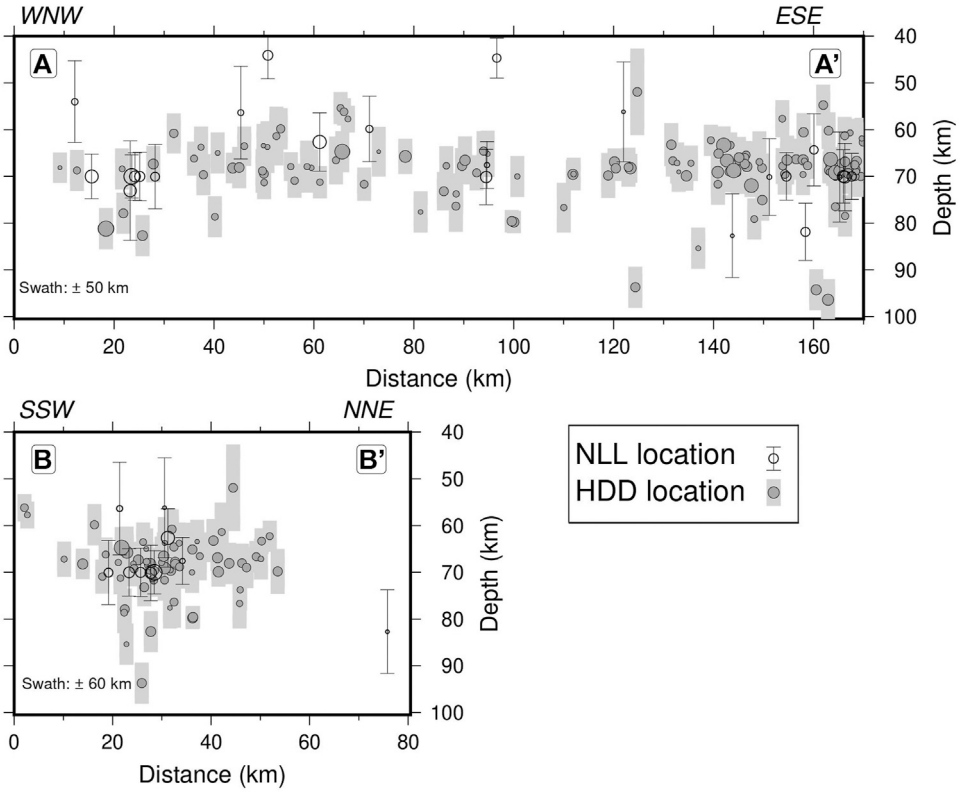

FIGURE 3 | Vertical cross-sections of earthquake hypocenters. Dark gray and black open circles depict the relative and absolute earthquake locations' hypocenters. Earthquake location uncertainties are shown as vertical black and light gray bars, respectively. The locations of cross-sections A–A′ are marked in **Figure 2**. Earthquakes within 50 and 60 km on either side of the cross-sections are shown. Note that cross-sections are slightly vertically exaggerated and the size of the symbols are scaled to their respective magnitudes.

activity range from 40 to 100 km (average focal depth of 65.8 km). Estimated local magnitudes M_L range from 0.79 to 4.51. The overall spatial distribution of seismicity is similar to those observed by previous studies (e.g., Pandey et al., 1999; Monsalve et al., 2006; de la Torre et al., 2007; Velasco et al., 2007; Diehl et al., 2017).

The majority of the intermediate-depth earthquakes (248 events) are clustered in a region near southern Tibet and northeastern Nepal (box in **Figure 2**) with hypocentral depths generally larger than 60 km. Epicenters within this cluster of events align on a west-northwest to east-southeast oriented sub-linear structure in the vicinity of the Higher Himalayas. We refer to this cluster as "Cluster 1" hereafter. Cluster 1 is composed of two main linear features, one strikes at west-northwest to east-southeast (N ~105°), and one strikes northwest to southeast (N ~140°), as it can be clearly seen in the inset of **Figure 2** highlighted by the cross-sections A–A′ and C–C', respectively. The two main linear features appear not to merge at their endpoints but rather slightly to the west of the eastern end of the N ~105° segment. The lateral termination of seismicity in Cluster 1, especially at its western edge, is considered a natural feature and not an artifact observed due to limitations of the seismic network.

The hypocentral distribution of seismicity in Cluster 1 is generally uniform, with a mean value of 68.7 km. **Figure 3** depicts the hypocentral depths along the profiles highlighted in the inset of **Figure 2**. Seismicity depths are generally constant along the length of the profile A–A′ ranging from 58 to 78 km within their respective hypocentral errors. Seismic deformation occurs within a ~150 km long and ~35 km wide (across strike) zone (profile B–B′). In the southeastern section of Cluster 1 (**Figure 4**), depths range mostly between 60 and 75 km within uncertainties. Seismic deformation there takes place in a narrower zone compared to profile A–A' (~60 km long and ~30 km wide zone) and seismicity rates are higher here compared to near A–A′ profile. A significant number of events along C–C′ are clustered near the 70 km depth velocity model layer boundary, which represents the Moho, as distance to closest station increases from C to C'. This location artifact is due to the velocity jump in the 1D velocity model we use here that causes discontinuities in the travel times (e.g., Havskov and Ottemöller, 2010). For more details on this, refer to the **Supplementary Section 1.2**.

We also observe another cluster of intermediate-depth earthquakes (depths generally >35 km) located in southeastern Nepal (Cluster 2; **Figure 2**). This cluster forms a east-northeast to west-southwest structure and is very close to the hypocenter of the lower crustal M 6.5 1988 Udayapur earthquake (Chen and Kao, 1996). Previous studies (e.g., Pandey et al., 1999) that used a different dataset than the one presented here, suggested that Cluster 2 seismicity there might be

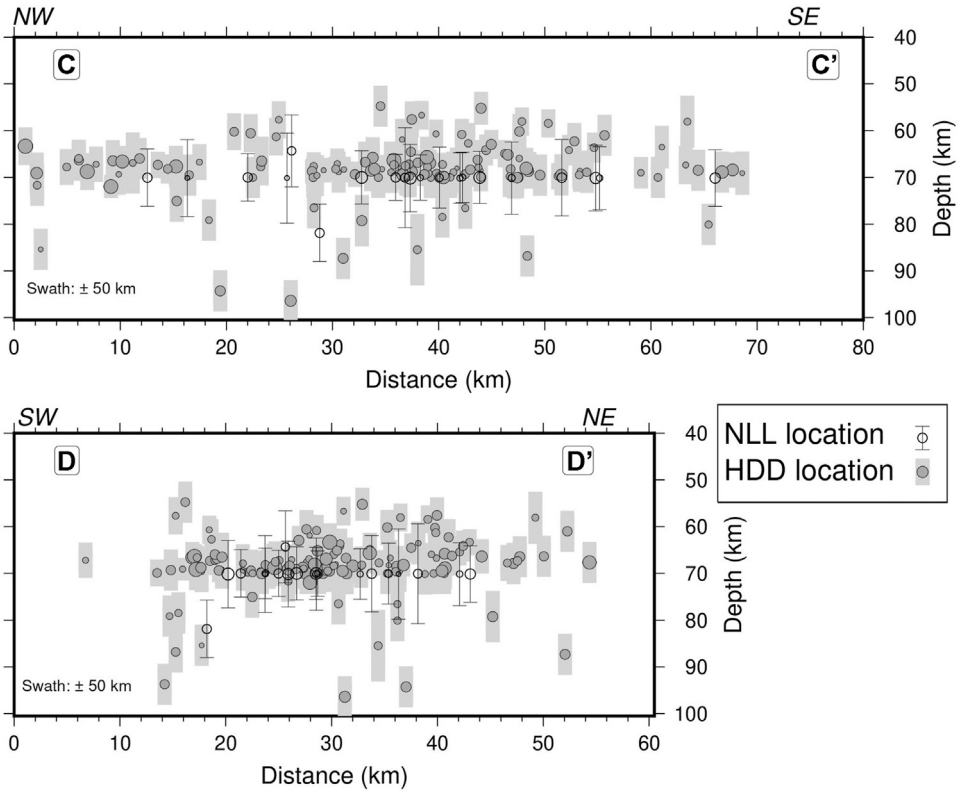

FIGURE 4 | Same as **Figure 3** but for cross-sections C–C′ and D–D'. Earthquakes within 50 km on either side of the cross-sections are shown. Note that cross-sections are vertically exaggerated and the size of the symbols are scaled to their respective magnitudes.

related to the aftershock sequence of the M6.5 Udayapur earthquake. Given the time span of our dataset here (19 months), we can not conclude whether Cluster 2 is part of the aftershock sequence or not, as there is no noticeable decrease in the frequency or magnitudes of the events with time (see **Figure 5**). Shallow seismicity (<40 km; **Figure 2**) delineates the seismicity at the mid-crustal ramp on the southern front of High-Himalaya, as well as the Dhubri-Chungthang fault zone (DCFZ) across southwestern Bhutan previously highlighted by (Velasco et al., 2007; Diehl et al., 2017).

3.2 Spatio-Temporal Evolution

In the following sections we examine a number of different properties of the seismicity: rate of seismicity, inter-event times, magnitude frequency distributions, and potential spatial migration rates.

3.2.1 Rate of Seismicity and Inter-event Times

Seismic activity near southern Tibet and Northeastern Nepal (Cluster 1) is remarkably continuous throughout the examined period (**Supplementary Figure S13** in supplementary material). **Figure 5** shows the distribution of magnitudes with time for the two defined clusters. The magnitude detection threshold is ~1.4 for the examined time period (lower detection threshold of around 1.0 in mid-2002 for Cluster 1). Cluster 1 contains several M > 4.0 events that do not appear to have any clear aftershocks. That is to say, magnitudes between the largest event and the next largest event is very small (e.g., 0.2 magnitude units). In contrast, for a mainshock-aftershock sequence, the magnitude difference between the mainshock event and the largest aftershock is usually 1.2 magnitude units (Båth, 1965). Cluster 2 has a steady occurrence rate for events with magnitudes ranging from 3.0 to 3.5.

The rate of seismic activity is relatively constant for the full catalog with sporadic slight accelerations (**Figure 5**). We also observe a change in seismicity rates with the evolution of the seismic network that coincides with the start of operation of the Hi-CLIMB network and the occurrence of several events in western Nepal (October 2002; **Figure 5**). Cluster 1 exhibits the high and constant rates until mid-late October 2002 (end of operation for HIMNT network) and later on, seismicity rates decrease significantly. Cluster 2, near Udayapur, has a relatively constant detection threshold and remarkably low seismicity rates, suggesting a balance in stress release.

The time between successive events, inter-event times, for the two clusters is shown in **Figure 6**. The majority of events from Cluster 1 exhibit relatively large inter-event times of between a day and 10 days. Cluster 2 has the largest inter-events times (>2 days on average). The lowest inter-event times (between a couple of hours to 15 min) are presented by events outside the two defined clusters (gray crosses in October 2002; **Figure 6**). These events are located in the western Nepal region. There is no apparent indication of mainshock-aftershock

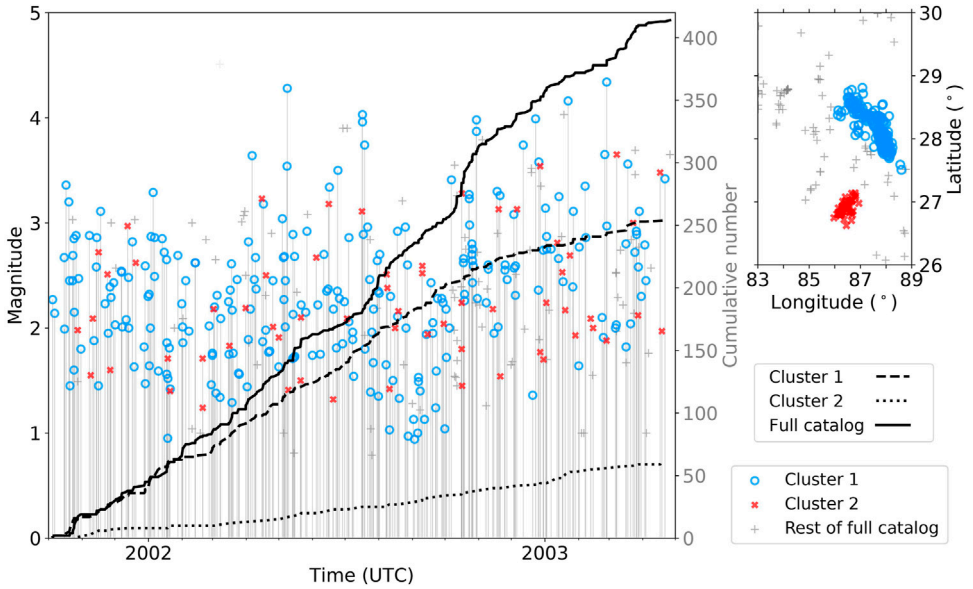

FIGURE 5 | Local magnitudes of earthquakes versus time for Cluster 1 (blue circle), Cluster 2 (red cross) and the remaining events of the full catalog (gray cross), are shown in the left axis. Solid, dashed and dotted black lines represent the cumulative number of events versus time for the full catalog, Cluster 1 and Cluster 2, respectively (right axis). Inset depicts the spatial distribution of the events.

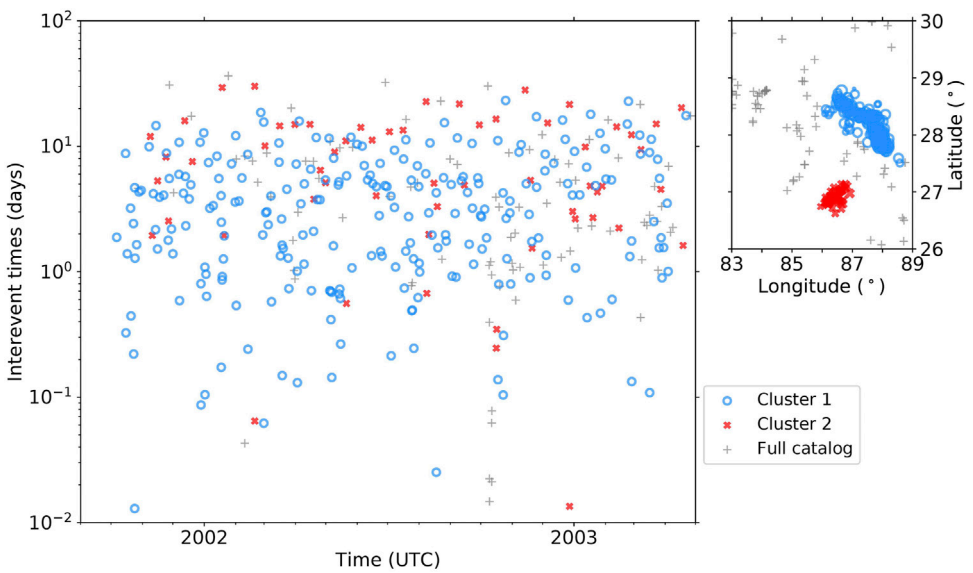

FIGURE 6 | Inter-event times for the intermediate-depth earthquakes (>40 km) that occurred between 2001 and 2003 for Cluster 1 (blue circle), Cluster 2 (red cross) and the rest of the events in the catalog (gray cross). Inset depicts the spatial distribution of the events.

sequence that would be highlighted by a series of short inter-event times.

3.2.2 Magnitude Frequency Distribution

Gutenberg-Richter distributions are generally used to describe the relative numbers of small and large earthquakes (Gutenberg and Richter, 1942). Local magnitude estimates in the full catalog range from 0.79 to 4.51 with a magnitude of completeness of $M_c = 2.4$. We calculate M_c with the maximum curvature method (Wiemer and Wyss, 2000), applying 0.4 magnitude units upward correction similar to Woessner and Wiemer (2005). We calculate b-values by fitting the cumulative density function with a power-law above the magnitude of completeness and obtain a b-value of 0.91 ± 0.004 for the full catalog (**Figure 7**). Cluster 1 has a larger

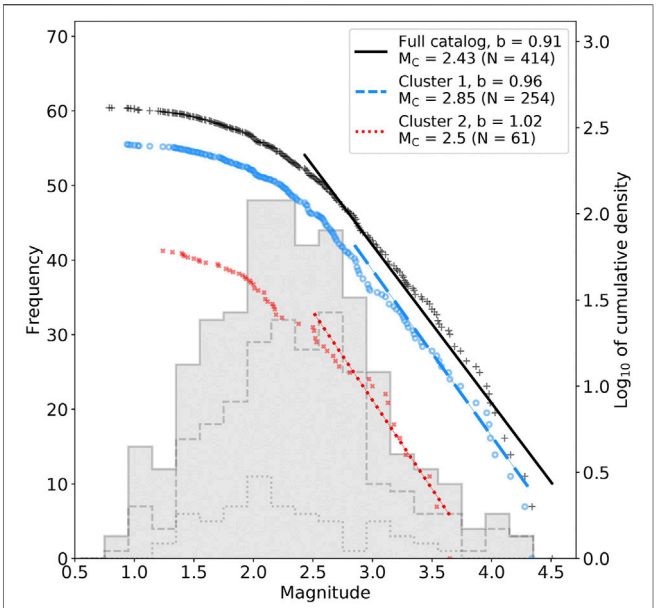

FIGURE 7 | Magnitude frequency distribution of earthquakes for full catalog, Cluster 1, and Cluster 2. Left axis (Frequency) shows the number of earthquakes in each magnitude bin. The magnitude bin used here is 0.2 magnitude units. Right axis (logarithm of cumulative density) depicts the cumulative number of earthquakes of magnitude M_L and higher. The magnitude of completeness is calculated using the maximum curvature method (Wiemer and Wyss, 2000) applying 0.4 magnitude units upward correction. The b-values are calculated by fitting the cumulative density function with a power-law above a magnitude threshold.

magnitude of completeness (i.e., M_c = 2.85) and a slightly higher b-value (0.96). Clusters 2 has a relatively small number of events (61) to obtain a robust b-value estimate.

3.2.3 Seismicity Migration Rates

We seek to identify any potential seismicity migration pattern focusing on Cluster 1 that lies beneath and North of the high Himalayas and Mount Everest. Spatial or temporal seismicity migrations generally occur within swarm sequences and not within mainshock-aftershock sequences (e.g., Vidale and Shearer, 2006; Fischer and Hainzl, 2021). Seismicity migrations can be used as proxies for pinpointing potential mechanisms as drivers for seismogenesis (e.g., Shapiro et al., 1997; Lohman and McGuire, 2007; De Barros et al., 2020).

We visually examine the earthquake's occurrence time versus the distance along strike and perpendicular to cross-section A–A′ from **Figure 2** to identify any potential patterns. **Figure 8** depicts the evolution of seismicity in time and space within cross-section A–A'. Data points are color-coded according to the along-strike distance, by doing so we ensure that any observed perpendicular to the strike pattern occurs in the same place and not far away from each other. We observe a sequence of 5–6 events that could potentially be characterized as seismicity migration (i.e., the sequence on November 17, 2001 in **Figure 8** highlighted by a black arrow). We do the same for cross-section C–C' (**Figure 9**) and do not observe any clear example of a sequence of events that stand out with a similar number of events.

To examine this potential migration pattern in more detail and possibly identify more sequences, we perform additional analysis (see supplementary material for detailed information). In this analysis, we examine the evolution of all succeeding events in our catalog by calculating the difference in time and distance of each event to its successive events and keeping those groups that are sufficiently close within a 3D volume with respect to any first event (time and space window of 20 days and 20 km). We found four such sequences that satisfy these criteria and exhibit apparent migration patterns. This relatively small number of sequences does not allow a robust quantitative estimation for diffusion rates, directivity, magnitude variation, or migrations velocities. We can, however, report that all the examined sequences generally fit with simple models of linear or diffusive migration, with rates of the same order of magnitude: for linear seismicity migration velocities at < 1.0 km/day, and for hydraulic diffusivity values <1.0 m^2/s.

4 DISCUSSION

We present the most detailed intermediate-depth earthquake catalog, comprised of 414 events with high-quality locations for the central Himalayas to date. Combining this with information from previous seismicity studies (e.g., Diehl et al., 2017), we have been able to observe a potential connection of the intermediate-depth seismicity across the DCFZ to the Shillong plateau for the first time. We start with continuous data and apply a systematic processing routine to all the available data. By applying this analysis that includes modern detection techniques (e.g., Mousavi et al., 2020), we avoid inconsistencies that may arise by combining earthquake catalogs constructed using different detection, picking and location methods and extend the number of intermediate-depth earthquakes previously located in the region (i.e., 139 events; Monsalve et al., 2006).

Using this earthquake catalog, we examine the seismicity characteristics at depths >40 km beneath southern Tibet and the central Himalayas. Overall, we observe a mostly monotonous pattern of seismicity: no clear mainshock-aftershock sequences, relatively large inter-event times, almost constant seismicity rates, small difference in magnitude units between largest and second largest events, and potential indications for spatial migrations based on a few examples. The nearly continuous seismic activity and the evidence of potential seismicity migration within sequences of succeeding events at reasonable rates we observe here allow for the interpretation that fluids and metamorphic dehydration reactions to play a role in seismogenesis within a hydrous ILC beneath the high Himalayas. Laboratory experiments on natural hydrous granulites deformed at various pressure-temperature conditions fracture within both granulite and eclogite stability fields (Incel et al., 2017). Metamorphic dehydration reactions densify rocks (i.e., reduction in volume) and create a network of fractures in the ILC where at least locally permeability can be high. This behavior and relation to dehydration embrittlement is also suggested by a moment tensor solution that includes a clear isotropic component, obtained for one of the largest intermediate-depth events calculated by Alvizuri and Hetényi

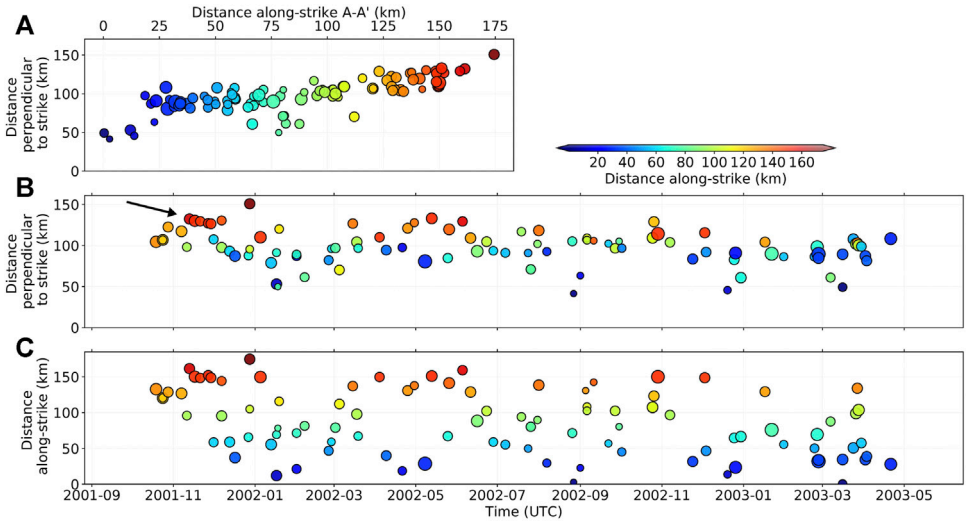

FIGURE 8 | Graph visualizing the space and time evolution of the hypoDD relocated seismicity along strike and perpendicular to Cluster 1. Circles are colored according to the distance along strike of cross-section A–A'. **(A)** Rotated map view of seismicity along cross-section A–A' (strike) and B–B' (perpendicular to strike). **(B)** Distance perpendicular to strike vs. time. **(C)** Distance along strike vs. time. Figure format is adapted from Shelly et al. (2007). The black arrow highlights the November 17, 2001 sequence.

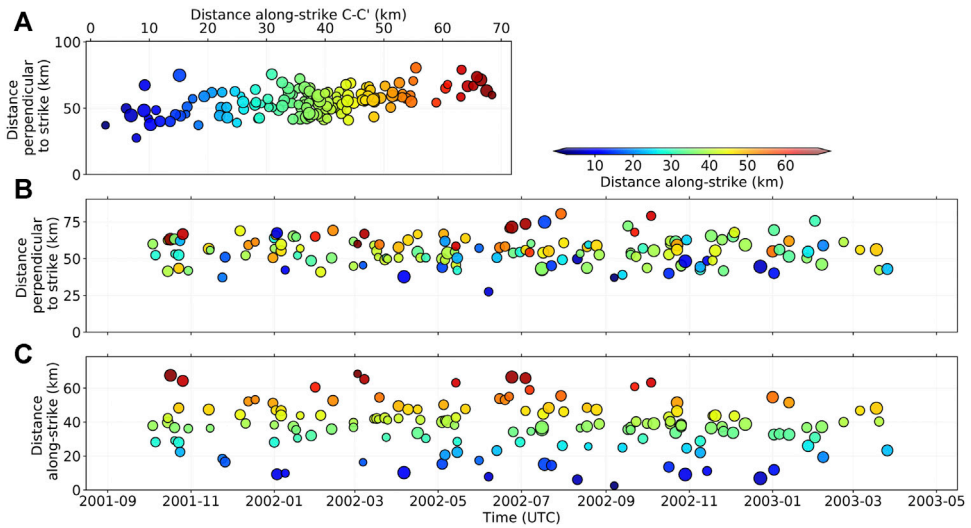

FIGURE 9 | Same as **Figure 8** but for cross-sections C–C′ and D–D'.

(2019) that is also within our catalog (focal mechanism VII in **Figures 1**, **2**). This interpretation could be strengthened with additional analyses, including stress drop estimations, but the limited data and lack of path and site terms restricted this possibility. While the few sequences we identified here could represent fluid migration following dehydration reactions, metamorphic arguments can be put forward for single events as well. An example of such a single event includes a magnitude 4 earthquake (M_L = 4.5, 6th of June 2013, 19:01:03 UTC) that occurred in the lower crust at ~76 km depth in northern Bhutan, a region covered at the time by GANSSER temporary seismic network (Diehl et al., 2017; Singer, 2017). Despite the dense coverage of the seismic network, no aftershock was observed for at least a year (e.g., Diehl et al., 2017). This single event could be an indication that rocks near the earthquake's hypocenter have undergone metamorphic reactions. The freed fluids likely escaped on pre-existing pathways and no further surrounding rock masses were ready to react similarly, hence the dehydration process triggered a single event and no aftershocks.

As an alternative interpretation, the nearly constant seismic activity could be due to the background microseismicity of the area and depth range. In that case, tectonics can be the

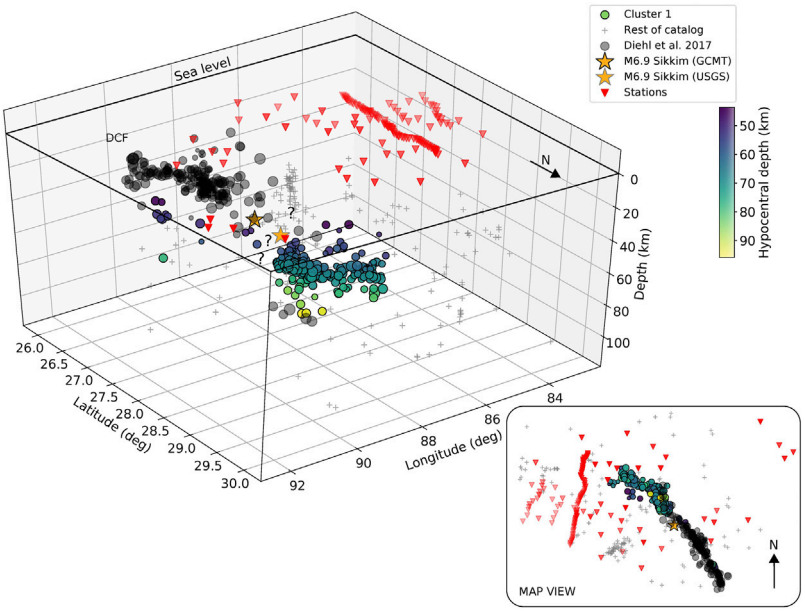

FIGURE 10 | Three dimensional view of seismicity near Dhubri-Chungthang fault zone (DCFZ) and Cluster 1. Hypocenter locations determined in this study, located in Cluster 1, are colored according to their hypocentral depths (see color scale) and the rest of the events in the catalog are depicted with gray crosses. Black circles show the seismicity located by Diehl et al. (2017) in the vicinity of DCFZ. Stars show the M6.9 2011 Sikkim Himalaya earthquake hypocenters provided by the U.S. Geological Survey (USGS) and the Global Centroid Moment Tensor (GCMT). Question marks depict the region where the DCFZ seismicity could be connected to Cluster 1, possibly through the M6.9 event. Inset shows the map view of the seismicity. For a more detailed view of the seismicity see also **Supplementary Video S1**.

mechanism controlling seismogenesis at such depths beneath the central Himalayas. One could expect tensional fracturing due to the bending of the Indian plate from north-dipping back to horizontal; however, the observed focal mechanisms (**Figure 1**; de la Torre et al. (2007)) show mostly strike-slip and some transtensional events along the N105° striking part of Cluster 1. The strike-slip component here can be explained with the dextral basement fault zone that separates the Shillong block and India (Vernant et al., 2014), with active seismicity (see next paragraph); it can also be an inherited tectonic feature, continuing the rift zone related to the formation of the Shillong Plateau as presented in (Talwani et al., 2016).

The linear N140°-striking part of Cluster 1 (**Figure 2** including the shallow seismicity <40 km depths) appears to be a continuation of the Dhubri-Chungthang fault zone (DCFZ) that is identified from the NW corner of the Shillong Plateau, crossing southwestern Bhutan and then beneath Sikkim (e.g., Diehl et al., 2017). A more detailed view of this can be found in **Figure 10** (and **Supplementary Video S1**) that shows a 3D view of the intermediate-depth earthquake hypocenters in conjunction with the shallower events located near the DCFZ zone by Diehl et al. (2017). The hypocenter of the M6.9 2011 Sikkim Himalaya earthquake is also shown in **Figure 10** (both GCMT and USGS solutions). The significant discrepancies in location from different seismological institutions for the M6.9 2011 Sikkim Himalaya earthquake make it rather unclear whether the earthquake occurred within Cluster 1 or farther away to the southeast. Considering the location uncertainties and a ~50 km of subsurface rupture length obtained by empirical relations of Wells and Coppersmith (1994) for the M6.9 2011 Sikkim Himalaya earthquake, this major event could represent the connection between the DCFZ and the N140°-striking part of Cluster 1, and propagate the dextral deformation further beneath the orogen, possibly continuing as a tear fault along the N105°-segment (see focal mechanisms in **Figure 1**). The counterargument for this tectonic interpretation is the lack of a mainshock-aftershock sequences in our catalog. But a longer catalog and therefore observation time is required.

The intermediate-depth seismicity analyzed here is likely to include hypocenters that occurred both in the lower crust and in the upper mantle. It has to be stressed though, that the hypocenter uncertainties in our earthquake locations make it impossible to determine whether the intermediate-depth seismicity takes place below or above the Moho (70–75 km in Southern Tibet by receiver function analysis; Schulte-Pelkum et al., 2005; Nábělek et al., 2009), or, likely, both; similarly, it is currently impossible to estimate how thick the Moho as a vertical velocity-transition is. Further analysis (e.g., waveform fitting analysis) is required to distinguish between lower crustal and upper mantle events, which is beyond the scope of this paper. It should also be noted that the catalog presented here is relatively sparse due to the network's geometry and the large hypocentral depths, and thus a more dedicated seismic network could provide a more complete and higher resolution picture of seismicity. In addition to this, our catalog only covers a year and half of the

ongoing seismic deformation with high-quality locations, that is only a small snapshot with respect to typical dehydration periods (~1,000 years) compared to calm metamorphic times (Malvoisin et al., 2020). Therefore, potential future directions should include longer and denser seismic networks in the region that can help provide more robust locations along with modeling studies of rock mechanics. More detailed intermediate-depth event sequences could afford comparisons with sequences in shallower contexts that could potentially shed more light on whether these intermediate-depth events are tectonic, fluid related, or a mix of the two.

5 CONCLUSION

We present the most comprehensive, high-quality catalog of 414 intermediate-depth earthquakes that occurred in the central Himalayas between late 2001 and mid-2003. Intermediate-depth earthquakes are mainly concentrated in a 55–80 km deep cluster within two linear interconnected segments: a N105°-striking segment in southernmost Tibet adjacent to northeast Nepal, and a N140°-striking segment. The latter segment is likely connected to the M6.9 2011 Sikkim earthquake and the Dhubri-Chungtang fault zone cutting across the Himalayas, a connection that is observed for the first time. Seismicity there presents the following characteristics: 1) absence of mainshock-aftershock sequences, 2) small largest to next largest magnitude differences, 3) relatively constant seismicity rates, 4) inter-event times mostly >1 day, 5) a few sequences with potential spatial migration of generally <1.0 km/day. Our results, and particularly the absence of mainshock-aftershock sequences, suggest that eclogitization reactions that densify the hydrous Indian lower crust (ILC) could locally increase permeability and cause brittle failure. On the other hand, a tectonically inherited dextral deformation zone propagating beneath the orogen, and continuing as a westward tear fault beneath southernmost Tibet, is also a plausible scenario. We note that these two explanations are not mutually exclusive, and given the available data, no argument can be made on which one plays the most important role for seismogenesis. Further advances in this research can be obtained with longer observation times, as well as by opening access to seismological waveform data from all past, ongoing and forthcoming seismic networks and experiments.

DATA AVAILABILITY STATEMENT

The continuous seismic data from the three temporary networks used in this study can be found at the Incorporated Research Institutions for Seismology Data Management Center (IRIS-DMC; https://ds.iris.edu/ds/nodes/dmc/) with the following network codes: HIMNT, YL; Hi-CLIMB, XF; BPE, XA. The details of the intermediate-depth earthquakes catalog constructed in this study are available in the supplementary material in CSV and QuakeML format.

AUTHOR CONTRIBUTIONS

KM led the project and performed the analyses. GH provided initial ideas for the research and guidance. NC contributed by providing catalog data and discussions from early drafts of the manuscript. KM lead the manuscript writing, with input from GH and NC. All authors have read and approved the final version of the manuscript.

FUNDING

This work was funded by the Swiss National Science Foundation project OROG3NY (Grant *PP*00*P*2_187199).

ACKNOWLEDGMENTS

We thank the National Earthquake Monitoring and Research Center (NEMRC) of Nepal and John Nabelek for sharing catalog data and Benjamin Malvoisin for helpful discussions on seismicity migrations. We also thank Calum Chamberlain for useful feedback with the matched filter detection analysis and Maria Mesimeri for providing bootstrap analysis codes.

SUPPLEMENTARY MATERIAL

The Supplementary Material for this article can be found online at: https://www.frontiersin.org/articles/10.3389/feart.2021.742700/full#supplementary-material

REFERENCES

Acton, C. E., Priestley, K., Mitra, S., and Gaur, V. K. (2011). Crustal Structure of the Darjeeling-Sikkim Himalaya and Southern Tibet. *Geophys. J. Int.* 184, 829–852. doi:10.1111/j.1365-246X.2010.04868.x

Adhikari, L. B., Gautam, U. P., Koirala, B. P., Bhattarai, M., Kandel, T., Gupta, R. M., et al. (2015). The Aftershock Sequence of the 2015 April 25 Gorkha-Nepal Earthquake. *Geophys. J. Int.* 203, 2119–2124. doi:10.1093/gji/ggv412

Alvizuri, C., and Hetényi, G. (2019). Source Mechanism of a Lower Crust Earthquake beneath the Himalayas and its Possible Relation to Metamorphism. *Tectonophysics* 769, 128153. doi:10.1016/j.tecto.2019.06.023

Austrheim, H. (1987). Eclogitization of Lower Crustal Granulites by Fluid Migration through Shear Zones. *Earth Planet. Sci. Lett.* 81, 221–232. doi:10.1016/0012-821X(87)90158-0

Baillard, C., Lyon-Caen, H., Bollinger, L., Rietbrock, A., Letort, J., and Adhikari, L. B. (2017). Automatic Analysis of the Gorkha Earthquake Aftershock Sequence: Evidences of Structurally Segmented Seismicity. *Geophys. J. Int.* 209, 1111–1125. doi:10.1093/gji/ggx081

Båth, M. (1965). Lateral Inhomogeneities of the Upper Mantle. *Tectonophysics* 2, 483–514. doi:10.1016/0040-1951(65)90003-X

Bettinelli, P., Avouac, J. P., Flouzat, M., Jouanne, F., Bollinger, L., Willis, P., et al. (2006). Plate Motion of India and Interseismic Strain in the Nepal Himalaya from GPS and DORIS Measurements. *J. Geodesy* 80, 567–589. doi:10.1007/s00190-006-0030-3

Bilham, R. (2019). Himalayan Earthquakes: A Review of Historical Seismicity and Early 21st century Slip Potential. *Geol. Soc. Spec. Publ.* 483, 423–482. doi:10.1144/SP483.16

Caldwell, W. B., Klemperer, S. L., Lawrence, J. F., Rai, S. S., and Ashish (2013). Characterizing the Main Himalayan Thrust in the Garhwal Himalaya, India with Receiver Function CCP Stacking. *Earth Planet. Sci. Lett.* 367, 15–27. doi:10.1016/j.epsl.2013.02.009

Carpenter, N., Nabelek, J., and Braunmiller, J. (2010). South-central Tibetan Seismicity from HiCLIMB Seismic Array Data. M.S. Thesis. Corvallis: Oregon State University.

Chamberlain, C. J., Hopp, C. J., Boese, C. M., Warren-Smith, E., Chambers, D., Chu, S. X., et al. (2017). EQcorrscan: Repeating and Near-Repeating Earthquake Detection and Analysis in Python. *Seismological Res. Lett.* 89, 173–181. doi:10.1785/0220170151

Chen, W.-P. (1988). A Brief Update on the Focal Depths of Intracontinental Earthquakes and Their Correlations with Heat Flow and Tectonic Age. *Seism. Res. Lett.* 59, 263–272. doi:10.1785/gssrl.59.4.263

Chen, W.-P., and Kao, H. (1996). Seismotectonics of Asia: Some Recent Progress. *World Regional* 1, 37–62.

Chen, W.-P., and Molnar, P. (1983). Focal Depths of Intracontinental and Intraplate Earthquakes and Their Implications for the thermal and Mechanical Properties of the Lithosphere. *J. Geophys. Res.* 88, 4183–4214. doi:10.1029/jb088ib05p04183

Chen, W.-P., Nabelek, J. L., Fitch, T. J., and Molnar, P. (1981). An Intermediate Depth Earthquake beneath Tibet: Source Characteristics of the Event of September 14, 1976. *J. Geophys. Res.* 86, 2863–2876. doi:10.1029/jb086ib04p02863

Cotte, N., Pedersen, H., Campillo, M., Mars, J., Ni, J. F., Kind, R., et al. (1999). Determination of the Crustal Structure in Southern Tibet by Dispersion and Amplitude Analysis of Rayleigh Waves. *Geophys. J. Int.* 138, 809–819. doi:10.1046/j.1365-246X.1999.00927.x

Craig, T. J., Copley, A., and Jackson, J. (2012). Thermal and Tectonic Consequences of India Underthrusting Tibet. *Earth Planet. Sci. Lett.* 353-354, 231–239. doi:10.1016/j.epsl.2012.07.010

De Barros, L., Cappa, F., Deschamps, A., and Dublanchet, P. (2020). Imbricated Aseismic Slip and Fluid Diffusion Drive a Seismic Swarm in the Corinth Gulf, Greece. *Geophys. Res. Lett.* 47, 1–9. doi:10.1029/2020GL087142

de la Torre, T. L., Monsalve, G., Sheehan, A. F., Sapkota, S., and Wu, F. (2007). Earthquake Processes of the Himalayan Collision Zone in Eastern Nepal and the Southern Tibetan Plateau. *Geophys. J. Int.* 171, 718–738. doi:10.1111/j.1365-246x.2007.03537.x

de la Torre, T. L., and Sheehan, A. F. (2005). Broadband Seismic Noise Analysis of the Himalayan Nepal Tibet Seismic experiment. *Bull. Seismol. Soc. Am.* 95, 1202–1208. doi:10.1785/0120040098

DeMets, C., Gordon, R. G., and Argus, D. F. (2010). Geologically Current Plate Motions. *Geophys. J. Int.* 181, 1–80. doi:10.1111/j.1365-246x.2009.04491.x

Diehl, T., Singer, J., Hetényi, G., Grujic, D., Clinton, J., Giardini, D., et al. (2017). Seismotectonics of Bhutan: Evidence for Segmentation of the Eastern Himalayas and Link to Foreland Deformation. *Earth Planet. Sci. Lett.* 471, 54–64. doi:10.1016/j.epsl.2017.04.038

Efron, B., and Robert, T. (1994). *An Introduction to Bootstrap*. New York: Chapman & Hall.

Fischer, T., and Hainzl, S. (2021). The Growth of Earthquake Clusters. *Front. Earth Sci.* 9, 1–13. doi:10.3389/feart.2021.638336

Gutenberg, B., and Richter, C. F. (1942). Earthquake Magnitude, Intensity, Energy, and Acceleration. *Bull. Seism. Soc. Am.* 32, 163–191. doi:10.1785/bssa0320030163

Hainzl, S., and Ogata, Y. (2005). Detecting Fluid Signals in Seismicity Data through Statistical Earthquake Modeling. *J. Geophys. Res. Solid Earth* 110, 1–10. doi:10.1029/2004JB003247

Hauksson, E., Ross, Z. E., and Cochran, E. (2019). Slow-Growing and Extended-Duration Seismicity Swarms: Reactivating Joints or Foliations in the Cahuilla Valley Pluton, Central Peninsular Ranges, Southern California. *J. Geophys. Res. Solid Earth* 124, 3933–3949. doi:10.1029/2019JB017494

Havskov, J., and Ottemöller, L. (2010). *Routine Data Processing in Earthquake Seismology: With Sample Data, Exercises and Software*. Netherlands Dordrecht: Springer Science & Business Media. doi:10.1007/978-90-481-8697-6

Henry, P., Le Pichon, X., and Goffé, B. (1997). Kinematic, thermal and Petrological Model of the Himalayas: Constraints Related to Metamorphism within the Underthrust Indian Crust and Topographic Elevation. *Tectonophysics* 273, 31–56. doi:10.1016/s0040-1951(96)00287-9

Hetényi, G., Cattin, R., Brunet, F., Bollinger, L., Vergne, J., Nábělek, J. L., et al. (2007). Density Distribution of the India Plate beneath the Tibetan Plateau: Geophysical and Petrological Constraints on the Kinetics of Lower-Crustal Eclogitization. *Earth Planet. Sci. Lett.* 264, 226–244. doi:10.1016/j.epsl.2007.09.036

Hetényi, G., Chanard, K., Baumgartner, L. P., and Herman, F. (2021). Metamorphic Transformation Rate over Large Spatial and Temporal Scales Constrained by Geophysical Data and Coupled Modelling. *J. Metamorph. Geol.*, 1–13. doi:10.1111/jmg.12604

Hetényi, G., Godard, V., Cattin, R., and Connolly, J. A. (2011). Incorporating Metamorphism in Geodynamic Models: The Mass Conservation Problem. *Geophys. J. Int.* 186, 6–10. doi:10.1111/j.1365-246X.2011.05052.x

Hoste-Colomer, R., Bollinger, L., Lyon-Caen, H., Adhikari, L. B., Baillard, C., Benoit, A., et al. (2018). Lateral Variations of the Midcrustal Seismicity in Western Nepal: Seismotectonic Implications. *Earth Planet. Sci. Lett.* 504, 115–125. doi:10.1016/j.epsl.2018.09.041

Hoste-Colomer, R., Bollinger, L., Lyon-Caen, H., Burtin, A., and Adhikari, L. B. (2017). Lateral Structure Variations and Transient Swarm Revealed by Seismicity along the Main Himalayan Thrust north of Kathmandu. *Tectonophysics* 714-715, 107–116. doi:10.1016/j.tecto.2016.10.004

Huang, G. C. D., Wu, F. T., Roecker, S. W., and Sheehan, A. F. (2009). Lithospheric Structure of the central Himalaya from 3-D Tomographic Imaging. *Tectonophysics* 475, 524–543. doi:10.1016/j.tecto.2009.06.023

Incel, S., Hilairet, N., Labrousse, L., John, T., Deldicque, D., Ferrand, T., et al. (2017). Laboratory Earthquakes Triggered during Eclogitization of Lawsonite-Bearing Blueschist. *Earth Planet. Sci. Lett.* 459, 320–331. doi:10.1016/j.epsl.2016.11.047

Jackson, J., Austrheim, H., McKenzie, D., and Priestley, K. (2004). Metastability, Mechanical Strength, and the Support of Mountain Belts. *Geology* 32, 625–628. doi:10.1130/G20397.1

Jackson, J. (2002). Strength of the continental Lithosphere: Time to Abandon the Jelly sandwich? *GSA Today* 12, 4–10. doi:10.1130/1052-5173(2002)012<0004:sotclt>2.0.co;2

Kennett, B. L., and Engdahl, E. R. (1991). Traveltimes for Global Earthquake Location and Phase Identification. *Geophys. J. Int.* 105, 429–465. doi:10.1111/j.1365-246X.1991.tb06724.x

Kind, R., Yuan, X., Saul, J., Nelson, D., Sobolev, S. V., Mechie, J., et al. (2002). Seismic Images of Crust and Upper Mantle beneath Tibet: Evidence for Eurasian Plate Subduction. *Science* 298, 1219–1221. doi:10.1126/science.1078115

Krischer, L., Megies, T., Barsch, R., Beyreuther, M., Lecocq, T., Caudron, C., et al. (2015). ObsPy: A Bridge for Seismology into the Scientific Python Ecosystem. *Comput. Sci. Discov.* 8, 0–17. doi:10.1088/1749-4699/8/1/014003

Lemonnier, C., Marquis, G., Perrier, F., Avouac, J. P., Chitrakar, G., Kafle, B., et al. (1999). Electrical Structure of the Himalaya of Central Nepal: High Conductivity Around the Mid-crustal Ramp along the MHT. *Geophys. Res. Lett.* 26, 3261–3264. doi:10.1029/1999GL008363

Liang, X., Zhou, S., Chen, Y. J., Jin, G., Xiao, L., Liu, P., et al. (2008). Earthquake Distribution in Southern Tibet and its Tectonic Implications. *J. Geophys. Res. Solid Earth* 113, 1–11. doi:10.1029/2007JB005101

Lohman, R. B., and McGuire, J. J. (2007). Earthquake Swarms Driven by Aseismic Creep in the Salton Trough, California. *J. Geophys. Res. Solid Earth* 112, 1–10. doi:10.1029/2006JB004596

Lomax, A. (2005). A Reanalysis of the Hypocentral Location and Related Observations for the Great 1906 California Earthquake. *Bull. Seismol. Soc. Am.* 95, 861–877. doi:10.1785/0120040141

Lomax, A., Virieux, J., Volant, P., and Berge-thierry, C. (2000). "Probabilistic Earthquake Location in 3D and Layered Models," in *Advances in Seismic Event Location* (Springer), 101–134. doi:10.1007/978-94-015-9536-0_5

Maggi, A., Jackson, J. A., McKenzie, D., and Priestley, K. (2000). Earthquake Focal Depths, Effective Elastic Thickness, and the Strength of the continental Lithosphere. *Geology* 28, 495–498. doi:10.1130/0091-7613(2000)028<0495:efdeet>2.3.co;2

Malvoisin, B., Austrheim, H., Hetényi, G., Reynes, J., Hermann, J., Baumgartner, L. P., et al. (2020). Sustainable Densification of the Deep Crust. *Geology* 48, 673–677. doi:10.1130/G47201.1

Matoza, R. S., Shearer, P. M., Lin, G., Wolfe, C. J., and Okubo, P. G. (2013). Systematic Relocation of Seismicity on Hawaii Island from 1992 to 2009 Using Waveform Cross Correlation and Cluster Analysis. *J. Geophys. Res. Solid Earth* 118, 2275–2288. doi:10.1002/jgrb.50189

Menke, W., and Schaff, D. (2004). Absolute Earthquake Locations with Differential Data. *Bull. Seismol. Soc. Am.* 94, 2254–2264. doi:10.1785/0120040033

Michailos, K., Smith, E. G. C., Chamberlain, C. J., Savage, M. K., and Townend, J. (2019). Variations in Seismogenic Thickness along the Central Alpine Fault, New Zealand, Revealed by a Decade's Relocated Microseismicity. *Geochem. Geophys. Geosys.* 20, 470–486. doi:10.1029/2018GC007743

Michelini, A., and Lomax, A. (2004). The Effect of Velocity Structure Errors on Double-Difference Earthquake Location. *Geophys. Res. Lett.* 31, 1–4. doi:10.1029/2004GL019682

Miller, K. (2002). Bhutan Pilot Experiment. Other/Seismic Network. International Federation of Digital Seismograph Networks.

Mitra, S., Priestley, K., Bhattacharyya, A. K., and Gaur, V. K. (2005). Crustal Structure and Earthquake Focal Depths beneath Northeastern India and Southern Tibet. *Geophys. J. Int.* 160, 227–248. doi:10.1111/j.1365-246x.2004.02470.x

Molnar, P., and Chen, W. P. (1983). Focal Depths and Fault Plane Solutions of Earthquakes under the Tibetan Plateau. *J. Geophys. Res.* 88, 1180–1196. doi:10.1029/JB088iB02p01180

Molnar, P., and Tapponnier, P. (1975). Cenozoic Tectonics of Asia: Effects of a continental Collision. *Science* 189, 419–426. doi:10.1126/science.189.4201.419

Monsalve, G., Sheehan, A., Rowe, C., and Rajaure, S. (2008). Seismic Structure of the Crust and the Upper Mantle beneath the Himalayas: Evidence for Eclogitization of Lower Crustal Rocks in the Indian Plate. *J. Geophys. Res. Solid Earth* 113, 1–16. doi:10.1029/2007JB005424

Monsalve, G., Sheehan, A., Schulte-Pelkum, V., Rajaure, S., Pandey, M. R., and Wu, F. (2006). Seismicity and One-Dimensional Velocity Structure of the Himalayan Collision Zone: Earthquakes in the Crust and Upper Mantle. *J. Geophys. Res. Solid Earth* 111, 1–19. doi:10.1029/2005JB004062

Mousavi, S. M., Ellsworth, W. L., Zhu, W., Chuang, L. Y., and Beroza, G. C. (2020). Earthquake Transformer An Attentive Deep-Learning Model for Simultaneous Earthquake Detection and Phase Picking. *Nat. Commun.* 11, 1–12. doi:10.1038/s41467-020-17591-w

Mugnier, J. L., Gajurel, A., Huyghe, P., Jayangondaperumal, R., Jouanne, F., and Upreti, B. (2013). Structural Interpretation of the Great Earthquakes of the Last Millennium in the central Himalaya. *Earth-Science Rev.* 127, 30–47. doi:10.1016/j.earscirev.2013.09.003

Nábělek, J. L., Hetényi, G., Vergne, J., Sapkota, S., Kafle, B., Jiang, M., et al. (2009). Underplating in the Himalaya-Tibet Collision Zone Revealed by the Hi-CLIMB Experiment. *Science* 325, 1371–1374. doi:10.1126/science.1167719

Nelson, K. D., Zhao, W., Brown, L. D., Kuo, J., Che, J., Liu, X., et al. (1996). Partially Molten Middle Crust beneath Southern Tibet: Synthesis of Project INDEPTH Results. *Science* 274, 1684–1685. doi:10.1126/science.274.5293.1684

Pandey, M. R., Tandukar, R. P., Avouac, J. P., Lavé, J., and Massot, J. P. (1995). Interseismic Strain Accumulation on the Himalayan Crustal Ramp (Nepal). *Geophys. Res. Lett.* 22, 751–754. doi:10.1029/94gl02971

Pandey, M. R., Tandukar, R. P., Avouac, J. P., Vergne, J., and Héritier, T. (1999). Seismotectonics of the Nepal Himalaya from a Local Seismic Network. *J. Asian Earth Sci.* 17, 703–712. doi:10.1016/S1367-9120(99)00034-6

Paul, H., Mitra, S., Bhattacharya, S., and Suresh, G. (2015). Active Transverse Faulting within Underthrust Indian Crust beneath the Sikkim Himalaya. *Geophys. J. Int.* 201, 1072–1083. doi:10.1093/gji/ggv058

Paul, H., and Mitra, S. (2017). Three-Dimensional Crustal Architecture beneath the Sikkim Himalaya and its Relationship to Active Deformation. *J. Geophys. Res. Solid Earth* 122, 7860–7878. doi:10.1002/2017JB014506

Pavlis, L. G. (1986). Appraising Earthquake Hypocenter Location Errors: A Complete, Practical Approach for Single-Event Locations. *Bull. Seismol. Soc. Am.* 76, 1699–1717. doi:10.1785/bssa0760051514

Petley-Ragan, A., Ben-Zion, Y., Austrheim, H., Ildefonse, B., Renard, F., and Jamtveit, B. (2019). Dynamic Earthquake Rupture in the Lower Crust. *Sci. Adv.* 5, 1–8. doi:10.1126/sciadv.aaw0913

Priestley, K., Ho, T., and Mitra, S. (2019). The Crustal Structure of the Himalaya: A Synthesis. *Geol. Soc. Spec. Publ.* 483, 483–516. doi:10.1144/sp483-2018-127

Priestley, K., James, J., and Mckenzie, D. (2008). Lithospheric Structure and Deep Earthquakes beneath India, the Himalaya and Southern Tibet. *Geophys. J. Int.* 172, 345–362. doi:10.1111/j.1365-246X.2007.03636.x

Rawles, C. J., and Thurber, C. H. (2015). A Non-parametric Method for Automatic Determination of P-Wave and S-Wave Arrival Times: Application to Local Micro Earthquakes. *Geophys. J. Int.* 202, 1164–1179. doi:10.1093/gji/ggv218

Ross, Z. E., Cochran, E. S., Trugman, D. T., and Smith, J. D. (2020). 3D Fault Architecture Controls the Dynamism of Earthquake Swarms. *Science* 368, 1357–1361. doi:10.1126/science.abb0779

Schulte-Pelkum, V., Monsalve, G., Sheehan, A. F., Shearer, P., Wu, F., and Rajaure, S. (2019). Mantle Earthquakes in the Himalayan Collision Zone. *Geology* 47, 815–819. doi:10.1130/G46378.1

Schulte-Pelkum, V., Monsalve, G., Sheehan, A., Pandey, M. R., Sapkota, S., Bilham, R., et al. (2005). Imaging the Indian Subcontinent beneath the Himalaya. *Nature* 435, 1222–1225. doi:10.1038/nature03678

Shapiro, S. A., Huenges, E., and Borm, G. (1997). Estimating the Crust Permeability from Fluid-Injection-Induced Seismic Emission at the KTB Site. *Geophys. J. Int.* 131, 5–8. doi:10.1111/j.1365-246X.1997.tb01215.x

Sheehan, A. F., de la Torre, T. L., Monsalve, G., Abers, G. A., and Hacker, B. R. (2014). Physical State of the Himalyan. *J. Geophys. Res. Solid Earth* 119, 567–580. doi:10.1002/2013JB010601

Shelly, D. R., Beroza, G. C., and Ide, S. (2007). Non-volcanic Tremor and Low-Frequency Earthquake Swarms. *Nature* 446, 305–307. doi:10.1038/nature05666

Singer, J. (2017). Tectonics of the Bhutan Himalaya: New Insights from Seismic Tomographic Images of the Lithosphere. Ph.D. Thesis. ETH Zurich.

Styron, R., Taylor, M., and Okoronkwo, K. (2010). Database of Active Structures from the Indo-Asian Collision. *EOS* 91, 181–182. doi:10.1029/2010EO200001

Talwani, M., Desa, M. A., Ismaiel, M., and Sree Krishna, K. (2016). The Tectonic Origin of the Bay of Bengal and Bangladesh. *J. Geophys. Res. Solid Earth* 121, 4836–4851. doi:10.1002/2015JB012734

Unsworth, M. J., Jones, A. G., Wei, W., Marquis, G., Gokarn, S. G., Spratt, J. E., et al. (2005). Crustal Rheology of the Himalaya and Southern Tibet Inferred from Magnetotelluric Data. *Nature* 438, 78–81. doi:10.1038/nature04154

Velasco, A. A., Gee, V. L., Rowe, C., Grujic, D., Hollister, L. S., Hernandez, D., et al. (2007). Using Small, Temporary Seismic Networks for Investigating Tectonic Deformation: Brittle Deformation and Evidence for Strike-Slip Faulting in Bhutan. *Seismol. Res. Lett.* 78, 446–453. doi:10.1785/gssrl.78.4.446

Vernant, P., Bilham, R., Szeliga, W., Drupka, D., Kalita, S., Bhattacharyya, A. K., et al. (2014). Clockwise Rotation of the Brahmaputra Valley Relative to India: Tectonic Convergence in the Eastern Himalaya, Naga Hills, and Shillong Plateau. *J. Geophys. Res. Solid Earth* 119, 6558–6571. doi:10.1002/2014jb011196

Vidale, J. E., and Shearer, P. M. (2006). A Survey of 71 Earthquake Bursts across Southern California: Exploring the Role of Pore Fluid Pressure Fluctuations and Aseismic Slip as Drivers. *J. Geophys. Res. Solid Earth* 111, 1–12. doi:10.1029/2005JB004034

Waldhauser, F., and Ellsworth, W. L. (2000). A Double-Difference Earthquake Location Algorithm: Method and Application to the Northern Hayward Fault, California. *Bull. Seismol. Soc. Am.* 90, 1353–1368. doi:10.1785/0120000006

Waldhauser, F. (2001). HypoDD - A Program to Compute Double-Difference Hypocenter Locations. USGS Open File Report 01-113. Available at: http://geopubs.wr.usgs.gov/open-file/of01-113/.

Wang, Y., Deng, Y., Shi, F., and Peng, Z. (2020). The Indo-Eurasia Convergent Margin and Earthquakes in and Around Tibetan Plateau. *J. Mineral. Petrol. Sci.* 115, 118–137. doi:10.2465/jmps.190927

Wells, D. L., and Coppersmith, K. J. (1994). New Empirical Relationships Among Magnitude, Rupture Length, Rupture Width, Rupture Area, and Surface Displacement. *Bull. Seismol. Soc. Am.* 84, 974–1002.

Wiemer, S., and Wyss, M. (2000). Minimum Magnitude of Completeness in Earthquake Catalogs: Examples from Alaska, the Western United States, and Japan. *Bull. Seismol. Soc. Am.* 90, 859–869. doi:10.1785/0119990114

Wittlinger, G., Vergne, J., Tapponnier, P., Farra, V., Poupinet, G., Jiang, M., et al. (2004). Teleseismic Imaging of Subducting Lithosphere and Moho Offsets beneath Western Tibet. *Earth Planet. Sci. Lett.* 221, 117–130. doi:10.1016/s0012-821x(03)00723-4

Woessner, J., and Wiemer, S. (2005). Assessing the Quality of Earthquake Catalogues: Estimating the Magnitude of Completeness and its Uncertainty. *Bull. Seismol. Soc. Am.* 95, 684–698. doi:10.1785/0120040007

Wolfe, C. J. (2002). On the Mathematics of Using Difference Operators to Relocate Earthquakes. *Bull. Seismol. Soc. Am.* 92, 2879–2892. doi:10.1785/0120010189

Yin, A., and Harrison, T. M. (2000). Geologic Evolution of the Himalayan-Tibetan Orogen. *Annu. Rev. Earth Planet. Sci.* 28, 211–280. doi:10.1146/annurev.earth.28.1.211

Zertani, S., Labrousse, L., John, T., Andersen, T. B., and Tilmann, F. (2019). The Interplay of Eclogitization and Deformation during Deep Burial of the Lower Continental Crust A Case Study from the Bergen Arcs (Western Norway). *Tectonics* 38, 898–915. doi:10.1029/2018TC005297

Zertani, S., Vrijmoed, J. C., Tilmann, F., John, T., Andersen, T. B., and Labrousse, L. (2020). P Wave Anisotropy Caused by Partial Eclogitization of Descending Crust Demonstrated by Modeling Effective Petrophysical Properties. *Geochem. Geophys. Geosys.* 21, 1–18. doi:10.1029/2019GC008906

Zhu, L., and Helmberger, D. V. (1996). Intermediate Depth Earthquakes beneath the India-Tibet Collision Zone. *Geophys. Res. Lett.* 23, 435–438. doi:10.1029/96gl00385

Conflict of Interest: The authors declare that the research was conducted in the absence of any commercial or financial relationships that could be construed as a potential conflict of interest.

frontiers in Earth Science

ORIGINAL RESEARCH
published: 08 October 2021
doi: 10.3389/feart.2021.680361

Tomographic Image of Shear Wave Structure of NE India Based on Analysis of Rayleigh Wave Data

Amit Kumar[1,2], *Naresh Kumar*[3], *Sagarika Mukhopadhyay*[1]* and *Simon L. Klemperer*[4]

[1]Department of Earth-Sciences, IIT Roorkee, Roorkee, India, [2]Geoscience, National Centre for Polar and Ocean Research, ESSO, Ministry of Earth Sciences, Government of India, Headland Sada, Vasco Da Gama, India, [3]Wadia Institute of Himalayan Geology, Dehradun, India, [4]Department of Geophysics, Stanford University, Stanford, CA, United States

The major scientific purpose of this work is to evaluate the geodynamic processes involved in the development of tectonic features of NE India and its surroundings. In this work, we have obtained tomographic images of the crust and uppermost mantle using inversion of Rayleigh waveform data to augment information about the subsurface gleaned by previous works. The images obtained reveal a very complicated tectonic regime. The Bengal Basin comprises a thick layer of sediments with the thickness increasing from west to east and a sudden steepening of the basement on the eastern side of the Eocene Hinge zone. The nature of the crust below the Bengal Basin varies from oceanic in the south to continental in the north. Indo-Gangetic and Brahmaputra River Valleys comprise ~5–6-km-thick sediments. Crustal thickness in the higher Himalayas and southern Tibet is ~70 km but varies between ~30 and ~40 km in the remaining part. Several patches of low-velocity medium present in the mid-to-lower crust of southern Tibet along and across the major rifts indicate the presence of either partially molten materials or aqueous fluid. Moho depth decreases drastically from west to east across the Yadong-Gulu rift indicating the complex effect of underthrusting of the Indian plate below the Eurasian plate. Crust and upper mantle below the Shillong Massif and Mikir Hills are at a shallow level. This observation indicates that tectonic forces contribute to the uprising of the Massif.

Keywords: NE India, surface wave, group velocity, tomography, Vs

OPEN ACCESS

Edited by:
György Hetényi,
University of Lausanne, Switzerland

Reviewed by:
Emanuel David Kästle,
Freie Universität Berlin, Germany
Bernhard Maximilian Steinberger,
German Research Centre for Geosciences, Germany

***Correspondence:**
Sagarika Mukhopadhyay
sagarfes@gmail.com

Specialty section:
This article was submitted to Solid Earth Geophysics, a section of the journal Frontiers in Earth Science

Received: *14 March 2021*
Accepted: *16 August 2021*
Published: *08 October 2021*

Citation:
Kumar A, Kumar N, Mukhopadhyay S and Klemperer SL (2021) Tomographic Image of Shear Wave Structure of NE India Based on Analysis of Rayleigh Wave Data. Front. Earth Sci. 9:680361. doi: 10.3389/feart.2021.680361

KEY POINTS

1. Our new Rayleigh wave tomography of NE India provides a 3D view of the complex interaction between Indian, Asian, and Burma plates.
2. Moho geometry shows expected crustal thinning beneath Bengal Basin and thickening beneath the Himalayas, but also pronounced Moho shallowing beneath Shillong Plateau/Mikir Hills.
3. Low-velocity bodies in the mid-crust of southern Tibet/Lhasa blocks likely indicate partial melts or fluids that are not only restricted to beneath the narrow surface graben.

INTRODUCTION

A long span of convergence between Indian and Eurasian plates has caused subduction, underthrusting, and extrusion resulting in widespread lithospheric deformation (Molnar et al., 1977;

Molnar, 1984; Tapponnier et al., 2001; DeCelles et al., 2002; Nábělek et al., 2009). Recently and in the past, the NE Indian region has experienced a frequent occurrence of moderate to large-size earthquakes due to ongoing active tectonic convergence (Ni and Barazangi, 1984; Pandey et al., 1995; Parvez and Ram, 1997; Kayal, 2008; Baruah et al., 2014, 2016; Le Roux-Mallouf et al., 2020). In response to the collision, the lithospheric part of these three plates experiences horizontal shortening and surface uplift. Elevated Tibetan plateau, Indo-Burma Ranges (IBR), and the Himalayas are the result of the collision and crustal thickening, which is associated with mountain building phenomena and crustal shortening (Burchfiel and Royden, 1985; England and Houseman 1989; Murphy and Copeland, 2005; Thiede et al., 2006). The study region includes Brahmaputra River Valley (BRV), Shillong Massif (SM), Mikir Hills (MH), Indo-Burma Ranges (IBR), Bengal Basin (BB), southern Tibet, eastern Himalayas, and part of central Himalayas (**Figure 1A**), characterized by the diverse geological setup and a very high variation in topography. The overall study region is demarcated by latitude 22°N to 32°N and longitude 85°E to 98°E. Detailed geological and tectonic studies were carried out by Krishnan (1960), Evans (1964), Desikachar (1974), and Nandy (1980).

In NE India, the Indian plate is supposedly simultaneously underthrusting beneath Eurasia and subducting below Burmese microplate in the north and east, respectively (Kayal, 2008; Sarkar et al., 2013; Kumar et al., 2015; Raoof et al., 2017). Le Dain et al. (1984) proposed that in the early Cenozoic period, the Indian plate subducted below the Burma microplate and presently the hanging lithosphere is being dragged northward. Mukhopadhyay and Dasgupta (1988), Kayal (1989, 1996), and Satyabala (2003) opined that the Indian plate is actively subducting below the Burma plate. GPS measurements in this area and Myanmar suggest EW convergence with a shallow dip of the Indian plate beneath Myanmar, which is locked along a megathrust further down-dip (Gahalaut et al., 2013; Steckler et al., 2016). Steckler et al. (2016) and Gahalaut et al. (2013) suggest that the active subduction has stopped, whereas Steckler et al. (2016) inferred active subduction despite the highly oblique plate motion and presence of thick sediment.

The convergence of Indian and Eurasian plates causes N-S compression mainly within the Himalayas and E-W extension within the Tibetan plateau (Armijo et al., 1986; Angelier and Baruah, 2009; Sarkar et al., 2013). Several workers suggested that low-velocity material is present within southern Tibet as a result of EW extension along several rifts (Kind et al., 1996; Cogan et al., 1998; Jiang et al., 2014) due to clockwise deformation with respect to the northeast corner of NE India. Extension-related normal faults have been identified (Kayal, 2001, 2008; Hintersberger et al., 2010) mostly within the Tibetan plateau and also in some cases in the Higher and Lesser Himalayas. Focal mechanism solutions in the eastern Himalayas expose the direction of compression from NNW-SSE to N-S from Arunachal Pradesh, Mishmi hills to Bhutan. However, in the IBR, NE-SW directed average compression is observed (Angelier and Baruah, 2009). IBR is under compression due to oblique subduction of the Indian plate below the Burma plate, where the NE-SW directed stress across the inner and northern arc is switched to the E-W directed stress near the Bengal Basin. Within NE India and SM, Baruah et al. (2016) made an investigation on tectonic stress through inversion of the stress tensor. They observed that compressional stress direction changes from NNW-SSE in the western part of the massif to the NNE-SSW direction in its eastern part. Oblique subduction of the Indian plate underneath the IBR causes compression along the NNE-SSW direction (Baruah et al., 2013, 2016). The available data set make it possible to study the crustal and upper mantle structure of Lhasa/southern Tibet and IBR.

Eastern Himalayan syntaxis (EHS) is a complex triple junction of Indian and Eurasian plates with the northern end of the Burma plate (Curray, 1989). A study of active tectonics in EHS was done by Holt et al. (1991). They identified an oblique thrust based on focal mechanisms and it shows the movement of the Indian plate directed toward NNE as it underthrusts below this region. Baranowski et al. (1984) found that radial directed slip in the Himalayas causes extension within Tibet; however, it is possibly half of the rate of under-thrusting taking place within the Himalayas. Holt et al. (1991) found that slip vectors are generally not orthogonal to the strike of the Himalayas.

Different workers have proposed different tectonic processes for the formation of SM. Evans (1964) postulated that the Dauki fault is a strike-slip fault along which SM has moved ~250 km eastward to its present position. Oldham (1899) concluded that movement along a thrust-plane or thrust planes and along secondary thrusts and fault planes may be the cause of the 1897 great Earthquake. Bouguer and isostatic anomalies indicate that high-density crustal/upper mantle strata are present beneath SM (Verma and Mukhopadhyay, 1977). Kailasam (1979) suggested that isostatic adjustment may have caused uplift of SM but positive Bouguer and isostatic anomalies over it imply that it should sink. Dziewonski and Anderson (1983) estimated the P-wave travel time residual beneath the Massif to be −0.57 s, indicating that the subsurface has higher velocity material than the surroundings. Many researchers suggested that the uplift of SM is influenced by active tectonics between NE India and the NE Himalayas (Chen and Molnar, 1990; Khattri et al., 1992; Mukhopadhyay et al., 1993, 1997; Najman et al., 2016; Govin et al., 2018). Mukhopadhyay et al. (1997) opined that the Massif has overthrusted southward above the Indian plate along the Dauki fault. Bilham and England (2001) and England and Bilham (2015) proposed that SM uplifted abruptly by ~11 m during the 1897 Shillong earthquake and suggested that it is a "pop-up" structure, whereas Raoof et al. (2017) suggested that it is the crest of the buckled-up part of the Indian plate. Clark and Bilham (2008) suggested that convergence of India and Eurasia in this part is shared between the Bhutan Himalayas and the Shillong Massif. Strong et al. (2019) stated that the Massif is affected by active uplifting as well as erosion.

From this discussion, it is obvious that there are several postulates about the tectonics and geodynamic characteristics of this area that has led to such a complex crustal/lithospheric structure. Hence, this area needs detailed investigation. The availability of a dense seismic network in NE India makes it possible to carry out such investigations for this region. The study

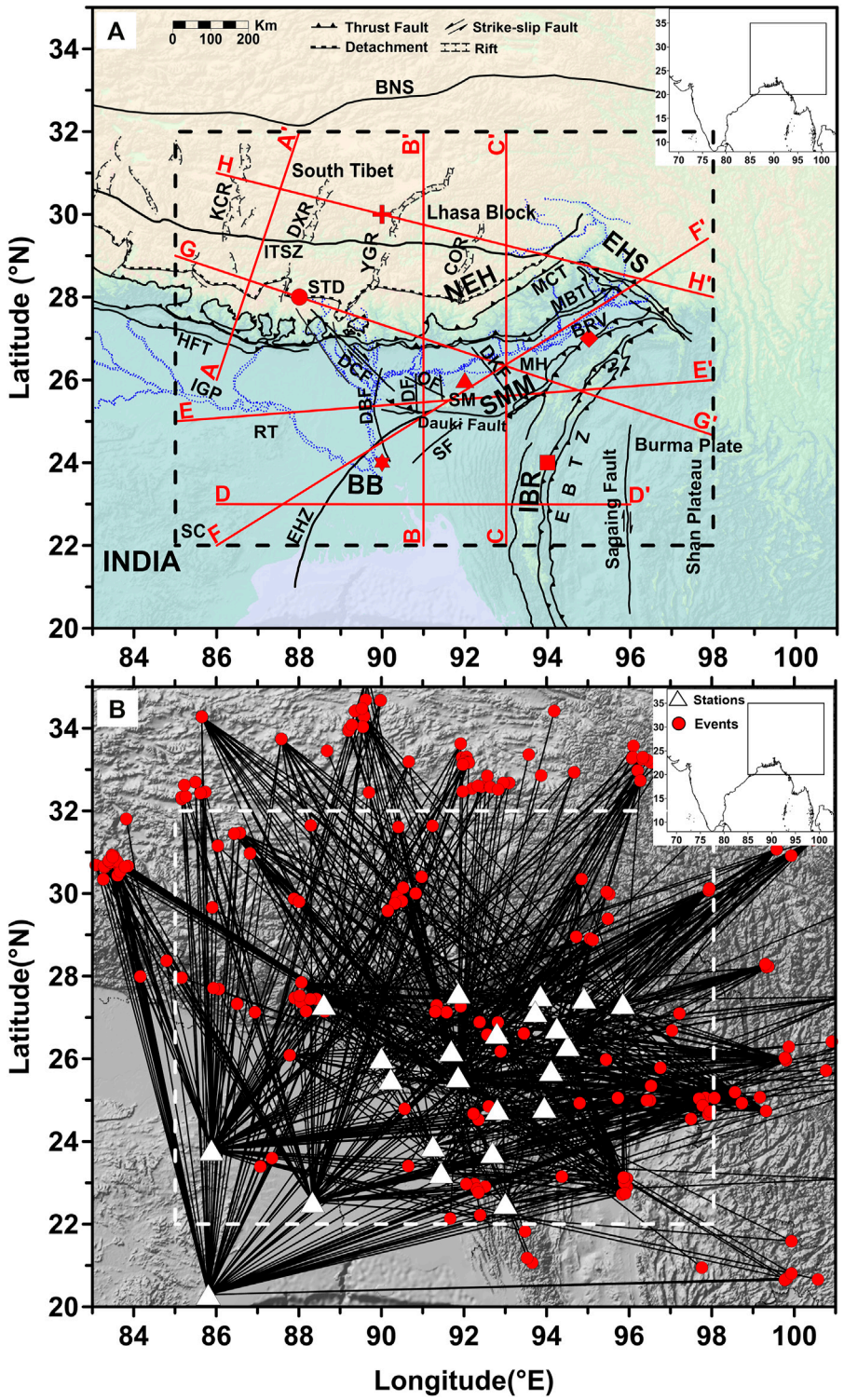

FIGURE 1 | Tectonic map of NE India and the surrounding area (GSI, 2000). Red symbols (shapes same as corresponding curves): location of six points for which Rayleigh wave dispersion curves are shown in **Figure 4**. Red lines: location of profiles for S-wave structures (**Figure 8)**. Rectangle (dash line) encloses the area for which results are used for interpretation. Abbreviations—IBR: Indo-Burma Ranges; NEH: Northeastern Himalaya; EHS: Eastern Himalayan Syntaxis; SMM: Shillong-Mikir Massif; SM: Shillong Massif; MH: Mikir Hills; BRV: Brahmaputra River Valley; BB: Bengal Basin; EBTZ: Eastern Boundary Thrust Zone; BNS: Bangong-Nujiang Suture; ITSZ: Indus-Tsangpo Suture Zone; STD: Southern Tibetan Detachment; MCT: Main Central Thrust; MBT: Main Boundary Thrust; HFT: Himalayan Frontal Thrust; IGP: Indo-Gangetic Plain; SC: Singhbhum Craton; RT: Rajmahal Trap; SF: Sylhet fault; DBF: Dhubri fault; DKF: Dhansiri-Kopili fault; DF: Dudhnoi fault; EHZ: Eocence

(*Continued*)

FIGURE 1 | Hinge Zone; OF: Oldham fault; KCR: Kung-Co Rift; DXR: Dinggya-Xainza Rift; YGR: Yadong-Gulu Rift; COR: Cona-Oiga Rift; DCF: Dhubri-Chungthang Fault Zone. **(B)**: Location of epicenters (solid red circle) and stations (white triangle) used for this study. Event-station path coverage at 12 s period is shown by black lines. **Inset**: Map of India showing the study region. Only those earthquakes are shown whose data are used in this analysis.

region is selected because it shows complex variations in plate motion that may affect the subsurface structure and properties of the lithosphere. In this study, we decipher subsurface characteristics to understand the effects of NS underthrusting and EW subduction in NE India and its surroundings. Most of the geophysical investigations were carried out on collision zones either toward the north or northeast of SM (Singh et al., 2015 and the references therein). However, the southern side of SM and that of BB have not been studied much due to unavailability of sufficient data. Thick sediments within BB make it challenging to delineate the underlying oceanic and/or continental crust (Alam et al., 2013). Sediment thickness and crustal structure of BB have been investigated by Currey (1991), Brune et al. (1992), Mitra et al. (2011), and Singh et al. (2016). The extent of sediment deposition and the nature of the crust in BB are required to be properly investigated. We have estimated the lateral variation in sedimentary layer thickness in BB. Although Bangladesh seismological data were not incorporated in the present work, there are stations in the surrounding part of India that gave good coverage of this zone.

We made use of new data sets covering NE India and surrounding areas and tried to solve several issues, such as Moho depth variation, nature of crust and sedimentary layer thickness variation in BB, deformation, and upliftment of SM in response to active NS and EW compression, geodynamic inferences related to oblique subduction of Indian plate below IBR, indentation of EHS and occurrence of low-velocity material in mid-crust of SE Tibetan plateau. To obtain the subsurface crustal and lithosphere S-wave velocity (Vs) image of the study area, surface wave tomography technique developed by Ditmar and Yanovskaya (1987), Yanovskaya and Ditmar (1990), and Yanovskaya et al. (1998) is applied. Tomographic image of the study area is obtained up to ~90 km depth, which elucidate the geodynamics of NE India through high-resolution data.

DATA

Surface wave data recorded by a network of 20 broadband seismic stations in NE India and three other stations (Kolkata, Bhubaneswar, and Bokaro) operated by the India Meteorological Department (IMD, India) were used in the present study (**Figure 1B**; **Table 1**). The last three stations provide better path coverage for BB. The instruments used in these seismic stations (**Table 1**) include Trillium-240, STS-2, RT151-120, and CMG40T with natural periods of 240, 120, 120, and 30 s, respectively. The data for 201 earthquakes (**Figure 1B**, **Supplementary Table S1**) used for this study were recorded at local and regional epicentral distances in the range of ~160–~1800 km. Surface waves of good signal strength recorded for wave period >1 s generated by earthquakes of focal depth ≤50 km and magnitude ≥5 were used. Shallow focal depth earthquakes generate higher surface wave amplitudes, and therefore even lower magnitude (M~5) records at regional distances have good surface wave signals. Based on selected stations and event locations, we have obtained maximum 753 source–receiver paths (**Figure 1B**; **Table 2**), which covers a broad range of azimuths and path lengths within the area of investigation. **Supplementary Figure S1** shows ray path coverage for periods between 8 and 60 s.

Data processing was performed in four steps: 1) estimation of fundamental mode Rayleigh wave dispersion curves, 2) construction of group velocity maps at different grid points of specified spacing for good resolution, 3) inversion of dispersion curve of each grid for obtaining 1D S-wave (Vs) velocity structure, and 4) construction of 2D and 3D images of Vs.

ESTIMATION OF GROUP VELOCITY

Pre-processing steps were carried out to remove the mean value, linear trend, and avoid spectral leakage (using tapering window) from raw data. The data were also converted into ground motion (displacement) units using the frequency response of the recorders. Fundamental mode dispersion curves of Rayleigh wave were estimated along each path between earthquake epicenter and the seismic station using the multiple filter technique (MFT) developed by Herrmann (2013) and Herrmann and Ammon (2002) based on the methodology of Dziewonski et al. (1969). MFT is a fast and efficient method used for analyzing multiple dispersed signals (Herrmann, 1973; Erduran et al., 2007). In this method, the Fourier transform of the signal selected for a given time window displays amplitude variation with frequency. In the next step, Gaussian filter is applied and followed by inverse Fourier transform to obtain the peak of the spectrum for a given time and frequency. The MFT uses phase-matched filtering to extract the dispersed waveform. It separates the other parts of waveform consisting of body waves, higher modes, and multipath effects (Kolinsky, 2004). Examples of dispersion curves are given in **Figure 2**.

Selection of range of periods of dispersion curves is based on the natural period of the seismometer, data sampling rate, noise level, and the distance between the epicenter and station along the great circle arc (Yao et al., 2006; Bensen et al., 2007; Yang et al., 2007; Guo et al., 2009; Kumar et al., 2017). The upper limit of the period up to which group velocity can be estimated also depends on the ratio of epicentral distance and the maximum wavelength of the recorded signal. The reliable maximum period of surface wave recorded at a given epicentral distance should have at least three wavelengths within that distance (Yao et al., 2006; Bensen

TABLE 1 | Detail information of seismic stations.

Station Code	Station Coordinates			Data Acquisition System	Seismic Sensor		Network	Data availability (Year)
	Lat (°N)	Long (°E)	Elev (m)	—	Sensor name	Period Range (Hz)	—	—
AGT	23.889	91.246	18	Reftek RT130	RT151-120	0.0083–50	NE Telemetry	2011–2013
AZL	23.738	92.690	969	Reftek RT1306	RT151-120	0.0083–50	NE Telemetry	2011–2013
BELO	23.249	91.447	20	Reftek RT130	RT151-120	0.0083–50	NE Telemetry	2011–2013
BWNR	20.296	85.806	46	Reftek 72A07	CMG40T	0.033–50	BBS	2004–2013
BOK	23.795	85.886	282	Quanterra Q680LVG	STS-2	0.008–50	GSN	2005-May 2008
BOK	23.795	85.886	282	Taurus	Trillium-240	0.004–35	RTSMN	May 2008-2013
DHUB	26.020	89.996	33	Reftek RT130	RT151-120	0.0083–50	NE Telemetry	2011–2013
DIBR	27.468	94.911	90	Reftek RT130	RT151-120	0.0083–50	NE Telemetry	2011–2013
GTK	27.319	88.602	1,348	Reftek RT130	RT151-120	0.0083–50	NE Telemetry	2011–2013
GUWA	26.193	91.691	88	Reftek RT130	RT151-120	0.0083–50	NE Telemetry	2011–2013
IMP	24.830	93.947	792	Reftek RT130	RT151-120	0.0083–50	NE Telemetry	2011–2013
ITAN	27.145	93.722	214	Reftek RT130	RT151-120	0.0083–50	NE Telemetry	2011–2013
JORH	26.743	94.251	79	Reftek RT130	RT151-120	0.0083–50	NE Telemetry	2011–2013
KOHI	25.720	94.108	1,353	Reftek RT130	RT151-120	0.0083–50	NE Telemetry	2011–2013
CAL	22.539	88.331	6	Reftek 72A07	CMG40T	0.033–50	BBS	2001–2009
LKP	27.333	95.846	139	Reftek RT130	RT151-120	0.0083–50	NE Telemetry	2011–2013
MOKO	26.321	94.516	1,353	Reftek RT130	RT151-120	0.0083–50	NE Telemetry	2011–2013
SAIH	22.500	93.000	729	Reftek RT130	RT151-120	0.0083–50	NE Telemetry	2011–2013
SHL	25.567	91.856	1,600	Reftek 72A07	CMG40T	0.033–50	BBS	2000 - May 2008
SHL	25.567	91.856	1,600	Taurus	Trillium-240	0.00416–32	RTSMN	May 2008–2013
SILR	24.781	92.803	18	Reftek RT130	RT151-120	0.0083–50	NE Telemetry	2011–2013
TAWA	27.594	91.867	297	Reftek RT130	RT151-120	0.0083–50	NE Telemetry	2011–2013
TEZP	26.617	92.799	83	Reftek RT130	RT151-120	0.0083–50	NE Telemetry	2011–2013
TURA	25.517	90.224	406	Reftek RT130	RT151-120	0.0083–50	NE Telemetry	2011–2013
ZIRO	27.527	93.850	160	Reftek RT130	RT151-120	0.0083–50	NE Telemetry	2011–2013

TABLE 2 | Group-velocity tomographic inversion details. Number of data (paths), final number of data after excluding outliers, initial rms residual (before tomography), final rms residual (after tomography), and averaged group velocity after tomographic inversion for different periods with mean error.

Period (s)	Number of initial data	Final number of data	Initial rms residual (s)	Final rms residual (s)	Mean Group velocity (km/s)	Mean Err. Group Velocity (km/s)
4	131	129	26.33	12.69	2.52	0.0680
6	574	567	33.99	17.24	2.55	0.0697
8	743	716	33.94	15.70	2.64	0.0637
10	784	746	33.50	13.89	2.70	0.0568
12	789	753	36.37	12.97	2.72	0.0537
14	793	741	36.90	12.14	2.74	0.0489
16	795	736	36.20	10.97	2.75	0.0456
18	794	749	35.73	11.82	2.76	0.0495
21	778	749	30.95	12.79	2.80	0.0552
24	755	722	25.52	11.13	2.85	0.0498
27	723	700	22.73	11.95	2.91	0.0561
30	673	650	20.39	11.23	2.97	0.0553
34	481	466	18.51	9.82	3.06	0.0512
38	447	424	18.40	8.25	3.13	0.0439
42	415	390	18.68	7.28	3.20	0.0398
46	392	382	20.56	9.33	3.28	0.0516
50	360	340	20.26	8.44	3.36	0.0487
55	311	302	18.64	8.62	3.44	0.0487
60	258	241	15.37	7.10	3.54	0.0442

et al., 2007; Yang et al., 2007; Guo et al., 2009). Based on these criteria, we could extract dispersion data for periods between 4 s and 60 s. Wave propagation path coverage for a particular period depends on the availability of good quality data. Path coverage in this study region varies (**Supplementary Figure S1**), and it has a maximum value at 12 s period (**Figure 1B**). In total, maximum 795 Rayleigh wave records were used. Minimum and maximum numbers of paths used for tomographic inversion of group velocity values are 129 and 753 at periods of 4 s and 12 s, respectively (**Table 2**).

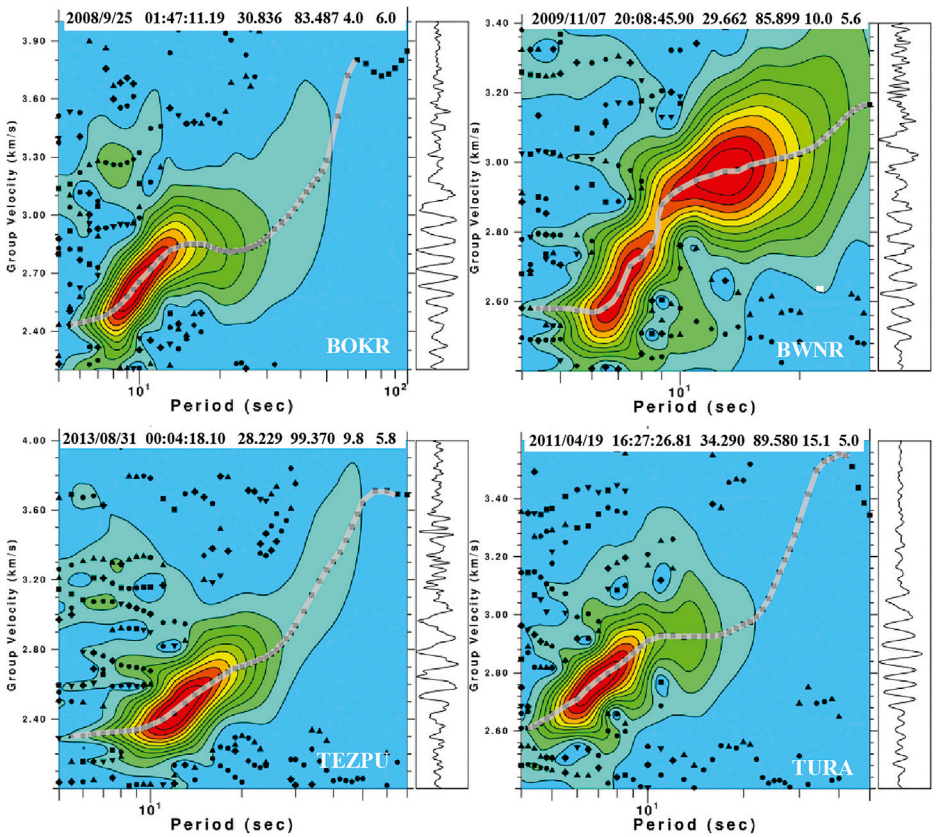

FIGURE 2 | Examples of dispersion curves obtained at four stations. Earthquake source parameters and the recording station names are mentioned on the dispersion curve plot. The range of the data of the dispersion curve used for further analysis is shown with a gray-color curve. The color in a particular contour defines the energy with blue representing minimum energy and its energy increasing trend from blue to cyan to green to yellow to red. Raw waveform is given in the right-hand rectangular block.

GROUP VELOCITY TOMOGRAPHY

Tomographic Inversion Method

Surface wave dispersion data were used to generate a map of spatial variation of group velocity for different periods within the study region. Surface wave velocity tomography maps are constructed through the inversion technique developed by Ditmar and Yanovskaya (1987) and Yanovskaya and Ditmar (1990). Dispersion curves obtained from the earthquake data are path specific, that is, each one gives average group velocity versus period for that particular path between earthquake epicenter and station location. It gives the group velocity for a particular period at different grid points of the study region. This inversion technique is robust and does not need any initial parameterization or truncation of Taylor series expansion of nonlinear equation because of its straightforwardness (Levshin et al., 1989). The basis functions for the inversion model are formed as a superposition of kernels of the group velocity travel time integral (Ritzwoller and Levshin, 1998). Measured group velocity is a function of the location described by $U(\theta,\phi)$ on a spherical surface. It is decomposed in different sections across the study region by taking the mean group velocity as a starting value and applying region-specific perturbations. Decomposed reference value U_0 and its location dependence perturbation are expressed by

$$U(\theta,\phi) = U_0 + \delta U(\theta,\phi). \tag{1}$$

Initially, this method leads to a search for smooth perturbation in group velocity from the reference model U_0 so that $U(\theta,\phi)$ gets fitted by N observed group travel times (t_i^{obs}). Smooth perturbation is based on the weighted least-squares technique. The above approach aims to minimize error function between observed and predicted values at each period and wave type through **Eq. 2**.

$$\sum_{i=1}^{N}\left[w_i\left(t_i^{obs}-t_i^{pred}\right)\right]^2+\gamma\int_s\left|\nabla U(\theta,\phi)\right|^2 dA=\min, \tag{2}$$

$$t_i^{pred}=\int_{P_i}U^{-1}(\theta,\phi)ds. \tag{3}$$

Here, P_i is the *ith* wave path, w_i is the associated weight through a map of group velocity $U(\theta,\phi)$, t_i^{pred} the predicted group travel time for the same path, and "S" denotes the study region. In **Eq. 2**,

γ is the regularization parameter and its selection controls the trade-off between the fit to the data and smoothness of the observed velocity map for each assessed period of the wave (Ritzwoller et al., 1998; Karagianni et al., 2002). The linearized inverse procedure is carried out with very small relative group velocity variations at each iteration for each period and wave type such that $\delta U(\theta,\phi)/U_0<<1$.

Tomographic images of Rayleigh wave group velocity were obtained at periods ranging between 4 s and 60 s on $1^\circ \times 1^\circ$ grid spacing. The regularization parameter is chosen such that the velocity range in the group velocity maps is identical or larger than the range of measured group velocities (Yanovskaya et al., 1998). To obtain an appropriate smoothed map, we have used several regularization parameters (γ) ranging between 0.05 and 0.4. The lateral variation in the group velocity and associated standard error for 12 s period for the different six regularization parameters are shown in **Supplementary Figures S2, S3**, respectively. Decrease in γ gives a sharp solution with large standard (solution) error and vice-versa. An increase in γ enhances the smoothness of the solution region (**Supplementary Figure S2**). Finally, the value of $\gamma = 0.3$ gives a relatively smoothed map with lesser solution error.

For best results in a tomographic study, the area of investigation should be covered uniformly by ray paths from all directions. Unfortunately, that is very rarely possible. Uneven distribution of ray paths may introduce some anomalous values to the solution. The solution is obtained after rejecting the data of a path with anomalous values categorized based on regularization parameters. The anomalous value represents a large deviation from the average velocity of a particular localized region. This error may be due to unresolvable lateral velocity variations, measurement errors, multipath effects, etc. (Yanovskaya and Kozhevnikov, 2003). The quality of the solution for the given regularization parameter is measured by comparing the initial and the remaining (unaccounted) mean square travel time residuals (Yanovskaya et al., 1998). Here, the initial means the travel time residual before the inversion based on the mean velocity of the data. The value of standard error (σ) was used for data selection. If an individual value of the travel time residual shows the value laying more than 3σ, the corresponding data were rejected from the data set and further recalculation of the solution is done. The observed values are almost comparable to the a priori errors resulting in fine velocity maps (**Table 2**). The standard errors associated with the evaluated group velocities are ≤0.07 km/s.

Ditmar and Yanovskaya (1987) and Yanovskaya et al. (1998) used two parameters, viz., mean size and stretching (ε) of the averaging area to prioritize lateral resolution. Yanovskaya (1997) adopted a technique similar to the one formulated by Backus and Gilbert (1968) for the 1D problem. This is formulated for 2D inversion through the calculation of the size of the averaging area S(x,y) for each point in different directions. Obtained resolution approximated by an averaging area over an ellipse centered at the point with S_{max} (x,y) and S_{min}(x,y) as the largest and smallest axes, respectively, over the area S (x,y) (Karagianni et al., 2002; Yanovskaya and Kozhevnikov, 2003). The mean size of the averaging area, $L=(S_{max} + S_{min})/2$, is the measure of the resolution for a particular point and these values for all grid points was used to calculate the lateral resolution of the area under investigation. The resolution depends on the path coverage between the epicenter and station as well as its azimuthal distribution (Gonzalez et al., 2007). The lateral resolution of the mean of the average area is less than 200 km in most of the regions under investigation (**Figure 3A** and **Supplementary Figure S4A**). The lateral resolution for the present data set was evaluated for different periods between 4 and 60 s. Its variation for a set of four periods (8, 12, 30, and 60 s) is shown in **Figure 3A**. Plots for the remaining periods are shown in **Supplementary Figure S4A**. It is noticed that the resolution is good between the 8 s and 30 s period. The evaluated 2D resolution dimension mainly portrays the propagation path geometry and its density as shown in **Figure 1B**; **Supplementary Figure S1**.

The stretching parameter (ε) indicates how uniform the spatial distribution of the path is (Gonzalez et al., 2007). The stretching (ε) of the averaging area is obtained by 2(Smax (x,y)-Smin(x,y))/(Smax (x,y)+Smin(x,y)), which describes the quality of the source–receiver path coverage (Kumar et al., 2019). Small values of the stretching imply that the paths are uniformly distributed in all directions, whereas large values indicate a preferred orientation of paths (Yanovskaya, 1997). Areas with stretching values ≤ 1.0 are considered to have a uniform azimuthal distribution of path and resolution is nearly the same along all directions. **Figure 3B** and **Supplementary Figure S4B** show stretching for the same periods for which resolution has been plotted. Tomographic images for group velocity and Vs are shown later for only the part where the resolution, as indicated in **Figure 3A**; **Supplementary Figure S4A**, is good.

Tomographic Images

Rayleigh wave group velocity tomograms for 16 different periods were obtained at 4, 6, 8, 10, 12, 16, 21, 27, 30, 34, 38, 42, 46, 50, 55, and 60 s to measure the spatial variation. Tomographic images are shown for the area where the spatial resolution is good (i.e., the mean size of the averaging area L ≤ 200 km). This encloses the area covered by the dense ray paths (**Figures 1B**, **3A**, and **Supplementary Figure S1**). Local dispersion curves obtained through tomography for six grid point locations (**Figure 1A**) are shown in **Figure 4** that indicates a high variation of group velocities at different periods from one place to another. Eight group velocity tomograms at 6, 10, 16, 24, 30, 38, 50, and 60 s are shown in **Figure 5**, and the rest are plotted in **Supplementary Figure S5**.

Rayleigh wave group velocity varies between ~1.80 km/s and ~4.15 km/s for periods ranging between 4 s and 60 s (**Figure 5**; **Supplementary Figure S5**). The data set is enough to investigate the crustal and uppermost mantle structures of the study region. Lateral variations of group velocities represent different geological and tectonic features. A shorter period of the Rayleigh wave group velocity map is very sensitive to Vs in the uppermost crust, whereas a longer period has deeper depth sensitivity depending on its wavelength. Lateral variation of group velocity can be discussed based on various geotectonic features.

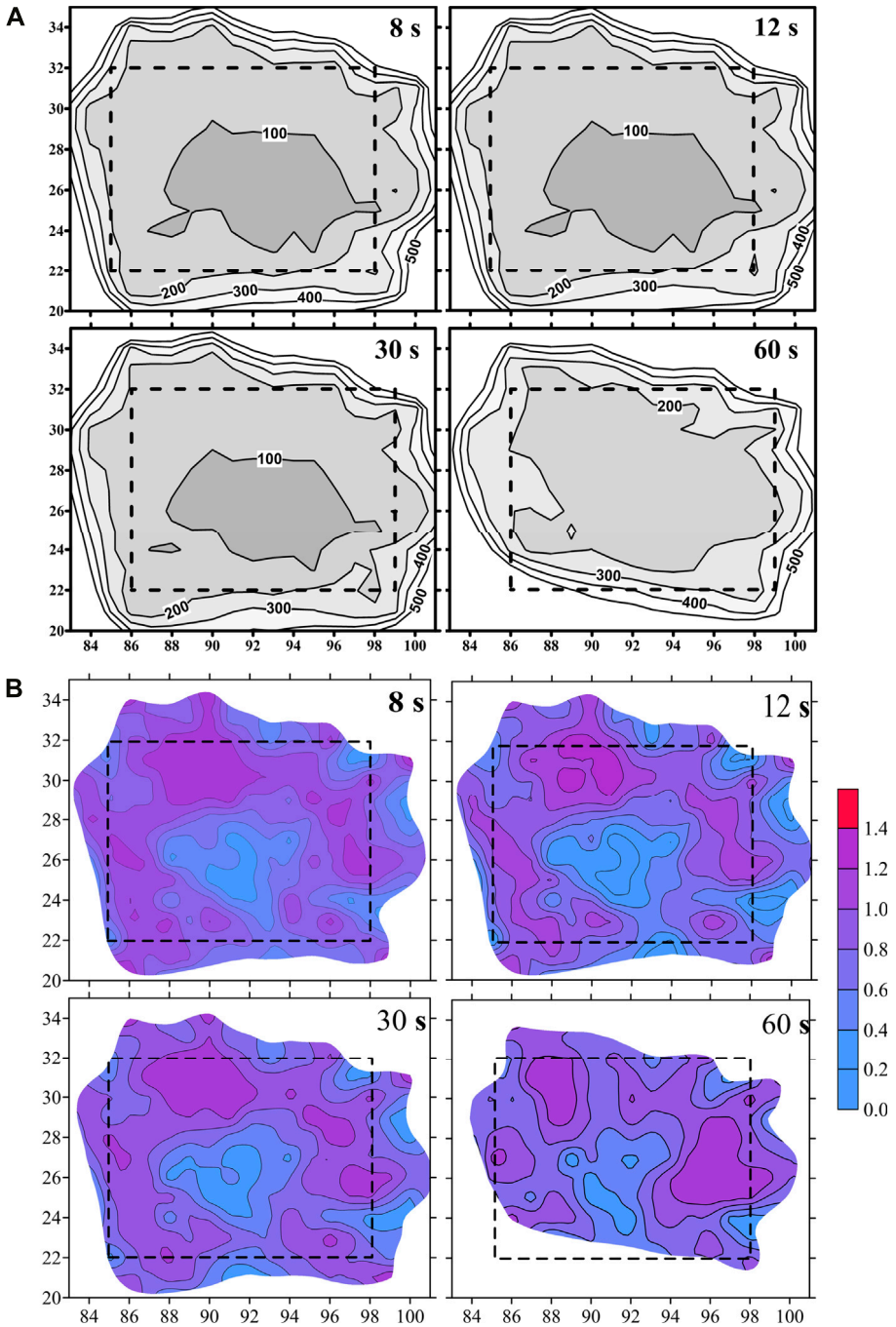

FIGURE 3 | Contoured diagrams of **(A)** mean size of averaging resolution length (in km) and **(B)** distribution of stretching parameter. Areas, where the resolution length of tomographic image >200 km, are clipped and shaded white. An area having a good resolution is demarcated by a rectangular box marked with dashed lines.

According to Mitra et al. (2006), group velocities at <22 s periods represent upper crust, between 25 s and 35 s are mainly influenced by lower crust and up to 60 s represents upper mantle structure. **Figure 4** shows that dispersion curves obtained for grid nodes (**Figure 1A**) located in the BB, IBR, and BRV have lower group velocity values at lower periods compared to those located at SM, STD, and Lhasa block. This indicates the effect of sediments at shallower depths in BB, IBR, and BRV regions. The rate of increase of group velocity value at periods greater than 20 s is very high except for the Lhasa block, indicating the presence of a low-velocity medium in lower crustal depth in the Lhasa block.

At periods ≤10 s, the entire BB, Indo-Gangetic Plain (IGP), eastern Nepal Himalayas, IBR, and parts of southern Tibet

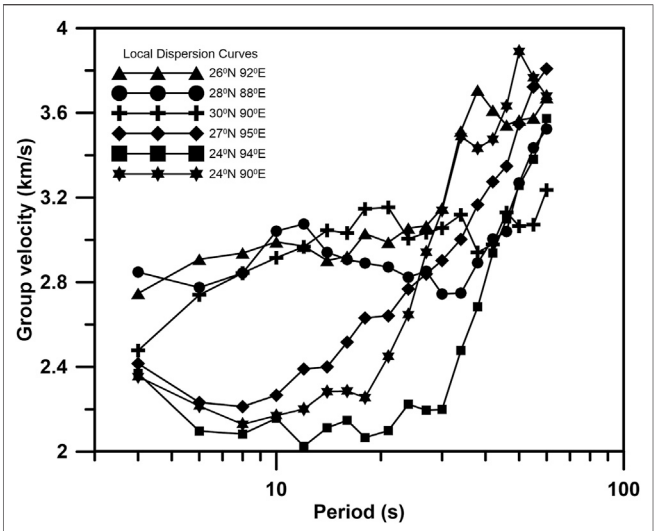

FIGURE 4 | Local dispersion curves for six different grid points (locations shown in **Figure 1A**).

show low group velocity values (**Figure 5**, **Supplementary Figure S5**). At 12–16 s, the values are still low for BB and the southern part of IBR. The low-velocity up to ~24 s Dhubri-Chungthang Fault Zone (DCF) demarcates a boundary suggesting a change in the sub-surface structure in the crust with similar observations by Diehl et al. (2017). The low-velocity zone systematically shifts south-eastward toward the southern part of the IBR with an increase in the period from 16 s to 42 s, and the group velocity value also increases within this zone with increasing period. The very low group velocity values (red color, **Figure 5**, **Supplementary Figure S5**) indicate the presence of sedimentary rocks. As group velocity at a higher period is affected by the Vs of the medium at greater depth, this shows that sedimentary rocks are present in BB and the southern part of the IBR up to greater depth. This observation for BB is supported by earlier investigations (Verma and Mukhopadhyay, 1977; Mitra et al., 2006; Acton et al., 2010), but for IBR, this is new information. Shifting of low group velocity from BB to IBR is supportive evidence of oblique subduction (Mitchell and McKerrow, 1975; Curray, 1989; Ni et al., 1989) of the Indian plate below the Burma plate. A higher velocity gradient in the western part of the BB relative to the eastern part of it shows that the basement depth increases from west to east. Low group velocity (from 4 s to 16 s) in BRV and IGP is also evidence of the presence of sediment at shallow depth (Kumar et al., 2018a). Kayal (2008) reported that the average sediment thickness in BRV is ~4 km. No anomalous change is found in this zone and a continuous increase in group velocity is observed, indicating a gradual increase in medium velocity with depth. The Singhbhum craton and Rajmahal trap in the Indian shields in the southwestern part of the study region are represented by relatively higher group velocity up to 30 s. A prominent increase in group velocity from 21 s along the NE direction of the Indian continent to SMM and EHS is observed. It may reflect upward crustal buckling at the middle of the study region as suggested by Raoof et al. (2017).

At all periods, SMM shows up as a zone of high group velocity indicating the presence of high-velocity crystalline rock bodies at all depth levels. A sudden decrease in group velocity is observed across the Dauki fault from north to south up to 21 s period. At periods >30 s, southern Tibet has lower group velocity compared to eastern Himalayas, NE India, and BB, indicating that at a deeper depth, the former region comprises lower velocity material. This corroborates the presence of thick crust in Tibet. This is also in accordance with the suggestion of the presence of partial melts and/or aqueous fluids in the mid-crust in Tibet (Brown et al., 1996; Cogan et al., 1998; Hetényi et al., 2011; Jiang et al., 2014). Such low-velocity zones in southern Tibet are observed in between 27 s and 50 s. Acton et al. (2010) also observed this type of change of velocity pattern between 50 s and 70 s and inferred that the crust below the Tibetan plateau is thick. Variation of group velocity all along the Himalayas, especially at lower periods, indicates the possible variation of crustal thickness along this tectonic trend as suggested by Raoof et al. (2017). In Nepal Himalayas, the low-velocity at short period has also been observed by Guo et al. (2009). The Gangetic plains adjacent to this region also have relatively lower group velocity with high gradients up to 16 s, which is similar to observations of Mitra et al. (2006).

INVERSION FOR CRUSTAL STRUCTURE

Tomographic maps provide averaged and smoothened group velocities estimated at discrete points at $1^{\circ} \times 1^{\circ}$ spacing within the area under investigation. These are described as the local dispersion curves of different grid points (ex. **Figure 4**). The smooth group velocity versus period data were inverted to obtain an average 1D Vs model at each grid node using CPS3.30 (Herrmann and Ammon, 2002; Herrmann, 2013). The lateral variation at each depth level from 4 to 90 km was obtained by contouring these values as per the procedure described by Kumar et al. (2019). In this process, the dispersion curve extracted from the group velocity maps at each grid point was inverted iteratively using the damped least-squares method. Selected grid points to the part of the study area where the resolution is at least 200 km (see **Figure 3**, **Supplementary Figure S4**) were inverted. The available path densities (**Table 2**, **Supplementary Figure S1**) show that the resolution for 8 s–30 s periods covers a very wide area (**Figure 3**, **Supplementary Figure S4**). For each data set, a fixed number of iterations were carried out. To avoid the trade-off between model variance and data variance, the selection of the damping factor is an important parameter to obtain the unbiased shear wave velocity structure. The damping factor is evaluated from the L curve of the trade-off between data variance and model variance for different damping values between 0.01 and 10 for single iteration inversion (Kumar et al., 2017) (**Supplementary Figure S6**). As an example, the optimum damping value obtained for the dispersion curve of one grid point is 1.1. The selected damping factor gives the smallest value which provides a balanced fit between the model and data from the L-curve

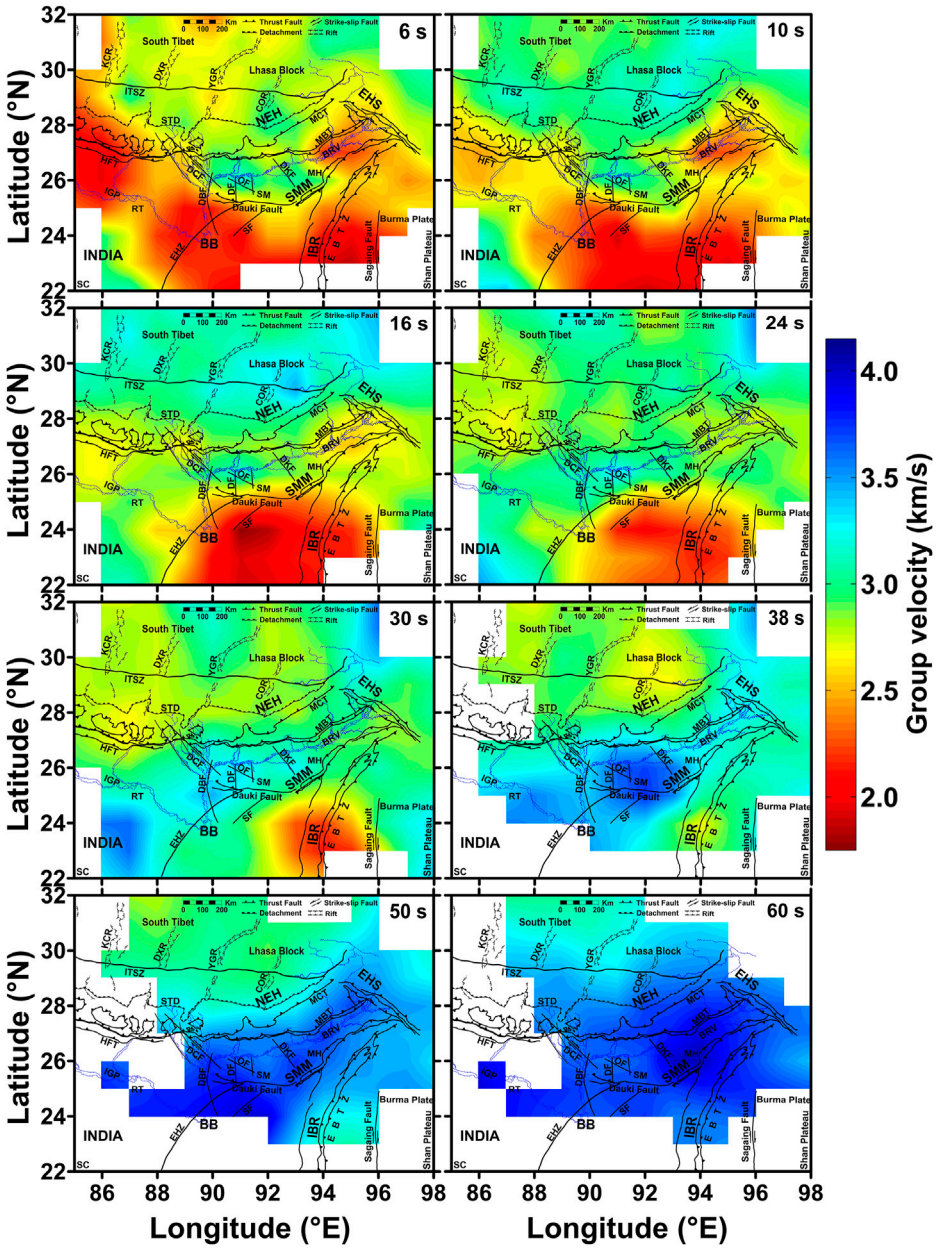

FIGURE 5 | Rayleigh wave fundamental mode group velocity tomographic images at different periods. Areas, where the resolution length of tomographic image >200 km, are clipped and shaded white.

(Gubbins, 2004). This procedure is adopted for obtaining the damping factor of each grid point.

To start inversion, an initial assumed velocity model is required (Yanovskaya et al., 1998; Bhattacharya et al., 2013; Motazedian and Ma, 2014). The inversion is mainly performed in two steps, in the first step, 30 different initial models are selected from the study region and adjoining parts of the Himalayas and IBR (Kumar et al., 2019 and references within). These initial models are used to invert each local dispersion curve for each model to obtain a priori Vs model. To overcome the dependency of the inverted model on the initial model, we constructed the average 1D Vs model at each grid node for each tomographic dispersion curve at the respective grid in this manner. In the next step, 250 randomly positive and negative anomalies were inserted in constructed average 1D Vs model for a wide range of perturbation at different depths and velocities. Thereafter, the inversion is performed for all these generated models at each grid nodes to obtain the respective output Vs models.

This brings the inverted model close to the local structure where perturbations minimize the dependency of inversion on the initial model. To follow the dispersion curve, a gradual

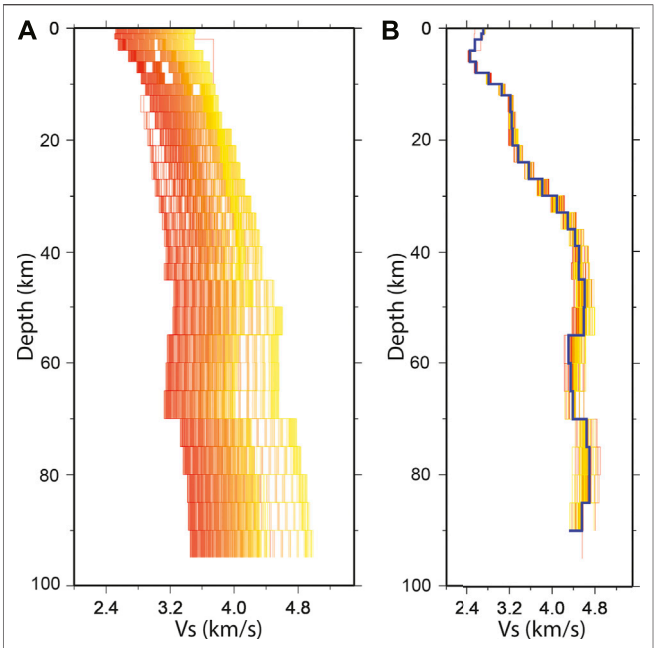

FIGURE 6 | (A) Initial 1-D models used for inversion and **(B)** corresponding inverted 1-D models. Blue line indicates the model chosen for further analysis.

increase in layer thickness and velocity is considered with depth. This process was carried out for each grid node within the study area separately by using the respective average dispersion curve of that grid. An example of initial and inverted models for the grid node at 24°N, 90°E are shown in **Figures 6A,B**, respectively. The best velocity model obtained from the weighted average of 250 output models is represented by a solid blue line (**Figure 6B**), which is based on the weighted average values for different depths from 250 output models. Our result indicates that the final model converges very well from a wide range of initial models and, therefore, the output is independent of initial values.

SHEAR WAVE VELOCITY STRUCTURE

Inverted 1D Vs models at all nodes are used to obtain lateral 2D variation (**Figure 7**, **Supplementary Figure S7**), and combining these 2D models, 3D velocity structure is obtained. 2D Vs map indicates ~2.8–3.0 km/s average velocity at 4 km depth in the southern Tibet and Lhasa block. It increases gradually to ~3.3 km/s at 6 km depth, to ~3.4–3.6 km/s at 10 km, and ~3.6–3.8 km/s at 24 km depth. The average velocity values at different depths match well with the 1D velocity results of Monsalve et al. (2008). A low-velocity zone is observed at the mid-crustal level (~27–50 km) for southern Tibet, which is similar to the observations of Jiang et al. (2011), Sun et al. (2010), and Kumar et al. (2018b; 2019). The ultra-low velocity (~3.3 km/s) zones in the mid-crust of southern Tibet have been suggested to be due to partial melting or aqueous fluid (Cogan et al., 1998; Makovsky & Klemperer, 1999; Unsworth et al., 2005; Jiang et al., 2014). Low-velocity derived in the present study is supported by previous geophysical studies, for example, observation of low-velocity anomaly (Kind et al., 1996; Hung et al., 2010; Hetényi et al., 2011; Kumar et al., 2019), bright spot (Brown et al., 1996; Makovsky et al., 1996), high electric conductivity (Chen et al., 1996; Wei et al., 2001), magnetotelluric study (Unsworth et al., 2004; Arora et al., 2007), and high heat flow (Francheteau et al., 1984).

Part of the Nepal Himalayas (between 85°E–~88°E) is located within the study area. Top ~8 km here contains low-velocity material (<2.8 km/s) that has a velocity lower than that in NE Himalayas at the same depth level (**Figure 7**, **Supplementary Figure S7**). Down to ~10 km depth, there is a variation in Vs along the Himalayas from Nepal to NE Himalayas. A positive velocity gradient is observed from 4 to 18 km depth (ranging from ~2.4 to 2.6 km/s to ~3.6–3.8 km/s) in the Nepal Himalayas. In NE Himalayas, this value varies from 3.0 to 3.6 km/s in the same depth range. Velocity gradient up to 18 km is relatively higher in the Nepal Himalayas as compared to that in the NE Himalayas and south Tibet (see also Raoof et al., 2017).

In the upper part of the crust down to ~21 km depth, Vs in BB is low compared to other parts of the study area (**Figure 7**, **Supplementary Figure S7**). This contrast is very high for the uppermost crust and distinctly visible between ~6 and 8 km depth indicating thick sediment depositions in the basin. The margin of low-velocity sediment deposition is demarcated by Dauki fault in the north. Although Vs increases gradually with depth, roots of low-velocity are visible down to ~21 km depth. Curray et al. (1982) and Brune and Singh (1986) also suggested that sediments/meta-sediments are present down to ~22 km depth in this region. Variation of sedimentary layer thickness in the BB observed by us is also seen by Singh et al. (2016). We find Vs representative of the crustal basement at depth below ~24 km. At depth ≥24 km, the Vs below BB is similar to that of oceanic crust (Sowers and Boyd, 2019) The basement also dips in the SE direction.

There are numerous active thrust faults in IBR (Le Dain et al., 1984). Low-velocity up to a depth of ~10 km is observed below the entire IBR. This could be because of several reasons, viz., presence of cracks, fluid, partial melting, or underthrusting of sediments. However, as Vs in this zone is similar to that observed in the adjacent BB, underthrusting seems most plausible. The low-velocity zone shifts southward along IBR. It is observed down to ~15–~18 km depth within the southern part of IBR. Below this depth, the velocity values are representative of crustal material. Therefore, the thickness of sediments below IBR increases from north to south. The high-velocity medium below 50 km depth may represent the subducting lithosphere as proposed by Raoof et al. (2017).

The BB, SMM, and BRV are trapped between two tectonic arcs. There is a very sharp change in velocity across the Dauki fault that separates BB from SMM with a very clear signature from ~4 to ~18 km depth (**Figure 7**, **Supplementary Figure S7**). This shows that the Dauki fault separates the deep-seated sediments of BB from the crystalline rocks of SMM. Low Vs in the upper ~4 km in IGP and BRV can be associated with thick sediment deposits (**Figure 7**, **Supplementary Figure S7**) (see also

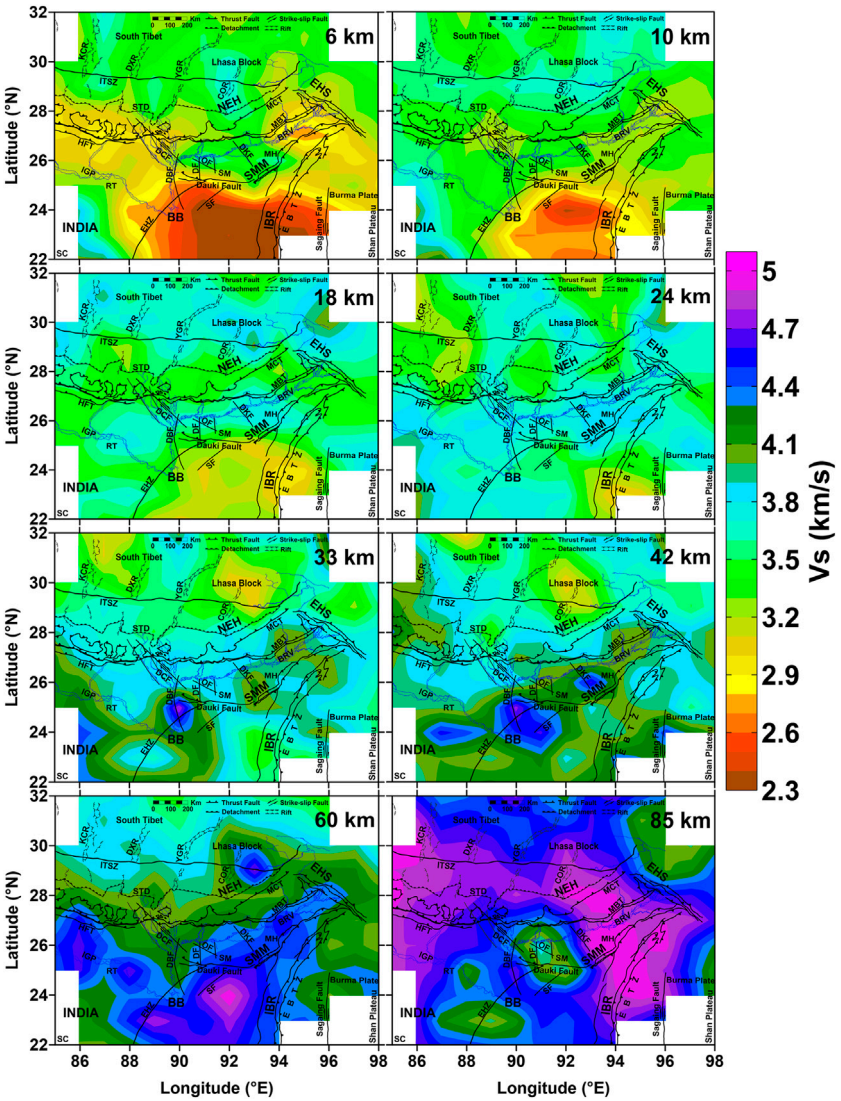

FIGURE 7 | Lateral variation of Vs at different depths. Abbreviations of tectonic features are as in **Figure 1A**.

Mitra et al., 2006; Suresh et al., 2008; Kumar et al., 2017). It is observed that sedimentary layer thickness varies in the IGP and especially in BRV. Within IGP and NE corner of BRV sedimentary rocks are observed up to 6 km depth, whereas within BRV north of SMM, its thickness is less than 4 km (**Figure 7**, **Supplementary Figure S7**).

To get a better perspective about the medium characteristics, S-wave velocity variation along eight profiles (**Figure 1A**) are presented (**Figure 8**). Profile AA' (**Figures 1A**, **8A**) is aligned SSW-NNE which crosses the IGP, Nepal Himalayas, and Tibetan plateau. Prominent tectonic features along this section are HFT, MBT, MCT, STD, and ITSZ. The surface wave is not sensitive to sharp discontinuities like Moho but gives absolute velocity for a depth section across the discontinuity. Kumar et al. (2019) correlated the Rayleigh wave tomography data with the receiver function of the Himalaya–Karakoram–Tibet region to evaluate 4 km/s S-wave contours of tomography results as the approximation of Moho discontinuity. Acton et al. (2010) obtained a 4.1 km/s contour of Moho based on the Rayleigh wave tomography data of the Indian continent and Tibet. Based on the receiver function analysis, Bora et al. (2014) obtained 4 km/s S-wave velocity for Moho in a large part of NE India. In the present study, Moho is marked at 4 km/s (**Figure 8**). **Figure 8A** shows that crustal thickness increases gradually from south to north which clearly shows the effect of underthrusting of Indian plate below the Himalayas. In the south beneath IGP, the Moho depth is ~30 km, which increases to ~80 km beneath Tibet. In the Nepal Himalayas, interfingering of high- and low-velocity material indicates repeated underthrusting and overthrusting of crustal and mantle material, respectively. Based on the receiver function analysis, Acton et al. (2011) observed imbrication of the crust

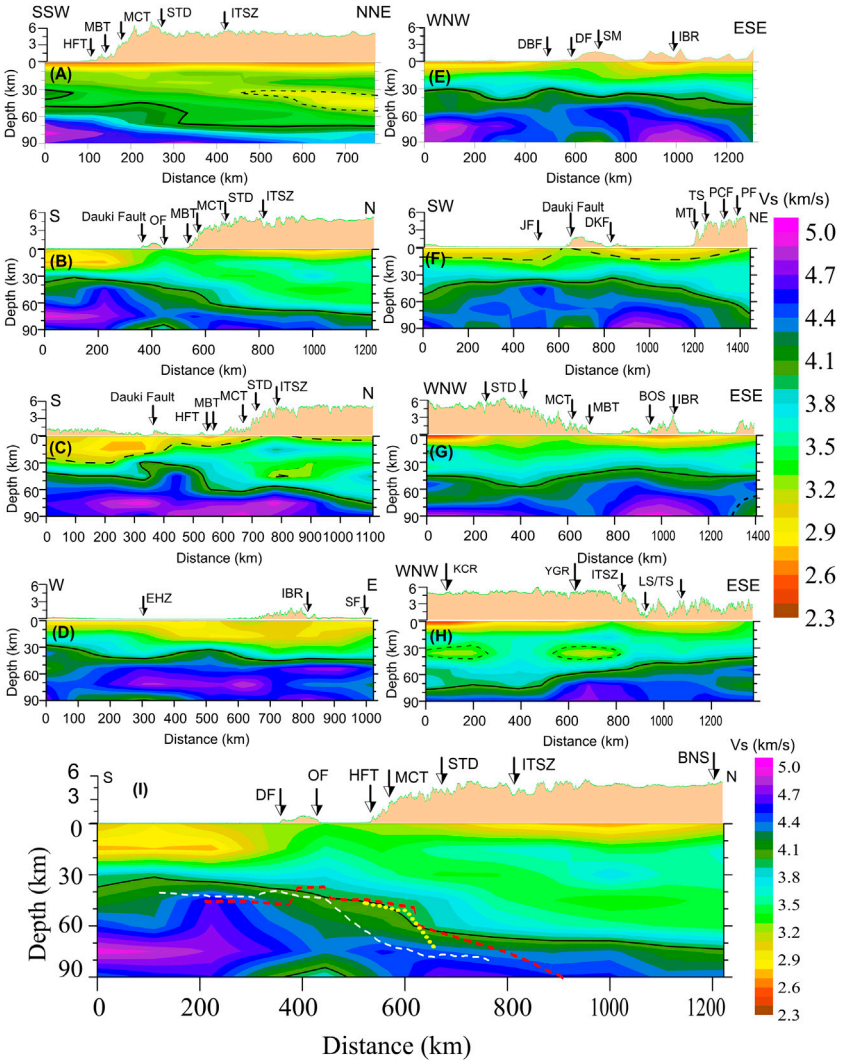

FIGURE 8 | (A–I) Vs structure along different profiles marked in **Figure 1**. Legend: solid line—Moho discontinuity, dashed line—sedimentary layer lower boundary, and dotted line—broken off part of uppermost mantle material (Panel 8G). Dashed lines in Panel 8H encompass low-velocity zones in mid-crust in Lhasa/south Tibet region. **(i)** Comparison of estimated Moho depth variation along profile BB' (black line, Panel 8B) with that obtained by Priestley et al. (2008) (white dash line), Mitra et al. (2005) (red dash line), and Singer et al. (2017) (yellow dotted line). Abbreviations: JF: Jamuna fault; MT: Mishmi Thrust; TS: Tidding Suture; PCF: Po Chu fault; PF: Parlung fault; BOS: Belt of Schuppen; SF: Sagaing fault; LT/TS: Lohit Thrust/Tidding Suture, and other abbreviations as in **Figure 1A**.

in the same region. This further supports our observation. A very low-velocity medium north of ITSZ near the Kung-Co rift at a depth range of 30–50 km probably represents a zone of partial melting and/or the presence of aqueous fluid (Makovsky and Klemperer, 1999; Unsworth et al., 2005; Klemperer, 2006). Our observation along this profile is showing good agreement with the finding of the presence of ramp-flat-ramp geometry of the Main Himalayan Thrust (MHT) in the Sikkim Himalaya using joint inversion of receiver functions and surface wave dispersions by Paul and Mitra (2017).

Profile BB' (**Figures 1A**, **8B**) starts from the BB; passes through the SM, NEH, and Lhasa block; and reaches the Bangong–Nujiang Suture (BNS) of south Tibet. The topography is highly variable (minimum and close to mean sea level at BB and BRV). The Moho depth is also highly variable from ~33 km beneath BB, gradually increasing toward the north up to the frontal Himalayas. Around SM, the crustal thickness is ~40 km. In the Himalayas from MBT to MCT, the Moho depth suddenly increases and mirrors the increase in topography height. In the Bhutan Himalayas, the Moho depth obtained in this study is similar to that obtained by Singer et al. (2017). Further north, it gradually increases to ~75 km depth. A very striking result is the low-velocity in the uppermost crust down to ~20–22 km in the BB for more than 200 km in the southern part. This suggests the presence of thick sediment deposits. The uppermost crustal velocity of SM is higher than that of BB and BRV. The boundary between the sedimentary rock and upper crust (dashed line) clearly shows that the Dauki fault

juxtaposes sediments of BB and crystalline rocks of SM. This also suggests that the Massif is either a pop-up structure (Bilham and England, 2001) or the crest of buckled-up Indian plate (Raoof et al., 2017).

Profile CC' (**Figures 1A**, **8C**) passes through the IBR, SM, MH, NEH, and southern Tibet and shows abnormal Moho depth in the central part of the profile. In the southernmost part, this discontinuity is marked at ~40 km depth with a gradual increase toward the north for about 300 km passing through IBR. South of Dauki fault, a sudden bend is detected in the Moho discontinuity with a sudden uplift in a localized zone of 200 km beneath MH. This observation is similar to Profile BB', where the sudden uplift is observed in the boundary between the sedimentary rock layer and the crystalline crust and supports the hypothesis that MH, like SM, is either a pop-up structure or it sits atop the crest of the buckled-up Indian plate. Moho depth is observed between ~30 and 32 km beneath the MH. Borah et al. (2016) obtained crustal thickness of 32–36 km north of SM based on the S-wave velocity model. The occurrence of thinned crust (30–32 km) beneath SM is also reported by Mitra et al. (2018) and Priestley et al. (2019). The sedimentary layer thickness progressively decreases from IBR to NEH. The low-velocity zone is seen in the mid-to-lower crust beneath Tibet and close to ITSZ that is also visible in Profile HH' (**Figure 8H**).

Profile DD' (**Figures 1A**, **8D**) starts from the west of BB and continues up to the Sagaing fault. An ~10-km thick layer of sedimentary rocks observed in the western part of BB up to EHZ increases down to ~20–21 km in the east beneath BB and IBR. Underthrusting of sedimentary wedge below the IBR is observed in both east and west. Moho depth varies between ~30 and 40 km.

Profile EE' (**Figures 1A**, **8E**) is along WNW-ESE from the IGP up to IBR. Within BB, low-velocity in the uppermost part is due to the thick sediments. In the west of the IBR, an ~20–21 km thick pile of sediment is visible. Moho is undulating and its depth is ~30 km at the WNW end and ~50 km at the ESE end.

Profile FF' (**Figures 1A**, **8F**), from the southwest of BB, crosses the BB, passes through SM, a long stretch of BRV, and then perpendicularly traverses the syntaxial bend of EHS. It is the longest section that stretches over 1,450 km and crosses many geological features and tectonic discontinuities. In the BB, it aligns nearly along the strike of EHZ. The profile crosses the Dauki fault to the south of SM and DKF to its northeast. Along the EHS, the section passes through the Mishmi Hills and several NW-SE trending faults. It shows low-velocity in the uppermost crust at both the sides of the SM related to thick sediment deposits of the BB and BRV. In the SM, the sedimentary rock layer thickness is very low. Crustal thickness varies between 35 and 70 km with the thinnest crust beneath the Massif and below the BRV close to the Massif and thickest in the northeast end beneath the EHS. Borah et al. (2016) obtained a crustal thickness of 36–40 km in the Assam valley using the S-wave velocity model. In BB, its value is between 40 and 45 km and decreases toward the northeast. Its thickest geometry in the EHS indicates subduction of the Indian plate. The increase in crustal thickness on either side of the Massif supports the observations of Raoof et al. (2017) suggesting upward crustal buckling beneath the Massif.

Profile GG' (**Figures 1A**, **8G**) is oblique to the Himalayan arc starting from the central Himalayas, crossing a narrow zone of the BRV, SMM, and further east perpendicular to IBR, then it crosses into the Burma plate. In the uppermost crust within the Himalayas and BRV, low-velocity is related to metasedimentary and sedimentary deposits of the Tethys and BRV, respectively. Borah et al. (2016) observed a 44 km thick crust beneath the lesser Himalayan region. Our result shows that the crustal thickness varies between 45 and 60 km with maximum thickness below the Himalayas.

Profile HH' (**Figures 1A**, **8H**) covers the Lhasa block and EHS. It starts from south Tibet near the Kung-Co rift, passes through the Yadung-Gulu rift, ITSZ, Mishmi Hills, and ends within the EHS. The topography in southern Tibet is high and the Moho depth is ~70–75 km for the initial 500 km of the profile. Crustal thickness suddenly decreases near the Yadong-Gulu rift and after that, it gradually decreases to ~40 km near the EHS. Beneath the Tibetan plateau/Lhasa block, two broad low-velocity zones are detected within ~30–40 km for a distance of about 300 km. Other workers (Brown et al., 1996; Kind et al., 1996; Nelson et al., 1996; Cogan et al., 1998; Hetényi et al., 2011; Jiang et al., 2014) also observed low-velocity medium in this region.

Priestley et al. (2008) and Mitra et al. (2005) using the receiver function estimated the Moho depth variation along an NS profile starting from 22.60°N and 91.25°E which is close to the profile BB' of this study (**Figure 8B**). In **Figure 8I**, the Moho depth reported by them is superposed on profile BB'. Our estimated Moho depth is shallower in most parts of the profile than their estimates. Although the Moho position estimated by them does not exactly match that of ours, the general trend of Moho depth variation is similar. Beneath the Higher Himalayas, the Moho depth suddenly dips toward north; similar observations are reported by Singer et al. (2017) and Mitra et al. (2005).

RESULT AND DISCUSSION

Bay of Bengal and Indo-Burma Range

The Bay of Bengal is characterized by the thickest sediment deposition in the whole world. Huge sediment deposition occurred in BB during the early-mid Miocene following collision between India and Eurasia (Alam et al., 2003). The large and quick influx of clastic sediments within the basin from the Himalayas in the north and IBR in the east led to sudden subsidence of the basin. At this stage, deep-marine sedimentation at the deeper part of the basin and deep to shallow marine sedimentation in the eastern part of the basin occurred (Alam et al., 2003). Mitra et al. (2018) observed the presence of 18–20 km thick sediment underlain by crystalline crust beneath the central BB. Our results show that sedimentary layer thickness is ~10 km in the western part of BB and it starts increasing rapidly east of EHZ with a maximum value of ~21 km at the eastern end of BB (**Figures 7**, **8**, **Supplementary Figure S7**). The margin of low-velocity sediment deposition is demarcated by the Dauki fault in the north and IBR in the east. Although Vs increases gradually with depth, low-velocity strata are visible down to ~21 km depth. Thick sediment

deposition in the BB camouflages basement configuration and makes it difficult to find the exact location of the boundary between oceanic and continental crusts (Alam et al., 2003). The oceanic crust contains only the mafic rock layer, whereas the continental crust has both the felsic layer overlying the mafic layer. Mafic rocks usually have higher P/S wave velocity than felsic rocks. Also, oceanic crust is thinner than the continental crust. It is observed that the crust underlying the thick sedimentary cover of BB has a thickness varying between ~10 and 18 km and Vs ~3.8 km/s (**Figures 7**, **8B**,**C, Supplementary Figure S7**), which is similar to that of oceanic crust (Gonzalez et al., 2007; Pasyanos and Walter, 2002). North of the Dauki fault, a crustal layer having an S wave velocity similar to that of continental crust (Vs ~3.4 km/s) overlying this layer is also observed and the total thickness of these two layers increases northward (*Data and Estimation of Group Velocity* in **Figure 7**). Hence, north of the Dauki fault crustal structure is similar to the continental crust. Based on these observations, we propose that BB is underlain by oceanic crust, and north of the Dauki fault, the crust is continental (**Figures 7**, **8B**,**C**, **Supplementary Figure S7**). Hence, we conclude that the Dauki fault represents an area where the transition of oceanic crust toward its south to continental crust toward its north occurs. Thus, we find clear demarcation between the oceanic and continental crusts. Based on paleomagnetic, gravity, and deep seismic sounding data, Talwani et al. (2016) too found the zone of transition from oceanic to continental crust near this area. Brune and Singh (1986) and Kumar et al. (2018a) found that average Vs in BB changes from oceanic type in its southern part to more continental type toward the north. Based on previous works using Rayleigh wave close to this study region (Acton et al., 2010; Bora et al., 2014; Kumar et al., 2019), 4.0 km/s contour is taken as the Moho discontinuity.

Numerous active thrust faults have been reported in Burma (Le Dain et al., 1984). Low-velocity up to a depth of ~10 km is observed below the entire IBR. With increasing depth, this low-velocity zone shifts southward along IBR with a gradual increase in velocity. It is observed up to ~15–~18 km depth within a very small portion representing the thickness of sediments as they match with velocity observed in the adjacent part of BB (**Figures 7**, **8**, **Supplementary Figure S7**). Below this depth, the velocity values are representative of crustal material. This shows that the depth up to which sedimentary rocks are present below the IBR increases from north to south. High-velocity medium below 50 km depth in this region may represent the subducting lithosphere (**Figures 7**, **8**, **Supplementary Figure S7**) as reported by Raoof et al. (2017). Based on local earthquake tomography over a part of the IBR and Burma plate, Zhang et al. (2021) too find evidence of eastward subduction of the India plate below the Burma plate.

Shillong-Mikir Massif, Indo-Gangetic Plain, and Brahmaputra River Valley

Low Vs in the upper ~4 km in the IGP and BRV is associated with thick sediment deposits. Evaluated Moho depth, based on 4 km/s velocity contour, varies between ~30 and 40 km (**Figures 7**, **8**). Thick sediments observed by us and highly oblique plate motion suggested by Kayal (2008) between India and IBR suggest the presence of active shallow dipping and locked megathrust faults (Steckler et al., 2016). We find a high Vs structure between ~50 and ~75 km (**Supplementary Figure S7**) within the BB formed due to crustal-scale buckling. At deeper depth, a high-velocity gradient shifted eastward and toward the IBR (**Figure 7**).

The SMM and BRV are sandwiched between two tectonic arcs where large earthquakes occur. Vs in SMM is representative of high-velocity crystalline rock bodies near the surface, whereas an ~6 km thick sediment is present in the BRV (**Figure 7**). A sharp change in velocity across the Dauki fault separating the BB from the SMM is observed, especially between ~6 and ~18 km depth. This shows that the Dauki fault separates the deep-seated sediments of BB from the crystalline rocks of SMM, where sediment thickness is negligible. High Vs beneath SMM reveals uplifted crust/uppermost mantle caused by it being in a vice-like grip between the Himalayas and IBR (**Figures 1A**, **8B**,**C**,**F**).

It has been suggested that upliftment of SM is caused by N-S compression due to Himalayan collision and E-W directed compression due to the Indo-Burman subduction (Chen and Molnar, 1990; Mukhopadhyay et al., 1997; Rao and Kumar, 1997; Najman et al., 2016; Govin et al., 2018). Upliftment of the SM is linked with kinematic changes in response to a collision between the Himalayas and the Indian plate and subduction of the Indian plate below the Burma plate cumulatively (Clark and Bilham, 2008). The crustal structure of NE India using the P-wave receiver function (Mitra et al., 2018) suggested that the SM uplifted due to thrust faulting on the Dauki fault, continent margin paleo rift fault, and back-thrusting Oldham fault. Strong et al. (2019) stated that the Massif consists of an actively uplifting block with associated continuous erosion processes.

Nepal Himalayas, Northeastern Himalayas, and South Tibet

A variation in Vs along the Himalayas from Nepal to NEH is noted down to a depth of ~10 km **(Figures 7**, **8)**. Velocity values at each of 12–24 km, 33–45 km, and 65–90 km depth range all along this zone are uniform. At other depth ranges, variation in velocity is observed along the trend of the Himalayas. This may be the effect of complex structural geometry in this region. Velocity gradient down to 18 km is relatively higher in the Nepal Himalayas than that in the NEH and south Tibet. Koulakov et al. (2015) estimated that the Moho depth varies both along and across the tectonic trend of the Nepal Himalayas and suggested that the first is due to the crumpling of the crust caused by the stress along the tectonic trend due to counterclockwise rotation of the Indian plate after the first contact with the Asian plate in the NW Himalayas. Observed lateral velocity variation along the tectonic trend in the NE and NW Himalayas (Koulakov et al., 2015; Raoof et al., 2017; Raoof et al., 2018) and our results in this study also support this contention.

Variation in Vs **(Figures 7**, **8)** in southern Tibet and the Lhasa block matches well with the 1D velocity model estimated by Monsalve et al. (2008) for this region. In the mid-crust

(~27–50 km), ultralow-velocity (~3.3 km/s) zone is observed which is also supported by other researchers using different geophysical studies (Francheteau et al., 1984; Brown et al., 1996; Chen et al., 1996; Kind et al., 1996; Makovsky et al., 1996; Nelson et al., 1996; Wei et al., 2001; Unsworth et al., 2004; Arora et al., 2007; Hung et al., 2010; Jiang et al., 2011). This may indicate partial melting or the presence of aqueous fluid. It is observed that the zones having partial melt/aqueous fluids do not form a continuous layer in southern Tibet but appear rather localized (**Figures 7**, **8**). Hetényi et al. (2011) too observed that zones having partial melts/aqueous fluids are discontinuous in nature.

Eastern Himalayan Syntaxis

EHS is the frontal part of the sandwiched Indian plate between the Eurasian and Burma plate. Sediment thickness of ~6 km is observed toward the northeast of BRV. An abrupt change in crustal thickness is observed in EHS between the F′ and H′ edges (**Figures 1A**, **8F**,**H**) of profiles FF′ and HH′, respectively. These two points are on the two sides of EHS, but they are quite close to each other. However, our study shows that the crust is 70 and 45 km thick near the F' and H' edges, respectively. Significant variation in crustal thickness within the northeast part of the EHS suggests that the nature of crustal deformation in the EHS is complex. Crustal thickness across the Tidding Suture is 55 km (Hazarika et al., 2012). An increase in crustal thickness within the EHS can be interpreted as an effect of indentation geometry of the Indian plate from the southwest direction. Convergence of Indian and Eurasian plates generates N-S and E-W compression within the NE India, leading to crustal buckling across the NE axis as shown in this work.

CONCLUSION

a) Bengal Basin is underlain by oceanic crust. Further north below the Shillong Massif/Brahmaputra River Valley, the crust changes to continental type.
b) Thickness of BB sediments increases from west to east. This inference is similar to previous estimates of sediment thickness for this area. The dip of the basement of this sedimentary basin increases suddenly to the east of the Eastern Hinge Zone.
c) Sediments are also getting underthrusted at the southern part of the Indo-Burma Ranges that lie within the study area.
d) In the Indo-Gangetic Plains and Brahmaputra River Valley, 5–6 km thick sedimentary layers are present. This observation is also reported by previous workers. However, north of SMM sedimentary layer is very thin.
e) Across the Dauki fault, low-velocity sediments of Bengal Basin are juxtaposed with high-velocity granitic/metamorphic rocks of the Shillong Massif and Mikir Hills. In the Shillong Massif and Mikir Hills, sedimentary layer cover is very thin or absent and crystalline rocks having higher velocity are present near the surface.
f) Shillong Massif and Mikir Hills lie atop the Indian plate that has buckled up because in this area, the Indian plate is in a vice-like grip between tectonically active Himalayan ranges toward the north, below which it is underthrusting, and the Indo-Burma Ranges toward the east, below which it is subducting (Grujic et al., 2018).
g) The Moho depth varies not only from south to north but also along the tectonic trends of the Himalayas.
h) Average Moho depth increases from ~40 km in the south to ~70 km in the northern part of the study area smoothly in most places but abruptly at other places.
i) In the eastern part of the Nepal Himalayas, the signature of repeated underthrusting and overthrusting is observed, whereas such a pattern is not observed further east along the trend of the Himalayas.
j) For southern Tibet/Lhasa block, two important findings are as follows 1) the Moho depth decreases from ~70 km west of the Yadong-Gulu rift to ~60 km toward the east which may be the effect of collision geometry to control the underplating of Indian plate in this section of southern Tibet/Lhasa block (Shi et al., 2015); 2) few low-velocity zones are observed in velocity sections at mid-crustal levels near or below the rift zones in the southern Tibet/Lhasa block. This could be due to the presence of zones having partially molten material and/or aqueous fluids. This observation is similar to many seismic and magnetotelluric studies in this area.

DATA AVAILABILITY STATEMENT

The original contributions presented in the study are included in the article/**Supplementary Material**; further inquiries can be directed to the corresponding author.

AUTHOR CONTRIBUTIONS

All authors listed have made a substantial, direct, and intellectual contribution to the work and approved it for publication.

ACKNOWLEDGMENTS

We are thankful to IMD for providing data. AK is thankful to the Ministry of Human Resource Development, Government of India, for the fellowship through grant #MHR01-23-200-428. AK also acknowledges NCPOR for partial completion of manuscript writing work in the institute through reference no. J-33/2021-22. This research did not receive any specific grant from funding agencies in the public, commercial, or not-for-profit sectors. The authors sincerely acknowledge editor György Hetényi and two reviewers for valuable suggestions for improvement of the manuscript.

SUPPLEMENTARY MATERIAL

The Supplementary Material for this article can be found online at: https://www.frontiersin.org/articles/10.3389/feart.2021.680361/full#supplementary-material

REFERENCES

Acton, C. E., Priestley, K., Gaur, V. K., and Rai, S. S. (2010). Group Velocity Tomography of the Indo-Eurasian Collision Zone. *J. Geophys. Res.* 115, 1–16. doi:10.1029/2009JB007021

Acton, C. E., Priestley, K., Mitra, S., and Gaur, V. K. (2011). Crustal Structure of the Darjeeling-Sikkim Himalaya and Southern Tibet. *Geophys. J. Int.* 184, 829–852. doi:10.1111/j.1365-246X.2010.04868.x

Alam, M., Alam, M. M., Curray, J. R., Chowdhury, M. L. R., and Gani, M. R. (2003). An Overview of the Sedimentary Geology of the Bengal Basin in Relation to the Regional Tectonic Framework and basin-fill History. *Sediment. Geology.* 155, 179–208. doi:10.1016/s0037-0738(02)00180-x

Angelier, J., and Baruah, S. (2009). Seismotectonics in Northeast India: a Stress Analysis of Focal Mechanism Solutions of Earthquakes and its Kinematic Implications. *Geophys. J. Int.* 178, 303–326. doi:10.1111/j.1365-246X.2009.04107.x

Armijo, R., Tapponnier, P., Mercier, J. L., and Tong-Lin, H. (1986). Quaternary Extension in Southern Tibet: Field Observations and Tectonic Implications. *J. Geophys. Res. Solid Earth* 91 (13), 803–813. doi:10.1029/jb091ib14p13803872

Arora, B. R., Unsworth, M. J., and Rawat, G. (2007). Deep Resistivity Structure of the Northwest Indian Himalaya and its Tectonic Implications. *Geophys. Res. Lett.* 34, L04307. doi:10.1029/2006GL029165

Backus, G., and Gilbert, F. (1968). The Resolving Power of Gross Earth Data. *Geophys. J. Int.* 16, 169–205. doi:10.1111/j.1365-246x.1968.tb00216.x

Baranowski, J., Armbruster, J., Seeber, L., and Molnar, P. (1984). Focal Depths and Fault Plane Solutions of Earthquakes and Active Tectonics of the Himalaya. *J. Geophys. Res.* 89, 6918–6928. doi:10.1029/jb089ib08p06918

Baruah, S., Baruah, S., and Kayal, J. R. (2013). State of Tectonic Stress in Northeast India and Adjoining South Asia Region: An Appraisal. *Bull. Seismological Soc. America* 103 (2A), 894–910. doi:10.1785/0120110354

Baruah, S., Baruah, S., Saikia, S., Shrivastava, M. N., Sharma, A., Reddy, C. D., et al. (2016). State of Tectonic Stress in Shillong Plateau of Northeast India. *Phys. Chem. Earth, Parts A/B/C* 95, 36–49. doi:10.1016/j.pce.2015.11.009

Baruah, S., Saikia, S., Baruah, S., Bora, P. K., Tatevossian, R., and Kayal, J. R. (2014). The September 2011 Sikkim Himalaya Earthquake Mw 6.9: Is it a Plane of Detachment Earthquake? *Geomatics, Nat. Hazards Risk* 7, 248–263. doi:10.1080/19475705.2014.895963

Bensen, G. D., Ritzwoller, M. H., Barmin, M. P., Levshin, A. L., Lin, F., Moschetti, M. P., et al. (2007). Processing Seismic Ambient Noise Data to Obtain Reliable Broad-Band Surface Wave Dispersion Measurements. *Geophys. J. Int.* 169, 1239–1260. doi:10.1111/j.1365-246x.2007.03374.x

Bhattacharya, S. N., Mitra, S., and Suresh, G. (2013). The Shear Wave Velocity of the Upper Mantle beneath the Bay of Bengal, Northeast Indian Ocean from Interstation Phase Velocities of Surface Waves. *Geophys. J. Int.* 193, 1506–1514. doi:10.1093/gji/ggt007

Bilham, R., and England, P. (2001). Plateau 'pop-Up' in the Great 1897 Assam Earthquake. *Nature* 410, 806–809. doi:10.1038/35071057

Bora, D. K., Hazarika, D., Borah, K., Rai, S. S., and Baruah, S. (2014). Crustal Shear-Wave Velocity Structure beneath Northeast India from Teleseismic Receiver Function Analysis. *J. Asian Earth Sci.* 90, 1–14. doi:10.1016/j.jseaes.2014.04.005

Borah, K., Bora, D. K., Goyal, A., and Kumar, R. (2016). Crustal Structure beneath Northeast India Inferred from Receiver Function Modeling. *Phys. Earth Planet. Interiors* 258, 15–27. doi:10.1016/j.pepi.2016.07.005

Brown, L. D., Zhao, W., Nelson, K. D., Hauck, M., Alsdorf, D., Ross, A., et al. (1996). Bright Spots, Structure, and Magmatism in Southern Tibet from INDEPTH Seismic Reflection Profiling. *Science* 274, 1688–1690. doi:10.1126/science.274.5293.1688

Brune, J. N., Curray, J., Dorman, L., and Raitt, R. (1992). A Proposed Super-thick Sedimentary basin, Bay of Bengal. *Geophys. Res. Lett.* 19, 565–568. doi:10.1029/91GL0313410.1029/91gl03134

Brune, J. N., and Singh, D. D. (1986). Continent-like Crustal Thickness beneath the Bay of Bengal Sediments. *Bull. Seismological Soc. America* 76, 191–203. doi:10.1785/bssa0760030903b

Burchfiel, B. C., and Royden, L. H. (1985). North-south Extension within the Convergent Himalayan Region. *Geol* 13 (10), 679–682. doi:10.1130/0091-7613(1985)13<679:newtch>2.0.co;2

Chen, L., Booker, J. R., Jones, A. G., Wu, N., Unsworth, M. J., Wei, W., et al. (1996). Electrically Conductive Crust in Southern Tibet from INDEPTH Magnetotelluric Surveying. *Science* 274, 1694–1696. doi:10.1126/science.274.5293.1694

Chen, W.-P., and Molnar, P. (1990). Source Parameters of Earthquakes and Intraplate Deformation beneath the Shillong Plateau and the Northern Indoburman Ranges. *J. Geophys. Res.* 95, 12527–12552. doi:10.1029/jb095ib08p12527

Clark, M., and Bilham, R. (2008). Miocene Rise of the Shillong Plateau and the Beginning of the End for the Eastern Himalaya. *Earth Planet. Sci. Lett.* 269, 337–351. doi:10.1016/j.epsl.2008.01.045

Cogan, M. J., Nelson, K. D., Kidd, W. S. F., and Wu, C.Project INDEPTH Team (1998). Shallow Structure of the Yadong-Gulu Rift, Southern Tibet, from Refraction Analysis of Project INDEPTH Common Midpoint Data. *Tectonics* 17 (1), 46–61. doi:10.1029/97tc03025

Curray, J. R., Emmel, F. J., Moore, D. G., and Raitt, R. W. (1982). "Structure, Tectonics, and Geological History of the Northeastern Indian Ocean," in *The Ocean Basins and Margins* (Boston, MA: Springer US), 399–450. doi:10.1007/978-1-4615-8038-6_9

Curray, J. R. (1991). Possible Greenschist Metamorphism at the Base of a 22-km Sedimentary Section, Bay of Bengal. *Geol* 19, 1097–1100. doi:10.1130/0091-7613(1991)019<1097:pgmatb>2.3.co;2

Curray, J. R. (1989). The Sunda Arc: A Model for Oblique Plate Convergence. *Neth. J. Sea Res.* 24, 131–140. doi:10.1016/0077-7579(89)90144-0

De Sarkar, S., Mathew, G., and Pande, K. (2013). Arc Parallel Extension in Higher and Lesser Himalayas, Evidence from Western Arunachal Himalaya, India. *J. Earth Syst. Sci.* 122 (3), 715–727. doi:10.1007/s12040-013-0298-7

DeCelles, P. G., Robinson, D. M., and Zandt, G. (2002). Implications of Shortening in the Himalayan Fold-Thrust belt for Uplift of the Tibetan Plateau. *Tectonics* 21 (6), 1–25. doi:10.1029/2001tc001322

Desikachar, S. (1974). A Review of the Tectonic and Geological History of Eastern India in Terms of Plate Tectonics Theory. *J. Geol. Soc. India* 15, 137–149.

Diehl, T., Singer, J., Hetényi, G., Grujic, D., Clinton, J., Giardini, D., et al.GANSSER Working Group (2017). Seismotectonics of Bhutan: Evidence for Segmentation of the Eastern Himalayas and Link to Foreland Deformation. *Earth Planet. Sci. Lett.* 471, 54–64. doi:10.1016/j.epsl.2017.04.038

Ditmar, P. G., and Yanovskaya, T. B. (1987). A Generalization of the Backus-Gilbert Method for Estimation of Lateral Variations of Surface Wave Velocity (In Russian). *Izv.Akad.Nauk Sssir, Fiz. Zemli* 6, 30–60.

Dziewonski, A., Bloch, S., and Landisman, M. (1969). A Technique for the Analysis of Transient Seismic Signals. *Bull. Seismological Soc. America* 59, 427–444. doi:10.1785/bssa0590010427

Dziewonski, A. M., and Anderson, D. L. (1983). Travel Times and Station Corrections for P Waves at Teleseismic Distances. *J. Geophys. Res.* 88, 3295–3314. doi:10.1029/jb088ib04p03295

England, P., and Bilham, R. (2015). The Shillong Plateau and the Great 1897 Assam Earthquake. *Tectonics* 34, 1792–1812. doi:10.1002/2015TC003902

England, P., and Houseman, G. (1989). Extension during continental Convergence with Application to the Tibetan Plateau. *J. Geophys. Res.* 94 (B12), 561–579. doi:10.1029/jb094ib12p17561

Erduran, M., Çakır, Ö., Tezel, T., Şahin, Ş., and Alptekin, Ö. (2007). Anatolian Surface Wave Evaluated at GEOFON Station ISP Isparta, Turkey. *Tectonophysics* 434, 39–54. doi:10.1016/j.tecto.2007.02.005

Evans, P. (1964). The Tectonic Framework of Assam. *Geol. Soc. India J.* 5, 80–96

Francheteau, J., Jaupart, C., Jie, S. X., Wen-Hua, K., De-Lu, L., Jia-Chi, B., et al. (1984). High Heat Flow in Southern Tibet. *Nature* 307, 32–36. doi:10.1038/307032a0

Gahalaut, V. K., Kundu, B., Laishram, S. S., Catherine, J., Kumar, A., Singh, M. D., et al. (2013). Aseismic Plate Boundary in the Indo-Burmese Wedge, Northwest Sunda Arc. *Geology* 41, 235–238. doi:10.1130/g33771.1

González, O. L., Alvarez, L., Guidarelli, M., and Panza, G. F. (2007). Crust and Upper Mantle Structure in the Caribbean Region by Group Velocity Tomography and Regionalization. *Pure Appl. Geophys.* 164, 1985–2007. doi:10.1007/s00024-007-0259-7

Govin, G., Najman, Y., Copley, A., Millar, I., van der Beek, P., Huyghe, P., et al. (2018). Timing and Mechanism of the Rise of the Shillong Plateau in the Himalayan Foreland. *Geology* 46 (3), 279–282. doi:10.1130/g39864.1

Grujic, D., Hetényi, G., Cattin, R., Baruah, S., Benoit, A., Drukpa, D., et al. (2018). Stress Transfer and Connectivity between the Bhutan Himalaya and the Shillong Plateau. *Tectonophysics* 744, 322–332. doi:10.1016/j.tecto.2018.07.018

Gubbins, D. (2004). *Time Series Analysis and Inverse Theory for Geophysicist*. Cambridge: Cambridge University Press

Guo, Z., Gao, X., Yao, H. J., Li, J., and Wang, W. M. (2009). Midcrustal Low-Velocity Layer beneath the central Himalaya and Southern Tibet Revealed by Ambient Noise Array Tomography. *Geochem. Geophys. Geosystems* 10 (5), Q05007. doi:10.1029/2009gc002458

Hazarika, D., Arora, B. R., and Bora, C. (2012). Crustal Structure and Deformation in the Northeast India-Asia Collision Zone: Constraints from Receiver Function Analysis. *Geophys. J. Int.* 188, 737–749. doi:10.1111/j.1365-246x.2011.05267.x

Herrmann, R. B., and Ammon, C. J. (2002). *Computer Programs in Seismology-3.30, Surface Waves, Receiver Functions and Crustal Structure*. Available at: http://www.eas.slu.edu/eqc/eqccps.html

Herrmann, R. B. (2013). Computer Programs in Seismology: An Evolving Tool for Instruction and Research. *Seismological Res. Lett.* 84, 1081–1088. doi:10.1785/0220110096

Herrmann, R. B. (1973). Some Aspects of Band-Pass Filtering of Surface Waves. *Bull. Seismological Soc. America* 63, 663–671.

Hetényi, G., Vergne, J., Bollinger, L., and Cattin, R. (2011). Discontinuous Low-Velocity Zones in Southern Tibet Question the Viability of the Channel Flow Model. *Geol. Soc. Lond. Spec. Publications* 353, 99–108. doi:10.1144/sp353.6

Hintersberger, E., Thiede, R. C., Strecker, M. R., and Hacker, B. R. (2010). East-west Extension in the NW Indian Himalaya. *Geol. Soc. America Bull.* 122, 1499–1515. doi:10.1130/b26589.1

Holt, W. E., Ni, J. F., Wallace, T. C., and Haines, A. J. (1991). The Active Tectonics of the Eastern Himalayan Syntaxis and Surrounding Regions. *J. Geophys. Res.* 96 (14), 14595–14632. doi:10.1029/91jb01021632

Hung, S.-H., Chen, W.-P., Chiao, L.-Y., and Tseng, T.-L. (2010). First Multi-Scale, Finite-Frequency Tomography Illuminates 3-D Anatomy of the Tibetan Plateau. *Geophys. Res. Lett.* 37, a–n. doi:10.1029/2009GL041875

Jiang, M., Ai, Y., Zhou, S., and Chen, Y. J. (2014). Distribution of the Low Velocity Bulk in the Middle-To-Lower Crust of Southern Tibet: Implications for Formation of the north-south Trending Rift Zones. *Earthq Sci.* 27 (2), 149–157. doi:10.1007/s11589-014-0080-1

Jiang, M., Zhou, S., Sandvol, E., Chen, X., Liang, X., Chen, Y. J., et al. (2011). 3-D Lithospheric Structure beneath Southern Tibet from Rayleigh-Wave Tomography with a 2-D Seismic Array. *Geophys. J. Int.* 185, 593–608. doi:10.1111/j.1365-246x.2011.04979.x

Kailasam, L. N. (1979). Plateau Uplift in Peninsular India. *Tectonophysics* 61, 243–269. doi:10.1016/0040-1951(79)90300-7

Karagianni, E. E., Panagiotopoulos, D. G., Panza, G. F., Suhadolc, P., Papazachos, C. B., Papazachos, B. C., et al. (2002). Rayleigh Wave Group Velocity Tomography in the Aegean Area. *Tectonophysics* 358, 187–209. doi:10.1016/s0040-1951(02)00424-9

Kayal, J. R. (2001). Microearthquake Activity in Some Parts of the Himalaya and the Tectonic Model. *Tectonophysics* 339, 331–351. doi:10.1016/s0040-1951(01)00129-9

Kayal, J. R. (2008). *Microearthquake Seismology and Seismotectonics of South Asia*. Springer, 503.

Kayal, J. R. (1996). Precursor Seismicity, Foreshocks and Aftershocks of the Uttarkashi Earthquake of October 20, 1991 at Garhwal Himalaya. *Tectonophysics* 263, 339–345. doi:10.1016/S0040-1951(97)81488-6

Kayal, J. R. (1989). *Subduction Structure at the India/Burma Plate Boundary: Seismic and Gravity Evidences*, 2. USA: 28th International Geological Congress, 164–165.

Khattri, K. N., Chander, R., Mukhopadhyay, S., Sriram, V., and Khanal, K. N. (1992). "A Model of Active Tectonics in the Shillong Massif Region," in *The Himalayan Orogen and Global Tectonics*. Editor A. K. Sinha (Delhi: Oxford and IBH), 205–222.

Kind, R., Ni, J., Zhao, W., Wu, J., Yuan, X., Zhao, L., et al. (1996). Evidence from Earthquake Data for a Partially Molten Crustal Layer in Southern Tibet. *Science* 274, 1692–1694. doi:10.1126/science.274.5293.1692

Klemperer, S. L. (2006). Crustal Flow in Tibet: Geophysical Evidence for the Physical State of Tibetan Lithosphere, and Inferred Patterns of Active Flow. *Geol. Soc. Lond. Spec. Publications* 268 (1), 39–70. doi:10.1144/gsl.sp.2006.268.01.03

Kolinsky, P. (2004). Surface Wave Dispersion Curves of Eurasian Earthquakes: the SVAL Program. *Acta Geodynamica Geomaterialia* 1 (134), 165–185.

Koulakov, I., Maksotova, G., Mukhopadhyay, S., Raoof, J., Kayal, J. R., Jakovlev, A., et al. (2015). Variations of the Crustal Thickness in Nepal Himalayas Based on Tomographic Inversion of Regional Earthquake Data. *Solid Earth* 6 (1), 207–216. doi:10.5194/se-6-207-2015

Krishnan, M. S. (1960). *Geology of India and Burma*. Madras, India: Higginbothams, 553.

Kumar, A., Kumar, N., Mukhopadhyay, S., and Baidya, P. R. (2017). Crustal and Uppermost Mantle Structures in the Frontal Himalaya and Indo-Gangetic basin Using Surface Wave: Tectonic Implications. *Quat. Int.* 462, 34–49. doi:10.1016/j.quaint.2017.02.035

Kumar, A., Kumar, N., and Mukhopadhyay, S. (2018b). Investigation of Azimuthal Variation in Seismic Surface Waves Group Velocity in the Western Part of Himalaya-Tibet Indo-Gangetic plains Region. *Himalayan Geology.* 39 (1), 33–46. doi:10.1111/1755-6724.13931

Kumar, A., Mitra, S., and Suresh, G. (2015). Seismotectonics of the Eastern Himalayan and Indo-Burman Plate Boundary Systems. *Tectonics* 34, 2279–2295. doi:10.1002/2015tc003979

Kumar, A., Mukhopadhyay, S., Kumar, N., and Baidya, P. R. (2018a). Lateral Variation in Crustal and Mantle Structure in Bay of Bengal Based on Surface Wave Data. *J. Geodynamics* 113, 32–42. doi:10.1016/j.jog.2017.11.006

Kumar, N., Aoudia, A., Guidarelli, M., Babu, V. G., Hazarika, D., and Yadav, D. K. (2019). Delineation of Lithosphere Structure and Characterization of the Moho Geometry under the Himalaya-Karakoram-Tibet Collision Zone Using Surface-Wave Tomography. *Geol. Soc. Lond. Spec. Publications* 481, 19–40. doi:10.1144/SP481-2017-172

Le Dain, A. Y., Tapponnier, P., and Molnar, P. (1984). Active Faulting and Tectonics of Burma and Surrounding Regions. *J. Geophys. Res.* 89 (B1), 453–472. doi:10.1029/JB089iB01p00453

Le Roux-Mallouf, R., Ferry, M., Cattin, R., Ritz, J.-F., Drukpa, D., and Pelgay, P. (2020). A 2600-Year-Long Paleoseismic Record for the Himalayan Main Frontal Thrust (Western Bhutan). *Solid Earth* 11, 2359–2375. doi:10.5194/se-11-2359-2020

Levshin, A. L., Yanovskaya, T. B., Lander, A. V., Bukchin, B. G., Barmin, M. P., Ratnikova, L. I., et al. (1989). "Recording, Identification, and Measurement of Surface Wave Parameters," in *Seismic Surface Waves in a Laterally Inhomogeneous Earth*. Editor V. I. Keilis-Borok (Dordrecht: Kluwer Academic Publisher), 131–182

Makovsky, Y., and Klemperer, S. L. (1999). Measuring the Seismic Properties of Tibetan Bright Spots: Evidence for Free Aqueous Fluids in the Tibetan Middle Crust. *J. Geophys. Res.* 104 (B5), 10795–10825. doi:10.1029/1998jb900074

Makovsky, Y., Klemperer, S. L., Ratschbacher, L., Brown, L. D., Li, M., Zhao, W., et al. (1996). INDEPTH Wide-Angle Reflection Observation of P-Wave-To-S-Wave Conversion from Crustal Bright Spots in Tibet. *Science* 274, 1690–1691. doi:10.1126/science.274.5293.1690

Mitchell, A. H. G., and McKerrow, W. S. (1975). Analogous Evolution of the Burma Orogen and the Scottish Caledonides. *Geol. Soc. America Bull.* 86, 305–315. doi:10.1130/0016-7606(1975)86<305:aeotbo>2.0.co;2

Mitra, S., Kainkaryam, S. M., Padhi, A., Rai, S. S., and Bhattacharya, S. N. (2011). The Himalayan Foreland basin Crust and Upper Mantle. *Phys. Earth Planet. Interiors* 184, 34–40. doi:10.1016/j.pepi.2010.10.009

Mitra, S., Priestley, K., Bhattacharyya, A. J., and Gaur, V. K. (2005). Crustal Structure and Earthquake Focal Depths beneath north Eastern India and Southern Tibet. *Geophys. J. Int.* 160, 227–248.

Mitra, S., Priestley, K. F., Borah, K., and Gaur, V. K. (2018). Crustal Structure and Evolution of the Eastern Himalayan Plate Boundary System, Northeast India. *J. Geophys. Res. Solid Earth* 123, 621–640. doi:10.1002/2017JB014714

Mitra, S., Priestley, K., Gaur, V. K., Rai, S. S., and Haines, J. (2006). Variation of Rayleigh Wave Group Velocity Dispersion and Seismic Heterogeneity of the Indian Crust and Uppermost Mantle. *Geophys. J. Int.* 164, 88–98. doi:10.1111/j.1365-246X.2005.02837.x

Molnar, P., Chen, W., Fitch, W., Tapponnier, P., Warsi, W., and Wu, F. T. (1977). Structure and Tectonics of the Himalaya: A Brief Summary of Relevant Geophysical Observations. *Ecologieet Geologie de l'Himalaya, Colloques internationaux du C.N.R.S.* 268, 269–294.

Molnar, P. (1984). Structure and Tectonics of the Himalaya: Constraints and Implications of Geophysical Data. *Annu. Rev. Earth Planet. Sci.* 12, 489–516. doi:10.1146/annurev.ea.12.050184.002421

Monsalve, G., Sheehan, A., Rowe, C., and Rajaure, S. (2008). Seismic Structure of the Crust and the Upper Mantle beneath the Himalayas: Evidence for Eclogitization of Lower Crustal Rocks in the Indian Plate. *J. Geophys. Res.* 113, B08315. doi:10.1029/2007JB005424

Motazedian, D., and Ma, S. (2014). Crustal Shear-Wave Velocity Models Retrieved from Rayleigh-Wave Dispersion Data in Northern Canada. *Bull. Seismological Soc. America, early edition* 104 (4), 1–13. doi:10.1785/0120130265

Mukhopadhyay, M., and Dasgupta, S. (1988). Deep Structure and Tectonics of the Burmese Arc: Constraints from Earthquake and Gravity Data. *Tectonophysics* 149, 299–322. doi:10.1016/0040-1951(88)90180-1

Mukhopadhyay, S., Chander, R., and Khattri, K. N. (1997). Crustal Properties in the Epicentral Tract of the Great 1897 Assam Earthquake, Northeastern India. *Tectonophysics* 283, 311–330. doi:10.1016/s0040-1951(97)00148-0

Mukhopadhyay, S., Chander, R., and Khattri, K. N. (1993). Fine Structure of Seismotectonics in Western Shillong Massif, north east India. *Proc. Indian Acad. Sci. - Earth Planet. Sci.* 102 (2), 383–398.

Murphy, M. A., and Copeland, P. (2005). Transtensional Deformation in the central Himalaya and its Role in Accommodating Growth of the Himalayan Orogen. *Tectonics* 24, a–n. doi:10.1029/2004TC001659

Nabelek, J., Hetényi, G., Vergne, J., Sapkota, S., Kafle, B., Jiang, M., et al.the Hi-CLIMB Team (2009). Underplating in the Himalaya-Tibet Collision Zone Revealed by the Hi-CLIMB Experiment. *Science* 325, 1371–1374. doi:10.1126/science.1167719

Najman, Y., Bracciali, L., Parrish, R. R., Chisty, E., and Copley, A. (2016). Evolving Strain Partitioning in the Eastern Himalaya: The Growth of the Shillong Plateau. *Earth Planet. Sci. Lett.* 433, 1–9. doi:10.1016/j.epsl.2015.10.017

Nandy, D. R. (1980). Tectonic Pattern of Northeast India. *Indian J. Earth Sci.* 7, 103–107.

Nelson, K. D., Zhao, W., Brown, L. D., Kuo, J., Che, J., Liu, X., et al. (1996). Partially Molten Middle Crust beneath Southern Tibet: Synthesis of Project INDEPTH Results. *Science* 274, 1684–1688. doi:10.1126/science.274.5293.1684

Ni, J., and Barazangi, M. (1984). Seismotectonics of the Himalayan Collision Zone: Geometry of the Underthrusting Indian Plate beneath the Himalaya. *J. Geophys. Res.* 89 (B2), 1147–1163. doi:10.1029/JB089iB02p01147

Ni, J. F., Guzman-Speziale, M., Bevis, M., Holt, W. E., Wallace, T. C., and Seager, W. (1989). Accretionary Tectonics of Burma and the Three Dimensional Geometry of the Burma Subduction Zone. *Geol. Soc. America* 17, 68–71. doi:10.1130/0091-7613(1989)017<0068:ATOBAT>2.3.CO;2

Oldham, R. D. (1899). Report on the Great Earthquake of 12th June 1897, Mere. *Geol. Surv. India* 29, 1–379.

Pandey, M. R., Tandukar, R. P., Avouac, J. P., Lavé, J., and Massot, J. P. (1995). Interseismic Strain Accumulation on the Himalayan Crustal Ramp (Nepal). *Geophys. Res. Lett.* 22, 751–754. doi:10.1029/94gl02971

Parvez, I. A., and Ram, A. (1997). Probabilistic Assessment of Earthquake Hazards in the North-East Indian Peninsula and Hindukush Regions. *Pure Appl. Geophys.* 149, 731–746. doi:10.1007/s000240050049

Pasyanos, M. E., and Walter, W. R. (2002). Crust and Upper-Mantle Structure of North Africa, Europe and the Middle East from Inversion of Surface Waves. *Geophys. J. Int.* 149, 463–481. doi:10.1046/j.1365-246x.2002.01663.x

Paul, H., and Mitra, S. (2017). Three-dimensional Crustal Architecture beneath the Sikkim Himalaya and its Relationship to Active Deformation. *J. Geophys. Res. Solid Earth* 122, 7860–7878. doi:10.1002/2017JB014506

GSI (2000). "Seismotectonic Atlas of India and its Environs," in *Geological Survey of India, Special Publication*. Editors P. L. Narula, S. K. Acharya, and P. Banerjee, 86.

Priestley, K., Ho, T., and Mitra, S. (2019). The Crustal Structure of the Himalaya: A Synthesis. *Geol. Soc. Lond. Spec. Publications* 483, 483–516. doi:10.1144/SP483-2018-127

Priestley, K., Jackson, J., and McKenzie, D. (2008). Lithospheric Structure and Deep Earthquakes beneath India, the Himalaya and Southern Tibet. *Geophys. J. Int.* 172, 345–362. doi:10.1111/j.1365-246x.2007.03636.x

Rao, N. P., and Kumar, M. R. (1997). Uplift and Tectonics of the Shillong Plateau, Northeast India. *J,Phys,Earth* 45, 167–176. doi:10.4294/jpe1952.45.167

Raoof, J., Mukhopadhyay, S., Koulakov, I., and Kayal, J. R. (2017). 3-D Seismic Tomography of the Lithosphere and its Geodynamic Implications beneath the Northeast India Region. *Tectonics* 36, 962–980. doi:10.1002/2016TC004375

Raoof, J., Mukhopadhyay, S., and Malik, J. N. (2018). "3-D Seismic Tomography of the Indo-Asian Collision Zone from Pamir-Hindu Kush in the West to Indo-Burma Ranges in the East: Geodynamic Implications," in AGU Fall Meeting, Washington DC, USA, Dec 10–14, 2018.

Ritzwoller, M. H., and Levshin, A. L. (1998). Eurasian Surface Wave Tomography: Group Velocities. *J. Geophys. Res.* 103 (B3), 4839–4878. doi:10.1029/97jb02622

Ritzwoller, M. H., Levshin, A. L., Ratnikova, L. I., and Egorkin, A. A. (1998). Intermediate Period Group Velocity Maps across central Asia, Western China and Parts of Middle-East. *Geophys. J. Int.* 134, 315–328.

Satyabala, S. P. (2003). Oblique Plate Convergence in the Indo-Burma (Myanmar) Subduction Region. *Pure Appl. Geophys.* 160, 1611–1650. doi:10.1007/s00024-003-2378-0

Shi, D., Wu, Z., Klemperer, S. L., Zhao, W., Xue, G., and Su, H. (2015). Receiver Function Imaging of Crustal Suture, Steep Subduction, and Mantle Wedge in the Eastern India-Tibet continental Collision Zone. *Earth Planet. Sci. Lett.* 414, 6–15. doi:10.1016/j.epsl.2014.12.055

Singer, J., Kissling, E., Diehl, T., and Hetényi, G. (2017). The Underthrusting Indian Crust and its Role in Collision Dynamics of the Eastern Himalaya in Bhutan: Insights from Receiver Function Imaging. *J. Geophys. Res. Solid Earth* 122, 1152–1178. doi:10.1002/2016JB013337

Singh, A., Bhushan, K., Singh, C., Steckler, M. S., Akhter, S. H., Seeber, L., et al. (2016). Crustal Structure and Tectonics of Bangladesh: New Constraints from Inversion of Receiver Functions. *Tectonophysics* 680, 99–112. doi:10.1016/j.tecto.2016.04.046

Singh, A., Singh, C., and Kennett, B. L. N. (2015). A Review of Crust and Upper Mantle Structure beneath the Indian Subcontinent. *Tectonophysics* 644-645, 1–21. doi:10.1016/j.tecto.2015.01.007

Sowers, T., and Boyd, O. S. (2019). *Petrologic and Mineral Physics Database for Use with the U.S. Geological Survey National Crustal Model*. Reston, VA: USGS Open File Report, 2019–1035

Steckler, M. S., Mondal, D. R., Akhter, S. H., Seeber, L., Feng, L., Gale, J., et al. (2016). Locked and Loading Megathrust Linked to Active Subduction beneath the Indo-Burman Ranges. *Nat. Geosci* 9, 615–618. doi:10.1038/ngeo2760

Strong, C. M., Attal, M., Mudd, S. M., and Sinclair, H. D. (2019). Lithological Control on the Geomorphic Evolution of the Shillong Plateau in Northeast India. *Geomorphology* 330, 133–150. doi:10.1016/j.geomorph.2019.01.016

Sun, X., Song, X., Zheng, S., Yang, Y., and Ritzwoller, M. H. (2010). Three Dimensional Shear Wave Velocity Structure of the Crust and Upper Mantle beneath China from Ambient Noise Surface Wave Tomography. *Earthq Sci.* 23, 449–463. doi:10.1007/s11589-010-0744-4

Suresh, G., Jain, S., and Bhattacharya, S. N. (2008). Lithosphere of Indus Block in the Northwest Indian Subcontinent through Genetic Algorithm Inversion of Surface-Wave Dispersion. *Bull. Seismological Soc. America* 98, 1750–1755. doi:10.1785/0120070254

Talwani, M., Desa, M. A., Ismaiel, M., and Sree Krishna, K. (2016). The Tectonic Origin of the Bay of Bengal and Bangladesh. *J. Geophys. Res. Solid Earth* 121, 4836–4851. doi:10.1002/2015JB012734

Tapponnier, P., Xu, Z. Q., Roger, F., Meyer, B., Arnaud, N., Wittlinger, G., et al. (2001). Oblique Stepwise Rise and Growth of the Tibet Plateau. *Science* 294, 1671–1677. doi:10.1126/science.105978

Thiede, R. C., Arrowsmith, J. R., Bookhagen, B., McWilliams, M., Sobel, E. R., and Strecker, M. R. (2006). Dome Formation and Extension in the Tethyan Himalaya, Leo Pargil, Northwest India. *Geol. Soc. America Bull.* 118, 635–650. doi:10.1130/b25872.1

Unsworth, M. J., Jones, A. G., Jones, A. G., Wei, W., Marquis, G., Gokarn, S. G., et al. (2005). Crustal Rheology of the Himalaya and Southern Tibet Inferred from Magnetotelluric Data. *Nature* 438, 78–81. doi:10.1038/nature0415410.1038/nature04154

Unsworth, M., Wenbo, W., Jones, A. G., Li, S., Bedrosian, P., Booker, J., et al. (2004). Crustal and Upper Mantle Structure of Northern Tibet Imaged with Magnetotelluric Data. *J. Geophys. Res.* 109, B02403. doi:10.1029/2002JB002305

Verma, R. K., and Mukhopadhyay, M. (1977). An Analysis of the Gravity Field in Northeastern India. *Tectonophysics* 42, 283–317. doi:10.1016/0040-1951(77)90171-8

Wei, W., Unsworth, M., Jones, A., Booker, J., Tan, H., Nelson, D., et al. (2001). Detection of Widespread Fluids in the Tibetan Crust by Magnetotelluric Studies. *Science* 292, 716–719. doi:10.1126/science.1010580

Yang, Y., Ritzwoller, M. H., Levshin, A. L., and Shapiro, N. M. (2007). Ambient Noise Rayleigh Wave Tomography across Europe. *Geophys. J. Int.* 168, 259–274. doi:10.1111/j.1365-246x.2006.03203.x

Yanovskaya, T. B., and Ditmar, P. G. (1990). Smoothness Criteria in Surface Wave Tomography. *Geophys. J. Int.* 102, 63–72. doi:10.1111/j.1365-246x.1990.tb00530.x

Yanovskaya, T. B., Kizima, E. S., and Antonova, L. M. (1998). Structure of the Crust in the Black Sea and Adjoining Regions from Surface Wave Data. *J. Seismology* 2, 303–316. doi:10.1023/A:1009716017960

Yanovskaya, T. B., and Kozhevnikov, V. M. (2003). 3D S-Wave Velocity Pattern in the Upper Mantle beneath the Continent of Asia from Rayleigh Wave Data. *Phys. Earth Planet. Interiors* 138, 263–278. doi:10.1016/S0031-9201(03)00154-7

Yanovskaya, T. B. (1997). Resolution Estimation in the Problems of Seismic ray Tomography. *Izvestia, Phys. Solid Earth* 33 (9), 762–765.

Yao, H., Van Der Hilst, R. D., and De Hoop, M. V. (2006). Surface-wave Array Tomography in SE Tibet from Ambient Seismic Noise and Two-Station Analysis - I. Phase Velocity Maps. *Geophys. J. Int.* 166, 732–744. doi:10.1111/j.1365-246x.2006.03028.x

Zhang, G., He, Y., Ai, Y., Jiang, M., Mon, C. T., Hou, G., et al. (2021). Indian continental Lithosphere and Related Volcanism beneath Myanmar: Constraints from Local Earthquake Tomography. *Earth Planet. Sci. Lett.* 567, 116987. doi:10.1016/j.epsl.2021.116987

Conflict of Interest: The authors declare that the research was conducted in the absence of any commercial or financial relationships that could be construed as a potential conflict of interest.

Publisher's Note: All claims expressed in this article are solely those of the authors and do not necessarily represent those of their affiliated organizations or those of the publisher, the editors, and the reviewers. Any product that may be evaluated in this article, or claim that may be made by its manufacturer, is not guaranteed or endorsed by the publisher.

Advantages of publishing in Frontiers

OPEN ACCESS
Articles are free to read for greatest visibility and readership

FAST PUBLICATION
Around 90 days from submission to decision

HIGH QUALITY PEER-REVIEW
Rigorous, collaborative, and constructive peer-review

TRANSPARENT PEER-REVIEW
Editors and reviewers acknowledged by name on published articles

Frontiers
Avenue du Tribunal-Fédéral 34
1005 Lausanne | Switzerland

Visit us: www.frontiersin.org
Contact us: frontiersin.org/about/contact

REPRODUCIBILITY OF RESEARCH
Support open data and methods to enhance research reproducibility

DIGITAL PUBLISHING
Articles designed for optimal readership across devices

FOLLOW US
@frontiersin

IMPACT METRICS
Advanced article metrics track visibility across digital media

EXTENSIVE PROMOTION
Marketing and promotion of impactful research

LOOP RESEARCH NETWORK
Our network increases your article's readership